Fraunhofer

IZFP

FRAUNHOFER-INSTITUT FÜR ZERSTÖRUNGSFREIE PRÜFVERFAHREN

Christian Boller, Hartmut Janocha (Eds.)

New Trends in Smart Technologies

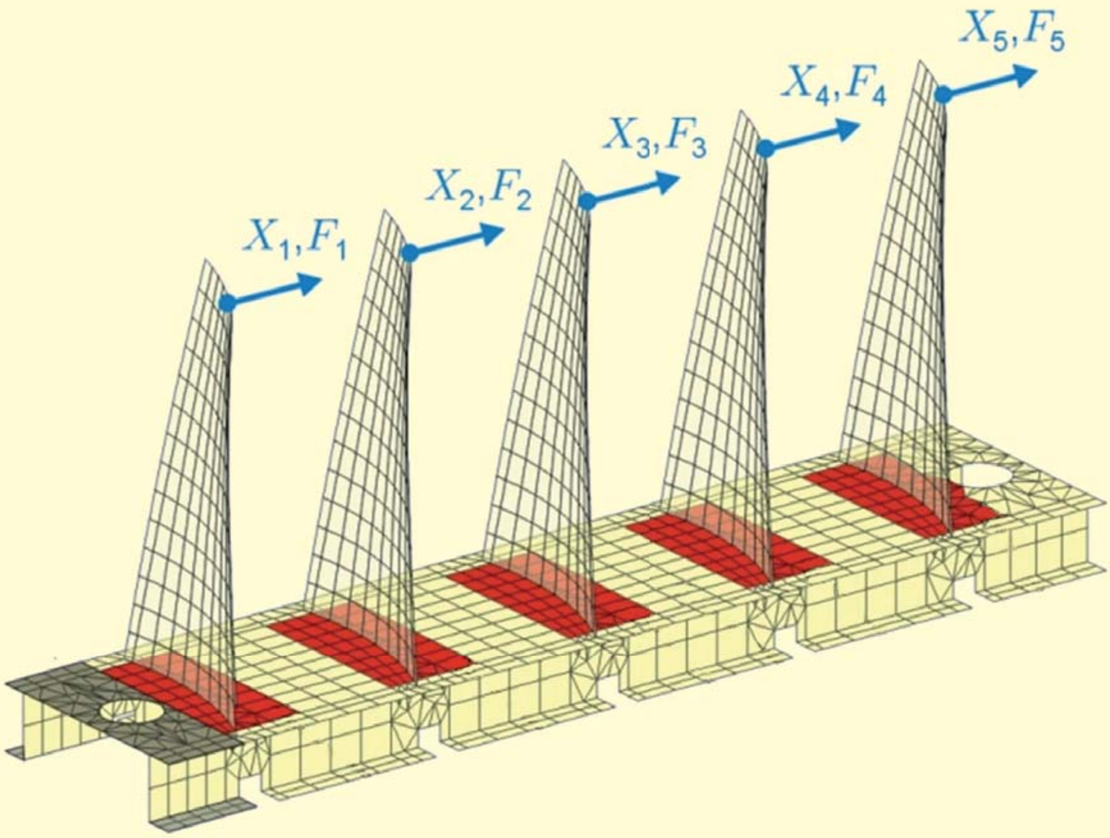

FRAUNHOFER VERLAG

UNIVERSITÄT DES SAARLANDES

Fraunhofer-Institut für
Zerstörungsfreie Prüfverfahren IZPF

Universität des Saarlandes

New Trends in Smart Technologies

Christian Boller
Hartmut Janocha (Eds.)

FRAUNHOFER VERLAG

Contact

Christian Boller, Prof. Dr.-Ing.
Chair of Testing and Quality Assurance, Saarland University and
Director of Fraunhofer Institute Nondestructive Testing IZFP
Campus E 3.1
66123 Saarbrücken/Germany
Phone +49 681 9302-3800
Fax: +49 681 9302-11-3800
E-Mail: christian.boller@izfp.fraunhofer.de
Website: www.izfp.fraunhofer.de

Members of staff:
Birgit Conrad-Markschläger, Roger Pfau

Bibliographic information published by Die Deutsche Bibliothek

Die Deutsche Bibliothek lists this publication in the Deutsche Nationalbibliografie; detailed bibliografic data is available in the Internet at <http://dnb.d-nb.de>.

Printing and Bindery:
Mediendienstleistungen des
Fraunhofer-Informationszentrum Raum und Bau IRB, Stuttgart

Printed on acid-free and chlorine-free bleached paper.

Fraunhofer Information-Centre for Regional Planning and Building Construction IRB
P.O. Box 80 04 69, D-70504 Stuttgart
Nobelstrasse 12, D-70569 Stuttgart
Phone +49 711 970-2500
Fax +49 711 970-2507
E-Mail : verlag@fraunhofer.de
URL www.verlag.fraunhofer.de

Contents

Preface

Fundamentals

Modelling

Applications

PREFACE

Adaptive, intelligent or *smart technologies, materials* and *structures,* or even expressions such as *Adaptronics* are now around within the scientific community for nearly three decades. It encompasses sensing, actuation and control capabilities to be combined from a systems approach would this happen on a macro, meso or even micro scale. S*mart technologies,* how it is considered as the summarizing term here, have generated a variety of interdisciplinary activities and fields. Starting from technology development in the early and mid-20th century technologies became increasingly specialized with the danger of loosing the view of an integrated systems approach. Many of the existing technical systems in transportation, manufacturing, processing, medicine, computation, electronics and others have made significant progress over the past centuries and decades. However a lot of concern also emerged with regard to technical governance over a society and as to where the human being and nature would find its role within the process. This concern has triggered a large amount of research in the area of *biomimetics* and *bio-inspiration* which has been an answer from biology's side to a natural and engineering science request. Structures (macro) as well as materials (micro) have been considered, drawing upon an understanding of materials and systems with sensing and actuation capabilities as well as control. This includes modelling, numerical simulation, realisation on a laboratory and finally also real application scale. The diversity of disciplines involved, comprising materials science and engineering, structural design, strength, dynamics and fatigue, control, electrical engineering, applied mathematics, signal processing, non-destructive testing, artificial intelligence and much more, makes up possibly one of the most interdisciplinary areas of engineering science history has ever seen.

Smart technologies have triggered a variety of new research areas which have gradually become subjects of their own or merged into further areas of engineering. As regards sensing structural health monitoring (SHM) is one of those topics which are increasingly discussed with respect to structural design, inspection and life cycle management. With respect to actuation and damping a lot of novel actuation principles have been established, starting from the generation of guided waves in the context of SHM, vibration dampers as a means of load alleviators and energy harvesters, or as elements of morphing structures that optimize their shape in accordance to operational conditions. What happens at the macro scale is allowed to also happen at the micro scale where micro electro-mechanical systems (MEMS) are still the major representatives. MEMS on the one side may be considered as a sensing system only but has to be considered as a smart system completely when it comes to drug delivery and other similar types such as considered within the biomedical sector. Progress in material science has provided a comprehensive and theoretical framework for implementing multi-functionality into materials, and the development of high speed digital computation has allowed that framework to be gradually transformed into methodologies to be considered for practical design and manufacturing. Actuation within a system is not possible without control. Enhancement in computation power and decentralization as well as cost has allowed control algorithms to be applied, that have not been applicable in the past. Development of products in the electronics entertainment and leisure industry is currently ongoing at such a pace, technical standard, and as a consequence of high volume production comparatively low cost, that smart technologies developed can virtually be obtained by 'cannibalizing' modern electronic toys towards a new smart system. A rewarding area where this is happening in this regard is robotics. Micro (unmanned) aerial vehicles with different sensors and morphing aerodynamic profiles have made a start with a trend of gradually applying technologies developed also to ground and possibly even under water vehicles. Such a fleet of specific small robotic vehicles being designed on a modular basis and operating even in swarms may be the automated inspection helpers in the not too far future.

The smart technologies' community nowadays meets at a variety of opportunities physically as well as intellectually. Those opportunities include R&D projects, conferences and seminars, journals and books. Many of these opportunities have been generated in a variety of locations around the globe over the past that are impossible to be mentioned here. The idea of compiling this book has been generated along the 5th ECCOMAS Thematic Conference on Smart Structures and Materials held in Saarbrücken/Germany in the summer of 2011. From the variety of papers presented at this conference a variety were considered worth to be expanded and to be compiled in a book providing recent trends with respect to the development and realization of smart technologies and which has become the result of the book presented here. The different articles provide an insight into where development in smart technologies stands today with a specific emphasis towards technology application.

This book is structured into three main sections including a) Fundamentals, b) Modeling and c) Applications. As regards the fundamentals, aspects related to different types of sensors and actuators are addressed as well as a system's reliability and risk assessment, the latter being a major issue not too much considered with regard to smart technologies so far. Within the modeling section different aspects are considered such as actuators, damage in composite materials, adaptive structures with regard to shape optimization, vibration absorption as well as probabilistic aspects within the frame of SHM. A large amount of the book is devoted to smart technologies' applications, starting from risk based inspections and looking into a variety of SHM-based applications related to metallic as well as composite materials and even addressing the topic of monitoring electric transmission lines. With a specific view on active blade damping and bridge hinge restrainers some recent developments with the actuation side are discussed as well as some recent developments in flow control including the aspect of morphing structures in micro aerial vehicles.

All of those smart technologies' solutions can have some inspiring impacts on next generation nondestructive technologies' development either from the sensing and sensor signal processing side with respect to SHM as well as from the robotics side with regard to inspection vehicles. Further impacts have to be seen in the wide field of engineering, materials technology and science and even medicine. All of those potential impacts have been a motivation to get this book edited. Therefore hoping this book to become another source of inspiration in engineering through smart technologies the editors want to thank Fraunhofer Gesellschaft for supporting this book to be published within the frame of Fraunhofer Publications not only in a printed but also as an open access electronic publication, which can be found under http://publica.fraunhofer.de/starweb/pub09/index.htm. Furthermore the editors want to thank all contributing authors for their willingness and effort to submit partially well extended articles that have gone through a peer reviewing process and the respective quality assurance process. Without their effort and support together with a variety of other editorial helpers this book would not have been possible.

Christian Boller & Hartmut Janocha

Saarbrücken/Germany, June 2013

Fundamentals

PREDICTIVE MODELING OF SMART STRUCTURES WITH IN-SITU SENSING CAPABILITY

Victor Giurgiutiu*
University of South Carolina, Columbia, South Carolina, USA,
*Corresponding author. E-mail: victorg@sc.edu

ABSTRACT

A methodology for the predictive modeling of smart structures with in-situ sensing capability is presented and discussed. First, the smart structures concept is briefly reviewed. Then, self-sensing smart structures with in-situ sensing capabilities are introduced. Focus is placed on active sensing methods using ultrasonic guided waves in thin-wall structures. The challenges of modeling ultrasonic wave propagation in realistic structures and the mesh-size and time-step convergence requirements are discussed. The recently developed hybrid models for modeling ultrasonic nondestructive evaluation using bulk waves are presented and their advantages are discussed as well. A new approach, the generic hybrid global-local (HGL) approach is presented. It builds upon previous work in hybrid methods and extends them to guided waves in thin-wall structures equipped with piezoelectric wafer active sensors (PWAS) capable of both transmission and reception of ultrasonic guided waves. The features of this proposed HGL approach, which is still under development, are discussed.

SMART STRUCTURES

The concept of smart structures (a.k.a., adaptive structures or intelligent structures) is usually derived through analogy with living organisms which can *sense* the environment, *interpret* the information sensed from the environment, and *react* to it appropriately. For example, sensors in my skin would sense the pricking of a rose's thorns and send the information to my nervous system which will interpret it and instruct my hand to let go and retreat. In order to achieve these functions, the living organisms possess sensing, data processing, and actuation capabilities embedded into their complex bodies. Similarly, a bio-inspired smart structure would be equipped with sensing, data processing, and actuation capabilities. A smart structure is a *multifunctional system* with capabilities well beyond the mundane load-bearing mission of conventional structures (Figure 1). Enabling technologies are active materials, integrated active sensors, fiber optics sensors, fiber optics communication, solid-state actuators, autonomous power and energy harvesting, multifunctional composites, self-healing materials, integrated electronics, reasoners, and microcontrollers, etc.

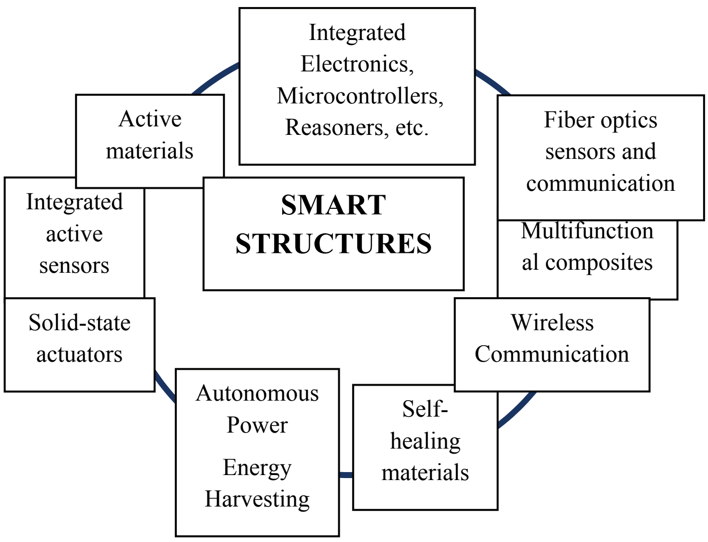

Figure 1: The smart structures constellation: functional attributes and technology enablers.

Smart-structure concepts have been developed for many engineering fields. A *smart building* or *bridge* would feel an earthquake and 'brace' itself to sustain it better; afterwards, it would quickly inspect itself to assess and control damage, if any. A *smart aircraft* would feel the effect of flight loads, operational environment, or enemy fire on its load bearing capability and would take corrective actions to arrive safely at destination. A *smart space antenna* would adapt its shape to maintain its focusing accuracy under uneven solar heating and micrometeorite impacts. A buried *smart pipeline* would monitor its state of corrosion, detect leaks, report its state of structural health, and even attempt self-repair. A *smart automobile* structure would adapt its suspension impedance according to the road type, i.e., make it stiffer for high-speed travelling on high way, while making it more complying for cross-country excursions. A *smart machine tool* will adapt the tool holder, pressure, feed, and impedance to optimize the machining process by increasing material removal rate while reducing chatter and vibration and minimizing energy usage. Recent advances in smart structures research and implementation can be traced along three major directions: (i) morphing structures; (ii) self-bracing structures; (iii) self-monitoring structures.

SELF-MONITORING SMART STRUCTURES

Self-monitoring smart structures are equipped with structural health monitoring (SHM) sensors and advanced data processing algorithms capable of structural diagnosis and prognosis. The goal of SHM is to develop a monitoring methodology that is capable of detecting and identifying various damage types during the service life of the structure, monitor their evolution, and predict the remaining useful life with a continuously updating structural model. SHM can be broadly classified into two categories: (a) passive and (b) active. **Passive SHM** (such as acoustic emission, impact detection, strain measurement, etc.) are relatively more mature; however, their utility is limited by the need for continuous monitoring and the indirect way in which damage existence is inferred. **Active SHM** aims at directly interrogating the structure on demand using guided wave ultrasonics and other methods. Active SHM resembles conventional nondestructive testing/evaluation only that the sensors are permanently attached to the structure and interrogated automatically without human intervention. Historical SHM data would allow projection of damage progression trends and estimation of remaining useful life. In critical situations, on board processing of SHM data would allow adaptive mission planning to ensure safe return to base. Smart structures with in-situ sensing capabilities are likely to increase their presence in aerospace because they can offer tangible evidence of the structural performance and state of health [1]. The benefits of monitoring the structural state include design feedback, performance enhancement, on-demand condition-based maintenance, and predictive fleet-level prognosis.

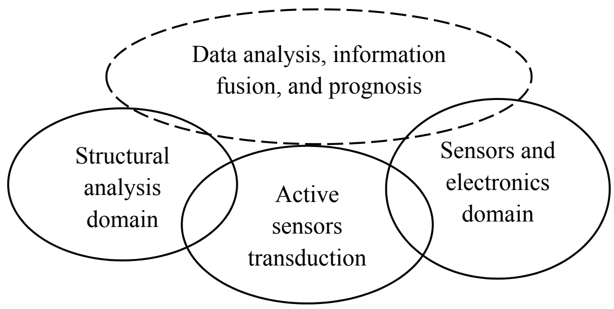

Figure 2: Venn diagram of the multi-domain interaction in a self-monitoring smart structure

On-board structural sensing systems have been envisioned for determining the health of a structure by monitoring a set of sensors over time, assessing the remaining useful life from the recorded data and design information, and advising of the need for structural maintenance actions. Figure 2 shows the Venn diagram of the interrelations inherent in a predictive methodology which will combine the structural analysis domain with the active sensors transduction domain and the sensors and electronics domain. The software domain of data analysis, information fusion, and prognosis is weakly bonded to this predictive methodology concept because it will utilize its signal products, process them, and then feed them back into the process to achieve structural prognosis that will forecast the future behavior of the structure. Figure 3 shows a possible implementation of an SHM system on board an unmanned aerial vehicle (UAV). Some active sensors are distributed in clusters around the structure targeting the „hot spot“ areas where structural problems are expected to happen, whereas wide-sensing active sensors will be evenly distributed around the structure to detect unexpected structural damage occurrences.

The sensor signals are fed into data concentrators that perform local processing of received data and distill pertinent critical information that is sent to the on-board processing unit for further data condensation and reasoning. If a critical situation is identified, then immediate remedial action is taken and the base-station is alerted for further instructions that may mean a change in flight plan, mission objectives, or even return to base.

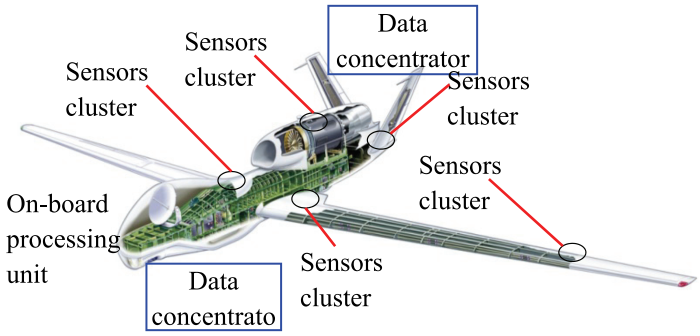

Figure 3: Possible implementation of a structural health monitoring (SHM) system on board an unmanned aerial vehicle (UAV).

Essential to the whole process is the availability of proper structural modeling methodologies and software, as discussed in the next section.

MODELING OF ULTRASONIC WAVE PROPAGTION

Finite element modeling of ultrasonic wave propagation in realistic structures is challenging because a very fine mesh is required in both time and space discretization to achieve a reasonable representation of the high frequency ultrasonic guided waves used in this process.

Analytical methods such as ray-tracing [2], beam/pencil [3], Green functions [4] can efficiently model wave propagation in simple geometries. Geometric theory of diffraction based on ray tracing was recently extended to efficiently calculate multiple echoes and scatter [5] but it cannot handle complicated defects or structures with complex geometries. Green functions give the displacement field at any point in a uniform elastic medium illuminated by ultrasonic waves using an integral formulation. Analytical Green functions exist for both bulk waves [4] and guided waves [6]; Green’s functions can be also determined experimentally [7]. However, scattering of ultrasonic waves from a complex-shaped defect cannot be achieved directly by analytical methods and needs the use of a numerical discretization approach such as finite differences, finite elements, boundary elements, etc.. Commercially available finite element (FE) codes (e.g., ABAQUS-CATIA, NASTRAN, ANSYS, COMSOL, PZFlex, etc.) are capable of capturing the structural details and offer convenient built in resources for automated meshing, frequency analysis, and explicit time integration of dynamic events. Even a relatively rough FE model would yield a ‘wave propagation’ output that is illustrative and instructive. However, to obtain accurate wave propagation solution at ultrasonic frequencies is computationally intensive and may become prohibitive for realistic structures [8,9]. Aldrin et al. [10] performed FEM studies of the scattering of guided waves from a multi-layer fastener site with cracks emanating from the hole and showed that the presence of a fastener insert can significantly change the scattering pattern if the insert is in full contact with the hole (i.e., stiff interface). However, they showed that considerable computational resources are needed to perform a full FEM simulation of this process, and proposed the use of analytical tools [11] that are much faster and more efficient.

CONVERGENCE OF FEM WAVE PROPAGATION MODELS

A recent systematic study of FEM convergence [12] has concluded that 25-30 nodes per wavelength, 5-10 nodes per thickness, and 15-20 steps per period would be required to obtain reasonable convergence in ABAQUS explicit code (Figure 4). Good-quality FE analysis can easily run into hundreds of millions of degrees of freedom and millions of time steps in order to satisfy the convergence and accuracy requirements (e.g., the analysis of a 1 m by 1 m specimen at 2 MHz would require at least 500 million degrees of freedom, and would run for many hours). It is apparent that brute-force FE analysis of ultrasonic damage detection is not appropriate for predictive simulation of structural sensing. When parameter studies, variability explorations, and sensor design options must be analyzed, a brute-force ultrasonic FE analysis would simply not do. Improved approaches to the FE method have been studied to increase efficiency while maintaining accuracy during ultrasonic simulation. Boundary element method [13] reduces mesh requirements by restricting the discretization to only the boundary of the domain under investigation, while the bulk of the domain is represented by analytical Green functions. When a crack is present, then the crack boundary should be also discretized since it is a part of the domain boundary. Roberts [14] used the boundary element method and the appropriate Green functions to model the propagation of ultrasonic plate waves across stiffeners integrally built into the plate. Spectral element method [15] overcomes the limitations of time domain integration by performing the analysis in the frequency domain; although increasingly popular [16,17], spectral elements have not been yet adopted in the commercial FEM packages. Another way to reduce the FE computational needs would be to have coarser meshes in the 'clean' parts of the structure and finer meshes around the structural features and the damage regions. However, it has been found that the variation in acoustic impedance in the transition zones between coarse and fine meshes results in a large amount of coherent noise [12]. Studies to adjust the material properties such as to facilitate a gradual variation of acoustic impedance have not been successful in the 2-D wave-propagation domain [18,19].

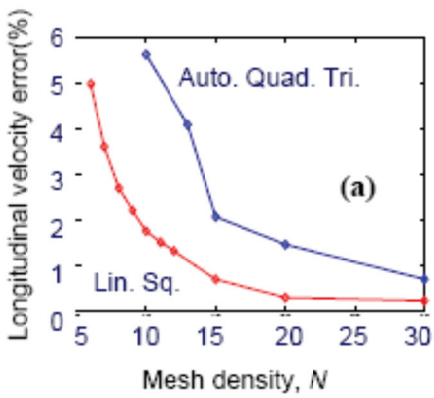

Figure 4: FEM convergence study [12]; *N* indicates the number of nodes per wavelength.

HYBRID MODELING METHODS FOR ULTRASONIC WAVE PROPAGATION

Several investigators have recently proposed to combine the efficiency of analytical methods with flexibility of discrete methods. Researchers at the French Commissariat for Atomic Energy [20] have developed the CIVA computational framework, which combines the *Champ-Sons* semi-analytical wave propagation model in the clean global region with the *Athena* FEM in the local region containing a defect. The general concept of this approach is shown in Figure 5a. Researchers at the Japanese Central Research Institute of Electric Power Industry [21] have developed a hybrid approach combining numerical FEM and analytical ray tracing method (Figure 5b). In these hybrid analyses, the FE mesh was usually confined to a small box region around the crack. The coupling conditions between the analytical region and the FE region were identified as a major challenge. Auld's reciprocity theorem [22] is used to couple two analysis states, one which is focused on global wave propagation, and another which deals with the interaction with the defect. In order to minimize the spurious diffractions at the global-local interface, Lin et al. [21] used a two-step transition layer with variable viscosity (FD in Figure 5b). The hybrid-method results were compared with conventional FE analysis. It was found that the signals predicted by the two methods were similar, while the number of elements used by the hybrid method was only 1/3rd of those used by the conventional FE, whereas the computational time was 1/10th. These hybrid approaches have been used to simulate the ultrasonic NDE process of detecting cracks in solid components using bulk waves and conventional NDE transducers. Validation and verification studies have yielded good agreement with full-power finite element analyses and with experiments [23-25].

The hybrid methods [20,21] could not be directly applicable to thin-wall structures because they were developed for solid parts interrogated with bulk ultrasonic waves, as appropriate for nuclear energy applications, whereas aerospace structures have a thin-wall construction and require guided waves for wide-area SHM applications. At present, only a few attempts have been made to develop the hybrid approach to the modeling of ultrasonic guided waves damage detection in thin-wall structures. In pioneering work, Mal et al. [26,27] extended the hybrid method to the study the interaction of guided waves with damage in thin plates. Notches and thickness removal (simulated corrosion) were analyzed with straight-crested 1-D models. For cracks emanating from rivet holes, a 2-D model employing circular crested guided waves and Bessel function was used. The damaged region was modeled with an FEM mesh that extended six times the plate thickness from the center of the hole. No systematic error analysis and convergence studies were reported. The model was validated with experiments and the comparison was quite good. More recently, Lanza di Scalea and his group at UCSD have used the HGL approach for the calculation of wave scatter from defects in 1D waveguides [28,29]. The effect of notches and corrosion in metallic rails, and delamination in composite stiffeners and spars were studied.

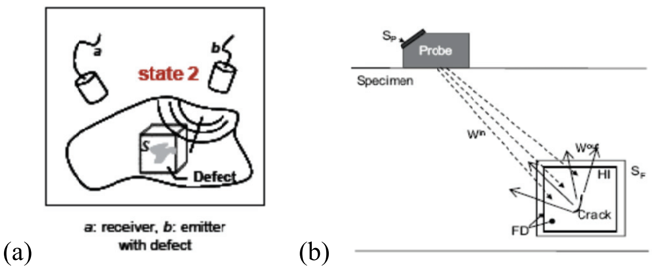

Figure 5: The hybrid method applied to the modeling of UT testing of a crack in a massive component: (a) French approach [20]; (b) Japanese approach [21].

PROPOSED HYBRID GLOBAL-LOCAL (HGL) APPROACH

We propose to build upon early pioneering work [11,20,21,26,27] and develop a **generalized hybrid global-local (HGL)** approach that will allow computationally-efficient multi-scale multi-domain modeling of structural sensing. The HGL approach will use **local FEM discretization** only in the critical regions (structural joints, discontinuities, flaws, damage, etc.) while using **global analytical solutions** (e.g., Green's functions) in the uniform outside region. The efficiency of the method resides in the fact that only local regions of interest will be meshed and solved with the FEM technique, whereas the uniform outside field will be solved analytically. Continuity and equilibrium conditions between the inner solution (FEM) and the outer solution (analytical) are imposed on the mesh boundary. We intend to develop the HGL method for multimode guided waves under full 2-D conditions as appropriate to aerospace thin-wall structures (Figure 6a). The waves originating from a transmitter PWAS propagate in circular wave fronts towards the local region containing the damage under investigation. The incoming waves enter the local region through the global-local (HG) boundary and interact with the damage generating a complicated scattering pattern. The scattered waves exit the local region through the GL boundary and are picked up by the receiver PWAS (as well as by the transmitter PWAS acting in pulse-echo mode).

It is expected that a major part of our effort will be concentrated on developing the **proper interfacing formulation** for the fully 2-D analytical solution of guided wave propagation in circular-radial geometry in interaction with a generically shaped FEM local region. The coupling of the local and global regions will be done by generic matching of the ultrasonic field (complex velocities and tractions) on both sides of the domain boundary (Figure 6b). The incident field is calculated analytically and then injected into the FEM boundary. The FEM response is calculated for two states ('pristine' and 'damage') and then ejected through the FEM boundary into the global domain to travel to the receiver sensor. We are aware that the coupling between the analytical and FEM regions plays an essential role in the solution accuracy. For example, the size of the FEM region must be selected sufficiently large to allow the entire incident ultrasonic field to enter before wave diffraction from the damage reaches the FEM region boundary. We would study carefully these aspects and apply algorithmic optimization to achieve best computational performance and meet convergence and accuracy criteria.

FEATURES OF THE PROPOSED GENERIC HGL MODEL

Building upon early pioneering work [11,20,21,26,27] we will incorporate features in the HGL approach to make generic and applicable to a variety of structural sensing situations.

The **FE meshing** will be generic, whereas previous investigation used mostly rectangular mesh and regular boundaries. Unlike previous work that used FEM boxes, the **shape of the local region** will be **generic**, i.e., a reproduction of the shape of interest but scaled up to match Saint Venant's principle (5 to 10 length scales). **Generic local regions** can be constructed not only around structural damage but also around the transducers and the salient structural features to capture special effects (e.g., nonlinear behavior). Reduced-order **nonlinear models** will be included in the local region.

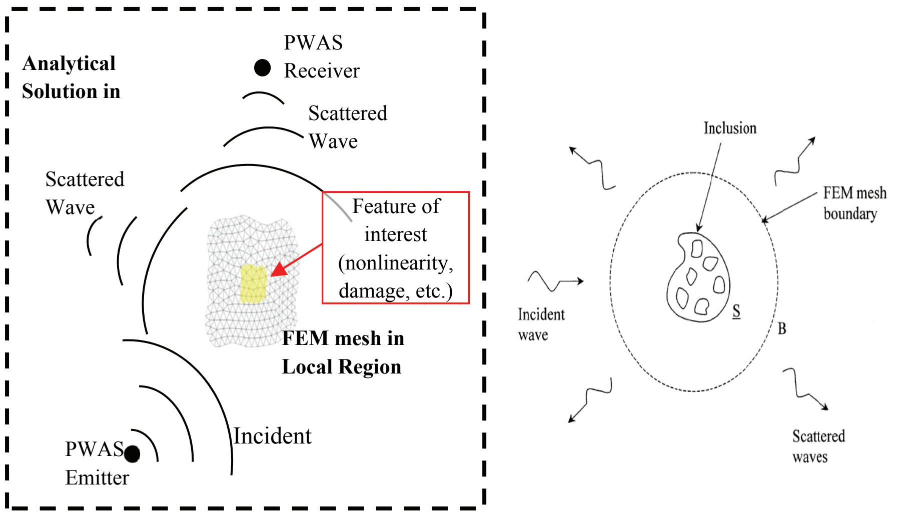

(a) (b)

Figure 6: Generalized setup of the hybrid global-local (HGL) method modeling of structural sensing: (a) overall model including PWAS transmitters and receivers; (b) Saint Venant's principle is used to define the local region (after Mal & Chang [27]).

Multi-domain analysis will be used to capture the conversion/transduction between electrical, mechanical, and ultrasonic domains. In preliminary work, we have experimented with ANSYS and ABAQUS multi-physics capabilities and obtained acceptable results. We were able to simulate both pitch-catch/pulse-echo wave propagation as well as E/M impedance standing waves using direct excitation of the piezoelectric wafer bonded to the structure using meshing of the entire problem, which required extensive computational resources. In the proposed work, we will **contain meshing to only the areas of interest, while maintaining the multi-physics capabilities**.

STRUCTURES AND MATERIALS CONSIDERED IN THE HGL SIMULATION

Unlike the previous work [11,20,21,26,27] our approach will be sufficiently generic to be easily generalized to various structural and material types (metallic, ceramic, composites, hybrids, etc.). It will be also open for generalization to other sensing principles besides piezoelectric ultrasonics. Once the HGL method is in place, we will be able to simulate different damage types that may occur in metallic and composite structures such as loose bolts in joints; disbonds in adhesive joints; degradation and delamination in composite material; corrosion in metallic materials; impact damage in composite material (cracks, delamination and fiber breakage); cracks in metallic components, etc. Analysis of integral rib stiffeners will periodic layout would be easily incorporated. The actual case studies to be considered will be selected through consultation with potential users.

CONVERGENCE AND ACCURACY CONTROL

If damage is not present inside the FEM region, then no wave scatter should take place. However, it is quite possible that numerical artifacts associated with the FEM discretization in the local region and with the GL interface would generate scatter even in a damage-free situation. The existence of such false-scatter artifacts will be an indication of deficient numerical modeling that needs to be corrected. Therefore, a possible figure of merit of the HGL modeling will be the relative smallness of the residual wave scattering in the case of a damage-free local region.

Another possible figure of merit of our modeling would be the energy balance between incoming and outgoing wave fronts. During our preliminary studies, we have identified convergence differences between the ABAQUS and ANSYS codes when analyzing the same geometric discretization with the same element type. Therefore, investigation of FEM convergence and development of convergence guidelines for multi-physics FEM simulation and HGL approach will play a major role in our investigation.

CONCLUSIONS

This paper has presented a proposed predictive methodology for multi-scale multi-domain modeling of smart structures with in-situ sensing capability. Such methodology would be able to predict the signal response of the structural sensors as a function of the structural state and/or the presence of structural flaws or damage, in linear and nonlinear regimes. The modeling is multi-scale because it has to incorporate (a) the macro-scale structural features; (b) the micro-scale flaw/damage; (c) the mezo-scale interfaces between structural parts and between sensor and structure. The modeling is multi-domain because the analysis is integrated over several physical domains, i.e., (a) structural mechanics; (b) electromechanical transduction in the sensors; (c) guided waves ultrasonics; (d) power and signal electronics, etc.

To achieve this proposed methodology for predictive modeling of smart structures with in-situ sensing capability, we are proposing a hybrid global-local (HGL) approach which achieves the integration of an analytically described ultrasonic field in the global region with a numerical discretized response in a local region around a structural feature, a damage site, sensor attachment, or other local region of interest. Multi-physics elements are used to model with the piezoelectric transduction in the sensors and actuators. The focus is on the study of guided wave propagation in thin-wall structures and their interaction with the structural damage/defects. The outcome of this endeavor will go beyond the state of the art with the following attributes: (a) 2-D thin-wall structure global domain; (b) guided waves; (c) local-global boundary of generic shape based on Saint-Venant's principle; (d) generalized matching condition on the global-local boundary; (e) zoom-in/zoom-out capabilities. At present this HGL methodology is under development and actual results will make the object of future presentations.

REFERENCES

[1] White, E. V., 2009. Structural Health Management: System Integration Challenges and Implications. *ASME 2009 Conference on Smart Materials, Adaptive Structures, and Intelligent Systems (SMASIS 2009),* Oxnard, CA, 21-23 Sept., 2009.

[2] Achenbach, J. D., Gautesen, A. K. and McMaken, H., 1982. *Ray Methods for Waves in Elastic Solids*. Pitman Books Ltd., London, UK.

[3] Gengembre, N., 2003. Pencil Method for Ultrasonic Beam Computation,. *Proceedings of 5th World Congress on Ultrasonics*, Paris, France, pp. 1533-536.

[4] Achenbach, J. D., 1973. *Wave Propagation in Elastic Solids*, Elsevier, Amsterdam.

[5] Fukutomi, H., Lin, S., Ogata, T., Yamada, H. and Ogata, T., 2009. Prediction of Received Signals in Ultrasonic Testing by Finite Element Method Combined with Geometrical Optics Theory. *CP1096 Review of Quantitative Nondestructive Evaluation*, D. O. Thompson and D. E. Chimenti (Eds.), AIP, 28, pp. 49-56.

[6] Achenbach, J. D. and Xu, Y., 1999. Wave Motion in an Isotropic Elastic Layer Generated by a Time-Harmonic Point Load of Arbitrary Direction. *Journal of the Acoustical Society of America* 106(1), pp. 83-90.

[7] Etaix, N., Fink, M., Ing, R-K. and Leblanc, A., 2010. Thickness and Phase Velocity Measurements Using the Green's Function Comparison Method. *IEEE Transactions on Ultrasonics*, Ferroelectrics, and Frequency Control, 57(8), pp. 1804-812.

[8] Cawley, P., Drozdz, M., Habgood, N., Lowe, M. S. and Russell, J., 2008. Finite Element Modeling of Elastic Wave Propagation and Defect Interaction in Large Complex Components. *CP975 Review of Quantitative Nondestructive Evaluation*, D. O. Thompson and D. E. Chimenti (Eds.), AIP, 27, pp. 99-106.

[9] Arritt, B., Brown, J., Doyle, D. and Reynolds, W., 2010. Wave Propagation in Rib-Stiffened Structures: Modeling and Experiments. *ASME 2010 Conference on Smart Materials, Adaptive Structure, and Intelligent Systems*, #SMASIS2010-3773.

[10] Aldrin, J. C., Chellapilla, S. S., Jata, K. V., Lindgren, E. A. and Medina, E. A., 2009. Analytical Model of the Scattering of Guided Waves from Fastener Sites with a Stiffness Interface. *CP1096 Review of Quantitative Nondestructive Evaluation*, D. O. Thompson and D. E. Chimenti (Eds.), AIP 2004 28, pp. 145-52.

[11] Aldrin, J. C., 2001. Models and Classification Procedures for Ultrasonic Inspection of Holes for Fatigue Cracks. *PhD Dissertation*, Northwestern University.

[12] Drozdz, M., Lowe, M. S. and Rajagopal, P., 2009. Towards Improved Finite Element Modeling of the Interaction of Elastic Waves with Complex Defect Geometries. *CP1096 Review of Quantitative Nondestructive Evaluation*, D. O. Thompson and D. E. Chimenti (Eds.), AIP, 28, pp. 49-56.

[13] Liu, Y., 2009. *Fast Multipole Boundary Element Method*, Cambridge Univ. Press.

[14] Roberts, R. A., 2007. Plate Wave Transmission/Reflection at Integral Stiffeners. *CP894 Review of Quantitative Nondestructive Evaluation*, D. O. Thompson and D. E. Chimenti (Eds.), AIP, 26, pp. 95-102.

[15] Doyle, J. S., 1997. *Wave Propagation in Structures: Spectral Analysis Using Fast Discrete Fourier Transforms*. Springer-Verlag, New York Inc.

[16] Chakraborty, A. Gopalakrishnan, S. Mahapatra, R. D. 2008. Spectral Finite Element Method. Springer-Verlag London Ltd.

[17] Lee, U., 2008. *Spectral Finite Element in Structural Dynamics*, Wiley, UK.

[18] Craster, R. V., Drozdz, M., Lowe, M. S. and Skelton, E., 2007. Modeling Bulk and Guided Waves in Bounded Media Using Absorbing Layers in Commercial Finite Element Packages. *CP894 Review of Quantitative Nondestructive Evaluation*, D. O. D. E. Chimenti and Thompson (Eds.), AIP, 26, pp. 87-94.

[19] Drozdz, M., 2008. Modeling Complex Defects Using Commercial Finite Element Packages. *PhD Dissertation*, Mechanical Engineering Dept., Imperial College, University of London.

[20] Fouquet, T., Gengembre, N., Lhemery, A., Omote, R. and Schumm, A., 2004. A Semi-Analytical-FEM Hybrid Model for Simulating UT Configurations Involving Complicated Interactions of Waves with Defects. *CP700 Review of Quantitative Nondestructive Evaluation*, D. O. Thompson and D. E. Chimenti (Eds.), AIP, 23, pp. 74-80.

[21] Fukotomi, H., Lin, S., Ogata, T. and Yamada, H., 2009. Prediction of B Scope Images for Ultrasonic Testing by Geometrical Theory of Diffraction. *CP1096 Review of Quantitative Nondestructive Evaluation*, D. O. Thompson and D. E.

[22] Auld, B.A. 1979. General Electromechanical Reciprocity Relations Applied to the Calculation of Elastic Wave Scattering Coefficients. Wave Motion 1(1), pp. 3-10.

[23] Cattiaux, G., De Roumilly, L., Lonne, S., Mahaut, S. and Lonne, S., 2006. Validation of CIVA Simulation Tools for Ultrasonic Inspection in Realistic Configuration. *ECNDT September 25-29*, 2006, Berlin, Germany, p. We.1.4.4 [online] Available at: http://www.ndt.net/article/ecndt2006/topic~31.htm

[24] Cattiaux, G., De Roumilly, L., LeBer, L., Lonne, S., and Mauhaut, S., 2006. Experimental Validation of CIVA Ultrasonic Simulation. *5th International Conference on NDE in Nuclear Industry*, San Diego, CA, USA, May 10-12.

[25] Leymarie, N., Lonne, S., Mauhaut, S,. Raillon, R. and Spies, M., 2009. *Results of the 2008 UT Modeling Benchmark Obtained with Two Semi-Analytical Models: Responses of Flat Bottom Holes at Various Depths under Interfaces of Different Curvatures.* [online] Available at: http://extende.com/wp-content/uploads/2010/02/QNDE2008_Benchmark_US.pdf

[26] Chang, Z. and Mal, A. K., 1999. Scattering of Lamb wave from a rivet hole with edge cracks. *Mechanics of Materials*, 31, pp. 197-204.

[27] Chang, Z. and Mal, A. K., 2000. A semi-numerical method for elastic wave scattering calculations. *Geophysical Journal International*, 143, pp. 328-34.

[28] Bartoli, F. L., Di Scalea, F. L., Sabra, K., Srivastava, A., 2007. Global-Local Ultrasonic Method Applied to the Quantitative Detection of Defects in Aircraft Panels. *6th International Workshop on Structural Health Monitoring*, Sep. 11-13, 2007, Stanford Univ., CA, pp. 1604-611.

[29] Srivastava, A., 2009. Quantitative Structural Health Monitoring Using Ultrasonic Guided Waves. *PhD Dissertation in Structural Engineering*, University of California, San Diego.

SMART ULTRASONIC THIN FILM BASED SENSORS SYSTEMS - INVESTIGATIONS ON ALUMINIUM NITRIDE FOR THE EXCITATION OF HIGH FREQUENCY ULTRASOUND

T. Herzog, S. Walter & H. Heuer

Fraunhofer Institute for Non-Destructive Testing, IZFP Dresden Branch, Maria Reiche Str. 2, 01109 Dresden/Germany

ABSTRACT

Many new materials and processes require non-destructive evaluation methods with high resolutions. Acoustic microscopes in a frequency range up to 250 MHz are frequently used because of their versatility, but need high inspection times due to the necessary mechanical scanning of the sensor. The efficiency of conventional acoustic microscopes can be enhanced by a combination with phased array ultrasonic techniques. With the phased array technique, the use of segmented transducers (i.e. into pixels divided sensors), it is possible to control the shape and the sound beam direction by a phase delayed excitation of the single elements and therefore evaluate specific volumes of the specimen without the need of mechanical scanning. The use of two-dimensional sensor arrays allows a three-dimensional steering of the ultrasound beam, which is beneficial due to the enormous reduction of the manipulation efforts.

Aluminium nitride is a promising material for the use as a piezoelectric sensor material in the considered frequency range and contains the potential for high frequency phased array application in the future. This work represents the fundamental development of piezoelectric aluminium nitride films with a thickness of up to 20 µm. Fraunhofer IZFP has investigated and optimized the deposition process of the aluminium nitride thin film layers regarding their piezoelectric behaviour. Therefore a specific test setup and a measuring station to determine the piezoelectric charge constant (d_{33}) and the electro acoustic behaviour of the sensor has been created. Large single element transducers were deposited on silicon substrates with aluminium electrodes, using different parameters for the magnetron sputter process, like pressure and bias voltage. Acoustical measurements up to 500 MHz in pulse echo mode were carried out and the electrical and electromechanical properties qualified. As a result, it was found out, that there are two parameter sets for the sputtering process to obtain an excellent piezoelectric charge constant of about 7.2 pC/N as a maximum.

INTRODUCTION

Ultrasonic microscopes are frequently used for the non-destructive evaluation of micro-technical components and structures, the reason being their versatility and efficiency. The frequency of an ultrasonic test system defines the attainable resolution and the penetration depth into a material. The higher the frequency the better the resolution is and the smaller the penetration depth becomes. The efficiency of conventional microscopes can be enhanced by a combination with high frequency phased array (PA) techniques. With the use of segmented transducers (i.e. sensors divided into pixels), it is possible to evaluate the complete volume of specimens in 3 dimensions. The advantage is that the ultrasonic transducer does not need to be manipulated mechanically by a scanner. The shape and the sound beam direction can be controlled on a large scale since each of the array elements can be pulsed with appropriate time delays. At present PA ultrasonic sensors with operating frequencies up to 20 MHz are available, but frequencies above 50 MHz are necessary for the applications that require a high resolution. Therefore development of new high frequency PA sensors has been required. A promising alternative piezoelectric material is aluminum nitride (AlN). Aluminum nitride is a piezoelectric but not ferroelectric material with a Wurtzite crystal structure. Compared to the widely used ferroelectric materials like PZT, AlN can not be electrically poled. Therefore piezoelectric activity can only be achieved with single crystals or with a polycrystalline structure with a strong crystal orientation.

To achieve a vibration of the sensor in thickness direction, a crystalline orientation in (001) direction is necessary (c-axis of the AlN crystalline structure being oriented perpendicular to the substrate surface). AlN in this condition exhibits several attractive properties that were verified in various publications (e.g. [1]) and in our own experimental work:

- Piezoelectric coupling coefficient of 20 %
- Piezoelectric constant d_{33} of about 8 pm/V
- Piezoelectric constant g_{33} of about 100 mVm/N
- High sound velocity for longitudinal waves 10700 m/s

- High dielectric strength of up to 20 MV/cm
- Low dielectric constant of 8.6
- High electrical resistivity of more than 10^{11} Ωcm
- High temperature stability (up to 1000°C)

Additionally the AlN thin film technology is compatible to CMOS technology and therefore interesting in MEMS (Microelectromechnical Systems) and MOEMS (Microoptomechanical Systems) fabrication. Recent publications show, that for these applications very thin films (below 1 µm, e.g. [2] were deposited with deposition rates between 5 nm/min [3] and 100 nm/min [4]. But until now AlN is seldom used for ultrasonic transducers. Only a few groups are working on single element ultrasonic transducers for low frequencies based on membrane vibration [5] or based on thickness vibration to reach a high resonance frequency of 100 MHz [6]. Further investigation on the behaviour of thin film AlN piezoelectric sensors and design consideration need to be performed.

Test Setup and Measurement Methods

A simple layout was used for optimization of deposition process in previous investigations [7,8]. Here additionally sensor investigations were carried out for high temperature storage and design considerations performed for different substrate materials with the same test layout. An electrode structure with 10 mm diameter was deposited on an isolated silicon wafer. An aluminium nitride film in a circle structure with a diameter of 13 mm was deposited, followed by a second aluminium electrode to fabricate the sensor and the interconnection pad on the top side as shown in Figure 1. The aluminum electrodes all have a thickness of 150 nm. These deposition processes were carried out at Fraunhofer Institute for Electron Beam and Plasma Technology - FEP in Dresden.

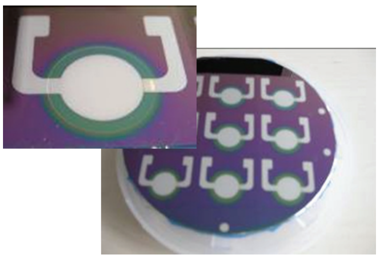

Figure 1: Ultrasonic sensors on silicon wafer.

Additionally design considerations were carried out with different electrode sizes. The layer thicknesses and sequence are same as we used in the first experiments. Only the layout was changed as can be seen in Figure 2. The bottom electrode is a square shaped aluminum electrode with a large ground area around for a better electromagnetic shielding. On top of the bottom electrode a square shaped AlN layer with a thickness of 10 µm and an edge length of 5 mm follows. The top electrode is also square shaped with the same edge length as the bottom electrode and a short track for the connection of the measurement tips. Sensors with edge lengths of 5 mm, 1 mm, 0.5 mm and 0.3 mm were manufactured with the optimized sputtering parameter sets on a 6” silicon wafer. The bottom electrode for the smallest electrode size of 0.3 mm was 0.5 mm to reduce effects caused by a misalignment of the masks.

The optimized unipolar and bipolar deposition parameters were used for the deposition of 6” isolated silicon wafers with 17 pieces of the same geometry on each substrate.

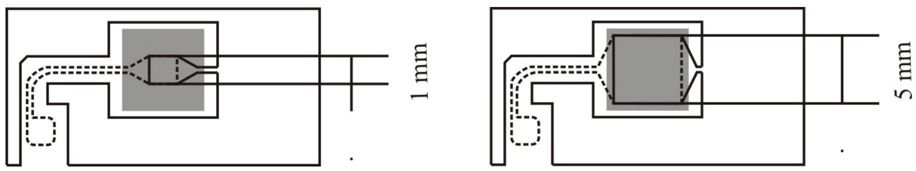

Figure 2: Layout for electrode size variation experiments with coaxial bottom electrode (full line), AlN layer (grey) and top electrode (dashed line), exemplarily for 1 mm² (left) and 25 mm² (right).

Pulse Echo Measurements

The sensor tests were performed with the pulse echo measurements too [7]. The AlN sensor served as an acoustic transmitter and receiver. The pulser and receiver DPR 500 (JSR Ultrasonics) was used to excite an acoustic sound wave. The ultrasound wave that propagates through the substrate, is reflected at the interface substrate-air and travels back to the AlN layer. There the ultrasound wave excites a voltage signal which can be measured and evaluated. The maximum amplitude of the received voltage signal was used to evaluate the AlN film quality depending on the deposition parameters. The measured voltage values were calculated to absolute voltage values without gain for a better comparability. Figure 3 shows a typical time response with multiple back wall echoes. To avoid an influence of the sending signal, not the first back wall echo but rather the fourth was evaluated.

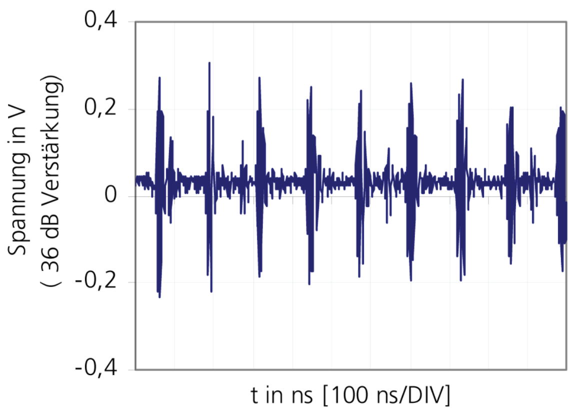

Figure 3: Echo pulse signal from silicon back wall reflection

Measurements of piezoelectric constant d_{33}

The piezoelectric charge constant d_{33} was determined with a conventional Berlincourt-Meter (Piezotest PM300). The samples were clamped and loaded with an alternating force. The generated electric charge was compared to the value of a reference sample to obtain the piezoelectric charge constant. The measurements were carried out by applying an alternating force of 0.25 N and a frequency of 110 Hz [7,8]. Additional test specimens with new substrate materials were created after the optimization of the AlN thin film deposition process. Different substrate materials like aluminium oxide, glass, quartz and aluminium were investigated. This is important for the sensor design considerations because different substrate materials have different mechanical and acoustic properties, which have an influence on the thin film ultrasonic transducers. The mechanical clamping of the thin film to the substrate plays an important role as well as the geometry dimensions. The relative big thin film sensor area versus the thin film thickness has a second influence on the d_{33} measurement with this method. This takes effect as a second clamping.

EXPERIMENTS AND RESULTS

Substrate variation and temperature storage

An acceptable piezoelectric activity could be proofed on a variety of substrate materials, which are common in electronics manufacturing, using sputtering parameter sets found in earlier investigations [8]. The d_{33}-meter can be used for a very fast estimation of the thin film quality for AlN sensors with the same substrate material and film thickness (see Figure 4). The measured value d_{33} is not the actual d_{33} value. This follows from the mentioned clamping of the thin film transducer on the substrate. During the testing with the d_{33}-meter the sample should only be loaded by the force head with a stress in thickness direction, which means parallel to the crystal orientation to obtain an unaffected d_{33} value.

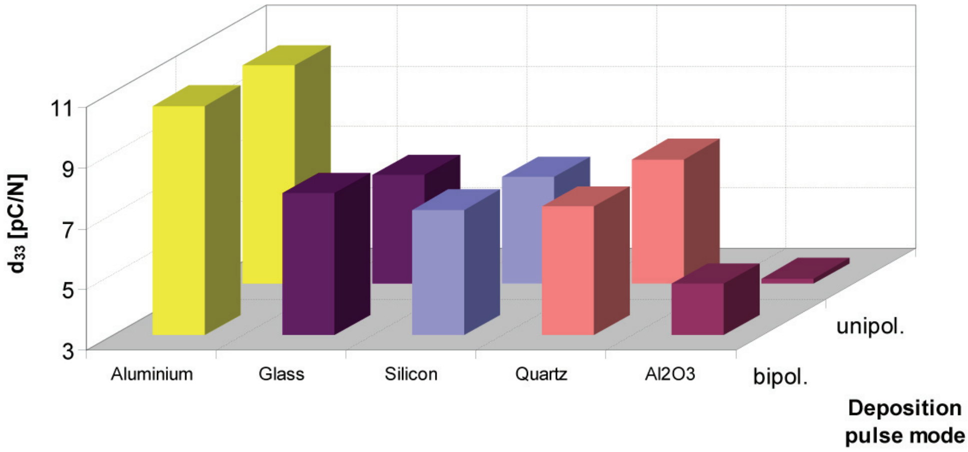

Figure 4: Results of d_{33} constants for AlN sensors deposited on different substrates.

In this case an additional stress in planar direction is induced, because of the clamping of the thin film on the substrate and because of the very low ratio of film thickness to diameter. Therefore the measured d_{33} value is lower than the true value and depends on Poisson's ratio of the substrate material. The lower the Poisson's ratio of the substrate is the lower the measured d_{33} value becomes.

The rather hard materials which have a lower Poisson's ratio and a lower elongation coefficient (e.g. 2.0 for silicon and 23.0 for aluminium in [10^{-6}/K]), show also lower d_{33} measurement results. This relationship can be seen in Figure 5. These results are similar for both deposition processes. Additionally the sensors were stored at high temperatures to evaluate the influence on the piezoelectric properties of the AlN and the substrate. The maximum signal voltages of the pulse echo measurements of all sensors were obtained, but a direct comparison was not possible because of the different substrate thicknesses and acoustical damping coefficients. Monocrystalline silicon has a much lower damping coefficient compared to the other substrate materials and therefore the maximum voltage received is much higher. For all materials it is obvious, that the temperature storage at 200°C had no significant influence.

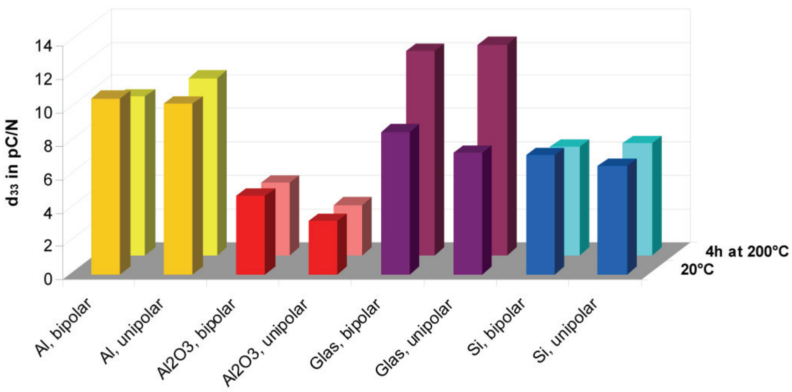

Figure 5: Piezoelectric charge constant of AlN thin film before and after temperature storage.

For aluminium, aluminium oxide and silicon no change in the d_{33} value could be observed but the d_{33} value of glass seemed to be much higher.

Due to the fact that there was no change in the measured back wall echo amplitude, it can be assumed that this effect is not caused by a change of the AlN properties, but by a change of the glass structure.

Electrode Size Variation

The variation showed a detectable reflected ultrasound wave for all electrode sizes. Sensors with the smallest electrode size and deposited with the bipolar mode could not be used for measurements. For these sensors a misalignment of the masks caused short circuits between the top electrode and the ground layer. The overview of the measured maximum signal amplitudes is shown in Figure 6. For both parameter sets the electrodes with 1 mm² showed the highest signal amplitude. All measurements were done with a conventional pulser-receiver with an input impedance of 50 Ω without additional impedance matching of the sensors. The impedance of the sensors with an electrode area of 1 mm² fits best to the characteristic impedance of the measurement cables used and the input impedance of the hardware. The reflection coefficient for these sensors is much lower than for the sensors with other geometries. The matching of the electric impedances, the sensor size and the film properties influence the maximum signal amplitude. Therefore there is no direct dependency visible between the maximum signal amplitude and the electrode area. But we could prove that it is possible to send and receive ultrasound waves with very small electrodes, which is important for an application of these films in phased array ultrasound transducers.

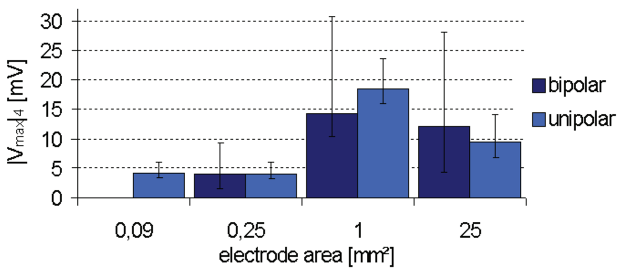

Figure 6: Maximum amplitude $|V\text{max}|$ of the 4th back wall echo without additional gain for square shaped electrodes with edge lengths of 0.3mm, 0.5 mm, 1 mm and 5 mm.

The variation of the mean values for the unipolar mode is between 7.5 % for the 1 mm² electrodes and 15.6 % for the 25 mm² electrodes. The variation of the values for the bipolar mode is higher. It varies between 15.7 % for the 0.25 mm² electrodes and 21.5 % for the 25 mm² electrodes.

Figure 7 shows the single values for the measured maximum amplitude of the different sensors for both deposition parameter sets. A dependency between maximum amplitude and sensor position on the substrate could not be found. Therefore a misalignment of the masks (e.g. offset or rotation) could not be the main reason for the higher scattering with the bipolar deposition mode. Furthermore there was no connection between low amplitude and the position of the sensor that was similar on all substrates. Thus a systematic variation of the film properties or crystal structure caused by the deposition process could be excluded.

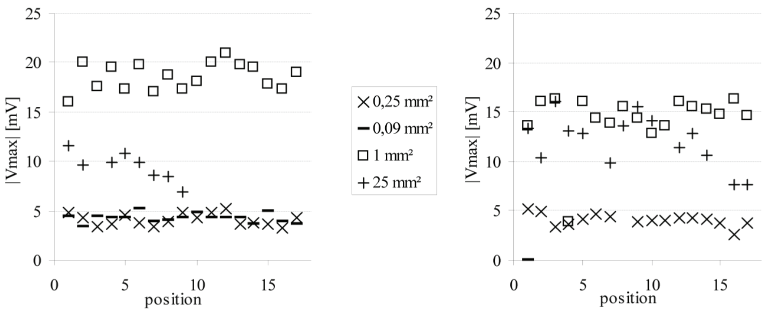

Figure 7: Maximum amplitude $|V\text{max}|$ of the 4th back wall echo without additional gain for square shaped electrodes against sensor position on the silicon substrate. Each electrode area was sputtered with unipolar (top) and bipolar (bottom) deposition mode.

CONCLUSION AND VISION

Basic investigations were carried out for different ultrasonic thin film AlN sensor designs, electrode sizes and substrate materials. It could be shown that the electrode size can be smaller than 1 mm square for use as high frequency sensors. Additionally tests of different substrate materials have shown that these sensor substrates can also be used in higher temperature applications up to 200 °C. The reason is the very good temperature resistance of the AlN thin film transducers.

The development of thin film based ultrasonic sensors should enhance the application range of ultrasonic microscopes. Especially the non-destructive evaluation becomes more and more important for micro-scaled components, heterogeneous structures, new materials like reinforced carbon fibre composites and thin film components in the flat screens or solar cells. Today these components were investigated with the ultrasonic microscope and mechanical scanning of single transducer during the components are placed in a liquid bath. The ultrasonic microscope is therefore very sensitive in case of delaminations, flaws, pores, cracks and gives important information about the consistence and quality of a product. The evaluations were carried out with single element transducer and frequencies from 5 MHz up to 200 MHz.

The measurement time is relative long caused by the necessary mechanical scanning and the lateral resolution limited by the scanner precision. For the scanning in z-direction also a parallel use of 2 to 4 single transducers focusing in different depth are necessary. With the use of phased array sensors working in higher frequency range and being available today, this technique will become more effective. The vision of the project idea is the development and demonstration of a new ultrasonic sensor test system with high frequency phased array transducers for the evaluation of complex three-dimensional components, structures or medical applications. Therefore a new phased array sensor has to be developed on the basis of piezoelectric thin films. A demonstrator working in a frequency range above 50 MHz in phased array technique with multi-channel electronic will be created in further investigations.

ACKNOWLEDGEMENTS

This work has been partially supported by a Grant-in-Aid for Technology Funding by the European Regional Development Fund (ERDF) 2007-2013 and the Free State of Saxony as well as by Fraunhofer-Gesellschaft. Many thanks also to Fraunhofer Institute for Electron Beam and Plasma Technology FEP in Dresden for the deposition processes and micro analyses by SEM and XRD, also to Polytec GmbH for the Laser vibrometer measurements.

REFERENCES

[1] Nicholson, P. S. and Patel, N. D., 1990. High Frequency, High Temperature Ultrasonic Transducers. *NDT International* 23(5), pp. 262-66.

[2] Conrad, H., Lakner, H., Pufe, W., Sandner, T., Schenk, H., Schmid, J. U. and Zimmer, F., 2009. Aluminum Nitride – A promising and Full CMOS Compatible Piezoelectric Material for MOEMS Applications. *Smart Sensors and Actuators*, Proc. of SPIE 7362.

[3] Akiyama, M., Nagao, K., Ueno, N., Tateyama, H. and Yamada, T. 2004. Influence of Metal Electrodes on Crystal Orientation of Aluminum Nitride Thin Films. Vacuum. 47, pp. 699-708.

[4] Clement, M., González-Castilla, S., Iborra, E., Ivira, B., Olivares, J,. Rastogi, A., Reinhardt, A., Rimmer, N. and Sangrador, J., 2008. BAW Resonators Based on AlN with Ir Electrodes for Digital Wireless Transmissions. *2008 IEEE International Ultrasonics Symposium Proceedings*, pp. 2189-192.

[5] Sevely, L. and Valbin, L., 2001. Piezoelectric Aluminum Nitride Thin Film for Ultrasonic Transducers MEMS Components and Applications for Industry. *Automobiles, Aerospace and Communication, Proceedings of SPIE*, 4559, pp. 95-102.

[6] Bond, L. J., Crawford, S. L., Good, M. S., Johnston, J. W., Martin, P.M. and Posakony, G.J., 2000. Piezoelectric Films for 100MHz Ultrasonic Transducers. *Thin Solid Films* 379, pp. 253-58.

[7] Bartzsch, H., Frach, P., Gittner, M., Gloess, D., Herzog, T,. Heuer, H. and Walter, S., 2011. Properties of piezoelectric AlN layers deposited by reactive pulse magnetron sputtering. *Proceedings of the 2011 Technical Conference of the Society of Vacuum Coaters*, 16-31 April 2011.

[8] Bartzsch, H., Gloess, D., Herzog, T., Heuer, H. and Walter, S. Smart ultrasonic sensors systems - Investigations on aluminum nitride thin films for the excitation of high frequency ultrasound. *Proceeding of the SPIE Microtechnologies*, Conference, 18.-20.04.2011, Prague.

SELF – SIMILAR PATTERNS ON Al SINGLE CRYSTAL FOILS UNDER CONSTRAINED CYCLIC TENSION AND THEIR CAPABILITIES FOR SMART SENSOR APPLICATIONS

P.V.Kuznetsov[1,2], Y.I.Tyurin[2], I.P.Chernov[2], T.I.Sigfusson[3]

[1]Institute of Strength Physics and Materials Science Siberian Branch of RAS, Tomsk, Russia

[2]National Research Tomsk Polytechnic University, Tomsk, Russia

[3]Innovation Center Iceland, Reykjavik, Iceland

ABSTRACT

In this article it is shown that the formation of particular self-similar patterns on Al single crystal foils (100)[001] under constrained cyclic tension is related to a surface effect of pure elastic origin known as the Grinfeld instability. The formation of structures in the Grinfeld instability condition could be considered as an additional channel of elastic energy dissipation alternative to dislocation glide in metal crystals under cyclic tension at stresses higher than the yield stress which can be considered as a means for stress monitoring in many regards.

INTRODUCTION

It was shown in [1-4] that Al single crystal foils (100) [001] fixed on plane high-strength alloy samples undergoing cyclic tension in the elastic region exhibit unusual properties. Al-foils are deformed plastically and the surface relief develops as a certain sequence of periodic structures of different scale whose quantitative and qualitative parameters correlate with the number of loading cycles. It was suggested by Gordienko et al. [1,2] to use such single crystal foils as sensors of fatigue damage accumulation in structural alloys. It was found in [5] that the structure formation on Al single crystal foils under cyclic tension is related to a common fundamental property of bilayer systems under external or internal perturbation fields. Particularly, according to [5] longitudinal macrobands on Al single crystal foils result from periodic distribution of compressive elastic misfit stresses resulting from tension of specimens with fixed Al foils due to the Poisson effect and the difference between elastic moduli of the substrate and the anisotropic one of foil.

Another type of structures observed on the Al foils after a various number of cycles is the periodic surface perturbations with different periods forming a cubic lattice with the sides oriented at an angle of 45° to the axis of tension [4,5]. A similar structure of micron range was observed in [6] under cyclic tension of bulk samples of Al single crystal (100)[001]. This structure was defined by Videm and Ryum [6] as a tweed structure. It was revealed in [5] that tweed structures resulting on Al foils are self similar in the size range from a few hundred nanometers to several hundred microns. These data are clear evidence of self-organization of the deformation structure of Al single crystal foils under constrained cyclic tension, and allow one to consider them as a smart material. Generally, smart materials are not ordinary materials. Rather, they are hybrid composites or integrated systems of materials such as shape-memory alloys, piezoelectric ceramics, magneto-(electro-)strictive materials, etc. A question arises: What intrinsic microstructure peculiarities of an ordinary FCC Al metal result in its sensory capabilities under cyclic tension. The aim of the present work is to clarify this question, to analyze possible generality of the observed phenomenon and its practical application.

MATERIALS AND EXPERIMENTAL PROCEDURE

The substrates were flat duralumin specimens of dimensions 150×30×4 mm3. The material to be studied was (001)[100] single crystal Al foils having dimensions 16×20×0.2 mm^3. The technology of growth of single crystals and manufacture of foils are described in [1,2]. The foils were attached to the central part of the surface of the flat duralumin specimens with glue. The composite duralumin - foil specimens were tested for low-cycle fatigue on a Schenck Sinus 100.40 testing machine with the following parameters: f= 1

Hz, σ_{max} = 200 MPa, σ_{min} = 0.1 σ_{max} and $\sigma_{mean} = (\sigma_{max} - \sigma_{min})/2$. Once a specified number of loading cycles was reached, the specimens were removed from the grips of the testing machine and the foils were studied with an Axiovert optical microscope, a Solver atomic force microscope (AFM), a Tesla BS 300 scanning electron microscope and a laser profilometer.

SELF-SYMILARITY SURFACE PATTERN OF DEFORMED METALS

In most cases, the main mechanism of stress relaxation under plastic deformation of metal crystals at room temperature is the generation and motion of dislocations leading to slip trace initiation on the surface.

The traces of slip on the surface of deformed materials sometimes exhibit self-similarity, which has been investigated by a number of authors [7-9]. It was shown that self-similarity of the slip traces is observed both at the stage of easy gliding [7,8] and at the stage of parabolic hardening [9] of the materials studied, but in all cases, the range of linear dimensions of self-similarity is in the nanometer - micrometer scale and is in no excess of (1 ÷ 1,5) order of length. The range of linear dimensions of self-similar tweed structures from a few hundred nanometers to several hundreds of microns observed on the surface of Al single crystals under cyclic tension [5] is not consistent with the assumption about their dislocation origin. It is assumed by Gordienko et al. [2] that the structures are formed on the foil surface because of self-organization of vacancy-type defects in mechanical stress fields. However, no specific mechanism of self-organization of defects was offered by the authors [2] and the question of the mechanism of deformation of Al single crystal foils under cyclic tension still remains open.

GRINFELD INSTABILITY

The analysis performed shows that the role of free surface of Al single crystal (100)[001] increases under cyclic tension, when the strain is higher than the yield strength, and a significant contribution to the relaxation of elastic energy is provided by a different mechanism - the Grinfeld instability [10]. The Grinfeld instability is of purely elastic origin and is as following: when a nonhydrostatically strained solid has a surface, where the material can be redistributed by some appropriate transport mechanism, the solid may reduce its elastic energy via surface modulation. The instability wavelength (λ_c,) is controlled by a balance between the elastic energy, which tends to roughen the surface, and the surface tension, which smoothens it, and can be estimated in the linear approach of the Grinfeld instability as [10]:

$$\lambda > \lambda_c = \frac{\pi\gamma E}{\sigma^2} \tag{1}$$

where γ, E, and σ are the surface tension, the Young modulus, and the stress, respectively. The destabilizing stress and the surface tension can be estimated within the approaches used in mechanics and AFM measurements.

INTERPRETATION OF EXPERIMENTAL DATA IN TERMS OF THE GRINFELD INSTABILITY

The tweed structure in micron range

Figure 1 shows tweed structures of various scales observed on Al single crystal foils under constrained cyclic tension [5]. The analysis carried out has shown that formation of these structures can be explained in terms of the Grinfeld instability.

It was shown for the first time in [11] that the tweed structure with period T_2 ~ 3 μm (Figure 1b) was formed under cyclic tension of single crystal Al foils at stresses higher than the yield stress under conditions of Grinfeld instability. This structure is formed in the region of positive periodic distribution of misfit stresses arising on the "foil – specimen" interface due to the difference between the elastic modulus of the foil and that of the high-strength alloy. The cross section of the region is about 120 – 140 μm. An estimation based on the Grinfeld model in the linear approximation in [11] T = 4 μm is in satisfactory agreement with the experimentally measured period of the tweed structure T_2 ~ 3μm. The change in the cross-sectional profile of the tweed structure with increase of the number of loading cycles qualitatively agrees with the results of numerical simulation of Grinfeld instability evolution in the nonlinear approximation [12,13]. On this basis a conclusion was made in [11] that a tweed structure with the period T ~ 3 μm was formed under the conditions of Grinfeld instability.

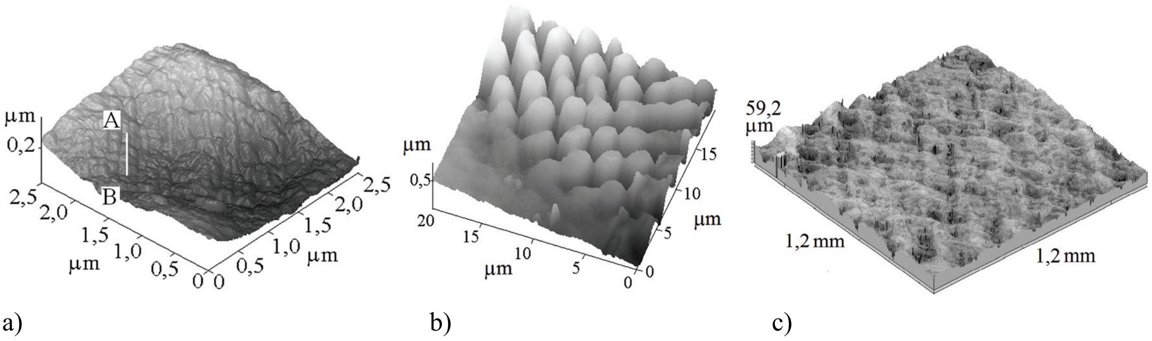

Figure 1: a) a fine tweed structure with period T1 ~0.3 μm, N =10000 cycles; b) a tweed structure with period T2 ~ 3 μm, N=10000 cycles; c) a coarse tweed structure with T3 ~ 320 μm, N=100000 cycles. a), b) AFM, c) laser profilometry.

A fine tweed structure

The fine tweed structure with the period T ~ 0.33 μm was found to form in the transition region between the longitudinal macroscopic bands and the tweed structure of micron range (Figure 2a) [6]. The area occupied by this structure is ~ 10-12 μm in width.

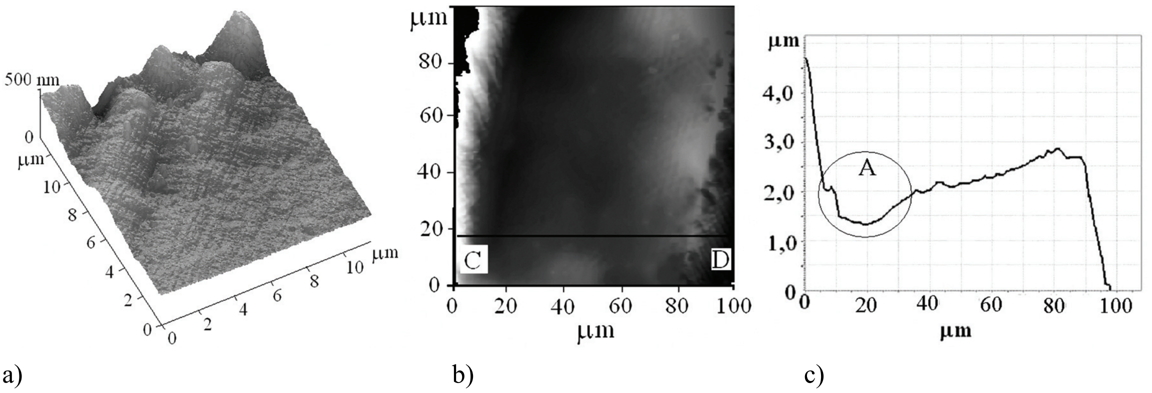

Figure 2: a) the fine tweed structure in the transition region. N ~ 10000 cycles; b) a macroband on the surface of the Al single-crystal foil; c) the cross-section along CD direction, indicated by the line segment in b). *N* ~ 100000 cycles. Atomic force microscopy.

Analysis of the experimental results shows that in the transition region between the macroscopic longitudinal bands and the tweed structure a local bending of the foil surface of an opposite sign is formed which gives rise to tensile and compressive normal stresses [14]. Pronounced curvature is clearly evident in the profilogram obtained by atomic force microscopy (Figure 2b, c). In the negative curvature region at the free surface of the foil, marked as circle A in (Figure 2c), an additional compressive stress (σ_a) arises, which leads to an increase in the local stress (σ_1) $\sigma_1 = \sigma_2 + \sigma_a$. In accordance with the Equation 1 it results in a decrease in the period of the tweed structure. Using the AFM data, the radius of curvature in the region A of the foil (Figure 2c) was measured to be equal to (24 ±6) μm and the extra stress (σ_a) was estimated as follows [15]:

$$\sigma_a = \sigma_0 (1 + 2\sqrt{a/\rho}) \tag{2}$$

where σ_0, α, ρ are the average stress, groove depth, and curvature in the stress concentrator region. The surface tension (γ) was estimated by Mullins' method [16] using the data from AFM profile measurement of the fine tweed structure (Figure3) along the direction AB shown in the (Figure 1a).

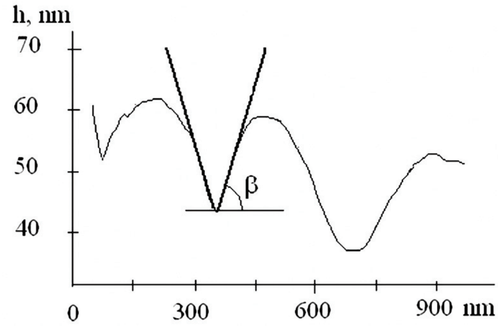

Figure 3: A cross section of fine tweed structure along the direction shown by AB in Figure 1a.

Figure 3 shows the tangent to two tweed structure protrusions at an angle β to the surface plane of the foil.

The resulting equation can be written as $2\gamma_s \sin\beta = \gamma_g$, [16], where γ_s and γ_g are the surface energy per unit area (γ_g = 1024 mJ/m^2 for Al [17] and the surface tension, respectively. The surface tension obtained as the average of about 25 tweed structure protrusions analyzed is ~ 430 mJ/m^2. Taking into account the above estimation of the additional local stress arising in the transition region, the period of the fine tweed structure in the model of Grinfeld instability was evaluated to be λ_{1G} = 0.35 μm, which is in good agreement with the experimental value λ_1 = 0.33 μm.

A coarse tweed structure

At N > ~ 40000 two systems of conjugate mesobands are formed on the foil surface in the direction of maximum shear stresses distributed over all their width d ~ 10 mm. The formation of bands of localized deformation leads to a partial relaxation of stresses in the foil which, according to Equation 1, causes roughening of the surface structure. Further cyclic deformation foil leads to a coarse tweed structure (Figure 1c). Using Equation 1and the period of the structure λ_3 =320 μm (Figure 1c), the residual stresses in the foil has been estimated. The surface tension was assumed to be equal to the surface energy of Al γ=1024 mJ/m^2 [17]. The value of σ_3 = 37 MPa obtained is higher than the yield strength of Al and comparable with the couple stress ~ 10 MPa occurring in the foil, due to eccentric load application [14]. This result suggests that in the process of surface coarsening the role of coupled stresses increases with the number of tension cycles. Thus, our analysis shows that the tweed structures of various scales observed on Al foils under constrained cyclic tension are described well in terms of the Grinfeld instability.

DISCUSSION

The Grinfeld instability is usually considered for nonhydrostatically loaded solids in contact with their own melt, solution, or vapor phase, which provides a redistribution of the material on the surface [10]. However, the formation of tweed structures under cyclic tension of aluminum crystals testifies to mass transfer in the absence of any external media. It can be naturally assumed that mass transfer on the foil surface is due by intrinsic point defects of aluminum, which form during cyclic tension of foils and appear to be rather mobile at the temperature of specimen testing. A micron tweed structure was observed on the surfaces of bulk plane samples of aluminum single crystals of cubic orientation [6,18] and on the mono- and polycrystalline aluminum foils glued on flat specimens of high-strength alloys [4,5,19] under cyclic tension. Therefore, this structure is possibly a result of crystal structure features of aluminium and is independent of the properties of the foil/sample interface.

As to other two tweed structures with λ_1 = 0.33 μm and λ_3 = 320 μm their formation is related both to the characteristics of point defects in aluminium and to the features of the foil/sample interface. Thus, the thin tweed structure with λ_1 = 0.33 μm, according to [5] (Figure1a), is formed in the transition region between the longitudinal stripes and the tweed structure of a micron range. Therefore, this structure is due to peculiarities of plastic deformation of a glued aluminum foil, in particular, to the stress and strain distribution on the foil /sample interface. The coarse tweed structure with λ_3 = 320 μm (Figure1c) seems to result from a high degree of plastic deformation of glued Al foils which can not be obtained under simple cyclic tension of bulk samples. Indeed, it is shown in [6] that the failure of bulk samples of pure aluminum single crystal with [001] orientation under cyclic tension at constant plastic strain amplitudes occurs approximately after N ~ 100000 cycles. Therefore, the coarse tweed structure observed at N ~ (100000 ÷ 150000) cycles in [5] corresponds to an ultrahigh degree of plastic cyclic deformation of the glued aluminum foils beyond cyclic durability of bulk aluminum samples.

In Al single crystals of cubic orientation under cyclic tension, four slip systems are simultaneously activated. Highly developed transverse slip leads to efficient generation of lattice defects. According to [20] an excess of strain induced defects in near-surface layers can be several orders of magnitude higher than their density in the material bulk. Therefore, a surface layer can be considered as an independent defect phase in contact with the Al crystalline phase. Analyses by Videm and Ryum [6] and Charsley and Harris [19] show that the temperature at which the specimens are subjected to cyclic tension affects the period of tweed structure and this is indicative of a peculiar role of heat-activation processes in the aluminum mass transfer.

The high mobility of point defects in aluminum crystals at room temperature suggests that the recrystallization temperature of aluminum crystals (T_r), 99.9999% purity according to [17], is T_r ~ -50 ° C.

Thus, the above analysis makes it possible to assume that the main reason of a ‘smart’ behavior of Al single crystal foils (100)[001] under constrained cyclic tension at stresses above the yield stress is due to the formation of a two-phase system "defective near-surface layer / base Al crystal". In this two-phase system there are conditions for Grinfeld instability, which result in formation of tweed structures. During cyclic tension of (100)[001] Al single crystal foil the nonuniform distribution of elastic energy density leads to nonuniform distribution of chemical potential along the surface of the Al foil [12,13]. In the field of nonuniformly distributed chemical potential along the Al - foil surface due to surface and/or volume diffusion, redistribution of aluminum mass occurs and results in the formation of tweed structures. The Grinfeld instability appears on the foils surface under certain boundary conditions which provides tweed structure formation in various scales and their self-similarity [5]. The nature of the Greenfield instability is universal, so we can assume that it may develop under certain conditions at cyclic deformation of other FCC crystals, such as copper.

The stacking fault energy of a Cu crystal γ = 67mJ/m^2 is smaller than the corresponding value for an Al crystal γ = 200 mJ/m^2 [17], therefore, the cross slip of dislocations and generation of point defects in Cu crystals are less developed than in Al crystals at room temperature. Conditions for mass redistribution on the surfaces of copper samples can be provided under cyclic deformation of samples at elevated temperature about ~(0.3 ÷ 0.5) homologous temperature, when the probability of cross slip of dislocations and the mobility of point defects increases. Interesting results, which seem to support the foregoing idea have been obtained in [21,22]. In this work, the effects of loading frequency and microstructure on the formation of thermal fatigue damage in thin Cu interconnects on <100> Si substrate were investigated.

Alternating current with different frequency was apapplied to the copper bands and produced temperature cycles with a range of 190 °C due to Joule heating. The cyclic temperature change gave rise to a cyclic strain in the Cu line due to the difference in the thermal expansion coefficient between the metal line and the wafer [21]. The cyclic deformation caused surface damages which depend on the copper band structure and deformation conditions [22]. It was found in [22] an unusual strain induced growth of grain in the [100] plane and a structure similar to a tweed structure observed in [4,5] on Al foils. According to [22] the observations show that the fatigue damage in thin Cu films is fundamentally different from that in coarse grained, bulk Cu and appears to be more and more controlled by diffusive mechanisms and interface properties rather than by dislocation glide. Unfortunately, no direct comparison of the experimental period of the structure observed in copper crystals with the Grinfeld model is possible because the theory is developed for isothermal conditions. A nature of Grinfeld instability is thermodynamic, and redistribution of material on the sample surface is not a direct result of dislocation gliding. Therefore the formation of structures in the Grinfeld instability condition could be considered as an additional channel of elastic energy dissipation alternative to dislocation glide in metal crystals under cyclic tension at stress higher than the yield stress.

POSSIBLE WAYS OF PRACTICAL APPLICATION

One can suggest several ways to develop practical applications based on the observed effects. The effect of frequency of mechanical loading on the period of a resulting tweed structure on single crystal foils of aluminum and aluminum alloy was observed in [3]. An increase in the frequency of cycling in the range (0.1 ÷ 10) Hz leads to a decrease in the period of tweed structure from ~ 3000 down to ~ 2000 nm.

Therefore, the effect of frequency of thermo-mechanical cycling in the kHz range on the nature of the relief formed on the samples of copper found in [22] supports the idea of authors [3] about the possibility of developing a new technology of self-assembling two-dimensional rectangular surface lattices of submicron (or maybe less) range by varying the frequency of cycling. The basic requirements to metal foils as multiscale sensors and the scope of their possible applications are discussed in [23]. In particular, it is shown in [23] that such foils can be used in aeronautics for load path detection, fatigue life sensing, and crack assessment. Appropriate techniques of acquisition and processing information based on optical means or measurement of eddy currents can be developed [23]. Self-similar structures formed on sensors under cyclic strain, allows us to use hierarchical non-linear approach to data analysis, including fractal analysis. Finally, the Grinfeld instability model makes it possible to get a quantitative relationship between the period of structures on the sensor surfaces and the stress in the sample.

CONCLUSIONS

Thus, it is shown that the formation of particular self-similar patterns on Al single crystal foils (100)[001] under constrained cyclic tension is related to a surface effect of pure elastic origin known as the Grinfeld instability. The formation of structures in the Grinfeld instability condition could be considered as an additional channel of elastic energy dissipation alternative to dislocation glide in metal crystals under cyclic tension at stresses higher than the yield stress. It is obvious that further experimental and theoretical studies of Grinfeld instability under cyclic deformation of metals are required with varying conditions of cyclic deformation (frequency of cycling, temperature, environment, etc.) and using different materials.

ACKNOWLEDGEMENTS

The work was partially supported by European Union INTAS grant 04-80-7078 and by the Governments of the Russian Federation grant № 11.G34.31.0003. The authors are thankful to Prof. E. E. Zasimchuk, Dr. Yu. G. Gordienko for provision with single crystal Al foils.

REFERENCES

[1] Gordienko Y. G., Karuskevich M. V. and Zasimchuk E. E., 1995. Forecasting the critical state of deformed crystal by the analysis of smart defect structure: fractal characteristics and percalationcrical indexes. *Proc. of Seventh Conference om Sensor and Their Application*. Dublin, Ireland, pp. 387-92.

[2] Gordienko Y. G., Zasimchuk E. E. and Gontareva R. G., 2003. Uncoventional deformation modes and surface roughness evolution in Al single crystals under restricted cyclic tension condition. *Journal of Materials Science Letters* 22, pp. 241-45.

[3] Gordienko Y. G., Gontareva R. G., Schreiber J. S., Zasimchuk E. E. and Zasimchuk I. K., 2006. Two-Dimensional Rectangular and Three-Dimensional Rhombic Grids Created by Self-Organization of Random Nanoextrusions. *Advanced Engineering Materials* 8(10), pp. 957 – 60.

[4] Gordienko Y., Kuznetsov P., Zasimchuk E., Gontareva R., Schreiber J. and Karbovsky V., 2008. Multiscale 2D Rectangular and 3D Rhombic Gratings Created by Self-Organization of Crystal Structure Defects under Constrained Cyclic Deformation and Fracture. *Materials Science Forum* 567-568, pp. 421 - 24.

[5] Kuznetsov P.V., Petrakova I.V., Gordienko Yu.G., Zasimchuk E.E. and Karbovskii V.L., 2009. Formation of self-similar structures on {100}(001) aluminum single-crystal foils under cyclic tension. *Phys. Mesomech*. 10(1-2, pp. 85 - 93.

[6] Videm M. and Ryum N., 1996. Cyclic deformation of [001] aluminium single crystals. *Materials science and Engineering* 219, pp. 1 - 10.

[7] Sprusil B. and Hnilica F., 1985. Fractal character of slip lines of Cd single Cristals. *Czech. J. Phys*. 35, pp. 897 - 900.

[8] Teplyakova L.A., Kunitsyna T.S. and Kozlov E.V., 1998. Distribution of the slip in single crystals of the alloy Ni3Fe. *Izv. Vuzov. Physics* 4, pp. 51-56.

[9] Kleiser T. and Boček M., 1986. The fractal nature of slip in crystals. *Z. Metallkde* 77, pp. 582–87.

[10] Grinfeld M.A., 1993. The stress driven rearrangement instability in ellastic crystals: mathematical models and physical manifestations. *J. Nonlinear Sci*. 3, pp. 35-83.

[11] Kuznetsov P.V., Panin V.E. and Petrakova I.V., 2010. Grinfeld instability in the formation of a tweed structure at the Al crystal surface under cyclic tension. *Phys. Mesomech* 13(1-2), pp. 70-78

[12] Yang W.H. and Srolovitz D.J., 1993. Cracklike surface instabilities in stressed solids. *Phys. Rev. Letters* 71(10), pp. 1593-596.

[13] Xiang Y. and Weinan E., 2002. Nonlinear evolution equation for the stress-driven morfologycal instability. *J. Appl. Phys* 91(11), pp. 9414-422.

[14] Kuznetsov P.V., Panin V.E. and Petrakova I.V., 2009. Structural and mechanical peculiarities of plastic deformation of (001){100}Al single-crystal foils on flat Al alloy substrates under constrained cyclic tension. *Phys. Mesomech* 12(3-4), pp. 180-89.

[15] Moroz L.S., 1984. *Mechanics and physics of deformation and fracture of materials.* Leningrad. Machinostroenie.

[16] Mullins W.W., 1957. Theory of thermal Grooving. *J. Appl. Phy.* 28(3), pp.333-39.

[17] Drits M.E. (Ed), 2003. *Properties of Elements*. Part 1. Moscow. Ruda i Metally. P.

[18] Vorren D. and Ryum N., 1988. Cyclic deformation of Al single crystals: Effect of the crystallographic orientation. *Acta Metall* 36, pp. 1443-453.

[19] Charsley P. and Harris L.J., 1987. Condensed dislocation structures in polycrystalline aluminium fatigued at 77K. Scripta Met 21, pp. 341-44.

[20] Alekhin V.P., 1983. *Physics of Strength and Plasticity of Materials Surface Layers*. Moscow. Nauka.

[21] Mönig R., Keller R.R. and Volkert C. A., 2004. Thermal fatigue testing of thin metal films. *Review of Scientific Instruments* 75(11), pp. 4997- 5004.

[22] Park Y.B., Mönig R. and Volkert C. A., 2007. Frequency effect on thermal fatigue damage in Cu interconnects. *Thin Solid Films* 515, pp. 3253–258.

[23] Paget Cr., 2008. Bonded thin metallic foil sensing elements application for structural health monitoring of aeronautical structures. *Phys. Mesomech* 11(5-6), pp. 308-13.

INFLUENCE OF PIEZOACTUATOR COUPLING DEGRADATION ON VIBRATION CONTROL EFFECTIVENESS

M. Pietrzakowski

Warsaw University of Technology, Institute of Machine Design Fundamentals, Warsaw, Poland

ABSTRACT

The study develops the modelling of piezoactuator edge delamination and analysis of active systems like beams or one-dimensional plates with this kind of imperfection. Delamination process is considered as a significant reduction of the bonding interlayer shear stiffness, which extends uniformly across the actuator from its ends to the centre. The governing equations are formulated separately for particular sections of the system and solved taking into account boundary and continuity conditions. For the steady-state case the influence of both the length and shear stiffness of the damaged region on the system's dynamic characteristics and control effectiveness is shown as well as the transverse displacement and shear stress distributions that have been numerically investigated and discussed.

INTRODUCTION

Techniques based on application of distributed piezoelectric transducers have found a relevant role in vibration control of thin walled flexible structures to improve their operational behaviour and ability to reduce unwanted vibration (see e.g. [1-5]). In order to achieve satisfactory control effectiveness relatively large deformations of piezoelectric actuators have to be generated during the control process. Large deformations of piezoactuator patches create severe interfacial shear stresses. Alternating in time shear stresses and also environmental conditions initiate geometrical and material degradation, which may progress and finally lead to a failure of the control system. The geometrical degradation is mainly introduced as delamination and refers especially to damage of a bonding interlayer of glue material. The glue damage is characterized by a local concentration of micro-cracks, which leads to reduction of the bonding layer shear stiffness decreasing significantly the coupling performance of piezoactuators and the control effectiveness. The actuator partial debonding was studied by Wang & Merguid [6] among others. In the field of damage detection techniques based on vibration responses are well established where a literature review has been provided by Zou et al. [7]. The modal frequency approach in a closed-loop detection of the piezoactuator damage was presented by Sun & Tong [8]. This study develops modelling of the actuator edge delamination. Instead of modelling delamination as a gap between the actuator and the main structure (c.f. [9,10]) the bonding interlayer is still considered. But within the damaged area the bonding layer shear stiffness is reduced depending on the phase of delamination process.

DESCRIPTION OF THE SYSTEM

The system considered herein is a simply supported one-dimensional plate with piezoelectric rectangular patches bonded to its both the upper and lower sides. Piezoelectric transducers operate as a collocated sensor/actuator pair in a closed loop control. The one-dimensional plate considered can be analysed as a beam modelled according to the Bernoulli-Euler theory due to its geometry and dimensions. Closed loop control with velocity feedback is applied to reduce transverse vibration excited by a time-dependant force $F(t)$. The physical model of the system with the sensor/actuator pair located between coordinates x_2 and x_5, the edge delamination regions indicated by coordinates x_2, x_3 and x_4, x_5 and loaded by the force acting at the x_1 cross-section is shown in Figure 1.

The delamination process is regarded as a local shear stiffness reduction of a massless viscoelastic bonding layer between the piezoceramic actuator and the main structure. It is assumed that the damaged section is characterized by a constant shear stiffness of the glue material and extends uniformly across the actuator to its centre. In the case of a relatively thin piezopolymer sensor the perfect bonding assumption is reasonable.

Viscoelastic properties of the system material components are approximated according to the Kelvin-Voigt relation.

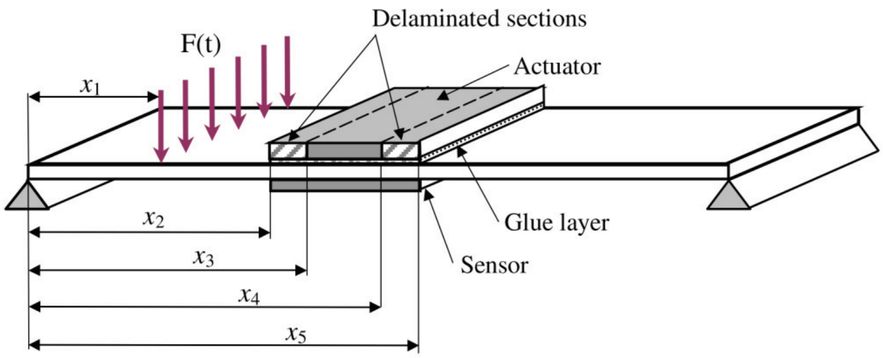

Figure 1: Model of the beam with partially delaminated piezoactuator.

EQUATIONS OF MOTION AND THE SOLUTION

For analysis the beam is divided into six sections due to the external force cross-section (x_1), the location of piezoelectric transducers (x_2, x_5) and the sections of the actuator delamination (x_2, x_3 and x_4, x_5) (Figure1). Taking the actuator extension into account, to which the inertial forces also contribute, and the shear stresses transmitted by the bonding layer, the motion of both the undamaged and damaged activated sections is described by two coupled equations related to the beam transverse displacements and pure longitudinal displacements of the actuator. They can be expressed in terms of beam surface strains ε_b and actuator strains ε_a in the following form

$$\begin{aligned} &\frac{\tilde{E} t_b^2}{12}\frac{\partial^4 \varepsilon_b}{\partial x^4} + \frac{t_b}{4}\frac{G_k}{t_g}\left(\frac{\partial^2 \varepsilon_a}{\partial x^2} - \frac{\partial^2 \varepsilon_b}{\partial x^2}\right) + \tilde{\rho}\frac{\partial^2 \varepsilon_b}{\partial t^2} = 0 \\ &E_a t_a \frac{\partial^2 \varepsilon_a}{\partial x^2} - \frac{G_k}{t_g}(\varepsilon_a - \varepsilon_b) - \rho_a t_a \frac{\partial^2 \varepsilon_a}{\partial t^2} = 0 \end{aligned} \qquad \begin{aligned} & x \in (x_2, x_3) \\ &\cup\, x \in (x_3, x_4) \\ &\cup\, x \in (x_4, x_5) \end{aligned} \tag{1}$$

Where the following parameters represent:

- t_a, t_b and t_g - actuator, beam and bonding layer thickness, respectively,
- $\tilde{\rho}$ - equivalent mass density of the activated beam section,
- ρ_a - actuator mass density,
- E_a - Young's modulus of the actuator material,
- $\tilde{E}$ - equivalent Young's modulus of the activated beam section,
- G_k - Kirchhoff's modulus referred to the undamaged ($k = u$) or damaged ($k = d$) actuator section, respectively.

The motion of other beam sections is described by the well-known equation

$$\frac{E_b t_b^2}{12}\frac{\partial^4 \varepsilon_b}{\partial x^4} + \rho_b \frac{\partial^2 \varepsilon_b}{\partial t^2} = 0 \tag{2}$$

where E_b, ρ_b are Young's modulus and mass density of the beam, respectively.

Supposing a viscoelastic material of the beam and the bonding layer, Young's moduli E_b, $\widetilde{E}$ and Kirchhoff's moduli G_u, G_d are complex. The governing equations formulation is described in details by Pietrzakowski [11] and Tylikowski [9].

The governing Equations 1 and 2 have to satisfy boundary conditions at the beam ends at $x = 0$ and $x = l$ for a simply supported beam, continuity of beam deflection, slope, curvature and transverse force at the borders of the sections at $x = x_1, x_2, x_3, x_4$ and x_5, free edge conditions at the actuator ends at $x = x_2, x_5$ and continuity of the actuator longitudinal displacements u_a and stresses σ_a at the borders between the actuator undamaged and damaged sections at $x = x_3, x_4$.

The normal stresses σ_a, uniformly distributed in the actuator cross-section, are given by the following relation

$$\sigma_a = E_a(\varepsilon_a - \lambda) \tag{3}$$

The continuity of stresses and displacements between the actuator sections yields

$$\sigma_a(x_3^-) = \sigma_a(x_3^+) \qquad \text{and} \qquad \sigma_a(x_4^-) = \sigma_a(x_4^+) \tag{4}$$

$$\int \varepsilon_a dx\Big|_{x=x_3^-} = \int \varepsilon_a dx\Big|_{x=x_3^+} \text{ and } \int \varepsilon_a dx\Big|_{x=x_4^-} = \int \varepsilon_a dx\Big|_{x=x_4^+} \tag{5}$$

The free edge conditions require zero normal stresses at the actuator ends and according to Equation 3 become

$$\varepsilon_a(x_2^+) = \varepsilon_a(x_5^-) = \lambda \tag{6}$$

The actuator strain $\lambda(t)$ is produced by the external voltage $V(t)$ applied to the actuator sections and is determined due to the general strain-voltage formula, which for the unconstrained transversally polarised one-directional actuator has the form

$$\lambda = d_{31}\frac{V}{t_a} \tag{7}$$

where d_{31} indicates the actuator piezoelectric constant. The voltage feeding the actuator is generated by the sensor and transformed according to the applied control function. In the case of perfectly bonded relatively thin sensor the voltage strictly depends on the beam deflection and due to the direct piezoelectric effect with the external electric field ignored can be approximated as follows

$$V_s = -\frac{d_{s31}E_s b_s}{c_s}\int_{x_2}^{x_5} \varepsilon_s dx \tag{8}$$

Where the following parameters represent:

d_{s31}- piezoelectric constant of the sensor,

E_s - Young's modulus,

c_s - sensor capacitance,

b_s - width of the sensor related to the effective electrode area.

The steady-state response of the active system discussed are harmonic single frequency functions with an angular velocity of excitation ω and can be written in the general form as

$$\begin{bmatrix} \varepsilon_a(x,t) \\ \varepsilon_b(x,t) \end{bmatrix} = \begin{bmatrix} \varepsilon_a(x) \\ \varepsilon_b(x) \end{bmatrix} \exp(i\omega t) \tag{9}$$

The spatial functions $\varepsilon_a(x)$ and $\varepsilon_b(x)$ are formulated using the modal superposition. They have the form dependent on the section of the beam or the actuator, which is determined by the boundary and continuity conditions. In order to solve the boundary-value problem for a viscoelastic system the complex moduli are used for material properties description. The surface strain spatial distribution in classical beam sections is described by the well-known formula

$$\varepsilon_b(x) = C_1 \exp(k_1 x) + C_2 \exp(-k_1 x) + C_3 \exp(ik_1 x) + C_4 \exp(-ik_1 x) \tag{10}$$

with the wavenumber $k_1 = \sqrt[4]{\dfrac{12\rho_b \omega^2}{E_b t_b^2}}$.

The activated beam sections ($x \in (x_2, x_3)$, $x \in (x_3, x_4)$, $x \in (x_4, x_5)$) are described by the following formulas for the beam surface strain and actuator strain, respectively

$$\varepsilon_b(x) = \sum_{n=1}^{6} D_n \alpha(k_n, \omega) \exp(k_n x) \tag{11}$$

$$\varepsilon_a(x) = \sum_{n=1}^{6} D_n \exp(k_n x) \tag{12}$$

where: $\alpha(k_n, \omega) = 1 - \dfrac{t_a t_g}{G_k}\left(E_a k_n^2 - \rho_a \omega^2\right)$.

As mentioned above Kirchhoff's modulus G_k with subscript $k = u, d$ describes the bonding layer properties of undamaged or damaged actuator section, respectively. The wavenumbers k_n are calculated from the algebraic equation

$$A_6 k_n^6 + A_4 k_n^4 + A_2 k_n^2 + A_0 = 0 \tag{13}$$

with the following coefficients: $A_6 = \dfrac{E_b t_b^2}{12} E_a t_a$,

$$A_4 = \frac{E_b t_b^2 t_a}{12} \rho_a \omega^2 - \frac{G_k t_b}{4t_g}\left(E_a t_a + \frac{E_b t_b}{3}\right), \quad A_2 = -\left(\frac{G_k t_a t_b}{4t_g}\rho_a + E_a t_a \tilde{\rho}\right)\omega^2$$

$$A_0 = \tilde{\rho}\left(\frac{G_k}{t_g} - \rho_a t_a \omega^2\right)\omega^2 . \tag{14}$$

In the system analyzed the thirty unknown coefficients $C_1, C_2, \ldots, C_{12}$ and $D_1, D_2, \ldots, D_{18}$ are calculated from the system of algebraic equations determined by boundary and continuity conditions after substituting the expected solutions.

RESULTS

Numerical calculations are performed for the beam of dimensions 380×40×2 mm³ loaded by the harmonic force $F = F_0 \exp(i\omega t)$ of amplitude equal to unity and acting at x_1 = 75 mm. The sensor/actuator pair is located between x_2 = 76 mm and x_5 = 114 mm with its centre placed on the fourth mode nodal line. The thickness of the PZT (lead-zirconate-titanate) actuator is t_a = 0.2 mm. The PVDF (polyvinylidene fluoride) sensor is of thickness t_s = 0.04 mm. The material properties of the beam and piezoelectric transducers are listed in Table 1.

Material parameter	Beam	Actuator (PZT)	Sensor (PVDF)
Mass density (kg/m^3)	7800	7280	1780
Young's modulus (N/m^2)	2.16×10^{11}	6.3×10^{11}	2.0×10^{9}
Piezoelectric constant (m/V)	-	1.9×10^{-10}	3.3×10^{-11}
Dielectric constant (F/m)	-	-	1.06×10^{-10}

Table 1: Material properties.

The actuator bonding layer within the undamaged section is of the shear stiffness parameter $G/t_g = 5\times10^{11}$ N/m^3. The beam and glue layer material damping of retardation time $\mu_b = 10^{-7}$ s and $\mu_g = 5\times10^{-5}$ s, respectively, is applied to limit the resonant amplitudes. Figures 2a, b show the beam deflection distributions which are induced by almost a static voltage (ω = 0.1 s^{-1}) of the amplitude V_0 = 100 V, and the voltage loading of the same amplitude value and frequency corresponding to the second mode, respectively. The diagrams show effects of the bonding layer stiffness in the one-side delaminated actuator comparing with the performance of the undamaged actuator. A constant length of the damaged section is assumed δ = 30%. The relative damage length parameter δ is defined as the ratio of the damaged section length to the total length of the actuator.

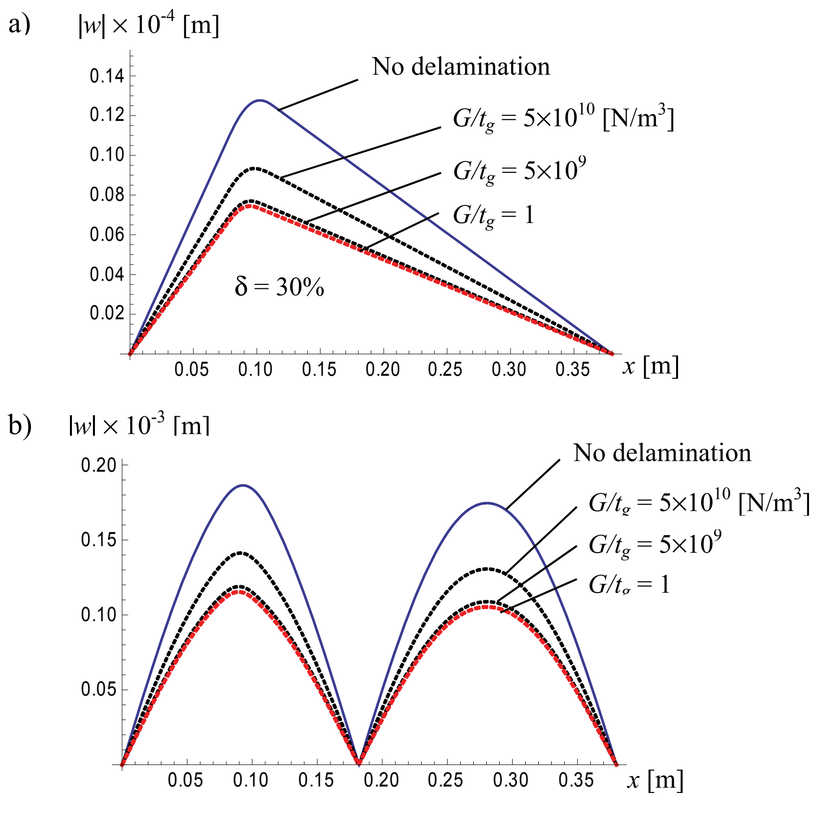

Figure 2: Influence of the bonding layer stiffness G/t_g within the damaged section on the beam deflection: a) quasistatic voltage loading, b) frequency excitation near the second beam resonance.

Comparison of the shear stress distribution along the actuator obtained for slowly varying external voltage of amplitude V_0 = 100 V is presented in Figures 3 and 4. Figure 3 shows the effect of variation in the bonding layer stiffness of the damaged section in the case of the one-side delamination pattern. It is seen that the bonding layer degradation strongly changes shear stress distribution comparing with the healthy actuator and for extremely low stiffness values (G/t_g = 1 Nm^{-3}) reduces the activated area to the undamaged section.

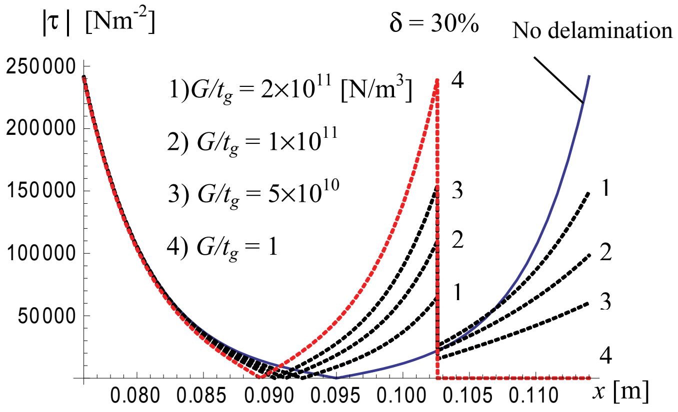

Figure 3: Effects of variation in the bonding layer stiffness G/t_g within the damaged section on the shear stress distribution for a quasistatic voltage loading (ω = 0.1 s^{-1}).

The influence of the delamination length parameter δ on the shear stress distribution is shown in Figure 4 for the actuator symmetrically delaminated on its opposite edges. Assuming a weak bonding layer (G/t_g = 1 Nm^{-3}) a decrease of the activated area caused by the damage expansion is shown clearly. The extreme shear stress values concentrate at the edges of the section where an accurate mechanical coupling exists.

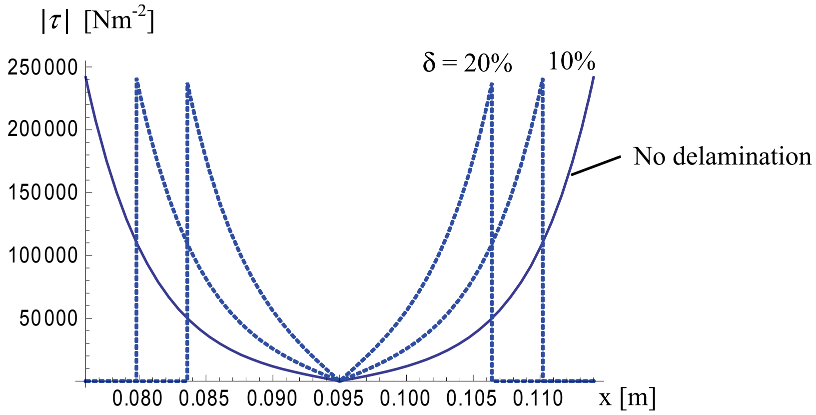

Figure 4: Effects of variation in the delamination length parameter δ on the shear stress distribution for the two-side damaged actuator at ω = 0.1 s^{-1}.

The results based on the analytical model considered in the case of a constant voltage loading have been verified using finite element method (FEM). The appropriate FE model of the beam with the actuator patch has been arranged. Generally 3D-solid, 8-nodes elements are applied, which for the piezoelectric actuator have additionally electric potential nodal quantity. The bonding layer consists of 8-nodes "cohesive" elements. For example, the simulation results in Figure 5 relate to diagrams in Figure 2a and show the effects of the glue layer stiffness degradation on the beam deflection. In Figure 6 the shear stress distributions are shown, which can be compared with analogous diagrams in Figure 3.

The results compared betwenthose obtained from FEM simulations and those from the analytical approach show quite a good agreement. Some differences noticed in the extreme values of deflection and stresses are caused by the analytical model simplification. Herein, the equivalent stiffness of the activated beam section is determined assuming a perfect bonding between the beam and the actuator. Hence it results in the system's global stiffness increase. Besides, in the analytical model of the actuator performance the bending effect is ignored.

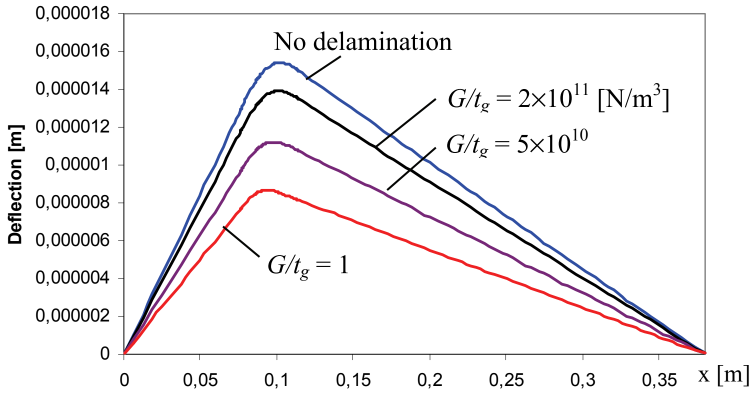

Figure 5: Influence of the bonding layer stiffness G/t_g within the damaged section on the beam deflection - FEM calculations.

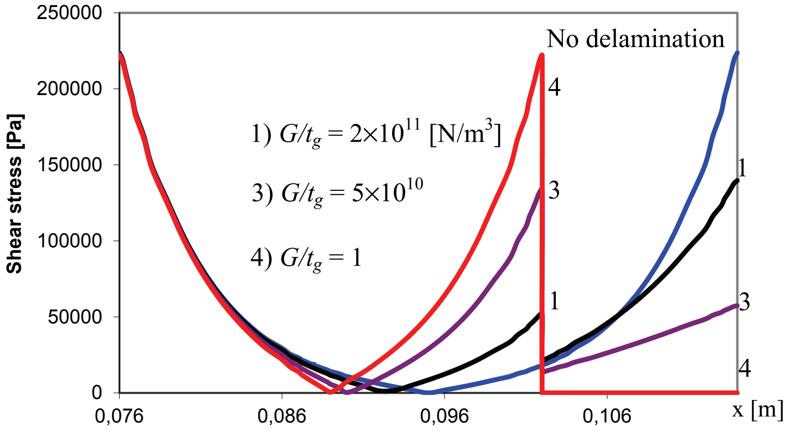

Figure 6: Effects of variation in the bonding layer stiffness G/t_g within the damaged section on the shear stress distribution - FEM calculations.

Deformation of the active beam segment including the damaged actuator section is presented in Figure 7. The bonding layer displacements and the stress concentration along the undamaged edge are also shown.

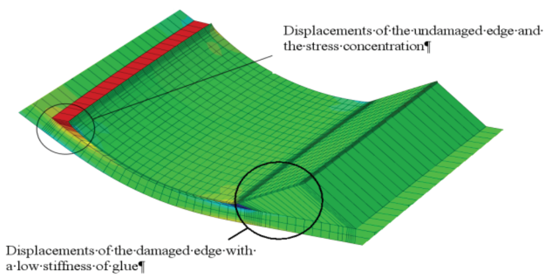

Figure 7: Deformation of the activated beam segment for a quasistatic voltage loading - FEM model.

The FEM calculations performed and the results obtained confirm the applied analytical model's correctness such that it can be used for dynamic analysis. Dynamic characteristics of the system considered are presented in terms of amplitude-frequency functions calculated at the activated field point x = 90 mm. The effects of the shear stiffness degradation for the one-side and two-side delamination patterns in the first resonance region are shown in Figures 8 and 9 respectively. The dynamic responses related to the symmetrically damaged actuator, which are obtained for various shear stiffness values within wide frequency range, are shown in Figure 10. The damage length parameter is assumed constant for both the left and right actuator edges and equal to δ = 30%. It can be seen that the amplitudes of the vibration modes tested increase significantly, as the bonding layer (due to the adhesive material degradation) becomes soft. In addition, the local stiffness changes affect the stiffness of the entire system, thus the resonant peaks appear at lower frequencies.

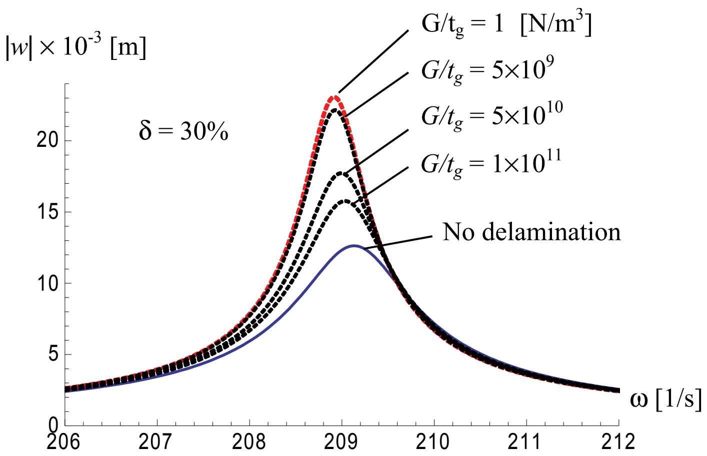

Figure 8: One-side damaged actuator. Effects of variation in the bonding layer stiffness G/t_g on the first mode active damping (δ = 30%).

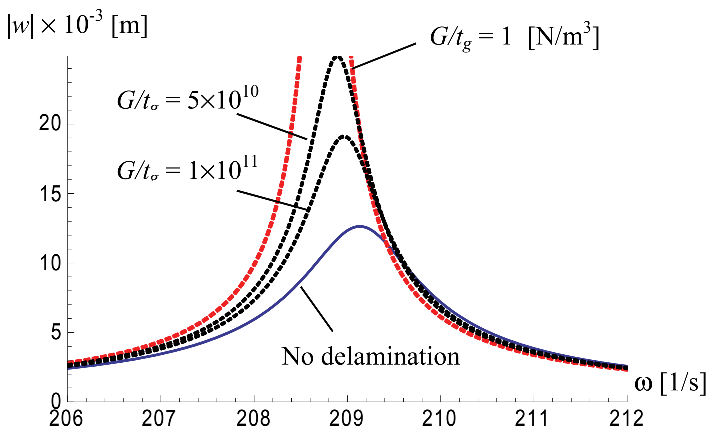

Figure 9: Symmetrically damaged actuator. Effects of variation in the bonding layer stiffness parameter G/t_g on the first mode active damping (δ = 30%).

The effect of variation in the relative length parameter δ on the beam dynamic response is numerically investigated for the two-side delamination described by the bonding layer of residual stiffness G/t_g = 1 Nm^{-3}. The results of calculation are presented in Figure 11 for the near-first resonance frequencies and in Figure 12 for a wide frequency range including the third resonance region.

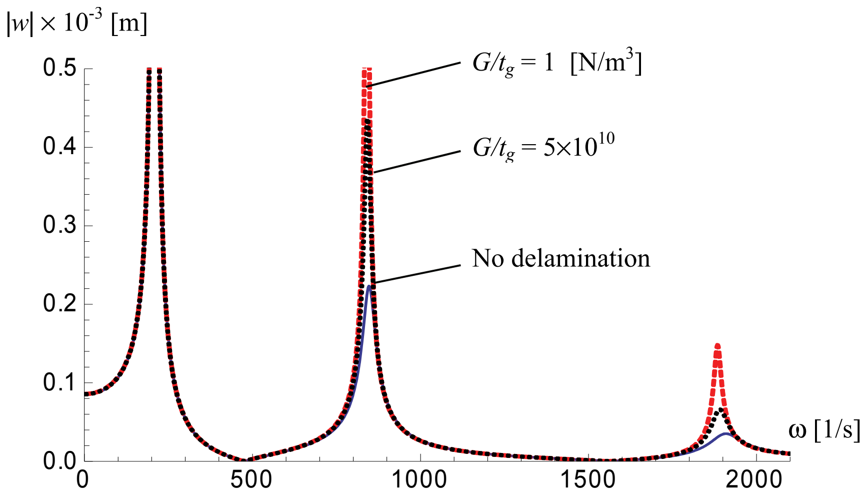

Figure 10: Symmetrically damaged actuator. Comparison of the dynamic responses in a wide frequency range depending on the bonding layer stiffness degradation (δ = 30%).

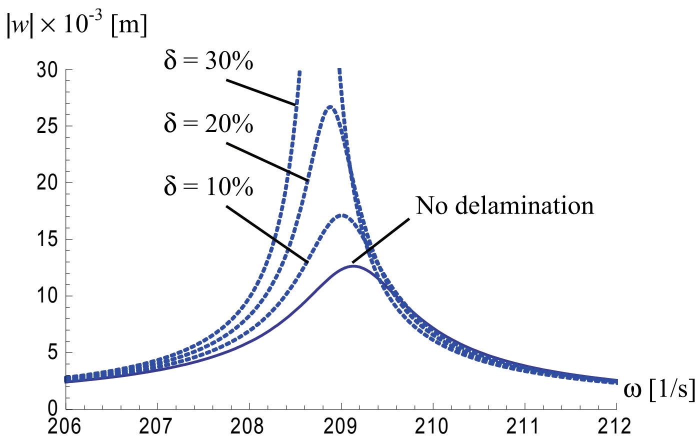

Figure 11: Effects of variation in the delamination length δ on the first mode active damping for the symmetrically damaged actuator ($G/t_g = 1$ [N/m^3]).

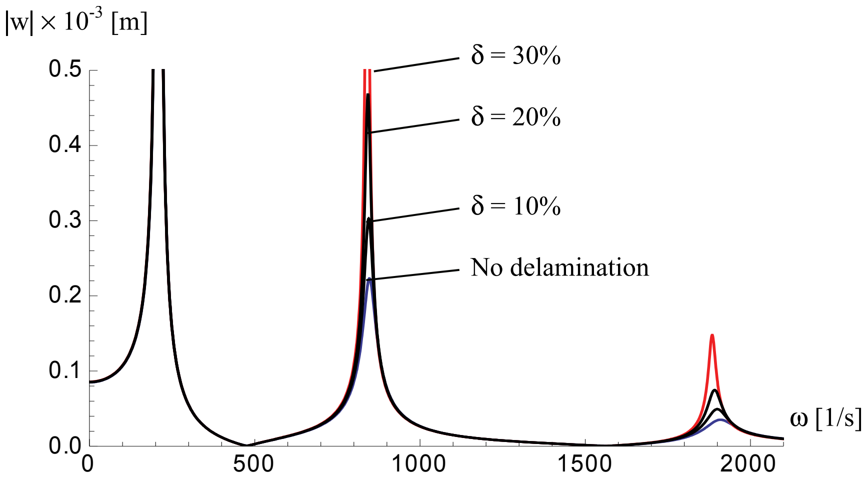

Figure 12: Effects of variation in the delamination length on the dynamic response in a wide frequency range for symmetrically damaged actuator ($G/t_g = 1$ [N/m^3]).

When comparing the plots a significant increase of the resonant amplitudes, caused by abbreviation of the actuator operational length, is noticed. Hence, the active damping effectiveness is reduced. Besides, the partly debonded actuator modifies the global stiffness of the system and a shift of the resonant peaks is observed. It can be concluded that the shear stiffness degradation and the increased length of delamination create qualitatively similar effects.

CONCLUSIONS

The model of the actuator edge delamination developed based on the bonding layer stiffness degradation is formulated and analysed. The numerical simulations show the influence of the delamination parameters on the transmitted shear force distribution, beam deflection and amplitude-frequency characteristics. The increased delamination length as well as the local bonding interlayer softening result in a disadvantageous modification of shear forces transmitted which diminishes the control system's effectiveness and leads to the modal frequency shift when related to the global stiffness reduction of the system. The changes in the modal frequencies can be used as a parameter for damage assessment.

The results presented and related discussion let us conclude that the stiffness of bonding layers within the damaged area has a harmful effect on the vibrational response and the active damping efficiency and can be used to describe the degradation process and estimate its progress. The proposed model of the actuator delamination offers a possibility of detecting the presence of damage and evaluating damage effects in active structures.

ACKNOWLEDGEMENTS

The work reported here was supported by the State Committee for Scientific Research (KBN), grant no 0673/B/T02/2008/35

REFERENCES

[1] Ha S. K., Keilers C. and Chang F.-K., 1991. Analysis of Laminated Composites Containing Distributed Piezoceramic Sensors and Actuators. *Journal of Intelligent Material Systems and Structures*, 2(1), pp. 59-71.

[2] Chandrashekhara K. and Agarwal A. N., 1993. Active Vibration Control of Laminated Composite Plates Using Piezoelectric Devices: A Finite Element Approach. *Journal of Intelligent Material Systems and Structures* 4(4), pp. 496-508.

[3] Reddy J.N., 1999. On Laminated Composite Plates with Integrated Sensors and Actuators. *Engineering Structures* 21, pp. 568-93.

[4] Benjeddou A., 2000. Advances in Piezoelectric Finite Element Modeling of Adaptive Structural Elements: a Survey. *Computers and Structures*, 76, pp. 347-63.

[5] Wang Q. and Quek S.T., 2001. Flexural vibration analysis of sandwich beam coupled with piezoelectric actuator. *Smart Materials and Structures* 10, pp. 229-39.

[6] Wang X.D. and Meguid S.A., 2000. On the Electroelastic Behavior of a Thin Piezoelectric Actuator Attached to an Infinite Host Structure. *International Journal of Solids and Structures* 37, pp. 2231-251.

[7] Zou Y., Tong L. and Steven G.P., 2000. Vibration-Based Model-Dependent Damage (Delamination) Identification and Health Monitoring for Composite Structures – Review. *Journal of Sound and Vibration* 230(2), pp. 357-78.

[8] Sun D. and Tong L., 2003. Closed-Loop Based Detection of Debonding of Piezoelectric Actuator Patches in Controlled Beams. *International Journal of Solids and Structures* 40, pp. 2449-471.

[9] Tylikowski A., 2001. Effects of Piezoactuator Delamination on the Transfer Functions of Vibration Control Systems. *International Journal of Solids and Structures* 38, pp. 2189–202.

[10] Nagendra Kumar D., Raja S. and T. Ikeda., 2007. Active Vibration Control of Smart Plates with Partially Debonded Multilayered PZT Actuators. *Smart Materials and Structures* 16, pp. 1584-594.

[11] Pietrzakowski M., 2001. Active Damping of Beams by Piezoelectric System: Effects of Bonding Layer Properties. *International Journal of Solids and Structures* 38, pp. 7885–897.

CARBON NANOTUBE-BASED ACTUATORS

S. Geier*, T. Mahrholz, P. Wierach & M. Sinapius

German Aerospace Center (DLR)

Institute of Composite Structures and Adaptive Systems Multifunctional Materials Lilienthalplatz 7, 38108 Braunschweig, Germany

*Corresponding author. E-mail Sebastian.Geier@dlr.de

ABSTRACT

This paper focuses on the electro-mechanical behaviour of a wide range of architectures based on pure carbon nanotubes (CNTs). The different types of architectures represent different qualities of CNT-alignment. The aim is to transfer the excellent micro-scale structural CNT-properties to the macro-scale anisotropic architecture. The main types of mentioned architectures are randomly oriented paper-like entangled CNTs, also called Bucky-papers, as a common reference. In contrast highly vertically aligned CNT-arrays are tested too. These are manufactured using two different techniques (chemical vapor deposition, CVD, and plasma enhanced CVD, PECVD) and substrates with decisive difference in result. As a linkage between the randomly oriented and highly aligned architectures, a manufacturing technique will be presented which transfers vertically aligned CNTs into a flat, horizontally aligned paper-like architecture.

The results of the active behaviour are correlated to findings of the various other material quality tests in order to clarify the composition and the origin of the active behaviour. The alignment is an important fact to distinguish between the possible actuation mechanisms, i.e. whether it is an electro-static or quantum-mechanical effect or caused by volume change. The type of actuation mechanism is crucial for future applications.

INTRODUCTION

One key issue of the future mobility is energy efficiency. Current research tries to improve it by using biological inspired adaptability in order to meet the actually most efficient condition. Until now it is common to realize adaptive systems via mechanical kinematics. The additional mass and complexity can be reduced by implementing multifunctional materials as part of the structural frame. These materials are able to convert e. g. electrical into mechanical energy. The aim of future research will be to develop manufacturing techniques which enable multifunctional materials to take on structural tasks.

At present reproducibility and economical production are the driving issues for successful use of smart materials. Focusing on electro-mechanical transducers there are three groups of active materials worth to be mentioned, which are well researched and partly commercially available (see Figure 1). Most of the realized adaptive systems are based on piezoceramics (see Figure 1, PZT) as electro-mechanical transducers. The active mechanism, called the inverse piezo-effect, can be explained by a crystalline deformation within an electric field. Characteristically high actuation frequencies up to 60 kHz and high stiffness (64GPa) are making them very attractive for applications. Inherent brittleness, low active strain (0.15%) and high operation voltage (200-2800V, [1]) are disadvantageous characteristics. In contrast to piezoceramics, shape-memory alloys (see Figure 1, SMA) generate high active strains up to 8% [2] by changing their crystalline, metallic configuration from austenite into martensite. Slow reaction and unstable long term behaviour are severe drawbacks.

Beside these established groups of active materials a third group, the electro-active polymers (see Figure 1, EAPs), found their way to application. Driven by an ion induced volume change or electrostatic-induced electrostatic attraction, free strains of 215% [5] and frequencies of 82 Hz ([5], depending on mechanism) can be reached. Their flexible base material with low stiffness does not allow highly loaded structural applications. Therefore this kind of actuator was mostly demonstrated as tensile loaded artificial muscle. With excellent electro-mechanical properties carbon nanotubes (CNTs) catch researcher's attention since years. Additionally it can be shown, that two dimensional architectures made of CNTs (called Bucky-paper) are reversely elongating when they are set up like a capacitor and electrically charged. Single CNTs (SWCNTs) are difficult to handle because of their nano-scale geometry. Therefore paper-like architectures of entangles and bundled SWCNTs are produced by filtration-techniques of aqueous dispersions made from commercially available powder consisting of agglomerated CNTs.

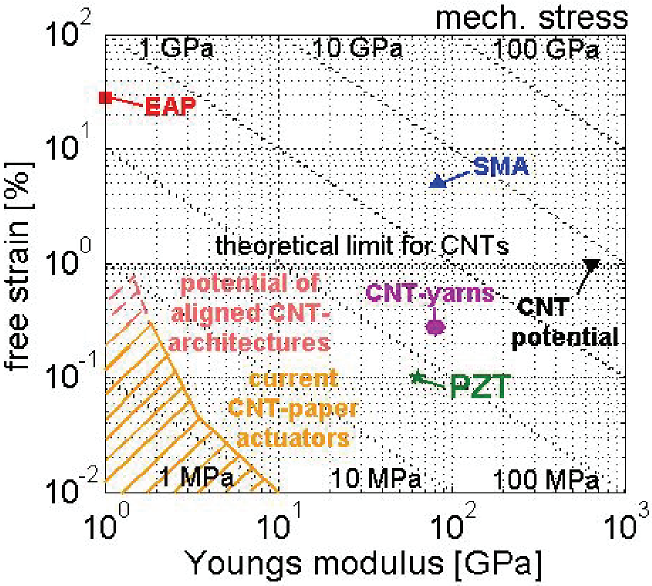

Figure 1: Overview of smart materials [2] in comparison to CNT-based materials, their potential and theoretical limitations [3,4].

These papers containing randomly oriented CNTs are responsible for the actuation behaviour. Bending cantilevers set-ups of CNT-papers are successfully demonstrated as electro-mechanical transducers [6]. The potential to combine low voltages of ± < 3V [6-8], theoretical high active strains 1% [3,4] and excellent mechanical properties make CNTs to be a promising candidate for a structural integrated actuators for future adaptive applications. The majority of research on CNT-actuators refers to extraordinary properties of CNTs like high Young's modulus of 1TPa [9] or thermal and electrical conductivities. Most of these values are related to ideal, single walled CNTs (SWCNTs) or theoretical calculations. In fact most of publications presented on CNT-actuation use macroscopic paper-like CNT-based architectures. Extensive studies [10-12] show that the mechanical results are essentially driven by the composition of the CNT-papers.

CNT-papers are a suitable configuration to make CNTs handable but they represent only partially the active behaviour of the single CNTs. To test this kind of model structure a number of test set-ups for deflection measurements were designed. Among these, two analysis-methods are well established now. The in-plain test set-up (see Figure 2) in which a CNT-paper is fixed on the one side and pre-stressed by a clamp on the other side is designed for symmetrical specimen [2,7,8,13]. The deflections of the actuated paper are detected by a distance laser sensor system along their direction of propagation. Often this test set-up is used for measurements within liquid electrolytes.

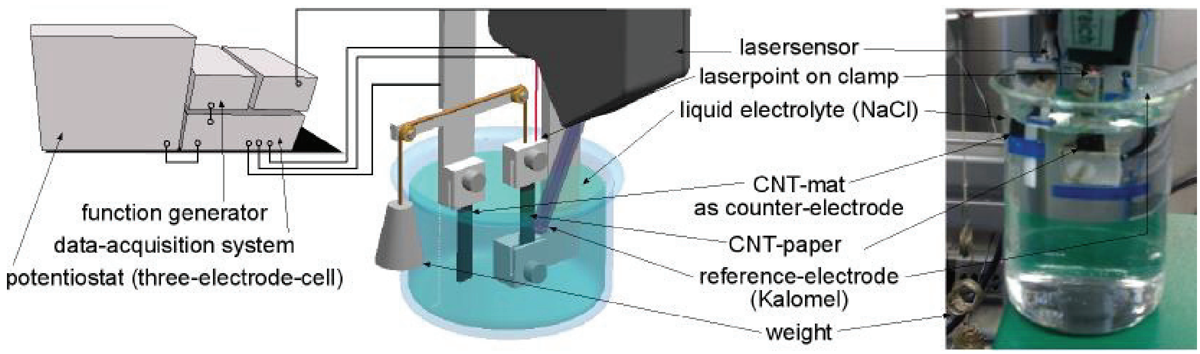

Figure 2: In-plane test set-up.

Unsymmetrical specimen build-ups, like it is the case for single side coated CNT-papers, are analysed within an out-of-plane test set-up [14]. This method is suitable for hybrid-testing, containing CNT-papers and solid electrolytes. By measuring the thickness change of the specimen secondary effects like thermal induced volume change or ion related mass-transfer can be clearly detected and compensated. Beside the diverging composition of the powder, the random orientation of CNTs generates an isotropic character of electro-mechanical properties. This is the reason for small measured strains. A possible solution is an aligned architecture, like vertically aligned CNTs grown as an array. The measurement along their geometric anisotropy offers a significant way to understand the actuation mechanism itself. From the mechanical point of view forces can also be transferred more efficiently along the aligned architectures (compare fiber-reinforced-plastics). That is the reason for intensive research on electro-magnetic alignment of CNTs in papers using powder based dispersions [15,16]. In the past several analysis-methods were used to identify the mechanism, but either the used material (CNT-papers with high density of different CNTs [17-19]) was not suitable for definite results or the analysis method (Atomic-Force-Microscopy scanning of activated single CNT) was carried out inconsequently [20]. The latest investigations on randomly oriented CNT-papers in use as actuators consider an important correlation between their mechanical properties and their active characteristics. Therefore an electrostatic effect as actuation mechanism is suggested instead of further preferred ion and charge transfer [21].

This conflicting message has driven the presented basic research in the field of CNTs: detailed analysis of CNT-papers and an evaluation of their contribution to the actuation mechanism, significant measurement of single SWCNTs or aligned CNT-based architectures because only their exact confirmation helps to evaluate the resulting measurements and to understand the actuation mechanism itself.

Understanding the Influence of CNT-Paper Composition

Prerequisites for excellent active properties are pure single walled dispersed metallic CNTs. Therefore SWCNTs of high purity are preferred. These CNTs show the highest specific surface area and their small diameter of 1-2 nm enables their geometric stability [22]. Within a comprehensive test campaign of rare SWCNT-material, suppliers (see Table 1) offering high purities were chosen. Their material is compared to powder of lower purity and powder mostly containing multi-walled carbon nanotubes.

Within a filtration process [23] a CNT-paper is formed of the powder. A high pressure source is added in order to improve the paper density and thereby the quality as a result of the higher compression (see Figure 3). For a more homogeneous dispersion the standard process of ultrasonic bath and afterwards manual homogenization can be optionally completed by a time variable (5 to 15 minutes at 4000*g*) centrifugation step (Universal 320, Hettich GmbH & Co. KG., Germany). Additionally other homogenizing techniques are tested like automatic high pressure homogenizing, ultra turrax and the efficiency of ultrasonic bath or ultrasonic horn without using the manual homogenizer first. The results presented refer only to CNT-papers made by the standard process described further below.

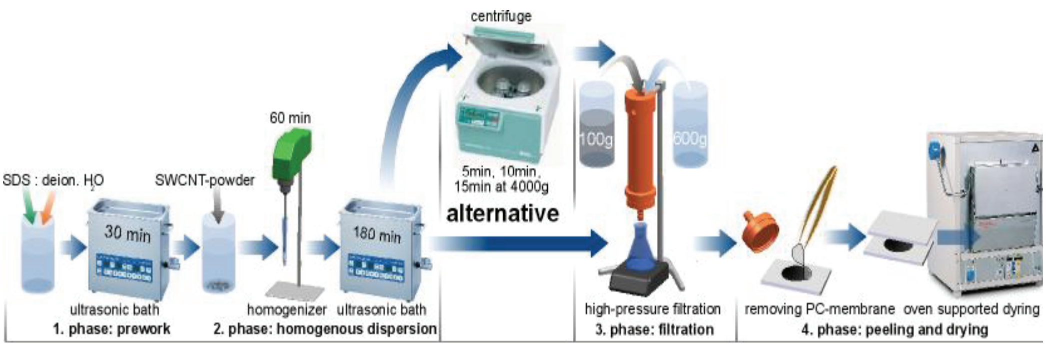

Figure 3: Process steps of CNT-paper manufacturing.

The powder handled is optically analysed via scanning electron microscopy (SEM, Leo 1550, Zeiss Jena AG, Germany) before processing. Thermo gravimetric analysis (TGA) of the powder are carried out by the suppliers. These tests are repeated later and compared to TGA-results of samples taken from CNT-papers. Each manufactured CNT-paper is also analysed by SEM afterwards. Additionally conductivity tests, measurements of the paper density and the specific surface area via the BET method (Nova 2000e, Quantachrome GmbH & Co. KG., Germany) are carried out. Moreover mechanical properties [24] are tested by a dynamic mechanical analysis-facility (DMA/SDTA861, Mettler Toledo Intl. Inc., Swiss) and the free strain is measured by the already mentioned in-plane test set-up (Figure 2). High resolution TGA-analyses (TGA Q500, TA instruments, US) of the papers are made for analysing the composition. This extensive quality assessment of the manufactured papers enables the comparison of different manufacturing processes, electro-mechanical properties and the powder and paper composition.

The selected powders analysed herein were used because of their high CNT purities as the decisive argument for a high conductivity. The correlation of the supplier information and the measured conductivity of the manufactured papers are shown in Table 1. The ranges for the standard process (with or without centrifuge) are presented in Table 2. It is evident that the purity offered does not guarantee the best conductivity, except the Unidym material. Even here additional process steps like centrifugation are required. MWCNT-papers have in fact a lower conductivity than all other SWCNT-papers, which can be attributed to their lower specific active surface also underlined by the range of the conductivity values. The variation of the standard manufacturing process has a decisive influence. Moreover it can be seen that different powders are not affected the same way. While the powders of Thomas Swan and Unidym show a significant improvement of the conductivity all other papers remain below 81 S/cm.

supplier	product	manu-facturing process	purity CNTs [%]	purity SWCNTs [%]	Conductivity of CNT-paper [S/cm]
Thomas Swan	Elicarb SW PR0925	CVD	70	unknown	62-241
Shenzhen Nano Tech Port Co. Ltd.	SWCNTs	CVD	>90	70	33-70
Unidym	super purified	HiPCO	>95	unknown	90-254
Nano-C Inc.	Nano-cpt Nano-capt	pyrolyse	unknown	>97	46-81
Bayer Materialscience AG	Baytubes C 150 P	CVD	>95	-	25-34

Table 1: Overview of CNT-suppliers and measured properties of the material.

Further CPS-measurement (CP24000, CPS Instruments, Inc., US) comparing the particle fraction of CNT-solutions made by different homogenizing techniques show that the standard process generates a double peak particle fraction with a small peak at 15 nm and the higher peak at 700 nm. Using just the ultrasonic bath inverts the proportions. Additional steps of pre-filtration with filtering-membranes and/or centrifugation of the dispersion, shifts the average x50 particle diameter to 25 nm. The mass loss during centrifugation ranges between 70-80%. Table 2 shows all measured values which are also plotted in Figure 4.

nr.	supplier	process-style	BP-conductivity [S/cm]	centrifuge-time [min]	Young's modulus [MPa]	free strain at +0.7V [%]	specific surface area [m^2/g]
1	T. S.	standard	103	0	994	0.12	294
2	T. S.	standard	161	5	2361	0.02	513
3	T. S.	standard	219	10	2414	0.03	350
4	T. S.	standard	228	15	3424	0.02	397
5	T. S.	high pressure	113	10	2010	0.007	472
6	U	standard	88	0	432	0.01	197
7	U	standard	128	5	1967	0.007	136
8	U	high pressure	250	0	2549	0.006	441
9	N-C hp.	high pressure	75	15	7385	0.005	233
10	N-C asp.	high pressure	80	0	3078	0.009	187
11	S	high pressure	42	0	945	0.012	331
12	S	high pressure	66	10	869	0.006	439
13	B	high pressure	26	0	776	0.02	209

Table 2: Overview of analysed CNT-papers:

T. S.: Thomas Swan, U: Unidym N-C hp: Nano-C high purity, N-C asp: Nano-C as produced,

S: Shenzhen, B: Bayer;

As a general trend the free strain decreases with an increasing specific Young's modulus. An increase of the mechanical properties seems only possible by using the additional process steps of centrifuging or high pressure homogenization. This increase is accompanied by higher specific surface areas and electrical conductivity. Nevertheless the high pressure process step does not increase the mechanical or active properties as far as the centrifugation step does, but it can reduce the extensive mass loss.

Also HR-TGA results show a great impact of the processing on the thermal stability of CNT-papers. As a reference untreated powder (Thomas Swan) was tested first. It was heated with 5K per minute up to 900°C within a nitrogen atmosphere. Afterwards it is cooled down until the heating chamber reached 25°C and heated up again within an oxygen atmosphere with the same routine. CNT-papers made from the stable fraction of 10 minutes centrifuged CNT-dispersion as well as papers made from the deposited CNT-residue of the same dispersion are tested this way. It is found that the mass loss increases by using a centrifuge step. The mass loss is related to unstable carbon-based material, which even degrades within the nitrogen atmosphere. The paper made of the centrifuged dispersion shows a loss of about 32wt% whereas the mat formed of deposited CNT-material looses 26wt% of relative mass. The neat powder used as reference shows less than 10wt% mass loss. This observation points out that the composition of the homogenously centrifuged CNT-dispersion tends to contain more unstable, amorphous material. This high fraction can also be seen as impact of the manufacturing process on the neat material by fragmentation of the CNTs via ultrasonic treatment.

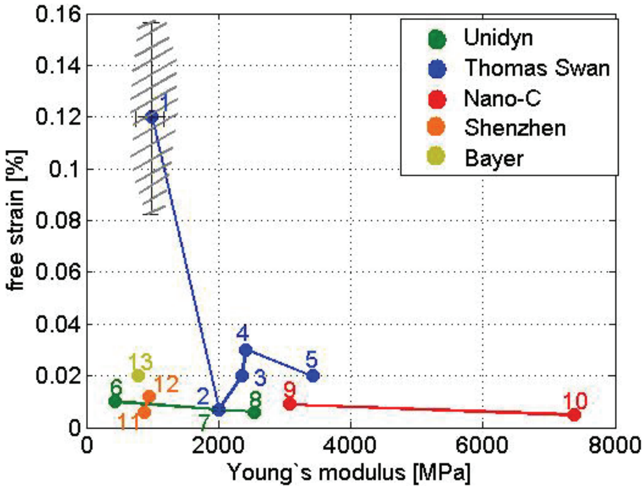

Figure 4: Overview of the results from Table 2 and Table 3.

In contrast DMA-analyses verify that centrifuging improves the values of electro-mechanical properties (stiffness, conductivity) and the specific surface almost twice and more. Although on SEM micrographs of the top side and bottom side of centrifuged papers almost no CNT-structures are apparent. Therefore CNT-bundles only become visible in cross section areas of cryogen broken papers or by using specific surface-scanning SEM-detectors. Moreover the papers show a typical layered structure (see Figure 9, middle micrograph) which suggests sedimentation levels. It seems to be possible that these levels consist of different sizes and therefore weights of powder agglomerates. An inhomogeneous build-up of centrifuged CNT-papers can also be the reason for out-of-plane bending, what can be observed in experiments using CNT-papers in ionic liquids. The diffusion of the ionic liquids seems to depend on the surface area. Smaller particles characterized by higher specific surface support the diffusion and layer building of the ions.

With this effect the paper swells asymmetrically and starts to bend out of plane although it is stressed in plane. This is a significant indicator for a global unsymmetrical build-up of a material with different levels of active surfaces. It is evident that both the electro-mechanical properties and active behaviour (free strain) cannot be improved simultaneously until now. Aspects like the layered build-up and the composition of a CNT-paper should open a discussion if results of measurements using CNT-papers are suitable for explaining the actuation mechanism itself. Table 3 gives detailed averaged results of four uncentrifuged CNT-papers. It can be seen that the standard process creates inhomogeneous papers with especially highly diverging results of free strain. With the totally similar paper production in mind, this result points out that the quality of CNT-papers is strongly affected by the human factor as well as the raw material quality. Both causes low reproducibility (grey shaded area in Figure 4).

	conductivity [S/cm]	bulk-density [g/cm^3]	Young's modulus [MPa]	free strain at +0,7V [%]	specific surface area [m^2/g]
average value	103	0.66	994	0.12	294
standard deviation [%]	37	9	19	31	18
median value	100	0.65	1050	0.12	282

Table 3: Results of four specimen of T. S. CNT-papers made by the same procedure.

Aligned CNT-architectures

There are different ways of manufacturing aligned architectures made of CNTs. While electrical field induced alignment points out to be energy and device intensive with often poor results an even more promising way opens up by using as produced vertically aligned CNTs, called CNT-arrays. Within the study described here multi walled carbon nanotube-arrays (MWCNT-arrays), produced at the partner institutes in Hamburg (TUHH) and Wismar (HSW) are used (see Figure 5).

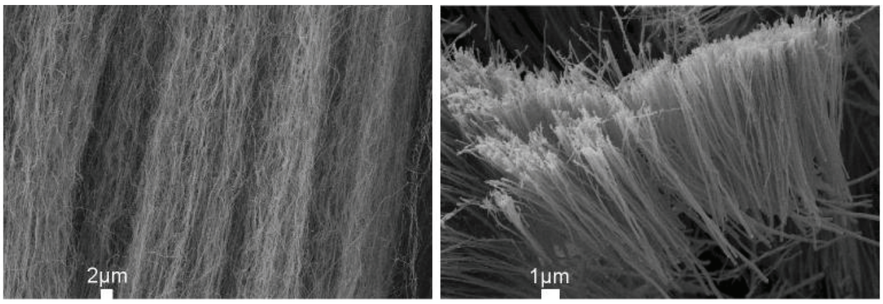

Figure 5: left: MWCNT-array with curly structure from the TUHH,
right: straight MWCNTs in array formation with short length of 10µm (HSW).

For the use as paper-like actuators a process inspired by Wang [25] is adapted (Figure 6). In this process the vertically aligned MWCNTs-array can be transferred into an almost horizontal position. This architecture is similar to the CNT-paper mentioned before. In a first step the substrate of the array is fixed at its bottom. In a second step the aligned CNTs are separated by a film of aluminum. The aluminum-covered arrays are rolled by a tube and flattened this way. An array bending can be avoided by pulling the film while the array is rolled in the same direction. The array is sheared within this process. This method enables the manufacturing of CNT-papers whose dimensions are only limited by the substrate geometry on which the CNTs are grown.

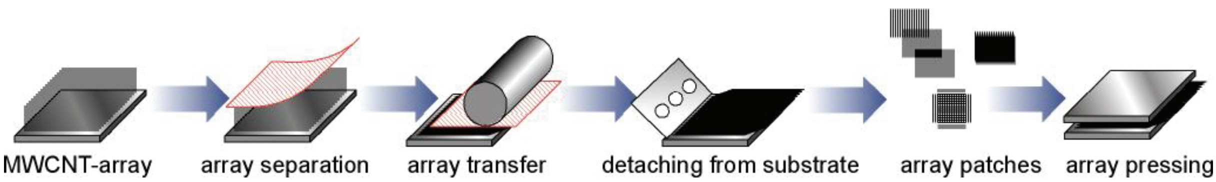

Figure 6: Process steps of transferring a MWCNT-array into an aligned paper.

Finally the idea of analyzing aligned structures is extended from aligned CNT-papers to unaffected arrays of free standing CNTs. A CNT-array is an ideal structure for measuring deflections because experiments show that their clamping can be suggested as fixed on the solid substrate. Straight CNTs of almost conform length are used like in Figure 5 (right) so that the actuation can be measured as the movement of the CNT-array top side. This can be transferred to covering bodies (glass tube) placed on the top of the arrays for which movements can be detected optically. This approach allows exact optical measurements out of any reflecting liquids on the one hand. On the other hand a complete wetting of the CNT-arrays by the electrolyte is ensured. The method allows measuring CNT-deflections provided that it is an ion and charge induced C-bond-lengthening. An out-of-plane test set-up is modified (see Figure 7) so that an array can be clamped and electrically activated.

A glass cylinder with a diameter of 3 mm, a height of 3 mm and a weight of about 0.06 g placed on the top of the arrays, transfers the deflection of the vertically aligned tubes out of the electrolyte. The measurements were carried out according to the in-plane measurements by charging the CNTs with different voltage steps around the zero potential of the electrical system. As a preparation of this test, different electrolytes were analysed for their wetting characteristics within a contact angle test set-up (contact angle system OCA20, DataPhysics Instruments GmbH, Germany). Deionized water, an one molar solution of sodium chloride as well as an ionic liquid, 1-ethyl-3-methylimidazolium bis(trifluoremethylsulfonyl)imide (EMITf$_2$N, supplied by Merck), are tested. The contact angle gives an idea about the wettability of the tested material (Figure 8).

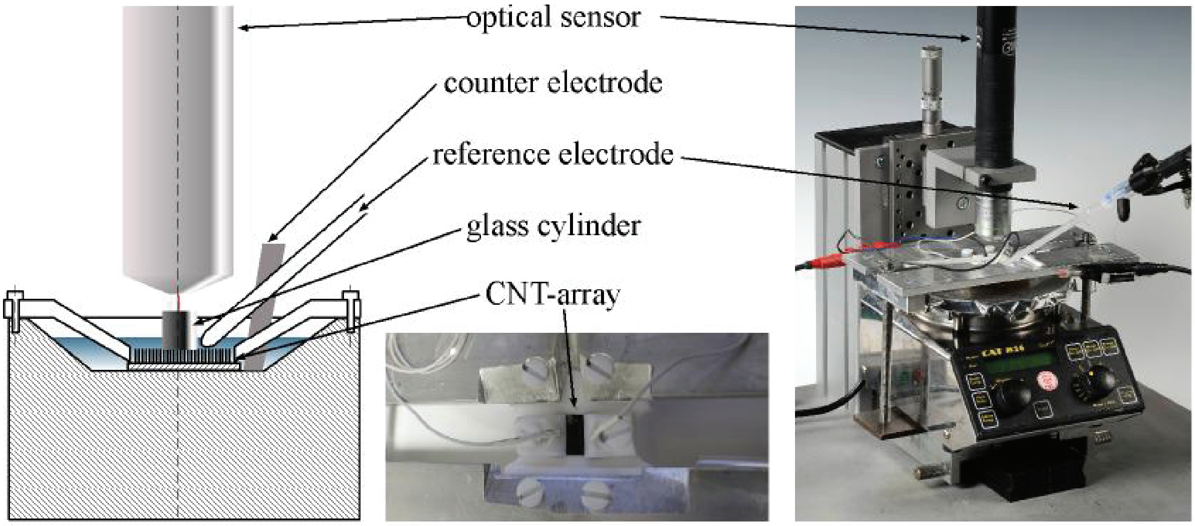

Figure 7: Different views of the out-of-plain test set-up: schematic graphic of the array testing (left), view from above onto the test bed (center), front view to the test set-up (right).

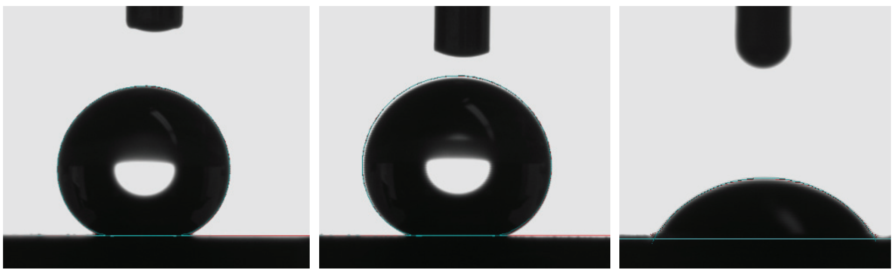

Figure 8: Wettability test of different electrolytes on MWCNT-arrays as substrate: 179.1° deionized water after 10 seconds (left), 169.1° one molar NaCl-solution after 10 seconds (center), 59.1° EMImTf$_2$N after 1second (right).

The more CNTs are covered by the electrolyte theoretically the more ion-transfer is enabled with increasing strain. The array is completely wetted by 11 g of the ionic liquid. Because of the slowly chemical reactions the tests are carried out at a frequency of 30 mHz. The reasonable activation voltage ranges for aqueous solution within ±1 V to avoid irreversible chemical reactions. In contrast ionic liquids can be used with rather high voltages of -2 V to 1.5 V (the ranges are supposed for 0 V as zero potential of the test system). Figure 8 reveals the ability of the ionic liquid only to diffuse into this strong hydrophobic material.

As a further development of randomly oriented CNT-mats, aligned papers can be produced successfully of CNT-arrays. Grown MWCNT-arrays with heights of more than 500 µm are successfully flattened to 2D papers. The alignment is proven by analyzing their conductivity along and crosswise the CNT direction. Due to a lower specific surface area MWCNTs are not able to reach the same conductivity as it can be measured for SWCNT-papers. The aligned papers show duplication of the conductivity values along the CNT alignment direction like with a crosswise alignment. All the measured conductivity values for aligned CNT-papers were even higher than they were found for filtrated MWCNT-papers as it can be seen from Table 2. Mechanical tensile tests are carried out but the aligned papers are still structurally too weak for measuring any values. Further thermal and manual processing in order to solidify the paper structure hadn't the yearned positive effect. The aim is to improve the paper density and thereby the adhesion between the CNTs (Van-der-Waals-forces) to get a higher quality of papers for practical application.

But even the incorporation of these papers into the measuring facility (DMA) failed. The left micrograph of Figure 9 shows a fold area of an aligned CNT-paper. It can be seen that the tubes slide easily on each other.

The Van-der-Waals couplings have to withstand all the stresses. In contrast to the aligned paper the fold edge of a tensile tested paper of randomly oriented CNTs looks like sharper with an inhomogeneous, layered build-up (Figure 9, middle picture). Higher resolutions reveal that the CNTs within the paper are not broken (Figure 9, left picture). The twisted bundles are pulled out of the paper and are aligned during the tensile test. The SWCNTs are even sliding on each other cutting in the SWCNT bundle until it consists of just one SWCNT. A randomly oriented CNT-paper is completely broken when all of these single tubes are pulled out completely. The stress-curve of the tensile test is qualitatively comparable to composite materials. The dominating mechanism of stiffness seems to be the high adhesion of SWCNTs within a bundle and the knotting of bundles within a CNT-paper which also contains a matrix of undefined material.

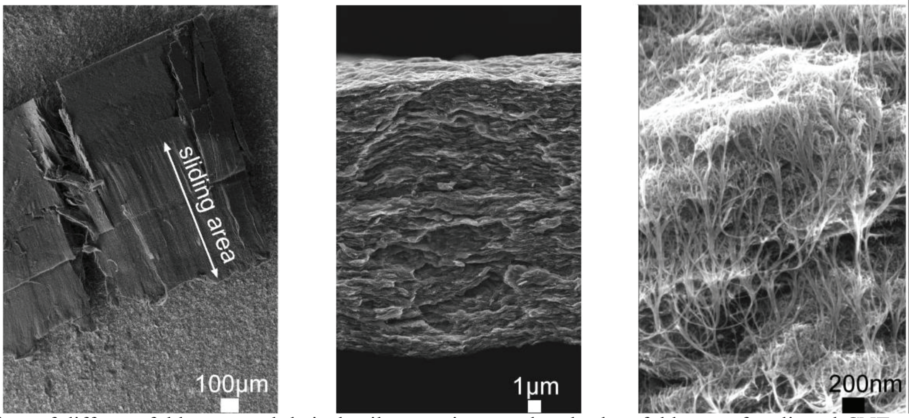

Figure 9: Overview of different fold areas and their details: top view on slant broken fold area of a aligned CNT-paper (left), fold line, cross section, of a CNT-paper of randomly oriented CNTs (center), details of fold line (right).

Figure 8 documents that tests of the active behaviour of MWCNT-arrays can only be carried out using ionic liquids because of the high hydrophobicity of CNT-arrays. For the presented measurements 1-ethyl-3-methylimidazolium bis(trifluoremethylsulfonyl)imide is used. During these analyses the almost same reaction is found like it is performed by CNT-papers in liquid electrolytes. The acquired data at -2 V is shown as an example in Figure 10.

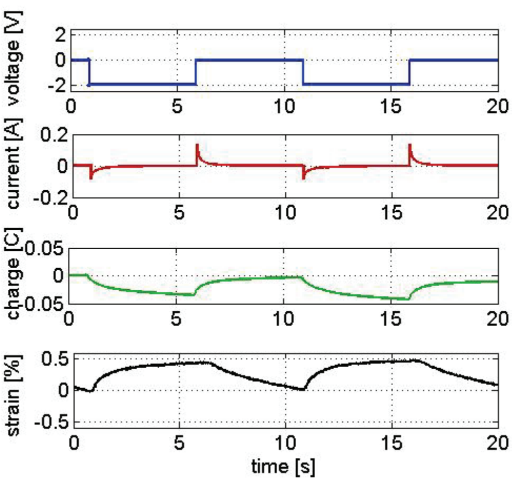

Figure 10: Data for voltage, current, charge and strain for -2 V.

Tests using activation voltages between -2 V to +1.5 V reveal a maximum free strain of 0.45% (see Figure 10 for activation voltages of -2 V). Negative potentials reach higher values of free strain in comparison to the positive charges. A possible reason can be found in the different structured ions provided by the electrolyte and their ability to form a double-layer around the CNTs.

To enable a better ion transfer without increasing the free strain significantly the test is carried out at different temperatures (22° C and 50° C). During the tests the ionic liquid changes its colour from transparent to yellow-brown. This effect refers to the ability of ionic liquids to solve any soiling from the electrodes (amorphous carbon, residues of the catalysis). It cannot be excluded that the solved particles affect the performance of the ionic liquid. Nevertheless the strain characteristics suggest that the used frequency is still too high for the different chemical processes to achieve the maximum strain (diffusion controlled process). Moreover the usage of SWCNT-arrays enables higher strain as well because of their higher active surface area, instead of using MWCNT-arrays. At least there are alternative ionic liquids available too. The diffuse process and chemical interactions between ionic liquids and the analysed CNT-structures have to be investigated in more detail in order to optimise the strain generation by synchronizing the interacting materials. Analysing these issues still enables to meet the CNT potential mentioned in Figure 1.

CONCLUSIONS

Different types of architectures made of carbon nanotubes are electro-mechanically tested to get an understanding of the actuation mechanisms. The wettability has decisive influence on the choice of the used electrolyte which can affect the paper by ion-transfer induced geometrical swelling. This fact points out an electrostatic behaviour of architectures made of entangled, randomly oriented CNTs. For reliable measurements architectures with symmetrical lay-up have to be preferred. As far as the presented tests show, this feature cannot be provided by randomly oriented CNT-papers. This behaviour results in a high deviation of results and an inverse relation between mechanical stiffness and free strain.

The presented manufacturing-process is a suitable technique to fabricate large two-dimensional CNT-papers. Although the neat vertically aligned CNT-arrays reveal a curly architecture with some entanglement, the aligned flattened papers suffer from less stiffness. Further steps to improve the friction by reducing free space between CNTs via manual compressing as well as thermal compacting show no significant effect on the mechanical properties. This type of architecture has to be developed further on for application.

The highly vertically aligned multi-walled CNT-arrays demonstrate the highest, reproducible result of all compared CNT-architectures by far. Taking the quality of alignment and the mounting on the specific substrate into account, the arrays made by PECVD and grown on glassy carbon are preferred. As far as the tests reveal the measured free strain has to be attributed to a quantum-mechanical elongation of the CNTs themselves.

These structures show the greatest potential for structure-integrated actuators in the near future.

ACKNOWLEDGEMENTS

This work is part of the basic research on future smart materials at the DLR - Institute of Composite Structure and Adaptive Systems. It was supported by the German Research Council (DFG) within the framework of the DFG PAK 355 - 'Basics for CNT-based Actuators' and the German Federal Ministry of Education and Research (BMBF) project Aktu_Komp.

Tribute has also to be paid to the colleagues of the Institute of Particle Technology of the Technical University of Braunschweig (IPat) for supporting the presented research with their analysis techniques and expertise.

PARTNERS

Technical University of Hamburg-Harburg

Polymer Composites M11

Swiss Federal Institute of Technology Zurich
Institute of Mechanical Systems
University of Applied Sciences, Technology, Business and Design
Institute of Surface and Thin Film Technology
Technical University of Clausthal-Zellerfeld
Institute of Particle Technology

REFERENCES

[1] Wierach, P. and Schönecker, A., 2005. Bauweisen und Anwendungen von Piezokompositen in der Adaptronik. *Adaptronik Congress,* pp. 1-11.

[2] Monner, H. P., Mühle, S., Wierach, P. and Riemenschneider, J., 2003. Carbon nanotubes - ein multifunktionaler Leichtbauwerkstoff für die Adaptronik. *Adaptronic Congress*.

[3] Guo, W. and Guo, Y., 2003. Giant Axial Electrostrictive Deformation in Carbon Nanotubes. *Phys. Rev. Lett.* 91(11), 115501.

[4] Ghosh, S., Gadagkar, V. and Sood, A. K., 2005. Strains induced in carbon nanotubes due to the presence of ions: Ab initio restricted hatree-fock calculations. *Chemical Physics Letters* 406, pp. 10-14.

[5] Pelrine, R., Kornbluh, R. and Kofod, G., 2000. High-Strain Actuator Materials Based on Dielectric Elastomers *Advanced Materials* 12(16), pp. 1223-225.

[6] Baughman, R.H., Cui, C., Zakhidov, A. A., Iqbal, Z., Barisci, J. N., Spinks, G. M., Wallace, G. G., Mazzoldi, A., Rossi, D. D., Rinzler, A. G., Jaschinski, O., Roth, S. and Kerzesz, M., 1999. Carbon nanotube actuators. *Science* 284, pp. 1340-344.

[7] Riemenschneider a, J., Mahrholz, T., Monner, H. P. and Melcher, J. 2007. System response of nanotube based actuators. *Mechanics of Advanced Material and Structure* 14(1), pp. 57-65.

[8] Riemenschneider B. J., Temmen, H. and Monner, H. P., 2007. CNT based actuators: Experimental and theoretical investigation of the in-plain strain generation. *Journal of Nanoscience and Nanotechnology* 7(10), pp. 3359-364.

[9] Yu, M.-F., Yakobson, B. I. and Ruoff, R. S., 2000. Controlled Sliding and Pullout of Nested Shells in Individual Multiwalled Carbon Nanotubes. *J. Phys. Chem. B Lett.* 104, pp. 8764-767.

[10] Grobert N., 2006. Nanotubes - grow or go?. *materialstoday* 9(10), pp. 64.

[11] Moon, J.-M., An, K. H., Lee, Y. H., Park, Y. S., Bae, D. J. and Park, G.-S., 2001. High-Yield Purification Process of Singlewalled Carbon Nanotubes. *J. Phys. Chem. B* 105 (24), pp. 5677–681.

[12] Itkis, M. E., Perea, D. E., Niyogi, S., Rickard, S. M., Hamon, M. A., Hu, H., Zhao, B. and Haddon, R. C. 2003. Purity Evaluation of As-Prepared Single-Walled Carbon Nanotube Soot by Use of Solution-Phase Near-IR Spectroscopy. *Nano Letters* 3(3) 309-14.

[13] Mazzoldi, A., Rossi, D. D. and Baughman, R. H., 2000. Electro-mechanical behavior of carbon nanotube sheets in electrochemical actuators, *SPIE, EAPAD*: 3987.

[14] Kosidlo, U., Weis, D. G., Hying, K., Haque, M. H. and Kolaric, I., 2007. Development of Measurement Set-up for electromechanical Analysis of Bucky Paper Actuators. *Journal of Nanotechnology Online* 3, pp. 1-11.

[15] Chen, C. and Zhang, Y., 2006. Manipulation of single-wall carbon nanotubes into dispersively aligned arrays between metal electrodes. *Journal of applied Physics* 39, pp. 172-76.

[16] Hone, J., Llaguno, M. C., Nemes, N. M., Johnson, A. T., Fischer, J. E., Walters, D. A., Casavant, M. J., Schmidt, J. and Smalley, R. E., 2000. Electrical and thermal Transport properties of magnetically aligned single wall carbon nanotube films. *Applied Physics Letters* 77(5), pp. 666-68.

[17] Gupta S., Hughes, M., Windle, A. H. and Robertson, J., 2003. Charge transfer in carbon nanotubes actuators investigated using in situ Raman spectroscopy. *Journal of applied Physics* 95(4), pp. 2038-048.

[18] Gupta S., Hughes, M., Windle, A. H. and Robertson, J. 2004. In situ Raman spectro-electrochemistry study of single-wall carbon nanotubes mat. *Diamond and related Materials* 13, pp. 1314-321.

[19] Gupta S., 2006. Electrochemical tuning and investigations on actuator mechanism of single-wall carbon nanotubes. *Diamond and related Materials* 15, pp. 378-84.

[20] Sippel-Oakley, J. A., 2005. *Charge-induced actuation in Carbon Nanotubes and resistance changes in Carbon nanotubes networks.* Ph.D. University of Florida, unpublished.

[21] Suppiger, D., Busato, S., Ermanni, P., Motta, M. and Windle, A., 2009. Electromechanical actuation of macroscopic carbon nanotube structures: mats and aligned ribbons. *Phys. Chem.* 11(25), pp. 5180-185.

[22] Krüger, A., 2007. *Neue Kohlenstoffmaterialien - Eine Einführung*. Wiesbaden, Teubner Studienbücher Chemie.

[23] Vohrer, U. and Zschoerper, N., 2007. Kohlenstoff-Nanoröhren – Phönix aus der Asche. *Vakuum in Forschung und Praxis* 19(2), pp. 22-30.

[24] Whitten, P. G., Spinks, G. M. and Wallace, G. G., 2005. Mechanical properties of carbon nanotube paper in ionic liquid and aqueous electrolytes. *Carbon* 43, pp. 1891-896.

[25] Wang, D., 2007. Highly oriented carbon nanotube papers made of aligned carbon nanotubes. *Nanotechnology* 19, pp. 1-5.

WORKING BEHAVIOUR AND CONTROL OF MAGNETORHEOLOGICAL DAMPERS

Felix Weber*

Empa, Swiss Federal Laboratories for Materials Science and Research, Überlandstrasse 129, 8600 Dübendorf, Switzerland

*Corresponding author. E-mail: felix.weber@empa.ch

ABSTRACT

Observations on a rheometer indicate that the MR damper force at currents different from 0 A is produced by the particle chains that act like brushes against the adjacent surfaces. Due to this brush analogy, a LuGre friction model-based feed forward control scheme is developed to track a desired dissipative force with a superimposed stiffness force. The measured tracking errors are mainly generated by the MR damper residual force. As a specific application study, a Bingham model-based feed forward is considered to track clipped viscous damping with negative stiffness for cable damping. The measured force tracking errors on the order of 20% are larger than for the LuGre approach. However, the Bingham approach leads to the cable damping ratio as expected from the theory and thereby indicates that models for feed forward control schemes do not require taking into account the pre-yield behaviour of MR dampers.

INTRODUCTION

Magnetorheological (MR) dampers have been installed on, e.g. stay cables, to semi-actively mitigate vibrations [1-3]. Also, MR dampers have been used for controlled vibration isolation and tuned mass damper systems [4-6]. For all these applications, the real-time control of the actual MR damper force according to the desired control force is a demanding task due to the non-linear characteristics of the MR damper force [7,8]. To compensate for the non-linear behaviour, the actual force is usually controlled by a model-based feed forward [9]. From the large variety of the existing feed forward control schemes, this paper presents two approaches. One is based on the LuGre friction model [10-12] and the other on the Bingham model [13], which is a simple modelling approach because it does not describe the pre-yield behaviour. Both approaches are experimentally validated for a desired dissipative force combined with a stiffness force. The results are discussed and conclusions are drawn.

WORKING BEAHVIOUR OF MR DAMPER

Observations at rheometer

A MR fluid sample is tested in shear deformation mode using the rheometer that is depicted in Figure 1. The test set-up is prepared such that the magnetic flux in the MR fluid sample is parallel to the rotation axis (Figure 2). Using an optical instrument which is similar to a microscope, it was observed that:

The MR fluid at 0 A and without remanent magnetization behaves similar to a viscous fluid. The viscous force is produced by the lubricant, which is visible in Figure 3(a), between the MR fluid sample and core plate.

The MR fluid at currents different from 0 A produces a predominant friction force by the friction between the particle chains and the core plate. This behaviour is shown in Figure 3(b) where the MR fluid sample was stretched after rotation in order to make the particle chains better visible. Figure 4 shows a snapshot from the video that was taken during rotation. It demonstrates that the MR fluid sample slides as an entire body against one adjacent surface and sticks to the other surface.

From these observations may be concluded that the predominant friction force of MR dampers is produced by the friction between the particle chains and the damper housing assuming that the chains stick to the cylinder of the piston where the magnetic flux density is large. Figures 5 and 6 explain schematically how the force is generated within the MR damper:

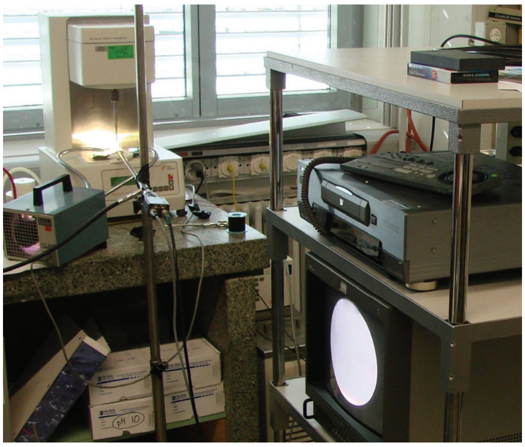

Figure 1: Rheometer and video camera.

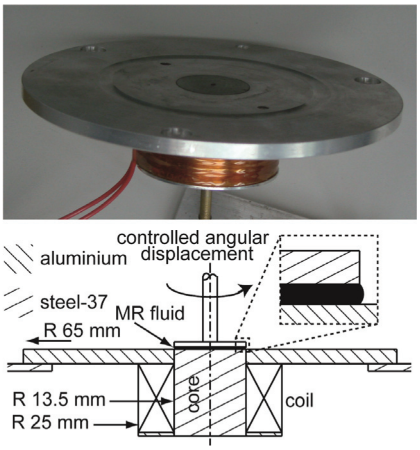

Figure 2: Details of rheometer set-up.

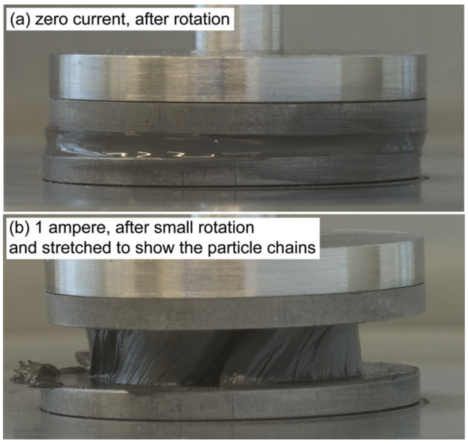

Figure 3: Particle chains visible in MR fluid.

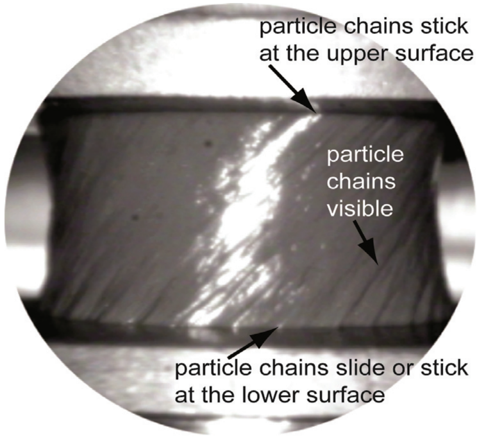

Figure 4: MR fluid during operation.

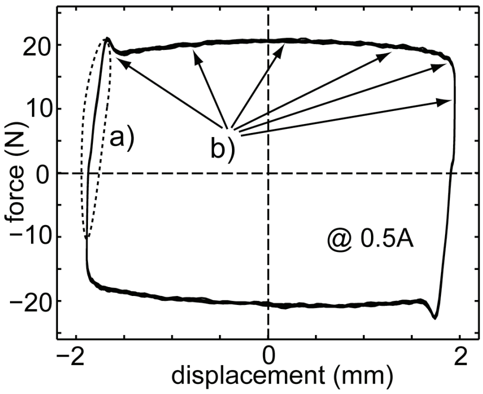

Figure 5: Force displacement trajectory at 0.5 A

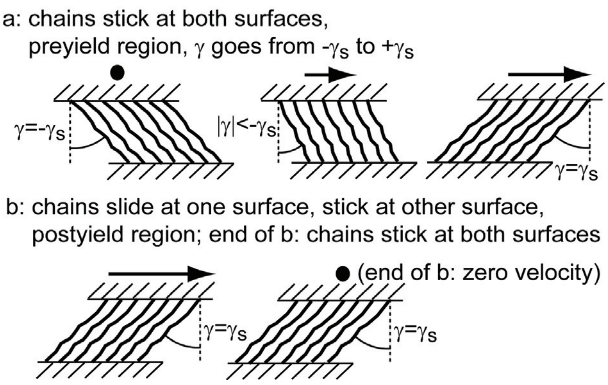

Figure 6: Sticking and sliding of chains during pre-yield and post-yield regions.

Section a): The displacement reaches its negative maximum where the particle chains stop to slide against the housing surface. Here, section a) starts which is commonly denoted as pre-yield region. During the entire section a), the particle chains stick to both surfaces, i.e. the damper housing and the rotating damper disc.

The angle of the particle chains changes from its negative sliding angle $\gamma = -\gamma_s$ to its positive sliding angle $\gamma = \gamma_s$. During this phase, the measured MR damper force is a pure stiffness force because the particle chains act like springs that are first compressed and then stretched due to the damper motion. This is visible by the very steep slope of the force displacement trajectory in section a. The end of section a) is characterized by the Stribeck effect [14] where the damper force changes from dry to sliding friction. The smooth transition may result from the fact that not all particle chains start to slide either against the damper housing or the rotating plate at the same time instant. The end of the Stribeck is interpreted as the time instant when all particle chains slide. Section b): This section starts when all particle chains slide relative to the damper housing or the rotating disc and stops when the particle chains stick again to both adjacent surfaces. The change from sliding to sticking is not characterized by a force increase as in case of the Stribeck effect since the brushes simply stop to slide. The section b) is commonly denoted as post-yield region. The maximum force is reached at approximately zero displacement where velocity reaches its maximum and thereby the sum of the friction force and the viscous force is maximized.

Response time of MR damper force

It is assumed that the MR damper produces a friction force f_1 at current i_1 and sliding angle $\gamma_s = \gamma_1$. Now, current steps up to $i_2 > i_1$. Then, the attraction force of the particle chains is increased instantaneously. Consequently, the chains stick to both surfaces. The MR damper force is then equal to the stiffness of the particle chains times the chain angle γ_1 which is the same as the sliding angle at i_1. Only if the chain angle becomes greater, the MR damper force can be increased. This can only be achieved by further rotation in the damper disc which is imposed by structural vibration. During the disc rotation, the chain angle and thereby the MR damper force increase continuously. The greater MR damper force is reached as $f_2 > f_1$ when the chains slide again relative to one surface at $\gamma_2 > \gamma_1$. The time needed go from γ_1 to γ_2 and thereby generate the force increase $f_2 > f_1$ represents an inherent response time of the MR damper force.

LuGre friction model of MR damper force

The LuGre friction approach is chosen to model the MR damper force due to the analogy between the brushes of this modelling approach and the particle chains of the MR fluid that are observed in the rheometer tests. The LuGre friction model was developed by researchers from Lund and Grenoble which explains the abbreviation LuGre [10]. The MR fluid parameters, i.e. slip stress, shear modulus and viscosity are identified from the rheometer tests [12]. These parameters and the results from tests on the entire MR damper device with sinusoidal motion at different amplitudes and frequencies are used for the modelling.

The model validation is depicted in Figure 7 which proofs that the LuGre friction approach is able to capture the MR damper force dynamics accurately.

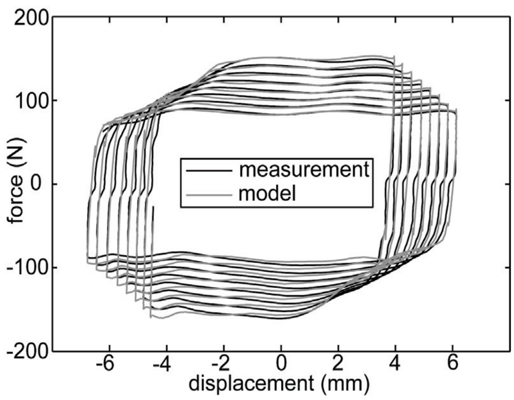

Figure 7: LuGre friction model validation.

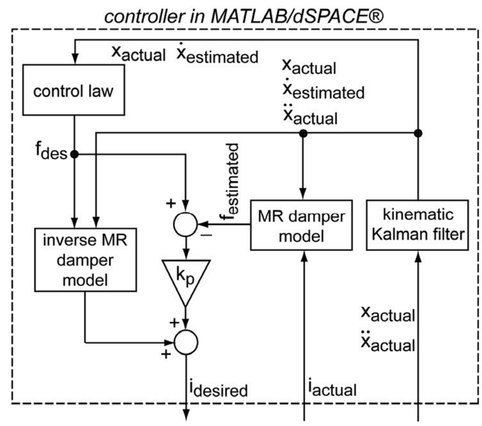

Figure 8: Model-based feed forward

EMULATION OF STIFFNESS WITH FRICTION AND VISCOUS DAMPING

Model-based feed forward control of MR damper force

The states used for the model-based feed forward control of the MR damper force are the actual damper displacement, acceleration and current (Figure 8). The damper velocity is estimated from the displacement and acceleration by a kinematic Kalman filter. The desired current is estimated from the inverse MR damper model which is derived from the validated LuGre friction model. The forward MR damper model, i.e. the validated LuGre friction model, estimates the actual MR damper force and thereby corrects the desired current generated by the inverse model.

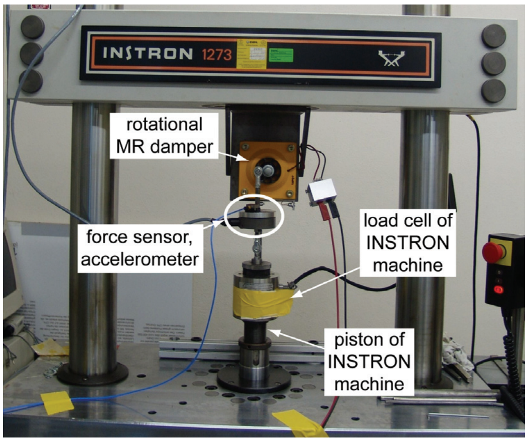

Figure 9: Validation of control approach on INSTRON machine

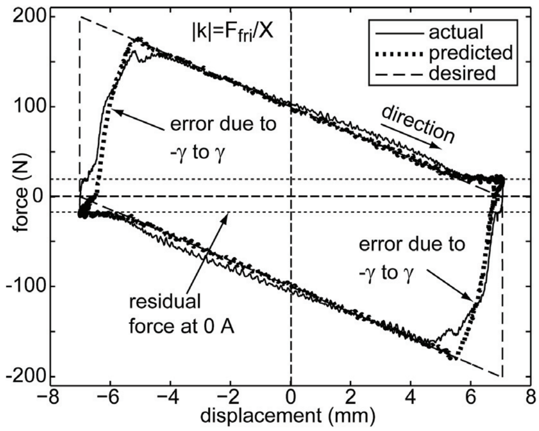

Figure 10: Tracking of friction with negative stiffness with $|k| = F_{fri} / X$

Hydraulic test set-up

The hydraulic machine of type INSTRON shown in Figure 9 is used to operate the MR damper at sinusoidal displacement with defined amplitudes and frequencies. The model-based feed forward control scheme is implemented in MATLAB/dSPACE® and runs at a sampling frequency of 1000 Hz. The desired current output is the command signal of the amplifier of type KEPCO that is operated in current control mode and thereby acts as current driver. The force sensor visible in Figure 9 is used to quantify the force tracking error but is not used as feedback for the force tracking task.

Friction damping with negative stiffness

The desired force f_{des} is the sum of a friction force and a positive or negative stiffness force

$$f_{des} = \begin{cases} \text{sgn}(\dot{x}) F_{fri} \pm k\,x & : |k| \le F_{fri} / X \\ 0 & : |k| > F_{fri} / X \end{cases} \tag{1}$$

where x denotes the damper displacement and $\dot{x}$ its velocity, F_{fri} is the friction force level and k is the stiffness coefficient. (1) results in active desired forces if

$$|k| > F_{fri} / X \tag{2}$$

where X denotes the damper displacement amplitude [15]. Then, (1) is clipped. The difference between the desired and actual forces in case of friction damping with negative stiffness is depicted in Figure 10 for $|k|= F_{fri}/X$ and in Figure 11 for $|k|> F_{fri}/X$. In addition, also the force predicted by the LuGre friction model is plotted. If

$|k| = F_{fri}/X$, the force tracking error mainly occurs when the desired force changes its sign and steps up to its maximum. The force tracking error then results from the inherent response time of the MR damper force as explained in the previous section. The rest of the tracking error is due to the residual force at 0 A. If $|k| > F_{fri}/X$, additional force tracking errors result from the semi-active constraint of the MR damper. The actual force cannot cross the displacement axis but has to follow the residual force until the displacement maximum is reached. Then, when the damper piston starts to move into the opposite direction, the force can change its sign and thereby track the desired force.

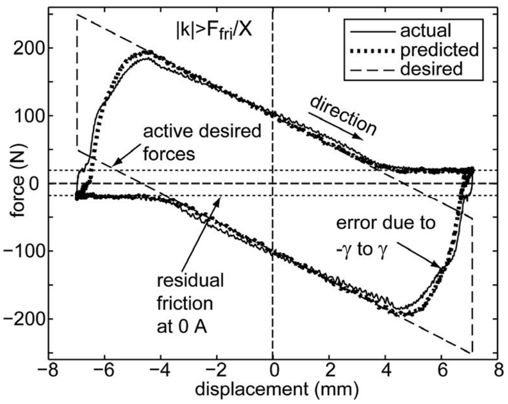

Figure 11: Tracking of friction with negative stiffness with $|k| > F_{fri}/X$

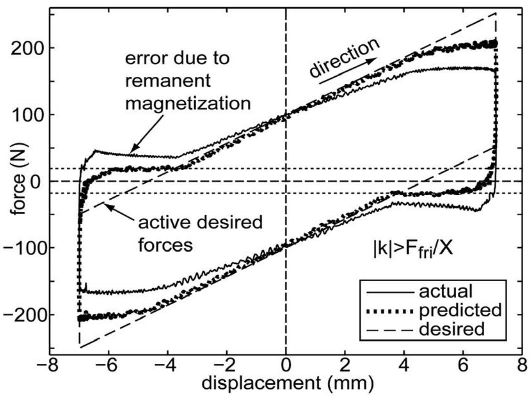

Figure 12: Tracking of friction with positive stiffness with $|k| > F_{fri}/X$

Friction damping with positive stiffness

Figure 12 shows that the force tracking error in case of positive stiffness with friction for $|k| > F_{fri}/X$ mainly occurs at large forces due to maximum current limitations and prediction errors of the MR damper force and when the desired force changes its sign.

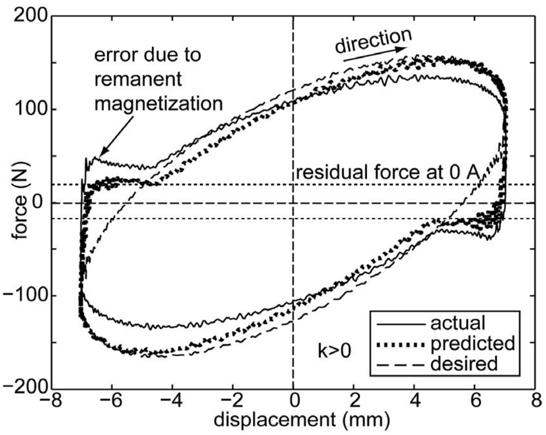

Figure 13: Tracking of viscous damping with positive stiffness with $|k| > 0$

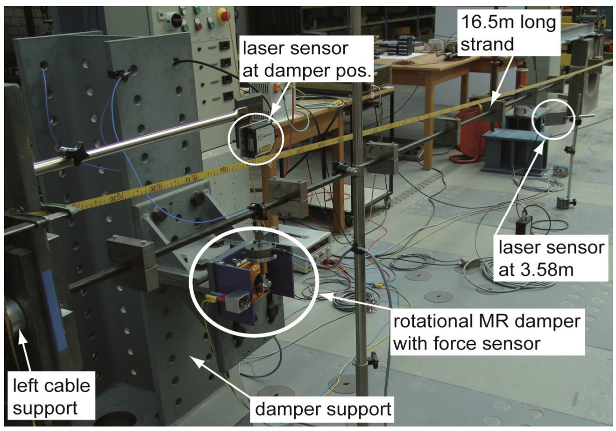

Figure 14: Rotational MR damper connected to 16.5 m long steel wire strand

This second source of force tracking error results from the remanent magnetization of the MR fluid particles and damper housing after the previous force maximum. The remaining magnetization yields increased forces at 0 A compared to the forces obtained from cyclic testing at 0 A [16].

Viscous damping with negative and positive stiffness

The desired force is the sum of a viscous force and a positive or negative stiffness force

$$f_{des} = \begin{cases} c\,\dot{x} \pm k\,x & :(c\,\dot{x} \pm k\,x)\,\dot{x} \geq 0 \\ 0 & (c\,\dot{x} \pm k\,x)\,\dot{x} < 0 \end{cases} \tag{3}$$

where c denotes the viscous damping coefficient. Equation (3) requires clipping independent of c and k. The emulation of Equation (3) is depicted in Figure 13 for positive stiffness which shows the same sources of force tracking error as for friction damping with positive stiffness except that the clipping leads to additional energy dissipation relative to the unclipped control force of Equation (3).

Cable damper set-up

The test cable is a 16.5 m long steel wire strand with rotational MR damper that is connected to the strand at 4% of the cable length from the left cable support (Figure 14). The actual damper displacement is measured by a laser triangulation sensor. The collocated velocity is derived in real-time from a kinematic Kalman filter. The force sensor is used to quantify the force tracking error. The damping performance of the controlled MR damper is assessed by the cable damping ratio of the first mode that is excited by hand. The cable damping ratio is estimated from the free decay response at 3.58 m cable length using the logarithmic decrement method. The control law in Equation (3) is implemented in MATLAB/dSPACE® and runs at 1000 Hz.

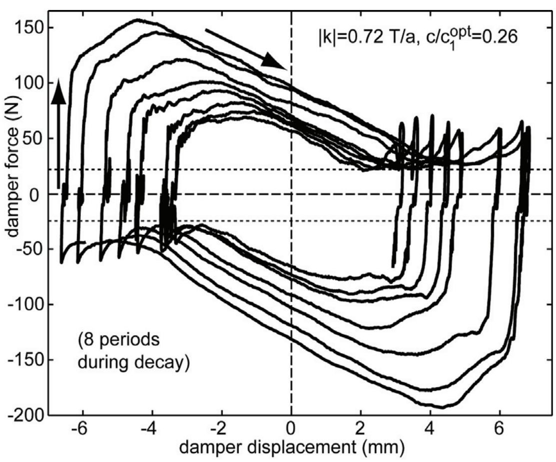

Figure 15: Force displacement trajectory for clipped viscous damping with negative stiffness

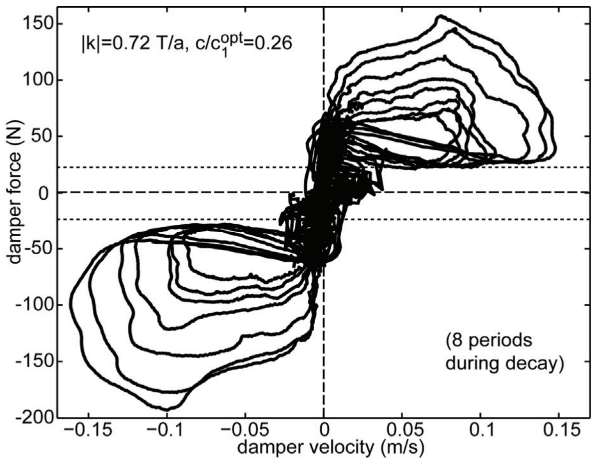

Figure 16: Force velocity trajectory for clipped viscous damping with negative stiffness

Measured clipped viscous damping with negative stiffness

A validated Bingham model of the MR damper under consideration is used for the model-based feed forward force tracking approach. Figure 15 depicts the measured force displacement trajectories during the free decay test due to the tuning $|k| = 0.72\ T/a$ and $c/\ c_1^{opt} = 0.26$. Here, T denotes the cable tension force, a is the damper position and c_1^{opt} is the optimal viscous damping coefficient of a transverse linear damper on a taut string for mode 1 according to Krenk [17]

$$c_{n=1}^{opt} = T\,/\,a\,/\,\omega_{n=1}\ . \tag{4}$$

The shape of the force displacement trajectories is similar to the one resulting from clipped LQR [15,18] which points out that Equation (3) is a simple method to generate almost optimal control forces for the damping of a cable with local damper close to one cable support. Force tracking errors mainly result from the residual force of approximately 22 N. The spikes of the actual force just before it changes its sign result from a too early increase of the damper current due to a slightly too early sign change in the estimated state variable $\dot{x}$. The measured force velocity trajectories in Figure 16 seem to show active force within the active quadrants. However, these forces are due to the pre-yield MR damper behaviour and consequently are not active forces.

Free decay test

Figures 17 and 18 display the time histories of the actual MR damper current and cable displacement at 3.58 m for a typical hand excited free decay test. The excitation level is adjusted such that the MR damper current is not constraint by its maximum of 3 A. Both the small variations of the point-to-point damping ratios and the good agreement between the exponential fit and the local maxima indicate that clipped viscous damping with negative stiffness yields almost amplitude independent cable damping despite of the clipping in (3). This results from the fact that (3) with clipping adjust the cycle energy in the MR damper approximately in proportion to the damper peak velocity and thereby approximately in proportion to the damper motion amplitude.

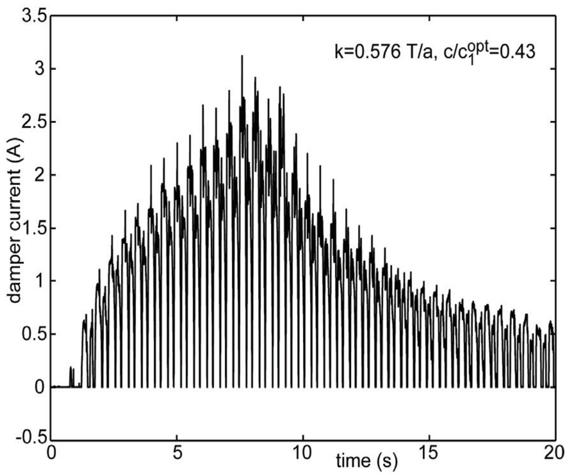

Figure 17: Current time history for clipped viscous damping with negative stiffness

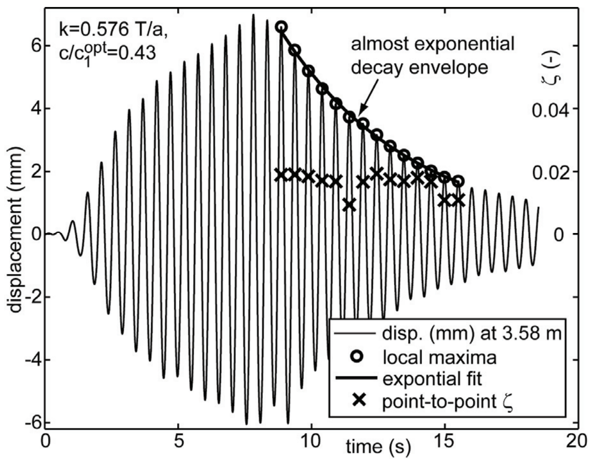

Figure 18: Cable displacement time history at 3.58 m for clipped viscous damping with negative stiffness

Measured cable damping ratio

The damping ratio of the first cable mode is measured for varied control law parameters c and k and also for pure viscous damping as benchmark damper where the MR damper emulates linear viscous damping with k =0 (Figures 19 and 20). According to Krenk [17], the theoretically achievable damping ratio of a taut string with optimal viscous damper is

$$\zeta_{theo} \cong a / L / 2 \tag{5}$$

where L denotes the cable length. Comparing Equation (5) with the results plotted in Figure 20, the emulation of viscous damping only yields 50% of ζ_{theo} .

The losses of 50% are explained by the flexural rigidity of the strand which evokes smaller damper motion [19] and reduces the achievable damping ratio to approximately 80% of Equation (5) [20]. The supplemental losses of 20%-30% are due to the force tracking errors which is discussed in detail in [15]. The experimental results due to clipped viscous damping with negative stiffness demonstrate that this approach generates approximately twice as much damping as optimal viscous damping which is in accordance with other researches [21,22].

A reasonably good tuning of Equation (3) without the danger of clamping effects due to too aggressive tuning is

$$c / c_1^{opt} \approx 0.5, \quad k \approx T / a \quad . \tag{6}$$

The achieved results also point out that fairly high damping in structures can be achieved by MR damper models that neglect the pre-yield region [23].

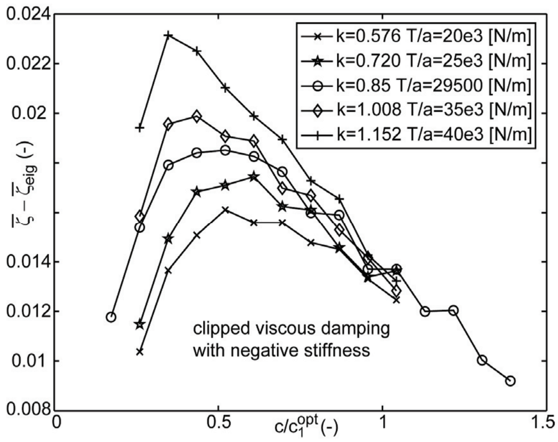

Figure 19: Measured damping ration due to controlled friction stiffness approach

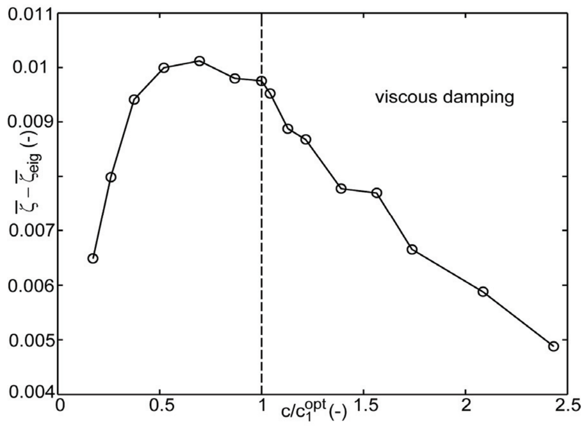

Figure 20: Measured damping ratio due to emulated viscous damping

SUMMARY AND CONCLUSIONS

From observations on a rheometer it is concluded that the MR fluid slides as an entire body relative to the damper housing and sticks to the rotating disc or moving cylinder of the piston where the magnetic flux density is higher. This behaviour generates the predominant friction within the post-yield region. When MR fluid sticks to both adjacent surfaces, then it behaves as a stiffness which is visible in the pre-yield region. Due to the brush analogy, the LuGre friction approach is considered for the MR damper modelling. The model validation shows precise prediction and the model-based feed forward force tracking control scheme leads to small tracking errors. The simpler Bingham model, which does not predict the pre-yield region, is then used to track clipped viscous damping with negative stiffness for cable damping. The resulting force tracking errors are slightly larger than those obtained from the more sophisticated LuGre friction approach. However, the feed forward control scheme based on the Bingham model is able to track sufficiently precise clipped viscous damping with negative stiffness. This is confirmed by the fact that it leads to twice as much damping as viscous damping only which is simpler to track.

INDUSTRIAL PARTNER

Maurer Söhne GmbH & Co. KG, Munich, Germany

REFERENCES

[1] Johnson E.A., Baker G.A., Spencer Jr. B.F. et al, 2007. Semiactive damping of stay cables. *Journal of Engineering Mechanics - ASCE* 133(1), pp. 1-11.

[2] Li H., Liu M., Li J., Guan X. and Ou J. P., 2007. Vibration control of stay cables of the shandong binzhou yellow river highway bridge using magnetorheological fluid dampers. *Journal of Bridge Engineering* 12(4), pp 401-9.

[3] Weber F., Distl H., Feltrin G. and Motavalli M., 2009. Cycle energy control of MR dampers on cables. *Smart Mater. Struct.* 18 015005, pp. 16.

[4] Stelzer G.J., Schulz M.J., Kim J. and Allemang R.J., 2003. A Magnetorheological Semi-active Isolator to Reduce Noise and Vibration Transmissibility in Atomobiles. *Journal of Intelligent Materials Systems and Structures* 14(12), pp. 743-65.

[5] Koo J.H., Ahmadian M. and Setareh M., 2006. Experimental robustness analysis of magneto-rheological tuned vibration absorbers subject to mass off-tuning. *Journal of Vibration and Acoustics – Transactions of the ASME* 128(1), pp. 126-31.

[6] Weber F., Boston C. and Maślanka M., 2011. Adaptive TMD based on the emulation of positive and negative stiffness with MR damper. *Smart Mater. Struct.* 20 015012, pp. 11.

[7] Choi S.B., Lee S.K. and Park Y.P., 2001. A Hysteresis Model for the Field-Dependent Damping Force of a Magnetorheological Damper. *Journal of Sound and Vibration* 245(2), pp 375-83.

[8] Sims N.D., Holmes N.J. and Stanway R., 2004. A unified modelling and model updating procedure for electrorheological and magnetorheological vibration dampers. *Smart Mater. Struct.* 13(1), pp. 100-21.

[9] Tse T. and Chang C.C., 2004. Shear-Mode Rotary Magnetorheological Damper for Small-Scale Structural Control Experiments. *Journal of Structural Engineering* 130(6), pp. 904-11.

[10] Canudas de Wit C., Olsson H., Alström K.J. and Lischinsky P., 1995. A new model for control of systems with friction. *IEEE Trans. Automat. Control* 40(3), pp 419-25.

[11] Jiménez R. and Alvarez-Icaza L., 2005. LuGre friction model for a magnetorheological damper. *Journal of Structural Control and Health Monitoring* 12, pp. 91-116.

[12] Boston C., Weber F. and Guzzella L., 2010. Modeling of a disk-type magnetorheological damper. *Smart Mater. Struct.* 19. 045005.

[13] Maslanka M., Sapinski B. and Snamina J., 2007. Experimental study of vibration control of a cable with an attached MR damper. *Journal of Theoretical and Applied Mechanics* 45(4), pp. 893-917.

[14] Stribeck R., 1902. Die wesentlichen Eigenschaften der Gleit- und Rollenlager – the key qualities of sliding and roller bearings. *Zeitschrift des Vereins deutscher Ingenieure* 46(38,39),pp. 1342-48; 1432-37.

[15] Weber F. and Boston C. 2011. Clipped viscous damping with negative stiffness for semi-active cable damping. *Smart Mater. Struct.* 20 045007, pp. 13.

[16] Oh H.-U. and Onoda J., 2002. An Experimental Study of a Semiactive Magneto-Rheological Fluid Variable Damper for Vibration Suppression of Truss Structures. *Smart Mater. Struct.* 11(1), pp. 156-62.

[17] Krenk S., 2000. Vibrations of a taut cable with an external damper. *Journal of Applied Mechanics* 67(4), pp. 772-6.

[18] Iemura H. and Pradono M.H., 2005. Simple algorithm for semi-active seismic response control of cable-stayed bridges. *Earthquake Engng Struct. Dyn.* 34, pp. 409–23.

[19] Boston C., Weber F. and Guzzella L., 2011. Optimal semi-active damping of cables with bending stiffness. *Smart Mater. Struct.* 20. 055005, pp. 8.

[20] Hoang N. and Fujino Y., 2007. Analytical Study on Bending Effects in a Stay Cable with a Damper. *Journal of Engineering Mechanics* 133(11), pp. 1241-6.

[21] Kurino H., Tagami J., Shimizu K. and Kobori T., 2003. Switching Oil Damper with Built-in Controller for Structural Control. *Journal of Structural Engineering* 129(7), pp. 895-904.

[22] Boston C., Weber F. and Guzzella L., 2009. Optimal semi-active damping of cables: evolutionary algorithms and closed-form solutions. *Smart Mater. Struct.* 18. 055006, pp. 5.

[23] Aguirre N., Ikhouane F., Rodellar J., Wagg D.J. and Neild S.A., 2010. Viscous and Dahl model for MR dampers characterization: A Real time hybrid test (RTHT) validation. *Proceedigns of the 14th European Conference on Earthquake Engineering*, August 30 - September 03. 2005. Ohrid, Republic of Macedonia.

UNCERTAINTY IN PASSIVE AND ACTIVE STABILISATION OF CRITICALLY LOADED COLUMNS

G. C. Enss*

System Reliability and Machine Acoustics SzM, TU Darmstadt, Darmstadt, Germany

R. Platz

Fraunhofer Institute for Structural Durability and System Reliability LBF, Darmstadt, Germany

H. Hanselka

System Reliability and Machine Acoustics SzM, TU Darmstadt and Fraunhofer Institute for Structural Durability and System Reliability LBF, Darmstadt, Germany

*Corresponding author. Email: enss@szm.tu-darmstadt.de

ABSTRACT

Sudden buckling of slender column structures may occur due to axial unforeseen overloads, imperfections or disturbances. Passive and active measures are presented to enhance the critical buckling load of a column to prevent buckling. Thus, uncertain buckling failure due to overloads may be controlled to reduce probability of failure. However, passive and active measures are subject to and also lead to uncertainties. Concepts of active buckling stabilisation are discussed with respect to uncertainties.

INTRODUCTION

Mechanical load-carrying structures may be exposed to mechanical stress, thermal stress, chemical stress and many other stresses during their lifetime, especially during operation. Load carrying structures are designed to withstand mechanical loads and may fail by overloads or fatigue. Whereas fatigue is generally a long-term failure due to relatively moderate loads, overloads may result in a sudden failure. An example for such sudden failure is buckling of axially compressed slender structures. If a slender column is loaded by a load above its critical buckling load, it may buckle. Eventually, this may lead to the collapse of an entire structure. In this article, different passive and active approaches for stabilisation of critically loaded columns and their uncertainties are discussed.

Active or adaptive mechanical systems gain importance in many fields in mechanical engineering. They are characterized by mechanical passive structural elements with functional integrated sensing and actuating capabilities. Active systems may be used in different operating conditions and may react to system changes by a suitable control algorithm [1]. Therewith, they have an augmented functionality and may be more reliable [2]. An overview of applicable smart materials for integration such as shape memory alloys or piezoelectric materials with sensing or actuation properties can be found in [3]. In lightweight structures, e. g. space truss structures, undesired vibrations play an important role as they often are low structural damped [4-6]. For vibration damping purposes, passive solutions are limited in their operating frequency bandwidth most times. Adaptive systems, however, may control broadband vibrations and even fulfill their requirements if system properties like eigenfrequencies of the passive structure change [6]. In machine tools, self excited vibrations may occur in machining centers due to combination of cutting parameters, machine stiffness, environmental conditions etc.

Those undesired vibrations may lead to an unstable cutting process and thereby, maybe, to a lower surface quality [7,8]. Other applications of adaptive mechanical systems can be found in the automotive and aeronautical industry [9,10].

The focus of work presented here lies in the stabilization of critically or over-critically loaded column structures against buckling. Stability of passive columns has been examined thoroughly for four different Euler boundary conditions [3]. The mathematical solution of the critical buckling load of axially compressed columns as well as beam columns loaded also by lateral forces is well documented in [11]. The dynamic behavior of axially loaded structures is extensively treated in [12]. In this work an existing highly sensitive active column system demonstrator is used to examine the effect of uncertain loading conditions on this system's uncertainty to buckle.

In first studies, active stability control was conducted only manually in one plane and in one direction in a simple column exposed to its buckling load [13]. A simple feedback control has been added to avoid buckling of the column in one plane and two directions by means of adaptive measures. These technological steps were accompanied by uncertainty description and assessment to, finally, control uncertainty from loading as well as uncertainties arising from the developed active stabilization technology. This work is part of the Collaborative Research Centre (Sonderforschungsbereich SFB 805): Control of Uncertainty in Load-Carrying Systems in Mechanical Engineering, which is publicly funded by the Deutsche Forschungsgemeinschaft DFG.

PASSIVE SOLUTIONS FOR STABILISATION

To prevent buckling, standards and design guidelines propose the use of safety factors from 3 to 10 against buckling, [14]. The system considered is a flat slender column of length l with a rectangular cross section bh, clamped at the base $x = 0$ and pinned at the upper end $x = l$, Figure 1.

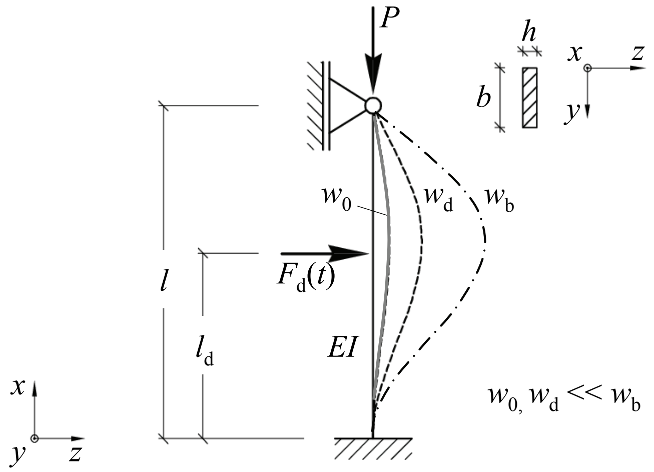

Figure 1: Column system with disturbance force $F_d(t)$

The column's geometric properties are length l and moment of inertia I and material with Young's modulus E. For the presented clamped-pinned column, critical buckling load P_{cr} is [3,11],

$$P_{cr} = \frac{\pi^2 \cdot EI}{(0.7l)^2} \tag{1}$$

that may lead to buckling deflection w_b.

In addition to the buckling deflection w_b other deflections that are non critical and are much smaller than w_b might occur. For example, the deflection w_d due to a lateral disturbing force F_d or a predeflection w_0 due to initial bending or imperfections in assembling the column are present. Selected passive modifications to reduce the structure's possibility of buckling are discussed in [15]. They are based on reducing the column length l, increasing moment of inertia I or reducing material property such as Young's modulus E. This could lead to more stability and an augmented buckling load increasing safety factors.

In technical structures, though, the possibility of changing the geometric or even the material properties of a structure is often not given due to strict boundary conditions and system specifications. If the structure is oversized by a predetermined high safety factor to avoid buckling, the additional weight may always be carried by the system even though only moderate or normal loads affect the structure most times.

To reduce weight, it would be more efficient to have a structure only slightly oversized that carries normal loads and may be stabilized actively just during the few occasions that the structure is overloaded. Furthermore, these passive modifications are still not able to prevent buckling initiated by disturbance forces F_d leading to a triggering deflection w_d, predeflection w_0 of the column or imperfections in its material that may lead to sudden buckling (Figure 1). Active solutions are a possible remedy to uncertainty in loading and system properties.

ACTIVE SOLUTIONS FOR STABILISATION

There is only little work available in literature on active buckling stabilization of column structures or active buckling control. One early approach was made in 1968 with a bracing of two electromagnets applying deflection proportional forces onto the column, resulting in a stabilization of the first buckling mode [16]. In other publications, concepts were presented applying bending moments through embedded shape memory alloys (SMA) in a pre-deflected composite column and experimentally validated with an increase of the buckling load of 11% [17]. Compared to piezoelectric actuators, SMA may apply large deflections at the expense of high applicable forces and high operating frequency. Therefore, their field of application is limited to non-repeated stabilization or static stabilization of already pre-deflected structures such as shown in [17]. Most of the work that followed was based on applying additional forces or bending moments on a column's surface or through clamped and pinned supports [18,19]. Work reported there has been based on shape control with actively applied bending moments distributed along the length of the column, using piezoelectric patch actuators attached to the column's surface. The use of piezoelectric patch actuators is, however, limited because of its inherent characteristics such as small available actuation strain of 0.1 to 0.2% [20].

Though, an increase of a column's critical buckling load up to a factor of 5.6 was achieved experimentally, stabilizing the first bending deflection shape of a thin pinned-pinned steel column with low bending stiffness and small control forces has been discussed in [18]. The column was externally stiffened by the attached piezoelectric patch actuators along its entire surface and additional stiffeners to cover gaps between the actuators. Also, by attaching piezoelectric patch actuators to a slender pinned-pinned plastic column with low bending stiffness, an increase of the buckling load by a factor of 8.8 was shown numerically by stabilizing its first and second bending deflection shape [19]. All of this work achieved active stabilization by controlling the first or higher bending deflection shapes actively. However, the work discussed uses additional devices as actuators and sensors along the column's surface that may not be suitable for example for outside application with environmental influences like humidity or other restrictions to have the surface of the column free from additional devices such as actuators. Furthermore, the influence of disturbances on the controlled system or the effect of uncertainty in operation was not investigated thoroughly. The concept presented in this article has the major advantage of leaving most of the column's surface unchanged without additional active devices and obstacles along the column's length. The actuation force for buckling control is realized close to the clamped end of the demonstrator system that is presented in section below.

DEMONSTRATOR COLUMN SYSTEM

A column system has been developed as a demonstrator to describe, assess and control uncertainties that may lead to buckling. For reasons of clearness, a system has been chosen that is highly sensitive against buckling due to uncertain loading. When an ideal column is loaded by an axial compressive force P equal to its individual critical buckling load P_{cr}, a critical stable equilibrium state occurs and it may buckle inevitably or stay in a straight line. In reality, however, an imperfect column may even buckle if loaded below its critical load due to imperfections in the system properties, for example due to an out of line deflection w_0 or material inhomogeneity. If the actual loading during the column's operation is not fully known, buckling becomes even more uncertain and may occur at lower loads. Generally, a load carrying passive structure should carry the load it is designed for at all times. In case of an active load carrying structure and in view of controlling uncertainty, active stabilization is intended to be activated to prevent buckling failure only if an overload or critical deflection is detected. This deflection may occur due to loading above the column's critical buckling load and a disturbance force F_d or a pre-deflection w_0.

Figure 2 shows the load carrying column system with time dependent active forces $F_a(t)$ near the fixed end to prevent buckling as a schematic sketch and a photograph of the real system. As a major allowance, the active force $F_a(t)$ is chosen to be applied close to the column's fixed end $x = l_a = l/30$ to keep the main part of the column's surface free from additional actuators. Furthermore, and comparing to other work presented in literature, the bending stiffness of this column with dimensions described in Figure 4 is more than 10 times higher [18,19]. High bending stiffness leads to higher necessary active loads along the column's surface that may not be generated by piezoelectric patch actuators any more.

The controlled active force $F_a(t)$ may be activated if the beam column needs to be stabilized quickly due to sudden but short-term axial overloading $P > P_{cr}$ or a lateral disturbance force $F_d(t)$ with $P \geq P_{cr}$. Like in prior concepts, the column is forced in its approximate second bending deflection shape w_2, but this time by active force $F_a(t)$, Figure 2a, instead of moments along the column's length like in [19]. The approximate second bending deflection shape w_2 occurs due to superposition of initial first buckling deflection shape due to F_d or $P > P_{cr}$ and deflection due to F_a [13]. Figure 2b shows the real demonstrator with the column, strain gauge sensors, actuators and a mass to generate the axial compressive load. The pendulum is used to reproducibly apply a disturbance force $F_d(t)$ and the guide rail facilitates the pinned boundary condition at the column's top. For an ideal system, forcing the column into its second bending deflection shape results in a reduction of the buckling length l to effective buckling length $l_d \approx 0.6\, l$ [21]. Thus, the critical load P_{cr} increases by a factor of 2.9 for the given boundary conditions theoretically because of the quadratic relationship of length l in Eq. (1) [11]. The control task is to keep the column deflected in the second bending deflection shape, i. e. keep deflection $w_2(l_d) = 0$ for the supercritically loaded column.

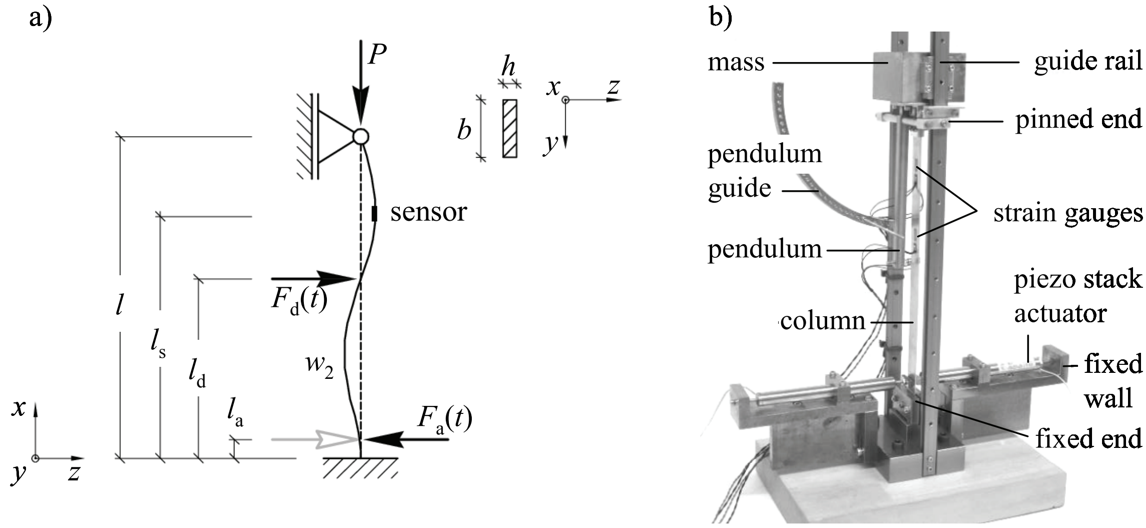

Figure 2: Active column system a) schematic sketch, b) real demonstrator

UNCERTAINTY IN ACTIVE COLUMN SYSTEM

This work deals with both, designing a suitable controller to stabilize the statically unstable system with active forces and studying uncertain disturbances on the actively controlled system critical to buckling. As a hypothesis in the SFB 805, uncertainty occurs when process properties of a system can not or only partially be determined. To describe uncertainties within this active column system, a process analysis was carried out in accordance with the consistent description of uncertainty in processes presented in [21]. Figure 3 shows the process chain for the active column system's life, including the processes 1 development, 2 production and 3 carrying load. At the beginning and at the end of each process, the state of the column system shown as a circle in Figure 3 is described via geometric, material, mechanical, electrical and other properties.

The states are described in detail in Figure 4. The properties of one state is valid for one time step t_n before and after a process with number of time steps $n = 1, 2, \ldots, N$. The aim of the active column system is to carry critical and overcritical loads, thus the process 3 of carrying load is shown in more detail. This enables the visualization and analysis of uncertainties in the corresponding subprocesses. The initial state 3 at time step t_3 just before process 3 of load carrying occurs characterizes the properties of the active column system after production (Figure 4). In this case it is assumed that it does not matter if the system is loaded for the very first time after manufacturing or later in its lifetime. The final state $4n$+3 at t_{4n+3} after process 3.4 generates an active force that is fed again as a loading input into process 3.1 within a feedback control loop. However, for the first time the column is loaded at t_3, the final state after process 3.4 active force generation exists at t_7 for $n = 1$. In the state matrices, major system properties are listed with corresponding categories of stochastic uncertainty (SU), estimated uncertainty (EU) and unknown uncertainty (UU) [22].

The geometric properties like column length l, thickness h, etc. are all categorized as EU as their design parameters vary from the production to the assembly process and uncertainties and information about their lower and upper design limits are given, e. g. l varies from 299.8 to 300.2 mm, but no further measurements were made for this evaluation.

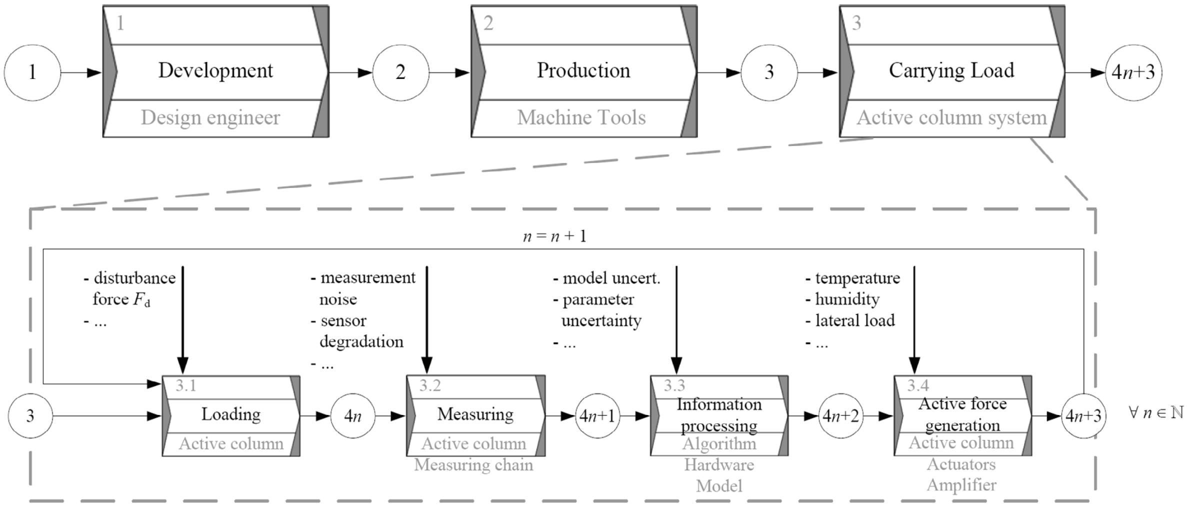

Figure 3: Detailed process chain of load carrying process of active column system

	Time	t_3		Uncertainty		
	Properties					
	Attribute	Nominal Value	Unit	Stochastic Uncertainty	Estimated Uncertainty	Unknown Uncertainty
Geometric properties	Length l	300	mm	-	[299.8, 300.2]	-
	Width b	20	mm	-	[19.9, 20.1]	-
	Thickness h	1	mm	-	[0.99, 1.01]	-
Material properties	Young's-Modulus E	70	kN/mm²	N(70,1)	-	-
Mechanical properties	Critical buckling load $P_{cr}(t)$	27.5	N	-	[27, 28]	-
	Disturbance force $F_d(t)$	-	N	-	-	x
	Active force $F_a(t)$	0	N	-	-	-
	Predeflection $w_0(x)$	-	m	-	-	x
	Measured deflection $w(x,t)$	0	m	-	-	-
	Measured strain $\varepsilon(x,t)$	0	-	-	-	-
Electrical properties	Strain gauge k-factor	1.76	V	-	[1.734, 1.786]	-

Figure 4: Full state matrix at t_3 before loading

Material properties like Young's modulus E are all known with SU, as many experiments exist for this material, giving information about nominal value $E = 70$ kN/mm² with deviations of $\sigma = 1$ kN/mm² being within normal distribution. Some mechanical properties are marked with an x as UU, e. g. the measured deflection w and stain ε, which remain unknown at time t_3 before the loading and measuring processes due to the force F_d at position l_d become relevant (Figure 4). Other mechanical properties are not categorized as uncertain because they simply do not exist on purpose, like the active force $F_a(t)$ is known to be zero before it is applied. Figure 5 shows an extracted section "mechanical properties" only of the state matrix at t_7 of the stabilised column after processes 3.1 loading, 3.2 measuring, 3.3 information processing and 3.4 active force generation shown in Figure 3 have been completed. Only mechanical properties are shown in Figure 5, as they are the major changing properties.

Regarding these four processes, the former uncertain deflection w_d due to the force F_d may now be detected by causing strain ε on the column's surface which can be measured by strain gauge sensors at x = 168 mm (Figure 5). Former unknown uncertainty marked with an x now becomes an estimated uncertainty by measuring deflection and strain tolerances and taking into account the data sheet of the strain gauge sensor. After measurements, the measured deflection $w(x,t)$ deviates between 694 and 706 µm. Furthermore, the process of information processing is introduced to convert the measured signals into control signals for the actuator. The active force F_a = 56 N is now applied and non-zero.

Due to active forces, the column may now carry up to 20% higher axial loads than the original non activated critical buckling load, experimentally. Compared to the uncontrolled passive system, the active system has the major advantage to control buckling failure due to unknown overloads and to react autonomous to a disturbance force F_d.

	Time	**t_7**		**Uncertainty**		
	Properties					
	Attribute	Nominal Value	Unit	Stochastic Uncertainty	Estimated Uncertainty	Unknown Uncertainty
Mechanical properties	Critical buckling load $P_{cr}(t)$	33.5	N	-	[33, 34]	-
	Disturbance force $F_d(t)$	0.15	N	-	[0.13, 0.17]	-
	Active force $F_a(t)$	56	N	-	[52, 60]	-
	Predeflection $w_0(x)$	500	µm	-	[200, 700]	-
	Measured deflection $w(x,t)$	700	µm	-	[694, 706]	-
	Measured strain $\varepsilon(x_i,t)$	42	µm/m	-	[41.6, 42.4]	-

Figure 5: Buckling control – extraction of section "mechanical properties" from full state, state matrix at t_7 of final state after process 3.4 active force generation.

CONCLUSION AND OUTLOOK

The main aim of this work has been to describe, assess and finally control uncertainty in a simple column sensitive to buckling. To achieve this aim, a technology for active stabilisation and disturbance compensation was introduced. Hence, uncertainty in loading may be controlled by an active technology forcing the column into a stabilizing approximate second bending deflection shape. Uncertainty within the active technology was analyzed according to the SFB 805 process model. Future work will focus on stabilization beams with circular cross section that may buckle in an infinite amount of directions. Also time-variant axial loads may be considered. Further in the timeline, the individual active column will be implemented in a truss structure that consists of single passive and active members.

ACKNOWLEDGEMENTS

This research has been funded by the Deutsche Forschungsgemeinschaft DFG within the Collaborative Research Centre (Sonderforschungsbereich SFB) 805.

REFERENCES

[1] Chopra, I., 2002. Review of State of the Art of Smart Structures and Integrated Systems. *AIAA Journal*, 40(11).

[2] Henning, E., Kopsch, D., Krämer, N., Pertsch, P., Pogodzik, N. and Richter S., 2006. Reliability of piezoelectric multilayer actuators. *Actuator 2006*, Bremen.

[3] Hering, E. and Modler, K.H., 2002. *Grundwissen des Ingenieurs*, Hanser, München.

[4] Aizawa, S., Arikabe, T., Fujita, T., Hatayama, T., Kamada, T., Murai, N. and Tohayama, K., 1997. Active vibration control of frame structures with smart structures using piezoelectric actuators. *Smart Materials and Structures* 6, pp. 448-56.

[5] Frapard, B., Lebihan, D., Petitjean, B. and Vaillon, L., 1999. Active isolation in space truss structures: from concept to implementation. *Smart Materials and Structures* 8, pp. 781–90.

[6] Preumont, A., 2002. *Vibration Control of Active Structures: An Introduction*, ISBN 1-4020-0496-6, Kluwer Academic Publishers, Dordrecht.

[7] Mussa, S. and Spath, D., 2001. Active Compensation of Machine Tool Errors with a Piezo Device. *Production Engineering* 8(2).

[8] Denkena, B., Sellmeier, V. and Will, J. C., 2006. Prediction of Process Stability and Dynamic Forces of an Adaptronic Spindle System. *Adaptronic Congress,* 2006, Göttingen.

[9] Harrison, A. J. L., Hillis, A. J. and Stoten, D. P., 2005. A comparison of two adaptive algorithms for the control of active engine mounts. *Journal of Sound and Vibration* 286, pp. 37-54.

[10] Costa, A. P. and Suleman, A., 2004. Adaptive control of an aeroelastic flight vehicle using piezoelectric actuators. *Computers & Structures* 82(17-19), pp. 1303-314.

[11] Gere, J. M. and Timoschenko, S. P., 1961. *Theory of elastic stability*, McGraw-Hill Book Company, 1961.

[12] Virgin, L., 2007. *Vibration of axially loaded structures*, Cambridge University Press, New York.

[13] Enss, G. C., Platz, R., and Hanselka, H., 2010. An Approach to Control the Stability in an Active Load-Carrying Beam-Column by One Single Piezoelectric Stack Actuator. *ISMA 2010 Int. Conf. on Noise and Vibration Engineering*, Sept. 20-22, 2010, Leuven/Belgium, pp. 535-46.

[14] ISO/TS 13725, 2001. Hydraulic fluid power cylinders – Method for determining buckling load.

[15] Enss, G. C., Hanselka, H. and Platz, R., 2011. A survey on uncertainty in the control of an active column critical to buckling. Proceedings of *Int. Conf. on Structural Engineering Dynamics ICEDyn*, June 20-22, 2011, Tavira/Portugal, #17.

[16] Jefferis, R. P., 1968. Feedback control of the buckling instability in an axially compressed thin elastic beam. *Ph.D. Thesis, Dept. of Electrical Eng.*, University of Pennsylvania.

[17] Choi, S., Choi, S. W., Lee, J. J., Seo, D. C., 1999. The active buckling control of laminated composite beams with embedded shape memory alloy wires. *Composite Structures* 47, pp. 679-86.

[18] Berlin, A. A., 1994. Towards Intelligent Structures: Active Control of Buckling, *Ph.D. Thesis, Dept. of El. Eng. and Computer Science*, Massachusetts Institute of Technology.

[19] Wang, Q. S., 2010. Active Buckling Control of Beams Using Piezoelectric Actuators and Strain Gauge Sensors. *Smart Mater. Struct.*, IOP Publishing Ltd. 19(6), 065022.

[20] Meressi, T. and Paden, B., 1993. Buckling control of a flexible beam using piezoelectric actuators. *Journal of Guidance, Control and Dynamics.* ASME 16, pp. 977-80.

[21] Eifler, T., Enss, G. C., Hanselka, H., Haydn, M., Mosch, L. and Platz, R., 2012. Approach for a consistent description of uncertainty in process chains of load carrying mechanical systems. *Applied Mechanics and Materials*, Trans Tech Publications 104, pp. 133-44.

[22] Birkhofer, H., Engelhardt, R. A., Enss, G. C., Hanselka, H., Kloberdanz, H., Koenen, J. F. and Sichau, A., 2010. A Model to Categorise Uncertainty in Load-Carrying Systems. *MMEP Modelling and Management of Engineering Processes*, July 19-20, 2010, Cambridge/UK, pp. 53-64.

HOW SIMULATION OF FAILURE RISK CAN IMPROVE STRUCTURAL RELIABILITY – APPLICATION TO PRESSURIZED COMPONENTS AND PIPES

Dragos D. Cioclov
Fraunhofer IZFP, Saarbrücken, Germany and D. Cioclov Consultant, New York, USA.
Dragos.cioclov@izfp.fraunhofer.de

ABSTRACT

Probabilistic methods for failure risk assessment are introduced, with reference to load carrying structures, such as pressure vessels (PV) and components of pipes systems. The definition of the failure risk associated with structural integrity is made in the context of the general approach to structural reliability. Sources of risk are summarily outlined with emphasis on variability and uncertainties (V&U) which might be encountered in the analysis. To highlight the problem, in its practical and analysis perspective, a short account is given on the nature of failures encountered in pressure vessels and pipe systems, with essential statistical data of service failure. Two engineering analysis tools are invoked: probabilistic fracture mechanics (PFM) and quantitative non-destructive inspection (QNDI). Probabilistic models for risk estimation, in terms of failure probability, are introduced in the classical view of full distribution approach (convolution integral computation) and direct Monte Carlo random simulation of the governing input variables implied in the failure model. The considered end-failure criterion operates with a performance function derived from the elastic-plastic Dugdale crack model, formalized in the failure assessment diagram (FAD) methodology. In the analysis are also integrated probability of detection (POD) models which quantify the chance of flaws/cracks detection by non-destructive inspection, applied intermittently or continuously in a structural health monitoring (SHM) system. he technique of construction of non-parametric confidence intervals on POD vs. crack size rule, by simulated bootstrap re-sampling is presented, in view of setting, presumably safe initial crack size used in fracture mechanics computations. By merging PFM and QNDI via POD, the benefit of applying non-destructive inspection for the purpose of increasing structural reliability is estimated in terms of the decrease of failure probability. The influence of the quality of non-destructive inspection is reflected by POD rule (model). The quantitative approach, structured as a computer code *pvRISK* is provided. A case study of failure risk assessment in PVs is presented and discussed in the context of failure risk management by intermittent inspection or by a SHM system. By sensitivity analysis, as concerns the variability of size of cracks that might subsist in the structure the benefit of applying NDI expressed in terms of reducing the probability of failure by fracture is evaluated.

ON THE MECHANICAL FAILURE RISK ASSESSMENT

The failure risk encountered in industrial components, pressure vessels (PV) included, may be defined by a combined measure of the potential for the component failure (usually by fracture or excessive deformation) and the consequences of the failure. Failure potential of a component is related with failure rate i.e. the frequency of its occurrence. Failure consequences are related with material, financial and image losses, environmental damage and, not ultimately, the danger upon human life. Globally, the risk of an accident may be quantified by the product of the accident frequency of occurrence and the resulted consequences, the latter, usually measured in terms of costs (e.g. [1,2]).
One possible general definition of risk is:

$$RISK\left(\frac{Consequence}{UnitTime}\right) = FREQUENCY\left(\frac{Event}{UnitTime}\right) \times SEVERITY\left(\frac{Consequence}{Event}\right) \tag{1}$$

According to this interpretation, risk frequency assessment may be made by statistical inference on past events (*a posteriori* analysis) or by probabilistic prediction (*a priori* prognostication). The assessment of severity is a matter of economic, social, environment or even of a political nature.
The background of failure risk assessment encompasses and synthesizes essential procedures from various fields of engineering:

1 Non-destructive inspection (NDI) techniques;
2 On-line continuous structural health monitoring (SHM);

3 Fracture mechanics (FM);
4 Reliability theory and probabilistic fracture mechanics (PFM);
5 Computer-assisted simulation of structural damage evolving in operation;
6 Damage tolerance concepts applied to structure with inevitable damage development and structural load-carrying capacity impairment by ageing;
7 Failure consequences evaluation as concerns economy, social and natural environment and, not ultimately, human life, at large.

The failure risk management and alleviation in load-carrying structures has at the core NDI technology. Nowadays, two ways of approach have been matured. On one way, (*i*) inspection is performed in intermittent sessions when the structure is retired from operation (revisions). Raw data resulting from intermittent inspections are processed by applying deterministic and probabilistic quantitative methods and, analysis evaluation and interpretation, the current state of the "structural health" is assessed. Forward in time prognostication of the damage evolution may be also made and, finally, decisions are taken on the further usage (repairs or retirement), maintenance timing during the remnant life. On the alternate way (*ii*), the well defined and scheduled inspection sessions of NDI are replaced by on-line continuously monitoring the "health" state of the structure under real-life operation conditions. Monitoring is achieved by sensing the damage in its various manifestations: cracks, corrosion, creep, wear, erosion, cavitation in hydraulic machinery, the enumeration being not exhaustive. In this approach to structural control and failure risk management, a new paradigm has evolved which is under vigorous development and is referred as structural health monitoring (SHM). It implies that monitoring sensors are permanently and intimately attached or implemented within the structure in "hot spots", usually in a network arrangement. Comprehensive monitoring of vital structures as in aerospace industry may imply networking of a large number of distributed sensors (e.g. [3,4]). The information gathered by sensors is transmitted by wired or, more advanced, by wireless channels to data processing hubs provided locally within the structure, centrally at the location of data processing and evaluation unit, for the entire system or to long distanced centers for global processing of information by expert systems which elaborate vital decision and prognostic of the risk evolution, together with devising, eventually, new maintenance strategies. The most advanced SHM systems, already implemented (aircraft and aerospace vehicles), or under development, present incipient attributes of artificial intelligence or even self-organization capability. SHM benefits from the tremendous development of micro- and nano-electronics, blended with ever increasing digital computation power.
It is worth to emphasize that, given the circumstances, both methods of failure risk management, by distinct session of NDI at scheduled intervals or by continuous SHM are currently applied and this dichotomy will continue for a long time from now. For the strategy based on inspection at pre-set intermittent intervals, methods have been developed for the evaluation of structural failure risk based on integrated probabilistic fracture mechanics (PFM) and quantitative non-destructive inspection (QNDI), (e.g. [5,6]). These already existing methods provide "ready-made" mathematical algorithms and procedures which are directly implementable in the continuous SHM assessing methodology.

In this view, the bases of probabilistic fracture mechanics and quantitative non-destructive inspection are first introduced, with emphasis on their practical aspects used for structural failure risk assessment under both circumstances, i.e. of distinct sessions of NDI and continuous SHM. The developed rationale of fracture risk is focused on pressure vessels and pipe (PV&P) components. In this context, a short outline is given on the ways of approach to the management of structural failure risk established nowadays: on the basis of the statistics of past failures and on the basis of *a priori* quantitative modeling of failure processes for the purpose of prognostication and gaining information for decisions making. In the latter case, probabilistic models in fracture analysis are highlighted according to the two analysis methodologies in use: direct convolution of the probabilistic distribution functions involved in the model and Monte Carlo simulation of model random variables implied in the failure model. Conjointly, it is evinced how QNDI is integrated with PFM via the key random variable which describes the probability of detection (POD) of a flaw (crack) of a certain size. The entire algorithmic construct is organized in *pvRISK* computation code.
The integrated PFM and QNDI construct aims to demonstrate and assess, explicitly, in terms of probability of failure the improvement of reliability which can be achieved by applying non-destructive inspection, intermittently or continuously, of a specified quality, quantified by POD.

FAILURE RISK ASSESSMENT IN PRESSURE VESSELS AND PIPE COMPONENTS

In PV&P current technology, one way to reduce failure risk of PVs is to inspect them periodically and repair or replace the part of the PV that shows signs of deterioration and damage, as is common in pipe lines. Inspection intervals are set on the basis of two main sources of information: past experience by processing historical failure data in terms of frequency and consequences and, prospective simulation, forward in time, using probabilistic models of the fracture process, in either analytical formulation or by Monte Carlo random sampling of key model random variables.

The results of analyses can be systematized in two-dimensional "risk matrix" that defines on one scale the categories of failure potential and, on the second one, the magnitude of consequences. This philosophy underlies the "Risk-Based In-Service Inspection" (RB-ISI) approach to pressure vessels and pipes reliability (see also [7,8]). This methodology is currently applied in nuclear power plants reliability management. Following this way of thinking, the risk matrix estimates enable to rank groups of PVs or parts of PVs systems. The higher ranked items are inspected more often and thoroughly (more on this philosophy is covered by Sundaramajan [9,10]). The key undertaking in ISI approach is the assessment of failure probability evaluated empirically, *a posteriori*, based on past events or *a priori*, prospectively, by modeling the failure as events governed by the random variables of the considered model. On conjoint approach of PFM and QNDI to mechanical failure risk assessment, methods have been tempted and reported, over the years, by the author (e.g. [5,6,11-14]). Obviously, organizations and many other authors have been embarked on this task. Without being exhaustive, because it is virtually impossible to provide a fair and comprehensive overview of this field, one can cite, in historical perspective, organization's guiding documents [8, 15-17] and milestones contributions by individuals or group of authors [7,18-24].

PAST EXPERIENCE ON THE SERVICE FAILURE OF PRESSURE VESSELS AND PIPE SYSTEMS

The failure modes of PVs and pipes systems can be classified as:

- Leak flaws that penetrate the component wall, resulting in visible sign of leakage, generally in limited amounts that comply with technical specifications for allowable limits;
- Failures characterized by larger leaks at rates greater than allowable limits;
- Rupture and breakage occurring on a significant portion of longitudinal or transverse cross-section of the pressure vessel or pipe.

The last category of failure is a serious event which needs a special attention and adequate measures for prevention of its repetition. Hence, a global characterization of failure modes for the purpose of statistical/probabilistic analysis may be accepted into two broad categories: leaks and ruptures. The broad conclusion of the past failures analysis of non-nuclear pressurized components, i.e. pressure vessels and pipes, can be seen in the rate of disruptive failure where rate is in the range of (1 to 5) x 10^{-5}. The rate of non-disruptive failures is about ten times greater, as results from the data given in Table 1 (e.g. [20, 25-29]).

Source	**Number PV & Pipes**	**Nb. in service PV/Year**	**Failures**		**Ruptures**	
			No. Events	**Rate 95% CL**	**No. Events**	**Rate 95% CL**
UK [31]	≈ 20 000	$3.1 \cdot 10^5$	65	$2.6 \cdot 10^{-4}$	5	$3.5 \cdot 10^{-5}$
Germany TÜV [32]	7 000	$6.7 \cdot 10^4$	30	$6.0 \cdot 10^{-4}$	0	$< 4.5 \cdot 10^{-5}$
USA NBBPVI [33]	536 000	$3.0 \cdot 10^6$	1.043	$(3.2 \cdot 10^{-4})$	115	$3.5 \cdot 10^{-5}$

CL – confidence limit; (…), supposedly, mean values

Table 1 – Failure and rupture statistics in PV & pipes. The data presented in this table do not encompass failures and rupture statistics for nuclear PV&Ps. Extensive information on the subject may be found in [15,19,25,29,30,31,32,33].

As concerns failure mechanisms related to PV&P (non- and nuclear) failure, they may be rationalized, as follows, without pretending to reflect a rating as concerns the frequency of occurrence and associated danger: Stress corrosion cracking (SCC) is caused by the simultaneous presence of tensile stress and corrosive medium. The governing variables in SCC-damage are: solution temperature composition and its P_H, metal composition and structures, impurity content and applied stress. The stress may arise from any sources such as, directly applied, residual or of thermal origin. While some of the factors outlined may be absent, the presence of stress above a certain threshold is a necessary triggering condition. Both intergranular and transgranular SCC has been observed.

1 Corrosion attack is induced by chemically active service fluids or microbiological species. Surface crevices and pitting typifies this damage.
2 Mechanical vibrations are induced by turbulent flow, pumps vibration or poor mechanical component design. Alternating stresses may be induced at values above the component fatigue limit prompting fatigue damage. Characteristically for this type of fatigue damage, almost the entire fatigue life of the component is consumed during the phase of crack initiation. Once crack initiated, it propagates steadily and ineluctably to failure.
3 Low cycle fatigue damage is related with repeatedly induced plastic deformation. Low cycle fatigue is generated at sites of severe deformation and geometric stress concentration under repeated pressurization. Under this circumstance the fatigue life can be as low as only some thousand of stress cycles.
4 Thermal fatigue damage is caused by cyclic stresses of thermal origin. High thermal gradients induce stresses in the plastic range. As thermal cycling proceeds the capacity of plastic deformation is exhausted and multiple cracks are generated at the metal surface. In some pipe segments, large radial temperature differences are generated by intermittent contact with cold and hot fluids. This condition, referred to as thermal stratification, tends to bow the pipe. The cyclic occurrence of this condition may result in large alternating global stresses.
5 Corrosion fatigue is the result of the synergic interaction of local corrosion and applied cyclic stress. Under this circumstance crack initiation is accelerated and the fatigue crack growth rate enhanced. Surface pits and crevices, induced in the incipient stage by corrosion attack, act as stress risers where fatigue cracks initiate. High tensile stress at such discontinuities, or at the tip of a propagating crack, cause local plastic strain (metal electric "positivity" is enhanced) and the rupture of the protective oxide film, hence promoting local electro-chemical corrosion processes.
6 Erosion induced damage, in a broad sense, covers metal loss by mechanical friction with the fluids mixed with solid particles.
7 Cavitation is an accelerated local damage caused by rapid pressure variations in the limited areas of restricted turbulent flaw.
8 "Water hammer" degradation is typical for pipes under rapid acceleration or deceleration of fluid flaw cause by pump start, outing or valves closure.
9 There is a rather large category of PVs and pipes failures which have the origin in the design, manufacture, inspection, maintenance and operation, or can be caused by natural events (e.g. earthquakes, winds, waves, freezing, etc.).

It is not uncommon that a failure implies a combination of the outlined damaging mechanisms with synergic conjunction of detrimental factors. In such cases a clear picture of the failure event may be difficult to be discerned.

It is obvious that in any failure event various degrees of variability and uncertainty are involved which renders a probabilistic aspect to failure events. Moreover, the failure risk evaluation in a PV or pipe segment results from the interplay between failure mechanism(s) and the applied NDI programs. A NDI procedure may be ineffective in assuring reliability against fracture if the possible failure event cannot be associated with an identifiable damage mechanism. Now, it is obvious that a strategy of PVs and pipes reliability management must be founded on the clear recognition of damage mechanisms, their physical backgrounds, coupled with plausible engineering models in order to enable quantitative analysis by computation. In mechanical risk analysis due account must be given to the parameters that have a stochastic/random nature. The final quantitative reliability assessment must also account on the quality of NDI techniques reflected in their capacity to sense defects, i.e. by their high probability of detection.

QUANTIFYING THE FAILURE RISK BY FRACTURE MECHANICS

The general context of fracture mechanics

Analytical failure risk assessment in load-carrying components and structures is mainly based on probabilistic fracture mechanics methods (e.g. [5,10,11,23,34]). Fracture mechanics, traditionally, is an engineering discipline that provides quantitative methods for assessing the circumstances under which a load bearing structural element can fail owing to the pre-existence of flaws or induced by outlined damage mechanisms. Once a flaw attains a dominant size, as a crack, it growths continuously under the actions encountered in service. The crack can grow at sub-critical rate, over an extended period of time, owing to cyclic loading and/or adverse environmental effects. The sub-critical growth of one dominant crack leads, inexorably, to the attainment of critical conditions, at which point, the crack rapidly extends in an unstable manner towards fracture. The key ingredients in a conventional deterministic fracture mechanics analysis are: the initial defect size, far-field applied stress, material properties which describe the resistance to sub-critical crack growth and the failure criterion which is associated with unstable, unbounded, crack extension until material separation/fracture. These circumstances are incorporated in the unifying concept of a driving force acting on the crack defect. Under linear elastic response of the loaded body, this concept is referred to the stress intensity factor (SIF). It embodies the intensity of the applied stress field σ_∞ and crack size, a. SIF is expressed in terms of stress intensity factor (SIF), $K = Y\sigma_\infty\sqrt{\pi a}$, where Y is a correction accounting on the geometry of the structural element. Mathematically, sudden fracture, occurs when SIF attains a critical material characteristic, the fracture toughness, Kc expressed in the same units as SIF. Apart from component geometry correction factor, Y, crack-tip plasticity corrections are introduced when the size of the crack-tip plastic enclave, which develops under load, is a non-negligible ratio of the crack size. When significant plastic deformation occurs at crack-tip the methods of elastic-plastic fracture mechanics apply. In this circumstance the Failure Assessment Diagram (FAD) methodology has been developed which is formalized by various prescriptions (e.g. [17,35,36]).

FAD methodology is implemented in *pvRISK* [40] algorithmic construct and code which will be further used to exemplify the failure risk assessment in pressure vessels. The end result of a deterministic fracture mechanics analysis, performed on this line provides for circumstances of monotonously increasing loading, the critical load at fracture or the component life set when loading is applied in cyclic sequences until failure. The evaluation of critical crack size associated with failure is the main part of the aims of the fracture mechanics approach.

Probabilistic models in fracture analysis

As a rule, input parameters in a fracture mechanics analysis are subjected to statistical variability and uncertainty (V&U). Variability is the effect of *chance* and is a function of the system. Variability is objective since it resides in the nature of the involved physical mechanisms underlying, in our case, material damage. It is not reducible by either study or further testing and measurements. It may be reduced, however, by changing the system. Uncertainty is the assessor's lack of knowledge about physical laws, parameters that characterize physical and technical systems. Belongs to sources of uncertainty even the unawareness stemming from semantics i.e. the meaning we attach to the vectors of communication. Uncertainty is reducible by further experiments and study. The alternate concept of the *degree of certainty* is our measure of how much we believe something to be true. In practice, certainty is validated by positive (confirming) experiments.

Variability and uncertainty act conjointly to erode our ability to predict the future behavior of a system. V&U are to be quantified when failure risk assessment is scrutinized. The most common methods available for this purpose are: probability theory, applied statistics, fuzzy logic, neural networks, and elicitation procedures. In the present study only methods pertaining to the theory of probability and applied statistics will be used.

Probabilistic formalism is constructed around the concept of *events* and their *probability of occurrence*. Probabilities are quantified by *random variables* (X) and their associated *distributions*. A specific type of distribution is described by its *repartition function*: $F(x) = prob(x \leq X)$ with $x \in (0,1)$ or by its probability density (PD) function, $f(x) = dF(x)/dx$.

In a probabilistic model some distributions are related with uncertainty about some parameters, other, reflect the variability, i.e. the random nature of underlying physical mechanisms. In the practice of mechanical failures modeling it is not easy to make this distinction so that, as a common rule, it is tacitly accepted that involved random variables reflect the contribution from both sources of randomness.
Quantitative probabilistic models are constructed on the basis of the theory underlying physical processes. Generally, in a probabilistic model, the description and interaction of the parameters governing the physical processes under study is made in terms of random variables. The main methods used to construct PMs pertain to: full distribution method implying the computation of multiple convolution integrals, Markov chains, Bayesian inference, or direct Monte Carlo random simulation. It is important not to forget that mathematical and physical models, fracture models included, are idealization of reality hence, strictly

speaking, all models are more or less accurate approximations. However, by increasing the accuracy of experiments and refining mathematical algorithms, models can approach reality ever more closely.

Full distribution approach to probabilistic fracture mechanics

Full distribution approach of failure risk assessment is formulated rigorously in terms of multiple convolution integrals. The first step on this line is to construct, on the basis of the underlying physical mechanisms, the key random variables, X_i, describing the relevant parameters of the material strength and the loading, together with the functional relationship among them: $Z=z\left(X_1,X_2,\dots X_n\right)$. The failure, or the limit state, is defined by the condition $Z \geq 0$ that represents the multi-dimensional failure surface. Function Z is also termed as performance function. Its representation marks the boundary between the safe and unsafe regions in the space of basic parameters X_i. Failure risk or reliability analysis can be developed in a form that is explicit or implicit in the random variables, X_i. Comprehensive presentation of this way of approach can be found in the literature [10,21,41,42].
Accounting that failure occurs when $Z \geq 0$ the probability of failure results as:

$$P_f=Prob[Z(X_1,X_2,\dots,X_n) \geq 0] \tag{2}$$

or, explicitly, by the convolution integral:

$$P_f=\int \dots \int_{Z(.)\geq 0} f_X(x_1,x_2,\dots,x_n)dx_1dx_2\dots dx_n \tag{3}$$

where $f_X\left(x_1,x_1,\dots,x_n\right)$ is the joint probability density (PD) function of $X_1,X_2,\dots,X_n$ random variables. The integration is performed over the region where $Z(.) \geq 0$.
If the random variables are probabilistically independent, the joint PD function may be replaced under integral sign by the product of mutually independent density functions, $f_{X_i}(x_i)$.

Rigorously, in a comprehensive approach, the joint PD function of random variables is in some degree correlated, making virtually impossible to define it in compact analytical form. Even if this function would be available, the direct evaluation of the multiple integral in Eq. 3 is extremely complicated. Analytical approximations of this integral, that are easy to compute, have been, nevertheless, proposed and are at the base of a multitude of computation algorithms. The majority of these approximations may be grouped into two classes referred to as: first- and second-order reliability methods (FORM and SORM, respectively). Detailed information on these methods can be found in the above mentioned literature and, more specifically, in the monograph of Madsen et al. [42]..

Direct Monte Carlo simulation of failure risk

For a given quantitative model conceived to predict the behavior of a system, Monte Carlo simulation consists of iterations of repeatedly sampling of random values of the model input variables according to theirs distribution. Distribution arguments are generated by inverse mapping a uniform distribution, defined over the interval $(0,1)$ using pseudo-random numbers[1] generated by computer (random numbers), onto the domain of definition of the considered random variable in the model. The sampled random values pertaining to all involved random variables, obtained in one iteration, are used as input in the model computation algorithm, in deterministic formulation and, after a large number of iterations (scenarios), the statistical response of the model is ascertained. On this basis probabilistic inferences on the system behavior may be performed.

Direct Monte Carlo simulation can be applied to estimate the probability of failure on the basis of performance function Z, (*see below*), rather than computing the convolution integral, Eq. 3, for probability

---

[1] Pseudo-random numbers are generated by mathematical algorithms having the property that the generated numbers appear to be independent observations from a uniform distribution defined on the interval $(0,1)$. It is conjectured that decimal digits of the number π are naturally occurring sequences random numbers. This conjecture seems reasonable in the light of Buffon's needle problem [54].

of failure estimation. By Monte Carlo simulation of failure, in every scenario the input variables are drawn automatically according to their probabilistic distributions implied in the model, and then fed into performance function *Z*. After *n* repetitions one counts n_f, the number of scenarios when the condition for failure is fulfilled, i.e. when $Z(.) \geq 0$. An estimation of the probability of failure follows as:

$$\overline{P}_f = n_f / n \tag{4}$$

As, $n \to \infty$, at limit, $\overline{P}_f \to P_f$, the true probability of failure.

The accuracy of Monte Carlo estimation depends on the number of simulation repetitions. It improves with the increase of the number of simulations. The accuracy can be evaluated by assuming that each simulation is a Bernoulli trial. Therefore, the number of failures in *n* trials can be considered to follow a binomial distribution. The coefficient of variation, *COV,* is a measure of statistical accuracy of the estimated probability of failure (e.g. [22,25,43], hence:

$$COV(\overline{P}_f) \cong \frac{1}{\overline{P}_f}\sqrt{\frac{(1-\overline{P}_f)\overline{P}_f}{n}} \tag{5}$$

Table 2 gives a view of the number of Monte Carlo simulations that are necessary to achieve a coefficient of variation of 10% for various levels of the estimated probability of failure $\overline{P}_f$.

Probability of failure $\overline{P}_f$	10^{-3}	10^{-4}	10^{-5}	10^{-6}
***n*- number of simulations**	10^5	10^6	10^7	10^8

Table 2 – Number of Monte Carlo simulation necessary to achieve a P_f accuracy of 10% COV (covariance).

It is obvious from the data presented in Table 2 that Monte Carlo simulation implies an extensive computer time. However, this is a diminishing drawback since the power of computer facilities increases rapidly at decreasing costs. Computer expenses implied in a sufficiently accurate Monte Carlo simulation are nowadays no higher than those associated with the numerical integration in Eq. 3.

PROBABILISTIC DESCRIPTION OF QUANTITATIVE NON-DESTRUCTIVE INSPECTION (QNDI)

Quantitative non-destructive examination encompasses flaws detection and their quantitative evaluation, together with assessing V&U associated with a specific NDI technique in terms of probability of detection (POD).

NDI systems are driven to their extreme capability to find small flaws. To extreme capability of NDI, not all small flaws are detected. V&U result. Because of V&U, NDI capability (implicitly, reliability) is characterized in terms of POD as a function of the flaw size, *a*. *POD(a)* function is defined as the proportion of all flaws of size *a* that will be detected by a given NDI system. Probability of non-detection (PND) is simply the complementary of POD, i.e. *PND=1-POD.*

The POD variation vs. flaw size displays, by the nature of physical limitations of NDI process, a minimum crack size threshold, a_o. This signifies that the flaw must be greater than a threshold a_o, for detection to be possible. Above this threshold POD increases with the flaw size. The POD curve eventually attains a maximum limiting value above which *POD* cannot be increased, presumably that other factors enter into play, such as human errors that might interfere in the detection process.

Probability of detection can be estimated only by statistically planned NDI experiments on specimens containing flaws of known size and position. A large experimental effort has been made in the last decades on this line and extended literature is available about this subject (e.g. [41,42]). Such experiments have enabled to derive various models of POD variation as against the flaw size. Here are some examples: Asymptotic exponential [20]; Log-logistic or log-odds [41]; Asymptotic of power-law type [43].

In handling POD data in fracture mechanics computation it should be taken into account that for a given NDI circumstance, the true probability of detection, as a function of crack size (length), will never be known exactly. The capability of a NDI technique in a given application can only be demonstrated through an experiment in which representative test components with known crack length are inspected and true POD is only estimated by the percentage of correct positive detections. The estimated POD is subjected to statistical variation that results from random influences in the flaws detection process stemming, basically, from random response to the non-destructive interrogation of the material which has, inherently, structural non-homogeneity. Nonetheless, unavoidable variations in the application of NDI technique are also incumbent. The variability reflected in POD is obviously more pronounced in manual NDI in relation either operators skill (human factor), being less dependent on this factor in automatic NDI. Under SHM, though the human factor is virtually non-existent, local failures in the embedded sensors networks, which may be ignored, makes, in the present capacity of SHM that POD is as a rule lower than in the case of NDI performed on the structure retired from service.

Unavoidable finite sample size in POD experiments and, possibly, systematic differences between inspection and in-service conditions introduces additional V&U in POD assessment used in risk assessments. However, statistical methods are available that yield confidence intervals (CI) on the true value of POD. CI derived for a specific sample, i.e. the set of experimental POD data, account for finite size of the sample and, indirectly, on the systematic errors reflected in the POD pattern of variation. Estimation of CI with bounding superior and inferior confidence limits (CL) offers an indirect way to achieve protection against making a wrong decision in choosing the relevant initial crack size on the basis of the capability of POD technique in fracture mechanics simulation of the fatigue crack growth and crack-conditioned sudden fracture.

Recently, new statistical methods have been developed for constructing CI, beyond the classical methodology which imposes, as premise, the knowledge of the theoretical statistical distribution obeyed by the sample (parent sample) under analysis (parametric approach). "Bootstrap" re-sampling method enables to construct CI relaxing this implied condition [44]. The author has developed a two-dimensional bootstrap technique for constructing CIs placed on the analytical form of POD vs. crack size variation (correlation). Figure 1 shows an example of bootstrap simulated re-sampling of POD vs. crack size for the set of data obtained by ultrasonic NDI [48]. Bootstrap simulation has been performed with *pFATRISK* simulation methodology and computer code developed for probabilistic failure assessment under circumstances of fatigue crack propagation in structural elements, specifically in aircraft fuselages treated as pressure vessel under fluctuating internal pressure in takeoff /landing cycles [46].

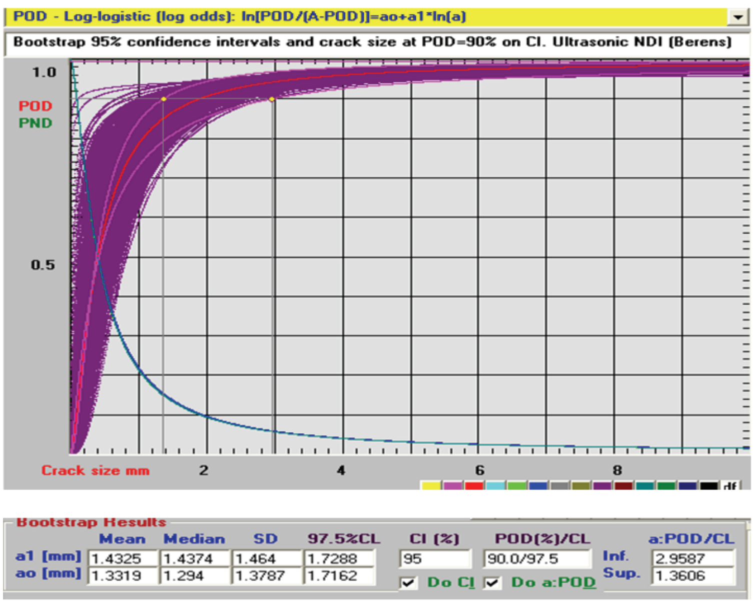

Figure 1 Bootstrap re-sampling of POD vs. crack size correlation and confidence interval construction with example of assessing the crack size at POD = 0.9 on the inferior confidence bound of 95% confidence interval.

In order to quantify and manage the failure risk in aerospace technology, damage tolerance of a structural component is demonstrated by the simulation of the fatigue crack growth. To ensure conservative design at very low levels of probability of failure, presumably lower than 10^{-9}, an equivalent initial flaw (EIF) size is adopted, as incipient flaw, for fatigue crack growth (FCG) simulation. EIF is set at the value of the crack size corresponding on the POD vs. crack size at a high POD value of 0.9 on the inferior confidence limit (CL) of 95% CI (e.g. [50]). This is an "operational", POD-related setting of EIF in FCG simulation in the structural components. For instance, Rummel and Matzkanin [48] give for various NDI techniques, materials and components geometry the value of a_{NDI} (95/90), i.e. the crack length for which it can be shown that there is 95 percent confidence that 90 percent of all cracks of this length will be found. Note that according to this rationale it is a chance (however, very small) that a crack longer than a_{NDI} (95/90) passes undetected through the NDI process. This chance depends not only on the capability of the NDI techniques but also on the distribution of crack length that are present in the component before inspection.

COMPUTATIONAL PROBABILISTIC FRACTURE MECHANICS (PFM)

Probabilistic fracture mechanics offers computational tools for quantifying in an *a priori* or *a posteriori* analysis the failure risk by fracture in terms of failure probabilities, P_f , or the complementary quantity, the reliability, expressed in terms of survival probabilities P_s. Obviously, $P_f = 1 - P_s$.
One way of approach of PFM is to account on the basic V&U encountered in structural design and operation and, on this basis, to evaluate the probability of failure under various loading and environmental circumstances such as static, fatigue, creep, wear, corrosion or a combination of these. Depending on the degree of complexity of the PFM model the following basic model parameters may be regarded as random variables:

1. Material fracture and strength characteristics under static (time independent) loading: ultimate tensile strength (UTS), yield point (YP), and fracture toughness (*Kc, Jc,* critical crck-tip opening displacement, *CTODc,* etc.).
2. Material characteristics related with time dependent damage and final failure. A wide variety of failure modes belongs to this category: material damage related with crack growth by fatigue under repeated loading (e.g. as described by Paris or Forman formalism); material damage by irreversible accumulation of deformation as activated by temperature and applied loading (creep, relaxation, plastic fatigue, thermal "ratcheting", etc.), combined modes with superimposed influence of active environment (corrosion, irradiation, etc.).
3. External loading intensity, statically or repeatedly applied.
4. Flaw size distribution in terms of size, orientation, location and frequency
5. The reliability of non-destructive testing as expressed by *POD(a)* functions.
6. Tentatively, quantification of human factor (reliability) in terms of probabilities to apply successfully a prescribed procedure.

Both probabilistic general methods, by convolution integrals computation and Monte Carlo simulation, are in current use. The models based on convolution integrals are rigorous and of wide generality. Unfortunately, on this line of approach, only few closed form analytical solutions can be obtained for the purpose of P_f or P_s computation and, moreover, these solutions correspond to highly simplified structural geometry and crack configurations (e.g. [11,12]). For structural geometry, loading and other conditions dictated by reality, the convolution integral method becomes very tedious. Nowadays, with the tremendous available computation power, Monte Carlo simulation is a reasonable alternative. Monte Carlo simulation methods are straightforward, of wide generality, with less restrictive assumption and with direct practical potential of application.

In the following, a case study is presented in which Monte Carlo simulation method will be exemplified in an exercise for assessing the failure risk in pressurized pressure vessels and pipes. For this purpose, *pvRISK*, a rationale and a computation code have been developed [37] which integrates PFM and QNDI.

AN OUTLINE OF THE *pvRISK* RATIONALE

General description

pvRISK is a rationale and a code platform devoted to perform fracture mechanics assessments. Failure Assessment Diagram (FAD), as specified in standards (see above), is the implemented failure criterion. This methodology encompasses both elastic dominated (brittle) and elastic-plastic dominated (ductile) fracture.
FAD approach to failure is a two-parameter criterion. One parameter, (K_r = *SIF / material fracture toughness*) pertains to pure fracture mechanics analysis. The other (L_r = *applied load / plastic collapse load*), is evaluated with the methods of plastic limit state theory (or by test). The interaction between the parameters results from Dugdale model of crack tip plasticity or from empirical corrections to this model.
For failures under singular loading (in one loading cycle) the performance function *Z* (see above) is implicitly implemented in FAD. There are enabled various formats of FAD in order to comply with national and international documents [17,36]). This methodology encompasses both elastic dominated (brittle) and elastic-plastic dominated (ductile) of fracture. Stress intensity factors (SIF) are calculated, according to *pvRISK* methodology, by analytical solutions of wide recognizance. There is a possibility to implement SIF fitted data obtained by finite element analysis.

The logic underlying *pvRISK* methodology in the context of analysis of mechanical reliability of load-carrying components is illustrated in Figure 2. Contributions and interactions pertaining to structural mechanics, probabilistic fracture mechanics, material testing, experimental loading evaluation and quantitative NDI are outlined. The main modules of *pvRISK* are:

- *Material module* for the input of material properties related to static fracture: UTS, YP, Kc, and others. All material properties are regarded as random variables (RV) following the most common distributions: Normal, log-normal and three parameters Weibull distribution. Fitted distributions are displayed in various representations as: cumulative probability (CP), probability density function (PDF), with evincing standard deviation (SD) intervals from 1 to 6.
- *Stress Intensity Factor (SIF) module* gives the possibility to choose among many geometry configurations which have compact analytical solutions given in the existing literature. Finite elements result in a table form, i.e. points of SIF geometry correction factor *Y* vs. crack size *a* may be given in the input. *Y(a)* functions and point estimations (Y_I, a_I) are graphically represented. For probabilistic analyses the crack size is defined as RVs with an input distribution, at choice, among several types: normal, log-normal, 3P-Weibull, logistic and extremal distribution or the distribution of statistically simulated crack size at various intervals during fatigue crack propagation.

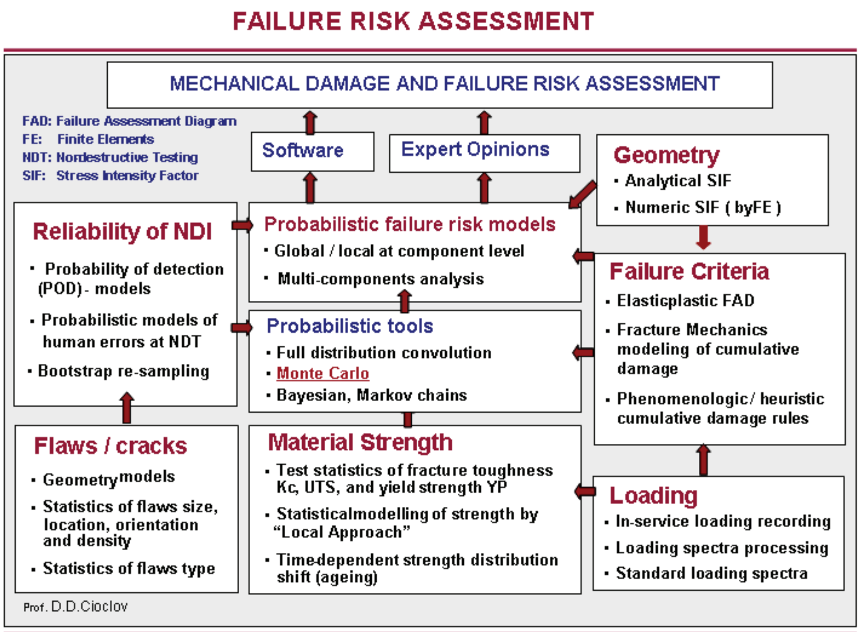

Figure 2 Probabilistic approach to failure risk assessment by the conjoint contribution of structural mechanics, probabilistic fracture mechanics, material testing, loading sensing/recording/evaluation and quantitative NDI.

- *Failure simulation module* (main module) performs static failure analysis under deterministic and probabilistic scenarios. In deterministic analysis, non-failure/failure circumstance is assessed by 2D FAD performance function formulated in two governing variables – K_r and L_r. In these variables, FAD formalism formulates the limit state of the component under analysis represented in K_r, L_r coordinates the boundary between non-failure/failure domains. A safety index is evaluated by the relative position of the component state representative point as against the limit state boundary. Parametric analysis enables to compute critical crack size, loading or material fracture toughness at failure. Probabilistic failure analysis is performed by Monte Carlo simulation of the RVs specified in the input (material strength parameters, crack size and loading intensity). In order to simulate failure vs. non-failure circumstance the Monte Carlo sampling of input parameters are feed into FAD formalism in one iteration. By a great number of iterations the probability of failure results as the ratio of the number of iterations resulting in failure to the total number of iterations. On-line (dynamic) graphical display of the state points in FAD representations portrays the points "cloud" that gives an overall perception of the failure occurrences. In this module the possibility to assess the influence of non-destructive inspection (NDI) via the concept of probability of detection (POD) as function of the flaw (crack) size is implemented. A straightforward evaluation of the failure risk mitigation can be made when a specific NDI procedure characterized by its POD capacity is applied as follows:
    - *POD module* enables to input the rule (distribution) of POD vs. crack size variation. Among the implemented analytical forms of *POD(a)* rules are: exponential, log-normal, logistic, log-logistic (odd-logistic), 3P-Weibull and asymptotic forms of power-law types. A unique feature is implemented in this module, namely, the possibility to perform bootstrap computer re-sampling (e.g. [47]) in the experimental (parent sample) (POD_i, a_i) data. By this procedure it becomes possible to construct non-parametric confidence intervals over the mean correlation POD vs. crack size, *a*. This technique is supplemented with algorithms pertaining to order statistics [5]. In this way conservative lower bounds of POD curves can be ascertained and the representative crack size, $a_{CL/POD}$, at specific confidence level, *CL*, and *POD* (e.g. $a_{90/95}$) can be set for the purpose of defining computational equivalent initial crack for the purpose of fatigue crack growth simulation.

pvRISK has been used mainly for *a priori* estimation (prognosis) of failure probability in pressure vessels and pipes and for *a posteriori* analysis of field failures. This software platform is under continuous development and can be customised for specific applications.

Application of pvRISK rationale to the analysis of failure risk in PVs and pipes

This section considers the case of a gas pipe which being in service for several years was found to be affected by stress-corrosion damage (see similar case descriptions in [49]. The pipe geometry was 610-9.5 mm (24-0.375 in) of API, grade B steel with nominal strength characteristics of UTS = 520 MPa and YP = 350 MPa.

The geometry of the pipe segment under analysis is shown in Figure 3 – together with the SIF correction factors, *Y,* vs. crack size, calculated at the depth tip (size *b*) and surface tip (size *a*) of the inner axial semi-elliptic crack. The internal pressure of the pipe segment is 80 bar.

An axial crack of approximately semi-elliptic geometry was found by ultrasonic NDI on the inner surface of the pipe. It was discerned that the crack depth was of some *b=5 mm* and the length (*2a*) emerging on the inner surface was about of *a=25 mm*. However, the crack length had a less accurately discernible boundary. Obviously, a probabilistic analysis is needed to evince how the failure risk is influenced by uncertainties in the knowledge of the crack size. This undertaken will be further outlined.

Failure risk assessment followed FAD methodology based on strip-yield model [50] underlaying *pvRISK* code which complies with R6/BS-7910 and SINTAP procedures. SIF analytic solution developed by Raju and Newman [51,52] is implemented in *pvRISK* methodology for *Y* factors computation. Figure 3 exemplifies *Y* factors for a crack aspect ratio of *b/a = 0.2*.

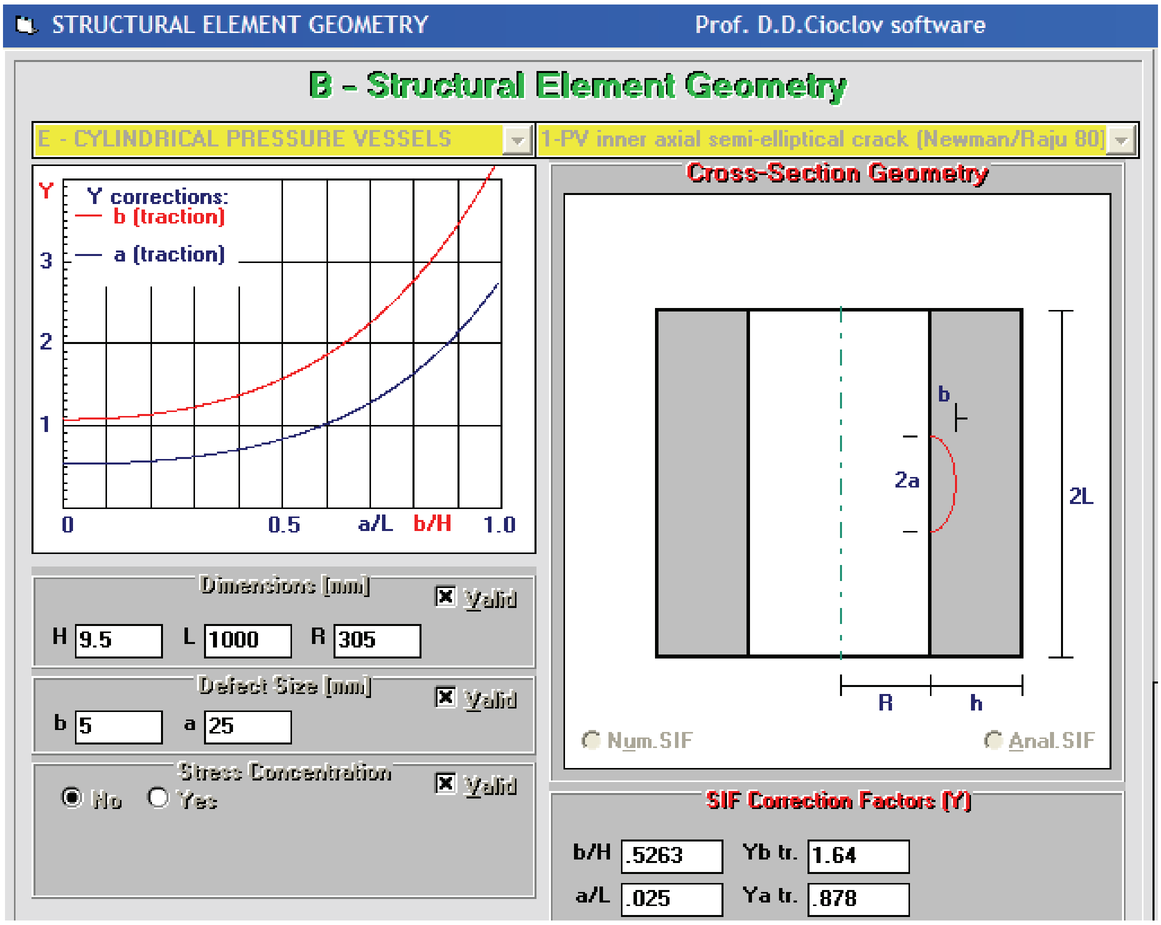

Figure 3 – Geometry characteristics of the pipe and stress intensity factor analysis according to *pvRISK* rationale.

Deterministic FAD analysis

In deterministic FAD analysis with *pvRISK* code, a strip-yield model (Dugdale) has been used. The steps in the analysis follow the R6/BS-7910 procedure. Nominal (mean) material strength parameters are given in Table 3. The results of the FAD analysis are contained in Table 4. Figure 4 shows the results of the deterministic FAD analysis.

Characteristics	**Mean**	**Lower threshold**	**Location param.**	**Shape param.**
UTS MPa	520	480	500	3.5
YP MPa	350	325	350	3.5
Kc $MPm^{0.5}$	100	100	175	4.0

Table 3 Parameters of 3P-Weibull distribution of strength and fracture toughness.

	K $MPm^{0.5}$	**Y**	**Kr**	**Safety Index**
At crack depth, *b*	34.498	1.6382	0.345	1.66
At surface crack tip, *a*	18.466	1.8769	0.185	1.69
Sr (#)	0.592	-	-	-

Table 4 Results of deterministic FAD analysis

It should be noted from data in Table 4 and Figure 4 that the point representation of the state related to the possibility of failure possibility or hence occurrence is seemingly not imminent. The safety index for failure triggering at the crack tip in depth (*b*) and at the surface crack tip (*a*) is 1.66 and 1,69, respectively at a loading intensity of approximately 60% of the plastic collapse load (*Sr* = 0.592). However, V&U which is compellingly involved makes the assessment of failure risk of the pipe component under study necessary by using probabilistic analysis.

Probabilistic FAD analysis

Probabilistic analysis has been made in a combined framework of expert judgment and the evidence of the trend of statistical data, as concerns material strength (UTS), deformation (YP) and fracture toughness characteristics (Kc) described by assumed 3P Weibull distributions, with the parameters outlined in Table 3. As concerns V&U in crack-size estimation, normal distribution has been hypothesized, a usual "custom" when there is no other specific information. The parametric (sensitivity) analysis performed, related to the scatter of the crack size, considers three scenarios of low, moderate and large scatter, parameterized by standard deviation (SD) as made explicit in Table 5.

Crack-size scatter	**Mean *b*/Mean *a***	**SD - *b***	**SD - *a***
Low	5 /25	0.5	2.5
Moderate	5 /25	1.0	5.0
Large	5 /25	1.5	7.5

Crack-size in mm.

Table 5 Parameters of the Normal distribution of the crack-size

In the probabilistic failure risk analysis, Monte Carlo method has been used in the format implemented in *pvRISK* rationale. By repeating a large number of FAD scenarios, Monte Carlo sampling of the key RVs, UTS, YP, Kc, *b* and *a*, has been performed in each of them. In each scenario deterministic FAD assessment has been made using temporarily sampled random key variables, according to their assumed distribution. A statement of failure/non-failure results is then made. The simulated probability of failure, P_f, results simply as the ratio of number of scenarios of simulated failures, n_f, to the total number of scenarios, n, attempted in Monte Carlo simulations:

$$P_f = \frac{n_f}{n} \tag{6}$$

For non-failure, representative points in FAD are positioned inside the domain bound by the limit-state curve, while for failure cases, outside. In the case when low probability values results in simulation, the number of iterations has been increased from 10^5 to 10^6 in order to improve the accuracy of the Monte Carlo simulation.

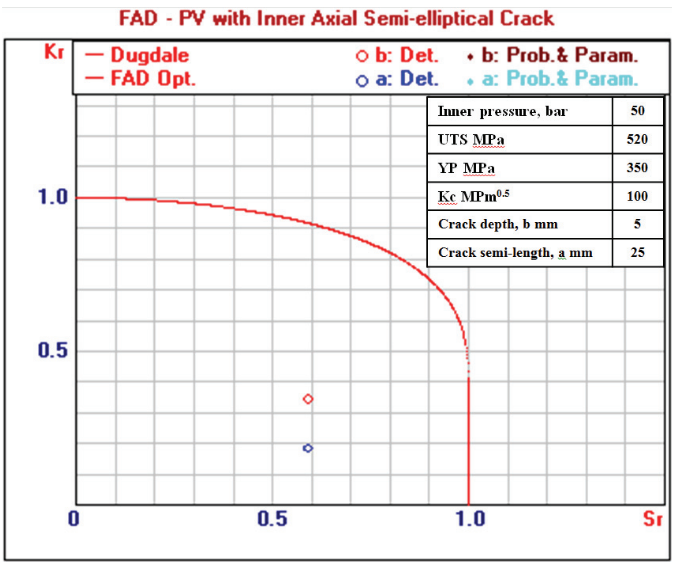

Figure 4. Deterministic FAD analysis representation with positions of points marking the state of flawed pipe as regards the risk of failure

Figure 5 illustrates the graphical display which visualizes the "cloud" of representative points. The "clouds" represent the state points on the FAD for every scenario of simulation with Monte Carlo random sampling of strength characteristics *UTS* and *YP*, fracture toughness *Kc* and crack size parameters *a* and *b*. It should be noted that representations in Figure 5 for series A, do not imply NDI performed before the analysis. The parameters of 3P-Weibull distribution of strength and fracture toughness characteristics are unchanged, as in Table 3. In Series A, no NDI was applied. In Series B, NDI was applied with POD capability as shown in Figure 6.

The trends, evinced by probabilistic analysis in Figure 5, for the case when no NDI is applied, enable to discern some pattern of behavior. As the scatter of the crack size increases the failure risk manifestly increases; compare in Table 6 positions 1, 3 and 5 and the corresponding clouds of state points in Figure 5, positions A1, A2 and A3. While at low scatter estimated failure probability is virtually zero, a high probability of failure results for large scatter of the crack-size. This obvious trend emphasizes the necessity to master the knowledge of crack size statistics in a failure analysis in order to obtain consistent results.

Quantitative NDI

To explore how the application of NDI contributes to a decrease of failure risk the sensitivity analysis has been performed following the scenarios parameterized as given in Table 6. In Monte Carlo simulation, the crack size has the same nominal (mean) values and the same extent of the crack size scatter for the three analysis circumstances as given in Table 5.
The quality of applied NDI is quantified in this study by the probability of detection (POD) as a function of the crack size (here crack depth *b* is considered as the "hot spot" location where final fracture is triggered). Asymptotic exponential [20] POD rule has been considered in the construct of a failure simulation model exemplifying the merge of FAD analysis and POD capability. This POD rule, represented in Figure 6 has the equation:

$$POD = A\left[1 - exp\left(-\frac{a - a_0}{a_1 - a_0}\right)\right] \tag{7}$$

where a, is the crack-size, a_0 is the sensitivity of NDI procedure, i.e. the inferior crack-size threshold under which the crack cannot be detected owing to the limitation of the instrumentation; a_1 is a fitting parameter and $A<1$ signifies that for $POD>A$ no detection is possible, irrespective of the crack size. This circumstance is in the realm of defective NDI instrumentation or human errors in applying the prescribed procedure. In this case-study the following parameters of the asymptotic exponential POD rule have been used: $A = 0.995$, $a_o = 1mm$ and $a_1 = 1.5\ mm$. Figure 6 shows POD vs. crack size representation for these parameters.

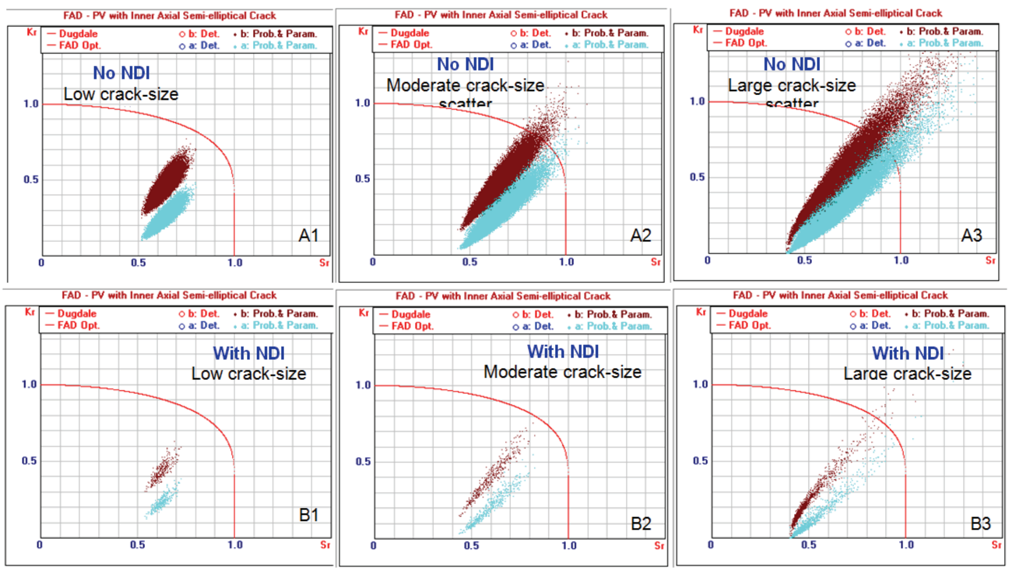

Figure 5. Probabilistic FAD analysis. Normal distributed crack size for low, moderate and large scatter of the crack size.

Implementation of POD rule in FAD methodology enables to evince scenarios when the crack size has the magnitude that might lead to failure but NDI technique is able to detect the flaw. In the simulation, once a crack is detected by the applied NDI, it is considered that efficient corrective measures have been applied implying that the element is repaired at the initial quality or is replaced with a new one. Hence, the scenario is counted as "non-failure", making in the overall counting, which yields the probability of failure, P_f ,

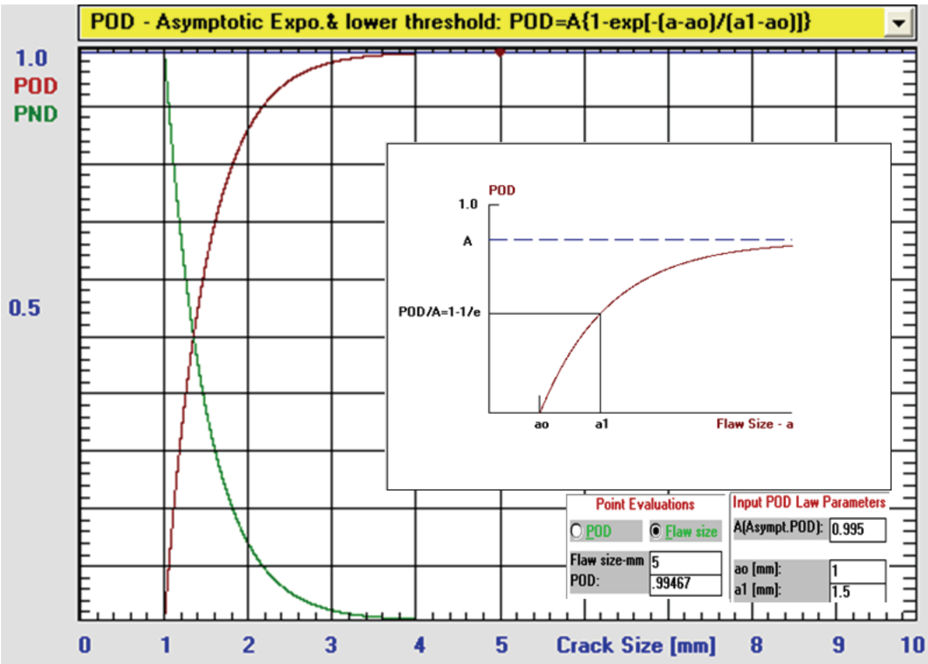

Figure 6 - Variation of the POD and PND as function of the crack size. Asymptotic exponential rule. $A = 0.995$, $ao = 1mm$ and $a1 = 1.5$ *mm*.

Eq. 6. as results from the simulation results, in terms of probability of failure (last column in Table 6), by application of NDI of high quality reflected in the POD vs. crack size curve shown in Figure 6 (POD=0.99467), the probability of failure decreases with nearly two orders of magnitude. When the crack size scatter increases the probability of failure increases but also in these circumstances the benefit of applying a NDI of quality is obvious.

It is worth to note that positions B1, B2 and B3, i.e. circumstances when NDI is applied shows a small number of FAD state representative points than when no NDI is performed. Obviously, the simulated detected cracks are considered as repaired or the element replaced with an unflawed one. However, though for large crack sizes, say over 5 mm, POD is very high, say beyond 0.995, a small chance ($1\text{-}A=0.005$) nevertheless remains that cracks that may escape NDI, irrespective of the crack size and, those in the realm of large cracks to provoke fracture.

No	FAD probabilistic	Crack size scatter	Nb. Simulations	Nb. Detections	Simul.POD[1)]	Nb. Failures	P_f
1	No NDE	low	100.000	-	-	0	0
2	With NDE	low	1.000.000	994.417	0.9944	0	0
3	No NDE	moderate	100.000	-	-	634	$6.34\ 10^{-3}$
4	With NDE	moderate	1.000.000	992.673	0.9927	33	$3.50\ 10^{-5}$
5	No NDE	large	100.000	-	-	4558	$4.56\ 10^{-2}$
6	With NDE	large	1.000.000	980.697	0.9807	189	$1.89\ 10^{-4}$

1) Theoretical POD = 0.99467 at b=5 mm, on source POD vs. crack size curve (Figure 6).

Table 6 – Results of comparative probabilistic analysis of the failure risk when NDI is applied and not-applied.

ON THE IMPLEMENTATION OF PFM & QNDI ANALYSIS IN STRUCTURAL HEALTH MONITORING

When combined PFM & QNDI analysis is performed, a clear differentiation of the circumstances should be stated. In the case under study which is reported in this paper, it was presupposed that combined FAD & POD analysis is performed intermittently, at pre-set timing (e.g. the pipe operation is shut-off or an aircraft is grounded for inspection). When continuous SHM is implemented, which parallels, on-line, the structure operation, the network system of sensors are "tuned" to provide warning at the attainment of a pre-set size,a_w, when it develops in the pipe. Obviously, the warning time, t_w, is random in nature, the randomness being conditioned by the V&U encountered in loading pattern, material response and POD of implemented sensing system. Warning time statistics at the attainment of a pre-set warning crack-size, a_w, can be simulated with *pvRISK* methodology, as detailed in Sect.7, resulting the probability of occurrence $P_t(a_w)$ associated with the warning time t_w, the relationship $t_w \Leftrightarrow P_t(a_w)$ being parameterized by a_w.

By setting the warning time early in the structures life, i.e. for small probabilities of occurrence, P_t , and performing the failure analysis as described in Sects 5 and 6 and 7, then, via P_t, the correlation of failure risk, P_f, with the level of warning crack size level a_w and warning time *tw*can be ascertained:

$P_f \Leftrightarrow P_t(a_w, t_w)$. The only difference in the failure risk assessment in the case of continuous on-line monitoring of the crack size is that in Monte Carlo simulation the crack size assumes a deterministic value at the warning level of the crack size, a_w. This way of approach is exemplified in a companion paper dedicated to failure risk assessment in riveted joints of fuselage structures provided [53].

DISCUSSION AND CONCLUSIONS

The study develops a methodology for integrating probabilistic fracture mechanics with quantitative NDE for the purpose of failure risk assessment in pressure vessels and pipe elements. The uncertainty in our knowledge and the intrinsic random variability implied in the physical mechanisms of fracture, confer an overall probabilistic character to the phenomenon of structural damage and failure. The estimation of the probability of failure may be achieved by integrating probabilistic fracture mechanics with quantitative non-destructive inspection using advanced computing technology.

For structural failure assessment, heuristic probabilistic models have been constructed on the basis of the principles of the probability theory. Key material, loading and crack-size parameters involved in the fracture process are modeled as random variables. Rigorously, probabilistic theoretical models of fracture are formulated in terms of direct distributions convolution which leads to a mathematical formalism expressed in multi-dimensional integrals. On this way, however, only highly simplified geometry of the structural elements can be approached and, few types of distributions describing the scatter of the crack size and material strength and fracture mechanics characteristics have been considered in order to obtain computationally efficient compact analytical solutions. Applied to more realistic structural geometry configurations, the direct distribution approach leads to tedious and, possibly, unpredictable errors that are unavoidable in the numeric approximations of the model multiple-integrals.

An alternate way of approach to failure models is offered by massive computer simulation of fracture models with Monte Carlo technique. Governing random variables of the underlying physical model are sampled according to their distribution functions and the evaluation of failure circumstance is made by a limit state criterion (performance function). In the *pvRISK* methodology the performance function is constructed on the principles of elastic-plastic fracture mechanics embodied in the Failure Assessment Diagram methodology. The accuracy of Monte Carlo simulation is straightforwardly assessed as function of the number of simulation. This relationship is outlined in order to substantiate the relevance of failure risk simulations using *pvRISK* rationale and the associated software. In this context, the concept of probability of detection is presented as being the quantitative framework which enables to take into account the quality of the applied NDI in prognostication of its influence on the reliability of the structure.

A case study is presented in which the application of *pvRISK* methodology to failure risk assessment in a pipe segment with inner semi-elliptic axial crack is exemplified. A parametric study of the influence of crack size scatter has been performed and the benefit of applying NDI is demonstrated in terms of the decrease in probability of failure.

It is obvious that application of NDI of proper quality reflected in the POD rule is beneficial in reducing the risk of structural failure. Applied in a reasonable time schedule by intermittent NDI or continuously by a SHM system, followed by repairs and/or replacements of the damaged components enables to increase structural reliability at levels where the probability of failure is very low.

REFERENCES

[1] RAE (2002). *The societal aspects of risk.* Royal Academy of Engineering, London. UK.

[2] Herkert, J.R. (1994). *Ethical risk assessment: Valuing public perception.* IEEE Technology and Society Magazine , Spring 1994, pp. 4-10.

[3] Boller, C. (2000). *Next generation structural health monitoring and its integration into aircraft design.* Int. J. Systems Sci. V.31, No.11, pp. 1333-1349.

[4] Boller, C., Chang, F-K and Fujino, Y. (2009). *Encyclopedia of Structural Health Monitoring.* Vol. 1-5. Wiley. Chichester.

[5] Cioclov, D.D. (2002), Failure Risk Simulation by Probabilistic Fracture Mechanics and quantitative NDI. *Third American-European Workshop on Reliability of NDI and Demining*, BAM-Berlin, Sept. 2002. *www.9095.net*

[6] Cioclov, D.D. (2006). Probabilistic Simulation of Fatigue Damage. Interaction with Quantitative Non-destructive Testing. Plenary Lect., Annual Assembly, IIW, Bucharest.

[7] Vo, T.V., Gore, E.J., Eschbach, E.J. and Simonen, J. (1989), Probabilistic risk assessment based guidance for piping in-service inspection. *Nuclear Technology,* Vol. 88, pp. 13-20.

[8] ASME (1991), *Risk- Based Inspection Development of Guide Lines.* Vol. 1 and Vol. 2, American Society of Mechanical Engineering, New York.

[9] Sundararajan, C. (1991), *Guide to Reliability Engineering: Data, Analysis, Applications, Implementation and Management.* Van Nostrand Reinhold Pub. New York.

[10] Sundararajan, C. (Ed.), (1995), *Probabilistic Structural Mechanics Handbook Theory and Industrial Applications.* Chapman & Hall, New York.

[11] Cioclov, D.D. (1986), A Model for Fracture Risk Analysis. *Rev. Roumaine des Sci. Techn. Série Mécanique Appliquée,* Tom 31, No. 6, pp 613-622.

[12] Cioclov D.D. and Kröning, M. (1999), Probabilistic fracture mechanics approach to pressure vessel reliability evaluation. PVP-Vol. 386, *Probabilistic and Environmental Aspects of Fracture and Fatigue.* (Ed. Rahman, S.), pp.115-125. The 1999 ASME Pressure Vessel and Piping Conference, Boston, Mss. 1-5 Auguest 1999.

[13] Cioclov, D.D. (1996), Meaning and techniques of risk based assessment of industrial components. Joint German-Indian Workshop, Madras Technological Center, Dec. 1996.

[14] Cioclov, D.D. (1997), Probabilistic vs. Deterministic Methods. Task Force / AG1 RIBA Meeting, Brussels, 20 May 1997, European Commission Directorate XI.

[15] RSS (1975), *Reactor Safety Study. An Assessment of Accident Risk in U.S. Commercial Nuclear Power Plants* - WASH 1400, NUREG - 75/014, Washington D.C., Nuclear Regulatory Commission, 1975.

[16] EPRI (1989), *Probabilistic Seismic Hazard Evaluation at Nuclear Power Plant Sites in the Central and Eastern United States. Resolution of the Charleston Earthquake Issue.* EPRI NP-6395-D (1989). Palo Alto, California; Electric Power Research Institute (EPRI), USA

[17] SINTAP (1999). *Structural integrity assessment procedure for European industry.* Final Procedure, Brite-Euram Project No. BE95-162, British Steel.

[18] Kihara, H. Oba, H and Susei, S, (1971), Precaution for avoiding of fracture of pressure vessels. In: *Practical Application of Fracture Mechanics to Pressure-Vessel Technology. Conference of Applied Mechanics Group of Institutions of Mechanical Engineers, 3rd-5th May, 1977*, pp. 183-189.

[19] Lidiard A.B. (1980). *Application of probabilistic fracture mechanics to light water reactor pressure vessels and piping*. Nuc. Engng. Design, V.60, pp.49-56.

[20] Marshall, W. (1982), *An Assessment of the Integrity of PWR Pressure Vessels: Summary of the Second of the Study Group on PWR pressure Vessel Integrity.* UKAEA, London.

[21] Toft-Christensen, P. and Baker, M.J. (1982), *Structural Reliability Theory and its Application.* Springer Verlag. New York.

[22] Cameron, R.F., Johnson, G.O. and Lidiard, A.B. (1987), The reliability of pressurized water reactor vessels. In: *Probabilistic Fracture Mechanics and Reliability.* Editor, J.W. Provan. Martinus Nijhoff Publishers, The Netherland.

[23] Provan, J.W. (Ed.), (1987), *Probabilistic Fracture Mechanics and Reliability.* Martinus Nijhoff Publishers, The Netherlands.

[24] Ayyub M. B. and McCuen R. (1995), Simulation-Based Reliability Methods. In: *Probabilistic Structural mechanics Handbook. Theory and Industrial Application*, Chapter 4. pp 53-69. Chapman & Hall, New York.

[25] Kellerman, O. and Seipel, H.G. (1967). In *On Containment and Sitting of Nuclear Power Reactors.* Int. Atomic Energy Agency Symp. Vienna.

[26] Engel, J.R. (1976). *Pressure vessel failure statistics and probabilities.* Nucl. Safety, V. 15, No.4, p. 387.

[27] Davenport, D.J. (1991). *A further survey of pressure vessel failures in the UK (1983-1988).* SRD Report , GNSR (HSE)-XSI 1/6.

[28] Nussey, C. (2006). *Failure frequencies for major failures of high pressure storage vessels at COMAH sites: A comparison of data used by HSE and the Netherlands.* www.hse.gov.uk/comah/highpressure.pdf.

[29] NASA (2009). *NASA Requirements for Ground-Based Pressure Vessels and Pressurized Systems. (PVS).* NASA-STD-8719.17.

[30] Smirth, T.A. and Warwick, R.G. (1981). *A survey of defects in pressure vessels in the UK for the period 1962-1978 and its relevance to primary circuits.* SRD report R203.

[31] Gibbons, W.S. and Hackney, B.D. (1964). *Survey of piping failures for the reactor coolant pipe rupture study* . Report GEAP-4574.

[32] Philips, C.A. and Warwick, R.G. (1968). *A survey of defects in pressure vessels built in high statdards of constructions and its relevance to nuclear primary circuit envelops.* AHSD, R 162,

[33] Lidiard, A.B. (1979). *Probabilistic fracture mechanic.* In: *Fracture Mechanics, Current Status, Future Prospects*. Pergamon Press, Oxford, U.K.

[34] HarrisD.O. , Lim, E.Y. and Dedhia, D.D. (1981). *Probability of pipe fracture in the primary coolant loop of a PWR plant.* Probabilistic Fracture Mechanics analysis, V.5 – Load Combination Program. NUREG/CR-2189, TI85 016245.Lawrence Livemore Laboratory, CA, USA.

[35] R/H/R6-Revision (1986): *Assessment of the Integrity of Structures Containing Defects. Authors*: Milne I., Ainsworth, R.A. Dowling, A.R. and Stewart, A. T. British Energy.

[36] BS – 7910 (2000). *Guide on Methods for Assessing the Acceptability of Flaws in Metallic Structures*. British Standard Institution.

[37] Cioclov, D.D. (1999). *pvRISK. A software for risk assessment in pressure vessels and pipes.* User's manual. IZFP Fraunhofer and CEC, Saarbruecken,

[38] Ang A.H.-S and Tang W.H. (1984), *Probability Concepts in Engineering Planning and Design,* Vol. II: *Decision, Risk and Reliability.* John Wiley & Sons, New York.

[39] Madsen, H.O. Krenk S. and Lind N.C. (1986), *Structural Reliability Analysis and Prediction.* Ellis Horwood, London.

[40] Melchers, R.E. (1987). *Structural Reliability and Prediction.* Ellis Harwood, London.

[41] Berens, A.P. and Hovey, P.W. (1981). Statistical Methods for estimation the crack detection probabilities. *ASMT Special Technical Publication,* STP 798, pp 79-94.

[42] Nichols, R.W. and Crutzen, S, (1988). *Ultrasonic Inspection of Heavy Section Steel Components: The PISC – II Final Report.* Elsevier Applied Science.

[43] Cioclov, D.D. (1998). *FATSIM –A Software for fatigue damage simulation*. Internal Note, Fraunhofer Institute of Non-destructive Testing – IZFP, Saarbrücken, Germany.

[44] Efron B. and Tibshirani,R.J. (1979). *An Introduction to the Bootstrap.* Chapman & Hall, New York.

[45] Berens, A.P. (1988). *NDE Reliability Data Analysis.* In: *ASM Metals Handbook*. Vol. 17, 19th Edition: *Nondestructive Evaluation and Quality* Control: 689-701. ASM International, Materials Park, Ohio.

[46] Cioclov, D. D. (2009). *Fatigue failure risk assessment in load carrying components. A probabilistic approach by integration fracture mechanics and quantitative non-destructive inspection.* In: Security and Reliability of Damaged Structures and Defective Materials – NATO Science for Peace and Security, Series C: Environmental., Ed. G.Pluvinage and A. Sedmak, pp. 25-74, Springer, Dordrecht, The Netherlands.

[47] Rummel, W.D. Hardy, G.L., and Cooper, T.D. (1989), *Application of NDE Reliability to Systems.* In: Metals Handbook*,* Vol.17 Nondestructive Evaluation and Quality Control, 9th ed. S.R. Lampman, Techn. Ed., Metal Park , Ohio, ASM International, pp 674-688.

[48] Rummel, W.D. and Matzkanin, G.A. (1996). *Nondestructive Evaluation (NDE) Capabilities Data Book.* Nondestructive Testing Information Analysis Center (NTIAC), Texas Research Institute Austin, TX.

[49] ASM (2002). *ASM Handbook Volume 11. Failure Analysis and Prevention.* Eds. Shipley, R.S. and Becker, W.T. ASM International. Materials Park, OH.

[50] Dugdale D.S. (1960). *Yielding of Steel Sheets Containing Slits.* Journal Mech. Phys. Solids. Vol. 8, pp 100-104.

[51] Raju, I.S. and Newman, J.C. (1980). *Stress-intensity factors for internal surface cracks in cylindrical pressure vessels.* Transactions of ASME, Ser. J, Journal of Pressure Vessel Technology. Vol. 102, pp. 342-346.

[52] Newman Jr. J.C. (1976). *Predicting Failure of Specimens with either Surface Cracks or Corner Cracks at Holes.* NASA TN D-8244, National Aeronautics and Space Administration, June, 1976.

[53] Cioclov, D. D. (2011). *Failure risk assessment by integration of probabilistic fracture mechanics and quantitative non-destructive inspection. A structural health monitoring view.* SMART11 Conference, June, IZFP Saarbrücken.

[54] Buffon, G. (1733). *Editor's note concerning a lecture given in 1933 to the Royal Academy of Science in Paris.* Histoire de l'Academie Royalle des Sciences, pp. 433-435. Paris.

Modelling

DIELECTRIC STACK ACTUATORS WITH INNOVATIVE ELECTRODE DESIGN

W.Kaal*, J.Hansmann & S. Herold

Fraunhofer Institute for Structural Durability and System Reliability LBF, Bartningstr. 47, 64289 Darmstadt, Germany
*Corresponding author. E-mail: william.kaal@lbf.fraunhofer.de

ABSTRACT

In this article a new design for dielectric elastomer stack actuators is introduced. In this approach the electrodes are metallic and therefore rigid compared to the elastomer. However, their perforated microstructure allows a local three-dimensional deformation of the elastomer, leading to a one-dimensional actuator movement. Compared to compliant electrodes metal electrodes promise to be more reliable, show less resistive losses and ease mechanical connections. To analyze the potential of this design a numerical model is set up and studied. Afterwards experimental tests on a variety of electrode designs and elastomer materials are performed. A demonstration actuator is finally designed and built that proves the potential of the concept. The actuator is electromechanically characterized and first reliability tests are carried out.

INTRODUCTION

In contrast to other smart materials dielectric elastomers are known to be capable of large deformations at moderate forces. They promise high potential in actuator applications in various fields, especially since they are likely to become much cheaper than e.g. piezoceramic actuators. To develop an actuator driven with moderate electrical voltage is one challenge to make industrial applications accessible. Therefore the elastomer films need to be manufactured extremely thin and with high precision. Another main technical challenge is to realize compliant electrodes with good electrical conductivity that can undergo large strains without adding too much stiffness. Metal electrodes are normally not feasible due to their high stiffness, though their electrical properties are excellent. Danfoss Polypower has developed a technique to realize flexible metal electrodes by coating a corrugated elastomer film with silver [1,2]. For stack actuators mostly carbon powder electrodes have been realized. Chuc et al. have successfully built a stack actuator with flexible electrodes made of carbon powder mixed in synthetic elastomer [3].

Although good performance can be achieved with these electrode materials in the laboratory they are possibly not favorable for industrial use. Beside their mechanical instability one of the main disadvantages of polymer stack actuators with flexible electrodes is the inhomogeneous strain distribution along its length (Figure 1). Since the outer bounds have to be rigid in order to realize mechanical connections a high strain gradient occurs in the boundary layers [4]. Especially for small actuators with a small number of layers these effects can become dominant.

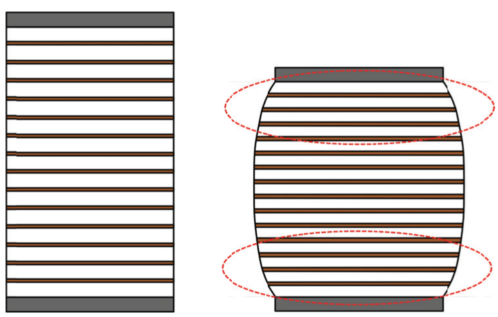

Figure 1: Disadvantageous strain constraint at conventional stack actuators.

In order to avoid an inhomogeneous strain distribution a new design approach is chosen. A stack actuator with rigid, perforated electrodes is considered (Figure 2). Here the whole actuator contracts in one direction only whereas all other directions remain undeformed macroscopically. Internally the elastomer is deformed in all three dimensions.

In this way it is possible to build actuators with only a few layers without losing performance by boundary effects. Mechanical connections to other systems are realized without loss of performance, too. For actuators with only a small number of layers this property is essential due to their performance.

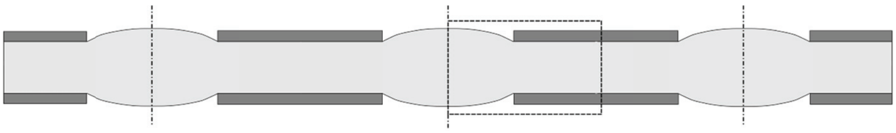

Figure 2: Deformation of elastomer film with structured electrodes (cross section).

NUMERICAL CONSIDERATIONS

In order to prove the performance potential of the new approach and to find an optimum geometry a parameterized finite element model has been set up. It represents one element of an active layer with a 60° hole pattern as shown in Figure 3.

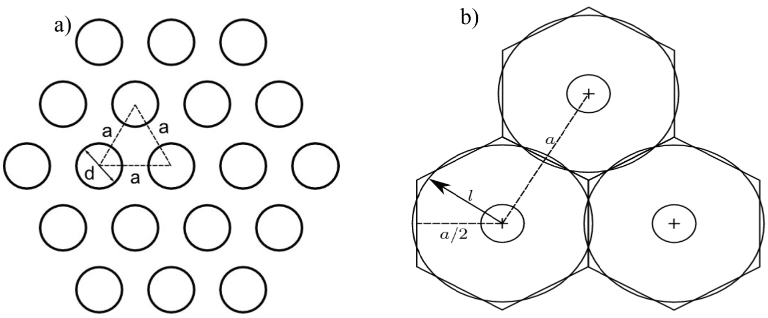

Figure 3: a) 60° hole pattern, b) approximation for 2D-model.

The hole pattern is characterized by two parameters, the hole distance *a* and the hole diameter *d* respectively. Another commonly used parameter for perforated material is the free area ratio ϕ, which can be derived from *a* and *d*:

$$\phi = \frac{\pi}{2\sqrt{3}}\left(\frac{d}{a}\right)^2 \quad (1)$$

To obtain a numerically manageable 2D model the hexagons are approximated by circles with the same area (Figure 3b). The outer radius *l* of the axisymmetric model is then calculated by

$$l = \sqrt{\frac{\sqrt{3}}{2\pi}a} \quad (2)$$

The 2D-representation is shown in Figure 3, which is the basis for the FE implementation. Two normalized dimensionless parameters are introduced to show the results independent of the model size:

$$\lambda = \frac{h}{l}, \quad \phi = \left(\frac{r}{l}\right)^2 \quad (3)$$

This simplified model is used to study the principle behavior of an actuator with perforated electrodes mechanically. It implies full adhesion between the elastomer and the electrode and assumes that the holes are located directly opposite each other. The elastomer is linear elastic (Young's modulus Y_P) and the electrodes are supposed to be much stiffer than the elastomer ($Y_P << Y_E$). Symmetry conditions hold true at the outer radius l. Moreover, the electrodes are constrained only to move in the vertical direction.

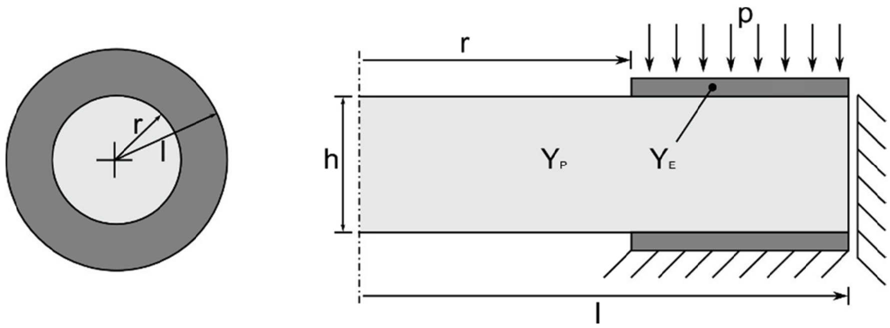

Figure 4. Mechanical 2D axisymmetric model.

As a first step the model is analyzed mechanically for all possible parameter combinations of λ and ϕ. The electrode is loaded with a uniformly distributed mechanical pressure *p* (representing Maxwell pressure) and the displacement of the upper electrode in vertical direction is evaluated. Figure 3 shows the normalized compliance ψ_1 in thickness direction, which is defined as

$$\psi_1 = \frac{x}{h}\frac{Y}{p}. \tag{4}$$

As can be seen for each ratio λ the compliance is largest for a different value of the free space ratio ϕ. The total maximum for the compliance is reached if ϕ tends towards 1 and λ tends towards zero. However, practically this is not a feasible combination, as that would mean an infinitely fine mesh with infinitely large holes. Even if amplitudes are largest here, the generated actuatoric forces apparently go to zero. Therefore, the compliance is multiplied by the solid area ratio ($1-\phi$). That results in a quantity for the work potential of the actuator, assuming that the actuator force is proportional to the electrode area.

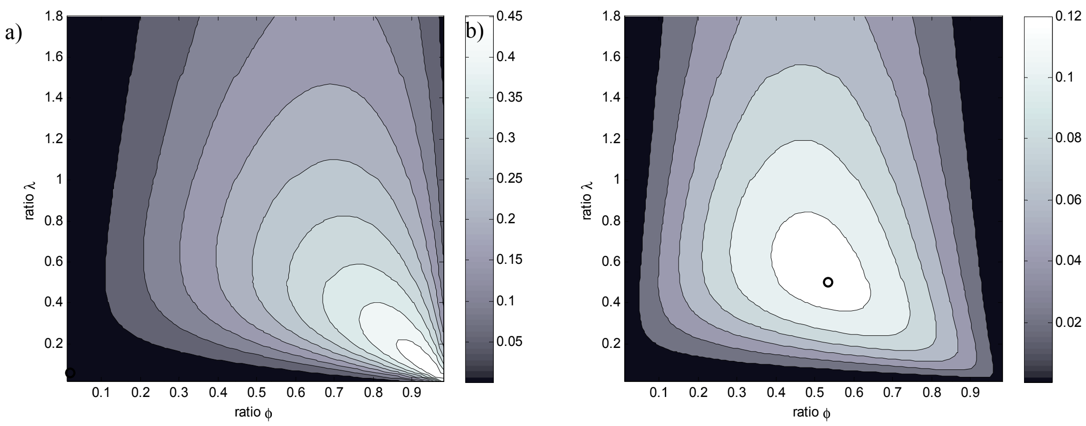

Figure 5: Simulation results of mechanical model: a) ψ_1 b) $\psi_1(1-\phi)$.

Apparently there is a certain optimum for the free area ratio and the thickness ratio if a maximum actuator work is demanded. Both the free area ratio and the thickness ratio should be approximately 50%, resulting in hole diameters that are double the size of the film thickness. Therefore, since the film thickness will have to be 20 to 100 μm in order to keep voltages manageable, the aperture size of the electrode will have to be in the same order of magnitude. The mechanical model is helpful for getting a general insight into the influence of the parameters. However, it does not take into account the inhomogeneous electric field distribution nor higher order effects arising from the electromechanical coupling and is therefore infeasible for exact calculations. It also does not consider the medium in the holes (normally air), which will have an influence on the formation of the electric field. Therefore the FE model is adapted and electromechanical elements for the elastomer and the medium in the holes are used. It can be used to directly calculate the capacitance of the element as well as the free stroke and the blocking force of the actuator. A sketch of the model is shown in Figure 6.

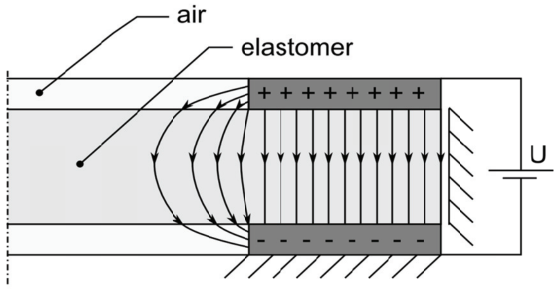

Figure 6: Sketch of the 2D-axisymmetric model with electromechanical coupling.

The following figures show some of the simulation results for an element with a free area ratio of 42%. A small radius at the aperture side was implemented to avoid singularities in the solution, and the FE-mesh was refined around it (Figure 7a). The potential distribution (Figure 7b) is influenced by the air in the holes, leading to an electric field that is mainly concentrated between the electrodes, but also extends in the hole region (Figure 8a). The mechanical strain distribution is quite complex (Figure 8b), the maxima occur at the aperture edges. Therefore the manufacturing quality of the aperture border will define the long-life cycle of the actuator. The deformation in horizontal and vertical direction (Figure 9a and 9b) proves the correctness of the boundary conditions and the symmetric deformation behavior.

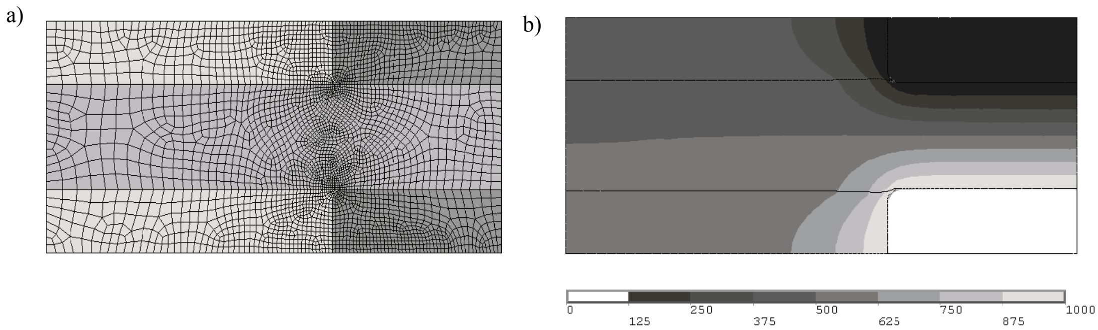

Figure 7: Electromechanical 2D-FE model: a) elements, b) potential distribution.

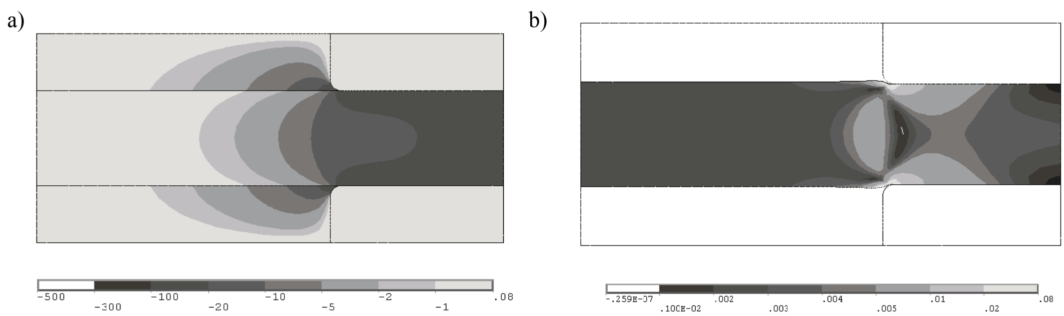

Figure 8: 2D-FE model: a) electric field, b) strain distribution.

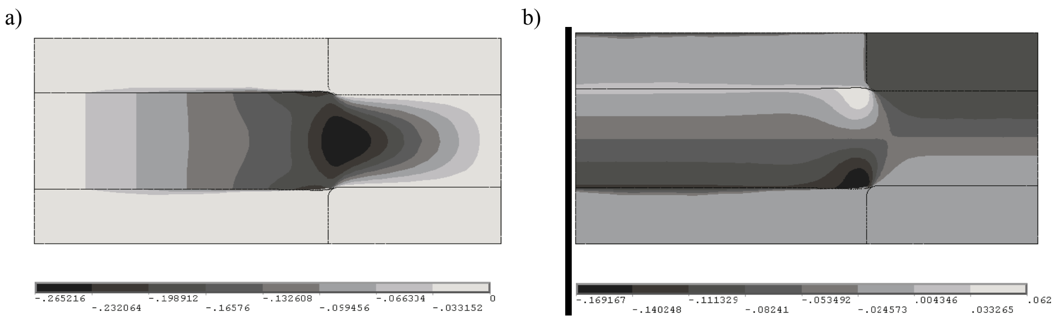

Figure 9: 2D-FE model: deformation in a) horizontal and b) vertical direction.

The electromechanical model can be used to estimate the performance of an actuator with perforated electrodes compared with an “ideal” stack actuator with completely compliable electrodes. Figure 10 shows the result of the simulation of an elastomer of 1MPa, a permittivity of 5 and an electric voltage of 1kV at 50 µm film thickness. It can be seen from Figure 10a that for free area ratios larger than 60% the strain in thickness direction can even exceed that of a stack actuator with ideally flexible electrodes (relative strain 1). But even if the strain is below the ideal strain, an actuator with perforated electrodes may outperform a conventional stack actuator, since in reality the finite compliance of the electrode will add stiffness to the system, thus reducing the actuator’s stroke. The capacitance of the perforated element is of course always below the value for the ideal actuator (Figure 10b). This is a positive effect, because it means that the same stroke can be realized at a smaller capacitance and thus at lower electric input energy.

Especially for dynamic applications the reduction of the actuator’s capacitance will enable the system to be driven with lower currents, allowing the use of smaller voltage amplifiers.

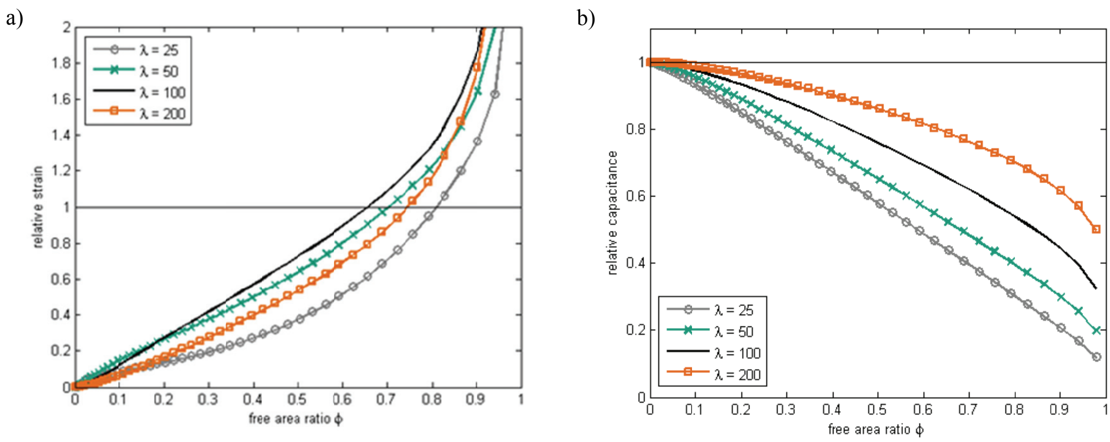

Figure 10: Comparison of a) stroke and b) capacitance of actuators with perforated and compliant electrodes.

The numerical considerations so far have given much insight into the phenomena of the new design approach for stack actuators. Effects arising from misaligned (overlapping) electrode geometries, material nonlinearities (e.g. hyperelasticity) and contact behavior between elastomer and electrode have also been considered, but are not discussed here.

REALIZATION OF AN ACTUATOR

To prove the simulation results and the theoretical considerations different combinations of elastomer and electrode are experimentally analyzed regarding their actuatoric potential. A test stand as shown in Figure 11a is used to characterize stack actuators for static and dynamic input signals. Each electrode can be connected separately to the high voltage source, and the stack is mechanically preloaded with a mass. The dynamic behavior of the system is analyzed by measuring its movement with a laser triangulator, a laser vibrometer and an accelerometer (measurement equipment not shown in Figure 11a).

a) b)

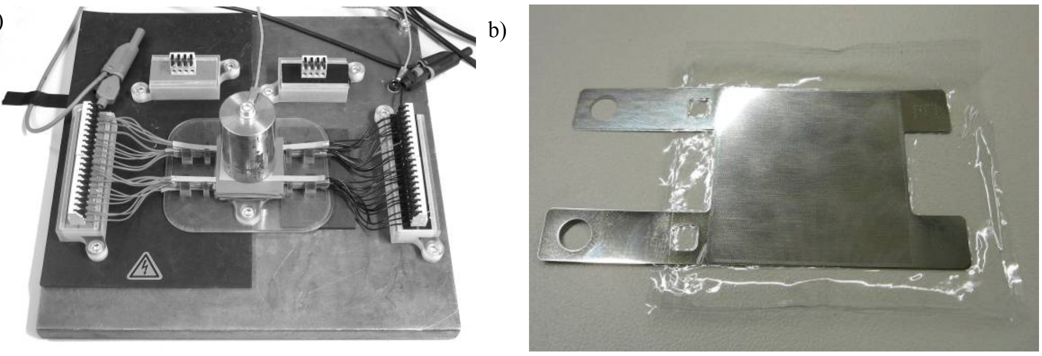

Figure 11: a) Test stand for dynamic characterization of stack actuators b) 4-layer stack actuator with 5 electrodes and PU elastomer.

Figure 11b shows an assembly of four electrodes with three layers of elastomer in between. The hole pattern is placed on a square area of 30 x 30 mm² inside a 0.5 mm width border which is necessary for mechanical stability of the electrodes.

On the left side are the connection lugs for electrical contacting of the electrodes. The cut-outs in the connection lugs are used for geometric alignment of the electrodes when building an *actor* with a larger number of electrodes, as well as the square lugs on the right side.

ELECTRODES AND ELASTOMERS

The actuators were built and tested with different electrodes. Figure 12a and 12b show a microscope photo of two general types that are both manufactured in an electroforming process. The surface of the first electrode type is smooth and the holes are sharp, the holes of the second type are conically shaped, resulting in a more mountainous surface. The thickness of the electrodes was in a range from 0.05 mm to 0.2 mm.

a) b)

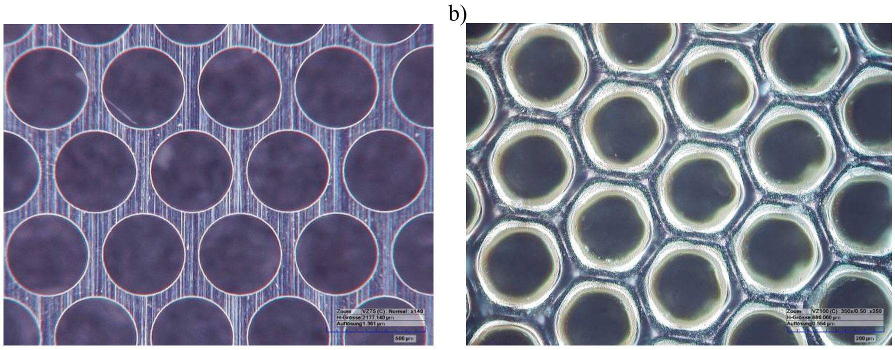

Figure 12: Microscope pictures of different electrode types a) cylindrical holes, b) conically shaped holes.

Different elastomer materials like silicone, natural rubber and polyurethane elastomers were tested likewise. These materials differ in their mechanical and electrical properties. Layers in a thickness range from 35 µm to 200 µm were tested.

FIRST TESTS ON RELIABILITY AND FAILURES

During the tests some actuator assemblies failed based on an electric breakthrough. Figure 12 shows a microscope photo of such a failure. The voltage level at which this failure appears depends theoretically only on the elastomer, its dielectric breakdown strength and thickness. However, the condition of the used electrodes will practically reduce the maximum voltage. Possible causes are sharp edges and burrs that can arise in the manufacturing process of the electrode.

Another source of possible early failures are small particles (dust, dirt, swarf etc.) which are on the electrode. Therefore high demands on a clean assembly environment are necessary. Polluted electrodes should first be cleaned e.g. in an ultrasonic bath. The aim of the actuator design was to have a closed and encapsulated device. The parts of the actuator were manufactured using a rapid prototyping printer (photopolymer jetting).

Figure 13a shows a CAD rendering of the actuator. The housing is shown as a transparent contour. Inside the housing is the stack of electrodes and elastomers which is held between two mounting plates. The lower mounting plate connects the stack with the housing; the upper mounting plate holds a thread which is lead through the housing to connect something to the actuator. The housing itself can be mounted by two M6 screws. The outer dimensions of the actuator are 89x45x13 mm³. Figure 13b shows a photo of the actuator mounted on a base plate with the cover removed. The stack is prestressed using a rubber band. Figure 14 depicts one of the experimental results of the quasistatic measurements. The actuator is driven with a high voltage sinusoidal input and the mechanical response is measured using a laseroptic system. The stroke increases with the voltage almost linearly, although the physical effect is quadratic in nature. The nonlinear stiffness of the system however seems to linearize the overall actuator again, which is a positive effect for most applications. At 1.9 kV the actuator displacement is about 200 µm, which equals about 5.8 % material strain in thickness direction.

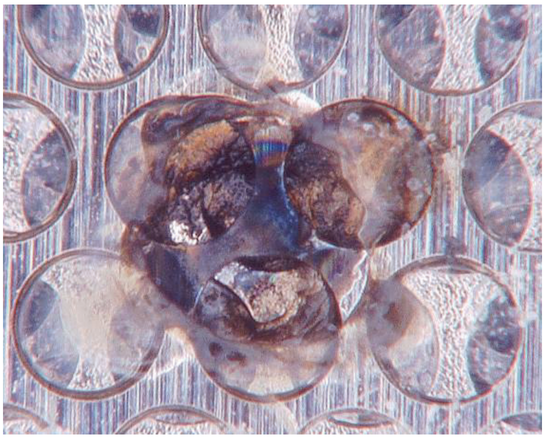

Figure 13: Microscope photo of electric breakthrough.

a) b)

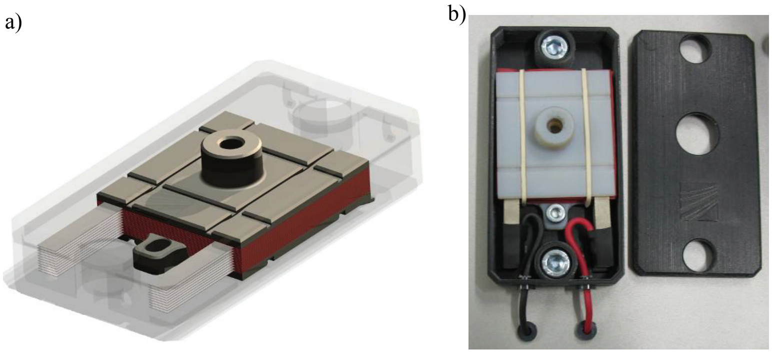

Figure 13: a) CAD rendering of the actuator, b) Actuator with removed cover.

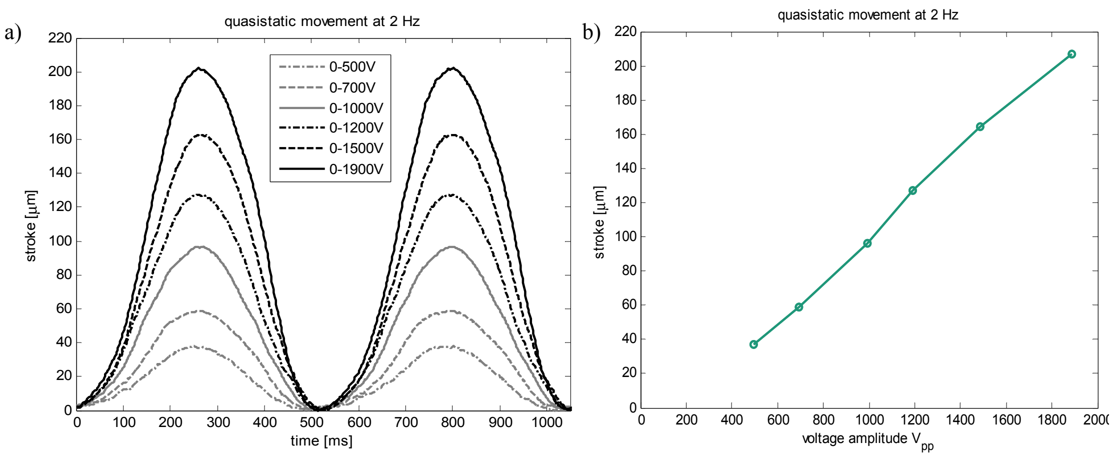

Figure 14: Actuator performance - quasi static movement at 2 Hz.

CONCLUSIONS

The new design seems to be a promising approach to build tailorable electro-active polymer (EAP) actuators for a wide variety of applications. More work will be necessary to optimize the electrode design and to standardize the manufacturing process. One of the mainly still unexplored areas is that of the reliability of EAP actuators. To get a first impression of the reliability of the stack actuator a long term test was carried out. The actuator was mechanically preloaded (*m*= 0.3 kg) and driven for approximately 17 hours in the overcritical state with a 200 Hz signal, which results in ~10^7 load cycles. The velocity was detected with a laser vibrometer. As can be seen from the result shown in Figure 15 the performance increased constantly during the first few hours and reached a saturation level afterwards. The physical effects responsible for that will have to be studied in the future.

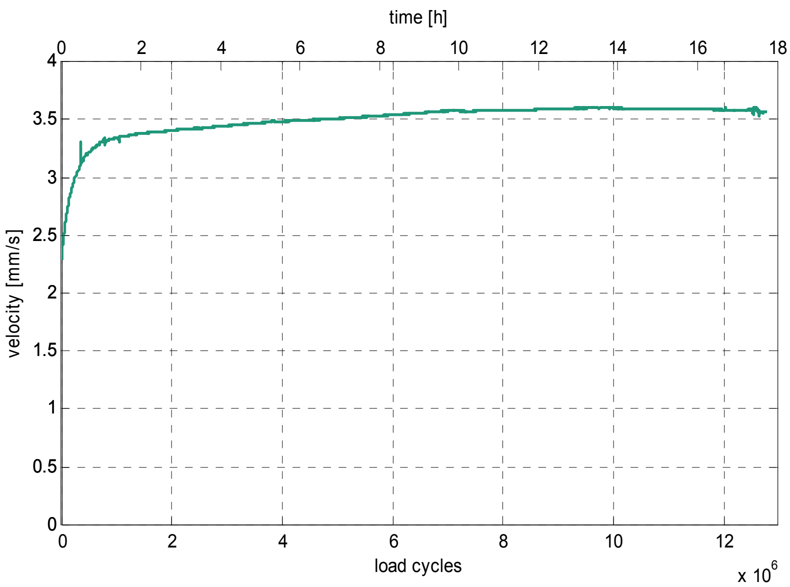

Figure 15: Velocity over time for 10^7 load cycles.

REFERENCES

[1] Wang, P., Lassen, B., Jones, W. R., and Thomsen, B., 2009. Multiscale modeling of a Composite Electroactive Polymer Structure, *20th International Conference on Adaptive Structures and Technologies.*

[2] Jones, W. R., Peng Wang, Lassen, B., and Sarban, R., 2010. *Dielectric elastomers and compliant metal electrode technology*. MELECON 2010 - 2010 15th IEEE Mediterranean Electro-technical Conference, pp. 368-373.

[3] Chuc, H. N., Park, K. J., Thuy, V. D., Kim, S. H., Koo, C. J., Lee, Y., Nam, J.-d., and Choi, R. H., 2007. *Multi-stacked Artificial Muscle Actuator Based on Synthetic Elastomer*, Proceedings of the 2007 IEEE/RSJ International, pp. 771-76.

[4] Kovacs, G., Düring, L., Michel, S., and Terrasi, G., 2009. Stacked dielectric elastomer actuator for tensile force transmission, *Sensors and Actuators A: Physical* 155(2), pp. 299-307.

DEVELOPMENT OF A DAMAGE QUANTIFICATION MODEL FOR COMPOSITE SKIN-STIFFENER STRUCTURES

R. Loendersloot[1], T.H. Ooijevaar[2], A. de Boer[1], & R. Akkerman[2]

[1]University of Twente, Faculty of Engineering Technology, Structural Dynamics & Acoustics, P.O. Box 217, 7500AE Enschede, The Netherlands
[2]University of Twente, Faculty of Engineering Technology, Production Technology, P.O. Box 217, 7500AE Enschede, The Netherlands

ABSTRACT

The development of a model-based approach for a damage severity assessment applied on a complex composite skin structure with stiffeners is presented in this article. Earlier investigations on composite structures with stiffeners revealed that a vibration based structural health monitoring approach employing the Modal Strain Energy Damage Index algorithm can detect and localise delaminations. The next step performed in the part of the research presented is to assess the severity of the damage. It is shown that parametric studies enhance the reliability of the damage severity assessment based on measured data, since a wide range of damage cases can be studied in advance, possibly under variable environmental conditions. The benefit of numerical models is also found in the ability to select measuring points in a smart way, hence optimising the efficiency of the data acquisition system. The amount of damage related information is maximised for a minimal number of sensor positions.

INTRODUCTION

A substantial amount of research effort is spent recently on Structural Health Monitoring (SHM) for civil, offshore, oil and aerospace applications [1,2]. The latter is a still relatively new area of research. This is due to the complexity of the components and the high demands on safety and reliability of the SHM-system. A range of technologies, comprising structural vibration and propagating wave technologies is employed for health monitoring purposes. The first method provides data that is relatively easy to interpret and relatively complex structures can be analysed but damage identification is limited to relatively large damages such as delaminations [3]. Wave propagation technologies employing higher frequencies, are considered to be more powerful as they are capable of detecting small damages such as cracks [4-6]. The downside is the more complex interpretation of the data, in particular in case it concerns non-flat structures.

Here, the structural vibration approach is selected because both the structure (panel with stringers) and the material (multi-layered composite) are relatively complex and the initial goal is to identify relatively large damages such as delamination (hence: no micro cracks). A limitation of the current SHM technologies is the ability to estimate the severity of the damage accurately. The evolution from level 2 to level 3 (diagnostic, see [3]) damage identification will be a crucial step forward to realise SHM-applications. Damage severity indices related to the modal strain energy are introduced [7-9] but lack confidence. It was suggested by others (i.e. [10]) that changes in the modal parameters can be used for a damage severity assessment, despite their damage localisation deficits. The combination of technologies is a potentially strong alternative and therefore explored here.

COMPOSITE SKIN-STIFFENER STRUCTURES

This research is part of a series performed by the authors concentrating on carbon fibre reinforced thermoplastic (PEKK) skins with multiple stiffeners, which are vulnerable for delamination damage. An overview of the studies is found in Table 1.

These studies showed that delamination damage can be detected and localised by vibration based technologies combined with the Modal Strain Energy Damage Index (MSE-DI) algorithm (first introduced by Stubbs et al. [7]). The experiments were performed using a shaker induced random force excitation and a laser vibro measuring system. The numerical models were implemented in a commercial Finite Element package. The current research focuses on the panel, depicted in Figure 1.

The plate consists of a 16-layer, quasi-isotropic midsection and 44-layer and 30-layer end sections. The stiffeners are made of a 15-layer quasi-isotropic stack (middle layer is a 90° layer). The geometry of the plate is shown in Figure 2. The properties of the PEKK UD composite are listed in Table 2.

Structure	Stringers	Dimensions	References
Beam	1	1000 mm × 100 mm	Loendersloot et al., 2009 [11]; Ooijevaar et al., 2010 [12]
Plate	2	300 mm × 282 mm	Ooijevaar et al., 2010 [13]; Loendersloot et al., 2010 [14]
Panel	3	1304 mm × 456 mm	Ooijevaar et al., 2011 [15]

Table 1: Overview of the structures investigated by the authors.

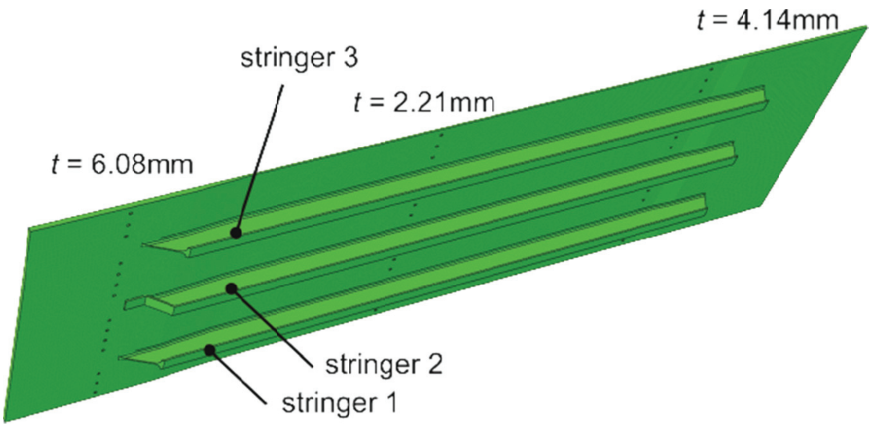

Figure 1: Three dimensional view of the panel with three stringers (stiffeners).

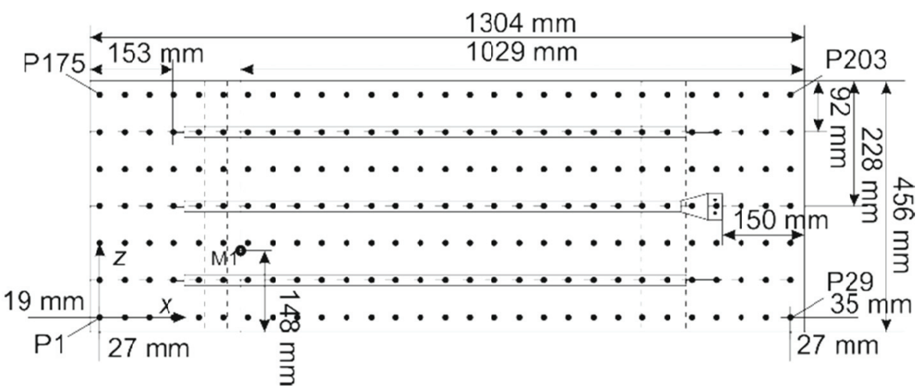

Figure 2: Bottom view of the panel, indicating the dimensions and locations of measuring points (dots) and location of the added mass (M1). The dashed lines indicate the edges of the transition zones between the sections with different thicknesses.

E_1 [GPa]	E_2=E_3 [GPa]	ν_{12} [-]	ν_{13}=ν_{23}	G_{12}=G_{13}=G_{23} [GPa]	ρ [kg·m^{-3}]
134	9.65	0.3	0.45	5.3	1590

Table 2: Material properties for uni-directional carbon fibre reinforced PEKK.

An earlier result [14] pointed out that an impact damage is relatively uncontrollable. A controllable damage is preferred for validation purposes of the numerical model. This was achieved by adding a small mass to the structure (see Figure 2, for the exact location M1 where the mass was added).

Dynamic measurements using a laser-vibrometer were performed on the structure with and without an added mass weighing 42 grams (~1.1% of the total weight).

The measurements are discussed in [15]. A model-based approach is opted based on the previous experiences with both experimental work and numerical models. Combining these improves the interpretation of the data measured in an actual application. The numerical model is implemented in Abaqus®. Shell elements are employed, combined with the composite lay-up option implemented in Abaqus®, hence allowing specifying each individual layer of UD material separately, respecting its orientation relative to the global coordinate system. The transition zones from the thicker end sections to the 16-layer mid-section are modelled according to the lay-up specifications provided by Fokker Aerostructures.

DAMAGE DETECTION, LOCALISATION AND SEVERITY

A distinction can be made between damage identification models that use frequency and modal parameters directly (*direct modal based models*), such as the natural frequencies and *Modal Assurance Criterion* (MAC) values [16], and those using derived modal parameters (*extended modal based models*), such as the modal flexibility and strain energy based algorithms [7,17]. The first type of models is generally only capable of detecting damage (level 1 damage identification [3]). The second type of models is also capable of localisation of the damage (level 2 damage identification [3]).

The *modal strain energy damage index* (MSE-DI) algorithm is applied in this research and those referred to in Table 1. The motivation to use an extended modal based damage identification algorithm is twofold: Firstly, these algorithms tend to be more sensitive to damage, enhancing the detectability compared to direct modal based algorithms. Secondly, extended model based algorithms allow for damage localisation, hence allowing the step from level 1 damage identification to level 2. The natural frequencies and the mode shapes can be determined directly from the measurements. The response of a damaged structure will exhibit a shift of the natural frequencies and subtle change of the mode shapes compared to [16]. Both *Experimental Modal Analysis* (EMA) and *Operational Modal Analysis* (OMA) can be employed to extract the modal parameters from measurements, whereas general eigenvalue problem solvers (for example a Lanczos solver), combined with a frequency response analysis are used for numerical models.

The change in the mode shapes (or difference between mode shapes if experimental and numerical results are compared) can be determined based on the MAC. This criterion is a mathematical comparison between to vectors φ_1 and φ_2 defined as

$$MAC = \frac{\left(\varphi_1^T \varphi_2\right)^2}{\left(\varphi_1^T \varphi_1\right)\left(\varphi_2^T \varphi_2\right)} \tag{1}$$

The MSE-DI algorithm belongs to the category of extended modal based identification methods. It is widely used and has also appeared in a number of different variants to improve the performance and robustness of the algorithm.

The main characteristics of the algorithms are discussed prior to proceeding to a quantitative severity estimation of the damage. The base of the algorithm is found in the strain energy. The structure investigated in this research is bending compliant. Hence, the theory presented is limited to the bending strain energy U, which for a beam reads

$$U = \frac{1}{2}\int_0^l \left[EI_y \left(\frac{\partial^2 u_z(x)}{\partial x^2} \right)^2 \right] \mathrm{d}x \tag{2}$$

with l the length of the beam EI_y the bending rigidity and $u_z(x)$ the z displacement as a function of the x coordinate. The relations for a plate, derived by Cornwell et al. [18], merely leading to more tedious equations. Hence only the one-dimensional case is addressed. In a linearized system, a superposition of a number of modes N_{freq} can describe the vibrations of the structure sufficiently accurate. Secondly, the beam is discretised in N elements over the length of the beam. Hence, the contribution of each element of each of the participating mode shapes $u_z^{(n)}(x)$ to the total strain energy is proportional to

$$U = \sum_{n=1}^{N_{freq}} \left(\alpha_n \sum_{i=1}^{N} u_i^{(n)} \right) = \sum_{n=1}^{N_{freq}} \left(\alpha_n \sum_{i=1}^{N} \left(\frac{1}{2} \int_{z_{i-1}}^{z_i} \left[\left(EI_y \right)_i \left(\frac{\partial^2 u_z^{(n)}(x)}{\partial x^2} \right)^2 \right] \mathrm{d}x \right) \right) \tag{3}$$

where the sub- or superscript n denotes the mode number, i the element number and α_n the modal participation factor. The various definitions of the damage index all compare the modal strain energy in the intact and damaged case (indicated by tilde sign). It is generally assumed that the total strain energy and total stiffness do not change significantly and that the damage is primarily located in a single element or a relatively low number of elements [17,18]. As a result, the change in the ratio of the strain energy in a single element over the total strain energy is of interest.

Following the definition proposed in [18], the ratio of fractional element stiffnesses of the damaged over the reference structure provides the base of the damage index:

$$\frac{\tilde{\gamma}_j^{(n)}/\tilde{\gamma}^{(n)}}{\gamma_j^{(n)}/\gamma^{(n)}} = \frac{\left(\int_{z_{i-1}}^{z_i} \tilde{w}^{(n)}(x)\mathrm{d}x \right)\left(\int_{z_{i-1}}^{z_i} w^{(n)}(x)\mathrm{d}x \right)}{\left(\int_0^l w^{(n)}(x)\mathrm{d}x \right)\left(\int_0^l \tilde{w}^{(n)}(x)\mathrm{d}x \right)} \tag{4}$$

where $w^{(n)}(x)$ represents the second term in the integrand of Equation 2 (the first term of the integrand, EI_y, is dropped as it is assumed to remain constant) and $\gamma_j^{(n)}$ the integral of $w^{(n)}(x)$ over element j and $\gamma^{(n)}$ the integral of $w^{(n)}(x)$ of the entire length l of the structure. This ratio is defined for each mode shape (superscript n). The information in each of the mode shapes is combined in the damage index β. There are several ways to achieve this. The most common methods are summarised in Equation 5, including references to various authors who introduced or used the method. In short it depends on how the modal information is summed. The value of one is added to both the numerator and denominator in Equation 4 for the first three equations (Equation 5a-c) by various authors, resulting in the second set of equations (Equation 5d-f).

$$\beta_j = \frac{\sum_{n=1}^{N_{freq}} \left[\tilde{\gamma}_j^{(n)}/\tilde{\gamma}^{(n)} \right]}{\sum_{n=1}^{N_{freq}} \left[\gamma_j^{(n)}/\gamma^{(n)} \right]}$$ (Cornwell et al [18]; Ooijevaar et al [12,13]; Loendersloot et al. [11,14] (5a)

$$\beta_j = \frac{\sum_{n=1}^{N_{freq}} \left[\tilde{\gamma}_j^{(n)} \gamma^{(n)} \right]}{\sum_{n=1}^{N_{freq}} \left[\tilde{\gamma}^{(n)} \gamma_j^{(n)} \right]}$$ Choi et al. [19,20] (5b)

$$\beta_j = \frac{1}{N_{freq}} \sum_{n=1}^{N_{freq}} \frac{\left[\tilde{\gamma}_j^{(n)}/\tilde{\gamma}^{(n)} \right]}{\left[\gamma_j^{(n)}/\gamma^{(n)} \right]}$$ Alvandi and Cremona [17] (5c)

$$\beta_j = \frac{\sum_{n=1}^{N_{freq}} \left[\left(\tilde{\gamma}_j^{(n)} + \tilde{\gamma}^{(n)} \right)/\tilde{\gamma}^{(n)} \right]}{\sum_{n=1}^{N_{freq}} \left[\left(\gamma_j^{(n)} + \gamma^{(n)} \right)/\gamma^{(n)} \right]}$$ Srinivasan and Kot [21] (5d)

$$\beta_j = \frac{\sum_{n=1}^{N_{freq}}\left[\left(\tilde{\gamma}_j^{(n)}+\tilde{\gamma}^{(n)}\right)\gamma^{(n)}\right]}{\sum_{n=1}^{N_{freq}}\left[\tilde{\gamma}^{(n)}\left(\gamma_j^{(n)}+\gamma^{(n)}\right)\right]}$$ Stubbs et al. [7]; Farrar and Jauregui [22,23](5e)

$$\beta_j = \frac{1}{N_{freq}}\sum_{n=1}^{N_{freq}}\frac{\left[\left(\tilde{\gamma}_j^{(n)}+\tilde{\gamma}^{(n)}\right)/\tilde{\gamma}^{(n)}\right]}{\left[\left(\gamma_j^{(n)}+\gamma^{(n)}\right)/\gamma^{(n)}\right]}$$ Yang et al. [24] (5f)

The list of definitions and interpretations of the damage index β presented here is far from complete. Other variants, partly discussed by the authors named as well, for example drop the assumption of a constant rigidity ($EI_y \neq \tilde{E}I_y$). However, it is beyond the scope of this article to discuss all variants. These are the main approaches, covering the majority of the implementations of the MSE-DI algorithm.

The summation, whichever way it is done, is an important and powerful aspect of the MSE-DI algorithm. It is not required to know a-priori which modes are most sensitive to damage. This is an important characteristic, since the location of the damage will affect which modes are most sensitive. The downside is that the modes that are not affected in a certain damage case dampen the value of the damage index β. This can cause a drop of the damage index below significance, resulting in a false negative damage notification (no notification, damage present). The set of modes must therefore be selected carefully in order to maintain sufficient sensitivity to damage while reducing the chance of undetected damages (see [8]). The sensitivity of the parameter γ is relatively high, since the curvature of the mode shapes is used. A small change in the mode shape, only resulting in a minimal change of the MAC value, can have a significant effect on the curvature [25].

However, it also implies that the mode shapes must be determined with a high accuracy to avoid erroneous results due to a poor representation of the mode shapes. This results in a relatively high number of measuring points, whereas one of the objectives in the implementation of the MSE-DI algorithm also involves the reduction of the number of measuring points [11,12]. The participation of a mode in the actual vibration of the structure (α in Equation 3) is dropped in all formulations for the damage index β. This makes it impossible to link the value of the damage index directly to damage severity in terms of a stiffness loss ratio. The efforts done [8,9] resulted in an underestimation of the damage severity. The damage severity index is generally obtained by normalising the damage index β using the standard deviation σ and the mean μ of the damage index over all elements. This results in the value Z, defined in each element as:

$$Z_j = \frac{\beta_j - \mu}{\sigma} \tag{6}$$

This normalisation is applied for all definitions of the damage index β, both strain energy and compliance based. The advantages are an increased value of the index at potential damage location and the possibility to directly assign a significance level. Discretisation of the mode shape curvatures, based on cubic spline interpolations, is described in [12]. It should be noted that equidistant grids are required to avoid unintended weighting of nodal displacements, resulting in a nodal density dependent damage severity. The spline fit parameters itself also affect the damage severity and should therefore be chosen with care. Numerically determined mode shapes can be used as an alternative for spline fits. However, the discrepancy between experimental and numerical results for higher frequencies limits the use of this method [14]. According to Choi et al. [26], mass normalisation of the modes and highest value normalisation for the curvatures is required to avoid a disproportional contribution of higher order modes as they have higher curvatures. The latter counts for the damage index as defined in Equation 5b and 5c, whereas the definition of Equation 5a is based on fractional values only.

RESULTS AND DISCUSSION

A numerical model was made in the commercial Finite Element package Abaqus®. A frequency analysis, to extract the natural frequencies and mode shapes, and a harmonic response analysis to extract the frequency response functions were subsequently performed. The frequency range for the harmonic response analysis was set equal to the frequency range of the measurements that were performed in parallel: 50 – 1050 Hz

[15]. The experimental results are used for validation of the FE model but are not discussed in this article in detail. The numerical analyses are run for eleven different cases: the reference case and ten cases with an added mass of 10 to 100 grams (~0.25-2.5% of the total mass). Firstly, the natural frequencies and MAC-values are investigated. Secondly, the MSE-DI algorithm is applied to localise the added mass and finally an approach is discussed to estimate the added mass from the results, comparable to damage severity estimation.

A measurement grid of 29 times 7 points was used (see Figure 2). Nodes are defined at these locations to determine the mode shapes for comparison with the experimental results. The first 20 natural frequencies calculated by the numerical model for all damage cases and the experimental natural frequencies are mutually compared. A reasonable correspondence (MAC>0.8) is found for the first 10 to 15 modes according to Figure 3 (red markers, filled squared markers indicate the diagonal of the MAC matrix, the triangles and circles the off-diagonal values). Small differences between the model and the real panel measuring inaccuracies and the high modal density complicate the comparison between the numerical and experimental results for higher frequencies. Potential sources of deviations between the model and the experiments are variations in fibre angle orientation and in the thickness. In addition, the boundary conditions used may not represent the real situation correctly.

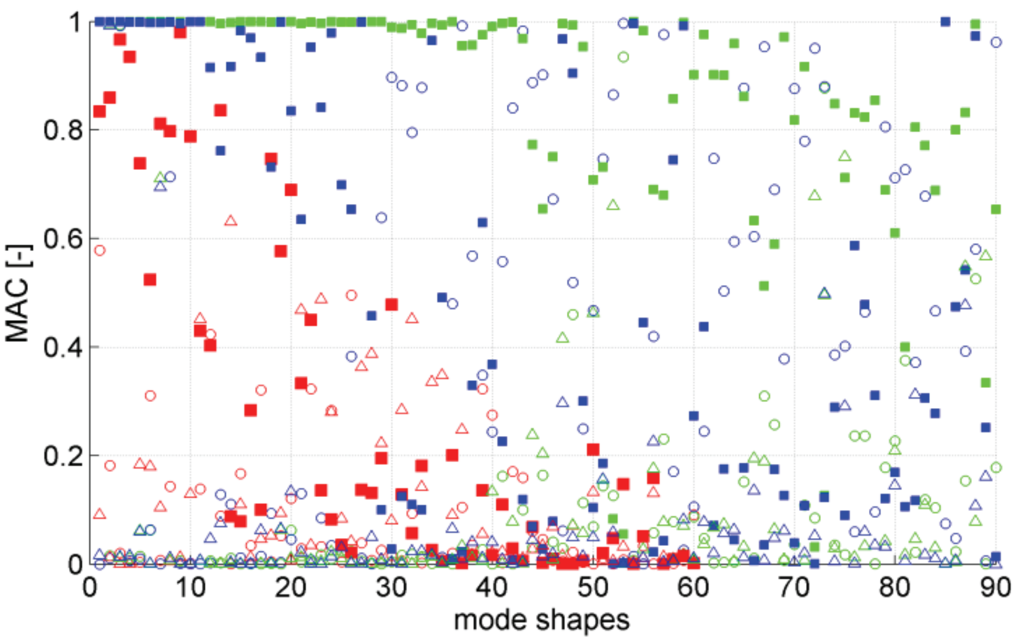

Figure 3: MAC values of the experimental versus numerical mode shapes (red markers, no added mass) and the MAC values for the numerical cases with an added mass of 10 grams (green markers) and 100 grams (blue markers). The filled, squared markers indicate the diagonal term of the MAC matrix, the triangles and circles indicate the off-diagonal terms.

The change of the natural frequencies due to the added mass varies per mode but is relatively small: 0.05% up to 5%, with an average of less than 1%. In general, it is smaller than the difference currently observed between the numerical model and the experiments. A significant change of the MAC values is observed comparing the (numerical) cases with the added mass (Figure 3, green and blue markers). Two cases are shown: an added mass of 10 grams and of 100 grams. The change in MAC values clearly indicates that a change in the structure has occurred, where the amount of change is a qualitative indication of the amount of added mass. The change in MAC-values only provides limited information on the location of the damage: A change of mode shapes due to the presences of an added mass is reflected in the decrease of the MAC value of a certain set of modes. However, a very low MAC-value implies that the modes do not match at all and as a consequence the curvatures will differ significantly over the entire mode shape, rather than only in the neighbourhood of the damage. This can lead to a number of erroneous peaks in the damage index (or ‘noise’), potentially even to false positives (indication of damage at a location where no damage is present).

To this end, the number of modes that participate in the MSE-DI algorithm is limited to those modes that have a MAC-value between 0.5 and 1.0. This range provided the best results here, but it should be emphasized that this is not true in general. A 1D MSE-DI algorithm is applied using cubic spline fitted mode shapes of 128 data points over the length of the panel. This results in seven data sets of the damage index *Z* over the width of the panel (Figure 2, first data set is based on P1-P29, the 7th on P175-P203). The reason to use a 1D algorithm is that the sensitivity of the damage index algorithm in the direction of the lower stiffness is significantly lower than that in the stiffer direction of the panel – which corresponds to the direction of the stiffeners [13,14]. However, this limits the localisation abilities in the width direction. The normalised damage index *Z* for the different damage cases is shown in Figure 4. A clear peak indicates the location of the damage. For all cases, the location of the damage is predicted to be approximately at $(x,y)=(1.025,0.068)$. The exact location of the added mass is $(x,y)=(1.03,0.08)$, resulting in a relative deviation of 0.5% in the length direction and 15% in the width direction. The high deviation in the width direction is evidently caused by the use of a 1D algorithm in length direction only. A 2D algorithm is required to improve the accuracy.

(a)

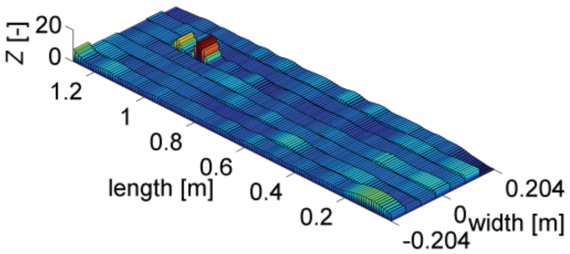

(b)

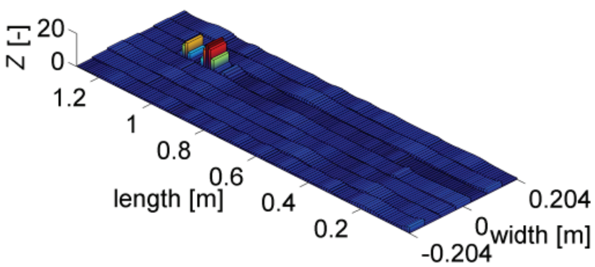

Figure 4: Normalised damage index *Z* for (a) an added mass of 10 grams and (b) an added mass of 100 grams.

A secondary peak is also present. This is either a false positive (indication of damage, but no actual change in the structure) or a secondary effect of the added mass caused by the set of modes included in the algorithm. The latter is assumed to be the most likely explanation given the height of the peak and the consistency in the location. It is also observed that the maxima of all peaks converge to the same value, irrespective of the amount of added mass. This is visualised in Figure 5, which shows the maximum values of all peaks as a function of the relative amount of added mass (compared to the total mass of the panel). The secondary peaks remain significantly lower than the maximum peaks, but raise above the significance level (which is generally 2 or 3 depending on the confidence desired). This situation may be comparable to a situation with multiple, different added masses. Also here, a 2D implementation may help to distinguish false negatives from true positives.

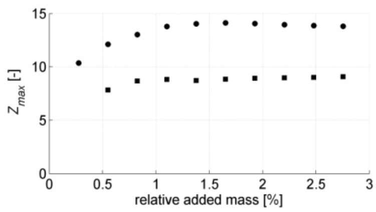

Figure 5: Maximum value for the normalised damage index *Z* as a function of the relative amount of added mass. The circles indicate the first peak, the squares the secondary peak.

The next step is to combine the results of the direct and extended modal based algorithms. The location of the damage is known (with certain accuracy) as well as the frequency response of the intact and damaged structure. The latter contains absolute values for the amplitudes and therefore has the potential to contribute to a more accurate severity estimation. The most apparent change in the frequency response function is the shift of the natural frequencies of some of the modes. An estimation of the damage severity (or: *amount* of added mass) requires a relation between the shift of the natural frequencies and the added mass. This relation is found by analysing the principle of generalised mass. The generalised mass matrix M_r is defined as:

$$M_r = \Phi_r^T M \Phi_r \tag{7}$$

with M the mass matrix and Φ_r the normalised mode shapes. The generalised mass matrix is a diagonal lumped mass matrix that is derived by adding small masses to the structure [27]. The generalised mass $m_r^{(n)}$ of a certain mode n can be written as

$$m_r^{(n)} = \frac{\left(\tilde{f}^{(n)}\right)^2}{\left(f^{(n)}\right)^2 - \left(\tilde{f}^{(n)}\right)^2} \sum_{j=1}^{N} \left(\Delta m_j \left(x_j^{(n)}\right)^2\right) \approx -\frac{f^{(n)}}{2\Delta f^{(n)}} \sum_{j=1}^{N} \left(\Delta m_j \left(x_j^{(n)}\right)^2\right) \tag{8}$$

with $f^{(n)}$ the n^{th} natural frequency (tilde refers to the damaged case), Δm_j the j^{th} of a total of N added masses, $\Delta f^{(n)}$ the frequency shift and $x_j^{(n)}$ the normalised displacement at the location of the j^{th} added mass of the n^{th} mode. The last step is achieved by ignoring the higher order terms and assuming that the frequency of the damaged case can be expressed as the frequency of the reference case plus a perturbation Δf. In this case N=1, for which case the relation between the frequency shift and added mass reads

$$\Delta m = \frac{2m_r^{(n)}}{f^{(n)}\left(x_j^{(n)}\right)^2} \Delta f \tag{9}$$

Analysing the structure for a range of added masses allows establishing the relation in Equation 9. Non-linearity can arise due to the higher order terms that were neglected in the derivation.

The relation in Equation 9 is depicted in Figure 6 for a number of modes, which were matched based on a minimum MAC value of 0.85 (between numerical modes). The dashed line is based on calculated frequencies shift (by the numerical model) and known added masses. The added masses and frequency shifts are expressed as a percentage of the total mass and the natural frequencies of the reference (undamaged) situation.

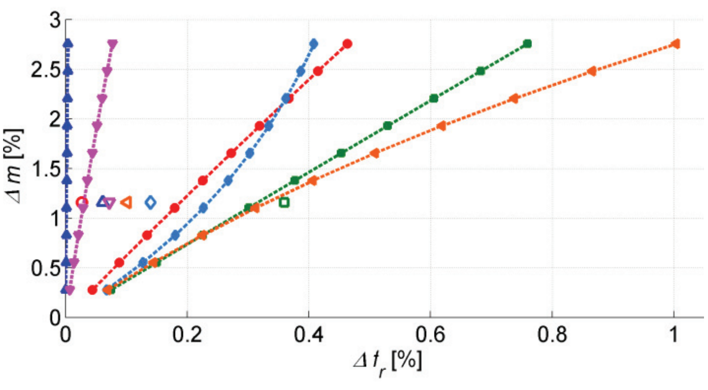

Figure 6: Relative mass change versus frequency shift for 6 cases. The lines connect the numerical results (filled markers) with 10 to 100 grams of added mass, whereas the open markers are based on the measured data. Red: mode 8, green: mode 9, blue: mode 10, magenta: mode 11, light blue: mode 14 and orange: mode 16.

The relation is linear in most cases as is expected for a limited change of the mode shapes. The generalised mass matrix is based on the concept of linear perturbation. It is assumed that the added masses do not affect the response $x^{(n)}$, which is strictly taken not to be the case here. The open markers in Figure 6 indicate the experimentally determined frequency shifts [15] for the given added mass of 42 grams. The colours and markers of corresponding modes are set equal. The discrepancy between the simulations and the experimental results are explained by the differences between the model and the experiments discussed previously. However, the relation between the frequency shift and the added mass depends on the generalised masses $m_r^{(n)}$ and frequencies $f^{(n)}$ of the reference state and on the response of the point $x^{(n)}$ of the damaged case. For the first two, accurate models can be developed, for example using model updating techniques or a comprehensive experimental program.

This only needs to be done once. The last parameter is obtained accurately employing a damage localisation method such as the MSE-DI algorithm discussed here. So far, the 'damage' was represented by an added mass. Normally, damage will be reflected in a decrease of the stiffness and an accompanying shift of the natural frequency. Hence, a similar procedure must be followed based on the generalised stiffness. However, the result of measurements on panels before and after a 10-50 J impact load [13,15] indicate lower shifts of the natural frequencies.

Hence, further experimental and numerical investigation will be required to successfully implement a stiffness based damage severity estimation.

CONCLUSION AND RECOMMENDATIONS

The work presented here reflects the challenges encountered in damage severity estimations. One of the conclusions that can be drawn is that the road from level 1 to level 3 and even 4 or 5 cannot be taken with a single method. The methods developed successfully enhance the detection and localisation of the damage, but lack the ability for a reliable quantitative estimation of the damage severity, since the damage index is merely a mathematical rather than a physical quantity. This first conclusion certainly does not judge the extended modal based damage identification algorithms. Their detection and localisation capabilities still outperform the direct modal parameter based model capabilities. In conjunction however, the two families of algorithms offer the potential to proceed to the next level of damage identification. The method of combining localisation methods with the theory of generalised mass is shown to relate frequency shifts with the change of the structure in a quantitative manner. The numerical model must be matched with the experimental results more than is necessary to acquire an accurate prediction of the location of the change in the structure. Some work is still ahead to improve this match for the current application. Moreover, future investigation is required to adapt the method proposed for a change in stiffness rather than a change in mass. Theory indicates the possibilities, but experimental results have already indicated that this is a challenging task.

ACKNOWLEDGEMENTS

The authors kindly acknowledge Fokker Aerostructures for manufacturing the composite panels on which the experiments were performed. This work was carried out in the framework of the European project Clean-Sky Eco Design (grant number CSJU-GAM-ED-2008-001).

REFERENCES

[1] Fan W. and Qiao P. (2011), Vibration based damage identification methods: A review and comparative study, *Structural Health Monitoring*, 10(1):88-111

[2] Montalvão D., Maia N.M.M. and Ribeiro A.M.R. (2006), A review of vibration-based structural health monitoring with special emphasis on composite materials, *The Shock and Vibration Digest*, 38(4):295-326

[3] Fritzen C.-P. and Kraemer P. (2009), Self-diagnosis of smart structures based on dynamical properties, *Mechanical Systems and Signal Processing*, 23:1830-1845

[4] Su Z., Ye L. and Lu Y., Guided Lamb waves for identification of damage in composite structures: a review, *Journal of Sound and Vibration*, 295(3-5):753-780
[5] Ihn J. and Chang F. (2008), Pitch-catch active sensing methods in structural health monitoring for aircraft structures, *Structural Health Monitoring*, 7(1):5-19
[6] Schulte R.T. and Fritzen C.-P. (2010), Modelling of Wave-Based SHM Systems Using the Spectral Element Method, *Proceedings in Applied Mathematics and Mechanics*, 10:15-18
[7] Stubbs N., Kim J.T. and Farrar C.R. (1995), Field verification of a nondestructive damage localization and severity estimation algorithm, In *Proceedings of the 13th International Modal Analysis Conference*, pages 210-218
[8] Choi S., Park S., Park N.-H. and Stubbs N. (2006), Improved fault quantification for a plate structure, *Journal of Sound and Vibration*, 297:865-879
[9] Li H., Fang H. and Hu S.-L. J. (2007), Damage localization and severity estimation for three-dimensional frame structures, *Journal of Sound and Vibration*, 301:481-494
[10] Ndambi J.-M., Vantomme J. and Harri K. (2002), *Damage assessment in reinforced concrete beams using eigenfrequencies and mode shape derivatives*, Engineering Structures, 24:501-515
[11] Loendersloot R., Ooijevaar T.H., Warnet L., Akkerman R. and Boer A. de (2011), Vibration based structural health monitoring and the modal strain energy damage index algorithm applied to a composite T-beam, in *Vibration and Structural Acoustics Analysis: Current Research and Related Technologies*, Springer Netherlands, 121-150, ISBN 97894007022
[12] Ooijevaar T.H., Loendersloot R., Warnet L.L., Boer A. de and Akkerman R. (2010a), Vibration based Structural Health Monitoring of a composite T-beam, *Composite Structures*, 92(9):2007-2015
[13] Ooijevaar T.H., Loendersloot R., Warnet L.L., Boer A. de and Akkerman R. (2010b), Vibration based structural health monitoring of a composite plate structure with multiple stiffeners. In *Proceedings of the European Workshop on Structural Health Monitoring*
[14] Loendersloot R., Ooijevaar T.H., Warnet L., Boer A. de and Akkerman R. (2010), Vibration based structural health monitoring of a composite plate with stiffeners. In: *International Conference on Noise and Vibration Engineering*, ISMA 2010, Leuven
[15] Ooijevaar T.H., Loendersloot R., Warnet L.L., Boer A. de and Akkerman R. (2011), Structural health monitoring of an advanced composite aircraft structure using a modal based approach, In: *International Workshop on Structural Health Monitoring*, IWSHM-8, Stanford, USA, 9 pages
[16] Salawu O.S. (1997), Detection of structural damage through changes in frequency: a review, *Engineering Structures*, 19(9):718-723
[17] Alvandi A.A. and Cremona C.B. (2006), Assessment of vibration based damage identification techniques, *Journal of Sound and Vibration*, 292(1-2):179-202
[18] Cornwell P., Doebling S.W., Farrar C.R. (1999), Application of the strain energy damage detection method to plate-like structures, *Journal of Sound and Vibration*, 224(2):359-374
[19] Choi S., Park S. and Stubbs N. (2005a), Nondestructive damage detection in structures using changes in compliance, *International Journal of Solids and Structures*, 42:4494-4513
[20] Choi S., Park S., Yoon S. and Stubbs N. (2005b), Nondestructive damage identification in plate structures using changes in modal compliance, *NDT&E International*, 38:529-540
[21] Srivnivasan M. and Kot C. (2004), Damage index algorithm for a circular cylindrical shell, *Journal of Sound and Vibration*, 215(3):587-591
[22] Farrar C.R. and Jauregui D.A. (1998a), Comparative study of damage identification algorithms applied to a bridge: I experiments, *Smart Materials and Structures*, 7(5):704-719
[23] Farrar C.R. and Jauregui D.A. (1998b), Comparative study of damage identification algorithms applied to a bridge: II numerical study, *Smart Materials and Structures*, 7(5):720-731
[24] Yang H., Li H. and Hu S. (2004), Damage localization for offshore structures by modal strain energy decomposition method, *Proceedings of the American Control Conference*, 4207-4212
[25] Pandey A.K., Biswas M., Samman M.M. (1991), Damage detection from changes in curvature mode shapes, *Journal of Sound and Vibration*, 252(2):223-238
[26] Choi F.C., Li J., Samali B. and Crews K. (2008), Application of the modified damage index method to timber beams, *Engineering Structures*, 30:1124-1145
[27] Dillinger S., Mühlbauer K., Gambietz W. and Gautier F. (2005), Determination of the generalized mass from vibration test data by adding mass, *IMAC-XXIII: Conference & Exposition on Structural Dynamics*, Orlando, Florida, USA

FEM-BASED SIMULATION, OPTIMIZATION AND CONTROL OF ADAPTIVE LIGHT-WEIGHT STRUCTURES

M. Fischer*, R. Wüchner & K.-U. Bletzinger

Chair of Structural Analysis, Technische Universität München, Munich, Germany

*Corresponding author. E-mail: m.fischer@tum.de

ABSTRACT

This contribution presents a finite element based approach for the virtual design and simulation of smart lightweight membrane structures. Form finding is used to determine the optimal structural shape of tensile structures from an inverse formulation of equilibrium. Also the cutting pattern generation of membranes is integrated in order to consider fabrication effects already in the earliest possible stage. Active control is adopted for vibration suppression under external loads like e.g. wind. Controller design is based on a state space model that is derived from the finite element model and that preserves the geometrically non-linear equilibrium state and the prestress effects of the membrane structure. Discrete time control via an optimal linear-quadratic-Gaussian (LQG) regulator is applied. The methods and algorithms of all simulation and design steps presented are illustrated and verified at the example of a controlled 4-point tent.

INTRODUCTION

Nowadays, the engineering design process commonly starts with computational simulations. The system under consideration can be analyzed, optimized and even redesigned by a virtual computer model before the first prototype is built. Simulations of flexible mechanical structures are generally based on the finite element method. In the case of thin and lightweight structures the aim of the computational design process is often to minimize weight while maintaining stress or vibration criteria. Prestressed membrane structures are well suited for lightweight structures due to the extremely low areal density and the optimal static load carrying behavior. Prominent examples in the civil engineering context are tents and stadium roofings. The numerical method of form finding is applied in order to determine structural shape from an inverse formulation of equilibrium. This approach is comparatively robust and also suited for complex shapes. The cutting pattern generation of membranes is integrated in the computational simulation process in order to include decisive fabrication effects already in the design stage.

This contribution presents a computational framework and the related algorithms for the virtual design and simulation of actively controlled lightweight membrane structures. Active control is adopted in order to reduce the vibrations induced by external loads. This is especially important in the context of lightly prestressed membranes, as they exhibit very low mode frequencies in the out-of-plane direction and are thus prone to vibration even for small disturbing loads. Thus control can be used to increase functionality, improve usability or to create even lighter structures [1,2]. In the context of structural control, it is a common approach to apply active or semi-active components in order to improve the behavior of an already given, passive system. In contrast to that, this work presents a design concept that aims for mechanically motivated control and adaptivity integration from the very beginning of the design process. The article will present the methods and algorithms of all design and simulation steps and will show a strategy about how to combine them into one computational simulation environment. The example of a controlled 4-point tent illustrates the methods and verifies the applicability of the approach presented.

FORM FINDING AND CUTTING PATTERN GENERATION

In a nonlinear continuum mechanical description, the unknown shape $\boldsymbol{x}$ of equilibrium can be identified as actual (deformed) configuration, which has to fulfill the equilibrium condition governed by the principle of virtual work. Using the prescribed Cauchy stress tensor $\boldsymbol{\sigma}$ and the external loading $\boldsymbol{q}$ (Figure 1, left), the total virtual work δw with its internal and external parts yields:

$$\delta w = \delta w_{int} - \delta w_{ext} = \underbrace{t\int_a \boldsymbol{\sigma} : \delta \mathbf{d},_{\mathbf{x}} \, da}_{\text{internal}} - \underbrace{\int_a \mathbf{q} \cdot \delta \mathbf{d} da}_{\text{external}} = 0 \tag{1}$$

$\delta d,_x$ is the derivative of the virtual displacement with respect to the geometry $\boldsymbol{x}$ of the surface in equilibrium. The integration domain is the area a of the final equilibrium surface. The thickness of the membrane is denoted by t.

Based on the second Piola-Kirchhoff stress tensor $\boldsymbol{S}$ and the deformation gradient $\boldsymbol{F}$, it is now possible to transform the integration domain of the original problem from the yet unknown equilibrium surface to a known reference configuration $\boldsymbol{X}$ (Figure 1, right). The internal virtual work of Equation (1) can be written as:

$$-\delta w_{int} = t\int_a \boldsymbol{\sigma} : \delta \mathbf{u},_x \, da = t\int_A \det \mathbf{F}\left(\boldsymbol{\sigma} \cdot \mathbf{F}^{-T}\right) : \delta \mathbf{F} dA = t\int_A \left(\mathbf{F} \cdot \mathbf{S}\right) : \delta \mathbf{F} \, dA \tag{2}$$

This transformation - often described as pull-back operation - is especially useful for the algorithmic solution of the form finding problem, as the known reference configuration can serve as a starting point for the solution. For the numerical solution, Equation (2) has to be discretized. Furthermore, as we are dealing with a geometrically nonlinear problem involving large displacements from the starting configuration to the actual equilibrium shape (Figure 1, right), a linearization of the resulting equation system is necessary, which follows the standard concept of incremental solution schemes [3].

As the geometry is coupled to the stress state of the structure, the equilibrium equations must be solved for the unknown geometry. However, a straightforward application of the method shown above is not possible due to the inverse nature of the problem: We are looking for the discretized equilibrium surface with a certain topology of the discretization parameters. However, the shape parametrization for the same geometry is not unique. That means that a generally applicable discretization technique like FEM must use some regularization methodology to circumvent the above mentioned singularities. In this context the similar nature of shape control [4] and form finding should be pointed out, as both approaches have to overcome the singularities of an inverse problem by regularization techniques. The most general method for regularization of the inverse problem of form finding is the updated reference strategy (URS).

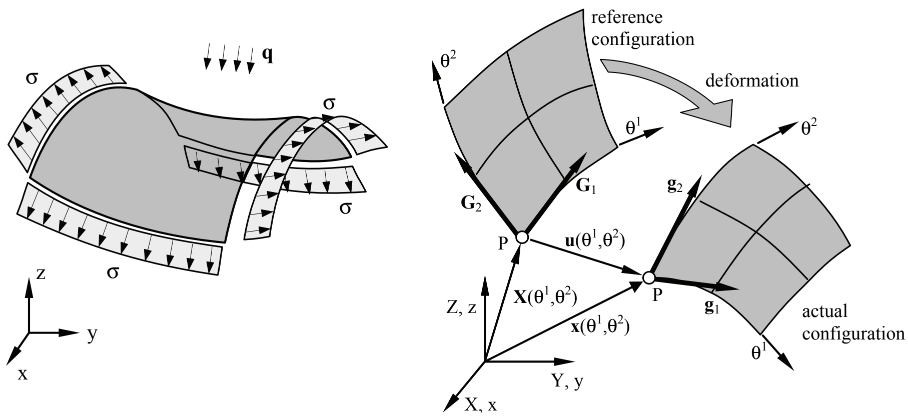

Figure 1: Left: Tangential surface stress field. Right: Deformation of surface from reference configuration to actual configuration.

This method is consistently derived from nonlinear continuum mechanics of elastic bodies and performs a homotopy mapping between the original, singular problem and a stabilization term [5]. Starting from Equation (2), one can introduce a continuation factor λ and formulate:

$$\delta w = \lambda \, t\int_A \det \mathbf{F}\left(\boldsymbol{\sigma} \cdot \mathbf{F}^{-T}\right) : \delta \mathbf{F} \, dA + (1-\lambda) t\int_A \left(\mathbf{F} \cdot \mathbf{S}\right) : \delta \mathbf{F} \, dA = 0 \tag{3}$$

Instead of assuming the Cauchy stress tensor $\boldsymbol{\sigma}$ of the unknown equilibrium surface to be given, the 2nd Piola–Kirchhoff stress tensor $\boldsymbol{S}$ referring to the arbitrary starting geometry is prescribed. If λ is chosen properly, the second term stabilizes the original expression and allows for the use of a standard finite element discretization and solution. This modification has the convincing property that it disappears at the solution surface. By using Equation (3), we are thus able to calculate a unique equilibrium surface for the given PK2 stress state. The modified and stabilized expression is nonlinear with respect to the final geometry x and must be solved iteratively applying a Newton-Raphson scheme. However, the resulting Cauchy stresses will differ from the targeted stress state depending on the choice for λ. This necessitates a second, outer iteration: The newly obtained actual configuration $\mathbf{x}$ of the modified system (Equation 3), which is closer to the final equilibrium shape, can be used to update the reference geometry $\boldsymbol{X}$ for the next form finding iteration. By repeatedly updating the reference geometry, the difference between the PK2 and Cauchy stresses is consequently reduced and the solution converges safely and robustly to the one of the unmodified problem (Figure 2). It should be noted that the speed of convergence is independent from the number of variables. Furthermore, the approach is capable of handling arbitrary stress states with or without external loading.

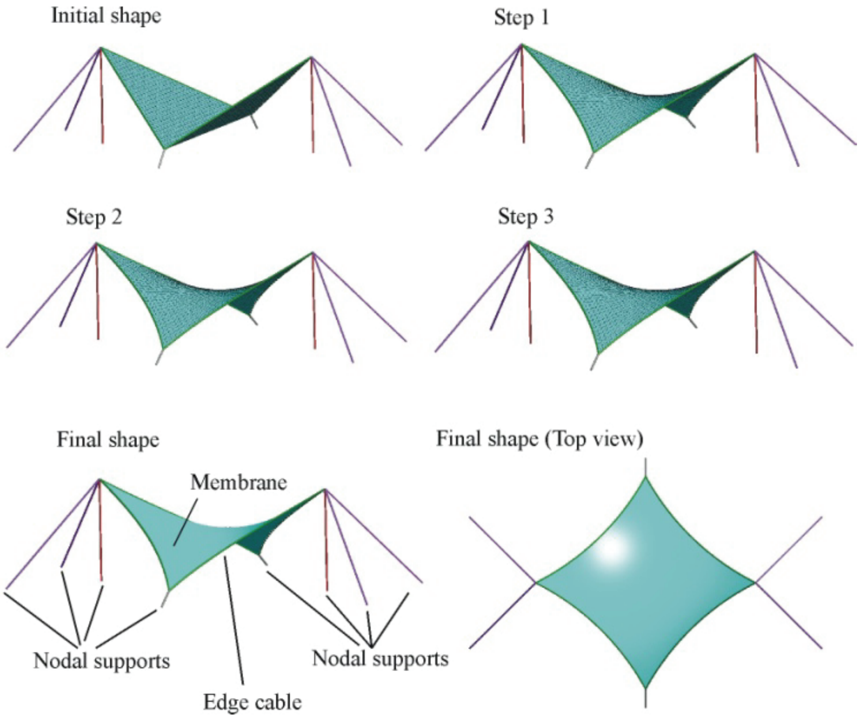

Figure 2: Application of form finding via the updated reference strategy to a 4-point tent: form finding steps and final geometry.

In general, membrane structures exhibit a doubly curved surface in order to establish a good load carrying behavior. This is important in the context of cutting pattern generation. For all surfaces that exhibit nonzero Gaussian Curvature, stresses occur through the flattening process. A very general approach for the generation of cutting patterns is the inverse engineering method [6] which is based on the description of the underlying mechanical problem. The three dimensional surface, which is defined through the form finding process, represents the final structure after manufacturing. For this surface the coordinates in three dimensional space Ω_{3D} and the finally desired prestress state $\boldsymbol{\sigma}_{prestress}$ are known. The aim is to find a surface in a two dimensional space Ω_{2D} which minimizes the difference between the elastic stresses $\boldsymbol{\sigma}_{el,2D \rightarrow 3D}$ arising through the manufacturing process and the final prestress $\boldsymbol{\sigma}_{prestress}$. Thus the cutting pattern generation leads to an optimization problem, were the positions of the nodes in the two dimensional space Ω_{2D} are the design variables. Furthermore, as the width of textile materials is usually limited in the practical manufacturing process, it is important to divide the structure into several parts in order to get appropriate cutting patterns. An appropriate way to avoid too much loss of material is the usage of geodesic lines for the definition of the cutting lines. Geodesic lines are characterized by connecting two points on a surface with the shortest amount of distance. The calculation of geodesic lines on discrete surfaces (e.g. finite element mesh) is performed in two steps (Figure 3). First of all an approximation of the geodesic lines along the edges of the elements of the discrete surface is calculated [7].

The second step is to perform an optimization of the approximated geodesic lines to get the “shortest path” between two given points [8]. It should be mentioned that this method is applicable for different element types and is able to consider different material models and arbitrary prestress states.

The final stresses under load and the boundaries of the structure are the major shaping parameters which clearly define the resulting geometry as shape of equilibrium.

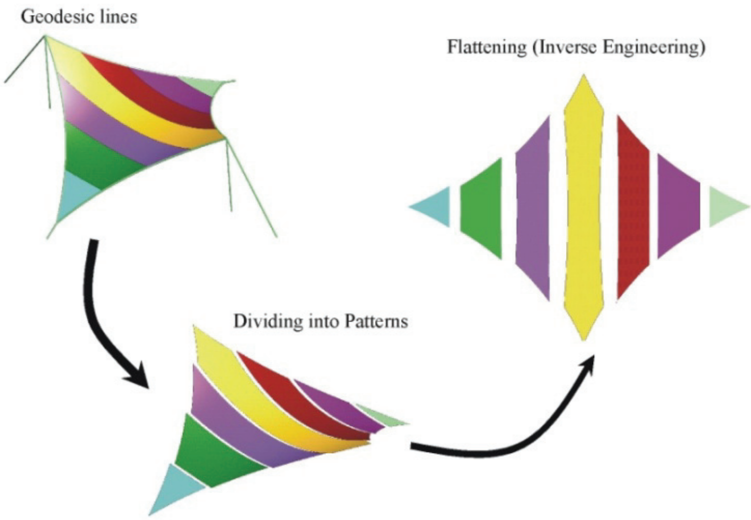

Figure 3: Cutting pattern process.

SIMULATION

The next step of the virtual design process is the geometrically nonlinear transient analysis of the structure. The consideration of geometrically nonlinear effects is here indispensable, as large displacements arise already from the starting configuration to the actual equilibrium shape of the prestressed membrane, even if external loads are neglected. Adding to the total virtual work δw of Equation 1, the dynamic contribution due to inertia forces yields:

$$\delta \mathrm{w} = \delta \mathrm{w}_{dyn} + \delta \mathrm{w}_{int} - \delta \mathrm{w}_{ext} = \delta \mathbf{d}^T \mathbf{M}\,\ddot{\mathbf{d}} + \delta \mathbf{d}^T \mathbf{r}_{int}(\mathbf{d}) - \delta \mathbf{d}^T \mathbf{r}_{ext}(t, \mathbf{d}) = 0 \tag{4}$$

Additionally introducing damping that is proportional to the velocity field, the geometrically nonlinear dynamic equation yields in its semi-discrete form:

$$\begin{aligned} &\mathbf{M}\,\ddot{\mathbf{d}} + \mathbf{C}\,\dot{\mathbf{d}} + \mathbf{r}_{int}(\mathbf{d}) = \mathbf{r}_{ext}(t, \mathbf{d}), \\ &\ddot{\mathbf{d}}(t = t_0) = \ddot{\mathbf{d}}_0,\ \dot{\mathbf{d}}(t = t_0) = \dot{\mathbf{d}}_0,\ \mathbf{d}(t = t_0) = \mathbf{d}_0 \end{aligned} \tag{5}$$

with the mass matrix $\boldsymbol{M}$, the displacement field $\boldsymbol{d}$, the vector of internal forces $\mathbf{r}_{int}(\mathbf{d})$ and the vector of external forces $\mathbf{r}_{ext}(t, \mathbf{d})$. The damping matrix $\boldsymbol{C}$ can be described in a simplified way as a linear combination of the mass matrix and stiffness matrix (Rayleigh damping):

$$\mathbf{C} = \alpha_1 \cdot \mathbf{M} + \alpha_2 \cdot \mathbf{K}_{el+geo} \tag{6}$$

Here, the stiffness matrix $\mathbf{K}_{el+geo}$ of the membrane equilibrium state after form finding is used in order to include the effects of prestress and geometrical nonlinearity also in the context of damping.

Even more realistic damping parameters can be obtained if the membrane structure is simulated and evaluated including the interaction effects with the surrounding air, as these fluid-structure interaction effects play a decisive role in the context of damping of membrane structures. For time integration, implicit methods like Newmark-β or Generalized-α are chosen. The solution of the related nonlinear equation system is done via complete linearization and iterative solution by the Newton-Raphson method with predictor-corrector scheme.

CONTROL

Structural control can now be applied to membrane structures in order to increase functionality, improve usability or to create even lighter structures. The design objective pursued in this contribution is to suppress vibrations in the membrane. This is challenging for the following reasons: Membranes, especially lightly prestressed ones, exhibit very low mode frequencies in the out-of-plane direction and are thus prone to vibration even for small disturbance loads. Beyond that, attaching many sensors, actuators or dampers directly on the membrane is not recommended, as this disturbs the optimal membrane stress state and results in a heavier system. The controller design for a flexible mechanical structure like a membrane represents in general a multiple input – multiple output (MIMO) system, where the application of nonlinear and large-scale finite element models is not suitable. Thus, as a first step, a linearization of the geometrically nonlinear system of Equation (5) is performed for controller design:

$$\mathbf{M}\,\ddot{\mathbf{d}} + \mathbf{C}\,\dot{\mathbf{d}} + \mathbf{K}_{el+geo}\mathbf{d} = \overline{\mathbf{E}}\mathbf{f}(t) + \overline{\mathbf{B}}\mathbf{u}(t) \tag{7}$$

Here, the stiffness matrix $\mathbf{K}_{el+geo}$ of the quasi-static nonlinear equilibrium state is used in order to include the effects of prestress, geometric stiffness and permanent loading also in the linearized model. The right hand side of Equation (7) contains the load contributions of external load and control input. The introduced matrices $\overline{\mathbf{E}}$ and $\overline{\mathbf{B}}$ link the degrees of freedom of the external load and the actuator signal to the time dependent functions of external load $\boldsymbol{f}$(t) and control input $\boldsymbol{u}$(t). The linearized representation of the finite element model obtained would in general yield to very high state-space dimensions. Thus an appropriate model order reduction scheme like the modal truncation technique has to be adopted. The latter method is commonly used in the context of flexible structures due to their low-pass characteristic, which allows for neglecting higher-frequency dynamics. Starting point is the linearized eigenvalue problem of the structure:

$$\left(\mathbf{K}_{el+geo} - \lambda_k \mathbf{M}\right)\varphi_k = \mathbf{0} \tag{8}$$

Figure 4 presents the three lowest axially symmetric eigenmodes of the 4-point tent. An evaluation of eigenmodes confirms that the vibrations of the membrane predominantly act in the out-of plane direction.

Solving Equation (8) for r eigenvectors yields the $(n \times r)$ modal matrix $\mathbf{\Phi} = [\varphi_1 \,|\, \varphi_2 \,|\, ... \,|\, \varphi_k]$ and the $(r \times r)$ spectral matrix $\mathbf{\Lambda} = diag(\lambda_k)$, where $\mathbf{\Phi}$ is orthonormalized with $\mathbf{\Phi}^T\mathbf{K}_{el+geo}\mathbf{\Phi} = \mathbf{\Lambda}$ and $\mathbf{\Phi}^T\mathbf{M}\mathbf{\Phi} = \mathbf{1}$. Inserting the modal coordinates $\mathbf{d} = \mathbf{\Phi}\mathbf{z}$ into Equation (7), the large finite element system with n degrees of freedom can be reduced to a decoupled equation system of r modal degrees of freedom:

$$\ddot{\mathbf{z}} + \mathbf{\Delta}\dot{\mathbf{z}} + \mathbf{\Lambda}\mathbf{z} = \mathbf{\Phi}^T\overline{\mathbf{E}}\mathbf{f}(t) + \mathbf{\Phi}^T\overline{\mathbf{B}}\mathbf{u}(t) \tag{9}$$

Based on this approach, the presented model is reduced from 2881 to 10 modal degrees of freedom.

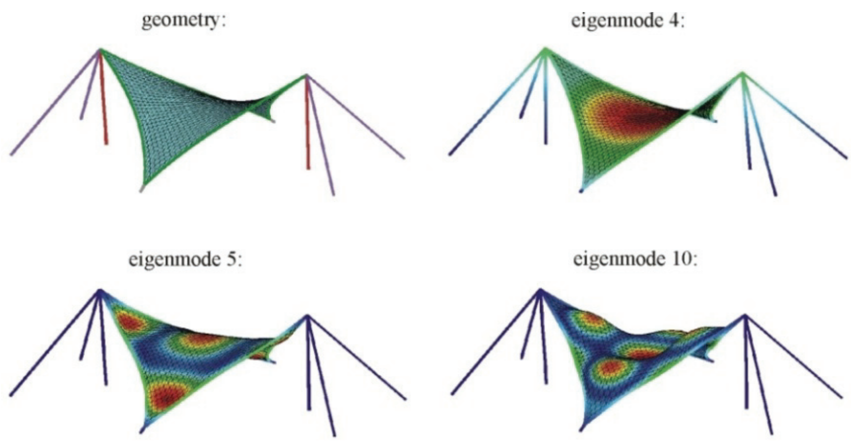

Figure 4: Eigenvalue analysis of the 4-point tent: Lowest three symmetric eigenmodes (scaled deformation and highlighted via contour plot).

Figure 5 shows exemplarily the displacement plot of the membrane midpoint by a transient analysis of the tent subjected to a half-sin pressure load of $q = 50\,N/m^2$ from below in the 4th eigenfrequency of the structure. The damping ratio for Rayleigh damping is set to 10%. The results of the nonlinear FE model, the linear FE model and the reduced model are compared. It can be observed that the linearization leads to an overestimation of the deformation, as displacement-dependent stiffness contributions are neglected. Beyond that, it can be seen that the reduced model is not able to exactly reproduce the initial deformation behavior, as the contributions of higher modes are missing. However, in general a good matching of the reduced model can be observed in this test example.

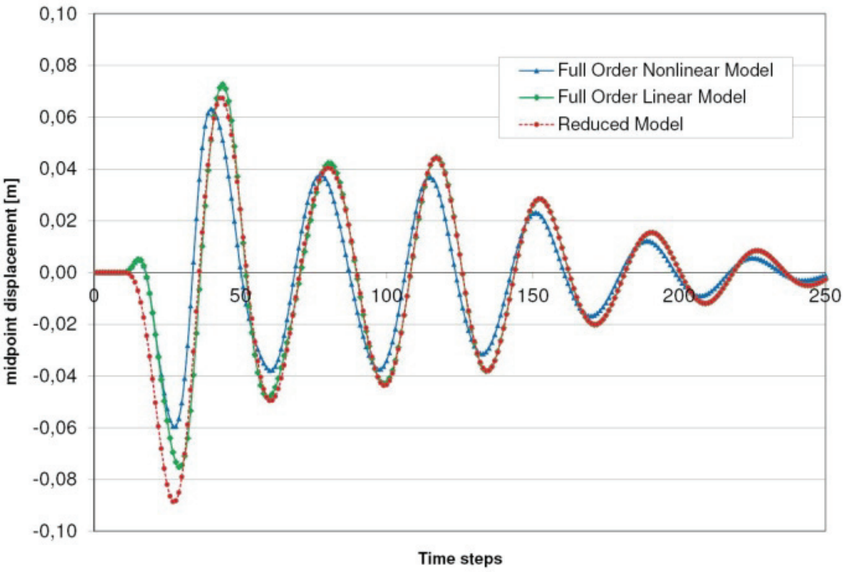

Figure 5: Transient analysis of the 4-point tent: Results of (a) the large nonlinear FE model, (b) the large linear FE model, (c) the reduced model.

For controller design, a transformation to the state space is performed. Based on the modal degrees of freedom of the reduced model, the state vector is defined by

$$\mathbf{x}_c = \begin{bmatrix} z \\ \dot{z} \end{bmatrix} \tag{10}$$

Using the state vector $\mathbf{x}_c$, the reduced model of Equ. (9) is transformed into the modal form of the state space equation:

$$\dot{\mathbf{x}}_c = \begin{bmatrix} \mathbf{0} & \mathbf{I} \\ -\boldsymbol{\Lambda} & -\boldsymbol{\Delta} \end{bmatrix} \mathbf{x}_c + \begin{bmatrix} \mathbf{0} \\ \boldsymbol{\Phi}^T \overline{\mathbf{B}} \end{bmatrix} \mathbf{u}(t) + \begin{bmatrix} \mathbf{0} \\ \boldsymbol{\Phi}^T \overline{\mathbf{E}} \end{bmatrix} \mathbf{f}(t) = \mathbf{A}\mathbf{x}_c + \mathbf{B}\mathbf{u}(t) + \mathbf{E}\mathbf{f}(t) \tag{11}$$

Besides to that, also the measurement equation can be formulated based on the finite element data:

$$\mathbf{y} = \mathbf{C}\mathbf{x}_c + \mathbf{D}\mathbf{u}(t) + \mathbf{F}\mathbf{f}(t) \tag{12}$$

Now the required information for controller design is prepared. It should also be pointed out that all matrices *A, B, E, C, D* and *F* are derived from the finite element model and the related modal truncation.

The selection and placement of sensors and actuators plays a decisive role in the design process of smart structures. This decision highly affects the controllability and observability of the controlled structure and has great influence on the required control effort to satisfy a given design objective and thus on the efficiency of the control system. As explained before, the vibrations of membranes act predominantly in out-of-plane direction, because the membrane's in-plane mode frequencies are much higher than those in the out-of-plane direction. Based on the evaluation of the dominant eigenmodes, the positions of 5 displacement sensors for the 4-point tent have been chosen according to Figure 6.

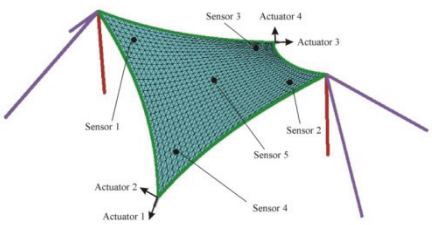

Figure 6: Active control of the 4-point tent: position of displacement sensors and force actuators.

The question of type and placement of effective actuators seems to be crucial, because attaching actuators directly on the membrane is in general not recommended due to detraction of the optimal membrane stress state. However, the presented form finding method itself suggests reasonable actuator types and places.

It has been shown that the form finding algorithm is a very effective alternative for the design of surface structures. The final stresses $\boldsymbol{\sigma}$ under load and the boundaries $\boldsymbol{\Gamma}$ of the structure are the major shaping parameters which have to be given and which clearly define the resulting geometry $\boldsymbol{x}$ as shape of equilibrium. These parameters can be chosen according to the individual preferences, e.g. depending on material, cross section, available design space, geometric restrictions etc. Beyond that, the prestress values and support conditions are as major shaping parameters predestinated to act as shape control parameters. By adaptively modifying the shape of the structure via the mentioned shaping parameters it is possible to maintain optimal behavior with respect to a specified criterion, like vibration reduction, while external effects like loading conditions are changing. Accordingly, four force actuators at the lower support cables have been chosen for the 4-point tent (Figure 6), two of them acting in-plane to the membrane and two of them acting out-of-plane. From the mechanical point of view, these two actuator groups have in general two different types of effects on the membrane structure: The in-plane actuators manipulate the prestress of the membrane, while the out-of-plane actuators actually change via deformation the Gaussian curvature of the structure. Summing up, the sensor and actuator positioning driven by form finding characteristics leads in this example to non-collocated sensors and actuators, as the different modal contributions to the displacement field can be best observed within the membrane, while actuator forces should be positioned at the supported corners of the tent.

The linearization at the operating state (prestressed membrane including permanent loads) led to the linearized state and output equations:

$$\begin{aligned}\dot{\mathbf{x}}_c &= \mathbf{A}\mathbf{x}_c + \mathbf{B}\mathbf{u} + \mathbf{E}\mathbf{f}\\ \mathbf{y} &= \mathbf{C}\mathbf{x}_c + \mathbf{D}\mathbf{u} + \mathbf{F}\mathbf{f}\end{aligned} \tag{13}$$

In this general form of the plant model according to Equation (13), $\mathbf{f}$ describes in general the disturbance which is assumed to be present in the state and the output equation.

For discrete controller design, it is necessary to derive a discrete-time state space model of the plant structure. Performing a discretization of equation (13) with an appropriate sampling time T yields:

$$\begin{aligned}&\mathbf{x}_c[k+1] = \mathbf{G}\mathbf{x}_c[k] + \mathbf{H}\mathbf{u}[k] + \boldsymbol{\varepsilon}\mathbf{f}[k]\\ &\mathbf{y}[k] = \mathbf{C}\mathbf{x}_c[k] + \mathbf{D}\mathbf{u}[k] + \mathbf{F}\mathbf{f}[k],\\ &\text{with: } \mathbf{G} = e^{\mathbf{A}T}, \quad \mathbf{H} = \int_0^T e^{\mathbf{A}T}\mathbf{B}\,d\tau, \quad \boldsymbol{\varepsilon} = \int_0^T e^{\mathbf{A}T}\mathbf{E}\,d\tau.\end{aligned} \tag{14}$$

For active control of the shown 4-point tent, a linear-quadratic-Gaussian (LQG) regulator is chosen (Figure 7).

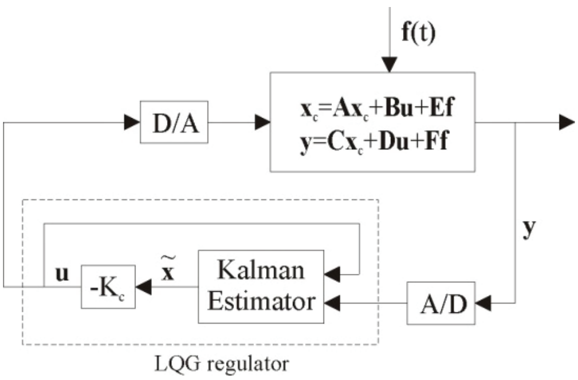

Figure 7: Closed loop LQG regulator.

A Kalman estimator is used to obtain a state variable estimation of the plant model based on the information of the five sensors placed on the membrane. Based on the estimation of the state, the state feedback gain $\mathbf{K}_c$ is used to generate the actuator signal:

$$\mathbf{u}(t) = -\mathbf{K}_c\tilde{\mathbf{x}}_c \tag{15}$$

Hereby the state feedback gain matrix $\mathbf{K}_c$ is chosen such that the feedback law of Equation 15 minimizes the performance index:

$$J = \frac{1}{2}\sum_{k=0}^{\infty}\left(\mathbf{y}[k]^T\mathbf{Q}\mathbf{y}[k] + \mathbf{u}[k]^T\mathbf{R}\mathbf{u}[k]\right) \tag{16}$$

where $\boldsymbol{Q}$ and $\boldsymbol{R}$ are symmetric, positive definite matrices. Taking again the 4-point tent example, an appropriate regulator is designed in Matlab/Simulink. The state space matrices $\boldsymbol{A}$, $\boldsymbol{B}$, $\boldsymbol{E}$ and $\boldsymbol{C}$ are derived from the data provided by the FE model. The matrices $\boldsymbol{D}$ and $\boldsymbol{F}$ are set to be zero. The sampling interval for discrete-time control is chosen to be T=0.01 sec. A pressure load of $q = 20N/m^2$ in the 5th eigenfrequency of the structure is applied as disturbing load case. Thus the possibility of resonance is provided. The weighting matrices for the optimal LQG controller design have been chosen like that: $\mathbf{Q} = \mathbf{I}_{5x5}, \mathbf{R} = 0.01 \cdot \mathbf{I}_{4x4}$. The following simulation results were obtained in Matlab/Simulink (Figure 8). The displacement amplitude is reduced by a factor of 2.6 at sensor 1 and 2, by a factor of 2.3 at sensor 3 and 4, and by a factor of 5.2 at sensor 5 (midpoint of the membrane). Error sources like measurement errors induced by the sensing device have been ignored in the analyses of this example for simplicity. In future studies, these assumptions should be relaxed and the effect of these errors should be investigated.

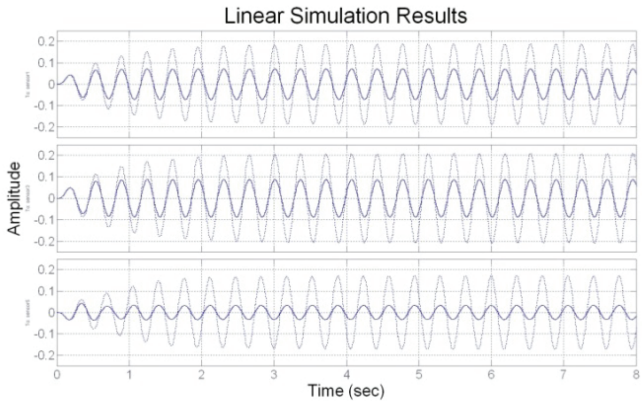

Figure 8: Sensor values for uncontrolled (thin line) and controlled (bold-printed line) system simulation in Matlab/Simulink.

SIMULATION INCLUDING CONTROL

In general, the feasibility of the structural behavior including control has to be verified and tested. Based on the large-scale and geometrically nonlinear finite element simulation it can be checked automatically, if e.g. wrinkling effects appear due to undesired compressive stresses in the membrane [9] or if all components comply with the maximum allowable stresses. The model described in the preceding chapters is now simulated including control based on the large-scale and geometrically nonlinear FE model. For time integration, the implicit Newmark β-scheme is chosen. Again, a pressure load of $q = 20N/m^2$ in the 5th eigenfrequency of the structure is applied as disturbing load case. Control is activated at time step 200. Figure 10 shows the resulting displacement of the membrane midpoint. Via control, a reduction of the amplitude of the midpoint displacement by a factor of 2.4 is obtained. Beyond that, it can be identified that the vibration of the midpoint is a bit shifted towards positive displacement values due to the control action. This is due to the fact that the actuators are only positioned at the lower tension cables of the 4-point tent (c.f. Figure 6).

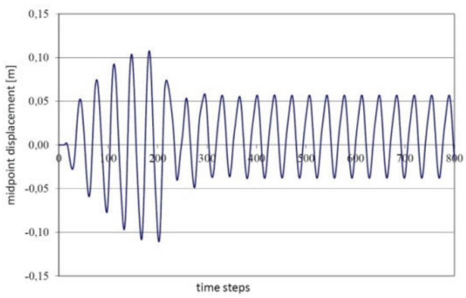

Figure 9: Geometrically nonlinear analysis of the 4-point-tent including control: Displacement of the membrane midpoint (control starts at time step 200).

COMPUTATIONAL FRAMEWORK AND OVERALL DESIGN PROCESS

The desired flexibility and variety to all these mentioned possibilities can only be guaranteed in a modular and modern computational framework. Flexible software modules for form finding, cutting pattern generation, structural analysis and structural optimization are part of the in-house finite element software Carat++ (see e.g. [10,11]). The program is completely written in C++ in order to take advantage of object-oriented programming features. Consequently, easier maintenance of the code, easier implementation of complex algorithms and higher flexibility is assured. The software is capable to perform the overall design process in a parallel computation. Besides to that, a data interface has been implemented for convenient controller design in Matlab/Simulink. All other steps of the design and simulation process (Figure 10) are performed in the software Carat++.

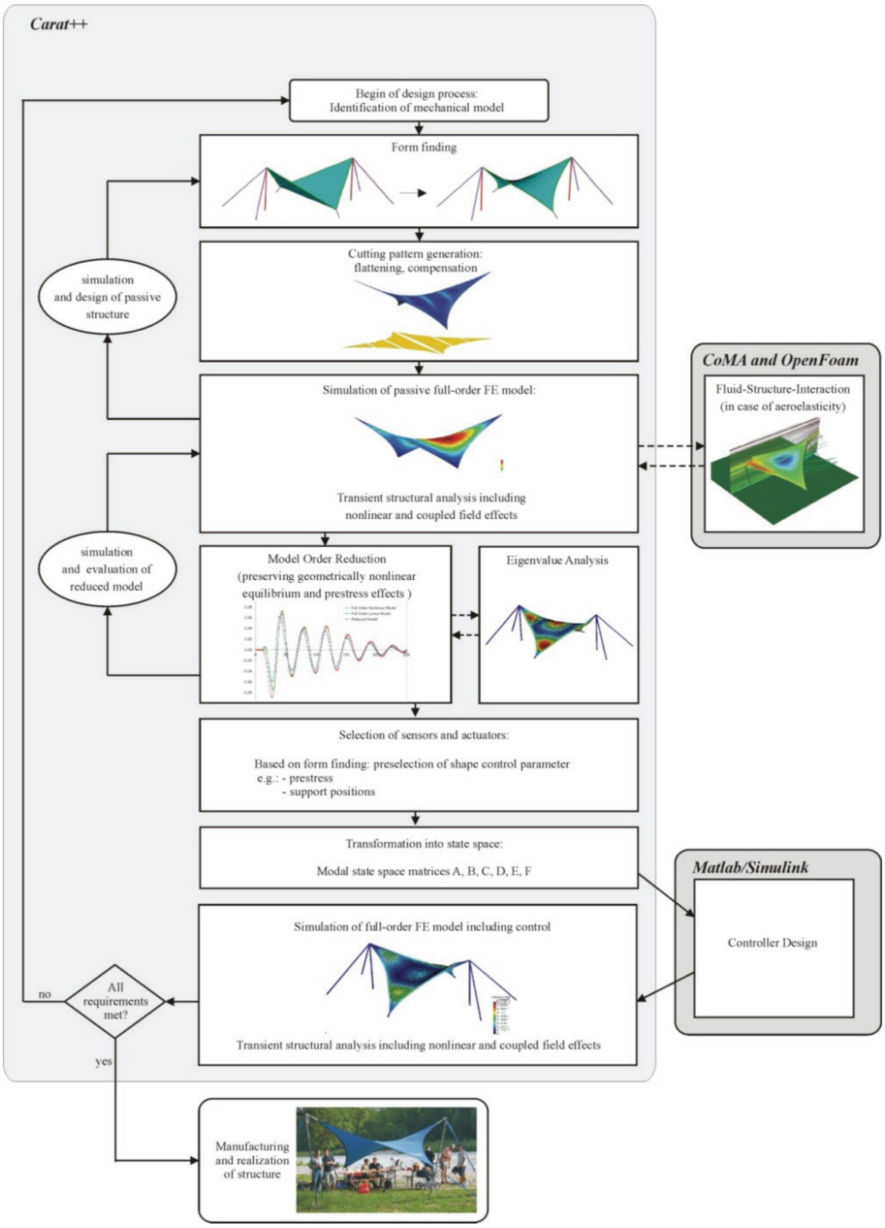

Figure 10: Overview of the overall design process and the used software packages.

CONCLUSION

An integrated computational framework and the related algorithms for the virtual design and simulation of controlled smart lightweight membrane structures have been presented. Form finding has been used to determine the optimal structural shape of tensile structures. Also the cutting pattern generation of membranes has been integrated in the design process in order to consider decisive fabrication effects already in the design stage. Active control for vibration suppression has been successfully adopted using a state space model that is derived from the finite element model and that preserves the geometrically nonlinear equilibrium state and the prestress effects of the membrane.

The methods and algorithms of all simulation and design steps presented have been illustrated and verified at the example of a controlled 4-point tent.

INDUSTRIAL PARTNER

FEMopt Studios GmbH, Germany

REFERENCES

[1] Bletzinger, K.-U., Fischer, M. and Wüchner, R., 2009. Computational framework for simulation and design of adaptive lightweight structures. *IV ECCOMAS Themaic Conference on Smart Structures and Materials*, Porto, Portugal.

[2] Bletzinger, K.-U., Dieringer, F., Fischer, M., Ionifelis, G. and Wüchner, R., 2010. FEM-Based Simulation, Design and Control of Adaptive Lightweight Structures. *Proceedings of the Tenth International Conference on Computational Structures Technology*, B. H.,V. Topping, et. al. (Editors), Civil-Comp Press, Stirlingshire, UK, Valencia, Spain, Sept. 14-17, pp. 68.

[3] Belytschko, T., Liu, W. K. and Moran, B., 2000. *Nonlinear Finite Elements for Continua and Structures*, Wiley, Chichester, England.

[4] Adelman, H. M. and Haftka, R. T., 1985. An analytical investigation of shape control of large space structures by applied temperatures. *AIAAJ* 23, pp. 450–57.

[5] Bletzinger, K.-U. and Wüchner, R., 2005. Stress-adapted numerical form finding of prestressed surfaces by the updated reference strategy. *Int. J. Numer. Meth. Engrg*. 64, pp. 143–66.

[6] Bletzinger, K.-U., Linhard, J. and Wüchner, R., 2008. Introducing cutting patterns in form finding and structural analysis. (E. Oñate and B. Kröplin, eds.) *Textile Composites and Inflatable Structures II*, Springer.

[7] Kimmel, R. and Sethian, J. A., 1998. Computing geodesic paths on manifolds. *Proceedings of the National Academy of Sciences* 95(15), pp. 8431–435.

[8] Wakefield, D.S., 1999. Engineering analysis of tension structures: theory and practice. *Engineering Structures* 21, pp. 680-90.

[9] Bletzinger, K.-U., Jarasjarungkiat, A. and Wüchner, R., 2008. A wrinkling model based on material modification for isotropic and orthotropic membranes. *Computer Methods in Applied Mechanics and Engineering* 197, pp. 773-88.

[10] Bletzinger, K.-U., Firl, M., Fischer, M. and Masching, H., 2010. Optimization of Nonlinear Structures based on Object-Oriented Parallel Programming. *Proceedings of the Seventh International Conference on Engineering Computational Technology*, B.H.V. Topping, et al. (Editors), Civil-Comp Press, Stirlingshire, UK, Valencia, Spain, September 14-17, paper 67.

[11] http://www.caratplusplus.de

ON MODELING OF ENERGY SELF-SUFFICIENT VIBRATION ABSORBER SENSOR MODULES

M. Kurch & D. Mayer

Fraunhofer Institute for Structural Durability and System Reliability LBF, Bartningstr 47, 64289 Darmstadt, Germany

ABSTRACT

Autonomous sensors enhance and widen the scope for structural health monitoring (SHM) of large lightweight structures, e.g. bridges, vessels. Systems for harvesting energy from vibrations on the basis of electromechanical transducers and mechanical resonators are often proposed for the power supply of those sensors. The utilization of mechanical vibration absorbers as resonators offers the perspective to integrate vibration reduction and structural health monitoring into a single device. The conversion of mechanical into electric energy for the supply of the sensor affects the necessary damping of the vibration absorber. Within this context it is essential to find optimum design parameters to maximize the energy generated and to provide the required damping. In this study described here a framework for the design of 'Energy Self-Sufficient Vibration Absorber Sensor Modules' is presented. After deriving the fundamental expressions for the power conversion, the framework is applied to an example application.

INTRODUCTION

Vibration phenomena are counted among the most challenging problems during the design and operation of lightweight structures, since they are the cause of cyclic fatigue, limited precision of machines and harmful noise radiation. Thus extensive work has been conducted during the last decades on passive and active systems for vibration reduction as well as on systems for structural health monitoring (SHM) and autonomous damage detection in mechanical structures [1]. On the other hand, vibrations are one of the preferred ambient energy sources being exploited by energy harvesting (EH) systems, which have been studied by several researchers during the last years [2]. In most cases, these systems aim at the supply of wireless sensor nodes, which are used to implement SHM systems at locations difficult to access or locations without an own power supply [3]. Potential applications include objects of civil infrastructure like bridges or mobile systems such as freight cars [4,5]. Within the work described here the integration of the basic principles of EH, SHM and vibration absorption into a single system is studied.

Mechanical resonators often serve as baseline structures for energy harvesting systems but when designed with respect to a feedback on the characteristics of the host structure they are applied to, they serve as tuned vibration absorbers (TVA). The combination of both aspects results in an 'Energy Self-Sufficient Vibration Absorber Sensor Module'. The design of the system is based upon data which can be gained from experiments, since in many practical situations no sufficient precise numerical models of the structure do exist. In the first step, the mechanical resonator is tuned to the structural vibrations and parameters for mass, stiffness and damping are estimated, which serve as input to the detailed design of the absorber-harvester system. A widely-used approach is the power harvesting from mechanical vibration energy by converting it into electric energy by means of piezoceramic (PZT) transducers. Among the different approaches the cantilevered beam with piezoceramic layers which is applied to a structure is the most popular harvester. The whole system is designed in such a way that the natural frequency where the strain in the PZT becomes maximum is tuned to the driving frequency. Therefore it is assumed that influence on this basis is negligible as the vibrating mass is small compared to the mass of the basis. A similar set up is chosen, when a tuned mass damper is mounted on structures to reduce the amplitude of mechanical vibrations. But for TVAs a significant influence has to be seen on the basis of the system feature. In the remainder of this article first the estimation of absorber parameters is described. Afterwards, the electromechanical design and the respective modeling method are introduced. In the last section, the application of the framework developed framework is discussed along an example of a freight car.

ESTIMATION OF SYSTEM PARAMETERS

Vibration absorbers are commonly realized by coupling a tuned single-degree-of-freedom oscillator to a vibrating structure. Energy harvesting systems can be designed in a similar way. The amount of power that is dissipated in the damping element can be regarded as an upper boundary for the electrical power that can be generated with the system [6]:

$$P = \theta \omega_T m \left|\Delta \dot{x}(j\omega)\right|^2 . \tag{1}$$

Here, m is the inertial mass, ω_T the tuning frequency and Θ is the damping ratio of the oscillator. Furthermore, the power is depending to the velocity $\Delta\dot{x}$ in the damping element. First, the case of the host structure being a simple spring-mass system is considered to compare the application of an oscillator designed as tuned vibration absorber to an energy harvesting system (Figure 1). The mass M of the system is chosen to be 1 kg and the resonance frequency f_0 to be 50 Hz respectively.

After setting the ratio μ of the two masses

$$\mu = \frac{m}{M} = 0.1, \tag{2}$$

the optimal mass and damping ratio of the TVA are calculated as described e.g. by [7]:

$$f_T = f_0 \frac{1}{1+\mu} = 45\,Hz \ , \tag{3}$$

$$\theta = \sqrt{\frac{1}{2}\mu}\ (1-\frac{\mu}{2}) = 0.2 . \tag{4}$$

In contrast to that, an energy harvesting system is not supposed to affect the host structure, thus the ratio μ is chosen quite small, e.g. 0.01. To illustrate both approaches the feedback on the host structure is analyzed by the respective input admittance while the energy dissipated in the damper is calculated according to Equation 1. As expected, the higher mass results in better vibration attenuation. The tuned vibration absorber also dissipated energy over a broader frequency range, while the energy harvesting system delivers a higher peak power in the resonance frequency. Clearly, the design of an energy harvesting absorber exhibits some challenges in balancing the targets of high vibration attenuation and effective power conversion. Indeed, vibration problems of technical structures often cannot be modeled by the above mentioned single-degree-of-freedom-oscillator. To estimate the effectiveness of the energy harvesting absorber system also for practical applications a description of systems with mobilities and impedances is proposed here. This method, also known as Analytical Testing was applied to predict the effects of tuned vibration absorbers to helicopter airframes [8]. The mobility of the host structure at the point where the vibration absorber should be applied is derived as a first step from the dynamic force excitation and the collocated velocity measurement:

$$Y_H(j\omega) = \frac{\dot{x}(j\omega)}{F(j\omega)} . \tag{5}$$

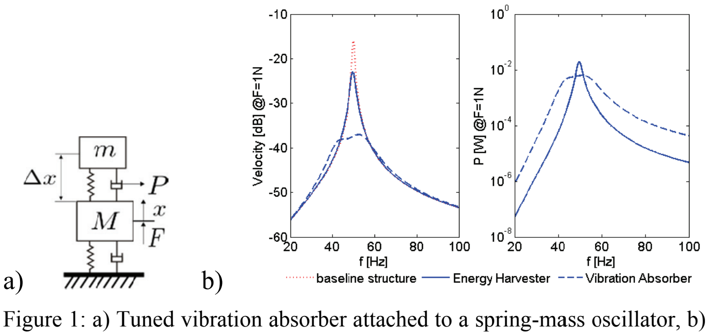

Figure 1: a) Tuned vibration absorber attached to a spring-mass oscillator, b) acceleration and dissipated power for EH system and TVA.

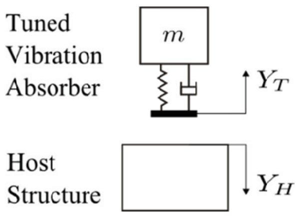

Figure 2: Mobility formulation of a tuned vibration absorber.

The mobility of a tuned vibration absorber with viscous damping can be calculated as:

$$Y_T(j\omega) = \frac{1}{m}\frac{j\omega^2 + j\omega 2\theta\omega_0 + \omega_0^2}{j\omega^2 2\theta\omega_0 + j\omega\omega_0^2}. \tag{6}$$

By coupling both systems, their respective mechanical impedances are connected in series, which results in a modified point mobility:

$$Y_{\text{mod}}(j\omega) = \frac{Y_T(j\omega)Y_H(j\omega)}{Y_T(j\omega) + Y_H(j\omega)}. \tag{7}$$

For the estimation of the vibration reduction under operational conditions the velocity spectrum $\dot{x}_H(j\omega)$ is measured at the designated coupling point. Under the assumption that the force causing the vibration does not change when the absorber is applied the resulting vibration spectrum can be calculated as:

$$\dot{x}_{\text{mod}}(j\omega) = \frac{Y_T(j\omega)}{Y_T(j\omega) + Y_H(j\omega)}\dot{x}_H(j\omega). \tag{8}$$

The difference velocity $\Delta\dot{x}(j\omega)$ between the absorber mass and the host structure (or the absorber's base, respectively) is:

$$\Delta\dot{x}(j\omega) = \dot{x}_{\text{mod}}(j\omega)\left(\frac{1}{j\omega m Y_T(j\omega)} - 1\right). \tag{9}$$

By substituting the predicted velocity spectrum from Equation 8 and using Equation 1 the power dissipated in a tuned vibration absorber applied to a host structure $Y_H(j\omega)$ and subject to operational vibrations $\dot{x}_H(j\omega)$ yields:

$$P = \theta\omega_T m\left|\frac{1 - j\omega m Y_T(j\omega)}{j\omega m(Y_T(j\omega) + Y_H(j\omega))}\right|^2 \left|\dot{x}_H(j\omega)\right|^2. \tag{10}$$

While the analytical framework was derived by mobilities and velocity spectra, it can easily be applied to accelerances and accelerations as well, which are commonly obtained from structural analyses. By solving Equation 9 and 10 for different configurations suitable parameters can be found for the mass, damping and stiffness of the absorber which both effect in a satisfying vibration reduction and a sufficient amount of energy dissipated in the damper. Indeed, the estimation of the power is rather rough. However it can serve well as a basis for the design of a vibration absorber with integrated energy harvesting transducers. In the real energy harvesting vibration absorber the dissipation of mechanical energy is realized by electromechanical energy conversion. Considering piezoelectric transducers for energy harvesting the model depicted in Figure 1 has to be enhanced by the electromechanical coupling α and the capacitance C_P of the piezoelectric transducer (Figure 3). By applying the electromechanical analogy, the electrical load R_L of the transducer can be integrated as a damping element into the model, while the capacitance is represented by a stiffness element.

Since the electrical load is coupled to the vibration absorber via the electromechanical coupling α and the capacitance, the power P dissipated will be much lower than in a mechanical damper mounted directly in parallel to the absorber stiffness k. Furthermore, the vibration absorber will always possess some pure mechanical damping, represented by the damper d in Figure 3, which partly dissipates the mechanical energy. Thus, the converted power of a real energy harvesting system may be much lower than estimated by Equation 10. As the coupling coefficient and the piezoelectric capacitance strongly depend on the actual design of the tuned vibration absorber and the integration of the transducer, a better estimation of the electrical power requires a detailed electromechanical design. The resulting models can hardly be formulated with simple analytical equations as shown above, but numerical models based on the Finite Element Method have to be used. In the following section, an example for the design and numerical analysis of a tuned vibration absorber with integrated piezoelectric energy harvesting is explained.

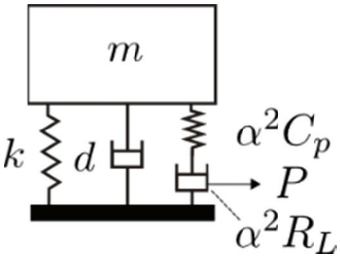

Figure 3: Equivalent model of the energy harvester including electromechanical coupling.

MODELLING OF THE PIEZOELECTRIC ENERGY HARVESTING SYSTEM

For the efficiency study of the electrometrical power conversion a model of the piezoelectric transducer is required. The model has to meet the requirements of the design framework introduced previously. The Finite Element simulation was performed to design a TVA and to calculate the generated electrical power. Vibration absorbers often consist of a cantilevered beam with a tip mass (Figure 4). When piezoelectric transducers are applied to the structure electrical energy is generated by the vibration. Therefore a generic Finite Element (FE) model was set up. The model which is depicted in Figure 5 represents a beamlike structure with a tip mass. The tip mass M_t was modeled as a lumped point element mounted at the cantilever's free end. The boundary conditions were applied at the point of origin. The supporting layer of the beam and the piezoelectric transducer were discretized using 20-node solid elements that exhibit quadratic displacement and voltage behavior [9,10].

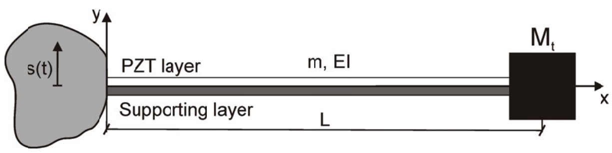

Figure 4: Schematic of the energy harvesting vibration absorber.

The piezoelectric element is discharged by the added resistor. The optimal harvested power flow can be achieved by tuning this load impedance to match the internal impedance of the piezoelectric generator. This yields the optimal resistance which maximizes the power [11] flowing into the electrical network. The impedance is calculated using either static or harmonic FE analyses. Since the applied PZT element and the shunted resistance are changing the dynamical system properties a harmonic analysis was conducted in order to calculate the new lumped mass, damping ratio and resonance frequency. These parameters take the TVA's feedback to the base into account, when energy is spent in the resistor. Using these parameters the resulting vibration spectrum can be calculated from Equation 8 and applied to the root point of the beam's Finite Element model. Thus, another harmonic analysis of a base excited oscillator has to be executed to get the motion of the absorber and the generated power which is consumed in the resistor. Indeed, the design of the vibration absorber presented is generic. But the model features all necessary properties for the study of energy harvesting vibration absorbers and can be extended easily for the analysis of more complex designs.

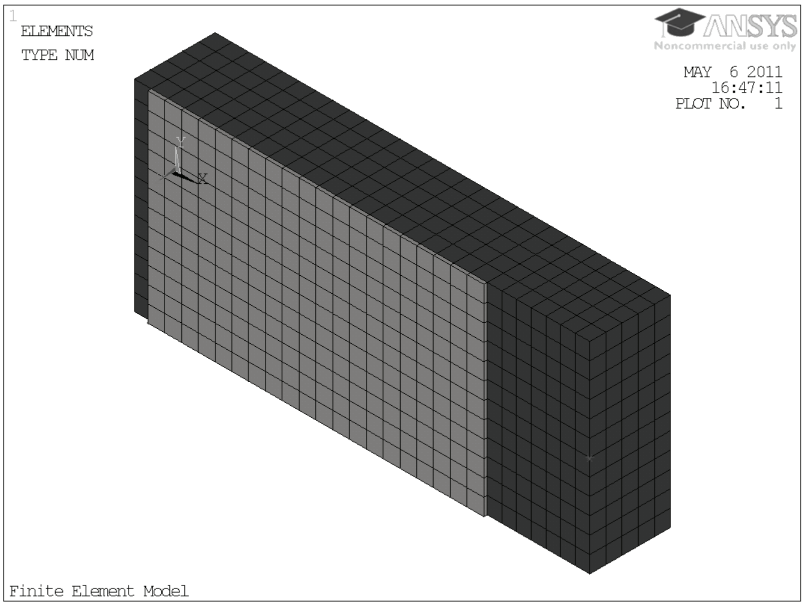

Figure 5: Generic Finite Element Model of the energy harvesting absorber.

EXPERIMENTAL VALIDATION

The method proposed is applied to design an energy harvesting vibration absorber for a freight car (Figure 6). The wheel set mount is chosen as a potential position for the installation of a the vibration absorber in order to reduce bending resonances of the wheel set axle and gain energy for a condition monitoring system of the bearing or the axle. The point mobility at the wheel set is obtained from an accelerance measurement with an impulse hammer and a collocated accelerometer (Figure 7, left). Furthermore, accelerations were acquired during operation of the freight car. The observed acceleration levels vary with the current operation condition (Figure 7, right). Obviously, accelerations of the wheel set are much higher when the car passes a track switch compared to normal driving on a straight line.

The vibration absorber is tuned to a resonance frequency of the wheel set at 189 Hz. First, the effect of different absorber masses on the potential vibration reduction and the dissipated energy is studied. For the first test, the damping coefficient is set to 0.03 and the mass is varied. As expected, a higher absorber mass effects in a better vibration reduction (Figure 8, left). The dissipated power in the absorber damper is calculated from Equation 10, using the acceleration spectrum measured during the passing of a track switch depicted above. The resulting power density spectrum is integrated in order to get the overall power. Obviously, a heavier absorber also dissipates more power. However, the power levels in the range of Watts have to be put into perspective: The necessary prominent acceleration levels only occur during the passing of a track switch, an event of a rather short duration which occurs only at certain times during operation.

Secondly, the effect of varying the damping coefficient is investigated, while the mass of absorber is retained at 10 kg. Neither very low nor very high damping coefficients lead to good vibration reduction (Figure 9), which is a well-known fact of tuned vibration absorber design. The dissipated power of the damper is also maximal for a certain value of the damping coefficient. Thus, in contrast to the mass of the absorber, the damping coefficient has to be chosen with respect to both, the goals of vibration reduction and energy harvesting. This can be obtained by a proper choice of the electrical load of the system and suitable design of the electromechanical transducer integrated into the absorber. A design optimization goes beyond the scope of this work. However, the workflow is illustrated by means of an example based on a generic design.

Figure 6: Freight car used for the experimental investigations.

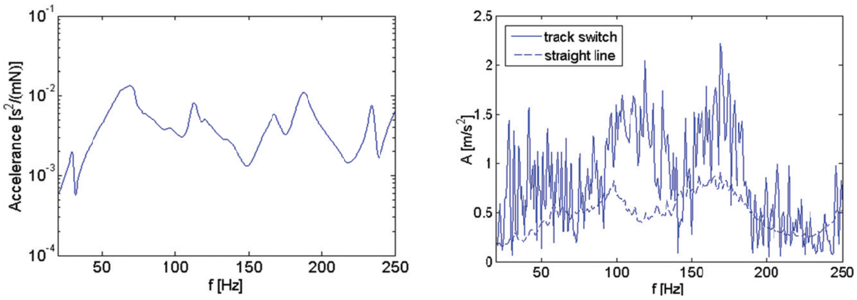

Figure 7: Accelerance at the wheel set mount (left), acceleration spectra during operation (right).

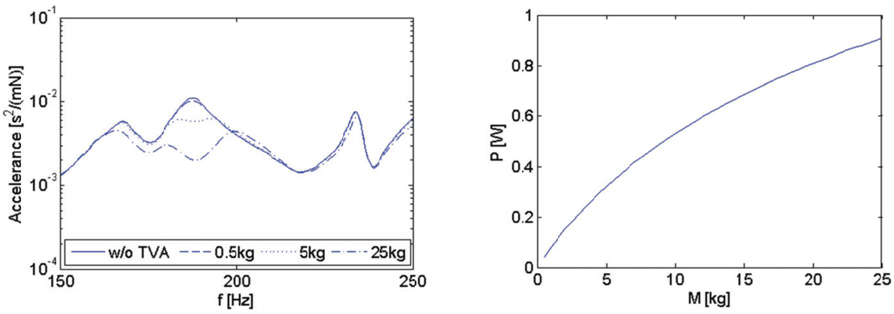

Figure 8: Effect of different absorber masses (left), overall power dissipated (right).

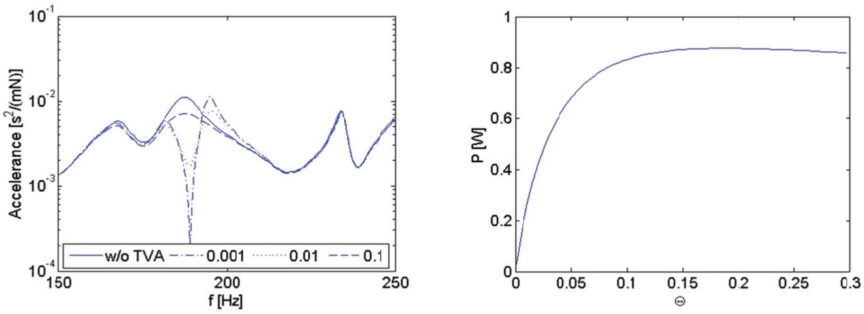

Figure 9: Effect of the damping coefficient (left), overall power dissipated (right).

The TVA has a tip mass of M_t = 5 kg and a mechanical damping ratio of Θ = 0.01. The material properties of X10CrNi18-8 spring steel (E = 195 GPa, ν = 0.29, ρ = 7900 kg/m^3) were chosen for the absorber spring. For the PZT layer the material properties of PIC 155 ceramic were applied.

First, the geometry of the absorber was varied and numerical modal analyses were conducted to tune the TVA to 189 Hz. The resulting geometries were 67.75 mm x 30 mm x 12 mm for the steel beam and 50 mm x 30 mm x 0.5 mm for the piezoelectric layer on top of the beam. Afterwards, a resistor of 26 kOhm was used as electrical load leading to additional damping of the absorber. The resulting damping coefficient obtained by a coupled numerical harmonic analysis was Θ = 0.0132. As described before, with those equivalent parameters for mass, resonance frequency and damping coefficient and the measured acceleration spectrum, the modified accelerance and acceleration spectrum were estimated using Equations 7 and 8. From the resulting acceleration the stroke x_{mod} (jω) at the absorber's mounting point was derived. The Finite Element model was used again for a harmonic analysis of the TVA including the electromechanical coupling and the load resistor using x_{mod} (jω) as base excitation in order to calculate the generated electrical power. The results are depicted in Figure 10. Obviously the power generated by PZT transducer is only a fraction of the whole dissipated power estimated with Equation 10. In the frequency range 180 - 200 Hz an amount of maximal 18 % and minimal 12 % is spent in the resistor, which matches well with the fact, that the electrical load of the system increases the damping only slightly from 0.01 to 0.0132, i.e. most of the damping is still caused by the mechanical system. However, the characteristics of both spectra in Figure 9 are quite similar. For example both the electrical and the overall dissipated power decrease next to the natural frequency of the TVA and rise towards higher and lower frequencies.

The maximum power is dissipated at 183 Hz. The reason for this effect is the relatively low damping of Θ = 0.01 for the mechanical system and Θ = 0.0132 for the coupled system. However, the application of poorly damped TVAs leads to two prominent natural frequencies to the left and right of the tuning frequency (see e.g. Figure 9).

In the case of the energy harvesting absorber, the strain in the PZT transducer increases for those frequencies and more power is generated. This effect vanishes when more damping is applied to the system, preferably by optimization of the electromechanical energy conversion. Therefore the accelerance at the TVA's resonance frequency will increase as well, and the energy harvester becomes more efficient.Thus, the estimation of the dissipated power by simple analytical calculations based on measurement results may serve well as a starting point for the detailed design of an electromechanically coupled TVA. For example, in the next step the thickness of the piezoelectric transducer could be increased and the effect on the vibration reduction and generated electrical power could be studied by stepping through the proposed workflow in a loop.

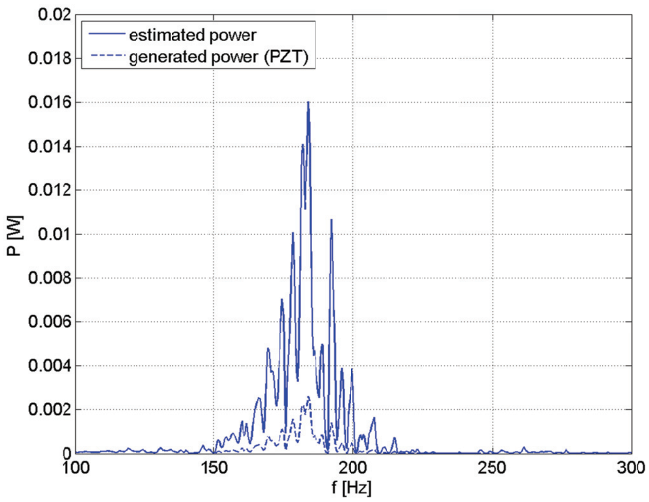

Figure 10: Numerical calculation of the generated electrical power in comparison to the first estimation.

CONCLUSIONS

This article presents a framework for the design of 'Energy Self-Sufficient Vibration Absorber Sensor Modules'. A method for the estimation of the effectiveness of the energy harvesting vibration absorber system for practical applications based on measurement data has been introduced and applied to a freight car. The analytical power estimation serves as an indicator for the potential of the system and for first parameter studies. For detailed investigations on the design, a generic Finite Element model was set which allows for the precise calculation of the expected power from the PZT transducer. The results showed that for the parameters considered only a fraction of the dissipated power is spent in the electrical network. This fraction has to be maximized in the further design process using the framework presented.

ACKNOWLEDGEMENTS

This work was conducted within the projects EA-TSM and PiezoEn, funded by the German Ministry of Education and Research BMBF under contract numbers W40027 and 16SV3398. The support is gratefully acknowledged. The authors also are indebted to Mr. Thiemo Engelbart, who conducted the measurements on the freight car, and the Railway Museum Darmstadt-Kranichstein for their kind support of the experimental work.

REFERENCES

[1] Farrar, Charles R. et. al., 2003. Damage Prognosis: Current Status and Future Needs. *Los Alamos National Laboratory Report*, LA-14051-MS

[2] Anton, S. R. and Sodano, H. A., 2007. A review of power harvesting using piezoelectric materials (2003-2006). *Smart Materials and Structures* 16(3), pp. 1-21.

[3] Spencer, B.F., Ruiz-Sandoval, M. and Kurata, N., 2004, Smart sensing technology: opportunities and challenges. *Structural Control and Health Monitoring* 11(4), pp. 349–68.

[4] Cunha, A. et. al., 2009. Identification, monitoring and control of bridges and special structures, Proc. *IV ECCOMAS Thematic Conference on Smart Structures and Material Systems*, Porto.

[5] Flammini, F. et.al., 2010. Towards Wireless Sensor Networks for railway infrastructure monitoring. *Proc. Electrical Systems for Aircraft, Railway and Ship Propulsion* (ESARS): 1-6.

[6] Elliott, S.J., Saba, R. and Baumann, O., 2008. *Vibration power harvesting from head motion*. Proc. Eurodyn, Southampton.

[7] Den Hartog, J. P., 1985. *Mechanical Vibrations*, Dover Publications.

[8] Bielawa, R.L., 1992. *Rotary Wing Structural Dynamics and Aeroelasticity*. Washington. AIAA.

[9] Allik, H. and Hughes, T., 1970. Finite element method for piezoelectric vibration. *International Journal for Numerical Methods in Engineering* 2(2), pp. 151-57.

[10] Zienkiewicz, O. C. and Taylor, R. L., 2005. *The Finite Element Method*, Butterworth Heinemann.

[11] Shu, Y. and Lien, I., 2006.Analysis of power output for piezoelectric energy harvesting systems Source. *Smart Materials and Structures* 15(6), pp. 499-512.

FAILURE RISK ASSESSMENT BY INTEGRATION OF PROBABILISTIC FRACTURE MECHANICS AND QUANTITATIVE NON-DESTRUCTIVE INSPECTION - A STRUCTURAL HEALTH MONITORING VIEW

Dragos. D. Cioclov

Fraunhofer IZFP, Saarbrücken, Germany and D. Cioclov Consultant, New York, USA.

Dragos.cioclov@izfp.fraunhofer.de

ABSTRACT

Intermittent non-destructive inspection has been used since long time for checking the integrity of load-carrying structures and mechanical components. With the tremendous contemporary development of sensor technology, in conjunction with advanced wireless communications and the support of the massive computation facilities, continuous monitoring of structural damage during operation and time-continuously assessment of structural integrity, for the prediction of structural remaining life, in conditions of reliable and optimized costs of operation, is, nowadays, a vigorous endeavour for the next years to come. The article addresses the scientific and engineering bases of Structural Health Monitoring (SHM) comparatively with the traditional approach to structural inspection and reliability assessment, outlining that beyond the new sensing sophisticated technology, much of the well-established methods based on models derived from fracture mechanics, quantitative non-destructive testing evaluation in probabilistic quantitative terms, are naturally integrated in SHM technology. The article is focused on civil aircraft structures outlining how the conjoint construct of Probabilistic Fracture Mechanics (PFM) and methods of quantitative non-destructive inspection (NDI) is implemented in SHM evaluations with the aid of massive computer simulations. Probabilistic substantiated of the warning time at the attainment of various levels of fatigue crack extension in the skin of a fuselage structure is assessed having as support a virtual SHM system which simulates acquired data processing performed on-board or in remote stations by wireless data transmission. A comparison of failure risk prediction is presented when aircraft operate under risk management applying intermittent NDI at scheduled inspection time (when the aircraft is grounded) on the one hand and continuous in time by SHM, on the other hand. The reported results are intended to demonstrate that by integration of existing assessment methodologies of PFM coupled with quantitative NDI can parallel SHM by massive computer simulation having as a result refined prognostics and management of failure risks and optimization of operational costs.

INTRODUCTION

Intermittent non-destructive inspection has been used since a long time for checking the integrity of load-carrying structures and mechanical components. Railroad hammer-tapping, in order to evaluate the emitted sound by “expert” interpretation, is a salient example. Developments along this way of approach have emerged in the nowadays state-of-the-art of non-destructive testing techniques (NDT). In this field, parallel inter-related developments are underway: improvement of sensing instrumentation, primary data processing quantitatively, in both deterministic and probabilistic format and, finally, their interpretation. Design and procedural inspection codes evolved on the basis of these developments having the main focus on assuring the structural integrity during the whole operational life, with maintenance costs kept as low as possible and, concurrently, assuring failure risks at very low levels, acceptable for the society from the standpoint of human life, environment and wealth protection. Obviously, there is conflicting interaction between high structural reliability and operational costs in which inspections, repairs or replacements of damaged parts of the structure may attain prohibitive expenditures. This issue has become more acute nowadays when increasing concern is manifested about the aging of load-carrying structures which operate under severe loading and environmental circumstances. From another perspective, with the development of a new generation of high-tech load-carrying structures, the benchmark of past experience and the ensuing projective model prediction methods become more and more irrelevant by obsoleteness.

To advance on this front, structural health monitoring (SHM) has been developed, recently, as a new paradigm, in response to the traditional approach to structural reliability and operational effectiveness. At the core of SHM is continuous, on-line sensing of localized damage in a multitude of locations, “hot-spots”, in the structure.

Concomitantly, the grate amount of recorded data is automatically processed, interpreted, ultimately, providing diagnosis of the current capacity of the structure to accomplish its operational tasks. Eventually, by means of automatic artificial intelligence, simulated suggestions may be stated for corrective measures for maintaining in further operations high standards of safety. There is accumulated a sound cognizance on the hot-spot locations in heavy duty structures based both on prior design considerations and the wealth of experience accumulated over the years in operation as result of maintenance inspections and, not ultimately, from failures. For instance, in aerospace load-carrying structures, multi-site fatigue damage in fuselage structures or corrosion in hidden hard-to-reach locations typify hot-spot locations where major flaws, mainly cracks, are prone to occur, inevitably, in aged aircraft.

These types of problems are addressed by SHM envisaged as a comprehensive rationale based on on-board implemented sensing network and subsequent data processing, locally, on-board and/or, wirelessly transmitted information to higher level data processing in a centralized monitoring station for decisions about adequate actions and information storage. There are many options for implementation of SHM in stationary structures, aerospace, automotive, on ground and see load carrying structures. Mostly used sensing systems are based, mainly, on ultrasonic and piezoelectric principles. Sensors of these types have miniature dimensions hence unobtrusive and easily implementable into the structure. Sensors with self excitation have being conceived which do not require cumbersome electric devices (e.g. Giurgiuţiu 2002). Selected overview information on SHM may be found in the works of Boller and Biemans [1], Boller and Mayendorf [2], Boller et al. [3], Giurgiuţiu et al. [4], Giurgiuţiu and Zagrai [5], Yolken and Matzkanin [6], Balageas et al. [7], Schmidt and Schmidt-Brandecker [8], Farrar and Lieven [9], Lloyd [10], Baker [11], Coppe et al. [12], obviously, the citation being by no means exhaustive.

A SHORT OUTLINE OF STRUCTURAL HEALTH MONITORING APPROACH

Continuous assessment of material damage during operation of a load-carrying structure is referred as structural health monitoring. It is a unifying view and a whole host of associated methods in structural integrity evaluation. SHM emerged from the tremendous developments in sensors technology, data acquisition and transmission, data processing and intelligent automatic evaluation for decision-making and mandating corrective measures in order to keep the failure risk at the lowest levels which are economically justified. Conceptual area of SHM incorporates various scientific and engineering approaches pertaining to structural integrity. Any physical system and process related with structural integrity can be envisaged as support for a SHM.

SHM implies evaluation of operational conditions, data acquisition, data processing and damage feature extraction in statistical format, models development of features conditioning structural damage, discrimination into damaged / un-damaged components, failure risk assessment, preventing measures formulation, prognosis of economic remnant life, input data for structures management strategies for devising satisfactory reliability versus costs trade-off. Figure 1 shows, schematically, the interplay between goals, means and specific methods involved in SHM. The nowadays sensors technology makes possible to monitor the whole history of a structure, locally, in “hot spots”, or globally, by a network of distributed sensors attached or incorporated within the structure. Hot-spots are identified according to the past experience, components and structures real geometry on which is exercised computer simulation of stress and strain distribution. Figure 2 exemplifies hot-spots in a civil aircraft load-carrying structure such as fuselage, wings and rear stabilizers.

Databases build-up in real time, together with computing algorithms appropriate to the specificity of the underlying materials damage mechanisms enable to project forward, in time, the evolution of the structural integrity. By this way, evolution of the material damage is brought under continuous scrutiny, enabling the prediction of the remnant life and further usage capacity, the risk of malfunction and, ultimately, the risk of failure, all being relevant information for decisions-making. Ascertainment of places or components that need overhaul or replacement becomes a part, in its own rights, in the management and supervision of structural operation. From a pragmatic standpoint, SHM is a comprehensive and continuous way of performing non-destructive inspection (NDI) with inter-inspections time-intervals vanishing, at limit, towards zero.

ON IMPLEMENTATION PFM & QNDI IN SHM SIMULATION

Data sources for monitoring fatigue damage by crack growth

Probabilistic fracture mechanics enables to model and simulate the statistic variability in the growth of an already initiated crack in a structural element subjected to variable loading. The information on the probabilistic pattern of fatigue crack growth (FCG) stems from two main sources. The first one pertains to the statistic of the parameters in the FCG model (Paris rule) [13] and the statistics of material strength and deformation characteristics entering in the model of the end failure, i.e. the fracture occurring the last cycle of survival of the loaded structural component. The set of parameters implied in the FCG model are assessed, experimentally, on standard specimens in fatigue tests, planned with the aim of extracting statistical information which is relevant for reliability assessments. Primary monitored data are the crack size, *a*, as function of the number, *n*, of applied loading cycles. Data are fitted to analytical models, one salient example being the Paris-Klensil rule with inferior threshold: $da/dn = C\left(\Delta K^m - \Delta K_{th}^m\right)$. Here, ΔK stands for the range of variation of stress intensity factor (SIF) – a global metric of the state of stress at the tip of an existing crack, of size a, and, ΔK_{th}, stands for the inferior threshold of SIF range under which fatigue crack growth becomes unobservable [13,14]. The end failure model adopted in this study pertains to the class of models based on the concept of Failure Assessment Diagram (FAD) which accounts on plasticity effects at the crack tip at the attainment of the critical (limit) state defined either by collapse in the cross-section owing to excessive plastic deformation spreading from the crack tip or, as in materials with low ductility, by component sudden fracture.

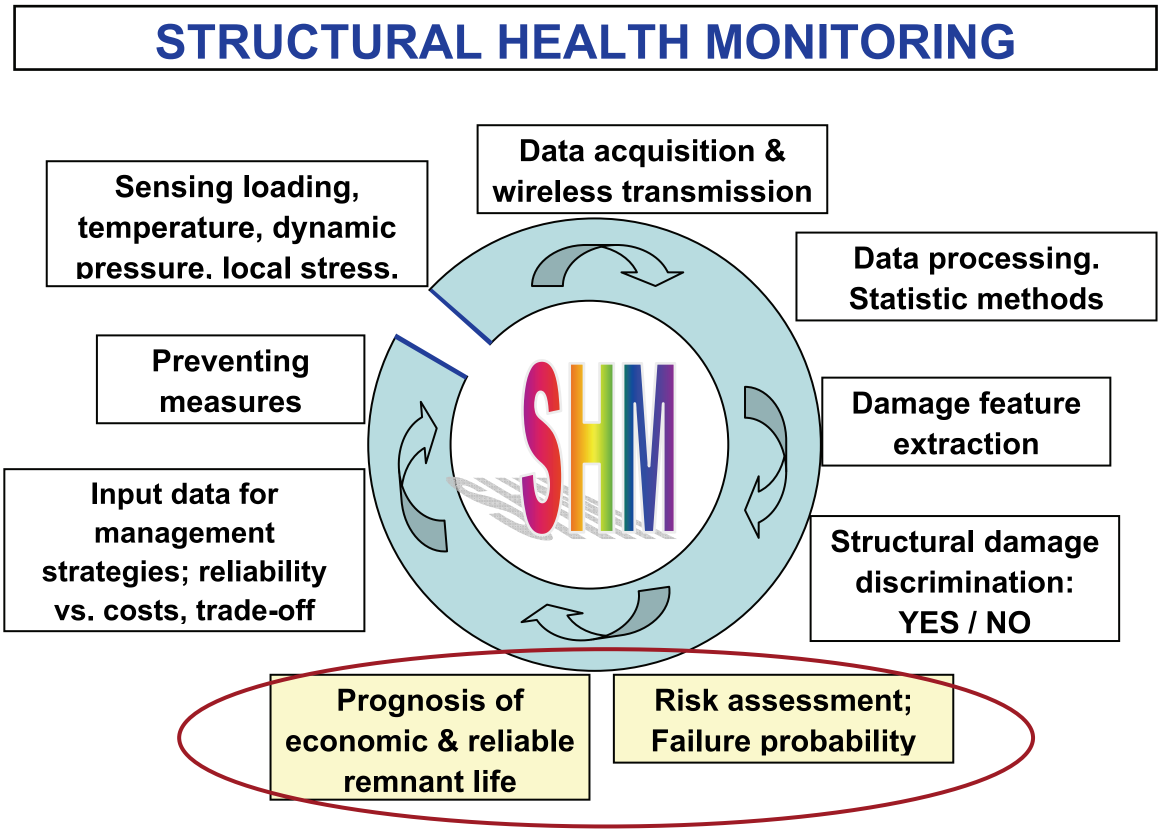

Figure 1: Rationale of SHM systems

FAD approach has at its base the Dugdale model of plastic deformation at the tip of a crack residing in a plate of rigid-perfect-plastic material. The theory and validation by experiments of FAD approach may be found in milestone references such as of Dugdale [15], R/H/R6 [16] and SINTAP [17], the citation being by no means exhaustive. Statistics of material parameters implied in FAD approach are: static fracture toughness, K_c, ultimate tensile stress (UTS) and yield point (YP).

The methodology of approach to fatigue damage owing to cracks growth under cyclic loading has been formalized in a probabilistic fracture mechanics construct by incorporating the outlined models of FCG and ultimate fracture, in the last survival loading cycle, as the end phase of the evolutionary damage process [18]. Analytics of the models in deterministic meaning are those which are well established in the present stage of fracture mechanics developments. As concerns the integration of probabilistic aspects of FCG, analytics of the models has been randomized by direct Monte-Carlo sampling of the basic random variables involved in the model, with distributions substantiated by statistical test. It should be emphasized that by this way it is circumvented the complicated probabilistic functionals, i.e. convolution integrals, which are intractable by finite functions requiring numeric approximations of doubtful degree of accuracy. Moreover, Monte Carlo simulation remains close to the physical phenomenology of FCG as it is reflected by the adequacy of prediction when it is adopted to the Paris-Klensil model of FCG. The main shortcomings of Monte Carlo simulation method is claimed for results obtained at very low probability levels ($<10^{-6}$) which requires a large number of sampling iterations ($>10^9$) to assure stable estimations. However, with the advent of massive computation technology this claim has fallen in desuetude. Another source of information derives from quantitative non-destructive inspection (QNDI). It encompasses flaws detection and their quantitative evaluation together with assessing variability and uncertainty (V&U) associated with a specific NDI technique. V&U encountered in NDI is quantified in terms of probability of detection (POD). Variability is the effect of *chance* and is function of the system. Variability is objective since it resides in the nature of the involved physical mechanisms underlying, in our case, material damage by fatigue. It is not reducible by either study or further testing and measurements. It may be reduced only by changing the system. Variability incorporates also our unawareness stemming from semantics, i.e. the meaning we attach to vectors of communication. Uncertainty associated with a probabilistic statement (as POD) stems from the assessor's lack of knowledge about physical laws and parameters that characterize technical systems. Uncertainty is reducible by further experiments and study. The alternate concept the *degree of certainty* is our measure of how much we believe something to be true. In practice, certainty is validated by positive (confirming) experiments.

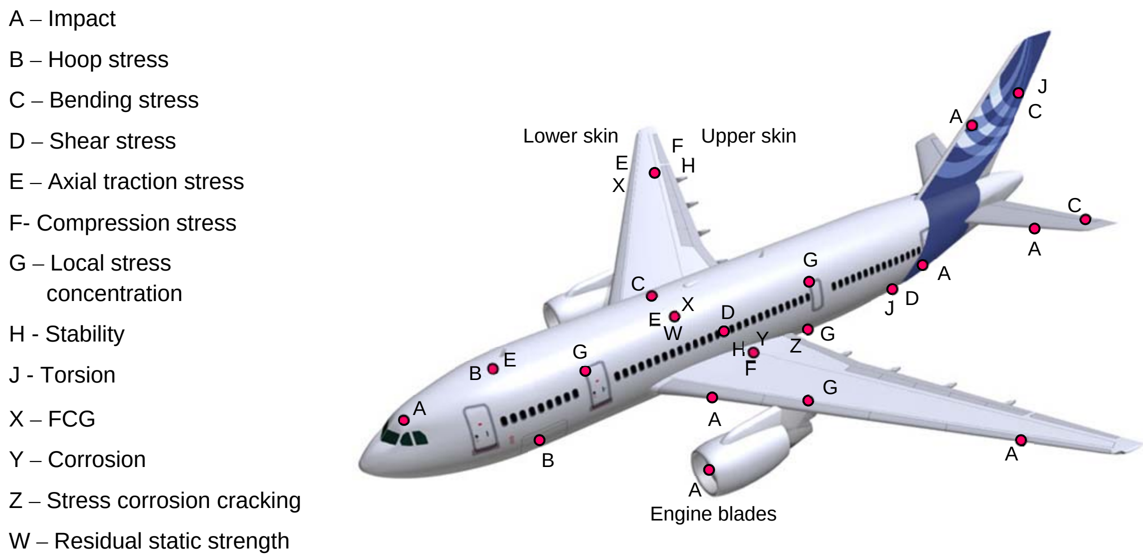

Figure 2**:** Hot-spot points prone for fatigue damage initiation and where SHM systems are usually implemented in the load-carrying structure of a civil aircraft. After [4] and [19].

NDI systems are driven to their extreme capability to find small flaws. To extreme capability, not all small flaws are detected owing to underlying V&U. NDI capability (reliability) is characterized in terms of probability of detection as function of the flaw size, *a*. A *POD(a)* function is defined as the proportion of all existing flaws of size *a* that will be detected by a given NDI system. Probability of non-detection (PND) is simply the complementary of POD, i.e. *PND=1-POD*. Probability of detection is estimated by statistically planned NDI experiments on specimens containing flaws of *a-priori* known size. A large experimental effort has been made in the last decades in order to elucidate this issue and extended literature is available about this subject (e.g. [20-22]). Integration of PFM and QNDI has been materialized in a theoretical construct transposed in a proprietary computer code and associated executable software identifiable under the acronym *pFATRISK* (see [18,23-26]). Figure 3 illustrates the main steps in probabilistic FCG simulation until the ultitimte state at fracture in the last survival cycle. The component geometry model consists in two symmetric through-thickness propagating cracks emerging from the boundary of a hole, placed symmetrically in a thin strip (coupon). The width of material ligament is determined by inter-rivets distance. It has been considered both determinstic cyclic loading with constant stress amplitudes and random cyclic loading with stress peaks following Pareto distribution, the latter loading history being able to model rare events of high stress peaks interspersed among near-constant amplitude cyclic loading. Plates in Figure 3 are arranged in the sequence which is followed along the simulation path according to *pFATRISK* rationale.

Figure 3 (*i*) portrays Paris-Klensil rule in deterministic and probabilistic format, in the latter case, with static strength parameters (UTS, YP and Kc) described by 3-parameters Weibull distribution and FCG governing parameters (*C*, *m* and ΔK_{th}) described by Normal distribution. Figure 3 (*ii*) shows SIF correction factors for the coupon geometry with two opposing pre-existent cracks as idealized body in which FCG occurs. Figure 3 (*iii*) shows the results of FCG simulation under constant amplitude loading (cycle ratio $\sigma_{min}/\sigma_{max}=0.1$) until the attainment of: case I - various pre-set crack sizes and case II – the attainment of a pre-set fatigue life. Concurrently is shown a FAD representation of FCG until failure. Figure 3 (*iv*) shows, in terms of cumulative probability density function (PDF), the fitting to a Log-Normal distribution of simulated data of the crack size, *a*, attained at a pre-set fatigue life (case II) and life scatter at pre-set warning crack size (WCS) level, case II. PDF vs. *a*, in case A is also shown. Figure 3 (*v*) exemplifies the deterministic assessment of the safety index (factor) accornding to FAD methodology and the counterpart probabilistic simulation (10^8 Monte Carlo iterations) of the failure risk in terms of probability of fracture or the inter-rivet ligament colapse by excessive plastic deformation. In this latter step the simulation of the influence of the quality of NDI can be implemented, quantified by experimentally-based POD. This part of *pFATRISK* simulation evinces the ample decrease in the probaility of failure by applying NDI of certain quality reflected in POD curves, having in mind the pre-supposition that a deffective element evinced in a simulation iteration is replaced or repaired at the initial load-carrying capacity. Obviously, this is an assessment at the time of inspection when the structure under consideration is at the disposal (e.g. an aircraft is grounded) for NDI according to regulatory prescriptions.

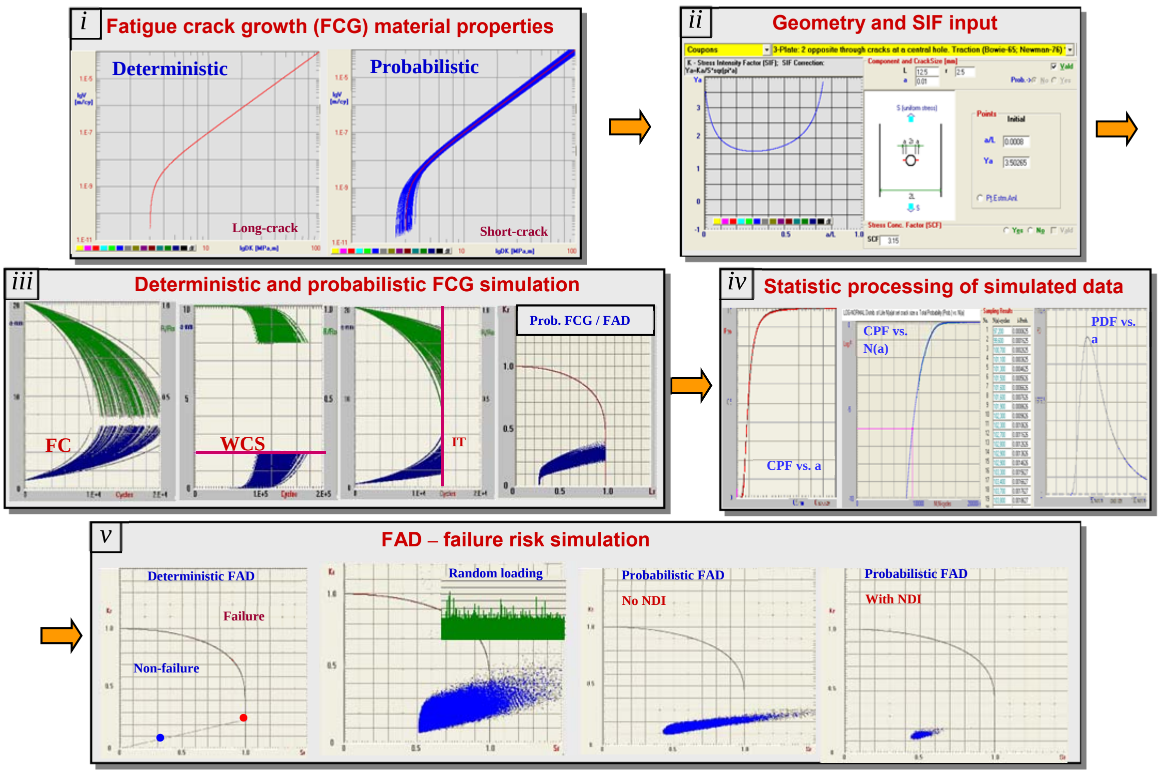

Figure 3: Probabilistic simulation of FCG in a coupon with central hole mimicking a rivet hole in the fuselage skin of an aircraft.

The thoretical bases and the computation path outline Figure 3 for assessing fatigue failure risk are adapted for the traditional approach to fatigue damage tolerance (DT), widely applied in aircraft structural design. It appears, however, that this construct, in its theoretical premises, algorithms and computation (programming) codes is logically implementable into SHM methodology. In fact what is nowadays the traditional damage tolerance approach to failure risk is a section, at a certain time, in the multi-dimensional space encompassing all relevant variables in the fatigue damage process. By contrast, SHM can follow, in principle, the same algorithmic construct but it is performed continuously in time requiring an explicit time dependence of random variables pertaining to the computation model.

However, as straightforward as it seems the similarity in algorithmic construct and the implementation in the damage models in the both ways of approach, the output of non-destructive sensing and the flow of monitored data towards processing places, locally or centrally in SHM assessments is significantly different in comparison with the traditional damage tolerance approach. Moreover, this difference imposes another decision making strategy and ensuing trade-off between reliability, maintenance and operational costs.

A case study of virtual structural health monitoring

In a real-life fleet of identical items, in the same congruent position of a specific hot-spot, the growth of a fatigue crack displays randomness owing to the variability of material properties, cyclic loading intensity, eventually, stemming from petite departures from constancy of manufacturing technology (e.g. riveting). Also due account is to be given to probabilistic uncertainties in data processing and interpretation. For setting warning at the attainment of a specific crack-size, beyond which the structural reliability is no more acceptable, probabilistic FCG simulation is the way to place this undertaking on the physics of the fatigue damage mechanisms and associated models. Under the given material response to loading circumstances, the knowledge of the variation of statistical scatter at achieving a pre-set crack size, sensed by SHM system, embodies the necessary input for the simulation of structural reliability. It may be expressed in various quantities. Most common is the probability of failure in the hot-spot location, a general index of the momentary dangerousness, but of equal importance is the prognostication of the remnant life (structural usage) associated with an estimated probability of incidence. Obviously, there is an interplay between the randomness of the warning time, at the attainment of a specific crack size, and the ensuing probability of failure. Smaller is the crack-size warning level, implicitly the time to reach it, the smaller is the expected probability of failure, i.e. the higher the structural reliability. Probabilistic simulation of this trade-off is the goal of integration of PFM and QNDI in a virtual SHM dedicated for a better substantiation of decision-making, either during operation or for setting the scheduled times for NDI (on grounded aircraft) and structural health evaluation. Virtual SHM, which will be further outlined, has a two-fold capability. I) to simulate the variability of FCG and evince the distribution of the time scatter for attaining a pre-set warning crack-size level. With other words, to estimate the probability of occurrence associated to a specific warning time. II) To simulate the crack-size statistics at pre-set warning time and, with this information as input, to assess the probability of failure. The latter assessment uses a model of end failure after stable FCG until the exhaustion of the component load carrying capacity. Figure 4 outlines the principles of this way of approach which has been carried on by simulation with *pFATRISK* methodology applied to fulfil task I and II outlined above.

This case study refers to a fleet of 9.999 identical geometry items (locations of analysis) under the same nominal loading. The failure risk, reflecting the variability of the FCG among locations, is simulated probabilistically, as outlined above and schematized in Figure 4. In the exercise it is presupposed that the structure has incorporated a generic SHM of FCG, which is capable to sense the size of cracks from micro (e.g. 0.1 mm) to macroscopic range. Specifically, the sizing covers the range from cracks nucleation to an extension which exhausts, locally, the load-carrying capacity of the ligament between two rivets. As fatigue testing data on riveted panels evinces, is in consonance with fatigue damage simulation evincing that in few loading cycles it is expected to be triggered wide spread of fatigue damage in the entire panel. Under task II, schematized in Figure 4, the analysis may incorporate the simulation of the benefit which might be gained by performing at pre-set scheduled time a NDI of quality reflected by POD vs. crack size correlation. Obviously, by corrective measures, ensuing the NDI, structural reliability is enhanced. A detailed presentation of this approach is to be found elsewhere [18].

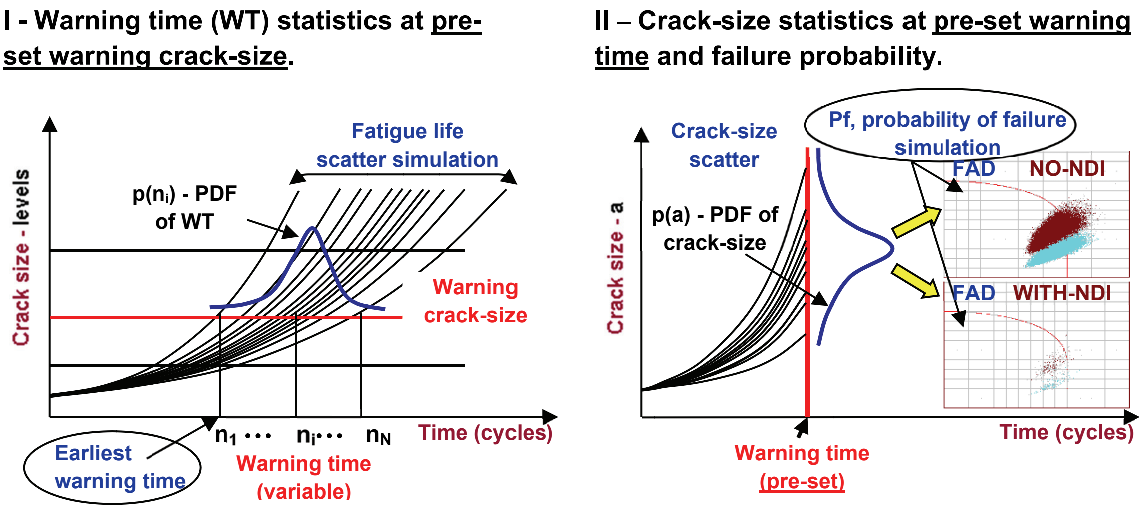

Figure 4: PFM & QNDI implementation in SHM. I – Simulation of warning time statistics at pre-set warning crack-size level. II – Simulation of crack-size distribution at pre-set warning time and probability of failure simulation according to FAD methodology, comparatively under non-application and application of NDI.

Probabilistic warning time simulation of fatigue damage in a virtual SHM system

For performing the task I of assessing the warning time statistics at pre-set crack size, probabilistic FCG simulation has been performed until the attainment of various warning crack-size (WCS) levels. Figure 5 shows the graphical representation, as generated automatically by *pFATRISK* software. Two concomitant parallel representations are shown: a) crack-size scatter vs. the number of applied loading cycles, shown in Figure 5a and, b) the probaility distribution function (PDF) of the number of loading cycles at the attainment of various crack-size warning levels in $N=9.999$ Monte Carlo iterations.

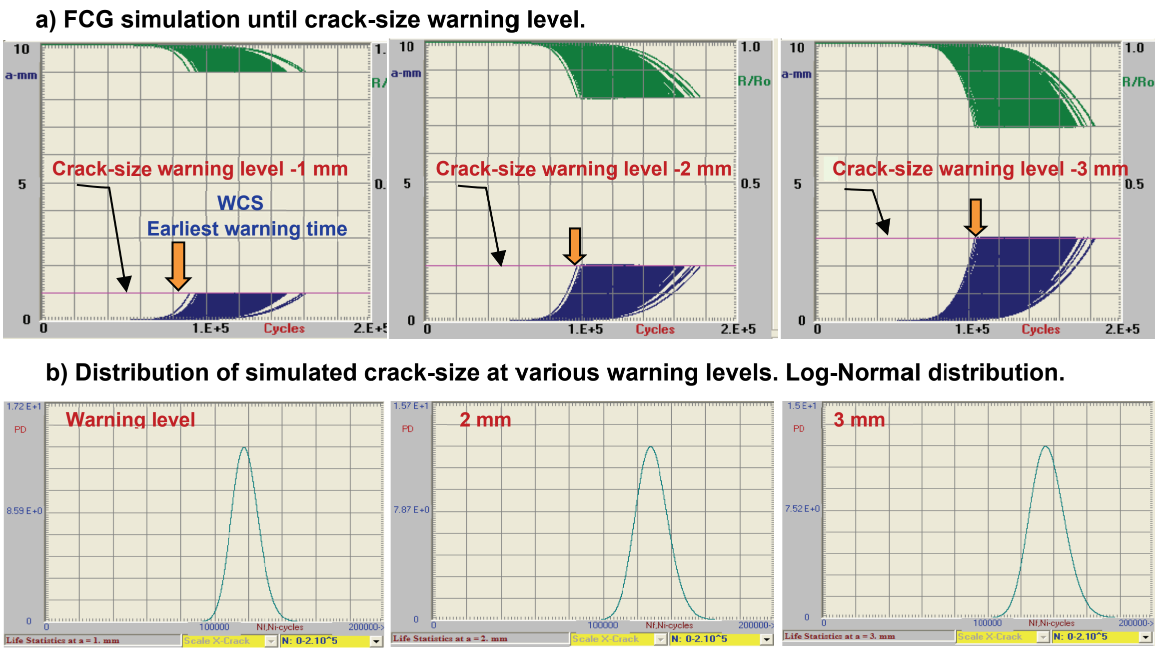

Figure 5: Fatigue crack growth simulation until the attainment the level of warning crack size of 1, 2 and 3 mm, respectively. *pFATRISK* simulation code.

Figure 5b illustrates the fitting in a Log-Normal distribution of simulated crack-size at various warning levels. The probability associated to simulated *i*-ranked values in the sample of N items has been computed with the formula: *Pi,N=(i-3/8)N* (e.g. [28,29]). The smallest ranked (*i=1*) values, corresponding to a specific WCS level, is assigned with the probaulity $P_{(i=1),N}$, as outlined above, resulting a probability of occurrence of 6.25 10^{-5}. Table 1 gives, the fatigue life, *N (i=1;WCS)*, at the smallest simulated rank, *i=1*, corresponding to various WCS levels. This may be interpreted as the minimum simulated life when the warning at the pre-set level is given in at least one item in the fleet. Table 3.1 also gives: the extrapolated warning life, at 10^{6} probability of occurrence, $N(P=10^{-6};\ WCS)$, a level of interest for reliability assessments according to the nowadays trends of airworthiness prescriptions.

By this analysis it is evinced, computationally, that when the WCS is 2 mm, the fatigue life attains, with a probability lower than 10^{-6}, at least 90.120 loading cycles. There are also given in Table 1 the median life *N(P=0.5; WCS)* and, for the purpose of comparison of the extent of the scatter of the warning time (*N*), it is given the simulated life at the highest probability of occurrence in the simulation session i.e., *N(P=0.99999;WCS)=190.659* cycles. It becomes obvious that the range of scatter of the fatigue life at warning, in the fleet stays in the ratio of two.

The results given in Table 1 are represented in Figure 6. The resulted functional relationship expresses the variation of warning reliable timing, probabilistically substantiated, as function of the pre-set WCS levels. However, the appropriateness of WCS levels is dictated by SHM detection capability and needs a specific analysis in terms of POD (e.g. [30]). It is apparent from Figure 6 that seting the probability of attaining the WCS at sufficiently low values (e.g. 10^{-6} or lower) mandates early, definitly on the safe side, timing for corrective measures: repaires or more in-depth intervention as overall inspection and further decisions for ovehaul or retirement for cause.

WCS mm	**Fatigue life (cycles) at warning crack-size**			
	Simulated*⁾ $N(i=1;WCS)$ **Prob.=0.0000625**	**Extrapolated** $N(P=10^{-6};WCS)$ **Prob.=0.000001**	**Median** $N(P=0.5;WCS)$ **Prob.=0.5**	**Extrapolated** $N(P=0.99999;WCS$ **Prob.=0.999999**
0,1	74.300	69.364	90.500	118.576
0.5	84.000	**80.463**	108.400	146.230
1.0	89.800	85.390	117.300	161.464
2.0	97.200	**90.120**⁾**	127.600	180.659
3.0	104.300	93.850	135.000	193.338
4.0	106.000	96.548	140.435	203.026
5.0	107.700	96.604	142.500	211.094

Table 1:*⁾ 9.999 simulation iterations. **⁾ case for further studies.

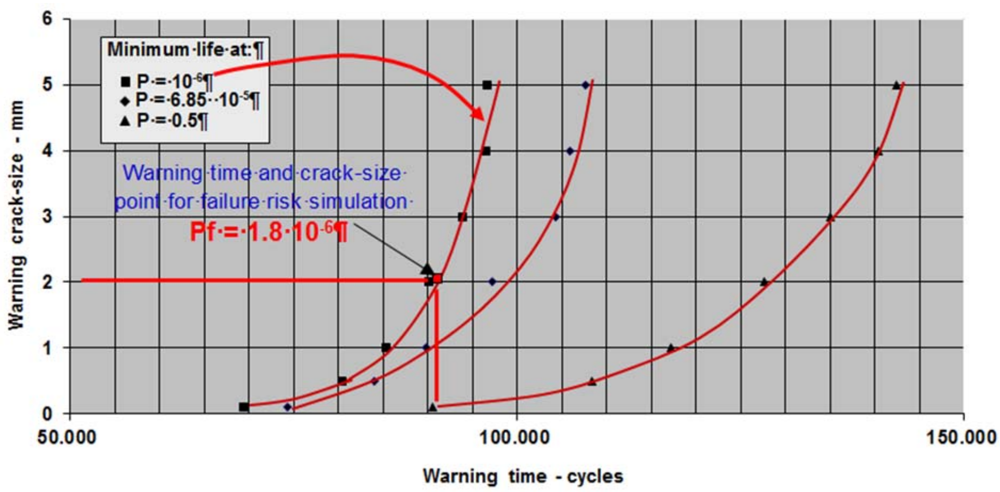

Figure 6: Warning time at various pre-set crack-size levels for low and median probabilities of occurence that crack-size attains the warning level.

These results outline the trade-off between SHM and continuous assessment of failure probability, general inspection schedule both issues being of relevance in structural failure risk management.It should be emphsize that data in Table 1 and represented in Figure 6 have been derived by probabilistic simulation of the fatigue crack growth over a cupon (Figure 3), a representative idealized spot of the material ligament between two rivets in the fuselage skin of an aircraft. Simulation in this exercise refers, globally, to fatigue damage as function of the number of flights in the phase prior to triggering of wide spread fatigue over the entire fuselage structure. FCG simulation may be performed as an idependent task or paralleling, virtually, real life crack-size monitoring. It enables to obtain a data base which can be processed locally or wireless transmited to central points in the SHM network and, eventually backward retransmitted for current operational guidance (see Figure 2). Globally, incorporating SHM and parallel performing computer simulation of the fatigue damage process, results in a better substantiation of current operational decisions and management regarding inspections timing, repairments or replacements and, not the last, the prediction of reliable remnant lives. In the next section, for the same circumstances of the case study, and following the same way of approach based on Monte Carlo FCG simulation, an execise of probaility of failure prognosis at various inspection times (IT) will be outlined.

Failure probabilities simulation for SHM at scheduled inspection time (IT)

Task II outlined in Figure 4, which performs the simulation of failure probability at pre-set inspection time, is demonstrated under the same premises as in the previous exercise of Task I. Simulation mimiks FCG in the model coupon under pressurization/ depressurization loading cycles encountered by the aircraft fuselage structures. Crack size scatter has been probabilistically simulated in 9.999 iterations (result values items) until the attainment of various levels of pre-set fatigue lives, envisaged as times for evaluation of failure risk in a continuous process or inspection/evaluation times when the structure is out of operation (aircraft is grounded). Massive Monte Carlo simulation, in 10^7iterations, has been performed in order to obtain stable values of the probability of failure. In one iteration, material strength UTS, YP and fracture toughness K_c, considered as random variables involved in the FAD failure model, together with already simulated crack size distribution at the evaluation (NDI) time, are Monte Carlo sampled and FAD assessment is performed in each iteration. If in one iteration the representation of the state point falls beyond FAD limit curve, then the iteration is counted as simulating the failure and, consequently, the structural element is considered replaced or repaired at the initial capacity. The ratio of the number of failures, N_F, to the number of total iterations, N , estimates the probability of failure: $\bar{P}_{fN} = N_F / N$. Further on, aligned to the suppositions taken in the case of task I (WCS=2 mm to which corresponds a fatigue life of approx. 900.000 cycles with probability of occurrence of 10^6), the simulated crack size distribution at this envisaged NDI time is used as probabilistic information for FAD analysis of the failure (fracture) risk, at this moment in the structure life. The crack-size warning level of 2 mm level is regarded, tentatively, as fairly detectable with nowadays SHM sensitivity (probability of detection) incorporating, nevertheless, a reasonable degree of conservatism against failure (mean FAD static safety index of 3.87, not documented here).

Figure 7 shows the results of probabilistic FCG simulation until the attainment of 90.000 loading cycles which corresponds, according to data given in Table 1, and Figure 6, with the time when, with a probability of occurrence of 10^{-6}, the propagating fatigue crack attains a size of 2 mm. Figure 7a illustrates the scatter of the crack size at the life of 90.000 cycles and Figure 7b gives the evolution of the state of damage in FAD representation until the attainment of this life. Though the scatter of the crack-size seems substatial (as apparently sugested by the enlarged view of Figure 7a, it encompasses, at the analysed time of loading history, crack-size values in the range of 0.02 to 0.7 mm. This fact makes that points “cloud” of the damage states in Figure 7b to be rather far-off the limit state FAD curve. However, it is important to stress that the representation in Figure 7 derives from the results from a session of only 9.999 simulations, not excluding the possibility of rare events with, for instance, 10^{-6}chances of occurrence which may arise in random Monte Carlo sampling of the variables governing FCG law. In this case, FAD representative points may fall in the failure domain. Figures 3, 5c and d show PDF representation of the fitted crack-size by two-parameters Weibull distribution of the inverse value of the crack size ($1/a$). PDF displays strong positive skewness evincing that cracks of large size associated with FCG, though rare events, are in the realm of possible occurence.

For the case of simulated crack statistics illustrated in Figure 7, the results of probabilistic FAD analysis are shown in Figure 8. For a sample of crack-size data, simulated until the attainment of 90.000 cycles, the probability of failure resulted in $\overline{P}_{fN} = 1.8\ 10^{-6}$. On the FAD simulation display it can be discerned, as is apparent in Fig. 8, few cases of failures which are in the realm of rare events, together with an overwhelming number of events of non-failures. Table 2 gives the simulated probabilities of failure as a function of the number of loading cycles experienced by the structure until various inspection times. For every pre-set inspection times, Monte Carlo simulations in 10^7 iterations have been repeated several times in order to check the stability of the estimated values of failure probabilities. Stable values have been obtained. However, at low probabilities, around 10^{-7}, the number of iterations should be increased with at least one order of magnitude for obtaining better convergence towards the true value of probability.

Figure 9 shows the graphical representation of the simulation results given in Table 2. A salient trend emerges from this part of the simulation exercise. The delay in application of an efficient NDI, beyond a life of 90,000 loading cycles (pressurizations / depressurizations in take-off / landing cycles), results, altogether, in a definitely increase of failure risk by FCG with nearly three orders of magnitude in a short interval from 90.000 to 105.000 loading cycles.

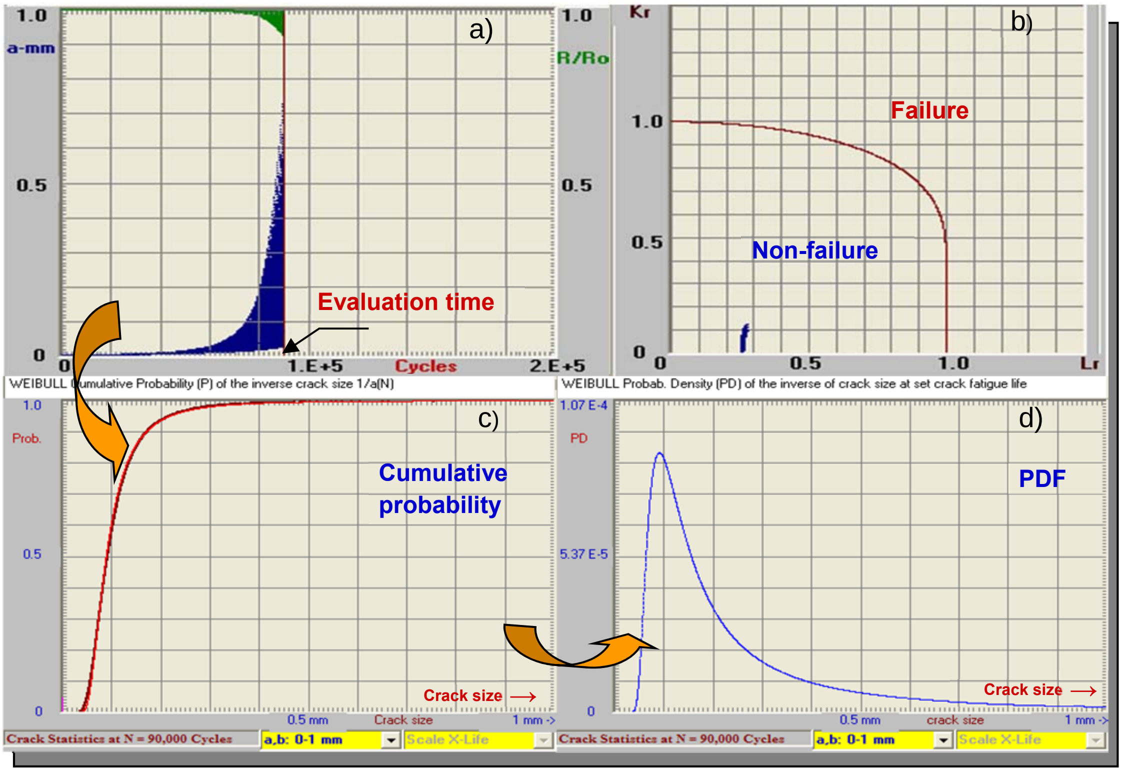

Figure 7: Probabilistic simulation of FCG until the pre-set NDI (evaluation) time at 90.000 cycles. Number of simulation iteration, 9.999. a) crack-size scatter; b) on-line FAD representation; c) crack-size data fitting into two-parameters Weibull distribution of the inverse value of the crack size (*1/a*), in cumulative probability representation; d) same as c) in PDF repesentation.

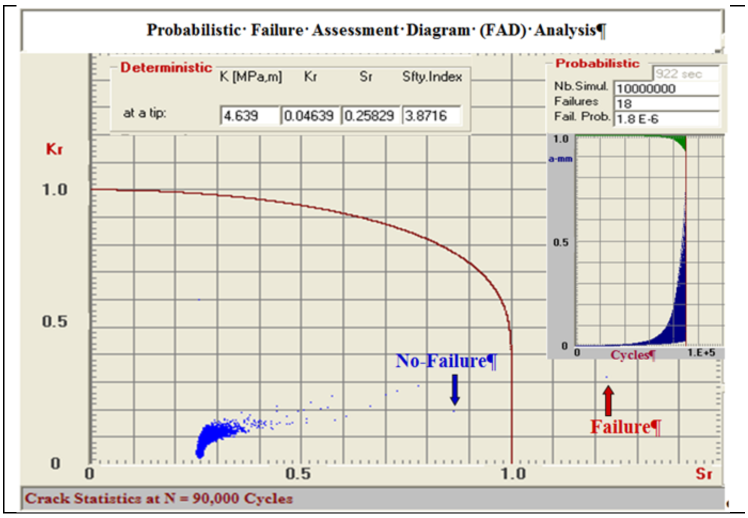

Figure 8: Probabilistic simulation of the failure risk in 10^7 Monte Carlo iterations. Probabilistic damage stage after 90.000 cycles of pressurization / depressurization of fuselage structure. The simulated probability of failure is 1.8 10^{-6}.

Number of loading cycles [1] at IT [2]	Crack size statistics at IT, mm		Probability $\overline{P}_{fN}$ at IT [4]
	Median	P=0.9999625 [3]	
80.000	0.0436	0.1692	$<10^{-7}$
90.000	0.0908	0.9125	$7.0\ 10^{-7}$ $1.1\ 10^{-6}$ $1.8\ 10^{-6}$ $2.8\ 10^{-6}$
95.000	0.1411	1.2347	$2.27\ 10^{-5}$ $2.53\ 10^{-5}$ $2.57\ 10^{-5}$
100.000	0.2267	2.1724	$1.54\ 10^{-4}$ $2.30\ 10^{-4}$ $2.46\ 10^{-4}$
105.000	0.3701	6.1578	$6.93\ 10^{-4}$ $7.78\ 10^{-4}$ $7.81\ 10^{-4}$

Table 2: [1] Constant amplitude loading $Smax/Smin=85/8.5\ MPa$; [2] IT - Inspection time; [3] Rank 9.999, the greatest crack-size in a sample of 9.999 Monte Carlo iterations; [4] 10^7 Monte Carlo simulation iterations.

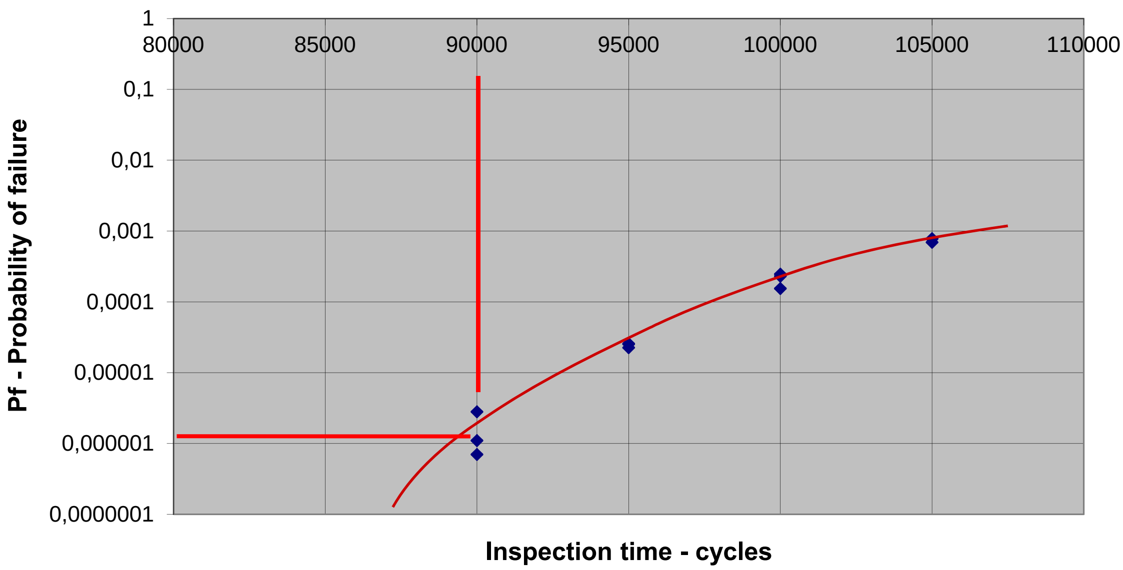

Figure 9: Monte Carlo simulated (10^7 iterations) of the probability of failure at various inspection / evaluation times.

DISCUSSION AND CONCLUSION

Computer simulation in science and engineering is gainning more and more areas of applications, being a rational way to enrich knowledge on the mechanisms underlying physical phenomena or to explore details not reachable by experiments. Structural health monitoring is a new paradigm emerged in the last two decades, aiming to predict future behavior of technical systems, to foster operational reliability concurrently with cost optimization. SHM is nowadays a comprehensive response to this challenge, beyond the means offered by traditional NDI.

The article atempts to evince how already existing concepts, models and computation algorithms of quantitative NDI and probabilistic approaches to structural failure risk are integrated, logically, in generic or dedicated SHM systems. For specific SHM applications to fatigue life and reliability management of aircraft structures, a way of approach is to make explicit the failure risk in probabilistic terms, in correlation with the capability of NDI and SHM. Inspection or monitoring quality in this commission is quantified with the aid of POD models which are already in use when damage tolerance strategy is followed. The generic SHM model reported has probailistic-statistic format materialized in the *pFATRISK* rationale and its associated mathematical algorithms and executable computer code. Statistic-probabilistic background of *pFATRISK* stems from the experimentally legitimated input as concerns data on material strength, deformation and fracture toughness, and the parameters of a fatigue crack growth model. By this way, uncertainty and variability features are taken into account. The rationale is capable to follow, virtually, by simulation of a real-life operating SHM systems. With the *pFATRISK* “tool”, an assessment has been performed with twofold aims: (*i*) to derive probabilistically founded safe warning times, as relevant information for warning at safe times for taking corrective mesures, or (*ii*) to set overall NDI timing, as a function of the pre-set levels of the warning crack-size, substantiated on the basis of simulated probability of failure assessed as a function of the elapsed time of the component life. Massive Monte-Carlo simulations of the FCG have been used in this undertaking.

The results obtained met in evidence the potential of integrated probabilistic methods of fracture mechanics and quantitative non-destructive inspection, supported by massive computer simulations, to parallel, virtually, SHM systems with the end aim of refining prognostications and management of operational failure risks, assuring, not the last, optimal cost.

REFERENCES

[1] Boller, C. and Biemans C.H.M., 1997. Structural health monitoring in aircraft- State-of-art, perspective and benefits. *Int. Workshop on Structural Health Monitoring*. 18-20 Sept. 1997. Stanford Univ. USA.

[2] Boller, C. and Meyendorf, N., 2008. *State-of-the-art in structural health monitoring for aeronautics*. Proc. Internat. Symp. On NDT in Aerospace. Fürth, Bayern, Germany.

[3] Boller, C., Chang, F-K and Fujino, Y., 2009. *Encyclopedia of Structural Health Monitoring*. Vol 1-5. Wiley. Chichester.

[4] Giurgiuţiu, V., Zagrai, A. and Bao, J.J., 2002. Piezoelectric wafer embedded active sensors for ageing aircraft structural health monitoring. *SHM - Structural Health Monitoring* 1(1), pp. 41-61. Sage Publications, USA.

[5] Giurgiuţiu, V. and Zagrai, A., 2005. Damage detection in thin plates and aerospace structures with the electro-mechanical impedance method. *Sage Publications* 4(2): 0099-20.

[6] Yolken, H.T. and Matzkanin, G.D., 2004. Recent trends in structural health monitoring. *The AMMTIAC Quarterly* 3(4). http://ammtiac.alionscience.com.

[7] Balageas, D., Fritzen, C.-P and Güemes, A. editors, 2006. *Structural Health Monitoring*. ISTE, London.

[8] Schmidt, H-J. and Schmidt-Brandecker, B., 2007. Design benefits in aeronautics resulting from structural health monitoring. Proc. Of the 6th Internat. *Workshop on Structural Health Monitoring*. DEStech Publ., pp. 762-69.

[9] Farrar, C. and Lieven, N., 2007. *Damage prognosis: the future of structural health monitoring*. Phil. Trans. Roy Soc. A. Published online, doi:10.1098/rsta.2006.1927.

[10] Lloyd, P.A., 2008. Structural health monitoring systems – benefits and airworthiness issues. *The Aeronautical J*. May, pp. 285-99.

[11] Baker, B., 2008. Improved generic strategies and methods for reliability-based structural integrity assessment. *Research Report RR642 for Health and Safety Executive*. University of Aberdeen, UK.

[12] Coppe, A., Hafka, R.T. and Kim, N.H., 2010. Uncertainty reduction of damage growth properties using structural health monitoring. *Journal of Aircraft* 47(6), pp. 2030-038.

[13] Paris, P.C., Gomez, M.P. and Anderson, W.E., 1961. A Rationale Analytic Theory of Fatigue. *The Trend in Engineering,* 13, pp. 9-14.

[14] Klensil, M. and Lukás, P., 1972. Influence of the Strength and Stress History on the Growth and Stabilization of Failure Cracks. *Engng. Fract. Mech.,* 4, pp. 77-92.

[15] Dugdale D.S., 1960. Yielding of Steel Sheets Containing Slits. *Journal Mech. Phys. Solids*. 8, pp. 100-04.

[16] R/H/R6, 1986. *R/H/R6-Revision 3. Assessment of the Integrity of Structures Containing Defects.* Authors: Milne I., Ainsworth, R.A. Dowling, A.R. and Stewart, A. T. British Energy (previously CEGB).

[17] Zerbst, U., Wiesner, C., Koçak, M. and L. Hodulak, 1999. *SINTAP: Entwurf einer vereinheitlichen europäischen Fehler-bewertungsprozedur – eine Einführung.* Autors: GKSS-Forschungszentrum Geesthacht, GmbH, Geesthacht, Germany.

[18] Cioclov, D.D., 2009. Fatigue failure risk assessment in load carrying components. *Security and Reliability of Damaged Structures and Defective Materials*, Eds. Pluvinage G. and Sedmak, A., NATO Science for Peace and Security Series – C: Environmental Security, pp. 25-74. Springer, Berlin.

[19] Speckmann, H., 2007. SHM: History and Future*. Conf. IWSHM, Stanford University*, 11-13 Sept. 2007, Stanford/CA, USA

[20] Berens, A.P. and Hovey, P.W., 1981. Statistical Methods for estimation the crack detection probabilities. *ASMT Special Technical Publication,* STP 798, pp. 79-94.

[21] Berens A.P., 1989. NDE Reliability Data Analysis. In: *Metals Handbook,* Vol. 17 *Nondestructive Evaluation and Quality Control,* 9^{th} ed. S.R. Lampman, Techn. Ed., Metal Park , Ohio, ASM International, pp. 689-701.

[22] Nichols, R.W. and Crutzen, S., 1988. *Ultrasonic Inspection of Heavy Section Steel Components: The PISC – II Final Report.* Elsevier Applied Science.

[23] Cioclov, D.D., 1998. *FATSIM. A Software for Fatigue Damage Simulation.* Proprietary Code Prof. D. Cioclov, C.E. Consulting, Saarbrücken, Germany.

[24] Cioclov, D., I. Altpeter, M. Kröning, 2005, Ein Beitrag der quantitativen ZfP mit Ultraschall im Zusammenhang mit probabilistischer Bruchmechanik zur Lebensdauerbewertung von Komponenten; Proceedings of: DVM Werkstoffprüfung 2005, Berlin/Germany

[25] Cioclov, D.D., 2011. *Failure risk assessment by integration of probabilistic fracture mechanics and quantitative non-destructive inspection. A structural health monitoring view.* SMART'11 Conference. Fraunhofer IZFP, Saarbrücken, Germany.

[26] Cioclov, D.D, Escobedo Medina, M.C. and Schmidt H-J., 2003. *On the probabilistic fracture mechanics simulation of the fatigue life and crack statistics for the purpose of damage tolerance assessment.* ICAF 2003, Fatigue of Aeronautical Structures as an Engineering Challenge. Ed. Guillome, M. V.1, pp. 189-209. EMAS Pub. Lucerne, Switzerland.

[28] Cioclov, D.D., 1975. *Strength and reliability under varying loading (in Romanian).* Facla Publishing House, Timisoara, Romania.

[29] Rinne, H., 1997. *Taschenbuch der Statistik.* Verlag Harri Deutsch, Thun and Frankfurt am Main, Germany.

[30] Aldrin, J.C., Medina, E.A. and Knopp, J., 2006. Cost benefit analysis tool incorporating probabilistic risk assessment for structural health monitoring. *Review of Progress in QNDE* 25, AIP, pp.1910-918.

Applications

APPLICATION OF RISK BASED INSPECTION TO HEAT EXCHANGERS OF A CHEMICAL PLANT

N. Farbas, A. Murariu, N. Pasca

National R&D Institute of Welding and Material Testing, ISIM Timisoara Romania

ABSTRACT

A risk-based inspection methodology is presented that is able to cope with systems consistingof a large number of components. By detailed analysis the components of high risk can be identified and analysed in further detail resulting in a risk-based inspection plan. One of the options considered is permanent monitoring of those critical components. The methodology is further illustrated along a case study performed on an isotopic echange installation in a heavy water plant.

INTRODUCTION

Periodical inspection (time based inspection) of industrial equipment is the common procedure applied in industry. It is necessary to verify the safety of complex installations after a given period of exploitation. In chemical or petrochemical plants where materials used are heavyly loaded, damage mechanisms like corrosion, fatigue, creep, stress corrosion cracking, and similar can appear. In order to monitor all these phenomena mainly non-destructive methods are involved. The national and international rules, regulations and standards prescribe very rigorous inspection intervals indicating what component has to be examined and which NDT method has to be taken. All the testing results are very scrupulously recorded so that the history of each component is well known. These periodical shutdowns of the equipment, foreseen by the regulations, but not by a real necessity, result in significant losses of production for the stakeholders. Taking into account that a chemical or a petrochemical plant has a daily production of many millions of Euros, it is easy to understand that the owners of these plants are not so happy to stop production when the compulsory periodical inspection is to be completed. The practical experience of inspection has indicated that many components of a complex industrial installation consisting of hundreds of individual parts are generally less affected by the exploitation condition than others. That means that the inspection activity made periodically on these parts may bring nothing, but may rather cost a lot of money. How can the cost of inspections be mitigated without affecting the safety of equipment? The answer to this question is given by the risk-based inspection and maintenance. This means to move away from time based inspection, often governed by minimum compliance with rules, regulations and standards for inspection. The result consists in planning and executing only those inspections that are needed and so providing economic benefits such as fewer inspections, fewer or shorter shutdowns and longer run lengths. All this is made by safeguarding the integrity and reducing the risk of failure.

RBI METHODOLOGY

Risk-based inspection (RBI) and maintenance concepts were developed in the U.S. between 1995-2005 [1,2], the first by API (American Petroleum Institute) in chemistry and petro chemistry, followed by EPRI (Electrical Power Research Institute) for nuclear and thermal power plants and then in the European Union within the RIMAP project [3] for every industry field. Recently, a new standard in the field of risk management has been jointly developed by ISO (International Organization for Standardization) and IEC (International Electrotechnical Commission) [4,5].

As other types of management systems (project management, human resource management, quality management), risk management system performs management of activities and processes, ensuring the appropriate risk management by integrating the new concepts on inspection and maintenance of equipment [6-9]: Fitness-For-Service (FFS), Risk Based Inspection (RBI), Reliability Centred Maintenance (RCM), in-service Inspection and monitoring the degradation state/ failure of components.

Risk-based inspection was developed because it was evident that some of the inspection activities seem to be not necessary on some components. Speaking in the spirit of components' failure consequences, it was demonstrated that in given equipment only some of them can generate major effects (financial losses, human injuries, environmental damage, etc). Here the so called 20-80 rule is applied: 20% of the components provide 80% of the total risk (Figure 1).

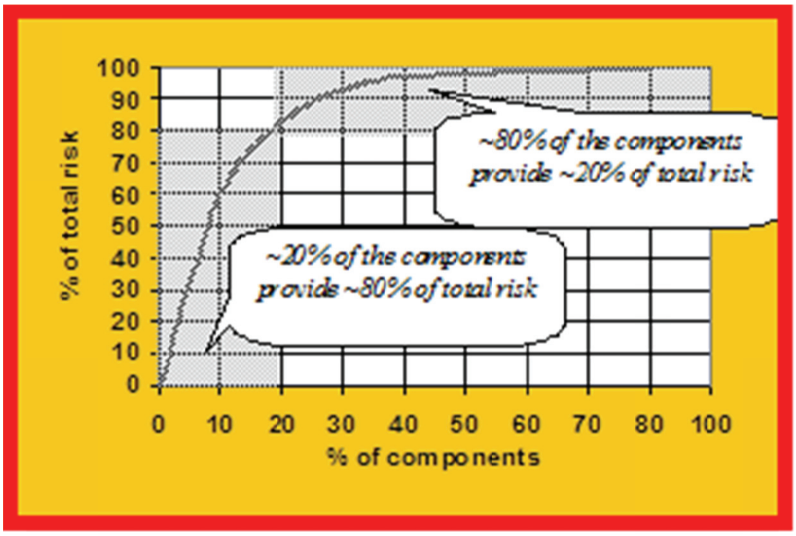

Figure 1 Definition of the 20-80 rule

Risk-based inspection is based on the definition of risk:

Risk = Probability x Consequence

That means that the risk is the product of the likelihood that a failure will occur and the consequence (cost) of that failure. The failure risk of a component is higher if the probability of damage is high and/or the consequences are high (huge production losses, large area around affected by the leakage of hazardous fluids, humans affected etc.). The total risk of an industrial installation is the sum of the risk calculated of all components included in that installation:

$$\mathbf{Risk_{total} = \Sigma\ (PoF_i\ x\ CoF_i)}$$

In order to perform a risk analysis of an industrial equipment it is necessary to decompose that equipment in separate components like shells, tubes, elbows, flanges, tube bundles, etc. For each of these components the probability of failure (PoF) and cost of failure (CoF) have to be evaluated to calculate the individual risk. The results of this evaluation are graphically represented into the risk matrix (Figure 2).

Normally the risk matrix has five categories for PoF and five for CoF [7]. Using these five categories it is possible to recognize four regions indicating the risk level: low risk, medium risk, medium high risk and finally high risk. To each component belongs a point in this matrix, so we can have an image about how much is the risk level of the whole equipment. Components in the low risk region can be disregarded in terms of inspection activities, which mean that the inspection intervals can be significantly enlarged without losses of installation's safety. The components having high risks associated have to be intensively checked in order to reduce either PoF or CoF. Generally it is difficult to mitigate the costs of failure of a component when environmental problems or production losses are involved. By intensifying the NDT through permanent monitoring of the components and by changing the process parameters (if possible) the probability of failure can be reduced up to an acceptable level. Based on the risk evaluation of the components an inspection plan is elaborated concentrated on high risk components, followed by practical intervention on the component consisting in replacement, repair of defects, etc.. When this operation is finished a new assessment of the components involved is made and the new risk level is estimated.

The whole process of RBI is summarized in the Figure 3. The risk analysis is made on two levels:

Level 1 – Qualitative risk analysis, simple brief prioritization of equipment (Screening)

Level 2 – Quantitative risk analysis (detailed analysis).

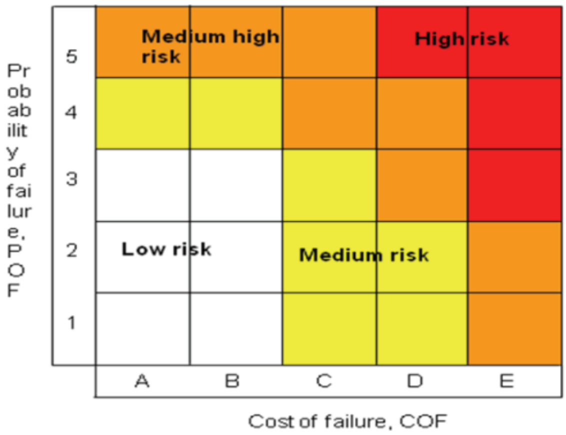

Figure 2 Schematic of probability of failure versus cost for a set of components of a system's installation

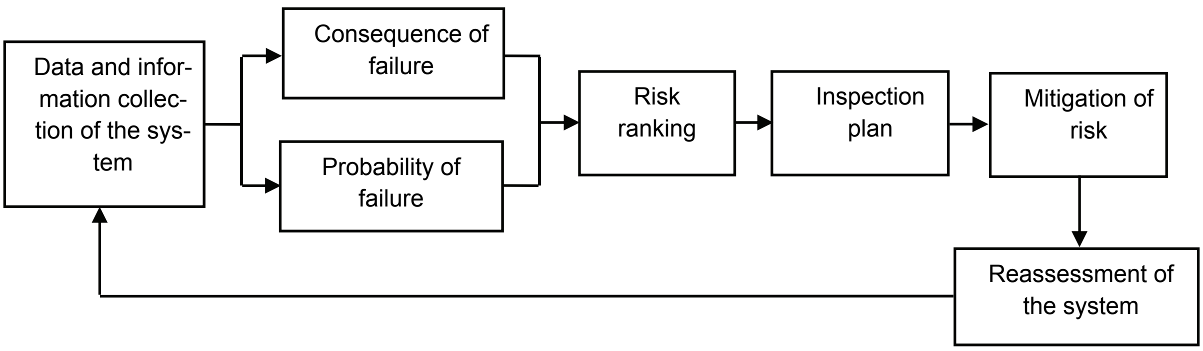

Figure 3 The Risk-Based Inspection (RBI) process

During the first level data and information existing at the stakeholder are evaluated and put in the risk matrix. Only components of the system showing high risk levels are involved in the second step of the risk analysis – the detailed analysis. The assessment procedure evaluates the remaining strength of the equipment in its current condition, which may be degraded from its original conditions. Common degradation mechanisms include corrosion, localized corrosion, pitting and crevice corrosion, hydrogen attack, embrittlement, fatigue, high-temperature creep, and mechanical distortion. Methods for evaluating the strength and remaining service life of equipment containing these types of degradation should be taken into account.

Thus the degradation mechanism, the influence of exploitation parameters on the material, the thinning of the wall thickness, and if possible new non-destructive examination and even destructive material testing performed is taken into account. Generally, a better knowledge of the component's behavior allows a better positioning in the risk matrix. After this the risk ranking is remade it becomes possible to provide the necessary information for the **risk-based inspection plan**. By application of the inspection plan the avoidance of unnecessary inspection is possible. Inspection intervals are based on the risks associated with the component and therefore inspection personnel can spend most of its time on the high risk areas and less time in the low risk areas.

The evaluation of risk in industrial equipment consisting of hundreds of components is not a simple work. This is why many institutes and software companies have developed specialised expert systems for different specific applications (chemistry, petro-chemistry, power plants, storage tanks, boilers, etc.). So on the market it is now possible to buy expert systems from API (USA), Det Norske Veritas (DNV - Norway), The Welding Institute (TWI -UK), Tischuk (USA), Bureau Veritas (Belgium/France) or Steinbeis Advanced Risk Technologies-R-Tech (Germany). Generally the expert system uses large data bases for materials, damage mechanisms, hazardous fluids, costs of failures, etc., all absolutely necessary for the risk ranking.

CASE STUDY

The risk-based analysis was made on some equipment from an isotopic exchange installation of a heavy water plant in Romania. For the isotopic exchange in extracting heavy water, hydrogen sulphide is use. H_2S is a very toxic chemical for humans and animals and is very corrosive for steels in general and for carbon steels in special. The screening risk analysis was made on 112 components on this complex installation. For the detailed analysis 8 heat exchangers connected together and one pressure release valve (Figure 4) were selected from the screening analysis results. These components were those having a high and medium high risk associated. The 8 heat exchangers were decomposed in 5 components each: the shell, the tube bundles, chamber, removable lid, and external lid. Together with the release valve 41 components were analyzed.

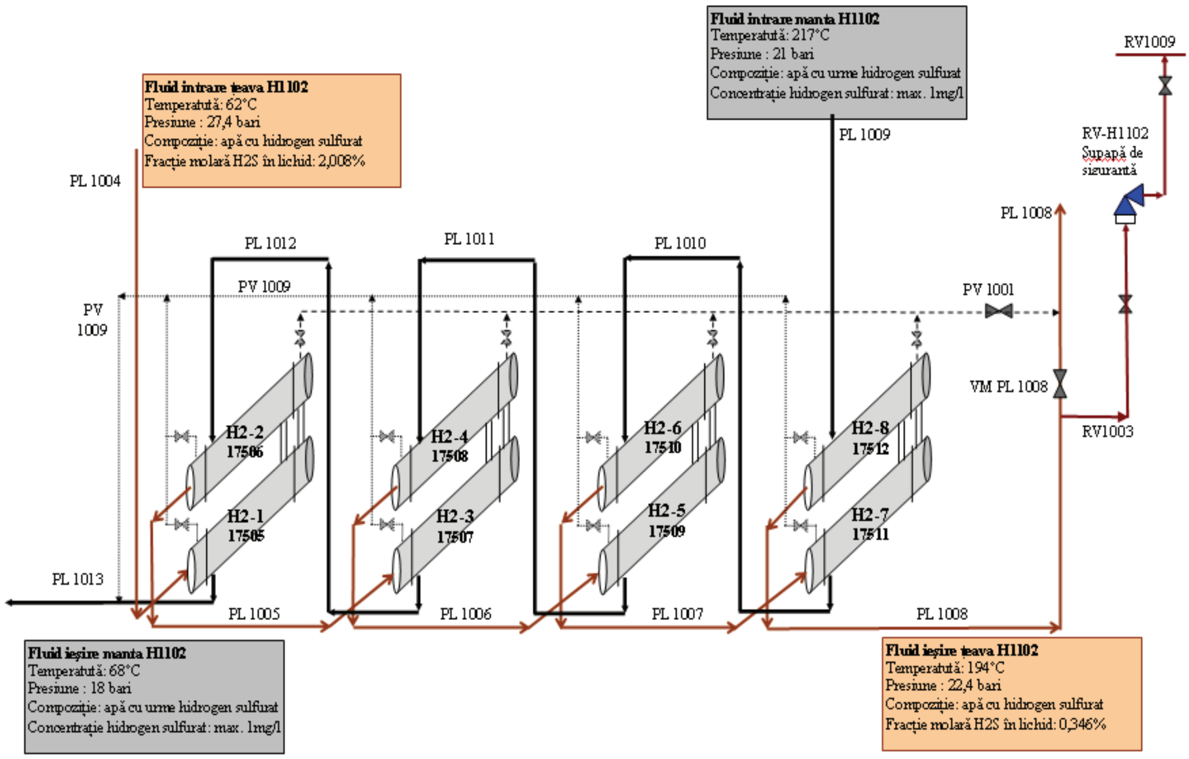

Figure 4 Schematic of an isotopic exchange installation of a heavy water plant

The input and output temperature, pressure and H_2S content of the fluids in the shell and in the tube bundles of the heat exchangers is given in the Table 1. For the evaluation of the risk level of the equipment's components the expert system from Det Norske Veritas (DNV) **Orbit-Onshore** was used.

Component	Temperature (°C)		Pressure		H_2S concentration in water (%)	
	input	output	input	output	input	output
Shell	217	68	21	18	Max. 0.0001	Max. 0.0001
Tube bundles	62	194	27.4	22.4	2.008	0.346

Table 1 Operational parameters heat exchangers considered

The screening analysis (level 1) needs introduction of a lot of data for each component (Figure 5) the expert system indicating if a detailed analysis is necessary. On the same output screen of the expert system the risk ranking of the component is made (in this case medium high).

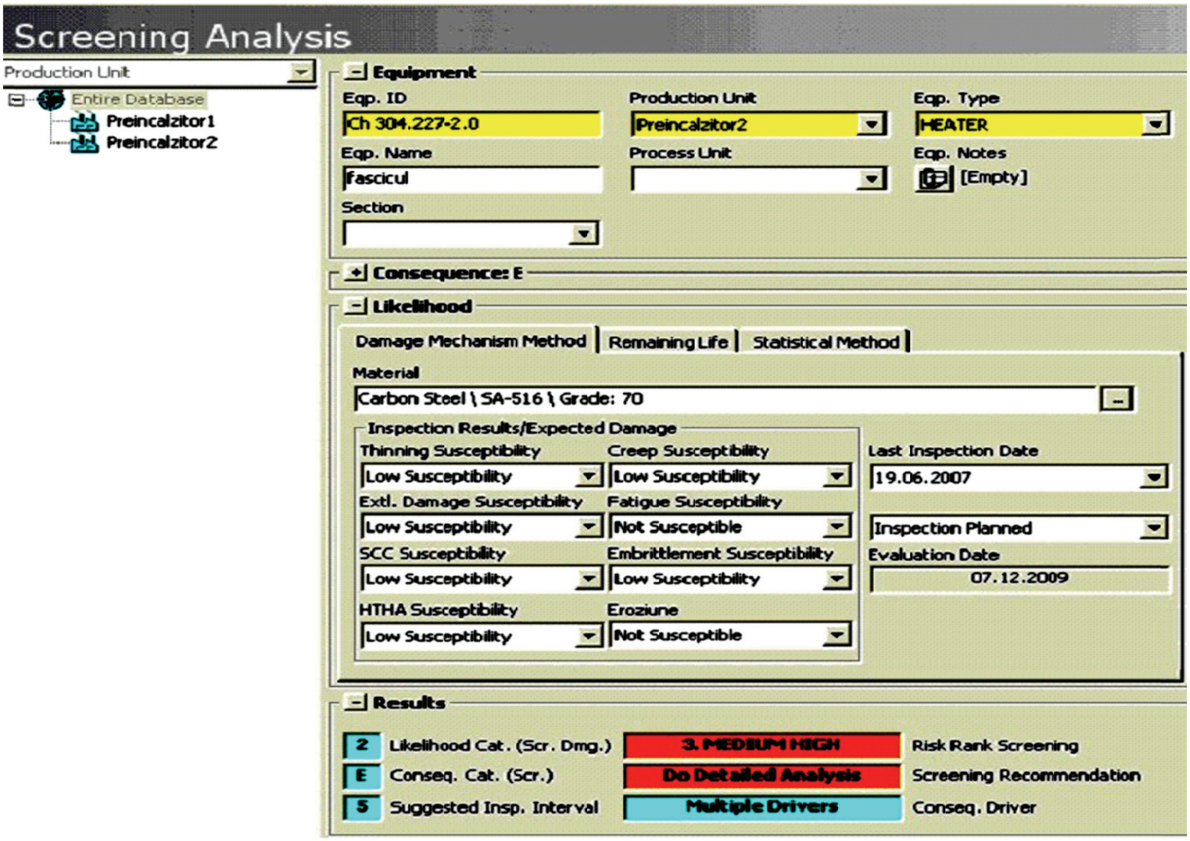

Figure 5 Example of the input screen for the screening analysis

The results of the screening analysis for the 112 selected components of the installation are indicated in the Figure 6. It can be seen that 87.5% of the results are in the medium high region, 2.68% are in the medium region and 9.82 % are in the low risk region of the risk matrix. For the detailed analysis, as already mentioned, 41 components of the system were selected. The expert system looks for information about material, fluids inside and outside, temperature, pressure, date of starting the exploitation, detailed damage mechanism, wall thinning diagram, consequence evaluation etc. Using all this information the expert system calculates the failure likelihood, the cost of failure and the risk of the component. The output form of the expert system for the tube bundles is shown in Figure 7.

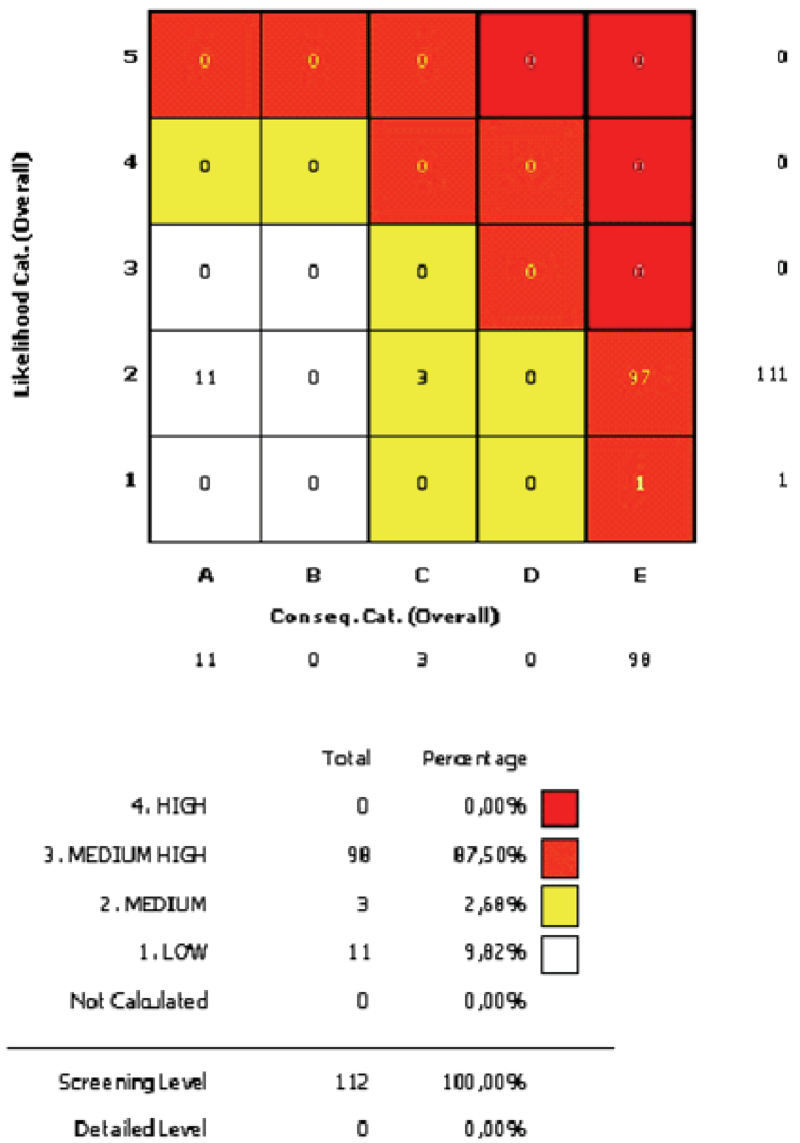

Figure 6 Results of screening analysis

The result of the evaluation by the detailed analysis using general data moves the component (in this case the tube bundles) from the medium high region of risk in the medium one. For all components a detailed analysis is made for hydrogen attack, piping fatigue calculation, wall thinning, external damage, stress corrosion cracking, and of course for the consequences. Very useful are former or new inspection results which are necessary to perform probability of failure calculation. As an overall result of the detailed analysis all evaluated components leave the medium high region (Figure 8).

The removable lids can be located into the low risk region and the external lids, the chambers and the pressure release valve are in the yellow region corresponding to the lowest likelihood category.

A little bit higher, in the yellow region, are the shells and the tube bundles. The detailed analysis for toxicity consequence (Figure 9) shows 8 components (approx. 20%) were placed in high risk areas, 25 components (60%) in medium - high risk level which all requires special treatment and 8 components (approx. 20 %) in low risk area. The detailed analysis for fatality consequence shows 25 components (60%) in medium - high risk level which all requires special treatment and 16 components (approx. 40 %) in low risk area.

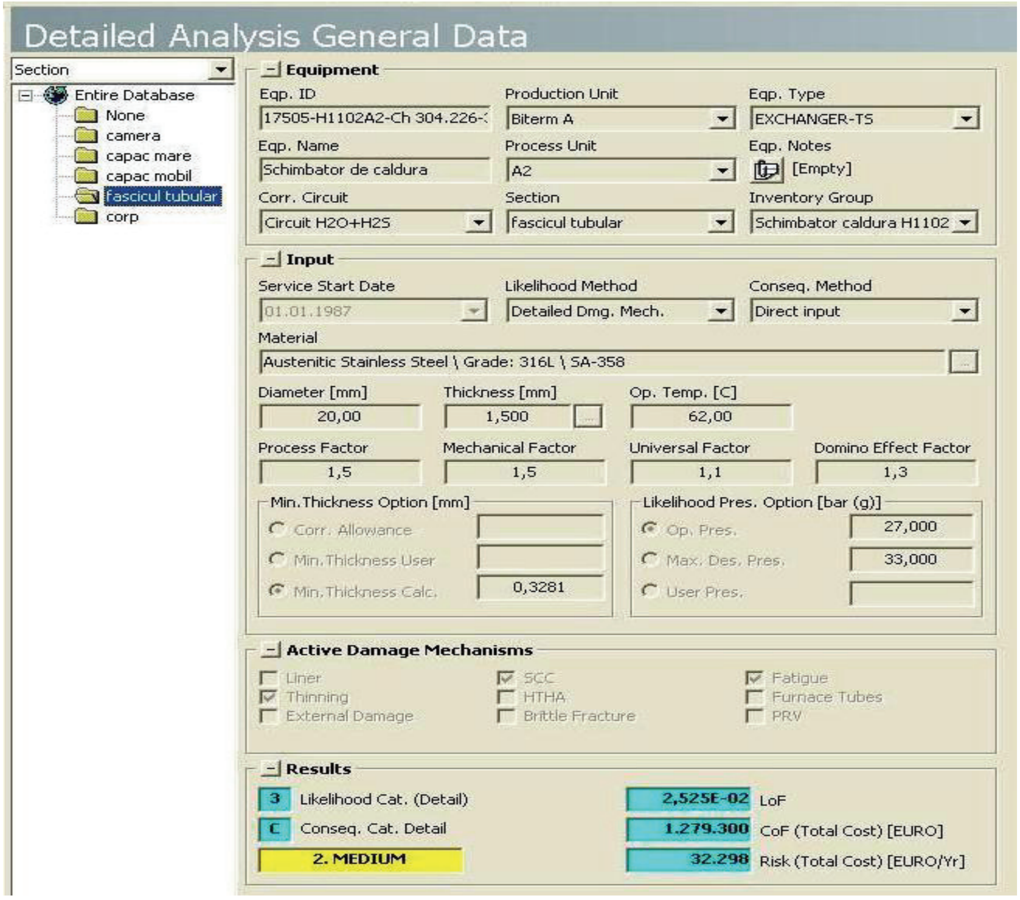

Figure 7 Example of output from expert system

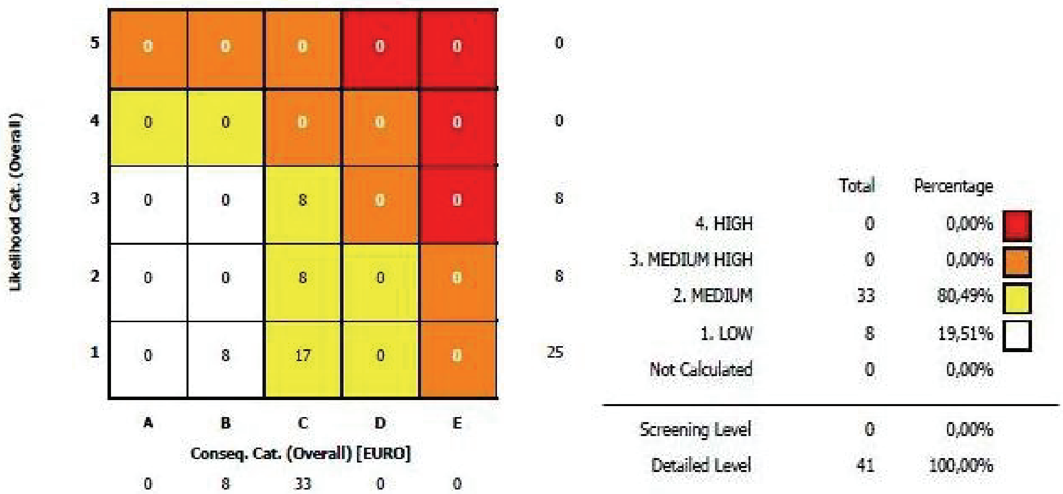

Figure 8 Result of a detailed analysis

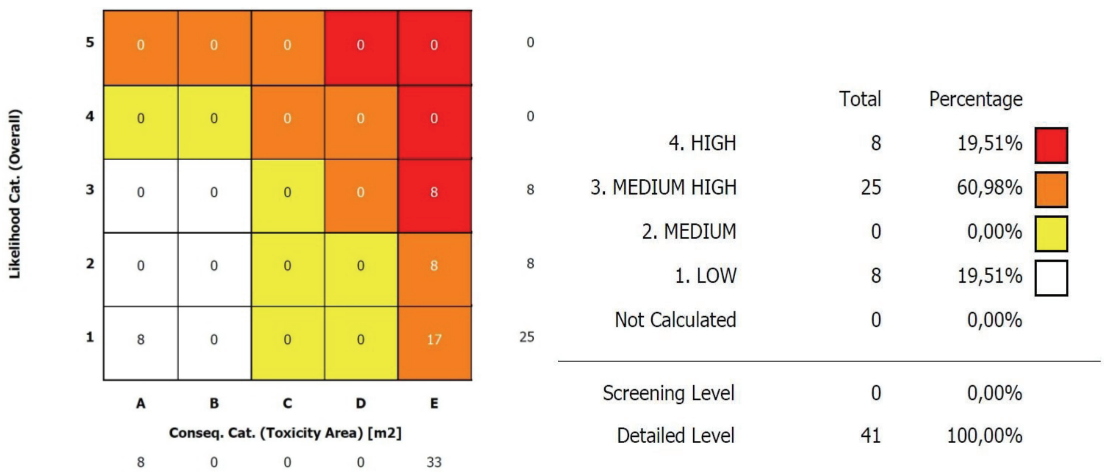

Figure 9 Results of detailed analysis for toxicity consequence

According to risk criteria the influent risk requires specific treatment. In order to treat components placed in high and medium-high risk level, a detailed inspection program has been developed and specific measures for risk mitigation by on-line monitoring of critical parameters has been taken. The inspection program is presented in Table 2.

*TM – Thickness Measurement; PT – Penetrant Test; VT – Visual Test

Component Type	**Likelihood category**	**Consequence category**	**Risk level**	**Inspection Type**	**Inspection interval [years]**
Chamber	1	C	2. MEDIUM	TM – layer, PT-welds	8
				VT	3
				TM – base material	15
External Lid	1	B	1.LOW	VT	3
				TM – base material	15
Removable Lid	1	C	2. MEDIUM	TM – layer, PT-welds	8
				VT	3
				TM – base material	15
Shell	2	C	2.MEDIUM	PT – welds	8
				VT	3
				TM – base material	8
Tube Bundle	3	C	2. MEDIUM	PT-welds	5
				VT	3
				TM – base material	5
Release Valve	1	C	2.MEDIUM	Test	5

Table 2 Detailed inspection programme considering risk mitigation by on-line monitoring

In an earlier period thickness measurements of the shell were performed regularly every 6 months and visual examination was performed for all components every annual review. By detailed analysis of operational parameters, materials and failure mechanisms of each component, using an expert system and the RBI method, the corrosion rate has been estimated (Figure 10) and the interval between successive inspections could be increased from initially 6 months to 8 years (Table 2).

From Figure 10 it is evident that a 6 months inspection interval is unjustified since it only increases inspection cost without any safety benefits.

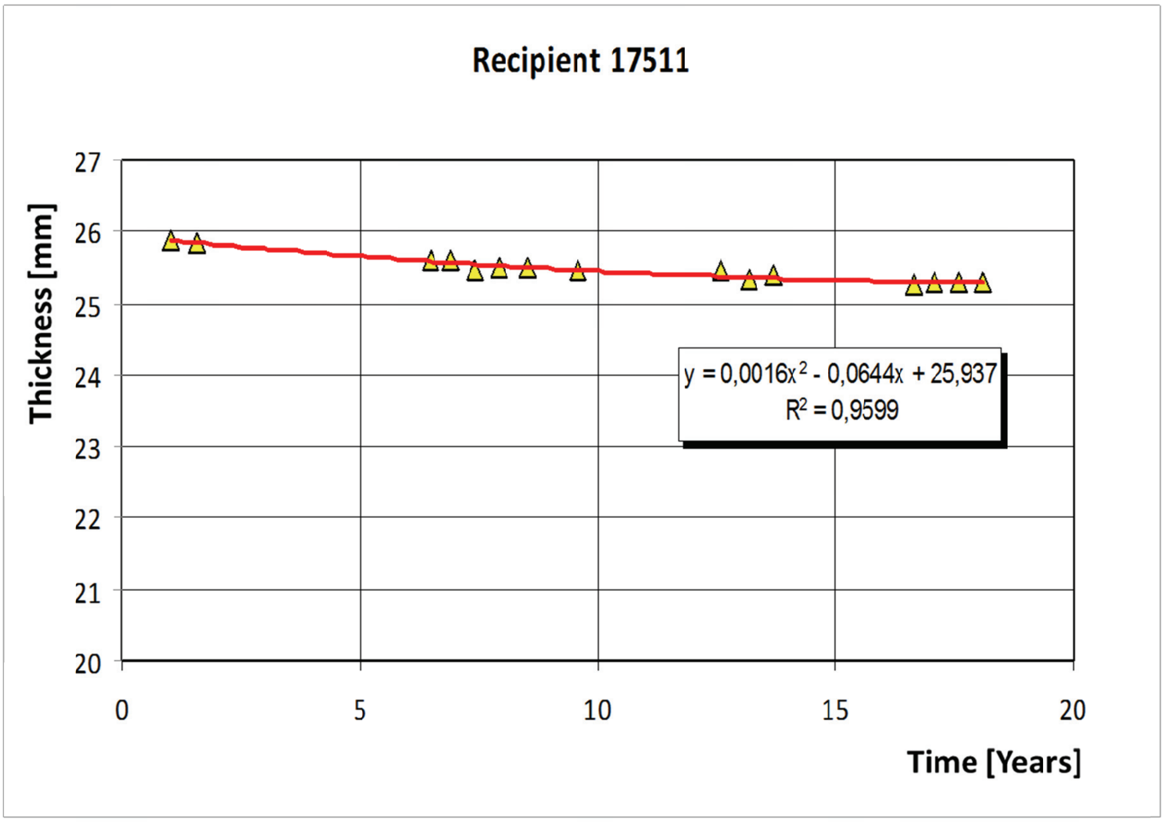

Figure 10 Estimation of corrosion rate through detailed analysis of parameters expressed in terms of thickness change of a shell

CONCLUSION

The risk-based inspection replaces the time-based inspection by evaluating every component of a complex industrial plant in terms of probability of failure and cost of failure. The risk ranking of all plants components allows identification of components having higher risk levels. Through the assessment of risk in two stages (by screening and detailed analysis) using risk based inspection concepts the time limits between inspections can be extended, thus making significant financial savings. Intensively testing and monitoring components with higher risk levels can be foreseen in the inspection plan. The economic benefits of applying risk-based inspection is provided by reducing shut-down periods, production losses, inspection duration and cost without reduction of a plant's safety.

ACKNOWLEDGMENT

This work was partially supported by the National Research Plan PNCDI 2: Frame 4: “Partnerships in priority areas”, project no.: 22-096, acronym: RBI, financed by the UEFISCDI and partially supported by contract C10/2009-2010 – RAAN ROMAG PROD Drobeta Turnu Severin.

REFERENCES

[1] Speck, J. B. and Iravani, A. T. M., 2002. Industry survey of risk-based life management practices. *ASME PVP 2002 Conference*, Canada.

[2] Patel, R. J., 2005. Risk Based Inspection-3rd MENDT. *Middle East Nondestructive Testing Conference & Exhibition,*- 27-30 Nov, 2005. Bahrain, Manama.

[3] RIMAP NAS Project, 2002-2005. Contract GIRT-CT-2001-05027. Commission of the European Communities, 2000. *RIMAP Project No., GROWTH Project G1RD-CT-2001-03008 'RIMAP': Risk Based Inspection and Maintenance Procedures for European Industry.*

[4] ISO 3100, 2009. Risk management — Principles and guidelines.

[5] ISO/IEC 31010, 2009. Risk management — Risk assessment techniques.

[6] API RP 580, 2009. Risk-Based Inspection, Second Edition.

[7] API RP 581, 2008. Risk-Based Inspection Technology, Second Edition.

[8] API 579-1 / ASME FFS-1, 2007. Fitness-For-Service, Second Edition.

[9] SAE JA1011, 2009. International: Evaluation Criteria for Reliability-Centred Maintenance (RCM) Processes.

EXPERIMENTAL DETERMINATION OF THE MULTI-AXIAL STRAIN TRANSFER FROM CFRP-LAMINATES TO EMBEDDED BRAGG SENSOR

N. Lammens*

Department of Materials Science & Engineering – Universiteit Gent, Gent/Belgium

*Corresponding author. E-mail: Nicolas.Lammens@ugent.be

ABSTRACT

The article deals with the numerical and experimental determination of multi-axial strain transfer in carbon-fiber reinforced laminated using fiber Bragg grating sensors integrated into the composite laminate. Based on small strain approximation theories a matrix formalism based on principal strains is formulated of which a core element is the multi-axial strain matrix *TC*. This matrix has been determined numerically and is further correlated with a K-matrix which is a correlation between wavelength-shifts and the strains respectively. A comparison between numerical and experimental results based on the TC-matrix has shown good coincidence.

INTRODUCTION

Superior design flexibility and fatigue performance render composite materials attractive successors for traditional construction materials. However, due to their anisotropic nature, isotropic material design procedures are no longer valid. Additionally, more complex strain distributions and failure modes exist. Therefore, internal strain information can provide useful knowledge concerning composite behavior both in material characterization and online health monitoring (e.g. smart structures). Embedding optical fiber Bragg gratings (FBG) can even provide multi- axial strain information. Determining the total strain field in composite structures is of upmost importance, since they render valuable information on the integrity of the structure.

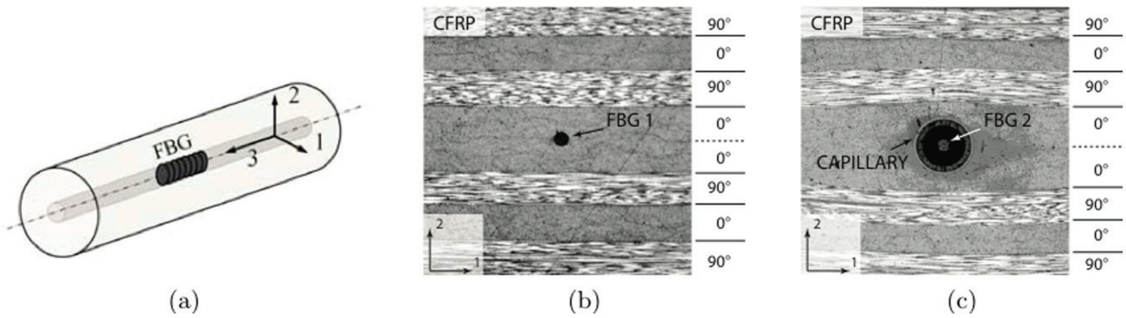

Figure 1: (a) The coordinate system used for all equations in this paper. (b) & (c) The cross-sections of a dual- FBG configuration inside a cross-ply composite material (b) the first FBG, (c) the second FBG en-capsulated inside a capillary.

In [1], the usability of 80 µm draw-tower gratings (DTG® [2]) embedded in carbon fiber reinforced composite is explored as a multi-axial strain sensor. DTGs are optical fibers in which the grating is inscribed during the drawing process with a single laser pulse. The response of such DTGs is, like any other FBG, dictated by Bragg's law.

Using a small-strain approximation and the centre strain theory (valid for conventional fibers), the temperature and strain sensitivity of an FBG along its polarization axes can be written as [3]:

$$\frac{\Delta\lambda_{B,1}}{\lambda_B} = \varepsilon_3 - \frac{\bar{n}^2}{2}\left[p_{11}\varepsilon_1 + p_{12}(\varepsilon_2 + \varepsilon_3)\right] + \beta\Delta T \tag{1}$$

$$\frac{\Delta\lambda_{B,2}}{\lambda_B} = \varepsilon_3 - \frac{\bar{n}^2}{2}\left[p_{11}\varepsilon_2 + p_{12}(\varepsilon_1 + \varepsilon_3)\right] + \beta\Delta T \tag{2}$$

in which p_{11} and p_{12} are the strain optic coefficients. The coordinate system is as depicted in Figure 1(a). The 1- and 2-axis are oriented according to the optical slow and fast axis. These will align with the principal directions of transverse strain. Using a dual-FBG configuration (Figure 1(b)-(c)), in which both FBGs are exposed differently to the strain field Equations (1)-(2) can be inverted to yield the strain-field from the measured wavelength shifts. In [1] and this paper, the second FBG is encapsulated in a capillary tube (Figure 1(c)), which isolates it from transverse stresses. As such, ε_1 and ε_2 are equal to $-\nu\varepsilon_3$, resulting in an equal shift of both wavelengths for this FBG. Temperature-compensation is achieved using an external sensor. The matrix-formalism yielding the principal strains from the measured wavelength shifts in this configuration can be written as:

$$\begin{bmatrix} -\frac{\bar{n}^2}{2}p_{11} & -\frac{\bar{n}^2}{2}p_{12} & 1-\frac{\bar{n}^2}{2}p_{12} \\ -\frac{\bar{n}^2}{2}p_{12} & -\frac{\bar{n}^2}{2}p_{11} & 1--\frac{\bar{n}^2}{2}p_{12} \\ 0 & 0 & \left(1--\frac{\bar{n}^2}{2}p_{12}\right)+\upsilon_f\frac{\bar{n}^2}{2}(p_{11}+p_{12}) \end{bmatrix}^{-1} \begin{bmatrix} \Delta\lambda_{B,1,a}/\lambda_{B,a} \\ \Delta\lambda_{B,2,a}/\lambda_{B,a} \\ \Delta\lambda_{B,b}/\lambda_{B,b} \end{bmatrix} = \begin{bmatrix} \varepsilon_1 \\ \varepsilon_2 \\ \varepsilon_3 \end{bmatrix} \tag{3}$$

with v_f , the Poisson-coefficient of the optical fiber. The matrix relating wavelength-shifts and strains are called the K-matrix.

STRAIN TRANSFER

The optical fiber can be regarded as an inclusion inside the material (Figure 1(b,c)). Because mechanical strains and stresses will be redistributed in the vicinity of the optical fiber, the mismatch in material properties between the composite and the optical fiber has to be taken into account (Figure 2).

As a result, the strains deduced from Equations (1)-(2), which represent those measured at the center of the optical fiber core, will differ from the actual strains that would exist in the undisturbed composite. When strain-gradients are limited, the strains that would occur in an undisturbed structure will be equal to the strains at a certain distance from the fiber. The multi-axial transfer of strain from the composite (e.g. the actual strains) to the fiber core (e.g. measured strains) was modeled in [4]. It was shown that axial strain transfer is usually in the vicinity of 100%, while transverse strain transfer is dependent on many parameters such as ply lay-up and material properties [4].

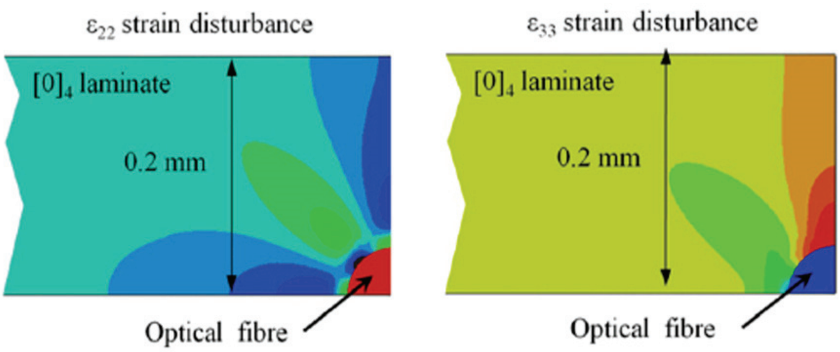

Figure 2: Transverse strain disturbance for a thin laminate [0]4 loaded in the transverse out-of-plane direction. The optical fiber sensor is embedded in the middle of the laminate [4].

In [4] a general method of modeling the strain transfer using matrix formalism is proposed:

$$[\varepsilon^c] = [TC][\varepsilon^s] \tag{4}$$

where ε^s symbolizes the sensed strains, and ε^c the composite strains, *TC* is called the multi-axial strain transfer matrix. Using numerical simulations, the *TC*-matrix has been calculated for the case of $[0_2, 90_2]_{2s}$ cross- ply carbon-fiber reinforced thermosetting polymer (CFRP) laminates with embedded 80µm optical fibers. The TC-matrix was found to be (The matrix was transformed to match the coordinate system in this paper (Figure 1)):

$$TC_{[0_2,90_2]_{2s}} = \begin{bmatrix} 7{,}64 & -1{,}23 & 0{,}82 \\ -1{,}24 & 7{,}62 & 0{,}81 \\ 0 & 0 & 1 \end{bmatrix} \tag{5}$$

Equation (4) can be extended with the aforementioned K-matrix, leading to a direct correlation between composite strains and wavelength shift:

$$[\varepsilon^c] = [TC][K]^{-1}\left[{}^{\Delta\lambda}/_{\lambda}\right] \tag{6}$$

EXPERIMENTAL RESULTS

Using Equation (6), the numerical TC-matrix has been validated experimentally. Different CFRP samples with $[0_2,90_2]_{2s}$ lay-up were created according to Figure 3.

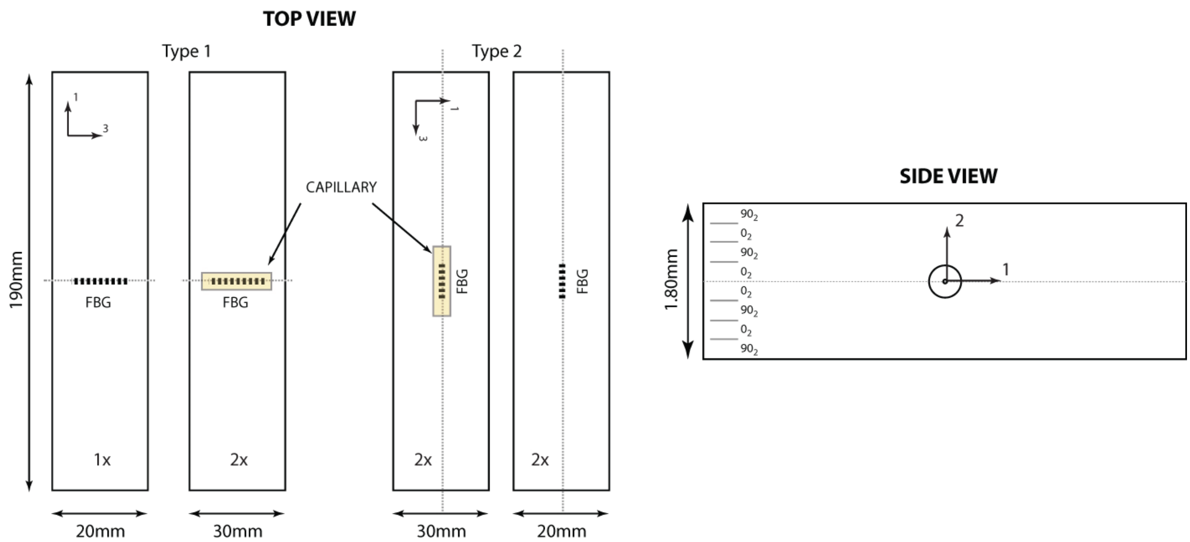

Figure 3: Dimension and lay-out of experimental samples.

According to [4] 3 different loading conditions are required to determine the TC-matrix. Both tensile loading in the length direction (1-direction for Type 1, 3-direction for Type 2) according to the ASTM D3039 standard and through-the-thickness compression loading (2 direction) were performed. All tests were performed three times. The wavelength shifts for the different loading conditions were recorded for the different samples (Figure 4). The results show an almost perfect linear behavior for loading along the 2-direction and 3-direction. Significantly more scattering is visible on the wavelength response of the capillary Type-1 sample (black squares in Figure 4(a)). In the future, more samples will be created to better study the behavior of this sample-type. These wavelength shifts are then translated to sensor strains (ε^s) using the K-matrix by substituting $v_f = 0.17$, $n = 1.456$, $p_{11} = 0.111$ and $p_{12} = 0.247$ in Equation (3).

The composite strains ε^c are determined using finite element simulations, for which the material properties have been determined previously. Using the three different strain fields ε^c and ε^s – corresponding to the three distinct loading conditions –, the TC-coefficients can be found from Equation (4).

$$TC_{[0_2,90_2]_{2s}} = \begin{bmatrix} 7{,}49 & -2{,}01 & 0{,}69 \\ -2{,}45 & 7{,}87 & 0{,}77 \\ -0{,}01 & -0{,}01 & 0{,}96 \end{bmatrix} \tag{7}$$

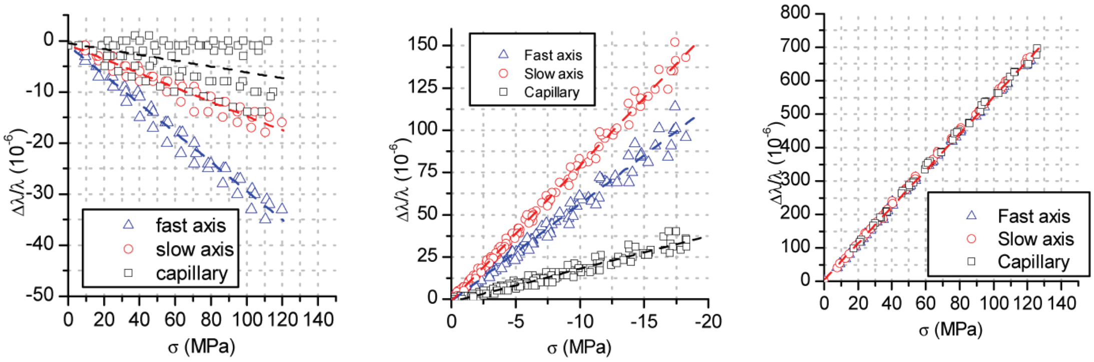

Figure 4: Wavelength shifts for loading in the (a) 1-direction, (b) 2-direction and (c) 3-direction.

If one compares Equation (7) to Equation (5), a more than decent correspondence between experiment and simulation has been found. Both matrices clearly show almost perfect axial strain transfer. In contrast, only a part of the transverse strains is transferred and both matrices show a significant cross-sensitivity to transverse strains. This cross-sensitivity is higher for the experimental matrix than for the numerical matrix. This could be caused by the large spread in the response of the capillary Type-1 sample. The good correspondence can be further validated and refined using additional testing.

CONCLUSIONS

Despite the manual lay-up procedure for the experimental samples it is clear that there is a strong correspondence between experimental and numerical TC-matrix described in Equations (7) and (5) respectively. This entails that numerical simulations can be used to determine the TC-matrix for more complex structures. Additionally, it is clearly illustrated that the proposed experimental set-up is capable of accurately determining the strain transfer. Finally, the experimentally and numerically determined TC-matrix shows the importance of translating the measured strains to the actual strains, which can significantly differ from each other.

INDUSTRIAL PARTNER

The author is funded by an EU FP7 project called SMARTFIBER. Therefore, the author likes to acknowledge the European Union and their partners IMEC, Airborne Technology Centre, FBGS Technologies, Xenics, Fraunhofer IIS and Optocap.

REFERENCES

[1] Ce Waele, W., Degriek, J., Lammens, N., Luyckx, G. and Voet, E., 2010. Multi-axial strain transfer from laminated CFRP composites to embedded Bragg sensor. *Proceedings OFS21*, Canada.

[2] Chojetzki, C., Mueller, H. R. and Rothhardt., 2004. High mechanical strength single-pulse draw tower gratings. *Int. Conf. on Applications of Photonics Technology*, Ottawa.

[3] Bennett, T., Lawrence, C., Nelson, D. and Udd, E., 1999. A fiber optic sensor for transverse strain measurement. *Experimental Mechanics,* 39(3), pp. 202–09.

[4] De Waele, W., Degrieck, J., Luyckx, G. and Voet, E., 2010. Multi-axial strain transfer from laminated CFRP composites to embedded Bragg sensor: I. Parametric study. *Smart Materials and Structures.*

IMPACT AND DAMAGE LOCALIZATION IN CARBON FIBER REINFORCED PLASTIC PLATES BY A PIEZOELECTRIC SENSOR NETWORK

A. Ungethüm and R. Lammering

Institute of Mechanics, Helmut-Schmidt-University/ University of the Federal Armed Forces Hamburg, Hamburg, Germany

ABSTRACT

A passively as well as an actively monitoring system for plate and shell structures is presented which allows for impact localization as well as damage detection and localization. The monitoring procedure proposed is based on the runtime of waves which are due to the impact or reflection at the damage and which are analyzed from data captured by a sensor network.

INTRODUCTION

With increasing application of advanced materials for lightweight structures, such as carbon fiber reinforced plastics, new types of damage occur, e.g. delamination, fracture of fibers or intermediate fiber fraction. These damages are often not perceptible visually from outside the structure, but cause especially under pressure load a strong loss in firmness and rigidity, cf. [1]. This may lead to failure of the entire composite structure. Apart from structural design methods which allow damage tolerance to be increased with respect to impact loading, there is a variety of other types of hybrid material systems and structures discussed as well as thermoplastic matrix or plies of the outside layers of those systems [2] and in that regard also methods are to be developed, which minimize the disadvantages of classical non-destructive testing of materials. The classical scanning procedures are either not applicable at all or only under inadequate effort. The time-consuming manual inspection of large surfaces, for example by ultrasonic, thermography, eddy current or X-ray techniques may be gradually replaced by integrated systems for monitoring a structure's load history or structural integrity. Therefore, approved monitoring methods have to be adapted to the specific needs required and new methods have to be developed in respective regards. Tobias [3] already presented a theory based on triangulation, which is able to detect damage in a plate by using three sensors. The underlying problem was modeled by three intersecting circles, which are in each case placed centrally around a sensor and whose radii are determined by the differences of the arrival times of wave packets at the sensors. Jeong and Jang [4], presented a similar triangulation-based model, which first evaluated the signals of two sensors. The location of the damage is defined by the intersection of two hyperbolas. Wang et al. [5] developed a four sensor model using an optimization strategy for the first time apart from the running time of wave packets. Further models of Kehlenbach and Hanselka [6], as well as of Sohn et al. [7] are based on the same principles. However, the signal analysis was extended by wavelet transformation in those cases. Common to all these models is their classification to structural health monitoring because all the investigations are related to active systems. In all of those cases piezo-electric patches were used as sensors and actuators. The continuous detection, analysis and evaluation of signals combined with the required efficiency of the algorithm necessary for passive monitoring systems in the sense of loads monitoring with regard to impact loading on composite structures have not been published in literature so far as to the knowledge of the authors.

This article intends to fill this gap by a migration-based optimization model for impact and damage detection and localization. The theoretical investigations are validated experimentally. For this purpose, a passively working loads monitoring system which allows for impact localization in plate and shell structures is presented. Monitoring is based on the runtime of waves which are due to the impact and which are detected by a piezoelectric sensor network which converts the deformations occurring due to mechanical waves into high frequency alternating current signals. Based on the same methodology, active damage localization becomes possible after integration of an additional actuator which generates elastic waves. Hence, statements about actual loads and damages, required maintenance and the residual structural life such as after impacts should become possible. Time and cost consuming maintenance procedures can be optimized and statements regarding life span consumption can be specified or predicted more precisely.

OPTIMIZATION MODEL FOR IMPACT AND DAMAGE LOCALIZATION

Waves propagating in thin elastic media, particularly in plates or shells, resulting from an impact load or being excited by a piezo-actuator result in guided or Lamb waves specifically, the latter being named after Horace Lamb. The respective equations are commonly given as Rayleigh-Lamb wave equations and read for structures with isotropic material behavior as follows [8]:

$$\frac{\tan(k_q h)}{\tan(k_p h)} + \left(\frac{4k^2 k_p k_q}{(k_q^2 - k^2)^2} \right)^{\pm 1} = 0, \tag{1}$$

with $$\mathrm{k}_\mathrm{q}^2 = \frac{\varpi^4}{\left(\frac{\lambda + 2\mu}{\rho} \right)^2} - \mathrm{k}^2 \text{ and } \mathrm{k}_\mathrm{p}^2 = \frac{\varpi^4}{\left(\frac{\mu}{\rho} \right)^2} - \mathrm{k}^2 .$$

Here, h is the plate thickness, ϖ the excitation frequency and k is the wave number. λ and μ are the Lamé coefficients and ρ the density. The exponent +1 describes symmetric, -1 antisymmetric wave modes. The group velocity c_g , interpretable as the propagation speed of a wave packet with slightly different frequency components, can be calculated by the differential relationship

$$\mathrm{c}_\mathrm{g} = \frac{\mathrm{d}\varpi}{\mathrm{dk}}$$

Yet, an analytical solution of equation (1) is not known.

Time of flight measurements and geometrical considerations allow for the determination of damage localization without use of the wave equation [4,9]. In case of isotropic material behaviour the wave front shape initiated by an impact or due to damage can be described by a circle. When the wave front reaches a sensor i, the source of the wave is located on a circle around this sensor. The running time of the waves $\Delta t_i = t_i - t_s$ describes the time that a wave needs for passing the distance S_i between the point of impact s and the sensor i. Thereby, t_s and t_i are the times when the wave is released in the point of impact and the wave arrives at the sensor i. The piezo-electric sensors used detect strains, which are caused by the wave propagation.

Introducing the velocity of the wave propagation c that is uniform in each direction, the distance covered by the waves can be written as $S_i = c(t_i - t_s)$. The point of impact with the coordinates (x_s; y_s) is the geometric locus, where the circles, defined by centre (x_i; y_i) and radius $r_i = s_i$, intersect each other. The centers of the circles (x_i; y_i) are also the positions of the sensors i.

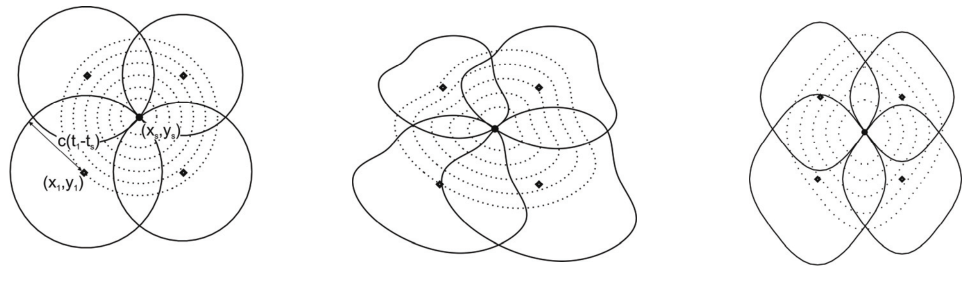

a) b) c)

Figure 1: Principle of migration based localization for a) isotropic, b) anisotropic and c) orthotropic material behavior with four sensors. Calculated location: intersection point; Propagating wave front shape: Dotted lines; Sensor: Rhomb.

The set of equations resulting from these considerations reads

$$(x_s - x_i)^2 + (y_s - y_i)^2 = c^2 (t_i - t_s)^2; \qquad i = 1..n \tag{2}$$

and contains the 4 parameters x_s, y_s, c and t_s which are computed from the n sensor signals. In anisotropic materials the velocity of the propagating waves is direction dependent (see Figure 1). To capture this effect, the set of Equations (2) is supplemented by the dimensionless propagation coefficient Ξ_i [10]:

$$(x_s - x_i)^2 + (y_s - y_i)^2 = \Xi_i^{\,2} c^2 (t_i - t_s)^2; \qquad i = 1..n. \tag{3}$$

The identification of the direction dependent propagation parameter $\Xi(\alpha_i)$ is based on material properties or experimental results by laser vibrometry (see Figure 2b).

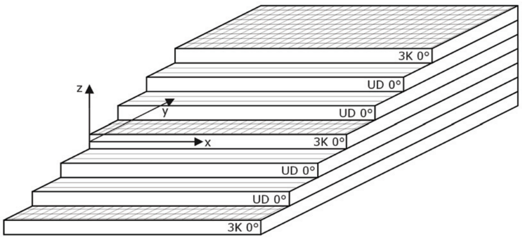

a)

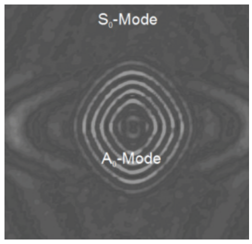

b)

Figure 2: a) Plate under consideration and b) measured form of the wave propagation [11].

Approximating the group velocity c_g of the first Lamb wave mode by the group velocity of a bending wave

$$c_b(\alpha) = \sqrt[4]{\frac{E(\alpha)h^2}{12\rho(1-\nu(\alpha)^2)}}\sqrt[2]{\varpi}, \tag{4}$$

the propagation form only depends on Young's modulus $E(\alpha)$ and Poisson's ratio $\nu(\alpha)$. Both material parameters can be calculated using classical laminate theory. For the plate under consideration (see Figure 2a) the results are shown in Figure 3.

Parameterization of the wave front shape in a polar coordinate system with azimuth α is possible by superposition of a_j-weighted ellipses with their principal axes in the dominant fiber directions ϕ_j of the laminate:

$$\Xi(\alpha) = \sum_j \sqrt{\frac{1}{1 - a_j \cos^2(\alpha + \phi_j)}}; \alpha \in [0; 2\pi]; a_j \in [0;1). \tag{5}$$

For the parameter $\Xi(\alpha_i)$ this yields to

$$\Xi(\alpha) = \sqrt{\frac{1}{1 - a_1 \cos^2 \alpha}} + \sqrt{\frac{1}{1 - a_2 \cos^2(\alpha + \pi/2)}}. \tag{6}$$

Replacing α by Cartesian coordinates one gets

$$\Xi(x_s,y_s,x_i,y_i)=\sqrt{\frac{1}{1-\frac{a_1(x_s-x_i)^2}{(x_s-x_i)^2+(y_s-y_i)^2}}}+\sqrt{\frac{1}{1-\frac{a_2(y_s-y_i)^2}{(x_s-x_i)^2+(y_s-y_i)^2}}} \tag{7}$$

Combining equation (3) with equation (7) the system of equations is rewritten as

$$(x_s-x_i)^2+(y_s-y_i)^2=\sqrt{\frac{1}{1-\frac{a_1(x_s-x_i)^2}{(x_s-x_i)^2+(y_s-y_i)^2}}}+\sqrt{\frac{1}{1-\frac{a_2(y_s-y_i)^2}{(x_s-x_i)^2+(y_s-y_i)^2}}}c^2(t_i-t_s)^2, \tag{8}$$

and still contains the 4 parameters x_s, y_s, c and t_s (see Figure 1c).

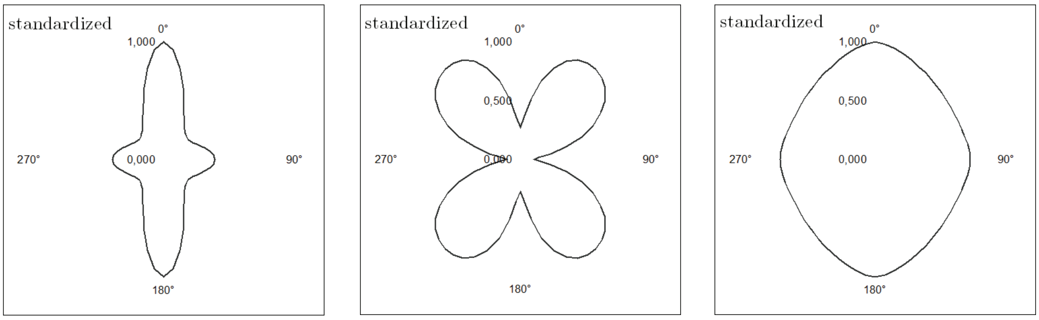

a) b) c)

Figure 3: Material parameters and calculated form of the wave propagation: a) $E(\alpha)$, b) $\nu(\alpha)$, c) $c_b(\alpha)$.

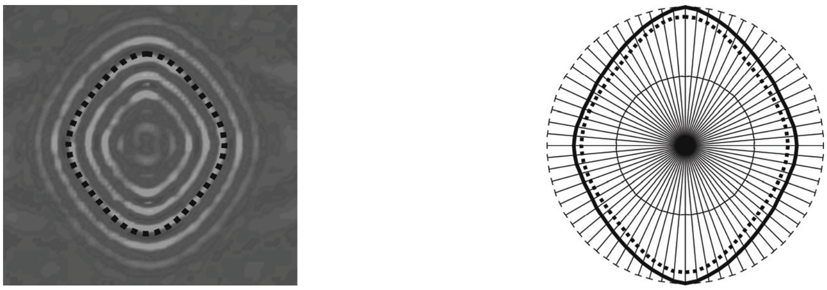

a) b)

Figure 4: Overlay of wave propagation parameter $\Xi(\alpha)$ (dotted): a) Result by laser vibrometry, b) $c_b(\alpha)$.

A typical method to find solutions to this ill-posed inverse problem is using optimization techniques. By squaring and adding Equations (8), an optimization problem with objective function F is formulated.

It allows for the integration of restrictions and for extension of the sensor number n:

$$F=\sum_n\left[(x_s-x_i)^2+(y_s-y_i)^2-\sqrt{\frac{1}{1-\frac{a_1(x_s-x_i)^2}{(x_s-x_i)^2+(y_s-y_i)^2}}}+\sqrt{\frac{1}{1-\frac{a_2(y_s-y_i)^2}{(x_s-x_i)^2+(y_s-y_i)^2}}}c^2(t_i-t_s)^2\right]^2\to\min \tag{9}$$

A robust and common algorithm for the solution of this global, non-linear optimization is the sequential quadratic programming (SQP) [12], which is used for all optimizations in this work. The SQP algorithm approximates the objective function for each iteration by a square function, while the constraints are replaced by linear approximations. The solution of the square sub-problem takes place under use of the reduced gradient method. The wave propagation due to damage is calculated by using the difference of the signals of the damaged and the undamaged structure (see Figure 5).

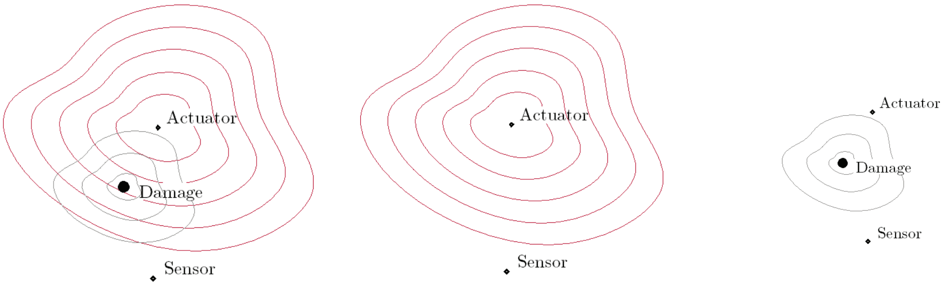

a) b) c)

Figure 5: Principal of damage localization: Wave propagation in the a) damaged and b) undamaged structure, c) due to damage by subtraction.

SIGNAL ANALYSIS

The difference in time-of-flight (TOF) is calculated by cross-correlation. Due to the low-frequency and broadband excitation of wave propagation of an impact it is advantageous to carry out a wavelet transformation in advance in order to allow for an unambiguous assignment (see Figure 6) [4,6,7]. A complex Morlet wavelet as mother wavelet is used to ensure precise identification of the time of arrival of the waves.

In the case of active damage detection the sensor signals are much more pronounced so that the arrival of the incoming wave can be determined without wavelet transformation.

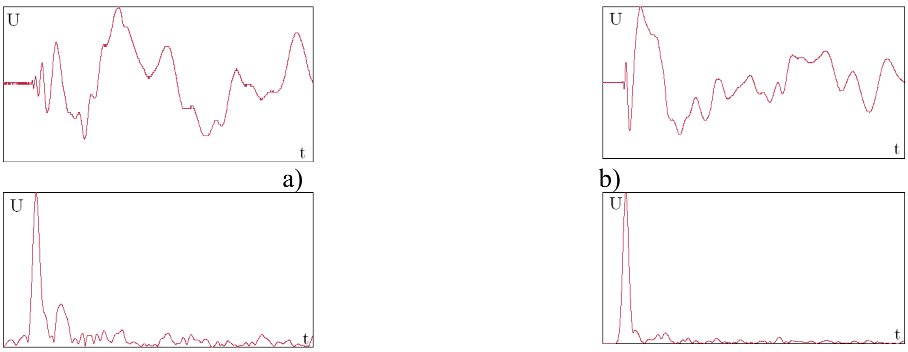

Figure 6: Captured sensor signals: a) Sensor 1, b) Sensor 2 and Wavelet transformed sensor signals: c) Sensor 1, d) Sensor 2.

EXPERIMENTAL VERIFICATION

For impact localization a carbon fiber reinforced plastic plate (1000 mm × 1000 mm × 2 mm) has been loaded by a hammer impact. Signal acquisition is done by 8 sensors glued to the plate. Edge reflections of the waves at the plate boundaries are absorbed with modeling clay. The electrical signals caused by the wave induced strains are measured with two four-channel persistence oscilloscopes (see Figure 7a). For validation of the computations the identification of 31 impacts at various locations is shown in Figure 8. The influence of the wavelet transformation is shown in Figure 9. Here, the localization errors of the 31 impacts shown in Figure 8 are depicted. Without the transformation less than 25% of the localization results are within an area of 1% of the plate surface around the real impact location. Using the complex Morlet wavelet transformation before cross correlation the results improve to more than 90% (see Table 1). Therefore, the precise determination of the time of flight must be considered as an important issue.

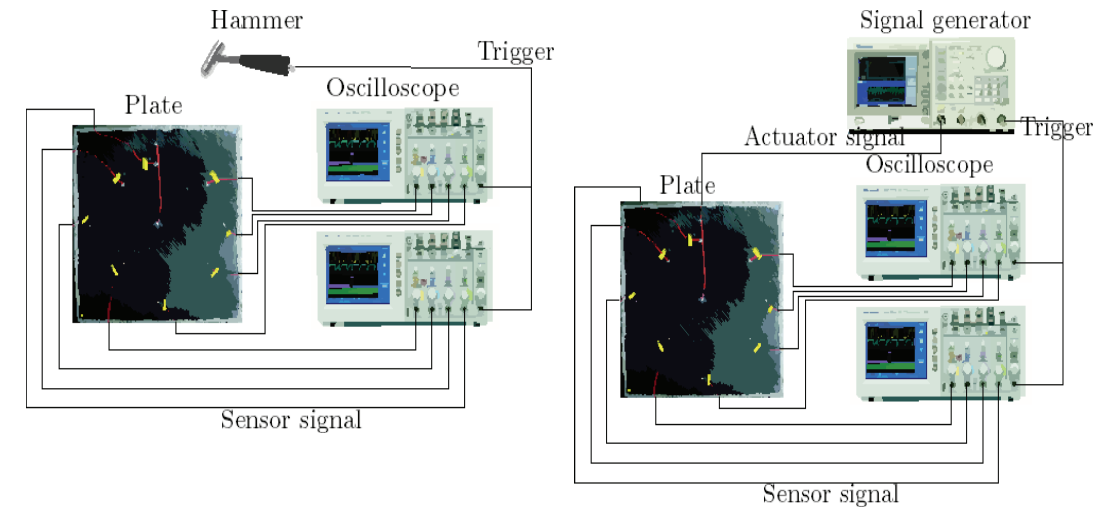

a) b)

Figure 7: Experimental setup for: a) Impact localization, b) Damage Localization.

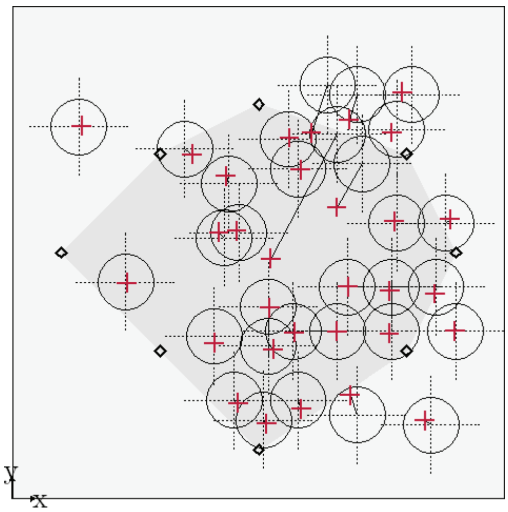

Figure 8: Calculated damage location using 8 sensor signals and wavelet transformation. Calculated location: Cross; Real impact: Crosshair with 1% plate surface marker; Sensor: Rhomb.

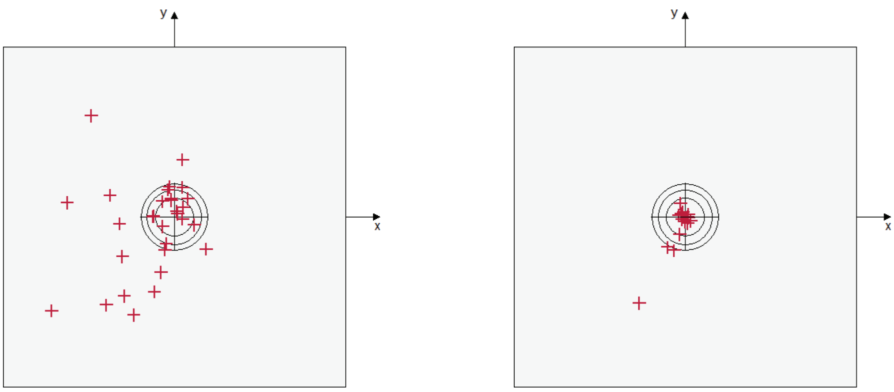

a) without wavelet transformation b) using complex Morlet wavelet

Figure 9: Error in the localization of 31 impacts. Accurate result: Crosshair with 1%, 2% and 3% plate surface marker; Cross: calculated result.

	Localization within			
	100%	3%	2%	1%
	of the plate surface			
Complete	15	4	5	7
Complex Morlet	3	0	0	28

Table 1: Influence of the wavelet transformation.

With increasing number of sensors evaluated , the accuracy and reliability increase and the result is less affected by measurement errors of individual sensors. This is shown in Figure 10. It is clearly visible, that results become more precise with increasing number of sensors. It should be noted that the impact location is close to the edge of the plate where reflections occur and being not within the inner area built by the 8 sensors.

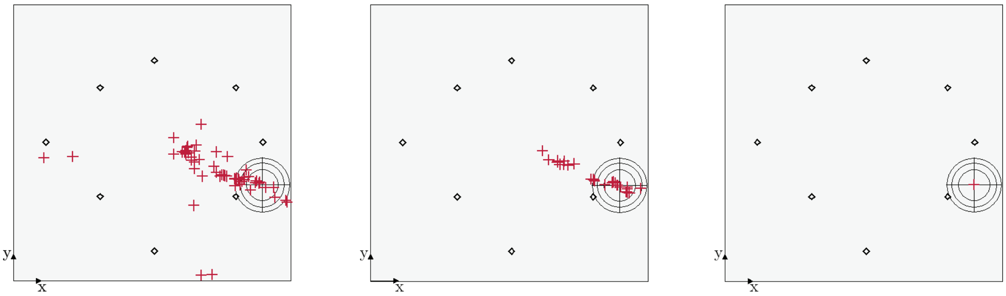

a) i=4 b) i=6 c) i=8

Figure 10: Calculated impact location with different number i of sensors. Calculated location: Cross; Impact: Crosshair with 1%, 2% and 3% plate surface marker; Sensor: Rhomb.

Finally, the methodology developed is used for damage detection. For this purpose, a sine signal with an amplitude of 2 V and a frequency of 25 kHz is sent to a piezoelectric actuator in the center of the plate (see Figure 7b). 76 different damage locations are simulated by means of magnets which are placed opposite at both plate surfaces and which work as additional masses. With one exception, all the damages were localized within 0.4% of the plate surface around the true location of the damage as can be seen in Figure 11. It is visible, that the precision of the damage localization is high in the inner area built by the actuators but that it becomes worse in the outer regions of the plate.

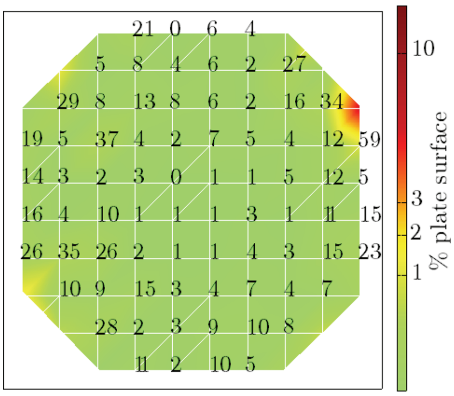

Figure 11: Localization error in [mm] and in [%] of the plate surface for 76 damage localizations using 8 sensor signals.

CONCLUSION

The intention of these investigations is the detection and localization of damaging events and damages at planar anisotropic structures by using a piezo-electric sensor network. For that purpose, an optimization model based on migration strategies has been presented. This model is able to localize the location on the basis of the form of the wave propagation and the signal running times of waves between the point of impact or damage and the sensor. The optimization model presented was verified with experimental measurement. The evaluation of the time signals provided by piezo-electric sensors as a reaction of the wave propagation provides information that the damages or damaging events can be detected and localized successfully. The difference between real and computed location during the experimental investigations are mainly based on inaccuracies of the signal analysis. The attainable accuracy allows now to apply subsequent scanning methods strictly locally.

REFERENCES

[1] Challenger, K.D., 1986. The damage tolerance of carbon fibre reinforced composites - a workshop summary. *Composite Structures* 6, pp. 295–318.

[2] Niu, M. C.-Y., 1992. *Composite Airframe Structures - Practical Design Information and Data*. Hong Kong: Hong Kong Conmilit Press Ltd.

[3] Tobias, A., 1976. Acoustic-emission source location in two dimensions by an array of three sensors. *NDT* 9(1), pp. 9–12.

[4] Jeong, H. and Jang, Y.S., 2000. Wavelet analysis of plate wave propagation in composite laminates. *Composite Structures*, 49(4), pp. 443–50.

[5] Wang, C.S. et al., 2001. Structure health monitoring from fiberreinforced composites to steel-reinforced concrete. *Smart Material Structures*, 10(3), pp. 548–52.

[6] Kehlenbach, M. and Hanselka, H., 2003. Automated structural integrity monitoring based on broadband lamb wave excitation and matched filtering. *Proceedings of the 44th AIAA/ASME/ASCE/AHS/ASC Structures, Structural Dynamics, and Materials Conference*, pp. 1486–1492. Norfolk.

[7] Sohn, H. et al., 2004. Wavelet-based active sensing for delamination detection in composite structures. *Smart Material Structures* 13(1), pp. 153–60.

[8] Rose, J.L., 1999. *Ultrasonic Waves in Solid Media. Cambridge*: Cambridge University Press.

[9] Hagedorn, J.D., 1954. *Seismic imaging - migration*. Technical report.

[10] Ungethüm, A. and Lammering, R., 2010. Impact and Damage Localisation of Carbon-Fibre-Reinforced Plastic Plates; *Proceedings of the 5th European Workshop on Structural Health Monitoring*.

[11] Neumann, M., 2009. *Experimentelle Untersuchung des Interaktionsverhaltens elastischer Wellen mit Strukturfehlern in dünnwandigen Strukturbauteilen.* Hamburg: Helmut-Schmidt-Universität.

[12] Boggs, P.T. and Tolle, J.W. 1995. Sequential quadratic programming. *Acta Numerica,* pp. 1–52.

FATIGUE CRACK DETECTION USING NONLINEAR VIBRO-ACOUSTIC MODULATIONS – COMPARATIVE STUDY OF PIEZO-BASED EXCITATION

R. B. Jenal

Faculty of Mechanical Engineering, Universiti Teknikal Malaysia, Malaka, Malaysia

W.J. Staszewski, A. Klepka & T. Uhl

Department of Robotics and Mechatronics, AGH University of Science and Technology, Krakow, Poland

ABSTRACT

Nonlinear vibro-acoustic modulations are used for crack detection in an aluminium plate. The focus is on the effect of low-frequency piezo-based excitation on modulation intensity. Two low-profile, surface-bonded piezoceramic actuators are used for low-frequency modal excitation in nonlinear acoustics tests. Low-frequency modal and high-frequency ultrasonic piezo-based excitations are introduced simultaneously to an aluminum plate. Modulated ultrasonic responses – due to fatigue crack damage – are captured using low-profile piezoceramic sensors. Both piezo-actuators used lead to similar nonlinear modulation effects despite different strain levels generated.

INTRODUCTION

Fatigue crack detection is of great importance in maintenance of many engineering structures. Ultrasonic testing is one of the most widely used approaches in practice. Various methods based on ultrasonic wave propagation have been developed over the last forty years. Recent developments include techniques based on nonlinear wave propagation phenomena. Classical approaches relate to frequency shifting and generation of higher harmonics well known for many years. Numerous inspection techniques based on generation of higher-harmonics, frequency mixing, analysis of slow dynamics, reverberation analysis and signal modulations have been developed. Literature examples include work from Van Den Abeele et al. [1,2], Duffour et al., [3], Nagy et al., [4], Guyer et al., [5], Parsons and Staszewski [6] and Antonets et al. [7]. It is generally agreed that nonlinear methods are more sensitive to detect small severities of damage than classical linear approaches.

More recently, non-linear vibro-acoustic modulations have been investigated [3,8-10]. The method utilises low-frequency modal excitation and high-frequency ultrasonic excitation for contact type damage detection. Ultrasonic wave modulations produced by nonlinear interactions are then used for damage detection. Nonlinear vibro-acoustic modulations approach has been used for crack detection in homogenous (e.g. aluminium) and micro-inhomogeneous (e.g. concrete) materials, crack detection in glass, damage detection in composites and composite sandwich structures or fracture detection in bones.

There are two major problems associated with this method. Firstly, physical understanding of various nonlinear mechanisms involved is not yet fully understood. Despite many research efforts, there is still very little understanding of what the physical mechanisms related to these nonlinearities are. These phenomena can be explained in many ways using: nonlinear elasticity (e.g. nonlinear form of the Hooke's law describing the relationship between stress and strain) [11], contact acoustics nonlinearity arising from the asymmetry of stiffness characteristics and leading to stiffness parametric modulations or unstable oscillations [12,13] or nonlinear coupling between strain and temperature field generated by damage [14-16]. A summary of recent developments in this area can be found in [16]. One of the main problems associated with the method is that similar nonlinear effects can be manifested by different mechanisms and vice versa. For example energy dissipation can be modeled using frictional, hysteretic or thermoelastic mechanisms. Hysteresis in turn involves both elasticity and dissipation, and could be linear or nonlinear. Nonlinearities not related to damage (e.g. due to boundary conditions or measurement chain) also contribute to the problem. It is often very difficult – if not impossible - to separate all these mechanisms involved.

Recent experimental research work presented in [16] show a strong evidence that nonlinear vibro-acoustic modulations are related rather to dissipative than to elastic effects. This confirms previously proposed physical models [15,17]. Secondly, previous experimental studies show that nonlinear vibro-acoustic effects are not unique to damage events. Modulation sidebands have been observed in non-damaged specimens due to material nonlinearity [15,18], boundary effects [19,20] and experimental measurement chain. The latter relates mainly to excitation methods and has not been fully investigated. Various methods of excitation have been used to analyse vibro-acoustic wave interactions. This includes audio speakers [18,21], shakers [20,22], hammers [21,23], lasers [24-26] and low-profile piezoceramic transducers [6,22,26]. Piezo-based excitation is very attractive in practical application. However, it is well known that piezoceramic transducers used for excitation are notoriously nonlinear devices. The major objective of the paper is to investigate low-frequency piezo-based excitation for fatigue crack detection.

The question is whether the application of different actuators leads to similar nonlinear phenomena associated with previously observed dissipative effects [16]. In order to achieve this objective the paper compares two low-profile, surface-bonded piezoceramic stack actuators used for low-frequency modal excitation in nonlinear acoustic tests in crack detection investigations. The structure of the article is as follows. Section 2 briefly introduces the nonlinear vibro-acoustic technique used for crack detection. Low-profile piezoceramic actuators are described in Section 3. Initial experimental investigations that lead to the selection low-frequency excitation are presented in Section 4. Modal analysis is used in these investigations. The experimental nonlinear vibro-acoustic tests for crack detection are reported in Section 5. Low-frequency modal and high-frequency ultrasonic piezo-based excitation is introduced simultaneously to an aluminium plate. Modulated ultrasonic responses – due to fatigue crack damage – are captured using low-profile piezoceramic sensors. Finally, the article is concluded in Section 6. The study demonstrates that different piezo-actuators produce similar nonlinear phenomena despite different generated strain levels.

NONLINEAR ACOUSTICS

The method of vibro-acoustic modulation relies on simultaneous excitation of test structures by high-frequency acoustic wave and low-frequency vibration. The method is illustrated schematically in Figure 1. A standing longitudinal ultrasonic wave (f_H) is introduced to one of the transducers. At the same time the structure is excited by low-frequency vibration (f_L) using the second transducer. Response signals are captured using the third transducer. If the specimen is undamaged, response signals exhibit the fundamental harmonics of both excitation components (i.e. high-frequency ultrasonic wave and low-frequency vibration) in the power spectrum. However, if the specimen is cracked, additional effects can be observed in the power spectrum of the response signal. Higher harmonics are generated and modulation sidebands are produced due to damage. Frequencies of modulation sidebands can be calculated as

$$f_n = f_H \pm n f_L \tag{1}$$

where n¬ =1, 2, 3, …, n indicates the n-th sideband, f_H is the frequency of acoustic wave and f_L is the frequency of vibration. Amplitude of these additional spectral components can be used to assess damage severity. The intensity of modulation – that relates to damage severity - can be evaluated using the amplitude of modulation components. Often modulation parameter R is used in practice.

This parameter is defined as

$$R = \frac{(A_1 + A_2)}{A_0} \tag{2}$$

PIEZO-BASED EXCITATION FOR NONLINEAR ACOUSTICS

Nonlinear acoustic tests can be carried out using different excitation techniques. Speakers, shakers, lasers, hammers or piezoceramic devices can be used in practice, as mentioned in Section 1. Selection of appropriate excitation method is important for practical implementation of the method. Type and amplitude level of low-frequency excitation has a significant effect on nonlinear phenomena and sensitivity of the method. Low-profile piezoceramic actuators offer portability and system integration. However, these actuators are well known for their nonlinear behavior. Piezoceramic transducers can be easily surface-bonded to monitor structures. Relatively low strain levels associated with these devices offer low-amplitude excitation that produce more non-classical (e.g. dissipation) rather than classical (e.g. elasticity) nonlinear effects, as demonstrated in [16]. The latter is more exhibited by higher levels of amplitude excitation.

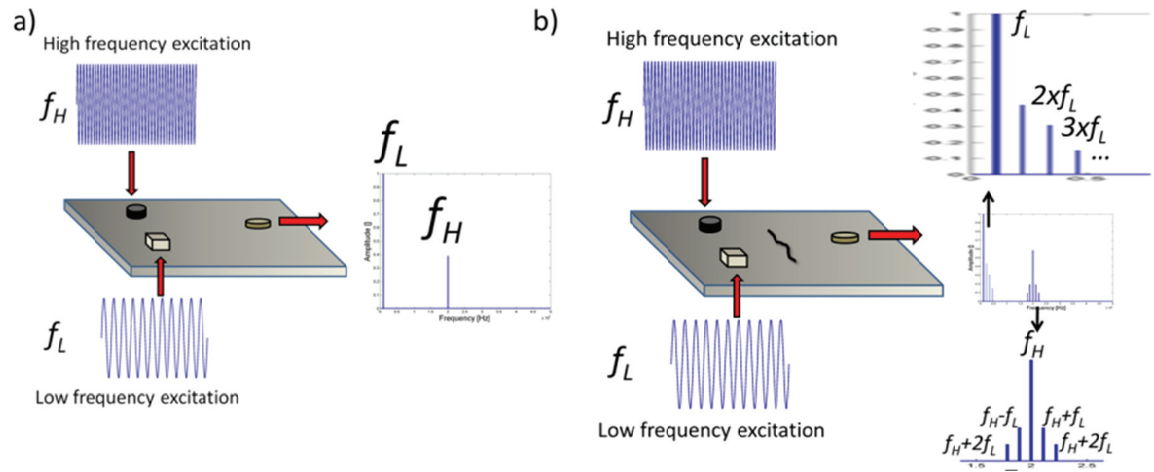

Figure 1: The principle of vibro–acoustic nonlinear modulation technique used for damage detection: a) undamaged structure; b) damaged structure.

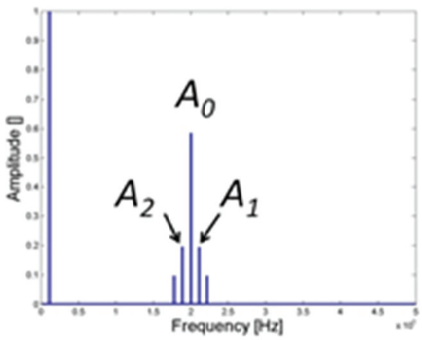

Figure 2: Power spectrum example illustrating vibro-acoustic modulation intensity.

Two piezoceramic transducers were used in the experimental work presented in this article. The first transducer was the PI Ceramics PL055.31 stack actuator with dimensions of 5x5x2 mm³. The second transducer was the NOLIAC CMAR03 12-mm ring actuator. Both actuators are shown in Figure 3. Table 1 gives specifications of the transducers.

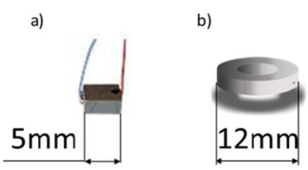

Figure 3: Piezoceramic actuators used in nonlinear acoustic test: a) PI Ceramics PL055.31; b) NOLIAC CMAR03.

	Dimensions [mm]	Nominal displacement	Blocking force [N]	Electrical capacitance [nF]	Resonant frequency [kHz]	Operating voltage [V]	Operating temp. [°C]
PL055. 31	5 x 5 x 2	2.2	>500	250	>300	-20 ÷+100	150
CMAR 03	12/6 x 2	2.8	2670	350	>500	20	200

Table 1: Transducers specifications.

INITIAL EXPERIMENTAL TESTS

This section briefly describes initial experimental tests undertaken to select frequencies for low-frequency excitation and assess strain levels associated with this excitation. The former is obtained using modal analysis, the latter utilizes the indirect approach that relates wave velocity to strain.

EXPERIMENTAL ARRANGEMENTS

A rectangular (400x150 mm²) aluminum plate of 2 mm thickness was used in these investigations. A fatigue crack was introduced in the middle of the plate.

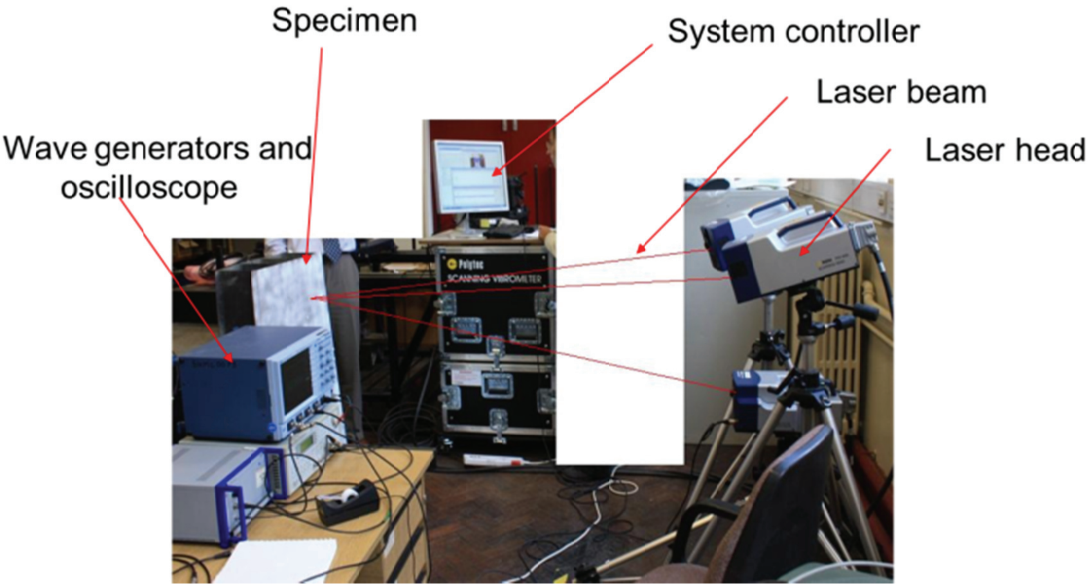

Figure 4: Experimental set-up used for vibration analysis.

This damage was formed by creating an initial notch before cyclically loading the plate to grow a crack. The maximum length of the crack investigated was equal to 69 mm. The instrumentation used was a two-channel TTi-TGA 1242, 40 MHz arbitrary waveform generator and a four-channel LeCroy Waverunner LT264, 350 MHz, 1 GS/s digital oscilloscope. The response of the structure was acquired using a 3-D PSV-400 Polytec laser Doppler vibrometer. Figure 4 shows the entire experimental set-up used for vibration and strain analysis.

MODAL ANALYSIS

The initial study involved experimental modal analysis to establish structural resonances. The plate was freely suspended and excited using the PI Ceramics PL055.31 piezoceramic stack actuator. Figure 5 shows the amplitude of the experimental Frequency Response Function (FRF). The experimental FRF was compared with the FRF estimated from Finite Element (FE) analysis. The first three excited modes – i.e. 65 Hz – 1st mode, 186 Hz – 3rd mode and 386 Hz – 6th mode - were selected for low-frequency excitation in nonlinear acoustic tests. Figure 6 shows the three vibration modes selected. The 1st and 3rd vibration modes are the first two bending modes whereas the 6th vibration mode exhibits mainly twisting action. These three modes, i.e. 1st, 3rd, and 6th were not only the first three vibration modes excited but also corresponded to three different crack modes, i.e. mode-I – crack opening, mode-III – crack tearing and mode-II – crack sliding, respectively. The action of the analysed crack modes were established using numerical simulations presented in [16].

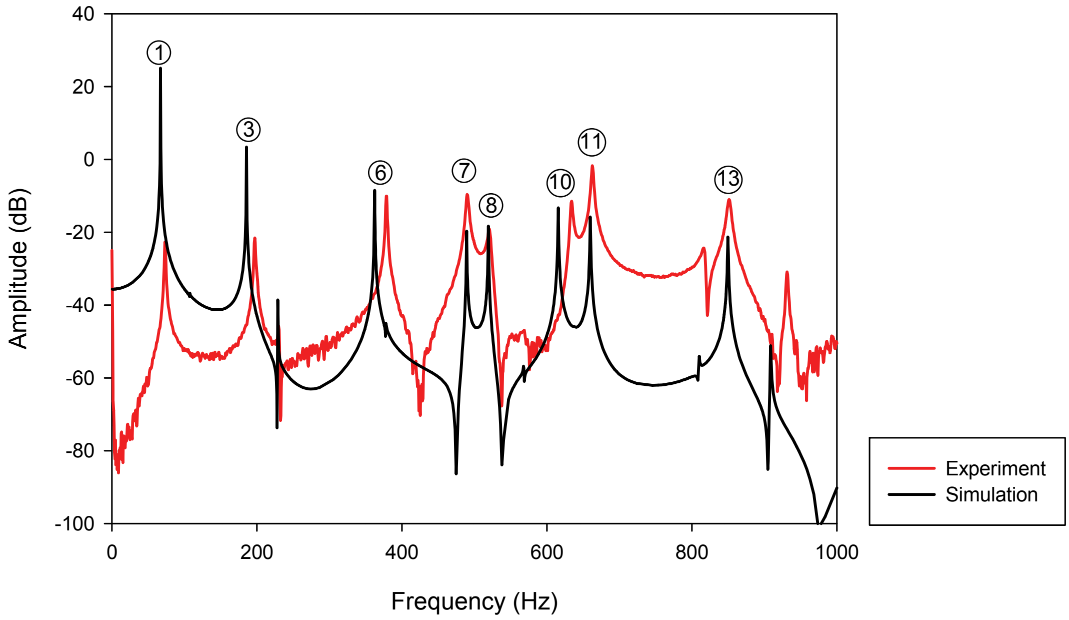

Figure 5: Frequency Response Function for the tested aluminum plate.

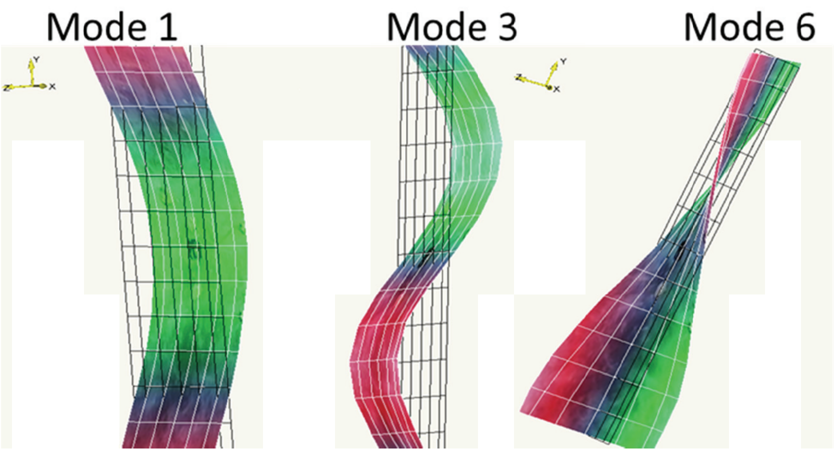

Figure 6: Vibration modes selected for low-frequency modal excitation.

STRAIN ESTIMATION

Once the frequency of modal excitation was established, a series of tests was performed to estimate strain levels in the vicinity of the crack for both stack actuators investigated. It is well known that laser vibrometers can be used for static and dynamic strain analysis when deflection measurements are performed. The relation of dynamic bending strain with measured velocity can be express as [27]

$$\xi(x,y,f) = \frac{K_{shape}}{c_L} v(x,y,f) \tag{3}$$

where $K_{shape} = \sqrt{3}$ is a non-dimensional shape factor and $c_L = \sqrt{E/\rho(1-\mu^2)}$ is longitudinal wave speed, ρ is density and μ is Poisson's ratio. The method is particularly useful when small strain levels involved are difficult to measure using classical electric or piezoelectric strain gauges. This approach was used to estimate strain levels associated with low-frequency modal excitation. The experimental results - for different vibration modes investigated and both piezoceramic stack actuators used - are given in Figure 7 and 8 (see next page). The results show that the strain level in the vicinity of the crack increases with the applied voltage, as expected. It is also clear that the estimated strain level for the *NOLIAC CMAR03* ring actuator is much larger than for the *PI Ceramics PL055.31* stack actuator for the same voltage applied. The out-of-plane vibration exhibits much larger amplitudes than the in-plane vibration for both actuators, as expected.

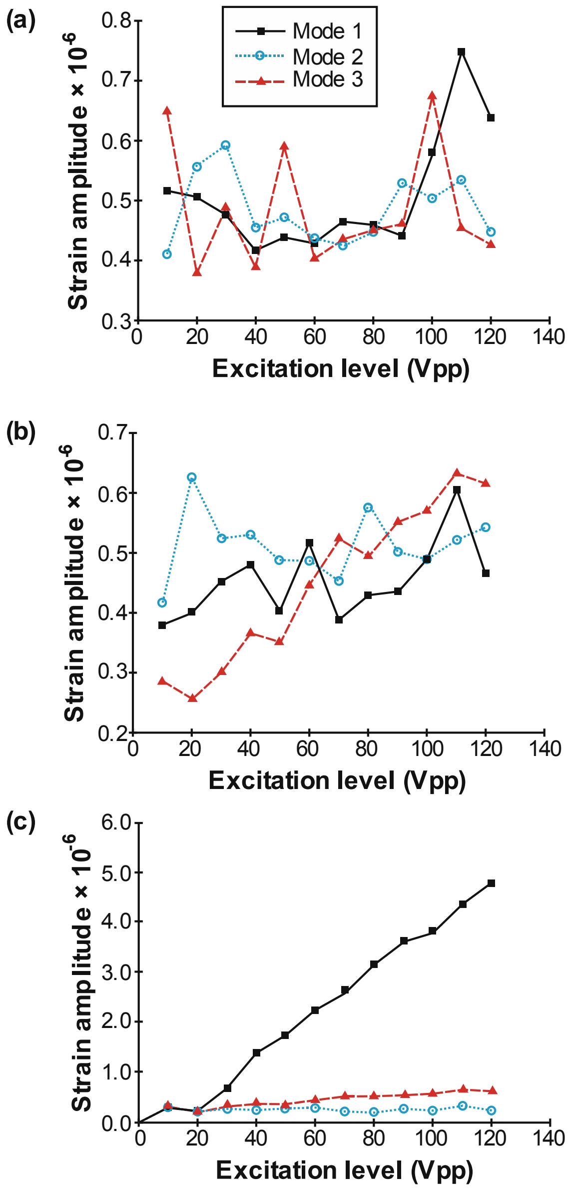

Figure 7: Strain amplitudes in:
(a) in-plane X-direction,
(b) in-plane Y-direction and
(c) out-of-plane Z-direction.
Aluminum plate was excited by the PI Ceramics PL055.31 stack actuator using the 1st, 3rd, and 6th vibration modes.

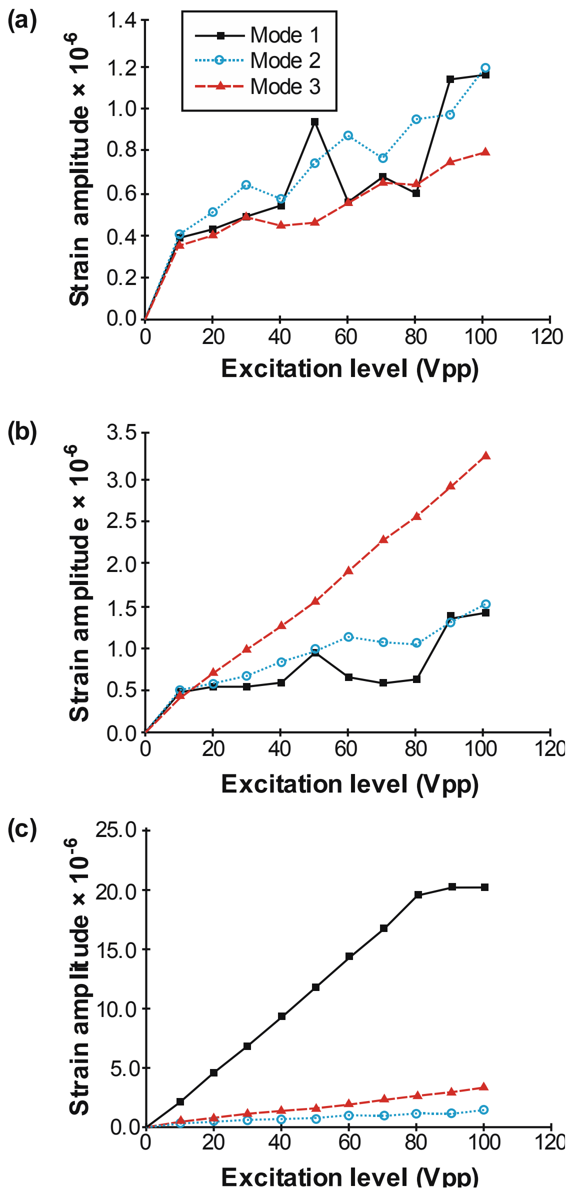

Figure 8: Strain amplitude in:
(a) in-plane X-direction,
(b) in-plane Y-direction and
(c) out-of-plane Z-direction.
Aluminum plate was excited by the NOLIAC CMAR03 ring actuator using the 1st, 3rd, and 6th vibration modes.

Most of the estimated dynamic strains in in-plane X- and Y-directions have values smaller than 1.0 μ-strain for the stack actuator. Although, the equivalent strain amplitudes for the ring actuator are of the same order (always smaller than 3.5 μ-strain), the results are less scattered and exhibit increasing trends with excitation amplitudes. The in-plane X-direction results are similar for all vibration modes investigated. The in-plane Y-direction strain levels exhibit the largest values when the plate is excited with the 6th vibration mode using the ring actuator. The out-of-plane Z-direction strain amplitudes always show the largest values for the 1st vibration mode and the smallest values for the 3rd vibration mode when both actuators are used. It is important to note that the method used for strain estimation is not accurate. However, the major interest in these investigations was in the order of the estimated strain and relative values with respect to different piezoceramic actuators and excitation frequencies used.

FATIGUE CRACK DETECTION USING NONLINEAR ACOUSTICS

Once the frequencies of modal/vibration excitation were established and strain levels near the vicinity of the crack estimated nonlinear acoustic tests were used for crack detection. In fact the focus of these investigations was rather not on crack detection but on the analysis of modulation intensity for various excitation actuators and frequencies used. The research performed attempts to answer a number of important questions: (a) which crack mode causes the largest intensity of modulations? (b) does modulation depend on the strain level in the vicinity of the crack? (c) are the results similar for different piezoceramic actuators used? The last question is the most important one in the work performed.

EXPERIMENTAL ARRANGEMENTS

The crack detection experiment with nonlinear acoustics utilized the piezoceramic stack actuators for low-frequency excitation. The ultrasonic continuous sine wave (frequency equal to 60 kHz and amplitude equal to 20 V) was introduced to the plate by a surface-bonded, low-profile PI Ceramics PIC155 transducer. The frequency of ultrasonic excitation was established using a trial-and-error approach to obtain good signal-to-noise ratio results. Once the ultrasonic wave propagated in the plate, the specimen was simultaneously vibrated using one of the piezoceramic stack actuators. The low-frequency excitation signal was also a continuous sine wave with the frequency equal to one of the selected vibration modes, as explained in one of the sections before. A PI E-505 LVPZT high-voltage piezo-amplifier was used to control the amplitude level for the PI Ceramics PL055.31 piezoceramic stack actuator. Figure 10 shows a schematic diagram illustrating experimental arrangements for the nonlinear acoustic test with piezoelectric excitation.

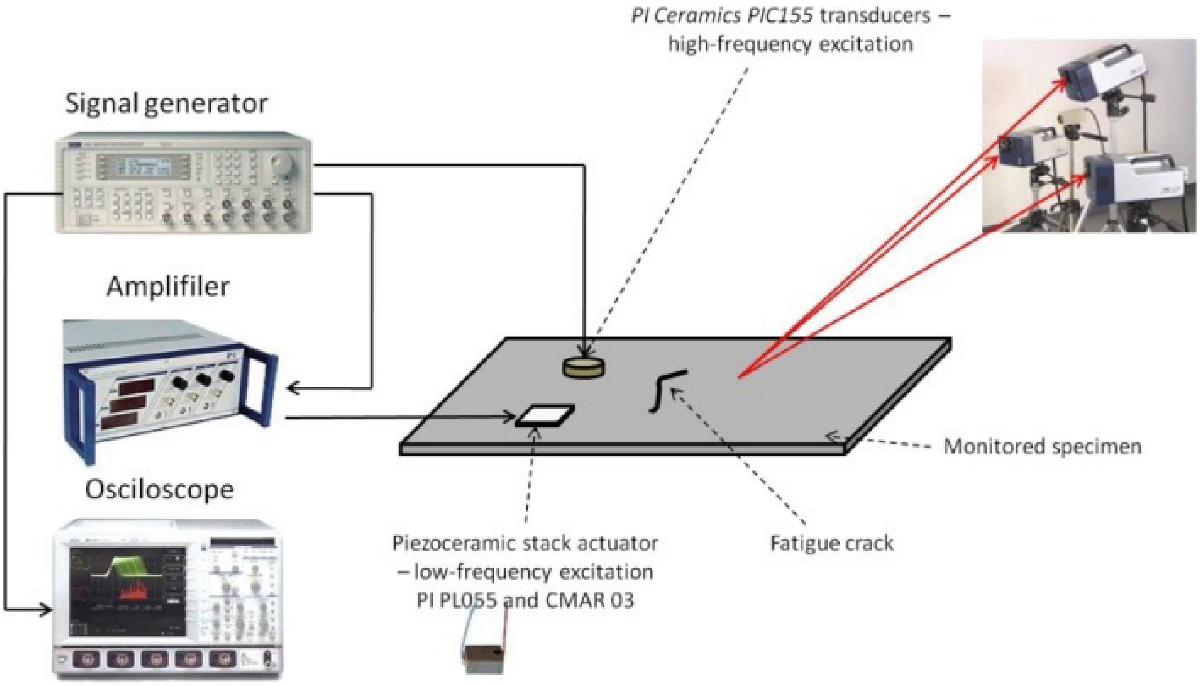

Figure 10: Experimental arrangements for the nonlinear acoustic tests.

VIBRO-ACOUSTIC NONLINEAR WAVE MODULATIONS – RESULTS AND DISCUSSION

Two experiments for both types of the piezoceramic stack actuators were conducted. Nonlinear acoustic tests were performed to assess the intensity of vibro-acoustic modulations due to wave interactions with the fatigue crack. The experimental results are presented in Figures 11 to 13. Firstly, the amplitude of the low-frequency (LF) and high-frequency (HF) spectral components was established for various levels of excitation voltage applied to the piezoceramic actuators. The experimental results - presented in Figures 11 and 12 - demonstrate that the type of actuator used for the low-frequency excitation has an impact on response amplitudes. Although for both actuators the LF amplitude always increases with the applied voltage – as expected - the NOLIAC CMAR03 actuator exhibits larger LF amplitude values for all vibration modes in Figure 11. When the ultrasonic wave propagates in the plate its HF amplitude increases with the applied voltage, as shown in Figure 12. However, the spectral amplitude of the HF wave is larger for the PI Ceramics PL055.31 stack actuator than for the NOLIAC CMAR03 ring actuator for all vibration modes investigated despite the fact that the latter produces larger strain levels for the same voltage amplitude applied (as shown in Figures 7 and 8). Figure 13 shows values of the modulation intensity parameter R plotted against the low-frequency (LF) spectral amplitude. The levels of R are roughly similar in both cases investigated for completely different levels of LF amplitude. Strain levels in the crack vicinity are several times higher for the NOLIAC CMAR03 ring actuator than for the PI Ceramics PL055.31 stack actuator for the same voltage amplitudes applied (as shown in Figures 7 and 8).

The 6th vibration mode (or in other words the crack mode-II) always produced the largest modulation intensities for both actuators used. The modulation intensity is much larger for this vibration mode than for the other two modes. Similar results were obtained for the same specimen when an electromagnetic shaker was used for low-frequency modal excitation in [16].

These results confirm that neither the excitation method nor the strain level associated with this excitation is the major factor behind nonlinear vibro-acoustic wave modulations. The sliding action of crack faces - associated with the crack mode-II – leading to energy dissipation is the most important factor, as explained in [16].

Modulation intensities for the 1st and 3rd vibration modes are much smaller when compared with the 6th vibration mode. When the PI Ceramics PL055.31 stack actuator was applied R values were larger for the 1st than for the 3rd vibration modes. It was the opposite situation in the case of the NOLIAC CMAR03 ring actuator. Interestingly, the strongest vibration mode (i.e. the 1st vibration mode) - associated with the largest strain levels in the vicinity of the crack – produced the smallest modulation intensities for the NOLIAC CMAR03 ring actuator.

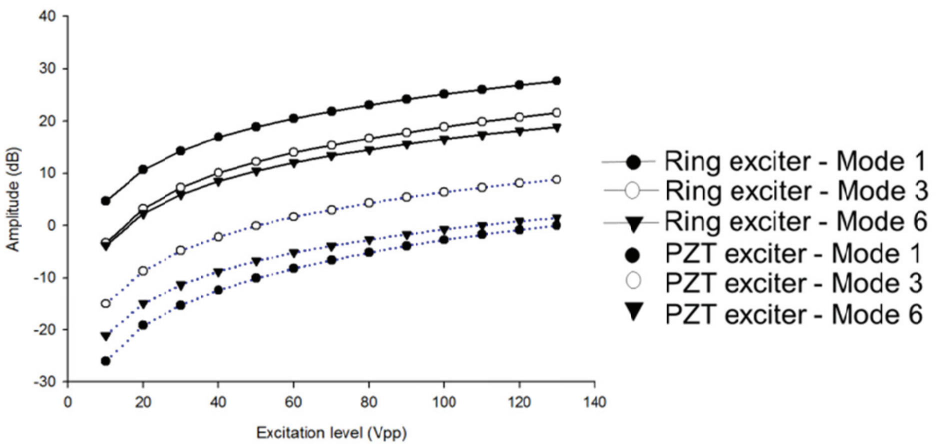

Figure 11: Low-frequency (LF) amplitude versus excitation voltage applied to piezoceramic actuators for the cracked aluminum plate excited by the NOLIAC CMAR03 ring actuator and PI Ceramics PL055.31 stack actuator for various vibration modes investigated.

CONCLUSIONS

Vibro-acoustic nonlinear wave modulations were used for fatigue crack detection in the aluminum plate. The study utilized low-profile, surface-bonded piezoceramic transducers for ultrasonic and vibration excitations.

The work performed aimed to compare the performance of piezoceramic stack actuators used for low-frequency vibration excitation. The actuators investigated produced different strain levels in the crack vicinity, as expected. However, the study performed indicates that neither strain level nor actuator type has the dominant effect on nonlinearities produced by crack-wave interactions. Further experimental work is needed to confirm these findings.

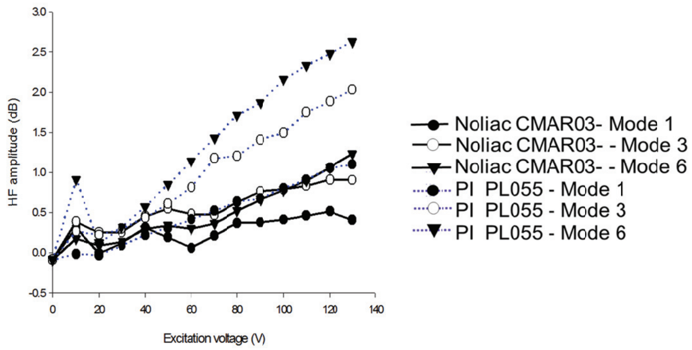

Figure 12: High frequency (HF) amplitude versus low frequency (LF) excitation voltage for the cracked aluminum plate excited by the NOLIAC CMAR03 ring actuator and PI Ceramics PL055.31 stack actuator for various vibration modes investigated.

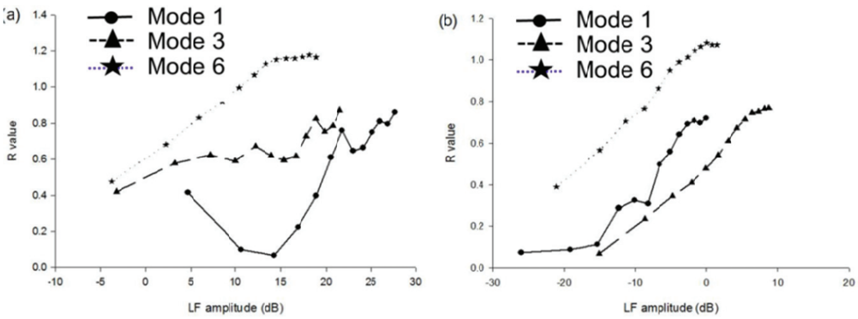

Figure 13: Modulation intensity R values versus low frequency (LF) amplitude for the cracked aluminum plate excited by different vibration modes using: (a) NOLIAC CMAR03 ring actuator; (b) PI Ceramics PL055.31 stack actuator.

ACKNOWLEDGMENTS

The work presented in this paper was partially supported by funding from two research projects MONIT (No. POIG.01.01.02-00-013/08-00) and WELCOME (Foundation for Polish Science, Project no. 2010-3/2).

REFERENCES

[1] Johnson, P. A., Sutin, A. M. and Van Den Abeele, K., 2000. Nonlinear elastic wave spectroscopy (NEWS) technique to discern material damage. Part I: nonlinear wave modulation spectroscopy. Rev Prog QNDE. 12(1), pp. 17–30.

[2] Carmeliet, T., Johnson, P. A., Tencate, J. A. and Van Den Abeele, K., 2000. Nonlinear elastic wave spectroscopy (NEWS) technique to discern material damage. Part II: single mode nonlinear acoustic spectroscopy. *Rev Prog QNDE*. 12(1), pp. 31–42.

[3] Cawley, P., Duffour, P. and Morbidini, M., 2006. *A study of the vibro-acoustic modulation technique for the detection of cracks in metals.* J Acoust Soc Am. 119, (3), pp. 1463–475.

[4] Adler, L., McGowan, P. and Nagy, P. B., 1990. *Acoustic nonlinearities in adhesive joints.* Rev Prog QNDE, 10B, pp. 1685–692.

[5] Guyer, R. A., McCall,, K. R. and Van Den Abeele, K., 1998. *Slow elastic dynamics in a resonant bar of rock.* Geophys Res Lett. 25, pp. 1585–588.

[6] Staszewski, W. J. and Parsons, Z., 2006. Nonlinear acoustics with low-profile piezoceramic excitation for crack detection in metallic structures. *Smart Mater Struc,* 15, pp. 1110–118.

[7] Antonets, V. A., Donskoy, D. M. and Sutin, A. M., 1986. *Nonlinear-vibro diagnostics of flaw in multilayered structures.* Compos Mater 15, pp.934–37.

[8] Johnson, P. A. and Sutin, A. M., 2004. Nonlinear elastic wave NDE II. Nonlinear wave Modulation spectroscopy and nonlinear time Reversed acoustics. *AIP Conference Proceedings* 760, pp. 385-92.

[9] Hu, H. F., Hu, N. Q., Jenal, R. B., Qin G. J. and Staszewski, W. J., 2010. Crack detection using nonlinear acoustics and piezoceramic transducers—instantaneous amplitude and frequency analysis. *2010 Smart Mater. Struct.* doi:10.1088/0964-1726/19/6/065017.

[10] Aymerich, F. and Staszewski, W. J., 2010. Experimental Study of Impact-Damage Detection in Composite Laminates using a Cross-Modulation Vibro-Acoustic Technique. *Structural Health Monitoring November 2010*, 9(6), pp. 541-53.

[11] Chick, B. B., Elbaum, C. and Hikata, A., 1965. Dislocatoin Contribution to the Second Harmonic Generation of Ultrasonic Waves. *Journal of Applied Physics*. 36(1), pp. 229-36.

[12] Busse, G., Krohn, N. and Solodov, I. Yu. 2002. *CAN:* an example of nonclassical acoustic nonlinearity in solids. *Ultrasonics,* 40, pp. 621–25.

[13] Mihara, T., Ohara, Y. and Yamanaka, K., 2006. *Effect of adhesion force between crack planes on subharmonic and DC responses in nonlinear ultrasound.* Ultrasonics, 44, pp. 194–99.

[14] Sas, P., Wevers, M. and Zaitsev, V., 2001. Nonlinear modulation methods of structural damage detection based on dissipative nonlinear effects. *Proceedings of the International Seminar on Modal Analysis*, pp. 233-42.

[15] Guyer, R. A. and Johnson, P. A., 2009. *Nonlinear Mesoscopic Elasticity: The Complex Behaviour of Rocks, Soil, Concrete*, Wiley.

[16] Iwaniec, J., Jenal, R. B., Klepka, A., Staszewski, W. J., Szwedo, M. and Uhl, T., 2011. Nonlinear acoustics for fatigue crack detection – experimental investigations of vibro-acoustic wave modulations. *Structural Health Monitoring*. 25, doi: 10.1177/1475921711414236.

[17] Castagnede, B., Gusev, V., Nazarov, V. and Zaitsev, V., 2006. Novel nonlinear-modulation acoustic technique for crack detection. *NDT & E Int*. 39, pp. 184–94.

[18] Johnston, P., 1999. *The new wave in acoustic testing.* Materials World. 7(9), pp. 544-46.

[19] Meo, M. and Zumpano, G., 2005. Nonlinear elastic wave spectroscopy identification of impact damage on a sandwich plate. *Computers & Structures* 71(3-4), pp. 469-74.

[20] Aymerich, F. and Staszewski, W. J., 2010. Impact damage detection in composite laminates using nonlinear acoustics. *Composites Part A: Applied Science and Manufacturing* 9(41), pp. 1084-092.

[21] Ballada, E. M., Vezirova, S. Yu., Pfleidererb, K., Solodovb, I. Yu. and Busse, G., 2003. *Nonlinear modulation technique for NDE with air-coupled ultrasound.* Ultrasonics 42 pp. 1031-036.

[22] Jenal, R. B., Klepka, A., Szwedo, M., Staszewski, W. J. and Uhl, T., 2010. Experimental analysis of vibro-acoustic modulations in nonlinear acoustics used for fatigue crack detection. *Proceedings of the fifth European workshop Structural Health Monitoring.*

[23] Donskoy, D., Ekimov, A. and Sutin, A., 2001. *Nonlinear acoustic interaction on contact interfaces and its use for nondestructive testing*. NDT&E Int. 34(4), pp. 231–38.

[24] Jerebtsov, S. N., Kolomenskii, Al. A. and Schuessler, H. A., 2003. Characterization of a polycrystalline material with laser-excited nonlinear surface acoustic wave pulses. *Fifteenth Symposium on Thermophysical Properties.*

[25] Jerebtsov, S. N., Kolomenskii, Al. A., Lioubimov, V. A., Jerebtsov, S. N. and Schuessler, H. A., 2003. Nonlinear surface acoustic wave pulses in solids: Laser excitation,propagation, interactions. *Review of scientific instruments* 74(1).

[26] Chen, S., Dajani, J. N., Gangarao, H. V. S., Petro, S. H. and Venkatappa, 1998. Damage detection using scanning laser vibrometer. *Proceedings of the 3rd International Conference on Vibration Measurements by Laser Techniques.* Ancona/Italy, June 16-19

[27] Karczub, D. G. and Norton, M. P., 2000. Correlation between dynamic strain and velocity in randomly excited plates and cylindrical shell with clamped boundaries. *Journal of Sound and Vibration,* 230(5), pp. 1069.

CRACK DETECTION BY WAVE PROPAGATION IN OVERHEAD TRANSMISSION LINES

L. Gaul, T. Haag, H. Sprenger, S. Bischoff
Institute of Applied and Experimental Mechanics, University of Stuttgart, Stuttgart/Germany

ABSTRACT

In this study, a concept of continuous monitoring for load-carrying cables of bridges and overhead transmission lines is considered. A sending/receiving piezoelectric transducer is used to generate an ultrasonic longitudinal wave in the cable strands. An interaction between the first longitudinal wave mode and vertical cracks in a single rod is investigated. Moreover, this work analyzes how the elastic energy of a propagating wave is distributed between adjacent wires via friction. An energy-based model is developed to approximate the coupling behavior in a two-rod system. Finally, the numerical predictions are verified by experimental data.

INTRODUCTION

The focus of this work is crack detection in multi-wire cables, which are widely used in numerous engineering applications, for example, as load-carrying structures of bridges, on elevators and as overhead power transmission lines. Cracks are usually caused by excessive mechanical loads from wind excitation or corrosive influences and can grow to large defects as cable age increases.
To detect deteriorations, power line installations are periodically inspected using both on ground and helicopter-aided visual inspections. Factors including sun glare, cloud cover, close proximity to power lines, and rapidly changing visual circumstances make airborne inspection of power lines a particularly hazardous task. To reduce the risk associated with aerial inspection of power line installations, the structural health monitoring of these cable structures is of importance.

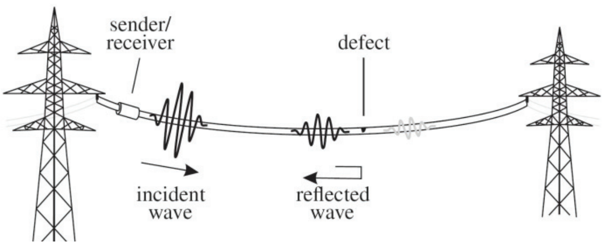

Figure 1: Interrogation of load-carrying structures of bridges using ultrasonic signals.

An experimental setup for identifying wire cracks in overhead transmission lines is illustrated in Figure1. A more detailed description can be found in [1]. As shown in Figure1, piezoelectric transducers serve as sender and receiver of elastic waves. The sending transducer converts the electric excitation signal into mechanical energy via the piezo-electric effect. In this way, an ultrasonic wave propagating in the axial direction is generated in the multi-wire cable, which is reflected at the surface crack and returns to the receiving transducer. If the amplitude of the reflected wave, sensed by the receiving transducer, is above a threshold value, the presence of a defect can be assumed.

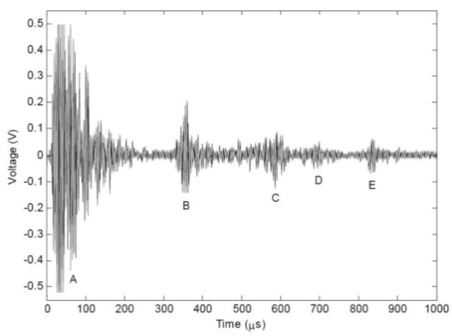

Figure 2: Time signal of excited wave (A), reflection at crack (B), reflection at free end (C) and further reflections (D, E).

In Figure2 the electrical output from the receiving transducer is depicted for an experimental investigation of a short cable with several wires. The initial signal burst (A) corresponds to the left bound wave after reflection, while the second signal burst (B) results from the right bound wave which has been reflected at a surface crack.

This work covers several aspects of analyzing defect cable structures. First, the interaction of guided waves in cylindrical structures with cracks is tackled, followed by a section on modeling energy propagation in friction coupled rods. Findings of both sections are incorporated in finite element and experimental analyses. It is shown that a wave traveling in one wire of a two-wire cable transmits energy to neighboring wires. This allows for the interrogation of subsurface cracks in a multi-wire cable, which cannot be detected by visual inspection. The two-rod system treated in this study serves as a fundamental concept for energy based descriptions of multi-wire wave propagation in cables. In future efforts, the energy based model will be validated for other frequency ranges and multi-wire configurations, including real twisted cable structures, such as overhead transmission lines and bridge cables.

WAVE PROPAGATION IN CYLINDRICAL STRUCTURES

Cable structures consist of several individual cylinders, which act as waveguides for ultrasonic waves featuring characteristic displacement fields (mode shapes). The displacement field of guided waves can be written as [2]

$$\boldsymbol{u}(x,y,z,t) = \hat{\boldsymbol{u}}(x,y)\, e^{j(kz-\omega t)}, \tag{1}$$

with stress field

$$\boldsymbol{\sigma}(x,y,z,t) = \hat{\boldsymbol{\sigma}}(x,y)\, e^{j(kz-\omega t)}, \tag{2}$$

by introducing circular wave number k, circular frequency ω and coordinate system (x, y, z), where the z-axis points in the direction of propagation.

In cylindrical waveguides, three types of propagation modes may be identified: longitudinal (L), flexural (F) and torsional (T) modes. For low frequencies, only three fundamental waves L(0,1), F(1,1) and T(0,1) propagate through cylindrical structures. For increasing frequency, complex roots in the k-plane move onto the real axis, i.e. evanescent modes transform into propagating modes for higher frequencies. The particular frequency at which a waveguide mode appears as propagating mode is referred to as cutoff frequency.

Moreover, diagrams in Figure3 illustrate that wave propagation is dispersive, i.e. group and energy propagation velocity of the distinct propagation modes depends on frequency.

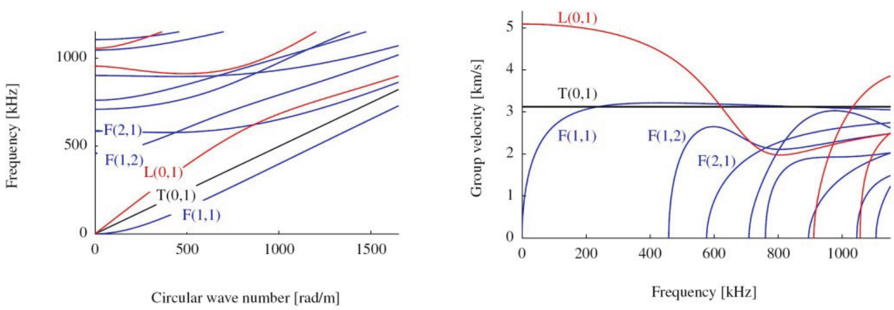

Figure 3: Dispersion curves for a cylindrical aluminum alloy waveguide with radius 2 mm.

DEFECT DETECTION STUDIES

Local Method

An experimental setup for identifying wire breaks in an overhead power line is depicted in Figure 4. The transmission line consists of a seven-wire stainless steel central load-bearing layer surrounded by 3 concentric layers of aluminum conductor wires (12, 18, 24 wires in the respective layers). The individual wires have diameters of 3.5 mm. Additionally, an artificial defect is generated by breaking a single surface wire at a distance of $\Delta z = 780$ mm from the sending transducer. A function generator drives a sending transducer with a single cycle of a 450 kHz sinusoid. The sending and receiving transducers (10 mm diameter, 2 mm thick, piezoceramic disc) are attached to the same surface wire on the transmission line. Experiments have shown that at this excitation frequency, the ultrasound is confined to the immediate vicinity of the driven wire, so that no significant mode structure in the transmission line as a whole is produced. The sending transducer converts the input electrical energy into mechanical energy via the piezoelectric effect, and a transient stress wave is thereby generated in the surface wire. The stress wave propagating through the surface wire, is reflected at the surface break, and returns to the receiving transducer. The mechanical stress is converted into an electrical signal at the receiving transducer via the inverse piezoelectric effect. The signal is amplified using a current amplifier, low-pass filtered, and finally sent to an oscilloscope for digital storage.

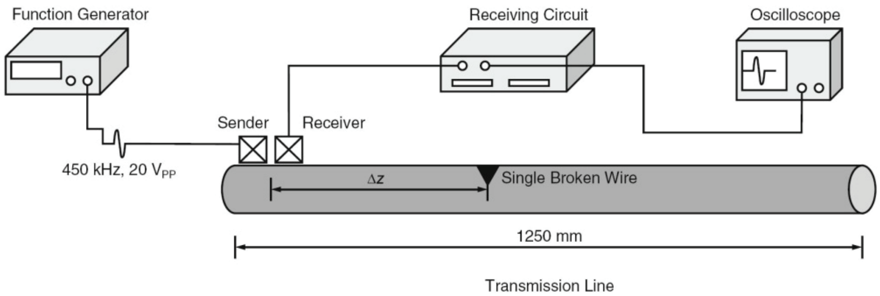

Figure 4: Experimental setup for local defect detection in a transmission line

The electrical output from the receiving transducer is depicted in Figure 2. The initial signal burst (A) is referred to as the “main bang”. It corresponds to the stress wave which is generated at the sending transducer and immediately sensed by the receiving transducer. Transducer ringing is evident in the main burst, but this ringing dies out relatively quickly. The second burst (B) corresponds to the stress-wave which has been reflected from the surface break. Time of flight calculations are used to predict the location of the break, and this value accurately predicts the physical location of the break. The additional bursts (C–E) in the diagram correspond to longer propagation paths of the elastic wave. Attempts at locating subsurface wire breaks using a single transducer pair located on the surface remain unsuccessful.
The local detection method allows for clear identification of a single broken surface wire using modest drive levels (20 V_{pp}) and a simple analog receiving circuit. Additionally, the 450 kHz excitation frequency (as opposed to lower frequencies) allows for better spatial resolution. The main disadvantage of the local method is that an array of transducers and an appropriate addressing scheme is required to ascertain the cable health. Single array elements could be individually addressed in order to assess the health of the surface wires; and, it might be possible to interrogate subsurface wires by addressing multiple surface transducers.

Global Method

An alternative wave-based detection method is described by Branham et al. [1]. In that study, a pulser-receiver is used to drive a piezoelectric ring with an electrical spike input, which in turn generates an elastic wave in a 33-wire transmission line having an overall diameter of 28 mm.

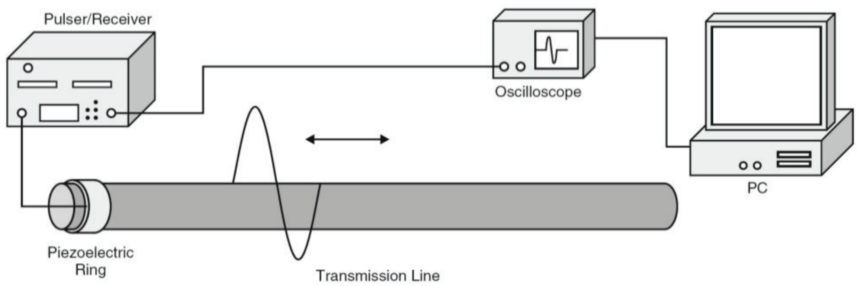

Figure 5: Experimental setup for global defect detection in a transmission line.

The experimental setup is shown in Figure 5. Since the inner surface of the piezoelectric ring is in contact with all of the surface wires, the elastic wave is globally generated at the surface of the transmission line.

The elastic wave is reflected from artificial cuts (ranging from a 2 mm deep cut to a complete cut) in the transmission line, and the reflected wave is sensed by the piezoelectric ring. The signal from the ring is received and amplified by the pulser-receiver.

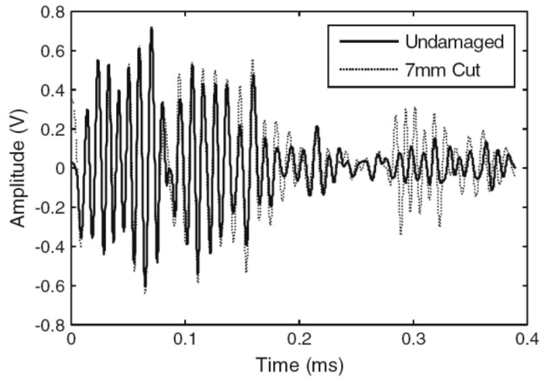

Figure 6: Transducer output for a damaged and an undamaged transmission line.

The time domain responses for cut and uncut transmission lines are compared in Figure 6. A discernible difference between the waveforms is seen around 0.3ms due to the reflection of the elastic wave from the cut. Laser-based measurements on the free cable end revealed the presence of elastic energy in all wires, including the innermost ones. As opposed to the local detection scheme, it can be concluded that there is appreciable coupling of energy between the wires at lower frequencies (~100 kHz in this global detection study), and thus, monitoring of subsurface wires is clearly possible. Although the global detection method allows for monitoring of both surface and subsurface wires, ringing of the transducer is problematic. That is, continued vibration of the ring transducer, even after removal of the drive signal, causes generation of voltage which can mask defect-reflected signals. Due to this ringing effect, the global method cannot reliably detect cuts whose depths are less than 25% of the transmission line diameter. Future work includes development of passive mechanical or active electrical means of transducer damping, which would lead to a more sensitive damage detection scheme.

ENERGY BASED MODEL

Due to computational limitations, transient analysis of ultrasonic wave propagation in real multi-wire cables using finite elements is virtually impossible. An energy based method has thus been developed to model wave propagation in adjacent rods. An extensive list of literature on energy flow analysis techniques can be found in [2]. To gain a better understanding of the coupling which occurs between adjacent wires in a cable, a simplified model is considered which consists of two straight rods having a friction contact between them. This can be considered as a precursor to multi-wire modeling.

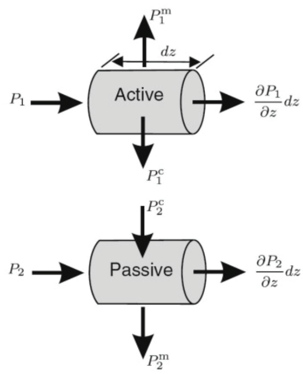

Figure 7: Power balance for a differential section of the coupled two-rod system

Figure7 depicts the power balance for a differential section of the two-rod assembly. Here, elements 1 and 2 are assumed to be cross sections of the active and passive rods, respectively. As a finite pulse of elastic energy traverses the element pair, a loss of energy in each element due to material damping and an exchange of energy due to friction coupling occur.

Including the effect of material damping and assumption of time-harmonic, longitudinal, elastic wave propagation the actual power P becomes [4]

$$P(z) = c_g \alpha \frac{|v_s|^2}{2} e^{-2k_2 z} \tag{3}$$

where c_g is the group velocity of the wave package, v_s the radial velocity component, α represents a constant and k_2 is the imaginary part of a complex circular wavenumber. The power loss from the i th rod element due to material damping is then given by

$$P_i^m = P_i(z) - P_i(z+dz) = -\frac{\partial P_i(z)}{\partial z} dz = c_m P_i(z) dz, \ i = 1, 2 \ , \tag{4}$$

where the superscript m indicates a power loss caused by material damping, and $c_m = 2k_2$, the material damping coefficient. According to Eq.(4), the average power loss due to material damping in a rod element is proportional to the input power and distance the elastic wave propagates. The energy coupling mechanism is modelled using a distributed dashpot which connects the differential elements. The instantaneous mechanical power transferred from/to the elements is

$$\begin{aligned} \widetilde{P}_1^c &= c_d v_1 (v_1 - v_2) dz \\ \widetilde{P}_2^c &= c_d v_2 (v_1 - v_2) dz \end{aligned} \tag{5}$$

where the superscript c indicates a power loss/addition due to inter-element coupling, c_d is the distributed dashpot coefficient, and v_1, v_2 are the instantaneous velocities of the differential rod elements. Since the square root of the time average power is related to the velocity amplitude, one obtains

$$\begin{aligned} P_1^c &= c_c \sqrt{P_1}\left(\sqrt{P_1} - \sqrt{P_2}\right) dz, \\ P_2^c &= c_c \sqrt{P_2}\left(\sqrt{P_1} - \sqrt{P_2}\right) dz, \end{aligned} \tag{6}$$

where c_c is the overall coupling coefficient. Finally, a balance of energy on the individual rod elements yields

$$\begin{aligned} \frac{\partial P_1}{\partial z} &= -c_m P_1 - c_c \sqrt{P_1}\left(\sqrt{P_1} - \sqrt{P_2}\right), \\ \frac{\partial P_2}{\partial z} &= -c_m P_2 + c_c \sqrt{P_2}\left(\sqrt{P_1} - \sqrt{P_2}\right). \end{aligned} \tag{7}$$

This set of nonlinear differential equations is solved using the ode45 routine in Matlab. The material damping parameter c_m, the coupling parameter c_c, and the boundary conditions, $P_1(z)\big|_{z=z_o} = P_1^o$, $P_2(z)\big|_{z=z_o} = P_2^o$, are determined using a least squares fit with experimental data [3].

NUMERICAL AND EXPERIMENTAL ANALYSES

In the following sections, the previously described energy based model of wave propagation in a two-rod system is used in simulations and predictions. Results are compared with experimental data and finite element simulations [4].

Experiment

The two-rod experimental setup is illustrated in Figure8. The rods are made from aluminum and have a length of 3 meters and a diameter of 4 mm. They are pressed together along the entire length using rubber bands. A piezoelectric transducer disc (10 mm diameter, 2 mm thick,) is glued to one end of the active rod [5]. The piezoelectric transducer is driven with 2 cycles of a 450 kHz sinusoid. A longitudinal elastic wave is thereby generated in the active rod. The energy is coupled to the passive rod along the line of contact as the elastic wave propagates. The radial surface velocity of the rods is measured at several points along the axial direction using a laser Doppler vibrometer.

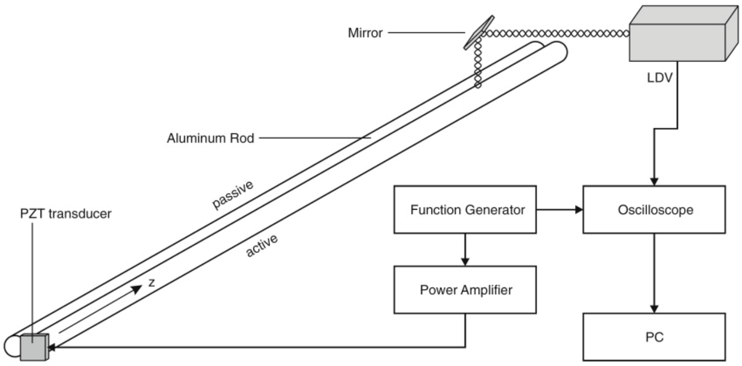

Figure 8: Experimental setup for measuring wave propagation in contacting rods.

The coupling of energy between the rods and the dispersive nature of the incident longitudinal wave is evident. The dispersive behavior of elastic waves in the cylindrical waveguide is predicted by the Pochhammer-Chree theory. An experimental group velocity of 4310 m/s has been determined at 450 kHz, which agrees well with predictions using the Pochhammer-Chree theory. At each measurement point the time average power is computed from the measured velocity. The dispersive nature of wave propagation complicated this computation. Therefore, the raw velocity signal is multiplied by a roving 4-period Hanning window with a 4-period width (based on a center frequency of 450 kHz) and is assumed to propagate with the experimentally determined group velocity at 450 kHz. Because the frequency content of the windowed signal is sufficiently narrowband, it propagates non-dispersive. Thus, the theoretical development in the previous section may be applied to compute the time average power.

In Figure 9, the experimental power distribution in the two-rod system is compared to that computed by the energy based model and the FE model [4]. There is consistent agreement between the experiment and the simulations. The FE simulation required ~2 hours, whereas the energy based model simulation required ~2 minutes. It is clear from these investigations that the energy based model can be used to accurately and efficiently predict wave propagation in a cable structure with several wires.

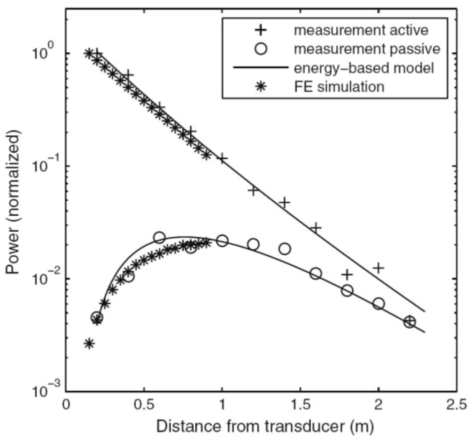

Figure 9: Measured and simulated time average mechanical power distributions in the two-rod system.

CONCLUSIONS

In this study a better understanding of the inter-wire coupling in cable structures with several wires was gained. Friction contact in a two-rod system was investigated and the results were confirmed experimentally. It was shown that a wave traveling in one wire of a two-wire cable transmits energy to neighboring wires. This allows for the interrogation of subsurface cracks in a multi-wire cable, which cannot be detected by visual inspection.
In future efforts, the energy based model will be validated for other frequency ranges and multi-wire configurations, including real cable structures, such as overhead transmission lines and bridge cables.

REFERENCES

[1] Branham, S.L., Wilson, M.S., Hurlebaus, S., Beadle, B.M., Gaul, L., “Nondestructive Testing of Overhead Transmission Lines”, Conference on Damage in Composite Materials, Stuttgart, 2006.
[2] Graff, K.F., “Wave Motion in Elastic Solids”, Dover Publications, Inc., New York, 1991.
[3] Czichos, H., Hennecke, M., Hütte, “Das Ingenieurwissen”, Springer-Verlag, Berlin, 2007.
[4] Gaul, L., Bischoff, S., Sprenger, H., Haag, T.. 2010. “Numerical and experimental investigation of wave propagation in rod-systems with cracks.” Engineering Fracture Mechanics, Vol. 77, pp. 3532–3540.
[5] Sprenger, H., Raman, S.R., Gaul, L., “Absorbing boundary conditions for solid waveguides”, Mechanics Research Communications, Vol.38, No.3, 2011.

VIBRATION DAMPING OF TURBOMACHINERY COMPONENTS

R. Bastaits[1], B. Mokrani[1], G. Rodrigues[1], I. Burda[2], R. Viguié[3], A. Preumont[1]
[1] Université Libre de Bruxelles, Brussels, Belgium
[2] Barbes-Bolyai University, Cluj-Napoca, Romania
[3] SAFRAN, Techspace Aero, Liège, Belgium

CONTEXT

Air transport is facing two major conflicting requirements in the ever-increasing demand, both for individuals and goods, and the ever-increasing ecological standards and price of energy. This calls for innovative solutions in the design and operation of aircraft, one of the main axes of improvement being the reduction of weight by increasing its functional efficiency. It can be performed through several aspects, such as the use of new materials, of lightweight structural design and of smart structures (see [1] e.g.).

Figure1 – Concept of the Bladed Drum (BluM®) [source: Safran – Techspace Aero]

These 3 aspects are coupled in our case study: the Bladed Drum (or BluM®) developed by Safran - Techspace Aero (Fig. 1) [2,3]. The low weight of this design with respect to the classical assembly approach comes at the expense of a very low level of inherent damping ($\xi \approx 0.01\%$) that, in more conventional bladed structures, is provided by the friction between the elements. It also cancels existing solutions to increase passively the damping, such as adding a layer of viscous material in the joints between the blades and the drum (e.g. [4]). Unfortunately, low levels of damping deteriorate the performance in terms of noise production, aerothermodynamics and high cycle fatigue, which is critical regarding safety. Therefore, the need for increasing the modal damping calls for new solutions amongst such as the use of shunted piezoelectric patches.

BASICS OF PIEZO-ELECTRIC SHUNT DAMPING

Piezoelectric materials have the ability to convert mechanical energy into electrical energy (a detailed discussion is provided in [5]); this property can be used to increase the structural damping. A patch of piezoelectric material, equipped with two electrodes on opposite faces, is glued on a structure (Fig.2). When subjected to mechanical loads (e.g. vibrations), electrical charges appear on the electrodes, as well as a voltage between them. This electrical energy, which is *extracted* from the mechanical one, may be dissipated in a dedicated shunt circuit, either passive or semi-active, connected to the electrodes of the patch, therefore inducing a dissipation.
The ability of a given patch to convert energy from a particular resonance mode is measured by its modal effective electromechanical coupling factor, K_i^2, eq.(1) [5]. The larger K_i^2, the larger the amount of mechanical energy from mode *i* that can be converted into electrical energy.

$$K_i^2 \approx \frac{k^2 v_i}{1-k^2} \quad (1)$$

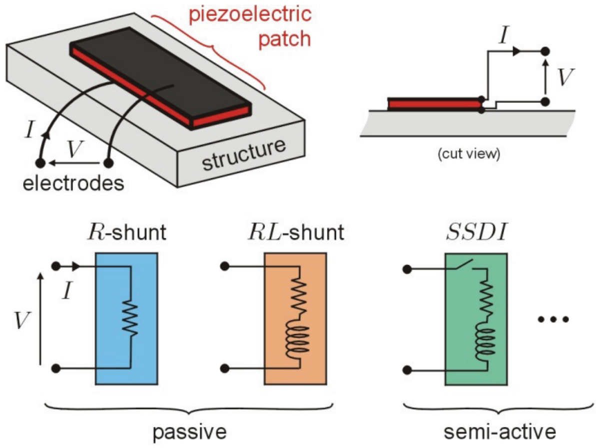

Figure 2 – Top: Patch of piezoelectric material glued on a structure. Bottom: Examples of circuits for shunt damping, either passive (*R* and *RL*-shunts) or semi-active (Switch Shunt Damping on Inductor – *SSDI*).

This equation shows the two contributions to K_i^2: k^2 is the electromechanical coupling factor, a *material* property that quantifies the efficiency of the energy conversion (expressed in *m*/*V*); v_i is the fraction of modal strain energy in the patch when the structure vibrates according to mode *i*, which is both a function of the *geometry* of the patch and of its *location* on the structure.

Classical passive shunts include the resistive *R*-shunt and the inductive *RL*-shunt [6]. Many semi-active solutions exist, some based on electronic switches that alternatively open and close the circuit to increase the performance, like the Switch Shunt Damping on Inductor (*SSDI*) [7,8,9,10]. Another interesting class of semi-active solutions is that combining a negative capacitance to the shunt circuit, to improve its performance by compensating most of the inherent capacitance of the piezo patch [11,12,6].

	Strengths	Weaknesses
R-shunt	- Simplicity - Robustness	Performance
RL-shunt	Performance	- Precise tuning - Synthetic L required
$SSDI$	- Performance - Smaller L required	- Switching logic - External power

Table 1 – Comparison of the classical shunt circuits.

A comparison of these 3 classical solutions for general applications is provided in Table 1 and Fig.3. *R*-shunt proves the simplest and most robust solution, but also provides the poorest performance. *RL*-shunts give much higher performance, but they require a precise tuning, and if weight is an issue, synthetic inductors may be required (making the circuit semi-active, thus requiring external power). Finally, semi-active solutions such as switch techniques may prove very efficient but require external power; moreover, the practical implementation of the switching logic proves difficult in real applications (broadband excitations, noise, need for a sensing device, …).

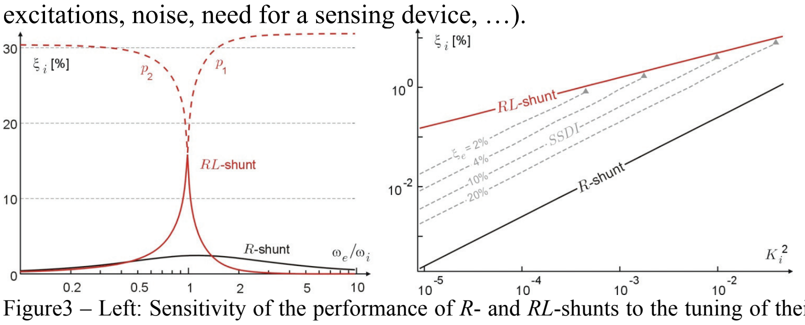

Figure3 – Left: Sensitivity of the performance of *R*- and *RL*-shunts to the tuning of their characteristic frequency with respect to that of the targeted mode [6]. Right: Comparison of the modal damping ξ generated by the 3 different shunts, as a function of K_i^2 (limited to values of practical interest) [12].

DAMPING BLADED STRUCTURES

The preceding discussion applies to any structure; for an application like the BluM®, the particular features of damping lightweight rotating bladed structures must be discussed. Fig. 4 illustrates the fact that resonance frequencies of blade modes families are very close: In the case depicted here, each step corresponds to modes where the blades of a given wheel vibrate according to their first bending mode (the geometry of the blades slightly changes from one wheel to another and, hence, so do their resonance frequencies). There are as many combinations of phase shifts between blades as there are blades per wheel (these modes are known as nodal diameters modes [13]). Moreover, the mode shapes and associated resonance frequencies are very sensitive to the elastic coupling between the blades and the drum, and to dispersion errors in the manufacturing of the structure, well known as the mistuning effect [14]. Therefore, in the view of providing a cost-effective solution for an industrial application, this calls for a choice of a shunt circuit that is both simple, systematic and robust to mistuning effects. The trade-off between performance and mass is also critical for an application like the BluM®.

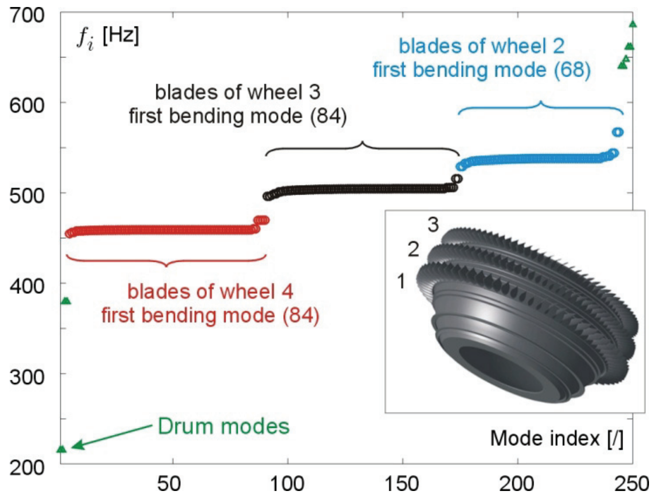

Figure 4 – First 250 resonance frequencies of a simplified finite element model of the BluM®.

The next issue is the location of the patches. Our goal is to damp bending and torsion modes of the blades. According to eq.(1), the location of the patch should be chosen so as to maximize the modal strain energy density v_i that is intercepted by the patch. For that purpose, maps of strain energy densities may be plotted, such as that presented in Fig.5. This map shows that, in the case of bladed structures, the ideal location of the patches is on the blades themselves, near their roots, where the strain energy is maximum. But the implementation of patches is difficult without affecting the flow in the booster or favoring a concentration of stresses. As a consequence, engine manufacturers won't consider this option as valid and develop methods of integration unless substantial benefits may be demonstrated. The alternative is to locate the patches on the support, under the root of the blades as, in the case of the BluM®, this space is empty and quite protected from severe environmental conditions. However, this comes at the cost of a substantial loss of efficiency (a decrease of the damping by a factor of roughly 10). Therefore only high performance shunt circuits can be considered for that purpose.

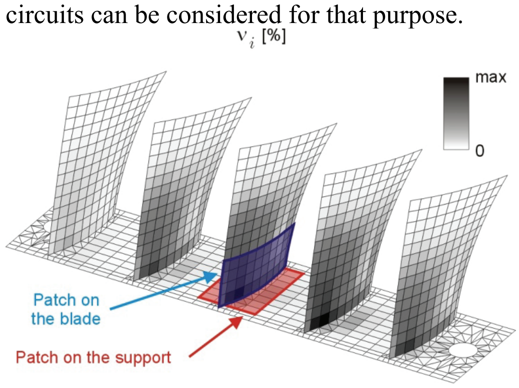

Figure 5 – Map of modal strain energy density of a bladed rail for a combination of first bending modes of the blades.

SENSITIVITY OF RL-SHUNTS TO MISTUNING

The approximate values of the inductance L_{OPT} and of the resistance R_{OPT} of an optimal RL-shunt can be approximated by [5]:

$$L_{OPT} = 1/(\omega_e^2\ C_{STAT})\ ,\ R_{OPT} = 2K_i/(\omega_e\ C_{STAT}) \tag{2}$$

where ω_e is the resonance frequency of the targeted mode [rad/s], C_{STAT} is the static capacitance of the piezoelectric patch [F] and K_i is the generalized electromechanical coupling factor of the targeted mode [eq.(1)]. It results that, for a given patch at a given location (i.e. given values of C_{STAT} and K_i), the value of the inductance is fully determined by the targeted frequency ω_e.

Fig. 6 shows a detailed plot of the influence of the tuning of the electrical circuit of a RL-shunt on the modal damping generated in the structure. It shows that an error on the tuning of 5% still guarantees that half of the optimal damping may be obtained. This fact is independent of the structure. Moreover, the frequencies of a family of blade modes of the BluM® are expected to lie in a tight interval (Fig.4) around a mean value: $\overline{\omega} \pm 5\%$ in the worst case expected (the half-length of the interval should lie between 3% and 5%). Therefore, a RL-shunt tuned with respect to the mean frequency $\overline{\omega}$ should still provide a significant level of modal damping for very lightly damped structures like the BluM®.

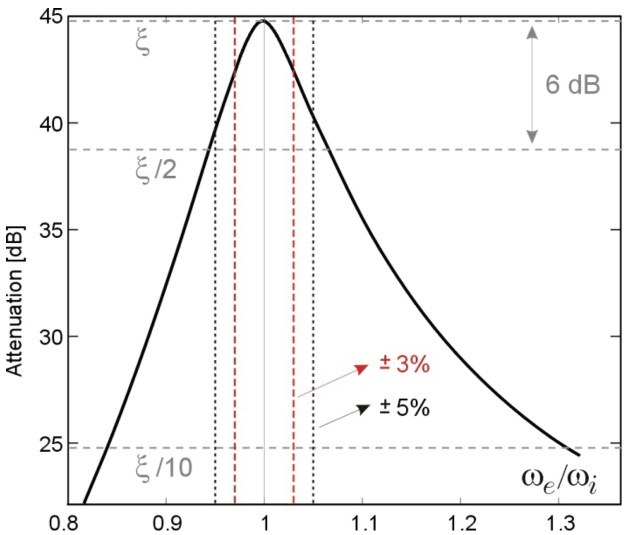

Figure 6 – Influence of the tuning of a RL-shunt ω_e with respect to the frequency of the targeted mode ω_i on the modal damping generated.

This fact has been demonstrated experimentally on a bladed rail that is representative of the BluM®, depicted in Fig.7. Two patches are glued under the support: One is used as the input to excite the rail, the other is used to create damping. The Frequency Response Function (FRF) as a function of the shunt circuit is depicted in Fig.8, where the frequency bandwidth shows 4 out of the 5 first bending modes of the blades. The attenuation provided is a function of the shift between the frequency of the mode and that of the RL-shunt (ω_e), *modulated* by the authority of the patch over the corresponding mode (given by K_i).

PROPOSED SOLUTION: “MEAN” RL-SHUNT

In the light of the general comparison of the shunt techniques and of the particular features of the dynamics of bladed structures, RL-shunts appear the most suitable solution as:

- R-shunts should be rejected because of their comparably much lower performance.
- The complexity of the trigger logic of switch techniques makes their sound implementation in structures like the BluM® very difficult.

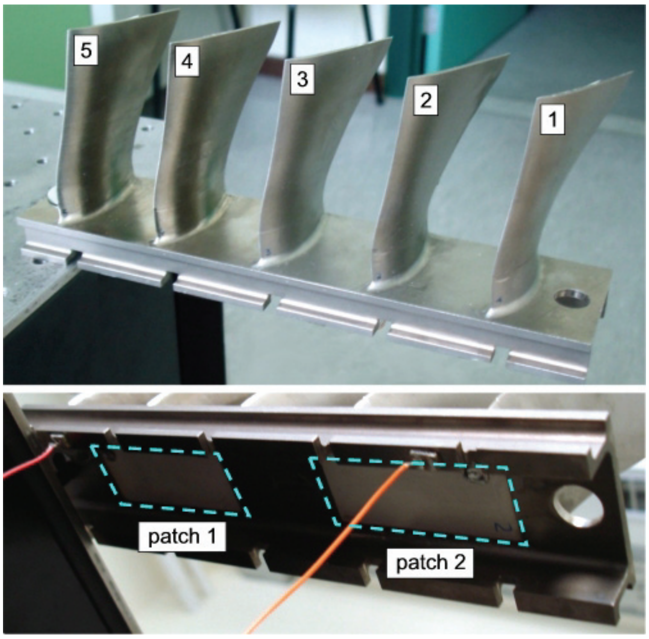

Figure 7 – Top: Bladed rail representative of the BluM®. Bottom: Two piezoelectric ceramic patches (55x25x0.3mm³) glued under the support of the rail.

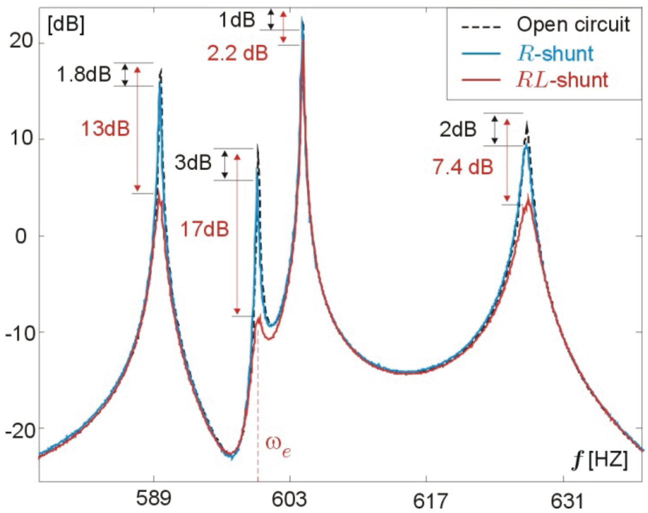

Figure 8 – Experimental measurements of the Frequency Response Function of the bladed rail between the tension applied to patch 1 and the displacement of blade 1 when patch 2 is used to provide damping (the frequency of the *RL*-shunt is given by ω_e). The intrinsic modal damping of the bladed rail ξ_i varies between 0.01% and 0.03%.

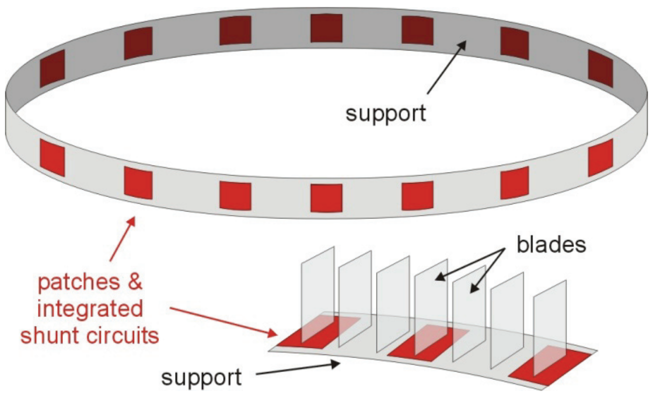

Figure 9 – Principle of the proposed solution to damp the BluM®.

The proposed approach, referred to as the "mean shunt" is the following:

- Several patches are distributed under the support (Fig.9), each patch having its own *RL*-shunt; each patch has a roughly additive contribution to the modal damping generated.
- All the *RL*-shunt circuits are built with the *same* components (R and L).
- The shunts are all tuned on the expected mean resonance frequency of the targeted family of blade modes $\omega_e^* = \varpi = \frac{1}{N}\sum \omega_i$; the tightness of the interval around ϖ ensures a good authority of the patches over the whole frequency bandwidth.
- R^*, is chosen using eq.(2); as a first approximation, K_i^* is taken as the maximum authority of the chosen patches over the modes of interest: $K_i^* = \max_{patch\ j} \max_{mode\ i} (K_{i,j})$.

This "mean shunt" approach tackles the high level of complexity and uncertainties of the structure by taking average values. It is very simple and robust. In the view of an easy gluing on a structure like the BluM®, one may imagine all the patches and their shunt circuits (in the form of integrated circuits) embedded in a soft strip that could be glued in place. For that purpose, Macro Fiber Composites may be used instead of ceramic patches. This implementation would meet the requirements of being lightweight and easy to implement in an industrial process.

MEAN SHUNT: NUMERICAL VALIDATION

The validity of the proposed solution has been studied numerically on the simpler structure of the bladed rail of Fig.7, supported by experimental tests (not reported here). A finite element model of the rail has been built in SAMCEF (Fig.10), including piezoelectric plate elements [15]. The modal analysis of this model is depicted in Fig.11, where the steps correspond to families of blade modes. In the following, we focus on the first bending modes of the blades (1F) (Fig.12).

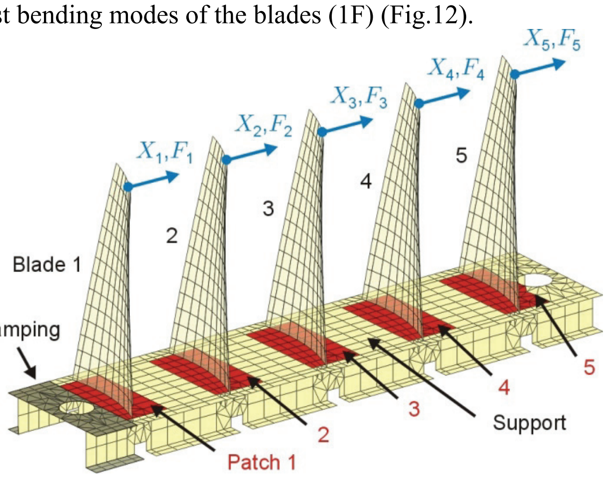

Figure 10 – Finite element model of the bladed rail.

Based on the model, the coupling factors K_i^2 of the 5 patches have been computed for each mode (Table 2). From this information, it is possible to select a minimum configuration of patches guarantying a reasonable authority over the 5 modes at the same time. In this case, we have favored combinations giving a better K_i^2 for the first and last 1F modes, as their frequencies are the furthest from that of the mean RL-shunt. For that purpose, we restrict ourselves to patches 1, 3 and 5 to generate damping. Using patch 2 or 4 instead of patch 5 would have increased the attenuation of mode 4 at the expense of that of mode 3. The performance of the "mean shunt" approach is compared in Fig.13 to that of a classical approach based on an independent tuning of the shunt circuits of each patch (patch 1 is tuned on mode 4, patch 3 is tuned between modes 3 and 5, and patch 5 between modes 1 and 2). Although the independent approach shows better results for the modes with the furthest frequencies, the performance of the mean shunt are still very good. Furthermore, the independent approach, although very simple in principle, is in fact difficult to implement, even in laboratory conditions, on a structure as simple as the bladed rail, because it requires the full characterization of the modes of interest. Therefore, it appears totally unpractical for an industrial application. In all cases,

these results show that a sound design allows the damping of the 5 modes with only three patches of reasonable size.
The robustness of the mean shunt approach with respect to the tuning frequency ω_e and to the value of the resistance R has then been tackled using the following procedure:

1. the design of the RL-shunts (ω_e and R) of *all* the patches is *identical*,
2. for each pair, the FRF is computed for a given input/output pair: $H_{ij}(\omega) = X_i/F_j$ (Fig.10),
3. the corresponding RMS response is computed according to $\sigma_{RMS}^2 = \int_0^\infty |H_{ij}(\omega)|^2 \; S_0(\omega)\, d\omega$, where $S_0(\omega)$ is a band-limited white noise (equal to 1 over the bandwidth of Fig. 13, and to 0 elsewhere). This value is compared to σ_0, the RMS response of the undamped rail under the same conditions.
4. the values of ω_e and R are changed and steps 2 and 3 are repeated.

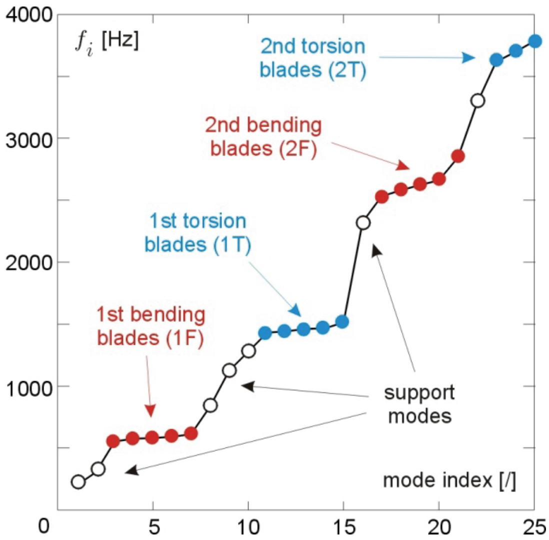

Figure11 – Modal density of the model of bladed rail.

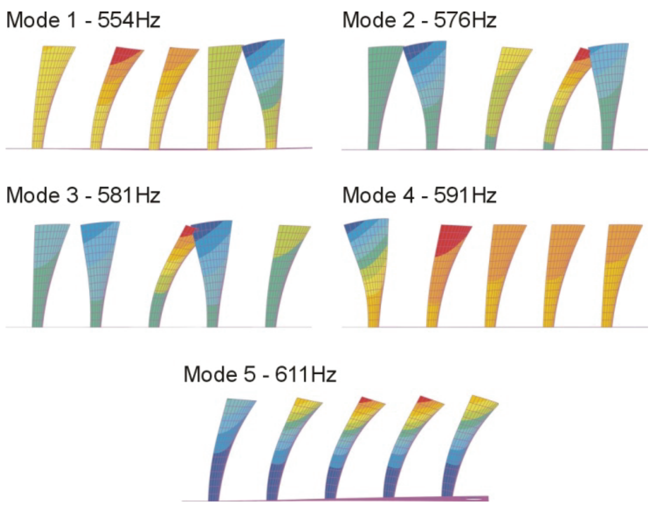

Figure12 – The family of the five first bending modes of the blades (1F).

Mode	ω_i [rad/s]	K_i^2 per patch P1	P2	P3	P4	P5
1	3483	2.8e-7	1.1e-4	7.7e-5	3.3e-6	2.2e-4
2	3620	3.1e-6	2.2e-4	2.7e-5	2.3e-4	7.3e-5
3	3653	1.4e-6	8.3e-5	3.1e-4	1.6e-4	1.6e-5
4	3720	2.2e-4	4.7e-5	2.9e-6	2.8e-6	7.6e-7
5	3843	4.2e-5	1.6e-4	2.1e-4	1.9e-4	9.2e-5

Table 2 – Effective electromechanical coupling factors K_i^2 of the 5 patches for the 1F modes.

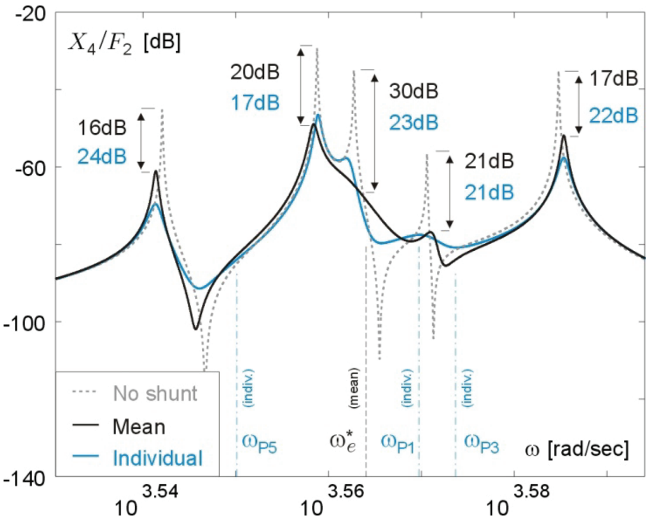

Figure 13 – FRF between F_2 and X_4 as a function of the type of shunt. The frequency of the mean shunt, $\omega_e^* = \bar{\omega}$ and those of the individual shunt are shown by the vertical dotted lines.

The results are depicted in Fig.14 for an input force on blade 2 and an output displacement measured at blade 4. The surface formed by the iso-curves exhibits a single minimum corresponding in a reduction of the RMS response of the blades of 71%. Moreover, in this region, the gradient is small enough to warrant a good robustness of the performance with respect to:

- changes in the resonance frequencies, of either the structure (ω_i) or of the circuit (ω_e, related either to the material properties and dimensions of the patch or to the electrical components);
- changes in the authority of the patches, either due to variations in the mode shapes or in the material properties [as $R \propto K_i$, eq.(2)], or to variations in the manufacturing of the resistors, or even to a drift in time.

As a consequence, although the performance using the simple design rule of the mean approach does not correspond to the optimum, it is still very close to it with a reduction of 69% in the RMS response. Such a reduction is significant in the context of resistance to fatigue. Furthermore, we see that the choice of R* does not require a precise knowledge of the K_i of the patches: Knowing its order of magnitude is enough, either from a finite element analysis (even quite rough) or from a measurement over a representative prototype. We finally note that the performance is quite robust to overestimations of R*.

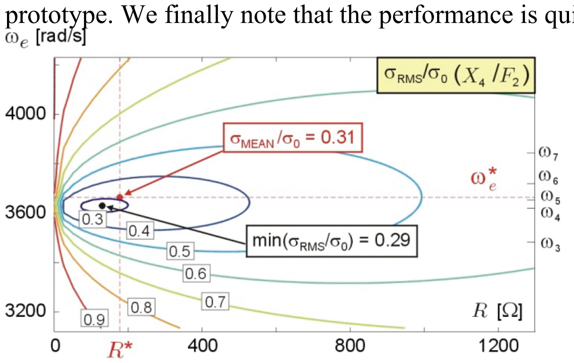

Figure 14 – Robustness of the mean shunt in the reduction of the RMS vibration of the blades, with respect to parameter changes. The dotted lines correspond to the mean shunt.

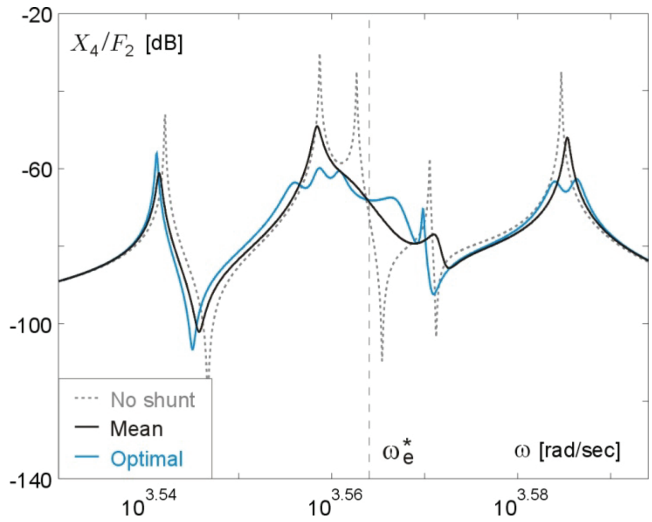

Figure 15 – FRF between F_2 and X_4 as a function of the type of shunt. The frequency of the mean shunt, $\omega_e^* = \overline{\omega}$, is shown by the dotted red line.

Fig. 15 compares the attenuation provided by the mean approach to that provided by an *independent* tuning of the 3 RL-shunts that minimizes the RMS response of the rail over the bandwidth of interest ($\sigma_{opt}/\sigma_0 = 0.18$). We can see that, although the mean approach provides less attenuation than the optimal solution for the given configuration, the difference remains moderate. Furthermore, it should be emphasized that such an optimal tuning would be very difficult (if not impossible) to achieve for a given bladed structure and, if achieved, the dispersion errors due to the manufacturing would make it less efficient for another similar structure.

σ_{RMS} is, in general, a function of the input/output pair considered and so is the ratio $\sigma_{mean}/\sigma_{opt}$. Curves similar to those of Fig.14 and 15, and the corresponding RMS values, have been generated for several input/output pairs (collocated or not) using the same configuration of 3 patches and the same general tendencies as above have been observed. Therefore, we can conclude that the mean approach provides a very simple rule of design for the RL-shunt, with a good level of attenuation and robust performance with respect to inherent mistuning phenomena.

COMMENTS

Some differences will occur when considering structures with a rotational symmetry, as opposed to the bladed rail considered here. In particular, the mode shapes will exhibit a more homogeneous distribution of the strain energy density at the level of the support. On one hand, this will induce a better distribution of the authority in the candidate locations for the patches, making the actual knowledge of the values of K_i^2 for each patch unnecessary for the choice of a subset of locations. On the other hand, this selection will have to take other considerations into account regarding nodal diameter modes or the breaking of the symmetry (to avoid creating an undamped subset of modes).

When considering a network with more patches, the results may be improved by dividing the patches in two sets, each with a different mean shunt approach designed to optimize the damping over half of the frequency bandwidth.

CONCLUSIONS

The damping of bladed structures with piezoelectric shunts, based on their specific features, has been briefly discussed. A design rule for RL-shunts has been proposed: The complexity and variability of the modal behavior is tackled by tuning the circuits to the mean value of the resonance frequencies. The proximity of these frequencies ensures a good attenuation of the blade modes over which the patches have a sufficient authority, in spite of the slight detuning. The choice of the resistance requires only a rough estimation of the coupling factors. This design rule is very simple, proves efficient and robust with respect to all parameters change in the system.

A campaign of laboratory tests is currently lead on a 1/2 scale model of a one-stage BluM®; one of the pursued goals is to assess the validity and the limits of the mean shunt approach.

INDUSTRIAL PARTNER

This research was performed in the "Health-Monitoring +" project supported by Skywin- Région Wallone, involving Safran– Techspace Aero as an industrial partner.

REFERENCES

[1] J. Williams, E. Starke, Progress in structural materials for aerospace systems, *Acta Materialia*, Vol. 51, 2003.

[2] J. Cortequisse, *One-piece bladed drum of an axial turbomachine compressor*, Patent US 2010 0158 690 A1, 2010.

[3] M. Wlasowski, *Reduced monobloc multistage drum of axial compressor*, Patent US 2011 0223 013 A1, 2011.

[4] D. Charleux et al., Numerical and Experimental Study of Friction Damping in Blade Attachments of Rotating Bladed Disks, *Int. Journal of Rotating Machinery*, Art. ID 71302, 2006.

[5] A. Preumont, *Vibration Control of Active Structures - An Introduction*, 3rd ed., Springer, 2011.

[6] B. De Marneffe, *Active and passive vibration isolation and damping via shunted transducers*, Ph.D. Thesis, Université Libre de Bruxelles, 2007.

[7] W. Clark, Vibration Control with State-Switched Piezoelectric Materials, *J. Intelligent Material Systems and Structures*, 11, 2000.

[8] C. Richard, D. Guyomar, D. Audigier and H. Bassaler, Enhanced semi-passive damping using continuous switching of a piezoelectric device on an inductor, *SPIE 3989*, 2000.

[9] D. Niederberger, *Smart Damping Materials Using Shunt Control*, PhD thesis, Swiss Federal Institute of Technology, 2005.

[10] M. Lallart, E. Lefeuvre, C. Richard, D. Guyomar, Self-powered circuit for broadband, multimodal piezoelectric vibration control, *Sensors and Actuators A,* 143, 2007.

[11] M. Date, M. Kutani, S. Sakai, Electrically controlled elasticity utilizing piezoelectric coupling, *J. Applied Physics*, 87(2), 2000.

[12] B. Mokrani, G. Rodrigues, I. Burda, R. Bastaits, A. Preumont, Synchronized Switch Damping on Inductor and Negative Capacitance, *J. Intelligent Material Systems and Structures*, in press.

[13] M. Singh, J. Vargo, D. Schiffer, J. Dello, SAFE Diagram - A Design and Relability Tool for Turbine Blading, *Proc. 17th Turbomachinery Symposium*, 1988.

[14] M. Castanier, C. Pierre, Modeling and analysis of mistuned bladed disk vibration: Current status and emerging directions, *J.Propulsion and Power*, 22, 2006.

[15] V. Piefort, *Finite Element Modeling of Piezoelectric Active Structures*, Ph.D. Thesis, Université Libre de Bruxelles, 2001.

BRIDGE HINGE-RESTRAINERS BUILT UP OF NITI SUPERELASTIC SHAPE-MEMORY ALLOYS

F. P. Amarante dos Santos* & Corneliu Cismasiu

Centro de Investigação em Estruturas e Construção - UNIC, Faculdade de Ciências e Tecnologia, Universidade Nova de Lisboa, Quinta da Torre, 2829-516 Caparica, Portugal

*Corresponding author. E-mail: fpas@fct.unl.pt

ABSTRACT

This paper analyses the seismic response of a viaduct equipped with a dual superelastic hinge restraining system. The influence of the superelastic restraining area on the structural behaviour of the viaduct is addressed through the analysis of the deck's displacements, velocities and accelerations, for several seismic events. The superelastic restraining system comprises two NiTi pre-strained elements, placed at the abutments of the viaduct. The study is based on a numeric implementation of a rate-dependent constitutive model for shape-memory alloys, calibrated with a set of experimental tensile tests.

INTRODUCTION

It is generally accepted nowadays that, for a modern transportation system to be reliable, the design process must ensure an acceptable earthquake risk for all bridge infrastructures. In the case of existing structures, unacceptable seismic safety conditions must be clearly identified and promptly corrected. Designers of bridge retrofit projects have to be able to understand the response of the structural system to potential earthquake ground motions and to design modifications aiming to change undesirable responses of the structure to the ones that satisfy the project performance criteria. Past earthquakes have demonstrated that the damage induced in bridges can assume a multitude of different forms, depending, among others, on factors like the ground motion itself, conditions depending on the building site, the adopted bridge structural solution and its specific detailing provisions. Unseating of the bridge superstructure at in-span hinges, or at simple supports, is one of the most severe forms of bridge seismic damage, leading to possible catastrophic consequences. In the case of simply supported bridges, unseating brings about the toppling of the spans from their supports, causing the structure to collapse. This type of failure is either due to shaking or to differential support movement associated with ground deformation. The problem of unseating is generally associated with inadequate seat lengths or restraint and it is enhanced by skewed, curved, or complex bridge configurations. The unseating mechanism of a multi-framed, simply supported bridge during an earthquake, associated with an in span hinge, is represented in Fig. 1.

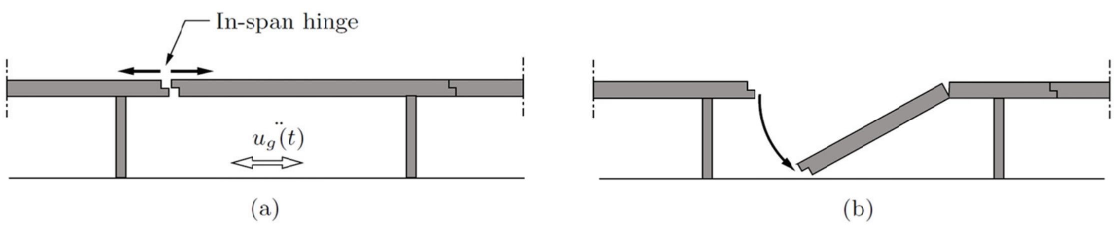

Figure 1: Unseating of bridge at in-span hinge during an earthquake.

In order to reduce the seismic response of bridge structures, they can be provided with special isolating devices called seismic links. According to Eurocode 8 [1], these connection devices may be responsible for the partial or full transmission of the design seismic action, provided that dynamic shock effects are mitigated and taken into account in the design. They are designed to ensure the structural integrity of the bridge and avoid unseating under extreme seismic displacements, while allowing the non-seismic displacements of the bridge to develop without transmitting significant loads. In order to avoid unseating, the code states that new bridges must be provided with appropriate overlap lengths between supporting and supported members at movable connections.

While these new design strategies aim to mitigate the potential unseating problems in new bridges, there are still many existing bridges susceptible to span unseating, due either to the lack of adequate seismic detailing, like the shorter seats usually associated with old constructions, either to potential stronger shaking than the one considered in the original design. These structures require seismic retrofitting in order to modify the seismic response of the bridge, controlling the deck displacements and preventing the unseating of spans. In the case of retrofitting existing bridges, connections implemented by seismic links may be used as an alternative to the provision of the minimum overlap length. Seismic links may also be used between adjacent sections of the deck, at intermediate separation joints, located within the spans. In this case, according to Eurocode 8 [1], the linkage elements may be designed for an action equal to 1.5 $g\ S\ M_d$, where g is the design ground acceleration on type A ground, S is the soil factor and M_d is the mass of the section of the deck linked to a pier or abutment, or the least of the masses of the two deck sections on either side of the intermediate separation joint.

The traditional approach for this type of restraining systems usually relies on the use of steel cables, which, if designed to remain elastic, lack the ability to dissipate energy and are responsible for the transmission of large seismic forces to other structural components. After yielding, these elements tend to accumulate plastic deformations in repeated loading cycles that can also result in unseating [2]. Several other devices have been presented in the past decades as unseating prevention devices for bridges, namely in the form of fluid-viscous dampers and metallic dampers [3]. Although these devices are able to dissipate energy, they lack the capacity for re-centering, which is a very important asset in order to control hinge opening in bridges during seismic actions. The installation of external hinge extenders prevents the supported section of the superstructure from dropping off from its support but has no effect on controlling the deck displacements, which may lead to structural damage in other important components. To overcome the limitations presented by these devices, and taking advantage of the recent advances in Material Sciences, an alternative solution for seismic retrofitting of structures has been proposed, based on the so called smart materials [2]. Among them the shape-memory alloys (SMAs), a unique class of metallic alloys, exhibit a peculiar thermo-mechanical property called superelasticity (SE). This property enables the material to withstand large cyclic deformations (up to 8%) without residual strains while developing a hysteretic loop, which translates into the ability of the material to dissipate energy. SMAs based seismic damping devices are aimed to concentrate energy dissipation in controlled locations by taking advantage of the superelastic effect. The high inherent damping exhibited by these alloys combined with repeatable re-centering capabilities and relatively high strength properties encouraged the research community to progressively introduce the SMAs in new technological applications related to energy dissipation in civil engineering structural design.

Several authors have studied the retrofit and rehabilitation of bridges using SMA restraining cables [2,4-7], confirming their efficacy when used as seismic links. Analytical models showed that the SMA restrainers reduce relative hinge displacements at the abutment much more effectively than conventional steel cable restrainers [5-7].

The main objective of this paper is to study the influence of the total cross-section of the SE restraining solution in the seismic response of a bridge. To perform this analysis, a numerical framework has been developed and a rate-dependent constitutive model has been implemented and calibrated with a set of experimental tensile tests.

CONSTITUTIVE MODEL

In a typical SMA constitutive model the mechanical law relates stress (σ) to strain (ε), temperature (T) and martensite fraction (ξ). Martensite fraction is an internal state variable that represents the extent of the transformation in the material and can be regarded as the fraction of the produced phase. The transformed phase fraction is considered to be in series with the elastic fraction of the response. Several approaches for the mathematical modeling of this elastic component exist in the literature [8]. Among them, the Voight model [9] used in the present paper contemplates two different crystallographic phases, austenite and martensite, not distinguishing between the twinned and the detwinned martensite. It considers a parallel distribution of austenite and martensite within the material and the corresponding Young's modulus is calculated by a rule of mixtures from the values of the pure austenite phase modulus EA, and the pure martensite phase modulus EM, yielding the following mechanical law,

$$\sigma = [\xi EM + (1 - \xi) EA] (\varepsilon - \varepsilon L) + \theta (T - T0) \tag{1}$$

where θ is the thermal coefficient of expansion, εL the maximum residual strain and $T0$ is the temperature at which the thermal strain is defined to be zero [10].

In order to complete the constitutive model, the mechanical law (1) is coupled with the transformation kinetic equations which describe the evolution of the martensite fraction with stress and temperature. Exponential kinetic relations, based on the Magee's transformation kinetics equations [11], are used in the present paper, yielding,

$$\xi AM = 1 - \exp [aM(Ms - T) + bM \sigma], \text{ with } \sigma > CM (T - Ms) \tag{2}$$

for the forward transformation, Ms being the temperature at which the transformation starts in the stress-free state, and

$$\xi MA = \exp [aA (As - T) + bA \sigma], \text{ with } \sigma \leq CA (T - As) \tag{3}$$

for the inverse transformation, where As is the temperature at which the transformation starts in the stress-free state. The temperatures at which the forward and inverse transformations end are defined as Mf and Af, respectively. The exponential law equations (2) and (3) are well known and widely used in the literature [12] once the material constants CM, CA, aM, bM, aA and bA are identified [13,14]. When quasi-static loading conditions are present, the heat exchanges between the SE material and its surrounding environment generates almost isothermic processes. However, as the rate of the dynamic loading increases the total amount of generated energy per time increases accordingly.

Since the dissipation capacity of the thermo-mechanical system is limited by the heat convection mechanism the generated and the dissipated energy become unbalanced for fast dynamic cycling causing changes in the specimen's temperature and the shape of its hysteretic loop. For a SMA constitutive model to conveniently apprehend this phenomenon it is necessary to couple an adequate heat balance equation together with the mechanical and kinetic transformation laws [12]. The heat transfer system consists of a cylindrical wire with circular cross section fixed at both extremities and surrounded by air at temperature Tf. There are internal energy sources within the wire deriving from the enthalpy of the martensitic transformations and internal friction, both occurring during a hysteretic superelastic cycle. Assuming the heat conduction through the wire's extremities to be negligible, the energy equation may be expressed [15] as,

$$- \rho\, c\, V\, dT / dt = h\, A (T - Tf) - qgen\, V \text{ with } T(0) = Tf \tag{4}$$

In the above equation ρ is the density of the material, c the specific heat, V the volume of the sample, A the interface surface and h the mean convection coefficient. The power generated per unit volume $qgen$ is defined [12] as,

$$qgen = cL\, \rho\, d\xi / dt + dW / dt \tag{5}$$

The first term is related to the martensitic fraction, assuming constant latent heat of transformation cL, and the second term to internal friction. In a complete tensile loading-unloading cycle the dissipated energy by internal friction corresponds to the total area enclosed by the hysteretic cycle. The total generated power during this cycle may therefore be computed by dividing the dissipated energy by the duration of the cycle.

ASSESSMENT OF THE CONSTITUTIVE MODEL

In order to assess its performances the model is used to simulate experimental superelastic hysteretic cycles obtained in classical uniaxial tensile tests. A Zwick/Roell Z050 testing machine was used to test a NiTi SE508 wire (*d* = 2.40 mm) with four different strain rates (0.008, 0.067, 0.250 and 0.333%/s). The tests were performed at room temperature (*Tf* = 20ºC) and the temperature of the SE wire is continuously monitored with a T-type thermocouple placed at the mid-section of the wire. The material properties used for the corresponding numerical simulations are presented in Table 1.

$E_A = 35000$ MPa	$E_M = 20000$ MPa	$M_f = -45°$ C
$M_s = -35°$ C	$A_s = -15°$ C	$A_f = -5°$ C
$C_M = 6.5$ MPaK^{-1}	$C_A = 6.5$ MPaK^{-1}	$e_L = 3.0\%$
$\rho = 6500$ kg m^{-3}	$c_L = 12914$ J kg^{-1}	$c = 500$ J kg^{-1}K^{-1}
$\overline{h} = 35$ W m^{-2} K^{-1}	$\theta = 0.55$ MPaK^{-1}	

Table 1: Parameters for the numerical simulation of the tensile tests.

The graphs in Fig. 2 show the simulated temperature time-history and the corresponding stress-strain diagrams for the quasi-static and dynamic situations against the experimental values. One can see that the implemented numerical model yields a set of very satisfying results, both for the temperature time-histories and the corresponding stress-strain diagrams. As the strain-rate of the dynamic loading increases from 0.008 to 0.333%/s, the amplitude of the temperature variation during the SE cycle increases in accordance with the experimental results. In what concerns the stress-strain diagrams for increasing strain-rates, the general shape of the hysteretic loops tends to be steeper and narrower in conformity with the trend observed in the experimental results.

SEISMIC SIMULATION OF NiTi SUPERELASTIC RESTRAINER CABLES IN A VIADUCT

The effect of a SMA-based passive control device on the seismic response of a railway viaduct is simulated next. The control device consists in two pre-strained NiTi superelastic wires working in phase opposition [16].

A common way to enhance the dissipation capacity of such devices is to pre-strain the SE wires [16-18]. The influence of the pre-strain is illustrated in Fig. 3, representing stress-strain diagrams resulting from a quasi-static harmonic cycle, yielding the full extent of the martensitic transformation in the wires.

The system with no pre-stress yields the stress-strain diagram indicated in Fig. 3(a), presenting the development of a full tension/compression SE hysteresis with an equivalent viscous damping of about 10%. When a 2% pre-strain is introduced in the wires the equivalent viscous damping increases to 23% as the hysteresis changes from two distinct SE areas to a single hysteretic curve, as illustrated in Fig. 3(b).

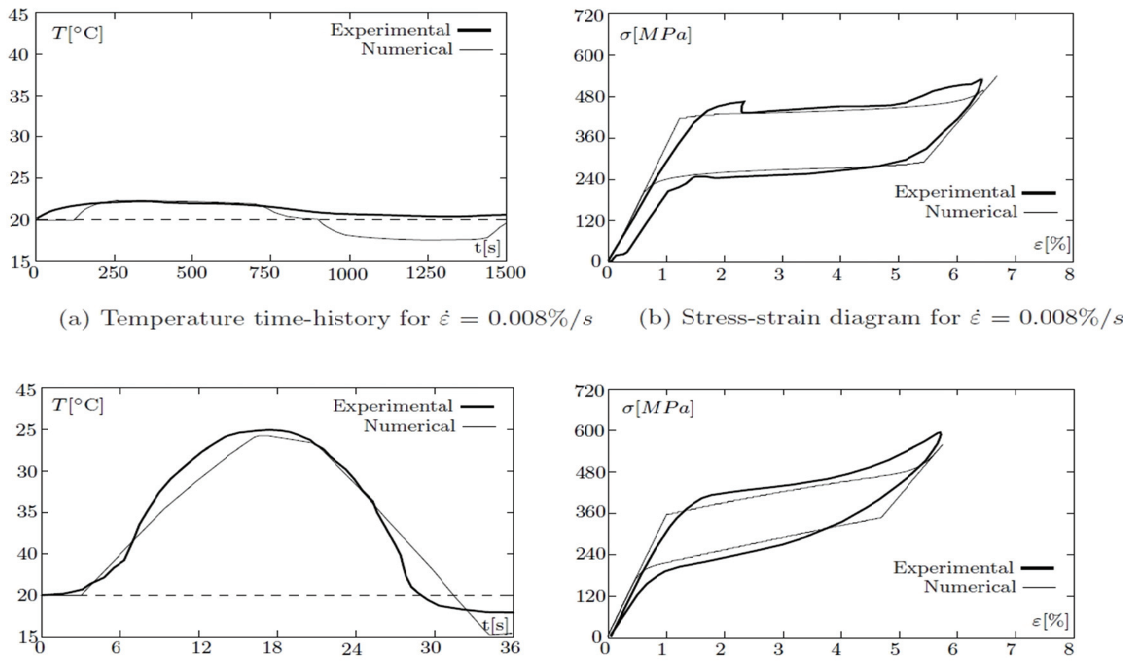

(a) Temperature time-history for $\dot{\varepsilon} = 0.008\%/s$ (b) Stress-strain diagram for $\dot{\varepsilon} = 0.008\%/s$

(c) Temperature time-history for $\dot{\varepsilon} = 0.333\%/s$ (d) Stress-strain diagram for $\dot{\varepsilon} = 0.333\%/s$

Figure 2: Numerical model vs. experimental data at temperature *Tf* = 20ºC, for increasing strain-rate.

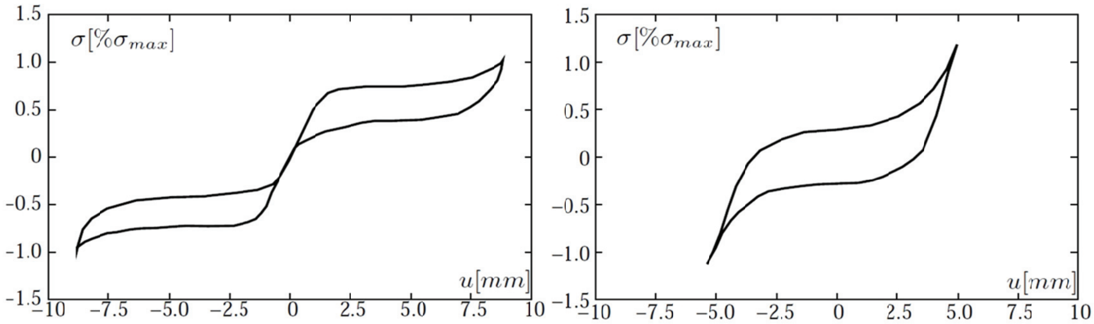

(a) Pre-strain = 0 (d) Pre-strain = 2.0%

Figure 3: Effect of the pre-strain in two SE wires working in phase opposition.

The structure used for the seismic simulation is the São Martinho railway viaduct [16]. This viaduct is a pre-stressed concrete railway viaduct with a total length between abutments of 852.0 m. It is built up of seven 113.6 m long independent segments and one segment of 56.8 m, adjacent to the south abutment. These segments are divided into 28.4 m spans and are structurally independent. The railway deck is a 13.0 m wide beam slab, comprising two 2.0 x 1.4 m main girders. The foundations are materialized by 1.2 m piles with an average length of about 30.0 m. The concrete piers are tubular and have an average height of 12.0 m. Each pier is supported by five piles.

A simplified numerical model of one of these segments was combined with a SE based passive seismic control device for the longitudinal analysis of the segment. The analysis was made assimilating it with a SDOF dynamic system with 4650 ton mass and stiffness of 355000 kN/m. Pre-strained NiTi SE restraining elements ($\varepsilon 0$ = 3.5%) were placed at the ends of the viaduct, one for each main girder, working in combination with the bearings. In order to clarify the effect of the SE elements in the dynamic behavior of the structure a parametric study considering a variation of the total SE restraining area up to an arbitrary value of A_{max} = 950 cm² was made. The structure of the viaduct is considered to behave elastically.

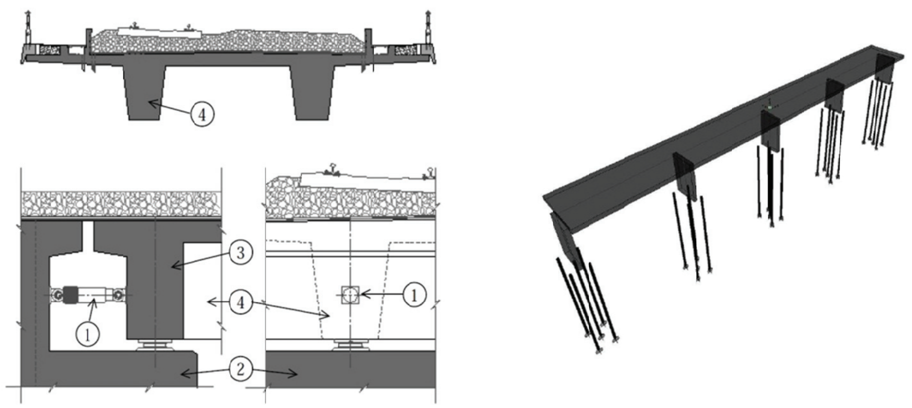

Legend: 1. SMA device, 2. Abutment, 3. Transverse girder, 4. Main girder

Figure 4: São Martinho railway viaduct: Mid-span cross section, SMA passive control device location and finite element model.

The seismic action is introduced in the system by means of artificially generated accelerograms using the design acceleration power spectral density functions. Given the random nature of these generated accelerograms the viaduct is submitted to six different series represented in Fig. 5. If the minimum stress to induce the martensitic transformation in the SE elements is not attained during the seismic events, the elements behave like additional linear elastic materials, increasing the system's stiffness. The displacement amplitude of the structure is hence decreased, but at the cost of increasing the system's natural frequency and leading to an undesirable increase in structural accelerations [19]. The introduction of a pre-strain in the SE elements facilitates the beginning of the martensitic transformation and the corresponding hysteretic energy dissipation.

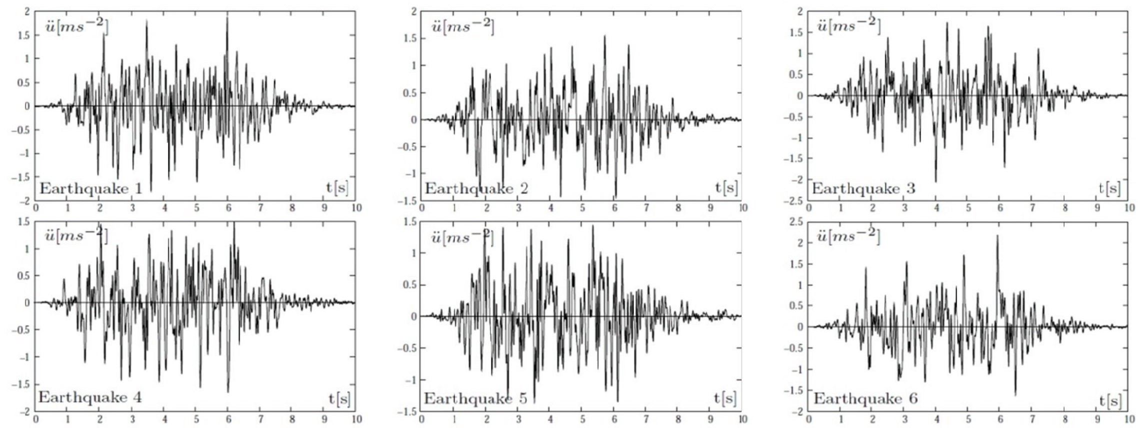

Figure 5: Generated accelerograms.

With illustrative purpose the seismic responses of the viaduct for a restraining area of 40 cm^2 (5% A_{max}), in what respect the longitudinal displacement, velocity and acceleration time-histories and the corresponding force-displacement diagram in the SE restraining elements is presented in Fig. 6 for earthquake 1.

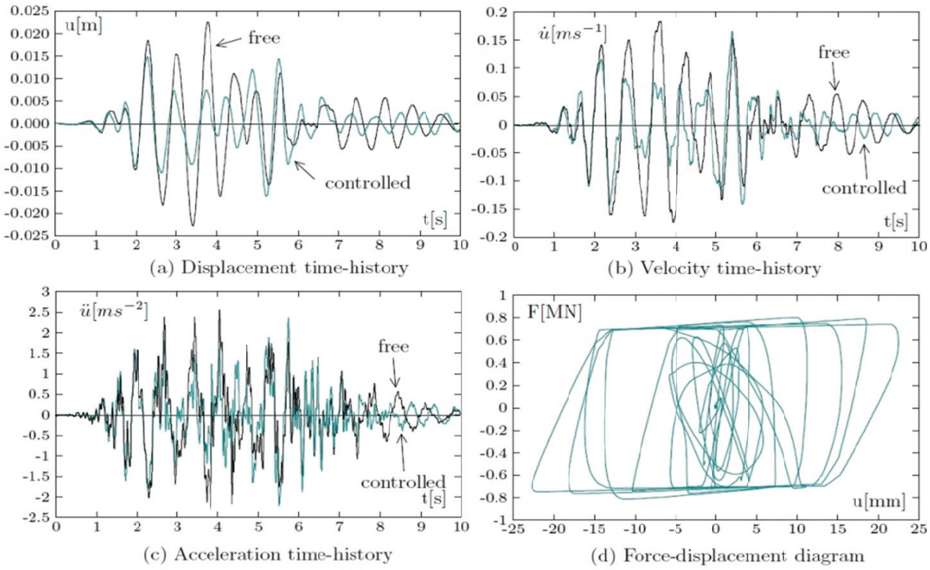

Figure 6: Seismic response of the viaduct for a restraining area of 5% A_{max}.

One can see that there is an important reduction of the amplitude of the longitudinal displacement of the viaduct as well as of the corresponding velocity and acceleration. Due to the presence of a loading plateau in the SE hysteresis, related to the forward martensitic transformation, the total SE force in the restraining elements is conveniently bounded, limiting the force which is transmitted to the structure during the seismic event.

The influence of the area of the SE restraining elements in the seismic response of the viaduct is translated in the curves presented in Fig. 7, obtained using the average value of the maximum response resulting from the set of six accelerograms. According to the obtained results one can see that for increasing areas of the SE restraining elements the mean longitudinal displacement and velocity of the deck decrease monotonously. In what concerns the mean longitudinal acceleration of the deck its value tends to decrease until it reaches a minimum threshold, which corresponds to about 20% of the maximum SE restraining area before starting to increase once more.

The shaded regions of the graphs represent the most effective SE restraining solutions for the passive control of the viaduct, where its seismic response in terms of displacements and velocity suffers the most important reduction of up to 40 and 50% respectively and the acceleration decreases up to 10%. Therefore one can say that with a SE restraining area of 20% of the maximum area considered one obtains an optimized solution for the seismic passive mitigation. If one increases the SE restraining area, one can further reduce the seismic response in terms of displacements and velocities, but at the cost of increasing the acceleration values. Regarding the acceleration time-history, one can say that, for a given seismic action, as long as the total area of the SE restraining elements enables a considerable extent of the martensitic transformation, the dissipation capacity of the system increases with the SE restraining area, decreasing the longitudinal acceleration of the deck. As the stiffness of the SE restraining elements continues to increase above a certain threshold, the extent of the martensitic transformation starts to decrease, the acceleration increases and the natural frequency of the viaduct is shifted to higher values.

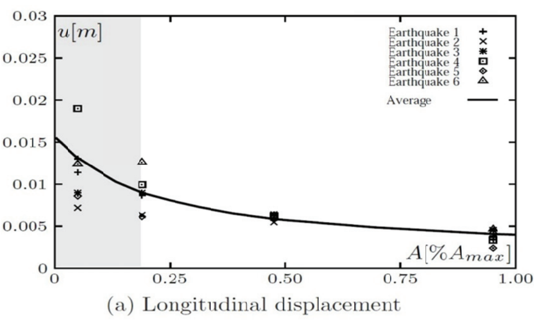

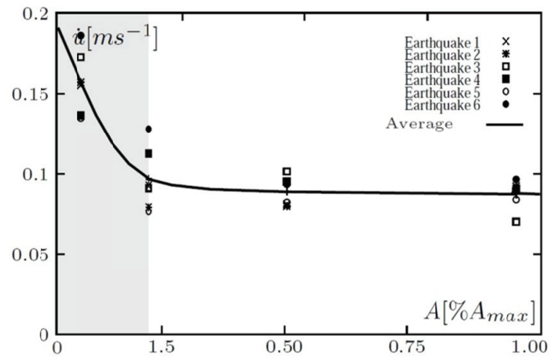

(b) Longitudinal velocity

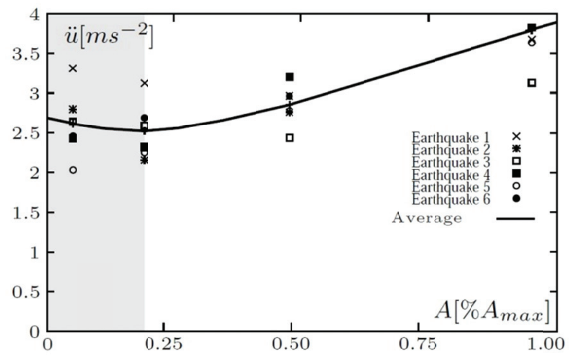

(c) Longitudinal acceleration

Figure 7: Longitudinal displacement, velocity and acceleration of the deck in function of the SE restraining area.

CONCLUSIONS

This article studies the retrofitting of a viaduct in order to modify its seismic response in terms of longitudinal deck displacement, velocity and acceleration, while preventing span unseating. The retrofitting solution is based on the use of SE SMA seismic links, featuring high dissipation and high re-centering capabilities. The analysis is based on the numeric simulation of the viaduct's longitudinal behavior together with SE restoring elements when subjected to a series of artificially generated accelerograms. The constitutive model describing the complex SE thermo-mechanical behavior of the seismic links is also presented and validated. In order to enhance the dissipation capacity of the SE restraining solution two pre-strained restoring elements working in phase opposition were used, which yield an equivalent viscous damping of about 23%. A parametric study concerning the SE area of the restraining system allows the optimal compromise between the cross-sectional area of the SE restraining elements and the seismic mitigation capacity of the system regarding the longitudinal deck displacement, velocity and acceleration to be identified. For the case studied, this optimal SE restraining window is bounded by a SE restraining area of about 190 cm², where the longitudinal displacement and velocity of the system are significantly reduced, together with a reduction of the corresponding acceleration field.

ACKNOWLEDGEMENTS

This work is part of the research developed in the Department of Civil Engineering, Faculdade de Ciências e Tecnologia, supported by contract SFRH/BD/37653/2007 with Fundação para a Ciência e Tecnologia.

REFERENCES

[1] CEN. Eurocode 8 - Design of structures for earthquake resistance - Part 2: Bridges. Ref. No. EN 1998-2:2005: E , 2005.

[2] J. E. Padgett, R. DesRoches, and R. Ehlinger. Experimental response modification of a four-span bridge retrofit with shape memory alloys. Structural Control and Health Monitoring , 2009.

[3] R. DesRoches. Application of shape memory alloys in seismic rehabilitation of bridges. Technical Report NCHRP-91, IDEA Program, Transportation Research Board, National Research Council, 2005.

[4] R. Johnson, J. E. Padgett, M. E. Maragakis, R. DesRoches, and M. S. Saiidi. Large scale testing of Nitinol shape-memory alloy devices for retrofitting of bridges. Smart Materials and Structures 17(3), 2008.

[5] B. Andrawes and R. DesRoches. Comparison Between Shape Memory Alloy Restrainers and other Bridge Retrofit Devices. ASCE Journal of Bridge Engineering , 12(6):700–709, 2007.

[6] R. DesRoches and M. Delemont. Seismic retrofit of simply supported bridges using shape memory alloys. Engineering Structures , 24:325–332, 2002.

[7] R. DesRoches, T. Pfeifer, R. T. Leon, and T. Lam. Full-Scale Tests of Seismic Cable Restrainer Retro?ts for Simply Supported Bridges. Journal of Bridge Engineering , 8(4):191–198, 2003.

[8] L. C. Brinson and M. S. Huang. Simplifications and Comparisons of Shape Memory Alloy Constitutive Models. Journal of Intelligent Material Systems and Structures , 7:108–114, 1996.

[9] C. Liang and C. A. Rogers. One-Dimensional Thermomechanical Constitutive Relations for Shape-Memory Materials. Journal of Intelligent Systems and Structures , 1:207–234, 1990.

[10] S. De la Flor and F. F. Urbina. Constitutive model of shape memory alloys: Theoretical formulation and experimental validation. Materials Science and Engineering A , 427(1-2):112–122, 2006.

[11] C. L. Magee. Nucleation of martensite. In ASM, editor, Phase Transformations , pages 115–156. 1970.

[12] A. Vitiello, G. Giorleo, and R. E. Morace. Analysis of thermomechanical behaviour of Nitinol wires with high strain rates. Smart Materials and Structures , 14:215–221, 2005.

[13] K. Tanaka, S. Kobayashi, and Y. Sato. Thermomechanics of transformation pseudoelasticity and shape memory effect in alloys. International Journal of Plasticity , 2:59–72, 1986.

[14] K. Tanaka, F. Nishimura, T. Hayashi, H. Tobushi, and C. Lexcellent. Phenomenological analysis on subloops and cyclic behavior in shape memory alloys under mechanical and/or thermal loads. Mechanics of Materials , 19:281–292, 1995.

[15] F. P. Incropera and D. P. DeWitt. Fundamentals of heat and mass transfer . John Wiley and Sons, Inc., 6th edition, 2006.

[16] C. Cismasiu and F. P. A Santos. Numerical simulation of superelastic shape memory alloys subjected to dynamic loads. Smart Materials and Structures , 17(2):25–36, 2008.

[17] M. Dolce, D. Cardone, and R. Marnetto. Implementation and testing of passive control devices based on shape memory alloys. Earthquake Engineering and Structural Dynamics , (29):945–968, 2000.

[18] Y. Zhang and S. Zu. A shape memory alloy-based reusable hysteretic damper for seismic hazard mitigation. Smart Materials and Structures , 16:1603–1623, 2007.

[19] S. Seelecke, O. Heintze, and A. Masuda. Simulation of earthquake-induced structural vibrations in systems with SMA damping elements. SPIE Smart Structures and Materials , 4697, 2002.

ACTIVE CONTROL OF FLOW-INDUCED ACOUSTIC RESONANCE INSIDE DOWNSTREAM CAVITIES THROUGH SURFACE PERTURBATION

L. Cheng, Z. B Lu, D. Halim,

Department of Mechanical Engineering, The Hong Kong Polytechnic University, Kowloon, Hong Kong

ABSTRACT

The control of the vortex-induced acoustic resonance inside a downstream cavity was experimentally investigated through actively controlled surface perturbation. The technique made use of piezo-ceramic actuators embedded on the surface of an upstream test model in a cross flow to generate a controllable motion to alter the vortex formation as well as the subsequent acoustic resonance. Experiments were conducted using various configurations using both open and closed-loop control. It was observed that, the flow-induced acoustic resonance could be effectively reduced after applying surface perturbation technique. This was caused not only from an impairment of the vortex shedding strength, but also from a shift in the shedding frequency resulting from the control action. The vortex strength abatement mechanism was discussed and the estimation of the frequency shift phenomenon as well as its effect on the impairment of acoustic resonance was experimentally assessed.

INTRODUCTION

Bluff bodies are widely utilized in various engineering applications, such as in the branches of aeronautics, mechanical, chemical and civil engineering. Downstream a bluff body placed in a cross flow, vortices can be generated, creating alternating lift and drag forces on the rear surface of the body [1]. This phenomenon, referred to as vortex shedding, can lead to potentially severe bluff body vibration and excessive acoustic noise at the same time. The problem is accentuated when a downstream cavity exists and the shedding frequency coincides with the natural frequency of the cavity [2,3]. This phenomenon is generally referred to as flow-induced acoustic resonance which can be classified as a type of flow-structure-sound (FSS) interaction problems. Because of the importance of FSS problems to a large variety of engineering applications, there has been a significant research interest in attempting to study these problems in the last few decades. Flow-induced acoustic resonance can be controlled by using passive or active control schemes [4]. The passive control schemes do not use an external energy input, and it may include surface modifications with roughness, splitter plate and small secondary control cylinder [5-7]. The active control scheme, on the other hand, injects external energy into the system to modifiy its characteristics using appropriate actuators.

The active control scheme can further be classified as open- and closed-loop control depending on whether feedback signals are used in the control process. Open-loop control includes rotary, streamwise, transverse oscillations of a bluff body and inflow oscillation [8-11]. However, the open-loop control performance is limited since the control actuation does not directly correspond to the system response. To get around this problem, active closed-loop control can be used by continuously adjusting the control actuation based on the system response, monitored via feedback signals acquired by sensors. Berger [12] introduced the single-sensor feedback control by actuating a bimorph cylinder with signals from a hot-wire sensor located in the wake. Huang and Weaver [13] utilized the fluctuating acoustic pressure inside the cavity as feedback signals, to drive the loudspeakers at the entrance of the tunnel. Cattafesta *et al*. [14-16] used an oscillating flap hinged near a cavity leading edge to disturb the shear layer separation, using feedback signals taken from the fluctuating acoustic pressure measured by a microphone within the cavity. These works, however, are mainly focused on controlling individual element such as the flow field, structural vibration or acoustic noise. Because of the coupling nature of vortex-vibration-noise system, it is reasonable to think that simultaneous control targeting all these elements can be more effective.

Based on this consideration, a surface perturbation technique was proposed by Cheng *et al.* [17], aiming at the simultaneous control of both flow field and structural vibration. The technique makes use of curved piezo-ceramic actuators, embedded underneath the structural surface, to generate a controllable transverse motion on a structural surface for altering fluid-structure interactions.

Using the THUNDER (THin layer composite UNimorph Driver and sEnsoR) actuators [18], the effectiveness of this control technique was experimentally assessed through a series of investigations in Zhang *et al.* [19-22]. The works demonstrated that the actively controlled perturbation could successfully alter the interactions by synchronizing the motion of the bluff body's upper surface and vortex shedding, leading to the simultaneous attenuation of both vortex shedding strength and the vortex-induced structural vibration. Using an open-loop control scheme with a similar arrangement of piezoelectric actuators, Zhang *et al* [23] further investigated the control of the flow-induced acoustic resonance in a duct system comprising an upstream structure as a vortex generator and a downstream acoustic cavity.

The work focused on controlling the acoustic resonance when the vortex shedding frequency coincided with the first acoustic resonance of downstream cavities. Experimental results demonstrated a 8.2dB reduction in the sound pressure level inside the resonant cavity due to the piezo-driven actuation. Apart from the apparent control performance, however, the underlying physical mechanism behind the control action still remained unknown. The sound reduction was interpreted as a direct consequence of the vortex strength impairment, the reason behind which, however, could not be explained either.

The present work reports an experimental study on the control of flow-induced acoustic resonance based on the surface perturbation technique. Major objectives are fivefold: 1) to provide a comprehensive assessment on the efficiency of the surface perturbation technique using an improved actuator configuration in the open-loop scheme. 2) to establish a general closed-loop control strategy using the surface perturbation technique. Due to the practical vibration characteristic limitation of the THUNDER actuators, the feedback signals used were dealt with a special signal processing which was based on the down-sampling theory; 3) to assess the effectiveness of the closed-loop control by comparing with the open-loop case. Closed-loop control test results provide additional evidence towards a better understanding of the underlying physics. 4) to provide experimental evidences for further explanation on the control mechanism of the surface perturbation technique in attenuating flow-induced sound. 5) to investigate the control mechanism behind the additional sound reduction in the cavity, as well as to formulate a mathematical description for predicting the perturbation-induced shedding frequency shift.

EXPERIMENTAL CONDITION

A closed circuit acoustic wind tunnel, with an 1820-mm-long square test section of 100mm x 100mm, was used to conduct the experiments as depicted in Figure 1. A parabolic contraction at the inlet was used to improve the uniformity of the flow velocity profile, and reduce the boundary layer thickness. A flat-walled diffuser at the downstream of the working section, with a half angle of 14°, was used to increase pressure recovery. The maximum flow velocity was 50m/s with a turbulence intensity of less than 0.1% in the upstream section. Low background noise was achieved in this wind tunnel since noise of the motor and fan was mostly absorbed by acoustic duct linings. A rigid thick plate with an angle of attack of zero, called the 'test model', was installed at 370mm downstream of the exit plane of tunnel contraction in the flow duct. The two ends of the test model were rigidly fixed on the walls of the duct and served as vortex generator.

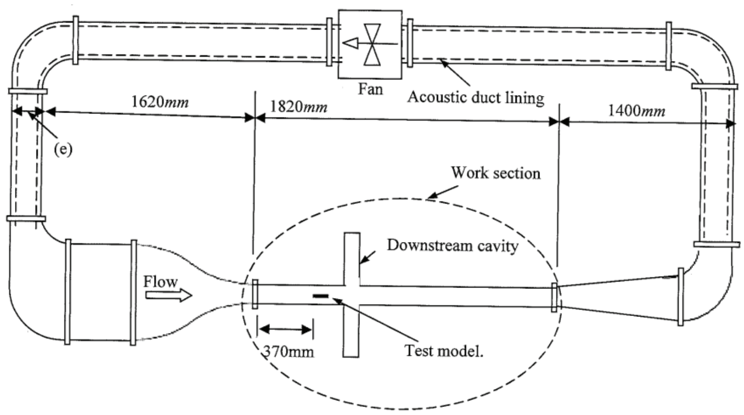

Figure 1: Sketch of the wind tunnel system.

At the downstream of the duct, two identical cavities with square cross sections were installed and they were symmetrical to the stream wise flow line. The test model, cavity dimension, and flow speed were set so that acoustic resonance took place inside the cavities at the vortex shedding frequency. Details of the test model are shown in Figure 2. It had a semi-circular leading edge and a height of h = 11mm and a width of w = 23mm. Its dimension w/h was within the range that ensured that only one vortex separated from the leading edge of the plate might develop along the plate at any instant [24]. Two curved THUNDER piezo-ceramic actuators, with a length of 63mm and a width of 14mm, were embedded in a slot of 16mm wide and 7mm deep on the top side of vortex generator and 1.0mm from the test model trailing edge. The actuators were installed in a cantilever manner to create a maximum perturbation displacement in the transverse y-direction. A thin plastic plate of 1.2mm thick, called a 'vibration plate', was mounted flush with the upper surface of the plate, and connected with the cantilevered end of the THUNDER actuators by using a double-sided tape. The vibration plate driven by the actuators would oscillate to create a span-wise uniform transverse vibration along the y-direction of the test model, which were confirmed by the measurement of velocity over the plate using a laser vibrometer. Figure 3 shows the entire test configuration together with the measurement system.

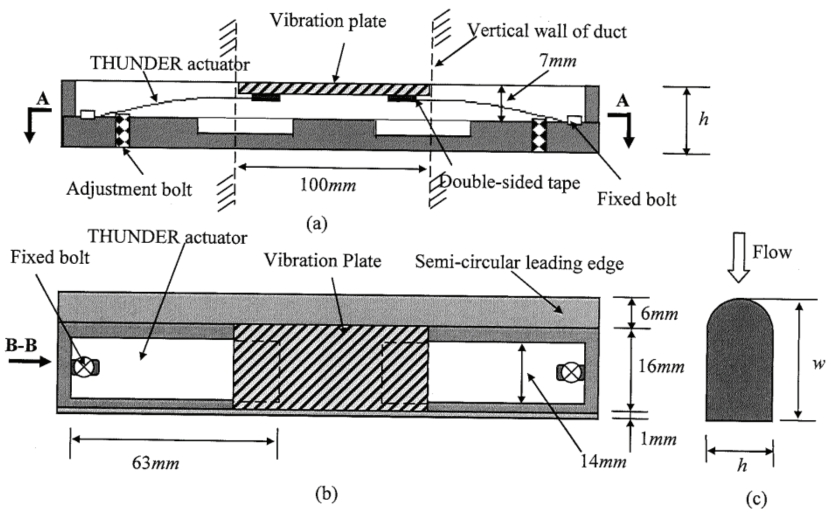

Figure 2: The test model in detail (a) Installation; (b) Top view A-A; (c) Side view B-B.

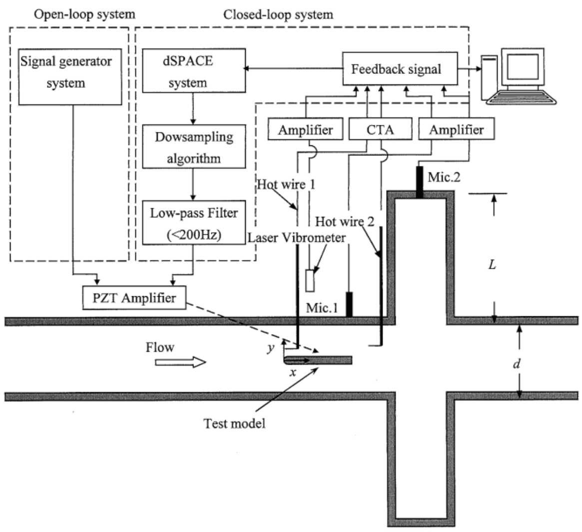

Figure 3: The experimental setup, control system and measurement system.

The depth (L) and width (B) of the two side cavities were chosen to be 487mm and 70mm, respectively. Based on the test configuration, the first acoustic resonance frequency of the cavity (f'_a) was estimated as $f'_a=c/(2(2L+d))\approx160$Hz [25], where c was the sound speed and d was the height of the duct. The corresponding critical flow velocity $U_{cr}=f_sh/S_t$ at resonance, when shedding frequency $f_s=f'_a$, was estimated to be about 8.2 *m/s*, using a Strouhal number S_t of 0.22, as suggested by Welsh *et al*. [26] for similar w/h ratios. The flow velocity was not very stable during the measurement, therefore, the vortex shedding frequency could only be adjusted approximately to f'_a. To generate the control perturbation, two cantilever actuators were simultaneously activated by a sinusoidal signal with controllable frequency, using the dSPACE rapid control prototyping system, and then amplified by a dual-channel PZT amplifier (Trek PZD 700), as shown in Figure 3. The actuators were simultaneously activated in two different ways: 1) by a sinusoidal signal at a tunable frequency to form an open-loop control scheme; 2) by feedback signals acquired from system response to form a closed-loop control scheme. The acoustic pressures were measured by two 1/2" condenser microphones (B&K 4189).

Microphone 1, referred to as Mic.1 hereafter, was flush-mounted on the top wall of the duct at x=23mm. Another microphone, Mic.2, was flush-mounted at the center of the top side-wall of the cavity. Two sets of 5 μm tungsten single hot wire were deployed to measure the fluctuating flow velocity at various positions around the test model. Hot wire 1 was fixed at the leading edge of test model at x=0mm and y=11mm, while hot wire 2 could be located at any positions around the test model depending on the requirement of the measurement. A Polytec Series 3000 Dual Beam laser vibrometer was also used to measure the perturbation displacement produced by actuators. All measurement signals were recorded for about 11*s* using a personal computer through a 12-bit A/D board at a sampling frequency of 5890Hz per channel. The closed-loop control process is described in Figure 3. In principle, the control can utilize any feedback signals acquired from the system, which may be from the hot wire 1, hot wire 2, Mic.1 or Mic.2. The feedback signal is then adjusted using the developed down-sampling algorithm via dSPACE system, before being applied to the PZT amplifier. The down-sampling theory used for control is detailed in the closed-loop section.

OPEN-LOOP CONTROL USING THE SURFACE PERTURBATION

The open-loop control using the developed surface perturbation configuration was investigated first in this work. Open-loop control experiments were carried out at $U_\infty = 8.2 m/s$ ($\mathrm{Re} = 5980$) and the control performance was evaluated in the sound field and flow field simultaneously. The control frequency f_p and control voltage V_p of the controller were first determined. It was observed that the best performance was obtained when f_p=30Hz with the highest permissible voltage of V_p=160V. Figure 4(a)-4(d) shows the sound pressure variation at the two microphone positions in time domain before and after control. All time-domain signals were filtered by a 5Hz-band-pass filter around the shedding frequency. It can be seen that, upon the control deployment, the sound pressure both in the duct and inside the cavity underwent significant reductions in the time domain. Noticing the difference in scale, the acoustic pressure was far more intense inside the cavity than that in the duct, due to the acoustic resonance effect. The reduction level inside the cavity after the control was also higher than that in the duct. For further observation in the frequency domain, the spectra of the signals were obtained using the Fast Fourier Transform with a frequency resolution of 0.1Hz.

The fine resolution was needed for an accurate determination of the locations as well as the values of the resonance peak corresponding to the shedding frequency. From the results shown in Figure5(a) and 5(b), upon the control deployment, the sound pressure level at Mic.1 decreased from 80.7dB to 64.8dB (a reduction of 15.9dB) at the shedding frequency as shown in Figure5(a). Meanwhile, Mic.2 recorded a decrease from 96.7dB to 76.0dB (a reduction of 20.7*dB*, as shown in Figure 5(b)), which was 4.8dB larger than the reduction measured by Mic.1. Meanwhile, higher order harmonics of the resonance frequency also experienced reduction to different extents after control. Based on the higher reduction of the acoustic resonance inside the cavity compared to that in the duct, one can surmise that, in additional to the reduction in the vortex strength which serves as the excitation of the acoustic field, there should be other important physical phenomena involved during the control process.

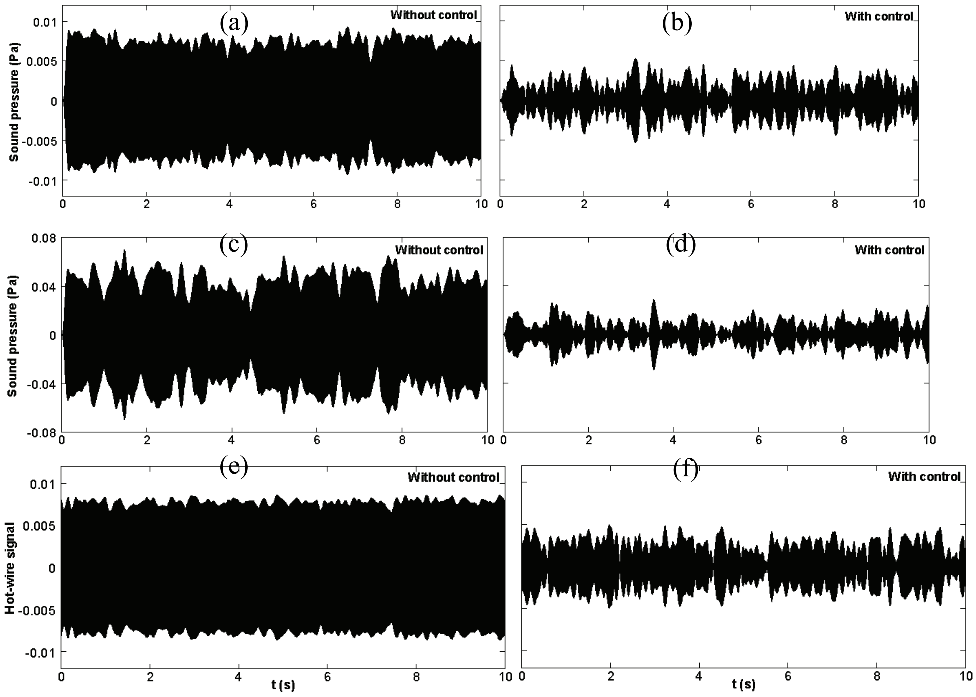

Figure 4: Time-domain results for the open-loop control performance in sound field; the signals were filtered by a 5Hz band-pass filter. The hot wire 2 was located at x = 34 mm and y =8.25 mm. (a) Without control: measured in the duct; (b) With control: measured in the duct; (c) Without control: measured inside the cavity; (d) With control: measured inside the cavity; (e) Without control: measured by hot wire 2; (f) with control: measured by hot wire 2.

A careful examination of the dominant peak revealed that, in the present case, the shedding frequency was shifted from 161.1Hz to 158.2Hz. This frequency shift phenomenon, albeit not very obvious, as well as its impact on the acoustic resonance inside the cavity, will be investigated further in the later section. Corresponding changes in the flow field, measured by hot-wire at x = 34mm and y=8.25mm, were examined in time domain (Figure 4(e) and 4(f)) and in frequency domain (Figure5(c)), respectively. It can be seen that control has also successfully reduced the vortex strength as evidenced by a significant reduction of the hot-wire signal in time domain, and the corresponding reduction in power spectral density *Eu* at the shedding frequency. In fact, *Eu* decreased from 4.1*e*-3 to 6.3*e*-4, corresponding to a reduction of about 85%.

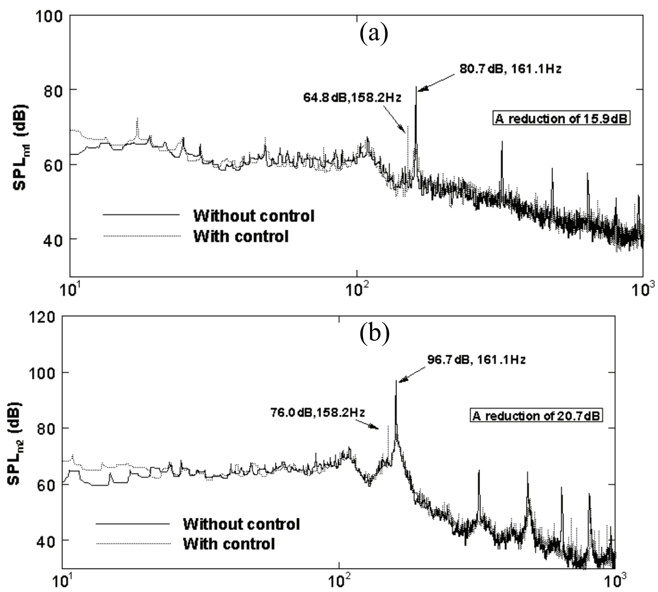

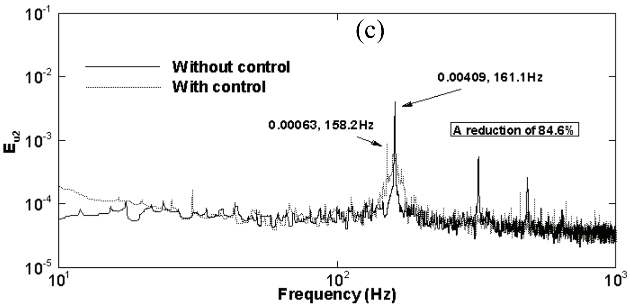

Figure 5: Control performance of open-loop control in the sound field and flow field. The hot wire 2 was located at x = 34 mm and y =8.25 mm. (a) SPL measured by Mic.1; (b) SPL measured by Mic.2; (c) Eu measured by hot wire 2.

CLOSED-LOOP CONTROL USING THE SURFACE PERTURBATION

Next, closed-loop control experiments were undertaken using the same surface perturbation configuration. In standard closed-loop control, a mainly-tonal feedback signal can be amplified by a control gain, resulting in a closed-loop control actuation dominated by the primary tone of the feedback signal. However, in the current experimental set-up utilizing THUNDER actuators, there was a main difficulty in directly implementing such a control configuration due to unique vibration response characteristic of THUNDER actuators. To illustrate this, the vibration characteristics of the test model, with embedded THUNDER actuators at a control voltage of 160V, were measured by using a laser vibrometer at varying control frequencies as shown in Figure 6.

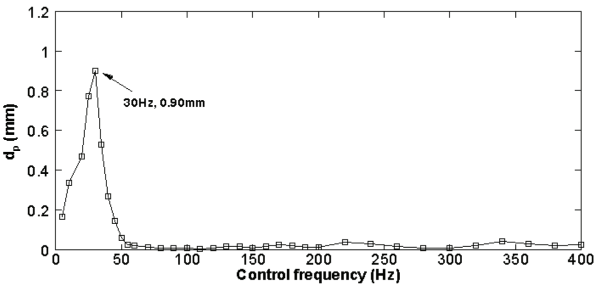

Figure 6: Vibration characteristics of the test model at various control frequencies. The control voltage was set to 160 V.

It was observed that the test model's frequency response peaked at around 30Hz, and rapidly decreased in magnitude as the control frequency increased. This also explains why the optimum excitation frequency for open-loop control was also 30Hz. The displacement of control actuation of the test model was measured to be only 0.016mm at the vortex shedding frequency of 160Hz, compared to the maximum displacement of 0.900mm at approximately 30Hz. Such a small actuation of only 1.8% of the test model's maximum capability would be insufficient for achieving a satisfactory control performance.

Therefore, to avoid such a control actuation problem, a down-sampling control method was proposed to bring down the frequency of the control actuation closer to the optimal operating frequency of test model at approximately 30Hz. Consider a feedback signal acquired from a sensor, containing information about the vortex shedding process. A typical Fourier spectrum of the vortex shedding system $U_0(f)$ with its dominant response at and around the vortex shedding frequency $f_{source}=f_s$ is shown in Figure 7. The spectrum is symmetric about zero frequency because the feedback signal is real-valued. Such a typical spectrum contains two dominant negative- and positive-frequency narrow-band spectrum around the negative and positive vortex shedding frequencies, each with the frequency bandwidth of BF. In this case, the frequency bandwidth for both narrow-band spectra is $f\in[-f_{source}-BF/2,-f_{source}+BF/2] \cup [f_{source}-BF/2,\ f_{source}+BF/2]$. These narrow-band spectra contain most of the spectrum energy associated with the vortex shedding and flow-induced acoustic resonance processes. Thus, it is imperative that the down-sampling method should focus on shifting these narrow-band spectra to lower frequencies with minimal distortion so effective control can be implemented to the system.

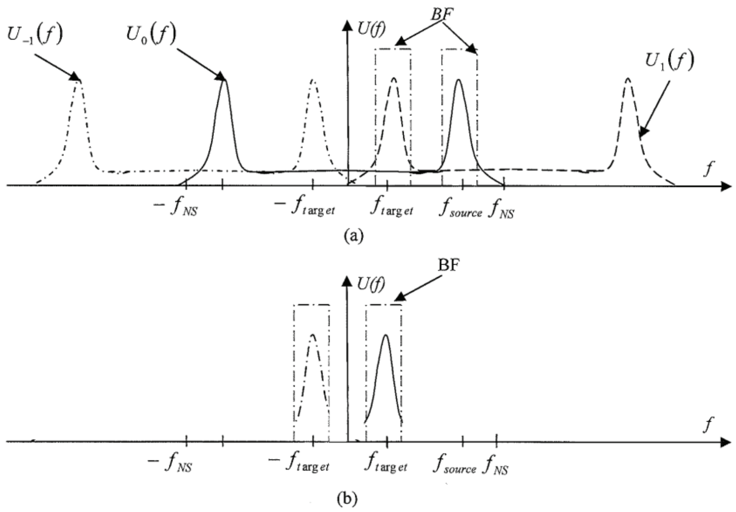

Figure 7: The schematic of the down-sampling process. (a) Original spectrum $U_0(f)$ and image spectra $U_{-1}(f)$ and $U_1(f)$; (b) Final spectra after down-sampling process.

As a consequence of sampling process, image spectrum are generated from the original spectrum shifted by integer multiples of the sampling frequency f_{NS} [27]. In a standard sampling process according to the Nyquist-Shannon sampling theorem [28], f_{NS} needs to be at least greater than twice the highest frequency of the band-limited continuous signal. This is to avoid the aliasing where the reconstructed sampled signal differs from the original continuous signal. However, the interest in this work is to generate the image narrow-band spectrum at low frequencies so that the reconstructed signal can be used as a feedback signal to drive the THUNDER actuator at its optimal operating frequency. To achieve this, a down-sampling method is utilized, using a sampling frequency lower than that recommended by the Nyquist-Shannon sampling theorem. Let spectrum $U_n(f)$, with subscript n being a non-zero integer number, to be the image spectrum associated with n multiples of f_{NS}. As shown in Figure 7, $U_1(f)$ is the image spectrum associated with $n\times f_{NS}(n=1)$ in the positive f axis, while U-1(f) is the image spectrum associated with $n\times f_{NS}(n=-1)$ in the negative f axis. To simplify the illustration, only spectrum $U_0(f)$, $U_1(f)$ and $U_{-1}(f)$ and are shown in the figure, excluding spectra with higher integer multiples of f_{NS}. The task now is how to choose an appropriate sampling frequency such that the peak of the narrow-band spectrum at the vortex shedding frequency f_{source} can be shifted to the target frequency f_{target} which is the THUNDER actuators' optimal operating frequency. Considering the original spectrum $U_0(f)$ and its positive-frequency image spectrum $U_1(f)$ in Figure 7, the target frequency can be related to the vortex shedding and down-sampling frequencies as follows:

$$f_{target} = f_{NS} - f_{source} \tag{1}$$

The significance of Eq. (1) is that since f_{source} can be evaluated based on the observation of vortex shedding process, one can choose a proper down-sampling frequency f_{NS} correspondingly to shift the narrow-band spectrum to a lower target frequency. As the result, two low-frequency narrow-band image spectra centered at $-f_{target}$ and f_{target} were generated as depicted in Figure 7. However, although the narrow-band image spectra have been shifted to lower frequencies, a problem still needs to be resolved. Due to the down-sampling process, overlapping image spectra associated with integer multiples of the sampling frequency f_{NS}, can in fact distort the overall spectrum, leading to a distorted reconstructed signal with multiple tonal components. To avoid such a distortion, a band-pass filter with the pass-band frequency of $f\in[f_{target}-BF/2, f_{target}+BF/2]$ is utilized to reject the off-bandwidth spectrum contributions as shown in Figure 7. This way, the narrow-band image spectrum located at and nearby the target frequency will be the only primary spectrum to be reconstructed.

Furthermore, although multiple narrow-band spectrum were also generated at integer multiples of down-sampling frequency, their spectrum contributions within the pass-band frequency BF, centered at f_{target}, are minimal because of their narrow-band spectrum characteristics. The down-sampled image spectrum can then be reconstructed to obtain the low-frequency continuous signal to be used for closed-loop control using the test model.

Based on the developed down-sampling method, a real-time closed-loop control experiment was performed. The closed-loop control was aimed to impair the vortex shedding process, whose shedding frequency was at approximately 160 Hz, by using the surface perturbation of the test model. The down-sampling frequency f_{NS} needed to be chosen first, considering the target frequency of 30 Hz, which was the optimal operating frequency of test model. For the simplicity of down-sampling implementation, f_{NS} was chosen to be an integer multiple of the original sampling frequency of 5890 Hz. Based on these control criteria, f_{NS} was determined to be 190Hz from Eq. (1). A real-time down-sampling control system was then implemented via dSPACE/Simulink system as shown in Figure 8.

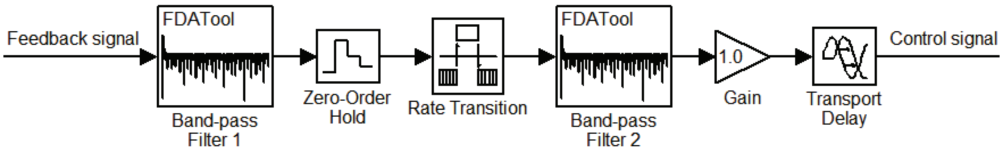

Figure 8: The down-sampling algorithm for closed-loop control.

The control modules consisted of the followings: (1) A band-pass filter with a pass-band frequency from 150 Hz to 170 Hz, called 'Band-pass filter 1', was used to capture components of feedback signal that contained most of the vortex shedding energy. (2) A Zero-Order Hold (ZOH) module was then used to down-sample the feedback signal from 5890Hz to 190Hz by holding the signal value fixed over a multiple-sample interval at a time step of $\Delta t = 0.00526\,s$, corresponding to the down-sampling frequency f_{NS} of 190Hz. (3) A Rate Transition module was used to update the sampling time step from the original $\Delta t = 0.00017\,s$ to the down-sampled time step of $\Delta t = 0.00526\,s$. (4) A narrow band-pass filter with a pass-band frequency from 29Hz to 31Hz , called 'Band-pass filter 2', was utilized to reject the off-bandwidth image spectra. (5) Finally, the Gain and Transport Delay modules were respectively used to adjust the magnitude A and phase delay $\emptyset$ of the down-sampled signal for closed-loop control.

With the proposed closed-loop control method, further experiments were performed to investigate the impact of closed-loop control to the flow and sound fields. Direct feedback control was implemented with 2 tunable primary control parameters, the magnitude A and phase delay $\emptyset$ relative to the down-sampled signal. The parameters could be systematically adjusted for control performance analysis and the identification of optimal control parameters. Initially, closed-loop control using multiple feedback signals from the hot wire 1, hot wire 2, Mic.1 and Mic.2 was investigated. Various measurements were conducted to check the control performance obtained by using the combination of feedback signals. However, it was found that no obvious improvement was obtained by using multiple feedback signals, compared to using a single feedback signal from hot wire 2. One plausible reason is that all signals contained the same information of the mainly tonal vortex shedding response in the flow or sound fields. Another reason is that microphones could be affected by the background acoustic noise, negating the advantage of having multiple feedback signals for control. Thus, it was decided that closed-loop control experiments would focus on using a single feedback signal from hot wire 2.

In the experiment, the phase delay was initially kept at $\emptyset=0$, whilst the control magnitude A was varied, causing the control voltage V_p to vary. The effect of varying V_p on the noise reduction of flow-induced acoustic resonance in the cavity is shown in Figure 9 in terms of sound pressure level reduction (ΔSPL). Note that for comparison, the open-loop control results are also included in the figure, which will be discussed further in the next section. The control voltage was limited by the maximum voltage allowable for THUNDER actuators, which was about 160 V. As expected, the closed-loop control performance at low control voltage was minimal, which justified the need to use the proposed down-sampling control method to optimize the control actuation of the test model. Furthermore, microphones in the duct and cavity both recorded the same general trend of increasing noise reduction as the control voltage was increased.

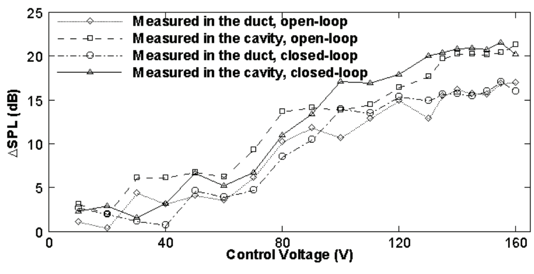

Figure 9: The open- and closed-loop control performance in terms of sound pressure level reduction for varying control voltages. The feedback signal was obtained from hot wire 2, which was located at x=35.5 mm, y=11.0 mm.

For the present case, the best control result was obtained when the control voltage V_p=155V, resulting in a SPL reduction of 17.1dB in the duct and 21.5dB inside the cavity, respectively. Figure 10 shows the control performance when the phase delay relative to the down-sampled signal was varied, whilst the control voltage was fixed at V_p=155V. The general trends of noise reduction measured by microphones in the cavity and duct were similar, indicating a consistent physical mechanism occurred in the system. The best control performance occurred when the control phase delay was approximately 288°, with the obtained noise reduction of 17.4dB in the duct and 22.6dB inside the cavity. The results thus indicate the existence of the optimal control phase delay for an efficient closed-loop noise control inside the cavity and in the duct.

Based on the optimal control voltage and phase delay configuration, the closed-loop control performance was investigated in both sound and flow fields. Figures 11(a) and (b) depict the sound pressure spectrum obtained from Mic.1 and Mic.2. It can be seen that, upon deployment of control, the sound pressures in the duct and inside the cavity underwent significant reductions. The spectrum indicated that with control, the SPL in the duct decreased from 81.3dB to 63.8dB (a reduction of 17.5dB) at the vortex shedding frequency. Meanwhile, the SPL measured inside the cavity decreased from 97.8dB to 75.1dB (a reduction of 22.6dB), which was much larger than the noise reduction measured in the duct. Such a phenomenon will be discussed in detail in the later section about the vortex shedding frequency shift.

The results demonstrated that an effective closed-loop control in the sound field could be achieved. Furthermore, the effect of closed-loop control in the flow field was investigated in terms of power spectrum density of flow velocity E_u measured by two hot wires, located at the leading edge with x=0mm, y=11mm and at downstream of the test model with x=34mm, y=11mm, again referred to as hot wire 1 and hot wire 2, as shown in Figs. 11(c) and (d). From the figures, it can be seen that E_u has decreased from 3.1e-4 to 4.4e-5 (a reduction of about 86%) measured by hot-wire 1 and 4.2e-3 to 7.2e-4 (a reduction of about 83%) measured by hot-wire 2. Therefore, the closed-loop control in the flow field was also effective in reducing the flow velocity strength caused by the vortex shedding. The corresponding control performances in time-domain were shown in Figures 12, where the signals were filtered by a 5 Hz band-pass filter centered at the vortex shedding frequency. Upon deployment of closed-loop control, the noise and flow velocity reductions were clearly observed in all four hot wire and microphone sensors, indicating that the vortex shedding was successfully impaired by the control action. These results demonstrate that the proposed closed-loop control using the down-sampling method can effectively alter the sound and flow fields generated by the vortex shedding with a desirable consequence of noise reduction inside the cavity.

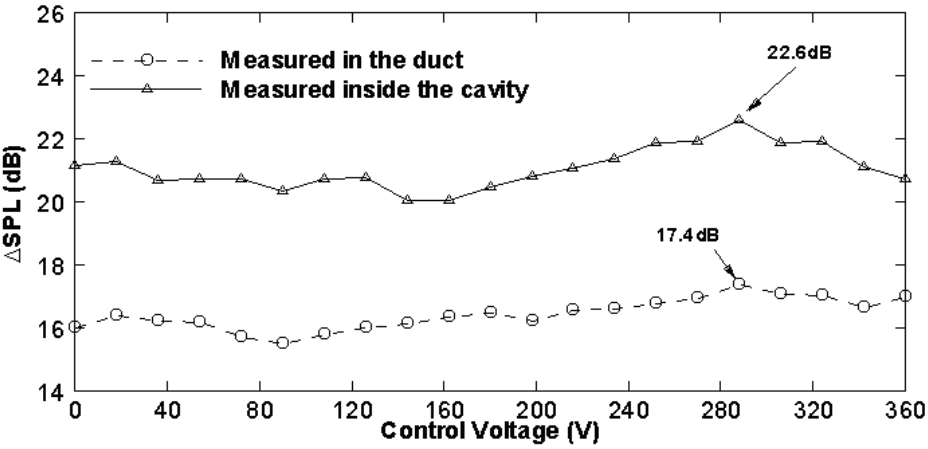

Figure 10: The closed-loop control performance for varying control phase delays. The feedback signal was obtained from the hot-wire 2, located at x=35.5 mm, y=11.0 mm. The control voltage was 155 V.

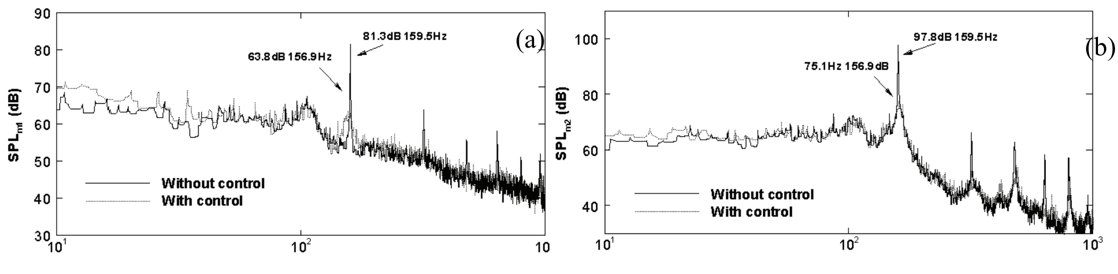

(c)

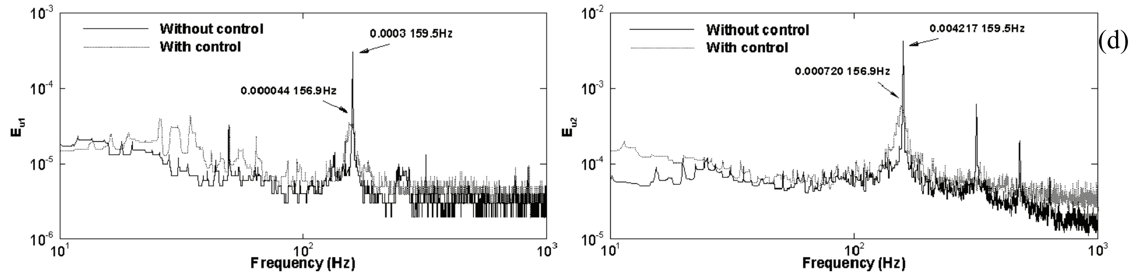

Figure 11: The best control performances in frequency-domain for closed-loop control. (a) Measured by hot wire 1 at x=0 mm, y=11.0 mm; (b) Measured by hot-wire 2 at x=34 mm; y=11.0 mm. (c) Measured in the duct; (d) Measured inside the cavity.

COMPARISON OF CLOSED-LOOP CONTROL WITH OPEN-LOOP CONTROL

To justify the use of closed-loop control over the open-loop one, closed-loop control performance was compared to that of open-loop control. The test model was actuated at varying control voltages and measurements from sensors were recorded. Figure 9 shows the level of sound pressure level reduction in the cavity when open-loop control was implemented. It can be observed that the open-loop and closed-loop control shared the same trend of sound reduction, although the closed-loop control could achieve a greater noise reduction. One plausible explanation is that the vortex strength abasement mechanisms for open-loop and closed-loop control are similar. A further observation on the open-loop control results shows that the best open-loop control performance achieved 1.3dB less reduction than that of the best closed-loop control performance as shown in Figure 10 Such results were expected because the open-loop control actuation was independent of what was occurring in the system, while the closed-loop control actuation was directly influenced by the system response as reflected by the feedback signal. The results show that the closed-loop control scheme can provide a more effective surface perturbation for impairing the generated vortices, leading to weaker vortex shedding and acoustic resonance inside the cavity.

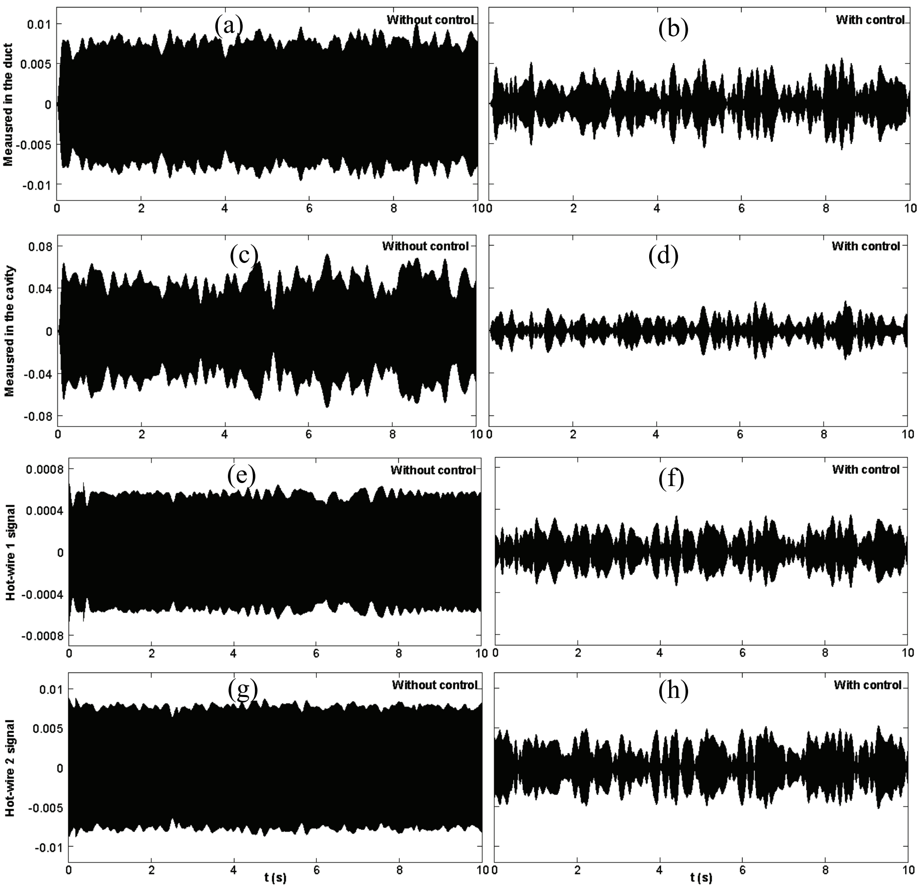

Figure 12: Time-domain results for the control performance in the sound field; the signals were filtered by a 5*Hz* band-pass filter: a) Without control, measured in the duct; b) With control, measured in the duct; c) Without control, measured inside the cavity; d) With control, measured inside the cavity. e) Without control, measured by hot wire 1; f) With control, measured by hot wire 1; g) Without control, measured by hot wire 2; h) With control, measured by hot wire 2.

Another experiment was done to further study the physical mechanisms of the vortex shedding process over the test model. For this purpose, the spectral phase relationship between two measured flow velocities along the up-surface of test model, u_1 and u_2, was analyzed. Here, u_1 was measured by hot-wire 1 which was located at leading edge with x=0mm, y=11mm, while u_2 was measured by hot-wire 2 which was moved along the line of y=11mm so the vortex shedding characteristic over the test model could be investigated. Figure 13 shows the spectral phase at the vortex shedding frequency for three different cases: without control, with open-loop control, and with closed-loop control. The results showed that without control, each cycle of vortex shedding began at the trailing edge of the test model. Between the leading edge and trailing edge, there was no clear vortex shedding as indicated by no significant spectral phase shift over this region. In this case, the flow over the leading edge and trailing edge was rather in-phase. The spectral phase for the region $0 \leq x \leq 5.5$mm was relatively small, however the spectral phase shift began to increase significantly for the region x>5.5mm. Such a spectral phase shift indicated that the flow structure over this region had started to change, leading to a full generation of vortex shedding at the trailing edge.

When either open- or closed-loop control was implemented using a surface perturbation in the region 5.5mm< x < 23.0mm, it was observed that there was generally no vortex shedding that dominated within this range. Instead, the boundary layer dominated the flow field in this region. Since the boundary layer was very complex, the measured spectral phase shift was rather irregular. However, at the trailing edge of the test model, vortex shedding was fully developed and propagated downstream. From Figure 13, a clear trend of monotonically decreasing spectral phase shift was observed. In the majority of regions downstream the test model, the value of the spectral phase shift for controlled system was larger than that of the uncontrolled system. The increase of the spectral phase shift value might imply that more time was required for a vortex to travel from the trailing edge to the downstream of the flow duct. This is consistent with the frequency shift phenomenon to be discussed in the later section where the vortex shedding frequency was slightly shifted to a lower frequency after control. However, further observation indicated that there was a generally larger spectral phase shift for system with closed-loop control than that of open-loop control, as can be seen in Figure 13.

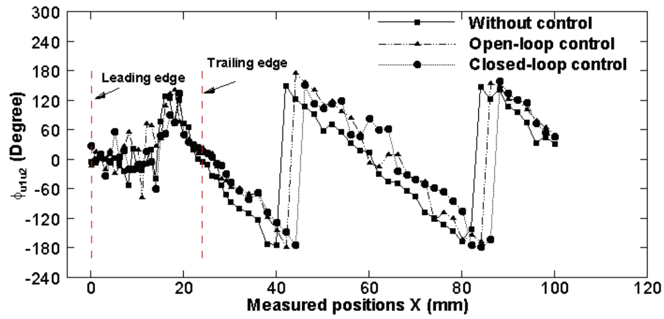

Figure 13: The spectral phase between u_1 and u_2 at the vortex shedding frequency. Here, u_1 was measured by hot-wire 1 which
was located at x=0 mm, y=11 mm, while u_2 was measured by hot-wire 2 which was moved along y=11 mm. The feedback signal was obtained from hot-wire 1 for closed-loop control.

The result suggests that for the closed-loop control, the active surface perturbation has generated a more significant change to the vortex shedding structure than that of open-loop control. This implies that the closed-loop control scheme could achieve higher reduction in the vortex energy and flow-induced noise in the duct and inside the cavity, compared to the open-loop control scheme. This is as expected since the closed-loop control utilized a feedback signal that contained the vortex shedding information, so an effective reduction of the vortex energy could be obtained. Based on this investigation, an optimal control strategy using the developed control technique could be proposed by optimally tuning the phase-delay term of the control actuation to create effective changes in vortex shedding structure, as observed by the spectral phase shift in the flow field.

VORTEX ABASEMENT MECHANISM

The observed control effect on vortex shedding may also be commented and explained from the pressure distribution viewpoint. Hourigan [29] showed that the trailing edge vortices can only be formed between the passing of leading edge vortices or the redeveloped shear layer. A pressure pulse from the vigorous trailing edge shedding then feeds back upstream and controls the redeveloped shear layer. The schematic of this feedback loop of vortex shedding for a semi-circular leading edge bluff body is shown in Figure 14. This process is called the impinging leading edge vortex instability (ILEVI), a combination of redeveloped shear layer and trailing edge vortex shedding (TEVS). Using the present system, measurements were carried out to identify the existence of the pressure pulse which was the key factor for the generation of TEVS. The peak values of E_{u2} (the auto-spectrum of signal from hot wire 2) at the vortex shedding frequency f_s for various hot wire 2 measurement positions in the duct were shown in Figure 15. It can be verified from E_{u2}spectrum that peaks in E_{u2}, albeit very small, existed even for measurement positions between the leading edge and the trailing edge. Since the TEVS only started from the trailing edge [23-25], therefore, the observed peak in E_{u2} at the vortex shedding frequency f_s for positions between the leading edge and trailing edge came from the pressure pulse. Compared with the peak value in the strongest vortex shedding region, the pressure pulse was indeed very small. After the open-loop control deployment, the pressure pulse was obviously reduced as shown in Figure 15. Based on the above observation, the reduction in the vortex strength due to the control can be further explained when taking the pressure pulse into account.

In the process of feedback loops of vortex shedding for a semi-circular leading edge bluff body, the pressure pulse is not very strong but it is a key factor for generating the subsequent vortex shedding. The surface perturbation generates a small local perturbation in the region between leading edge shear layer and trailing edge. This small local perturbation continuously changes the surface of the bluff body in a timely manner which disturbs the feedback of the pressure pulse on the trailing edge to the shear layer over the test model, and then damage the generation of next vortex shedding. More specifically, the perturbation velocity alters the flow structure around the surface of the test model, which further disturbs the entrainment of the leading edge shear layer to the trailing edge and the feedback of the pressure pulse to the leading edge shear layer. This process alters the generation of trailing edge vortex shedding, leading to a reduction of the vortex strength. This understanding is important for control design because this implies that a relatively small surface perturbation applied at correct timing can influence the vortex shedding generation effectively. This observation in fact confirms the previous investigation about the existence of optimal control phase delay, which is directly associated with the optimal timing for the surface perturbation used in the test model.

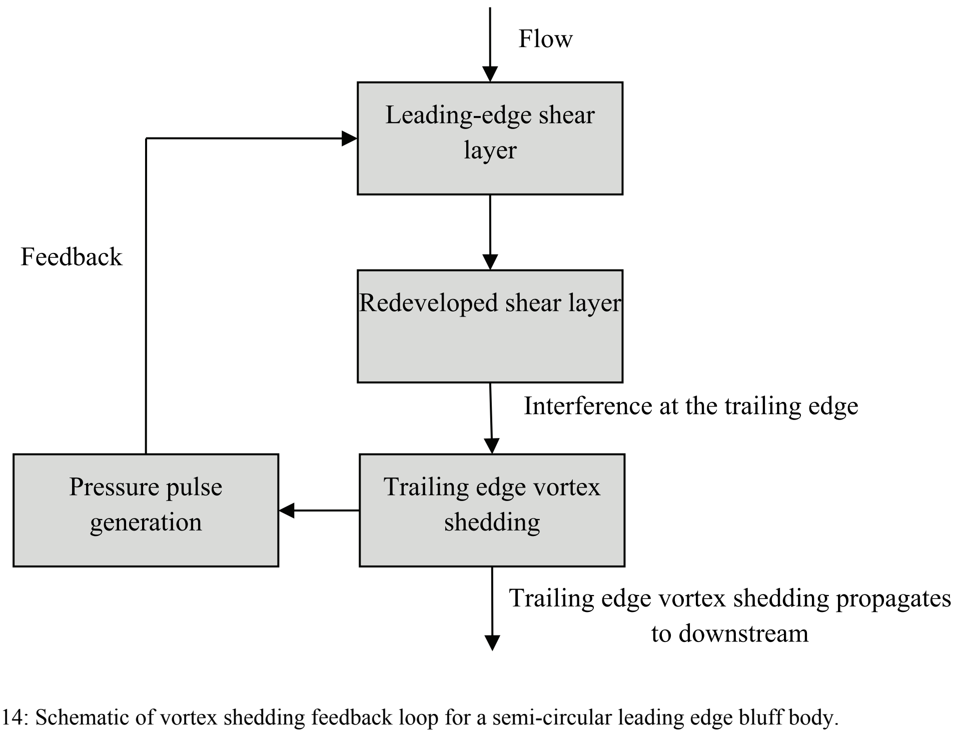

Figure 14: Schematic of vortex shedding feedback loop for a semi-circular leading edge bluff body.

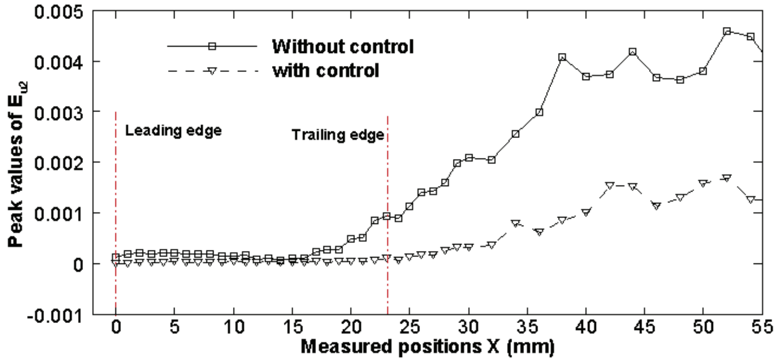

Figure15 Peaks of E_{u_2} measured by hot wire 2 from the leading edge to the downstream of test model.

VORTEX SHEDDING FREQUENCY SHIFT AND ITS IMPACT ON ACOUSTIC RESONANCE

Experiments have found so far that the sound reduction inside the cavity was larger than that in the duct. This work proposes an explanation for such a phenomenon based on the shedding frequency shift phenomenon. Initially, an investigation was undertaken by measuring the vortex shedding frequency f_s from Mic.1, for varying perturbation displacement of the vibration plate based on the open-loop scheme. The displacement of the vibration plate d_p was measured by a laser vibrometer at the center of the plate and the results are shown in Figure16. It was observed that the shedding frequency f_s generally decreased as the perturbation displacement level was increased. A trivial f_s reduction of less than 1 Hz occurred for a small perturbation level of typically less than 0.4mm.With a higher perturbation level d_p, however, the reduction in f_s became more appreciable. In particular at the optimum control configuration (f_p=30 Hz and V_p= 160 V) with d_p= 0.83 mm, the reduction in f_s reached 2.9 Hz. The effect of this frequency shift on the control performance turns out to be very important, which will be assessed next.

The shift of the shedding frequency to lower frequencies can be attributed to the effect of perturbation. In a way, the perturbation can be regarded as a way to increase the effective thickness of the test sample. Physically, the vortex shedding frequency is determined by the distance between two shear layers around the test model. Under the surface perturbation, the distance between two shear layers has actually changed, resulting in a shift in the vortex shedding frequency. The effect of the perturbation can actually be loosely represented by an equivalent increase ($\bar{d}_p$) in the thickness of the plate, h. The perturbed shedding frequency f_{sp} can be expressed as:

$$f_{sp} = S_t U_\infty / (h + \bar{d}_p) = S_t U_\infty / (h(1 + \bar{d}_p / h)) \tag{2}$$

Since h is much larger than $\bar{d}_p$, therefore $\bar{d}_p / h << 1$ and

$$f_{sp} = (S_t U_\infty / h)(1/(1 + \bar{d}_p / h)) \approx (S_t U_\infty / h)(1 - \bar{d}_p / h) = f_{s0}(1 - \bar{d}_p / h) \tag{3}$$

where f_{s0} is the unperturbed vortex shedding frequency. The corresponding frequency change Δf_{sp} can then be estimated by

$$\Delta f_{sp} = f_{s0} - f_{sp} = (\bar{d}_p / h) f_{s0} \tag{4}$$

Equation (4) shows that the reduction Δf_{sp} is linearly related to $\bar{d}_p$, which can be estimated by using the measured vortex shedding frequency shift data in Figure 16 and Eq. (3). To illustrate this, the variation of $\bar{d}_p$ relative to d_p for open- and closed-loop control schemes, is plotted in Figure 17. Furthermore, the relationship between measurement points can be approximated using a linear regression fitting line, with a gradient $\bar{d}_p/d_p$= 0.209 for the open-loop control scheme. The determined gradient for closed-loop control of 0.205 was in fact almost similar to that for open-loop control. Comparing two fitting lines for both open- and closed-loop control in Figure 17, it can be observed that the lines are relatively close to each other. This is reasonable considering uncertainties that normally arise for these particular experimental measurements. The results confirm that the vortex shedding frequency shift phenomenon occurs mainly due to the change of effective thickness associated with the surface modification of test model, regardless the control scheme used.

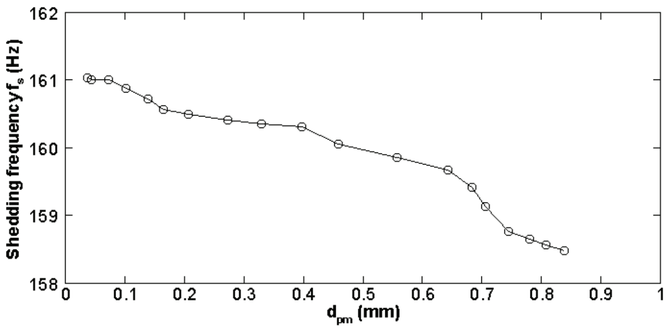

Figure 16: The shift of vortex shedding frequency at varying maximum displacement of the vibration plate d_p. The control frequency $f_p = 30Hz$, the shedding frequency was obtained in the data measured by Mic.1

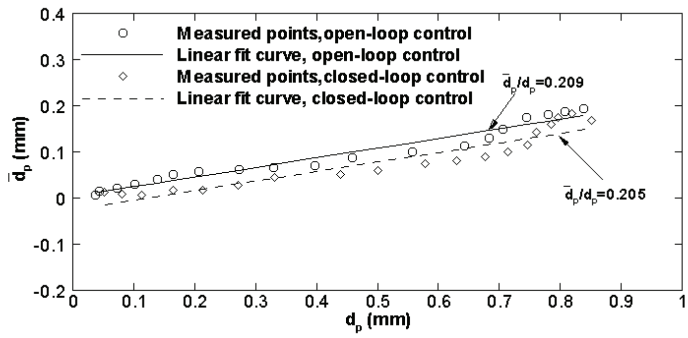

Figure 17: The effective perturbation displacement of the vibration plate, d_p was the displacement of the vibration plate measured by the laser vibrometer and $\bar{d}_p$ was the effective displacement of the vibration plate.

The sound pressure level spectra measured by the two microphones are compared in Figure 18 in terms of ΔSPL $=SPL_{m2}$-SPL_{m1}, with $SPL_{m2}$and SPL_{m1} being the sound pressure levels at Mic.2 and Mic.1, respectively. Three regions with unique characteristics can be identified from the figure. In the low frequency range (Region A), ΔSPL tottered around zero, indicating comparable SPLs in the duct and in the cavity. This suggests that the sound inside the duct was simply transported into the cavity. In a region around the first cavity resonance frequency f'_a (Region B), the SPL inside the cavity was obviously higher than that in the duct, indicating that sound was amplified by the cavity resonance effect. For example, the SPL difference reached about 20dB at the resonance $f=f'_a$. In the region further away from the resonance frequency (Region C), ΔSPL decreased, indicating a weaker acoustic field inside the cavity compared with that in the duct. One plausible reason is that at higher frequencies, sound dissipations increase with the decrease of wave length. Therefore, sound became much weaker when reaching the Mic.2 position which was at the far end of the cavity. In order to explain the higher noise reduction inside the cavity as compared to that in the duct, the acoustic resonance bandwidth was determined. To this end, a series of tests were conducted to document the sound pressure level measured by Mic.1 and Mic.2 at the shedding frequency f_s under varying flow velocities before the control was deployed. As shown in Figure 19, the peak values of sound pressure level at f_s measured by Mic.1, monotonously increased as the flow velocities increased. Furthermore, the peak values of sound pressure level at f_s measured by Mic.2, reached a peak value of 96.7dB when U_∞=U_{cr}= 8.2 m/s (i.e. f_s=f'_a=161.1 HZ, f'_a is the first resonance frequency of the downstream cavities).

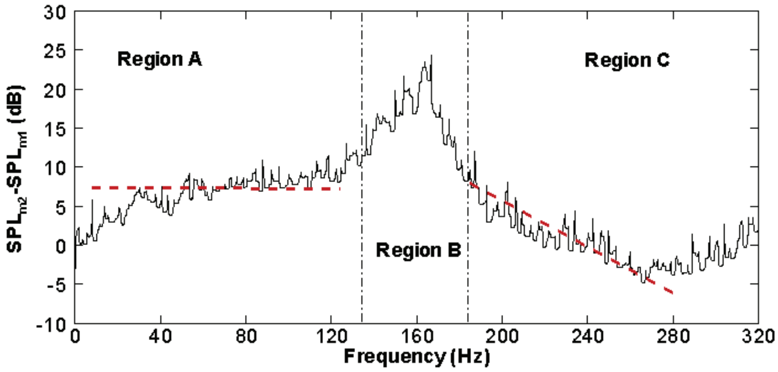

Figure18 The sound pressure level difference between the in the duct and inside the cavity. The depth of the downstream cavity was $L = 487mm$.

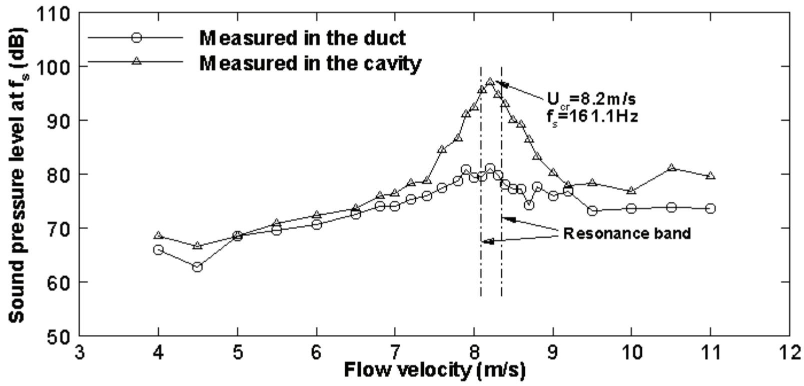

Figure 19 Sound pressure level obtained at the vortex shedding frequency at varying flow velocities. No control was deployed.

Using the conventional definition of the bandwidth corresponding to 3dB reduction from the peak value, the bandwidth of the resonance peak was determined as 3.4Hz from 159.0Hz to 162.4Hz, corresponding to a flow velocity variation from 8.0m/s to 8.3m/s. Furthermore, Figure 20 shows the effect of control on the previously defined ΔSPL at f_s at varying flow velocities with f_p= 30 Hz and V_p=160 V. It can be seen that apart from the resonance region, sound reductions in the duct and in the cavity were almost the same, which should be attributed to the weakened vortex strength discussed previously. Around the cavity resonance, sound reduction inside the cavity exceeded that in the duct by as much as 4.8dB. This can be attributed to the control-induced shift in the vortex shedding frequency. In fact, a 2.9 Hz shift in f_s exceeded the half bandwidth of the cavity resonance, and this alone should bring about at least 3 dB reduction in the *SPL*. Thus, the successful control of the acoustic resonance inside the cavity is the fruit of a dual process: the impairment of the vortex strength and the off-set of vortex shedding process away from the acoustic resonance due to the shift in vortex shedding frequency.

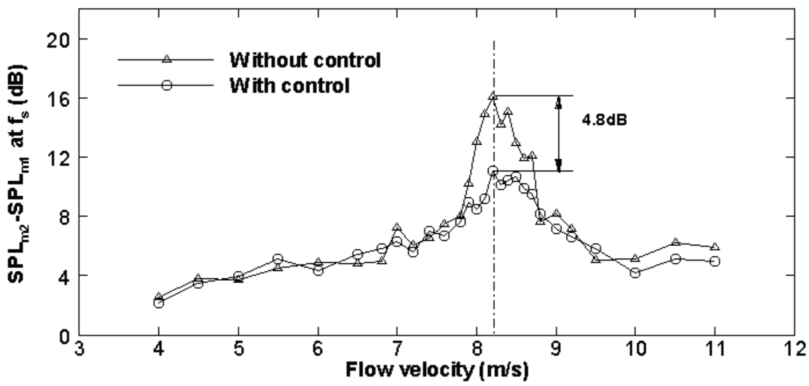

Figure 20 The effect of control on $SPL_{m2} - SPL_{m1}$ at f_s at varyings flow velocities in open-loop control scheme. Here, $f_p = 30Hz$ and $V_p = 160V$.

CONCLUSIONS

The control of flow-induced acoustic resonance was experimentally investigated by using active open-loop and closed-loop control schemes. It was found that the noise contributed by the flow-induced acoustic resonance could be effectively reduced by the implementation of the proposed surface perturbation technique. The present work leads to the following conclusions:

(1) Using the optimum open-loop control scheme, the sound pressure level at the vortex shedding frequency was reduced by 15.9dB in the duct and 20.7dB inside the cavity, respectively. This control performance was found to be repeatable and reliable.

(2) The closed-loop control method was developed by using a down-sampling method to utilize the high control actuation of THUNDER actuators embedded in the test model. It was found that the flow-induced acoustic resonance can be effectively reduced by the implementation of the developed closed-loop surface perturbation technique. At the optimum control voltage and control phase delay for the present experiment, noise reduction of 17.5dB in the duct and 22.6dB inside the cavity was obtained.

(3) The closed-loop control could achieve a better control performance than that of the open-loop control. The surface perturbation of test model in open-loop control scheme was independent of what was occurring in the system. In contrast, the closed-loop control scheme allowed the active surface perturbation to be adjusted according to the feedback response measured by a hot wire sensor. In particular, the phase delay of control actuation could be optimally tuned so that the strength of vortex shedding energy could be minimized, leading to a better noise reduction in the duct and cavity. This process was evident from the spectrum phase shift results for the closed-loop control case, where the vortex traveling time has been delayed at downstream of the test model. Therefore, an optimal control strategy was proposed by utilizing an optimal phase-tuned active surface perturbation to create sufficient changes in the vortex shedding structure, leading to an effective noise reduction in the system.

(4) The reduction of flow-induced noise in the duct is mainly due to the impairment of the vortex strength upon deployment of control. It is proposed that the local perturbation alters the flow structure around the surface of the test model, which further disturbs the entrainment of the leading edge shear layer to the trailing edge and the feedback of the pressure pulse to the leading edge shear layer. This process alters the generation of trailing edge vortex shedding, leading to a reduction in the vortex strength.

(5) The vortex shedding frequency shift phenomenon was observed in both open-loop and closed-loop control cases. This phenomenon allowed additional noise reduction inside the cavity than in the duct. The mechanism for the vortex shedding frequency shift in the closed-loop control is consistent with the open-loop control. As such, the frequency shift can be predicted based on the proposed formula given in Eq. (4). As observed from the open-loop control experiment, the frequency shift phenomenon led to a further sound pressure reduction of 4.8dB inside the acoustic cavity, compared to that in the duct. Therefore, two control mechanisms for flow-induced acoustic resonance had been demonstrated in this work: (a) The impairment of vortex shedding at downstream of the test model, influencing the correlated sound field inside the cavity. (b) The shift of vortex shedding frequency that allows additional noise reduction inside the cavity, particularly when the shedding frequency shift exceeds the acoustic resonance bandwidth.

ACKNOWLEDGEMENT

The authors wish to acknowledge support given to them by the Research Grants Council of HKSAR through Grant No. PolyU 5132/07E.

REFERENCES

[1] Gerrard, J. H., 1966. The mechanics of the formation region of vortices behind bluff bodies. *Journal of Fluid and Mechanics* 25, pp. 401-13.

[2] Bockholts, M., Hirschberg, A., Pascal, V. E. and Roozen, N. B., 1998. Vortex sound in bass-reflex ports of loudspeakers, Part I, Observation of response to harmonic excitation and remedial measures. *Journal of Acoustical Society of America* 104, pp. 1914–918.

[3] Novak, J. M., Radavich, M. and Selamet, A., 2001. A computational approach for flow-acoustic coupling in closed side branches. *Journal of Acoustical Society of America* 109, pp. 1343–353.

[4] Alvi, F., Cattafesta, L., Rowley, C. and Williams, D. *Review of active control of flow-induced cavity resonance*, AIAA 2003-3567.

[5] Coles, D., Roshko, A., Shih, WCL. and Wang, C., 1993. Experiments on flow past rough circular cylinders at large Reynolds numbers. *Journal of Wind and Industrial Aerodynamics Engineering* 49, pp. 351–68.

[6] Anderson, E. and Szewczyk, A., 1997. Effects of a splitter plate on the near wake of a circular cylinder in 2 and 3-dimensional flow configurations. *Experiments in Fluids* 23, pp. 161–74.

[7] Dalton, C., Owen, J. C. and Xu, Yu., 2001. The suppression of lift on a circular cylinder due to vortex shedding at moderate Reynolds numbers. *Journal of fluids and structures* 15, pp. 617–28.

[8] Baek, S. and Sung, H. J., 1998. Numerical simulation of the flow behind a rotary oscillating circular cylinder. *Physics of Fluids* 10, pp. 869–76.

[9] Choi, S., Choi, H. and Kang, S., 2002. Characteristics of flow over a rotationally oscillating cylinder at low Reynolds number. *Physics of Fluids* 14, pp. 2767–777.

[11] Blackburn, H. and Henderson, R., 1999. A study of two-dimensional flow past an oscillating cylinder. *Journal of Fluid and Mechanics* 385, pp. 255–86.

[12] Berger, E., 1967. Suppression of vortex shedding and turbulence behind oscillating cylinders. *Physics of Fluids* 10, pp. 191–93.

[13] Huang, X. Y. and Weaver, D. S., 1991. On the active control of shear layer oscillations across a cavity in the presence of pipeline acoustic resonance. *Journal of Fluids and Structures* 5, pp.207-19.

[14] Cattafesta III, L. N., Choudari, M., Garg, S. and Li, F., 1997, *Active control of flow-induced cavity resonance*, AIAA-97-1804 .

[15] Cattafesta III, L. N., Garg, S. and Shukla, D., 2001a. The development of piezoelectric actuators for active flow control. *AIAA Journal* 39, pp. 1562-568.

[16] Cattafesta III, L. N., Kurdila, A. and Mathew, J., 2001b. Modeling and design of piezoelectric actuators for fluid flow control. *SAE 2000 Tran. J. Aer.* 109, pp. 1088-095.

[10] Cetiner, O. and Rockwell, D., 2001. Streamwise oscillations of a cylinder in a steady current. Part 1: locked-on states of vortex formation and loading. *Journal of Fluid and Mechanics* 427, pp. 1–28.

[17] Cheng, L., Zhang, M. M. and Zhou, Y., 2003. Perturbed interaction between vortex shedding and induced vibration. *Journal of Fluids and Structures* 17, pp. 887-901.

[18] Cheng, L., and Marouzé, J. P., 2002. A Feasibility Study of Active Vibration Isolation THUNDER Actuators. *Smart Materials and Structures* 11, pp. 854-62.

[19] Cheng, L., Zhang, M. M. and Zhou, Y., 2004. Closed-loop-controlled vortex shedding from a flexibly supported square cylinder under different schemes. *Physics of Fluids* 16, pp. 1439-448.

[20] Cheng, L., Zhang, M. M. and Zhou, Y., 2006. Controlled flow-induced vibration on a fix-supported flexible cylinder in crossflow. *Journal of Sound and Vibration* 292, pp. 279-99.

[21] Cheng, L., Zhang, M. M. and Zhou, Y., 2006. Closed-loop controlled vortex-airfoil interactions. *Physics of Fluids* 18, 046102.

[22] Cheng, L., Zhang, M. M. and Zhou, Y., 2008. Control of post-stall airfoil aerodynamics based on surface perturbation. *AIAA Journal* 46, pp. 2510-519.

[23] Cheng, L., Zhang, M. M. and Zhou, Y., 2009. Asynchronous Control of Flow-induced Acoustic Cavity Resonance Using Imbedded Piezo-electric Actuators. *Journal of Acoustical Society of America* 126(1), pp. 36-45.

[24] Nakamura, Y., Nakayama, R., Ohya, Y., Ozono, S. and Tsuruta, H., 1992. A Numerical Study of Vortex Shedding from Flat Plates with Square Leading and Trailing Edges. *Journal of Fluid and Mechanics* 236, pp. 445–60.

[25] Shine, S. and Ziada, S., 1999. Strouhal numbers of flow-excited acoustic resonance of closed side branches. *Journal of Fluids and Structures* 13, pp. 127–42.

[26] Parker, R., Stokes, A. N. and Welsh M. C., 1984. Flow-Resonant Sound Interaction in a Duct Containing a Plate, Part I: Semi-circular Leading Edge. *Journal of Sound and Vibration* 95(3), pp. 305–23.

[27] Marks II, R. J., 1991. *Introduction to Shannon Sampling and Interpolation Theory*, Spinger-Verlag, New York.

[28] Shannon, C. E., Jan. 1949. Communication in the presence of noise, *Proc. Institute of Radio Engineers* 37(1), pp. 10–21.

[29] Hourigan, H., Tan, B. T. and Thompson, M. C., 2001. Self-sustained oscillations in flows around long blunt plates. *Journal of Fluids and Structures* 15, pp. 387-98.

METHOD OF IMPACT ENERGY DISSIPATION BY THE USE OF THE PNEUMATIC IMPACT ABSORBER WITH A PIEZO-VALVE

R. Wiszowaty, J. Biczyk, C. Graczykowski, G. Mikułowski

Institute of Fundamental Technological Research, Polish Academy of Sciences, Department of Intelligent Technologies, Warsaw, Poland

ABSTRACT

Presently, the important trend of "greening" the modes of transport is widely observed worldwide. One of the serious air-transport problems is the necessity of expensive recycling of degraded technical fluids, e. g. hydraulic oil, which is utilized in a wide class of air-vehicles being currently in service. Moreover, an important disadvantage of the hydraulic instal-lations in the aeronautic vehicles is their large weight. To overcome these problems (in the field of aircraft undercarriages) a new type of shock absorber has been proposed, which eliminates the usage of the hydraulic fluid. The device utilizes a gas cylinder with a piston equipped with a fast actuated valve in order to control the reaction force of the absorber in real-time. This paper presents a study on an impact energy dissipation method by the use of the pneumatic impact absorber and the results of an experimental verification of the concept based on a technical demonstrator of such device (a shock absorber for a landing gear fabricated for an UAV). The study focuses on the energy absorbing capabilities of the device. A landing gear shock absorber is used as an example, but the general idea of the device is considered to be useful in other fields of application.

INTRODUCTION

Presently, the important trend of "greening" the modes of transport is widely observed worldwide. One of the serious air-transport problems is the necessity of expensive recycling of degraded technical fluids, e. g. hydraulic oil, which is utilized in a wide class of air-vehicles being currently in service. Moreover, an important disadvantage of the hydraulic installations in the aeronautic vehicles is their large weight. To overcome these problems (in the field of aircraft undercarriages) a new type of pneumatic shock absorber has been proposed, which eliminates the usage of the hydraulic fluid. The device utilizes a gas cylinder with a piston equipped with a fast actuated valve in order to control the reaction force of the absorber in real-time. Pneumatic absorbers (e.g. protective air bags) are incorporated in some methods of minimizing the contact force between an impacting body and the obstacle during a collision. In classical solutions dedicated to the dissipation of the kinetic energy of the impacting body, no adaptive control of braking force is applied [1,2].

However, in some applications it is necessary to tune the level of the force during the process, in order to minimize its long term destructive influence [3-6]. The techniques proposed previously usually incorporated advanced fluids, which are expensive, heavy and difficult to recycle. Therefore, a new technique of the control of the deceleration process was proposed [7]. The adaptive impact absorber consisted of a cylinder with a piston and a piezo-valve in a by-pass configuration. The intensity of the gas flow through the valve in the by-pass was controlled in order to achieve the optimum deceleration level. The piezoelectric actuator was used to ensure sufficiently quick opening and closing of the valve. The advantage of the proposed semi-active approach was the decrease of the peak braking force in comparison to the passive braking of the impacting object. Furthermore, the semi-active control allowed to adapt the behaviour of the device to the predetermined level of the impact energy and therefore to optimize the braking process. Possible applications for the device are rail cars, landing gears, air-vehicles bogie dampers or precise docking systems.

The research presented was focused on an improved solution of the impact absorber with the piezo-valve positioned inside of the piston. This article presents a study on an impact energy dissipation method by the use of the pneumatic impact absorber as well as the results of an experimental verification of the concept based on a technical demonstrator - a shock absorber for a landing gear for Unmanned Aerial Vehicle (UAV). The study was focused on the energy absorbing capabilities of the device. The landing gear shock absorber was used as an example, but the general idea of the device is considered to be useful in other fields of application.

RESEARCH CONDUCTED

The investigation presented was divided into three phases: a) problem definition, numerical analysis and determination of design requirements, b) development and verification of the piezo-actuated valve, c) development and tests of the adaptive absorber with the valve. At the first stage, the concept of the valve actuated by piezoelectric stacks was developed and numerically proven. On the basis of numerical simulation the piezo-valve and absorber were designed and fabricated. The following studies were devoted to testing of the devices on dedicated laboratory stands.

NUMERICAL ANALYSIS OF ADAPTIVE PNEUMATIC LANDING GEAR

A numerical model of the adaptive pneumatic absorber was developed and analyzed by the authors and presented in [8]. The model utilizes the assumption of uniform distribution of gas parameters in each chamber and an analytical model of the gas flow through a controllable valve. The model proposed enables to conduct simulations of the process of energy dissipation and to test various strategies of valve opening. The aforementioned model was utilized to design the adaptive pneumatic landing gear intended to be applied on a UAV, i.e. to find optimal geometry of the absorber, optimal initial pressure and required properties of the valve. The initial data for the design of the landing gear included:

- mass of the UAV: $M = 8{,}5\,kg$, maximum touchdown velocity: $V_0 = 3{,}3\,m/s$
- maximum admissible vertical deceleration during landing: $a_{\max} = 70\,m/s^2$
- maximum overpressure in compressed chamber of the absorber: $p_2^{\max} = 15\,atm$.

Basic parameters of the adaptive absorber were determined by using the balance of the energy of the landing object and the conditions of the static equilibrium of the system after landing. With this the following parameters were obtained:

- length of the absorber: $h_0 = 0{,}11\,m$, length of the compressed chamber: $h_{02} = 0{,}095\,m$
- cylinder diameter: $d = 0{,}032\,m$,
- piston rod diameter: $d_T = 0{,}012\,m$
- initial pressure in absorber chambers: $p_0 = 6\,atm$

Furthermore the thermodynamic part of the model was utilized to determine the required parameters of the controllable valve:

- maximum pressure difference for which the valve remains airtight: $\Delta p = 8{,}5\,atm$
- maximum mass flow rate required: $q_{\max} = 14{,}8\,g/s$ (corresponding pressure difference: $\Delta p = 7{,}8\,atm$, corresponding upstream pressure $p_2 = 13{,}2\,atm$).

In the following step the numerical model of the pneumatic landing gear was developed and simulations of the landing process were conducted (see Figure 1).

Two control strategies were implemented:

- adjustment of time instant and level of constant valve opening,
- real-time control of the valve opening during landing (Pulse Width Modulation).

In the first strategy the valve remains closed during the initial stage of landing in order to enable a fast increase of the force generated by the absorber. The time of valve opening and flow resistance coefficient (representing valve opening) are adjusted by means of optimization procedure which minimizes force generated by the absorber, taking into account the constraint imposed on maximum absorber stroke. In the second strategy the valve also remains closed during the initial stage of the process. The optimum level of force generated by the absorber is determined by using the energy conservation law, which indicates the equality of potential and kinetic energy of the landing object and energy dissipated by the absorber and the wheel.

$$\Delta E_{K1} + \Delta E_{P1} + \Delta E_{K2} + \Delta E_{P2} = D_{ABSORBER} + D_{WHEEL}$$

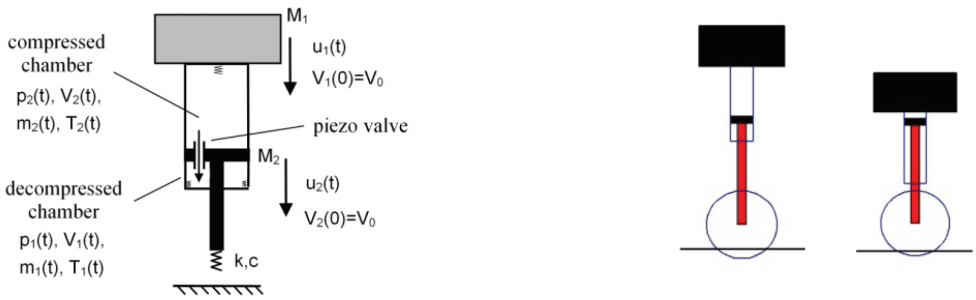

Figure 1: a) Considered model of adaptive pneumatic landing gear, b) Visualization of the landing process: intermediate and final stage of landing.

Alternatively, the time of valve opening can be determined from the kinematical condition:

$$a_1(t) = \frac{V_1^2(t)}{2(d_{\max} - (u_1(t) - u_2(t)))}$$

where $d_{\max} = 0{,}085\,m$ is assumed and denotes maximum stroke of the absorber. In a further part of the landing process the valve is simultaneously opened and closed in order to maintain constant force generated by the absorber. The signal that controls valve opening I_n depends on actual value of force generated by the absorber:

$$I_n = 1 \quad \text{if} \quad F > F_{OPT} + \Delta F_{TOL}$$

$$I_n = 0 \quad \text{if} \quad F < F_{OPT} - \Delta F_{TOL}$$

$$I_n = I_{n-1} \quad \text{if} \quad F_{OPT} - \Delta F_{TOL} < F < F_{OPT} + \Delta F_{TOL}$$

where: ΔF_{TOL} is assumed as the tolerance of the force level. The above strategy enables to stop the landing object by using a minimum level of the force generated by the absorber and therefore with minimum deceleration of the landing object.

During the final stage of the process, when velocity of the landing object is relatively small, the force generated by the absorber is gradually reduced in order to obtain the state of static equilibrium of the landing object. The results are depicted in Figures 2 to 4 and summarized in Table 1.

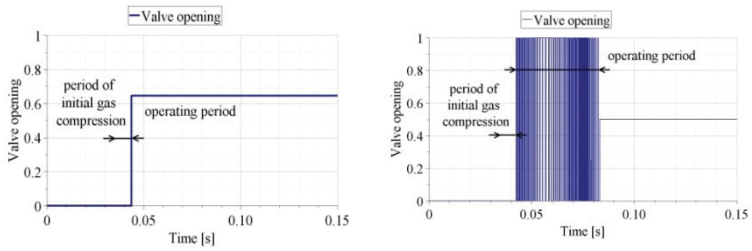

Figure 2: Control signal simulation with single-stage (left) and real-time control (right).

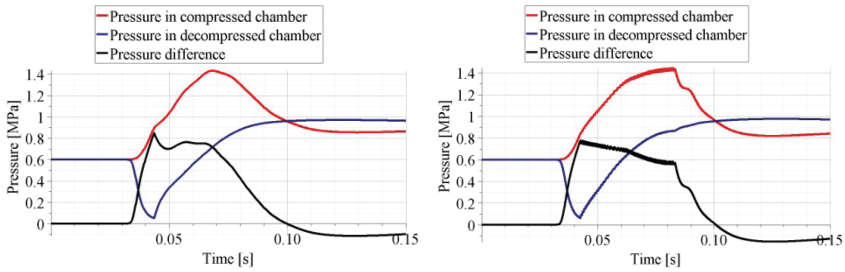

Figure 3: Numerical simulation of the landing with single-stage (left) and real-time control (right)

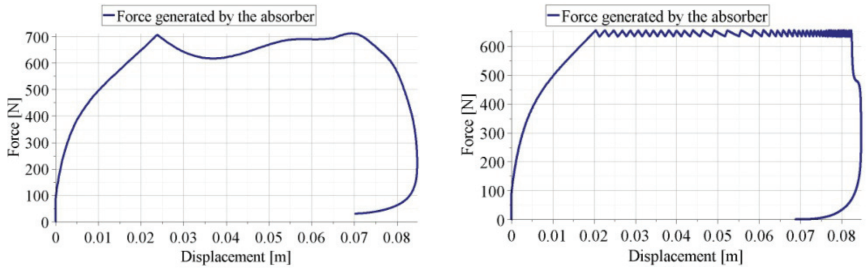

Figure 4: Force generated by the absorber with single-stage (left) and real-time control strategy (right).

TEST OF PIEZO ACTUATED VALVE

The core element of the Adaptive Impact Absorber (AIA) is a piezo-valve – shown in cross-section view in the two pictures below (Figure 5). This valve enables the flow of fluid between two sides of the piston inside the cylinder of the absorber. When the gas flow ratio is controlled, the reaction force of the absorber can be adjusted.

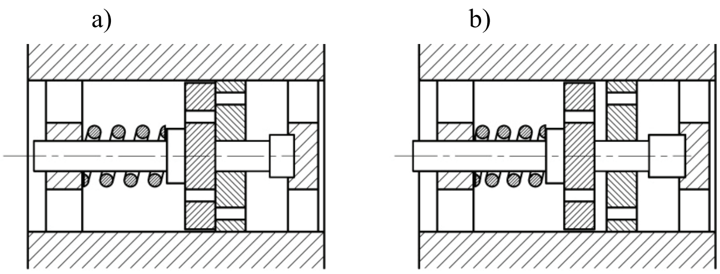

Figure 5: Cross-sectional view through the valve: a) closed, b) opened.

Figure 5 depicts the piezo-valve schematically in closed (a) and opened (b) position. Two plates with holes are tight when they are aligned. Moving one plate apart from the other enables the fluid to flow through the valve. To ensure small dimensions and a compact structure of AIA it is advisable to locate the valve in the piston of the absorber. This results in dimensional constraints of the valve. Short operating time also requires the use of the piezo-stacks for opening and closing the valve. As shown in the pictures, the opening of the valve is achieved by elongation of the piezo-stack (marked on the right hand sides of both pictures) and closing is done by the spring connecting one of the plates with housing.

To predict the value of the kinetic energy of the impacting body that could be efficiently dissipated by the use of the absorber equipped with the piezo-valve, a set-up was developed (Figure 6) consisting of two containers [9,10], three pressure sensors p_0, p_1, and p_2, three thermocouples T_0, T_1, and T_2, a pressure regulator and the piezo-valve investigated. In order to acquire its characteristics the valve was examined experimentally under a variety of flow conditions.

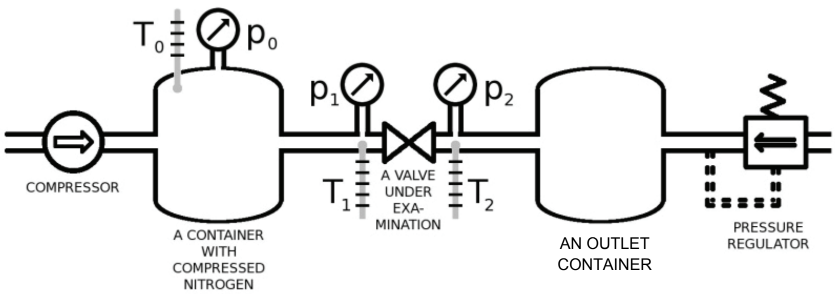

Figure 6: Scheme of the set-up applied to examination of the valve.

The dependencies of the mass flow rate in the function of inlet pressure p_1 and pressure drop on the valve p_1-p_2 were obtained (Figure 7). The surface presented resulted from was spanning the surface on the curves obtained in the series of experiments. The result shown indicates that mass flow rate depends on the pressure difference on the valve and on inlet pressure level.

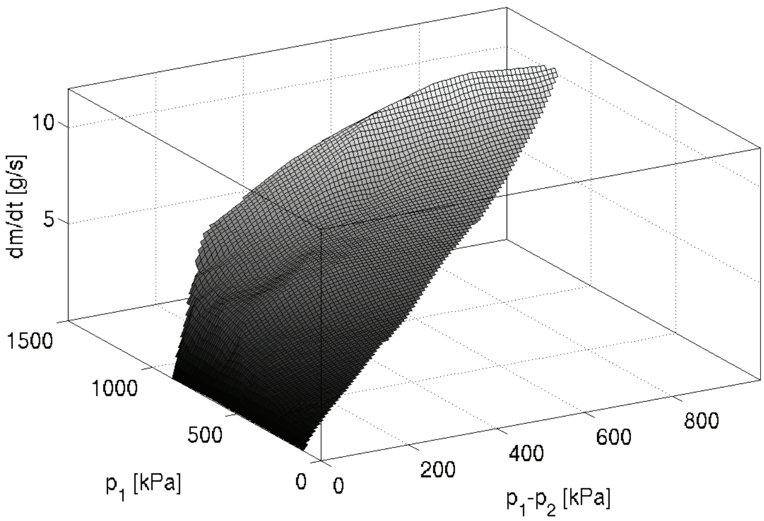

Figure 7: Mass flow rate dependency in the function of the inlet pressure p_1 and the difference between the inlet and outlet pressures (p_1-p_2).

EXPERIMENTAL VERIFICATION ON THE DROP TEST STAND

During the third phase of the investigation, the outcomes of the numerical computations were verified versus the results of experiments conducted with a model of the adaptive landing gear (Figure 8). The experimental program for the part of the research presented was aimed at confirming the design assumptions and correctness of the packaging concept. The development of the optimum control strategy for the device was outside of the scope of the study presented.

At the stage of the investigation presented the drop-test stand was used with the absorber mounted to the drop-weight of 9 kg at initial height of 0,1 m, which corresponds to the initial velocity of 1,4 m s^{-1}, where the impact energy was estimated for 8,3 J. The experimental procedure included two stages: the first, where the absorber operated as passive pneumatic device with the valve closed during impact and the second where the valve's operation was controlled in order to maintain a predefined value of pressure difference between the absorber's chambers and therefore to maintain the reaction force of the absorber on the predetermined level. In both cases the initial gas pressure in the absorber was 450 kPa and the predefined level of expected pressure difference was 210 kPa. The data acquisition setup included: gas pressure sensors inside the absorber's chambers, accelerometer fixed on the drop-weight, displacement sensor indicating position of the drop-weight in reference to the base plate of the stand.

Figure 8: Drop-test stand with adaptive absorber.

The results of the absorber's operation are presented in Figure 9. The graphs demonstrate the evolution of three parameters (drop-weight displacement, gas pressure difference, drop-weight deceleration) in time domain for two cases: passive and controlled. In the first tested case, when the absorber had almost an ideal elastic characteristic (except the friction losses) three bounces are shown at 0,1 s, 0,27 s and 0,58 s time instants respectively. In comparison, introduction of the controlled flow of the gas between the chambers allowed to dissipate the impact energy within the first compression stroke and to mitigate oscillatory movement after 0,35 s. Also the control procedure introduction decreased the maximum deceleration level of the drop-weight from 12 m/s^2 to 8 m/s^2. Figure 10 depicts the pressure difference between the absorber's chambers in the domain of the landing gear deflection during the impact loading. The efficiency of the landing gear calculated in accordance to the method proposed by [2,11] was 71% in the trial presented. The value is in agreement with the numerical predictions presented in Table 1 independently with respect to the impact energy.

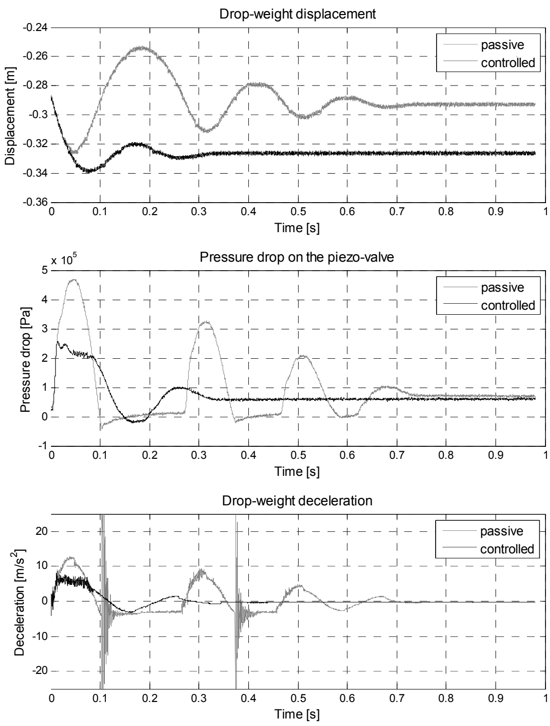

Figure 9: Comparison of two modes of the absorber operation: passive and controlled.

	Single-stage control	Real-time control
Maximum force generated	712N	654N
Maximum deceleration	79,19m/s^2	71,94 m/s^2
Absorber efficiency	83,9%	90,4%
Landing gear efficiency	72,6%	76,7%

Table 1: Comparison of quantitative results obtained for adaptive pneumatic landing gear with single-stage and real-time control strategy.

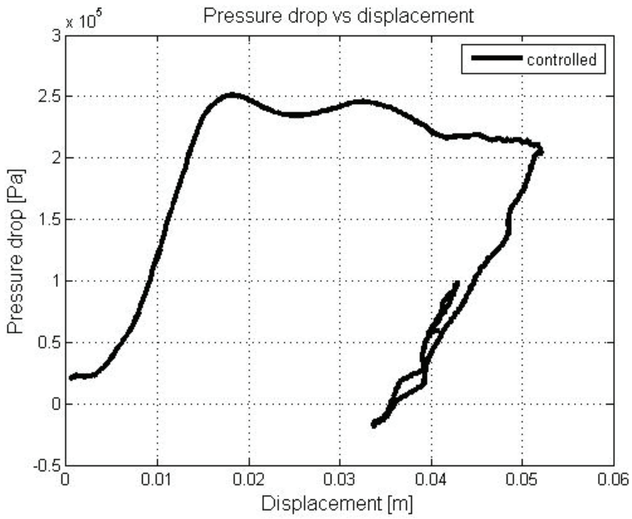

Figure 10: Pressure difference on the piezo-valve during the impact loading in the domain of the piston displacement.

CONCLUDING REMARKS

The study presented was divided into numerical and experimental phases. Numerical experiments conducted indicated that:

- the proposed concept of dissipating kinetic energy of the landing object by means of double-chamber pneumatic absorber is feasible.
- both control strategies proposed allow to avoid rebound of the landing object and to obtain favorable, almost constant level of force generated by the absorber. Real-time control of valve opening enables to obtain unprecedented very high efficiency of the absorber which exceeds 90%.

The results of experimental research indicated that:

- The maximum flow rate measured on the piezo-valve fabricated was in accordance to the numbers predicted for the numerical design.
- The absorber under impact loading responds fast enough to be controlled in real-time (0.5 kHz update rate).
- The measured efficiency of the landing gear was 71% and was in agreement with the numerical predictions.

REFERENCES

[1] Harris C. M. and Piersol A. G., 2002. *Shock and vibration handbook*, McGraw-Hill, London

[2] Conway H. G., 1958. *Landing gear design*, Chapman & Hall Ltd., London

[3] Mikułowski G. and Holnicki-Szulc J., 2007. Adaptive landing gear concept - feedback control valida-tion. *Smart Materials and Structures* 16, pp. 2146-158

[4] Batterbee D. C., Sims N. D., Stanway R. and Wolejsza, Z., 2007. Magnetorheological landing gear: 1. A design methodology. *Smart Materials and Structures* 16, pp. 2429.

[5] Batterbee D. C., Sims N. D., Stanway R. and Rennison M., 2007. Magnetorheological landing gear: 2. Validation using experimental data*, Smart Materials and Structures* 16(6), pp. 2441-452.

[6] Mikułowski G. and Jankowski Ł., 2009. Adaptive landing gear: Optimum control strategy and potential for improvement, *Shock and Vibration* 16, pp. 175-94

[7] Mikułowski G., Graczykowski C., Pawłowski P., Sekula K., Mróz A. and Holnicki-Szulc J., 2008. A feasibility study of a pneumatic adaptive impact absorber, *Proc. of the Fourth European Conference on Structural Control*, 4ECSC, St. Petersburg, Russia, 8 – 12 September 2008

[8] Mikułowski G., Pawłowski P., Graczykowski C., Wiszowaty R. and Holnicki-Szulc J., 2009. On a pneumatic adaptive landing gear system for a small aerial vehicle, *Proceedings of the IV Eccomas thematic conference on Smart structures and materials*, 13-15 July, Porto.

[9] Iwaszko J., 1999. *Opory przepływu powietrza przez elementy pneumatyczne*, Editing House of Warsaw University of Technology, Warsaw

[10] Beater P., 2007. *Pneumatic drives*, Springer-Verlag, Berlin

[11] Currey N., 1988. *Aircraft Landing Gear Design – Principles and practices*, AIAA

THERMOELECTRIC ENERGY HARVESTER FOR A SMART BEARING CONCEPT

Michał Lubieniecki & Tadeusz Uhl

AGH University of Science and Technology, Faculty of Mechanical Engineering and Robotics, Department of Robotics and Mechatronics, Al. A. Mickiewicza 30, 30-059, Krakow, Poland

ABSTRACT

The article presents fundamental design considerations of a thermoelectric harvester to be used in applications for machine condition monitoring (MCM) or condition based maintenance (CBM). The power to be harvested is the thermal power loss of the bearing. The aim of the harvester is to maintain the energy neutral operation. By the numerical analysis of the system equivalent model, the pulse width of the associated sensor active state is analyzed together with the power capacity of the harvester and its operation cycle length. The article contains an analysis of the influence of design parameters onto the system performance. The assumed design variables are: thermal resistances of the heat sink, insulating partition and the number of thermoelectric modules. The electrical circuitry is described by the energy buffer capacitance, sensor active state duration, equivalent resistance of the adjoined circuitry during the passive and active state. The continuous and burst mode of operation is taken into consideration. The preliminary experimental proof of the concept is presented as well.

NOMENCLATURE

I_{source}	– thermal power loss in a bearing [W]; equivalent current source	[A]
R_c	– thermal resistance of the rotating shaft resulting from convective heat transfer	[K/W]
R_{TEG}	– thermal resistance of the generator [K/W]; equivalent resistance	[V/A]
R_{HS}	– heat sink thermal resistance	[K/W]
R_{part}	– insulating partition thermal resistance	[K/W]
R_{str}	– thermal resistance of the structural system components	[K/W]
R_{conv}	– thermal resistance connected with the natural convection phenomenon	[K/W]
R_{cntct}	– contact thermal resistance	[K/W]
R_{hsin}	– thermal resistance of the heat sink	[K/W]
D_z	– outer diameter of a bearing	[m]
d_m	– mean diameter of a bearing	[m]
A	– surface area of the adjoined shaft	[m^2]
Ω,n	– angular velocity	[s^{-1}]
$\rho(T)$	– air density	[kg/m^3]
$\mu(T)$	– air dynamic viscosity	[$kg\ m^{-1}\ s^{-1}$]
$k(T)$	– air heat transfer coefficient	[$W\ m^{-2}\ K^{-1}$]
F_r	– radial load	[N]
F_a	– axial load	[N]
R_1, R_2, R_3	– rolling bearing geometry constants	[-]
S_1,S_2, S_3	– sliding frictional moment constants	[-]
X_{nteg}	– number of parallel thermoelectric generators	[-]

Voc	– open circuit voltage at the thermoelectric generator's terminals	[V]
α	– Seebeck coefficient	[V/K]
T	– temperature	[K]
I	– current in an equivalent electric circuit	[A]
V_{source}	– voltage output of the generator under load condition	[V]
R_s	– equivalent resistance of the sensor node in the sleep state	[V/A]
R_a	– equivalent resistance of the sensor node in the active	[V/A]
R_{inHV}	– internal resistance of the energy management unit being a function of V_{OC}	[V/A]
C	– storage buffer capacitance	[F]
E_0	– initial energy stored in the ideal energy buffer	[J]
η	– charging efficiency	[-]
P_s	– power output of the energy source	[W]
P_c	– power consumed	[W]
P_{leak}	– leakage power of the energy buffer	[W]

INTRODUCTION

As new constructions have to increasingly meet stricter demands with regard to reliability and functionality, a growing number of sensors and supplementary electronics are integrated into machines designed nowadays, to all of which power has to be supplied. Energy harvesting may be the answer to the energy needs of many of those decentralized measurement units. Various forms of energy are available for such systems. Most frequently referenced energy sources are: mechanical, thermal, solar, wind and acoustic [1]. A broad survey of the power density characteristic of different harvesting techniques can be found in [2,3], where the piezoelectric conversion of vibrational energy is said to be the most efficient way to power autonomous systems. However, some researches [4,5] have proven thermoelectricity to outperform the piezo-based harvester's power capacity. That is noteworthy, as the conversion efficiencies of the two mentioned technologies would equal for the characteristic number of the thermoelectric generator being 4 [6] what is not yet available among the commercial modules.

There are many examples of successful implementation of piezoelectric harvesting technology, mainly in the form of kinetic harvesters [7,8,9]. Despite their relatively high power density, piezo-based harvesters have limited application capability due to their narrow-band response and mechanical coupling issues [10]. On the other hand, thermoelectricity can operate well in industrial environment as long as persistent thermal gradients exist [9]. Still, low conversion efficiency is an obstacle in many potential applications [11]. The low efficiency results from the low achievable temperature gradients and energy cost of heat removal from the cold side of the generator, even though high efficiency (up to 18%) solutions are achievable in the form of combustion systems [12]. Many researches have been conducted on the topic of human body heat energy harvesting, starting with [13], through ones on Body Area Network applications [14,15], to those on implantable bio-sensors [16]. The wireless network based on a thermoelectric generator was presented in [17]. The theoretical considerations of such a network, from the point of view of a single node, are presented and analyzed in [18]. The possible power management strategies and adaptive duty cycling for the wireless sensor nodes are presented in [19].

Despite the fact that the first research on thermoelectricity and bearing cooling is dated back to 1963 [20], and continued in [21], the idea of an energy harvesting system using heat waste of rotating bearing was not introduced until the year 2004 [22] and in the form of housing-integrated device in [23]. There are no research papers on successful implementation of thermoelectric harvesters in the machine bearing node, however, the research topic has been noticed and is being explored [24-26]. The generator is located on the side of the still bearing ring working on a small thermal gradient (the research targets the specific application with favorable thermal conditions) or mounted on the rotating bearing ring and equipped with small heat sink as in [24]. None of the designs so far have assumed strong integration of the harvester and bearing housing. That makes the harvester rather a module than a mechatronic design. The article presents the concept of the energy harvester integrated in the bearing's housing. The influence of the design parameters on the system power output is presented from both, the mechanical and electrical domain of the system.

The article is organized as follows: section 2 introduces the general concept of the harvester. Section 3 presents methods for modeling the phenomena involved in the output power level computation. Section 4 shows the constraints imposed on the harvesting circuit as a result of the concept of energy neutral operation. Then, the influence of the design variables on the output power level is explained and, as a consequence, the power output available for continuous and burst mode operation is shown. In section 5 the proof of the concept is presented. The article is concluded in section 6.

SYSTEM TOPOLOGY

The general scheme of the bearing node with the harvesting circuit is shown in Figure 1. To adapt this scheme to the specific construction of a bearing node two topologies of the mechanical part of the system are proposed (Fig. 2): a) the bearing housing is thermally linked to the machine base but insulated from the bearing, additional heat sinks are required or b) the bearing housing is thermally insulated from the machine base and the heat source (i.e. bearing) to act as a heat sink. While the heat flux passes from the bearing to the environment, a bottleneck of that process are the natural convection boundary conditions, thermoelectric modules and insulating partitions that are all characterized by low heat conductivity values. Neglecting small thermal resistances of the bearing and housing components, the proposed model assumes that all surfaces of the system components are isothermal. This leads to significant simplification and as a result the problem is reduced to 2-dimensonal heat transfer.

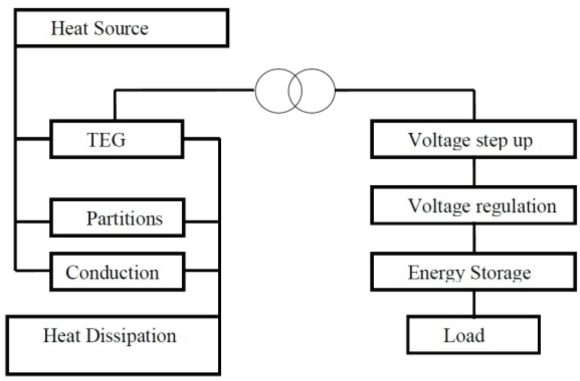

Figure 1: The general scheme of the harvester.

As electric analogy was used for the thermal system description, both solutions can be presented as resistive networks (the heat capacity is neglected as only steady state is being considered). Only the second system topology will be further investigated due to presumably higher volume energy density and its independency of other heat sources, what makes the considerations more general in nature.

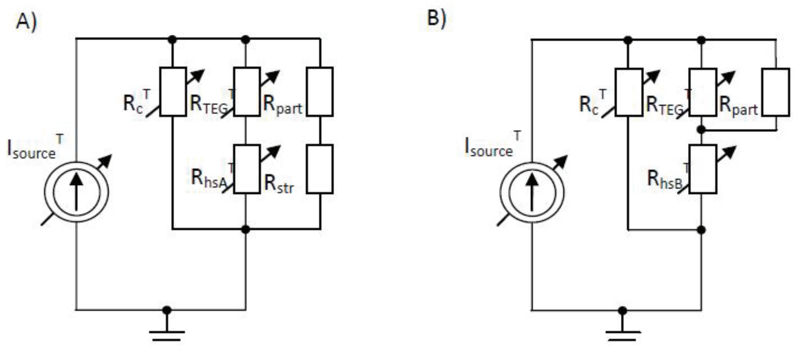

Figure 2: Proposed system topologies; a) The bearing housing is thermally linked to the machine base but insulated from the bearing, additional heat sinks are required; b) The bearing housing is thermally insulated from the machine base and the heat source and acts as a heat sink.

The above system representations result from the simplification of a more detailed system model presented below. This model can be used for analysis of all possible system configurations, regardless of the thermo electric generator's (TEG's) connection layout, mechanical layout or insulation partitions placement.

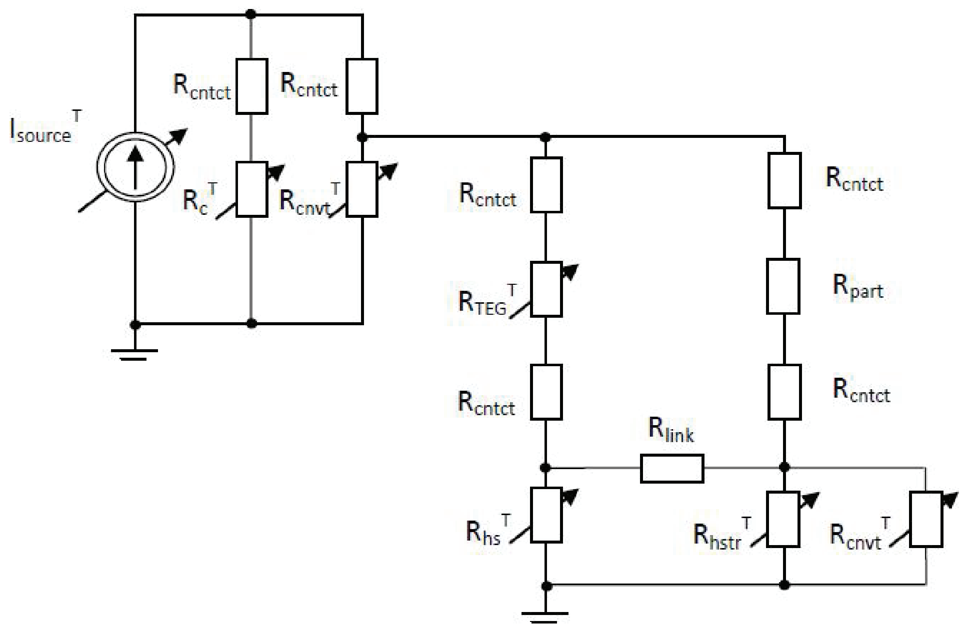

Figure 3: The general representation of the bearing housing with thermoelectric generators and possible insulating partitions.

Some thermal resistances can be assumed insignificant, e.g. the thermal resistance of the structure (due to relatively high thermal conductivity values), branch describing the natural convection on free housing surfaces (due to the limited surface area and low heat transfer coefficient for the convection process at the same time) etc. Although the contact resistances cannot be neglected while predicting the system performance, they will be omitted along this article as the goal is to show sensitivity of the design parameters, namely: thermal resistance of the insulating partitions, number of generators, heat sink thermal resistance and capacitance of an energy buffer.

MODELS OF APPLIED SUBSYSTEMS

There are several distinct elements of the housing that account for different physical phenomena. Those are: thermoelectric generator, heat sink, convective boundary condition on rotating shaft and bearing power loss. The models of each element are described below.

Thermoelectric Generator (TEG)

Different numerical models were tested and compared with the experiment, including finite element method (FEM), thermal network modeling (TNM) and analytic solutions. The experiment was organized as to keep constant ΔT across TEG while changing the load resistance and measuring the voltage output of the generator. The parameters describing thermoelectric generator model were assumed after Lineykin [27] and based on the data supplied by the module manufacturer. The energy generation rate was computed analytically on the basis of Rowe [6], assuming that the current involved phenomena are insignificant for small ΔT conversion. The ⟦Bi⟧_2 ⟦Te⟧_3 material parameters were considered temperature dependent. The results obtained analytically proved to be in good accordance with work of Jeagle [28] that additionally takes into account the generator geometry while solving the problem in Comsol Multiphysics. An Ansys solver was used for comparison. Some sample results are shown in Figure 4. The exact description of the performed experiment and numerical studies can be found in [29].

Heat Sink

A heat sink model and the convection boundary conditions were examined with the dimensional analysis and the models are described in [30]. Air properties change significantly with temperature which was introduced in the model equations. The model of isothermal u-channel fins of the heat sink is reported to agree well with the experimental figures for a Rayleigh number greater than 200, while beyond this limit giving the underestimated values of the heat transfer coefficient. The geometric shape of the heat sink was chosen because of this limitation as well as the assumptions of possible outline dimensions of the whole housing (Fig. 13).

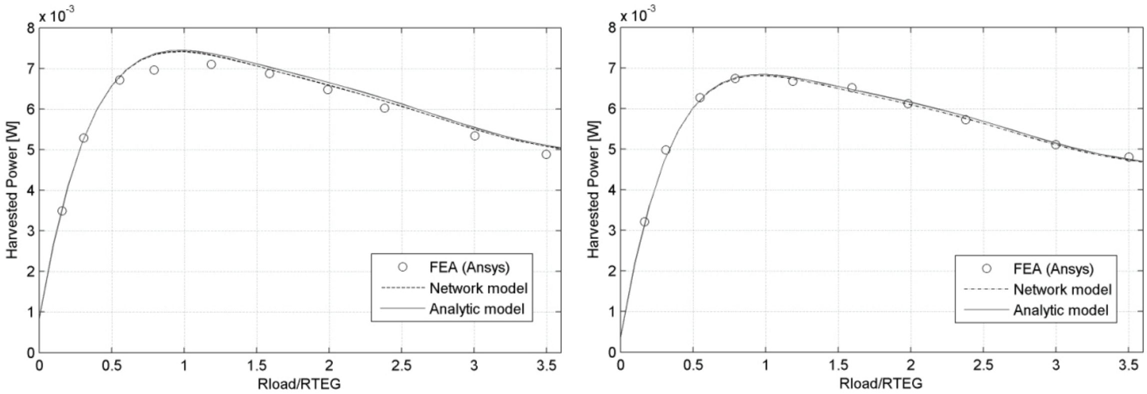

Figure 4: Numerical-experimental verification of the generator models ΔT=25K; left: no contact resistances included, right: thermal contacts included in the model; module consisted of 16 N-P pairs, module dimensions 8x8 [mm].

Rotating Shaft

The convective heat transfer from a horizontal rotating cylinder was described by Ozerdem [31]. The limitation of the model results from the rotating Reynolds number range (⟦Re⟧_r), however, for expected temperature range and rotating shaft speeds ⟦Re⟧_r it does not exceed the specified values. The thermal resistance of the rotating shaft can be described by Equation 1:

$$R_c = \frac{D_z}{0.318\left(\frac{\Omega D_Z^2 \rho(T)}{2\mu(T)}\right)^{0.571} k(T)A} \tag{1}$$

Bearing Power Loss

In comparison to the widely described and used Palmgren's model [32] the SKF bearing model [33] proved to be more precise when calculating the total frictional moment at a given load. The model was used together with the Walther viscosity model for grease lubricant.

$$M_{tot} = R_1 d_m^{1.97}[F_r + R_3 d_m^{3.5} n^2 + R_2 F_a] + S_1 d_m^{-0.12}[(F_r + S_3 d_m^{3.5} n^2)^{1.25} + S_2 F_a^{1.25}] \tag{2}$$

Circuit Analysis

Irrespective of the harvesting circuit operation being continuous or burst mode the energy neutral operation is guaranteed by maintaining the energy conservation law [34], that is:

$$E_0 + \eta \int_0^T [P_s(t) - P_c(t)]^+ dt - \int_0^T [P_c(t) - P_s(t)]^+ dt - \int_0^T P_{leak}(t) dt \geq 0 \ \forall T \in [0, \infty) \quad (3)$$

where []+ operation stands for: $[x]^+ = \begin{Bmatrix} x & x \geq 0 \\ 0 & x < 0 \end{Bmatrix}$

The first integral in the above equation represents the power that is being stored in the buffer during the passive sensor state, while the second integral represents the power consumed during the active sensor state. As the device is to operate continuously (no matter the duty cycle) assuming that the harvesting device (i.e. thermoelectric module) delivers the power at constant rate and the cycle time is so small that the influence of non-ideal buffer capacitance can be neglected, the time interval to be investigated can be limited to the single cycle duration and the above equation can be rewritten:

$$E_0 + \eta \int_0^{T_a} [P_s(t) - P_c(t)]^+ dt - \int_{T_a}^{T_c} [P_c(t) - P_s(t)]^+ dt \ \geq \ E_0 \ \ \forall T \in [0, T_c] \quad (4)$$

After n-cycles such that T_c n→∞ the operation is preserved to be neutral. However, the most power efficient operation does not allow the harvested energy to be shunted due to buffer overflow. The equation (Eq. 4) can be thus further reduced:

$$\eta \int_0^{T_s} [P_s(t) - P_c(t)]^+ dt = \int_{T_a}^{T_c} [P_c(t) - P_s(t)]^+ dt \ \ \forall T \in [0, T_c] \quad (5)$$

meaning that energy drop on the capacitor during the active cycle has to be compensated during the sleep time of the sensor which is satisfied when the P_s>P_c and by the long enough cycle T_C. As the energy drop of the capacitor is strictly connected with its voltage, as long as the voltage on the capacitor buffer can be restored during the passive cycle, the whole system maintains the energy neutral operation mode.

Continuous Operation Mode

Using the basic circuit algebra one can notice that the open circuit voltage on the single thermoelectric generator (circuit defined in Figure1) can be expressed as follows:

$$V_{OC} = \alpha \frac{I R_c R_{TEG}}{\left(R_{TEG} + R_{hs} + R_c + \frac{R_c(R_{TEG} + R_{hs})}{R_{part}}\right)} \quad (6)$$

It is obvious that if the R_{part} tends to zero, the heat flux bypasses the generator circuit and therefore there is no energy present for the smart bearing operation. If the thermal resistance of the insulation tends to infinity, the maximum power gained will be dependent on the power loss in the bearing, machine construction and heat sink resistance. The power capacity of the harvester for different load condition and wide speed range can be seen on Figure 5. Curves obtained are shaped mainly by the bearing power loss. The number of thermoelectric generators can be varied and result in harvester power density increase, however, the ratio of thermal resistance of the generators parallel/in-series connection and heat sink resistance plays a role of performance indicator. In this particular example with heat sink of fixed dimensions no more than 2 generators should be used (Figure 6) to observe any harvested power increase.

When the heat sink and thermoelectric generator compose an in-series circuit and the heat source can be treated as voltage source (isothermal), the optimal heat sink resistance is reported to be equal to the thermal resistance of the generator [6].

In the case of the system investigated, the smaller the heat sink resistance the more power is harvested (Figures 7 and 8). This is due to the fact that the heat source behavior can be represented by the current source rather than constant voltage source. Small heat sink resistance is also desirable as it influences the bearing temperature rise, which may influence the bearing lifespan for a heavy loaded bearing.

The heat sink resistance tends to increase for low thermal gradients that result from low bearing power losses. In such conditions R_a-number connected with convection on the heat sink boundaries approaches the limit and causes accuracy problems. In this condition the adopted model gives an evident increase in thermal resistance of the heat sink and lowers power gain. At the same time the thermal resistance of the rotating shaft decreases, what additionally influences the level of the power harvested.

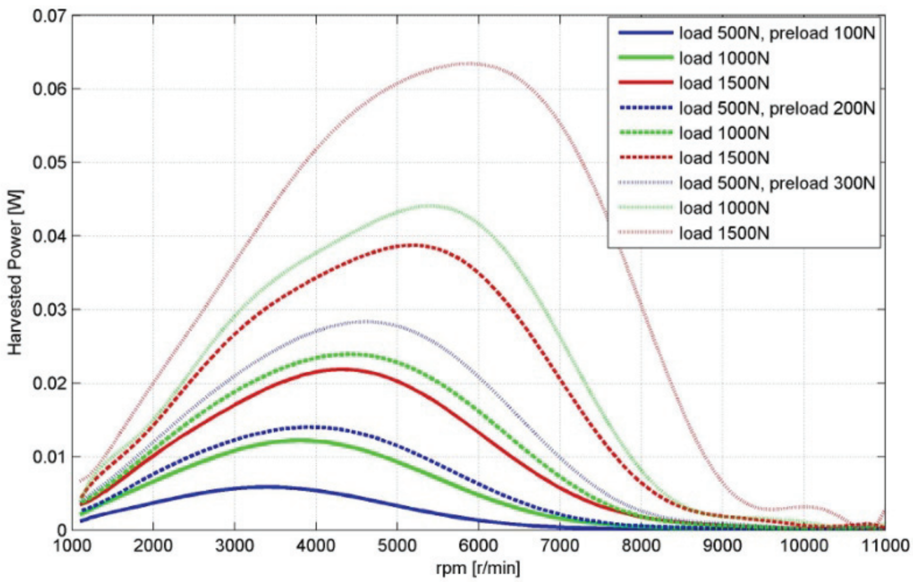

Figure 5: Power harvested as a function of rotating speed, preload and axial bearing load.

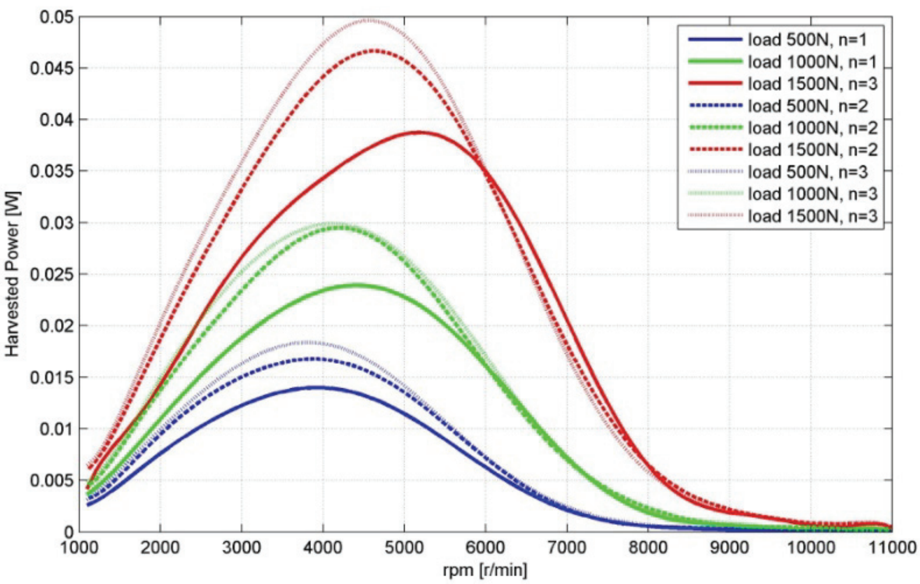

Figure 6: Influence of parallel connection of the generators; preload 200[N], number of generators alter from 1 to 3.

On the basis of the proposed model the trade-off between the thermal resistance of the insulating partition and the harvesting system performance can be determined (Figure 9). Moreover, the value is found to be independent of load conditions for constant shaft speed. The thermal resistance at the level of 5-7[K/W] is feasible and can be achieved in practical realization.

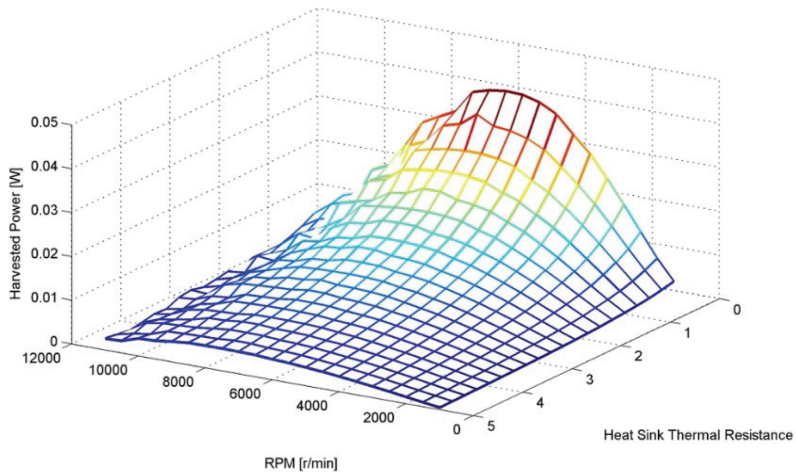

Figure 7: Influence of the heat sink thermal resistance to harvester power capacity; preload 200[N], load 500 [N]. Other load values make the relation analogous.

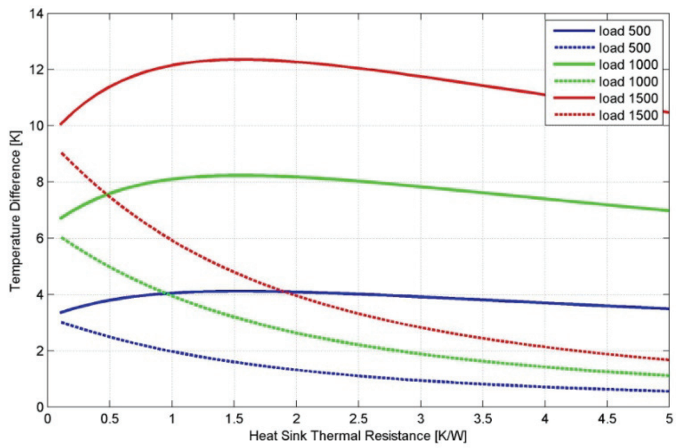

Figure 8: Maximum system temperature difference (solid) and the temperature difference on the generator (dashed), Sample curves for preload of 200N and rpm of 4000rpm;

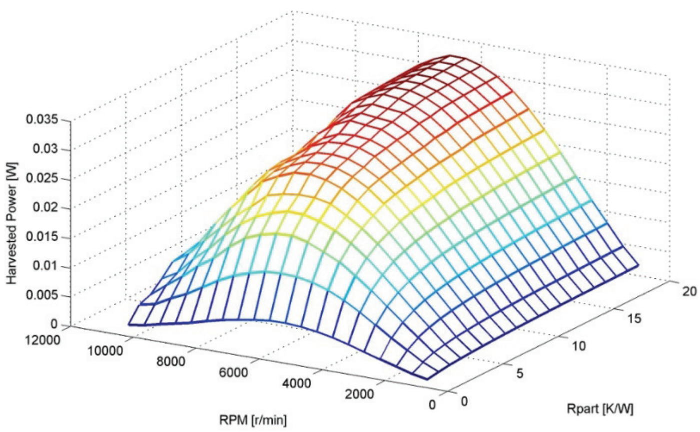

Figure 9: Influence of the insulating partition resistance on the harvester power capacity. Load 500N, preload 200N.

Burst Operation Mode

Any smart bearing operation will base on either continuous operation or burst mode composed of active and passive intervals. The section above shows the theoretical continuous power level that could have been harvested if only the load resistance was matched with the source (TEG). This assumption is usually not met and moreover, voltage levels have to be adjusted (DC conversion) and kept in regulation in order to successfully power more complex adjoined circuitries. The actual electronic devices for energy harvesting and energy management can rarely be represented by a simple set of switched resistances. Therefore, the following circuit topology is proposed for the whole energy harvesting circuit analysis (Figure 10). The circuit topology proposed by [18] assumes that the load can operate on arbitrary voltage, which in most cases is not true. The model referenced would be representative if the open circuit voltage of the generator would be at an appropriate level or the voltage step-up conversion would be nearly lossless. In the model proposed the current output of the harvester is an arbitrary function of voltage of the thermoelectric source under load condition. All following analyses were conducted with the use of a behavioral model of LTC3108 step-up converter and power management unit on assumption that the storage capacitor never reaches saturation i.e. it is charged or drives current to the load.

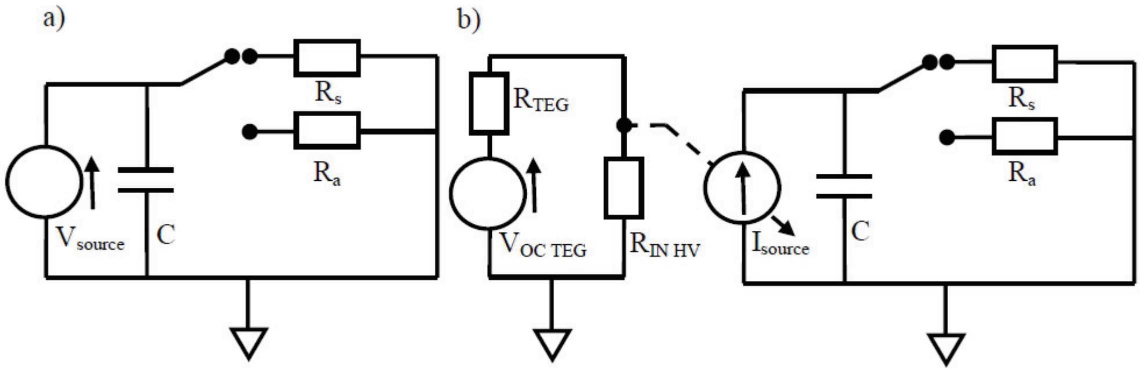

Figure 10: Left: Harvester topology by [9]; Right: Behavioral harvester model where $I_{source} = f(V_{Rin\ HV})$.

On the basis of findings described before it is assumed that the source voltage should never drop below a certain level, which could reasonably be 10% below the nominal value during the active cycle and the voltage should restore fully throughout the remaining part of the cycle:

$U_0 \geq U(t) \geq 0.9U_o$ - 10% voltage drop off acceptable, no saturation

$U(T_c) = U_0$ - full recuperation at the end of the sleep cycle

The voltage on storage capacitor can be expressed by the formula:

$$\frac{u(t)}{R} - I + \left(\frac{du(t)}{dt}\right)C = 0 \tag{7}$$

solving for the voltage:

$$u(t) = (u(0) - IR)e^{\frac{-t}{CR}} + IR \tag{8}$$

therefore: Maximum allowable burst time for energy neutral operation is:

$$T_a = R_a C log_e(\frac{10R_a I - 10u(0)}{10R_a I - 9U(0)}) \tag{9}$$

and required recuperation time for given T_a:

$$T_s = R_s C log_e\left(\frac{\left((R_s - R_a)e^{\frac{T_a}{R_a C}}\right)I - u(0)}{R_s e^{\frac{T_a}{R_a C}} I - u(0) R_s e^{\frac{T_a}{R_a C}}}\right) = R_s C log_e\left(\frac{U_{T_a} - R_s I}{u(0) - R_s I}\right) \tag{10}$$

which results in duty cycle of:

$$\frac{T_a}{T_s} = \frac{R_a log_e\left(\frac{10 R_a I - 10 u(0)}{10 R_a I - 9 u(0)}\right)}{R_s log_e\left(\frac{U_{T_a} - R_s I}{u(0) - R_s I}\right)} \tag{11}$$

The reciprocal relation of active and passive cycle duration time is determined by the open circuit voltage of the thermoelectric source.

Active burst duration is predominantly dependent on the capacitance while the constant power delivered by the harvester determines the recuperation time. The bigger the storage capacity the longer the allowable active state and the longer recuperation time are. For further analysis it is assumed that equivalent resistance in the active state is 100 [Ohm] and for passive or sleep state equals 100 [kOhm]. Active time of operation equals 50 [ms] and the cycle length results from the harvester output as well as capacitance of storage element (here ideal capacitor). The usable voltage output should be within the 2.97-3.3 [V] which means 10% permissible drop off. The above assures that during the active sensor time the near constant power will be driven to the sensor/load.

The power harvested in different operational conditions and conversion efficiencies were plotted in Figure 11 (top). It is important to notice the relation between the power generation rate with the minimum passive cycle length that was plotted on the same graph for clarity. Although the harvester energy level is capable to power the wireless sensor node, the efficiency of energy conversion is between 10-30% (Figure 11 bottom), which means the thermoelectric source has to be appropriately oversized. The higher the open circuit generator output is the smaller the difference in total cycle duration becomes. Lower conversion efficiency with respect to continuous operation mode (Figure 11, bottom) results from the fact that power harvested in this ideal case is always greater than with the use of any actual harvesting circuit due to the input impedance mismatch.

PROOF OF CONCEPT

The possibility of energy harvesting based on the power thermal loss in a bearing was experimentally verified. The experimental set up was organized as follows: the high-speed spindle drives a two point supported shaft, the third bearing on the shaft can be shifted giving only the radial load to the bearings. The bearings used are medium sized typical steel self-aligning ball bearings (bearing means a diameter of 46 mm). The power harvested was measured on the resistance matched for a single and in-series connection of up to 9 thermoelectric generators. The power output of the simple harvesting circuit was measured. For the sake of simplicity, after preliminary bearing model verification, the bearing was replaced by the controlled resistive heater and the power level harvested was measured. The bearing model verification was based on the measured temperature growth of the bearing and its housing during the work under constant load which was correlated to the thermal transient analysis of the detailed system model.

The power that could be harvested with respect to the theoretical power loss in a bearing is presented on Figure 12. The conversion efficiency drops as the bearing loss rises what agrees with the results of Section 4.

The power level available for burst operation mode is maintained at the proper level for a typical sensor and wireless transmission even for low power losses in a bearing. At the same time the total cycle length does not exceed 30 seconds, which means that the measurements can be taken twice a minute in the worst case scenario. That is sufficient in case of the bearing monitoring installations.

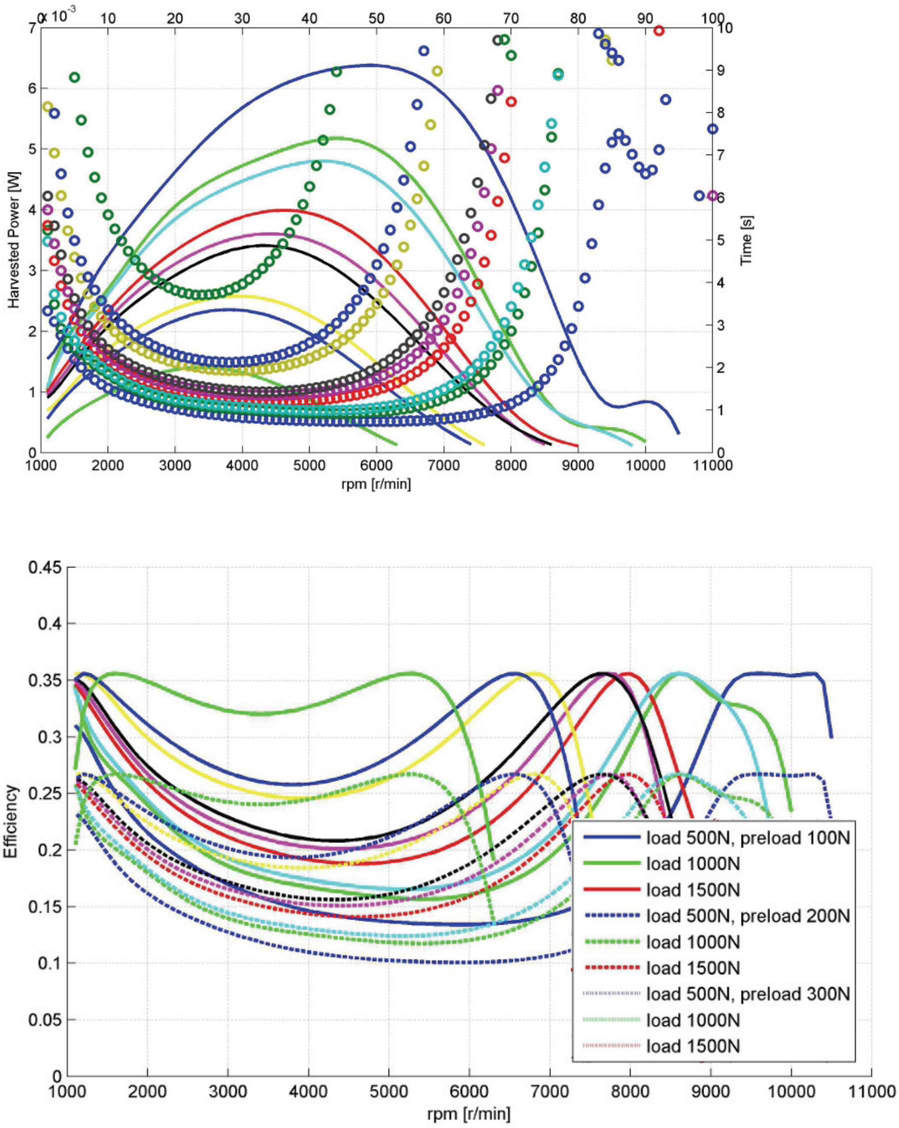

Figure 11: Top: Power harvested with respect to the rpm for different load values (solid);Recuperation time needed for T_a=0.05[s] (circles); Bottom: Energy conversion efficiency with respect to the matched resistance case in continuous operation mode.

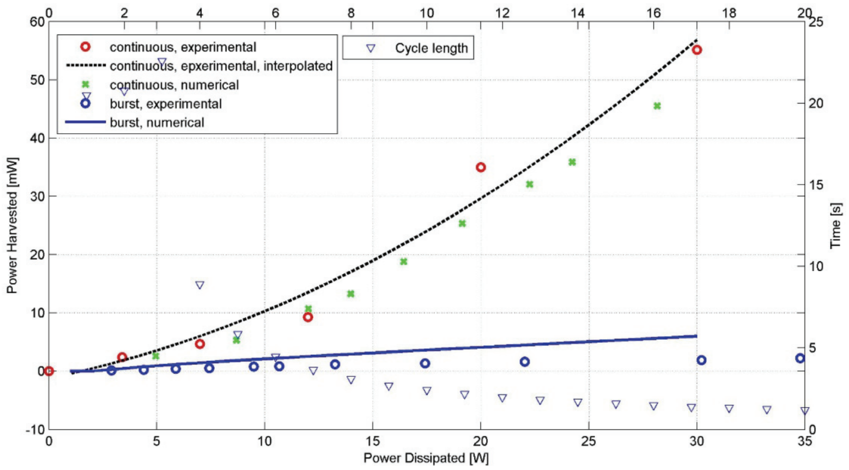

Figure 12: Theoretical power level harvested with respect to the power dissipated in a bearing during the continuous operation mode (red circles) and burst mode 0.05[s] (blue circles); The minimum cycle length (triangles, right axis) measured experimentally.

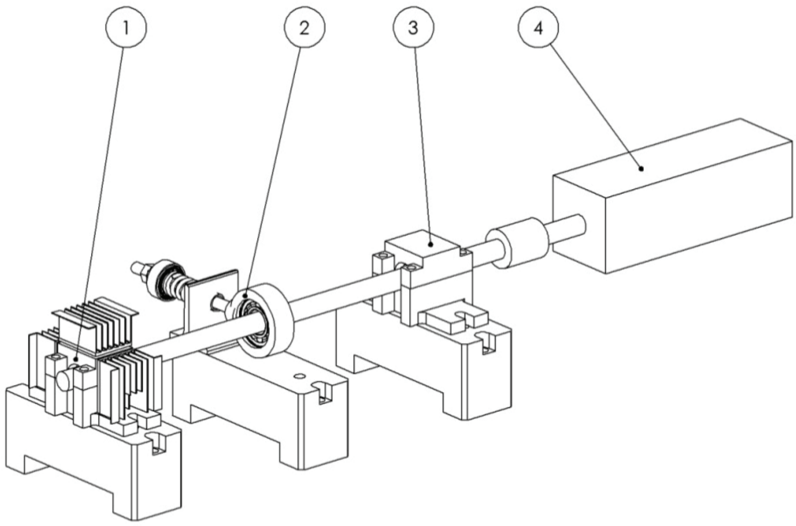

Figure 13: The experimental setup: 1) the bearing housing equipped with thermoelectric modules, 2) radial load excitation, 3) bearing housing, 4) high speed electric spindle.

CONCLUSION

The theoretical considerations lead to the conclusion that a standard medium sized bearing can be a sufficient source of power to be harvested for a continuous or cyclic operation of a measurement node. First of all the power capacity of a harvester circuit strongly depends on the bearing preload (that can also be a design parameter). For a system topology it was considered that heat sink thermal resistance is the second most important parameter. The thermoelectric generators can be stacked in series or put in parallel giving another 20% of energy on average. It was possible to find a feasible value of the insulating partition, however, it should be noticed that introducing thermal insulation may decrease the bearing node stiffness.

REFERENCES

[1] Chalasani, S. and Conrad, J. M., 2008. A survey of energy harvesting sources for embedded systems. *IEEE In Southeastcon*, IEEE (2008), pp. 442-47.

[2] Rabaey, J., Roundy, S. and Wright, P. K., July 2003. A Study of Low Level Vibrations as a Power Source for Wireless Sensor Nodes. *Computer Communications* 26(11), pp. 1131-144.

[3] Calhoun, B. H., Chandrakasan, A. P., Cho, S., Daly, D. C., Finchelstein, D. F., Verma, N., Wang, A. and Wentzloff, D. D., 2005. Design Considerations for Ultra-Low Energy Wireless Microsensor Nodes. *IEEE Trans on Computers*, June 2005, 54(6), pp. 727–40.

[4] Dereux, R., Inman, D. J., Simmers, G. E. and Sodano, H. A., 2004. Power Harvesting Using Thermal Gradients for Recharging Batteries. *Proceedings of 15th International Conference on Adaptive Structures and Technologies*, Bar Harbor, ME, October 25-27 2004.

[5] Dereux, R., Inman, D. J., Simmers, G. E. and Sodano, H. A., 2007. Recharging Batteries using Energy Harvested from Thermal Gradients. *Journal of Intelligent Material Systems and Structures*, January 1, 2007, 18, pp. 3-10.

[6] Rowe, D. M., 1995. *CRC Handbook of Thermoelectrics*. CRC-Press; 1st edition.

[7] Rabaey, J., Roundy, S. and Wright, P. K., 2003. A study of low level vibrations as a power source for wireless sensor nodes. *Computer communications* 26(11), pp. 1131-144.

[8] Williams, C. B., Yates, R. B., 1995. Analysis of a micro-electric generator for Microsystems. *Proceedings of the Transducers 95/Eurosensors* IX, pp. 369–72.

[9] Beeby, S. P., Tudor, M. J. and White N. M., 2006. Energy harvesting vibration sources for Microsystems. *Applications. Meas. Sci. Tech.* 17, pp. 175–95.

[10] Bottner, H. et al., 2004. New Thermoelectric Components Using Microsystem Technologies. *Journal of Microelectromechanical Systems*, June 2004, 13(3), pp. 414–20.

[11] Fleurial, J. P., Giauque, P. H., Herman, J. A., Nicolet, M. A., Shakkottai, P., Smart and M., Snyder, G. J., 2000. Miniaturized thermoelectric power sources. *Aip Conference Proceedings, Issue: January, Publisher: Aip*, 504, pp. 1500-507.

[12] Min, G. and Rowe, D. M., June 2007. Conversion efficiency of thermoelectric combustion systems. *IEEE Trans. Energy Convers.* 22(2), pp. 528–34.

[13] Starner, T., 1996. Human-powered wearable computing. *IBM Systems Journal* 35(3), pp. 618–29.

[14] Leonov, V. et al., May 2007. Thermoelectric Converters of Human Warmth for Self-Powered Wireless Sensor Nodes. *IEEE Sensors Journal* 7(5), pp. 650-57.

[15] Fiorini, P., Gyselinckx, B., Leonov, V., Ryckaert, J., Van Hoof, C. and Yazicioglu, R., 2005. Human++: Autonomous wireless sensors for body area networks. *Proc. Custom Integrated Circuit Conf. (CICC'05)*, pp.13–19.

[16] Mitcheson, P.D., 2010. Energy harvesting for human wearable and implantable bio-sensors. *Engineering in Medicine and Biology Society (EMBC)*, 2010 Annual International Conference of the IEEE, pp. 3432-436.

[17] Codrea, C., Lucas, N., Mateu, L., Pollak, M. and Spies, P., 2006. Energy harvesting for wireless communication systems using thermogenerators. *XXI. Conference on Design of Circuits and Integrated Systems (DCIS)*, Barcelona, Spain, November 22–24 2006.

[18] Dalessando, D. and Ortiz, A. et. al., 2007. Energy Harvester Power Management for Wireless Sensor Networks. *ACM Transactions on Embedded Computing Systems (TECS)* 6(4).

[19] Hsu, J., Kansal, A., Srivastava and V., Raghunathan., 2006. Harvesting Aware Power Management for Sensor Networks. *ACM/IEEE Design and Automation Conference*, San Francisco, CA Jul 24-28, 2006, pp. 651-56.

[20] Mims, B. L. et al., 1961. *Thermoelectric Cooling Assembly*, Patent US 30,097,027.

[21] Fumito, O. and Tadashi, R., 1983. *Cooling Device of Static Pressure Bearing*, Patent JP 58131430.

[22] Minoru, T., 2004. *Rolling Bearing,* Patent JP 2004332859.

[23] Kenji, N., 2008. *Rotatably Supporting Device With Generating Set*, Patent JPJP 2008223843.

[24] Micropelt GmbH, 2011. [online] Available at: http://www.micropelt.com

[25] Nextreme Thermal Solutions, 2011. Inc., [online] Available at: http://www.nextreme.com

[26] Sentient Corporation, 2011. [online] Available at: http://www.sentientscience.com

[27] Lineykin, S. and Ben-Yaakov, S., 2007. Modeling and Analysis of Thermoelectric Modules. *Industry Applications, IEEE Transactions*, March- April 2007 43(2), pp. 505–12.

[28] Jeagle, M., 2008. Multiphysics Simulation of Thermoelectric Systems – Modeling of Peltier-Cooling and Thermoelectric Generation. *Comsol Conference Proceedings*, 2008, Hannover.

[29] Lubieniecki, M. and Uhl, T., 2011. Thermoelectric energy harvester for a smart bearing concept. *Proceedings of IFFToM World Congress 2011*, Guanajuato, Mexico.

[30] Kreith, F., 2000. *CRC Handbook of Thermal Engineering*, CRC Press.

[31] Ozerdem, B., 2000. Measurement of convective heat transfer coefficient for a horizontal cylinder rotating in quiescent air. *International Communications in Heat and Mass Transfer* 27(3), pp. 389-95.

[32] Palmgren, A. *Ball and Rolling Bearing Engineering.* 3rd edn. SKF Industries, Philadelphia.

[33] SKF General Catalogue, 2003. *Catalogue 5000E*, June 2003.

[34] Hsu, J., Kansal, A., Srivastava, M. and Zahedi, S., 2007. Power Management in Energy Harvesting Sensor Networks. *ACM Transactions on Embedded Computing Systems (TECS)* 6(4).

STATIC-AEROELASTIC OPTIMIZATION OF SURFACE ACTUATED VARIABLE-CAMBER PIEZOCOMPOSITE MORPHING WINGS

O. Bilgen*, S. Barbarino & M. I. Friswell

College of Engineering, Swansea University, Singleton Park, Swansea, SA2 8PP, United Kingdom

*Corresponding author. E-mail: o.bilgen@swansea.ac.uk

ABSTRACT

A theoretical static-aeroelastic modeling and optimization of a variable-camber morphing airfoil that employs surface-induced forces via smart material actuators (instead of conventional internal and lumped mechanisms) is presented. The structural parameters are determined using a set of design criteria optimized via a Genetic Algorithm. The optimization is conducted to achieve maximum change-in-lift-coefficient-per-excitation-voltage. A coupled treatment of the fluid-structure interaction is employed which allows the realization of a design that is not only feasible in a bench top experiment, but that can also sustain aerodynamic loads in the wind tunnel.

INTRODUCTION

Smooth control surface designs have been a research interest since the beginning of modern aviation, the first controlled, powered and heavier-than-air flight by the Wright Brothers in 1903. During the past few decades, smart materials have been proposed and tested successfully to control the shape of smooth aerodynamic surfaces. There are several benefits of using shape control via solid-state smart materials over the discrete trailing-edge control using conventional control surfaces in aircraft. However, for smart material actuated morphing devices, the challenge is found in operating a relatively compliant structure (desirable for smart material actuators) at high dynamic pressures to extract controlling forces. Establishing a wing configuration that is stiff enough to prevent flutter and divergence, but compliant enough to allow the range of available motion is the central challenge in developing a morphing wing with smart materials.

The rapid development and the reduced cost of small electronics in the last decade led to the interest in using piezoelectric materials in small unmanned (and/or remotely piloted) fixed- and rotary- wing and ducted-fan aircraft. The 2002 Virginia Tech Morphing Wing Design Team (Eggleston et al. [1]) experimented with the use of piezoceramic materials, shape-memory alloys, and conventional servomotors in small unmanned aircraft.

Wind tunnel testing showed the feasibility of the smart material systems. Barrett et al. [2] employed piezoelectric elements along with elastic elements to magnify control deflections and forces in aerodynamic surfaces. Vos et al. [3,4] conducted research to improve the Post-Buckled-Precompression concept for aerodynamic applications. Roll control authority was increased on a 1.4 m span unmanned air vehicle. Kim and Han [5,6] designed and fabricated a flapping wing by using a graphite/epoxy composite material and a Macro-Fiber Composite (MFC) actuator. A twenty percent increase in lift was achieved by changing the camber of the wing at different stages of flapping motion. Bilgen et al. [7] presented an application for piezocomposite actuators on a 0.76 meter wingspan morphing wing air vehicle. Adequate roll control authority was demonstrated in the wind tunnel as well as in flight.

Bilgen et al. presented static flow vectoring via an MFC actuated thin bimorph variable-camber airfoil [8], and an MFC actuated cascading bimorph variable-camber airfoil [9,10]. Wind tunnel results and analytical evaluation of the airfoils showed comparable effectiveness to conventional actuation systems and no adverse deformation due to aerodynamic loading. Paradies et al. [11] implemented MFCs as actuators into an active composite wing. A scaled prototype wing was manufactured and models were validated with static and preliminary dynamic tests of the prototype wing. Wickramasinghe et al. [12] presented the design and verification of a smart wing for an unmanned aerial vehicle. The proposed smart wing structure consisted of a composite spar and ailerons that had bimorph active ribs with MFC actuators. The 2010 Virginia Tech Wing Morphing Design Team [13-15], of the Department of Mechanical Engineering) developed a completely servo-less, wind-tunnel and flight tested remotely piloted aircraft. The team designed and fabricated lightweight control surfaces and the necessary driving high-voltage DC-DC converters, culminating in a landmark first flight of the completely MFC controlled aircraft on April 29, 2010.

This vehicle became the first fully MFC controlled, flight tested aircraft. It is also known to be the first fully solid-state piezoelectric controlled, non-tethered, flight tested fixed-wing aircraft.

The motivation for the current research is to model and optimize the static-aeroelastic effectiveness of a variable-camber morphing airfoil. The proposed concept employs piezoceramic materials that provide the actuation forces and moments, and they also create the surface of the airfoil. The research focuses on 1) fundamental static-aeroelastic characteristics, quantified in terms of conventional two-dimensional aerodynamic coefficients and 2) optimization of the static-aeroelastic response.

STATIC-AEROELASTIC ANALYSIS

The high structural deflection requirement (of aerodynamic applications) creates the need for semi-solid-state mechanisms and distributed boundary conditions to be employed along with piezoelectric actuation.

A Macro-Fiber Composite actuator is chosen for actuation in the proposed concept. The MFC actuator was developed at NASA Langley Research Center [16,17] and offers structural flexibility and high actuation authority. The in-plane poling and subsequent voltage actuation allows the MFC to utilize the *33* piezoelectric effect, which is higher than the *31* effect used by traditional PZT actuators with through-the-thickness poling [18].

A piezocomposite airfoil was previously designed and evaluated in Bilgen et al. [19] and it serves as a baseline to the design proposed in this paper. The baseline design employs two active patches in the top and bottom surfaces of the airfoil which are pinned at the trailing-edge. These active surfaces are chosen to be MFC actuated bimorphs. A compliant parallelogram (box structure) is used to create the desired boundary conditions to the leading section of the curved bimorph surfaces. Wind tunnel experiments were conducted previously to compare the prototype variable-camber airfoil to other similar (in shape) fixed-camber airfoils.

The lift and drag measurements were conducted at 15 m/s and at a chord Reynolds number of 127,000. A lift curve slope of 0.144 per-degree was measured, which exceeds the NACA 0009 lift slope (0.083 per-degree) by 72%. The results showed the clear advantage of the lift generation by coupled camber-AOA change induced by voltage. The variable-camber airfoil produced a maximum lift-to-drag ratio (*L/D)* of 13.4 at 1500 V (AOA=5.78°) and an *L/D* ratio of -11.2 at -1500 V (AOA=-5.20°). The NACA 0009 airfoil produced a maximum *L/D* ratio of 16.3 at AOA=4.21° and an *L/D* ratio of -12.3 at AOA=-4.97°. The variable-camber airfoil has comparable *L/D* performance when compared to the fixed-camber airfoils with similar thickness. A relatively high experimental drag was observed for the morphing airfoil due to its blunt (elliptical) leading-edge (LE) when compared to the LE of NACA 0009 airfoil. The baseline variable-camber airfoil, described above, did not have a continuous surface as desired due to in-house fabrication limitations and this is one of the issues addressed by the current paper. In the prototype of the baseline design, the gap between the solid leading-edge and the variable-camber trailing-section (with variable-length) was covered using a flexible strip of plastic which allowed the active bimorph surface to slide forward and backwards with respect to the fixed LE geometry. Another issue is that the solid-state compliant box mechanism (formed by four "live" hinges) introduced extra weight and complexity due to limited in-house fabrication capabilities.

In the current concept, illustrated in Figure 1, the authors propose a continuous airfoil surface and a set of "simpler" boundary conditions to remedy these problems. The continuity in the airfoil surface is achieved by using a single substrate that wraps around the airfoil shape. This substrate forms the surface of the airfoil and it serves as the host material for the two cascading bimorph actuators. This airfoil is attached to a three-dimensional spar structure (e.g. a rectangular spar box with spanwise taper) at two locations. In Figure 1, the locations of these two boundary conditions (*Pin1* and *Pin2*) are exaggerated to aid visibility.

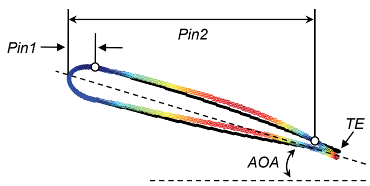

Figure 1: A simplified illustration of the variable-camber airfoil design. Actuated and non-actuated states are shown.

In Figure 1, the label “AOA” represents the geometric angle-of-attack. The boundary conditions in the design are pinned-pinned (similar to a simply-supported beam) for ease of implementation; however one can choose the second boundary condition (*Pin2*) as a slider (allowing motion in the chordwise axis and restricting motion in the lift axis). A pair of pinned-pinned boundary conditions theoretically creates a nonlinear displacement response but this is not a dominant effect in an actual implementation of the airfoil (with desirable aeroelastic characteristics). Starting with the baseline design, multiple configurations can be generated by changing the location of the pins. The two extreme configurations occur when: 1) the first pin is moved to the LE and the second pin is moved to the trailing-edge (TE) which is similar to a sail or a simply-supported beam; 2) both the first and second pins are moved to the leading-edge, hence the airfoil becomes equivalent to a cantilevered beam. The airfoil examined here (without electrical excitation and aerodynamic loading) has a profile that is similar to a NACA 0009 airfoil. The TE is formed by pinning the two bimorph surfaces and it is assumed to have a finite thickness of 0.05% chord.

STATIC-AEROELASTIC ANALYSIS METHOD

A thin shell-like morphing airfoil (with reasonable chordwise stiffness and displacement output) is possible with an MFC actuator given that the boundary conditions and structural features are favorable. Therefore, the support system for the variable-camber device is determined here using the static-aeroelastic model. A MATLAB [20] based program is used to solve the static fluid-structure interaction (FSI) problem by iterating between a panel method software XFOIL [21,22], and a finite element code ANSYS [23].

Before the iteration starts, the non-aero-loaded airfoil shape is analyzed in XFOIL to initialize the FSI. XFOIL calculates lift and drag coefficients and the pressure distribution and the program enters the iteration loop. First, the pressure distribution is applied to the airfoil geometry in ANSYS which calculates the aero-loaded (deformed) airfoil shape. Second, the deformed airfoil shape is analyzed in XFOIL to calculate change in the lift and drag due to the change in pressure induced deformation. These two steps are continued until no change is observed in the parameters of interest (i.e. deformation and aerodynamic coefficients). Due to the static nature of the problem, the solution converges after a few iterations. Note that the dynamic effects are known to be negligible (and ignored in the analysis) because of previous experimental observations. The analysis in this paper considers only chordwise distribution of aerodynamic loads and structural deformations.

For the XFOIL simulations, a 0.07% (of the mean velocity) turbulence level is assumed, which is consistent with the turbulence level in a typical wind tunnel. It must be noted that XFOIL predictions for AOA above the maximum lift angle are not accurate . Due to the limitation of the deflection of the piezocomposite bimorph, the XFOIL analysis presented here (for a 9.0% thick airfoil) never passes beyond this AOA. Approximately 400 panels are used in XFOIL to achieve numerical convergence for the airfoils considered in this section. As reported in the literature, XFOIL predicts slightly higher lift coefficients and lower drag coefficients when compared to experimental results; therefore the predictions must be viewed as an upper limit to the actual lift coefficient and lift-to-drag ratio.

The passive material in the airfoil is modeled as a homogeneous 2D area mesh using PLANE82 high-order quadrilateral (Q8) type element in ANSYS.

The MFC actuator is modeled as a monolithic piezoelectric layer using a homogeneous 2D area mesh consisting of PLANE223 high-order quadrilateral (Q8) coupled-field elements. The plane element type is chosen (instead of the beam element type) because of the dense, non-uniform and distributed loading at the leading-edge with significant components in the in-plane direction as well as the out-of-plane direction. An experimental evaluation of the peak-to-peak deflection-voltage relationship (deduced from previous data) is used to determine the material properties of the MFC actuator in the finite-element (FE) model. Approximately 20,000 elements are used to ensure convergence of the finite element model for all airfoil models evaluated in the study. The number of elements chosen is relatively high to accommodate the highly non-uniform pressure distribution data from XFOIL. Figure 2 shows an example of the finite element model used in the study. There is a high concentration of aerodynamic loading (shown with arrows normal to the surface) at the leading-edge. Note that most of the features on this figure are exaggerated to aid the visibility. In reality, the thickness of the substrate and the PZT layer is very small compared to the maximum thickness of the airfoil.

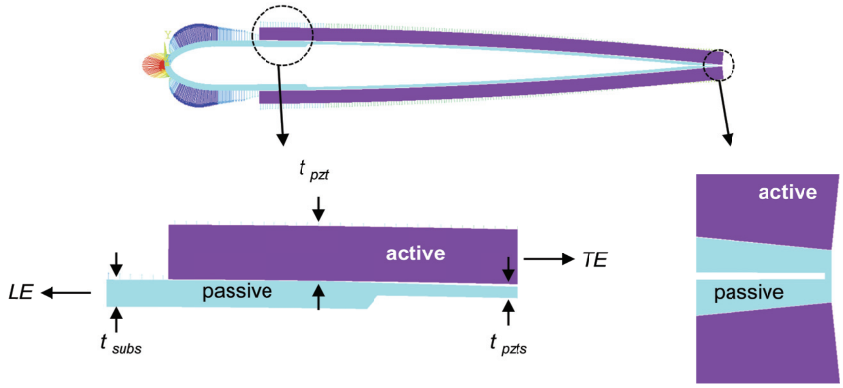

Figure 2: Example of the finite element model used in the parametric study.

The figure shows the whole airfoil and zoomed images of important areas. In addition to the effect of the location of boundary conditions, the substrate thickness is an important parameter assuming that the PZT layer thickness (t_{pzt}) is fixed. The MFC actuator has a fixed thickness of 300 µm. The leading section of the airfoil has a constant thickness of t_{subs}. This "stiff" substrate overlaps with a fraction of the active trailing section. This substrate is then reduced to a thickness of t_{pzts}. This arrangement has several advantages. First, the non-uniform aerodynamic pressure distribution has a much higher magnitude close to the LE. A thick (and therefore stiff) substrate is required around the LE. At the trailing section, the laminate formed by the active material and a thinner substrate has enough bending stiffness to carry aerodynamic loads. Another important reason for the stepped thickness is that the "optimum" leading section substrate thickness is more likely to be different than the "optimum" substrate thickness for a bimorph (or unimorph) actuator. These are expected results; however since these structural parameters are coupled with the aerodynamic state, a parametric analysis is presented next to understand the coupled behavior.

PARAMETRIC STUDY

A parametric study is conducted to understand 1) the sensitivity of aerodynamic output to the structural parameters and 2) the domain of structural parameters that result in feasible solutions. The main parameters of interest are 1) *Pin1* location, 2) *Pin2* location, 3) leading section substrate thickness, and 4) thickness of the substrate under the active material. The substrate material is assumed to be stainless-steel with a Young's modulus of 200 GPa. The first pin is fixed in both axes; in contrast the second pin is restrained only in the lift axis. The top MFC actuator is subjected to an effective +1500 V and the bottom MFC actuator is subjected to an effective -500 V.

Note that the actual applied electric field is adjusted so that the unimorph FE model has a matching transverse displacement response to the actual bimorph device. In addition, the electric field is also corrected for the fact that the *33* mode interdigitated MFC actuator is modeled as a *31* monolithic piezoceramic. First, the effects of pin locations on the lift coefficient and lift-to-drag ratio are investigated. The parametric analysis showed that placing *Pin1* close to the leading-edge results in the highest lift output.

The highest lift coefficient and lift-to-drag ratio are achieved for the configurations where *Pin2* is located between the leading-edge and mid-chord. Next, the effect of the leading section substrate thickness on the lift coefficient and lift-to-drag ratio are investigated. The analysis showed that using a leading section thickness in the range of 50.8 µm to 178 µm results in the highest aerodynamic output. Finally, the effects of the trailing section substrate thickness and *Pin2* location on the lift coefficient and lift-to-drag ratio are investigated. A fixed leading section substrate thickness (t_{subs} = 50.8 µm) and a fixed *Pin1* location (*Pin1* = 10%*c*) are assumed. Figure 3 shows the piezoelectric induced angle-of-attack of the variable camber airfoil (under aerodynamic loading).

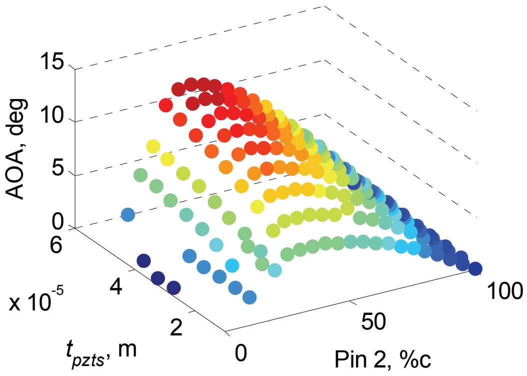

Figure 3: Theoretical angle-of-attack for the proposed airfoil subjected to a free-stream velocity of 15 m/s.

Figure 4 presents the lift coefficient and lift-to-drag ratio for the proposed airfoil subjected to a free-stream velocity of 15 m/s. Note that a fixed leading section substrate thickness and a fixed *Pin1* location are assumed.

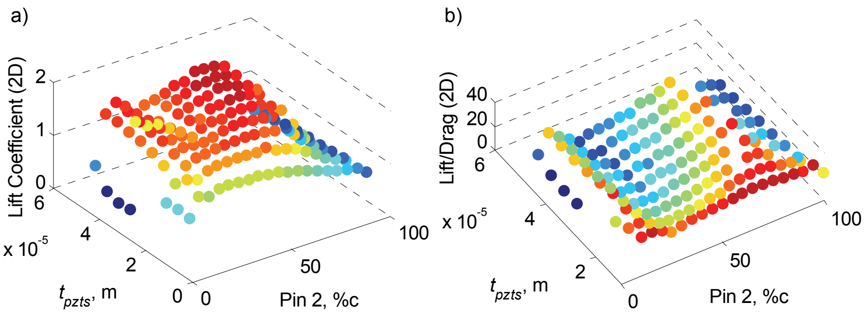

Figure 4: Theoretical (2D) a) lift coefficient and b) lift-to-drag ratio for proposed airfoil subjected to a free-stream velocity of 15 m/s. $Re_{chord} = 1.27 \times 10^5$.

The analysis shows that placing *Pin2* at or around 60%*c* and using a trailing section thickness of approximately 50.8 µm results in the highest lift output. Note that this is not the optimum solution (but a local-optimum) because the parametric study assumes other parameters as constants such as the *Pin1* location and leading section substrate thickness.

OPTIMIZATION STUDY

The approach to determine and optimize the internal passive structure of the variable-camber morphing wing is based on a Genetic Algorithm [24]. Genetic algorithms belong to the larger class of evolutionary algorithms, which generate solutions to optimization problems using techniques inspired by natural evolution, such as inheritance, mutation, selection, and crossover. Each individual (or configuration to be estimated) is characterized by its own "genetic code" or chromosome, generated as a set of values selected within suitable intervals for each optimization parameter. Some intelligence is integrated by the authors within the Genetic Algorithm in terms of parameters available to the optimization process, together with their degrees of freedom and constraints (range of variation for each parameter), to fulfill the proposed design criteria and achieve a suitable final structure.

The optimization process, illustrated in Figure 5, starts with the creation of a trial airfoil structure for each individual according to the genetic methodology, based on the random selection of a value, within the established range, for each parameter being part of the optimization.

The proposed static-aeroelastic analysis method, able to solve the static fluid-structure interaction problem, is then executed for each individual of a generation of individuals. The performance is estimated by the fitness function, quantified in terms of the change-in-lift-per-excitation-voltage ($F = \Delta Cl \;/\; \Delta V$) of the morphing wing. To maximize the objective function, the typical steps of genetic evolutionary algorithms are applied. Selection, cross-over and mutation operators are all executed to create a new generation starting from the best fit individuals of the previous one. Convergence towards the approximate global optima is achieved when a steady state is reached in the maximum fitness function (no more improvements, generation after generation, on the best fit individual). One must observe that the optimal solution is not only capable of maximum performance, according to the selected fitness function, but also satisfies the FSI problem. The structural solutions which are not capable of carrying aerodynamic loads are discarded. Figure 6 shows an example of the convergence of the maximum and average fitness for each generation.

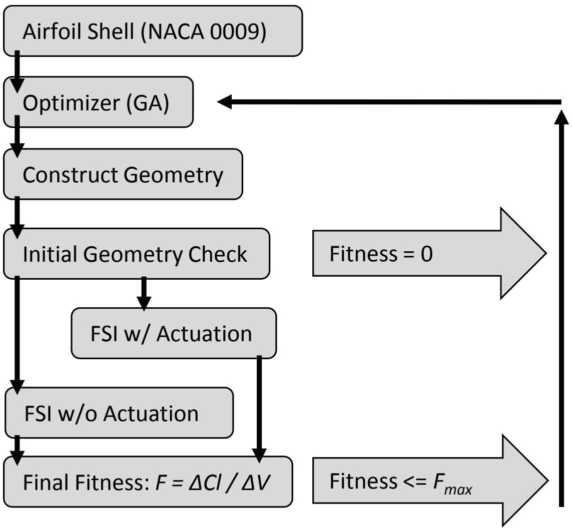

Figure 5: Genetic Algorithm optimization process.

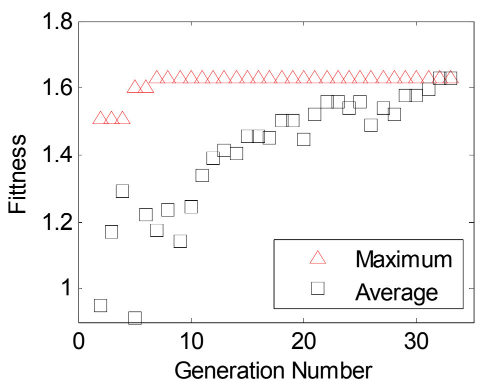

Figure 6: Convergence of fitness for the proposed airfoil at a free-stream velocity of 15 m/s. $Re_{chord} = 1.27x10^5$.

After the optimization is complete, the chromosomes of the best fit individuals are examined. The optimum structural parameters (for a free-stream velocity of 15 m/s) are: 1) *Pin1* location, *Pin1* = 0%*c*; *Pin2* location, *Pin2* = 50%*c*; 3) leading-section substrate thickness, t_{subs} = 178 µm; and 4) trailing-section substrate thickness, t_{pzts} = 50.8 µm. Figure 7 shows the operational response of the airfoil at 15 and 45 m/s free-stream velocities.

In the figure, two velocities are presented. At 15 m/s, the dynamic pressure is relatively low; therefore the flow induced deformations are small. Similar deformations are observed at 30 m/s (not shown here). At high dynamic pressures (i.e. 45 m/s) the flow induced deformations are significant. It is important to note that the identified optimum structural parameters apply to a specific range of dynamic pressures and when this range is exceeded, the structure is no longer "optimized" and the assumption of static-aeroelastic behavior will be invalid (i.e. at 45 m/s). Figure 8 shows three operational states of the optimum configuration. Note that the *x* and *y* axes are equally scaled.

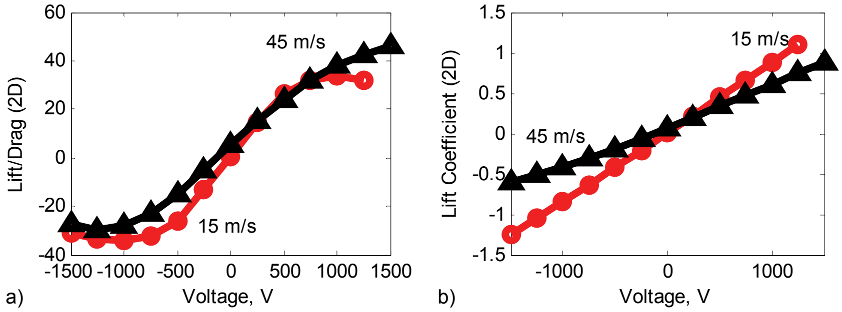

Figure 7: Theoretical (2D) static-aeroelastic response: a) lift coefficient and b) lift-to-drag ratio of the variable-camber airfoil to piezoelectric excitation voltage.

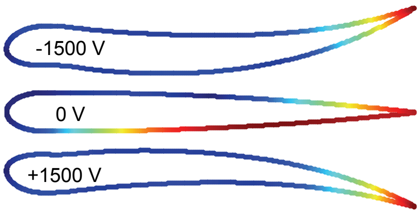

Figure 8: Operational states of the airfoil that corresponds to the highest change in lift coefficient output subjected to a free-stream velocity of 15 m/s. $Re_{chord} = 1.27 \times 10^5$.

CONCLUSIONS

This article presents the static-aeroelastic modeling and optimization of a variable-camber airfoil that employs surface-induced deformations instead of the more typical internal actuation.

The coupled treatment of the fluid-structure interaction allows the realization of a design that is not only feasible in a bench top experiment, but that can also sustain large aerodynamic loads. The effects of four important structural parameters are studied to achieve the highest possible lift coefficient. The highest lift coefficient change is achieved by the optimized configuration with the following parameters: 1) *Pin1* location at 0%*c*, 2) *Pin2* location at 50%*c*, 3) leading section substrate thickness of 178 µm and 4) trailing section thickness of 50.8 µm. The substrate material is assumed to be a stainless-steel, and the active material electromechanical properties are equivalent to the Macro-Fiber Composite actuator. The results are presented for a free-stream velocity of 15 m/s, chord Reynolds number of 127,000 and an assumed turbulence level of 0.07%. In comparison to the baseline variable-camber airfoil (with solid-state internal hinges and 9.0% chord thickness), the proposed airfoil (with a pinned and a pinned-sliding boundary conditions) produces a higher lift coefficient and a slightly lower lift-to-drag ratio. The advantages of the new concept are: 1) it has a continuous surface and 2) it requires more practical internal boundary conditions when compared to the baseline design.

ACKNOWLEDGMENTS

This work is supported by the European Research Council grant number 247045 entitled "Optimisation of Multi-scale Structures with Applications to Morphing Aircraft".

REFERENCES

[1] Eggleston, G., Hutchison, C., Johnston, C., Koch, B., Wargo, G., Williams, K. 2002. "Morphing Aircraft Design Team," Virginia Tech Aerospace Engineering Senior Design Project.

[2] Barrett, R. M., Vos, R., Tiso, P., De Breuker, R. 2005. "Post-Buckled Precompressed (PBP) Actuators: Enhancing VTOL Autonomous High Speed MAVs," 46th AIAA/ASME/ASCE/AHS/ASC Structure, Structural Dynamics & Materials Conference, AIAA 2005-2113, Austin, Texas, Apr. 18-21, 2005.

[3] Vos, R., De Breuker, R., Barrett, R., Tiso, P. 2007. "Morphing Wing Flight Control via Postbuckled Precompressed Piezoelectric Actuators," *Journal of Aircraft*, **44**(4).

[4] Vos, R., Barrett, R., Zehr, D. 2008. "Magnification of Work Output in PBP Class Actuators Using Buckling/Converse Buckling Techniques," 49th AIAA/ASME/ASCE/AHS/ASC Structures, Structural Dynamics, and Materials Conference, Schaumburg, IL, AIAA 2008-1705.

[5] Kim, D. K. and Han, J. H., 2006, "Smart Flapping Wing using Macro-Fiber Composite Actuators," Proceedings of SPIE Vol. 6173 61730F, pp. 1-9.

[6] Kim, D. K., Han, J. H., Kwon, K. J. 2009. "Wind Tunnel Tests for a Flapping Wing Model with a Changeable Camber using Macro-Fiber Composite Actuators," *Journal of Smart Materials and Structures*, **18**(2).

[7] Bilgen, O., Kochersberger, K. B., Diggs, E. C., Kurdila, A. J., Inman, D. J. 2007. "Morphing Wing Micro-Air-Vehicles via Macro-Fiber-Composite Actuators," AIAA-2007-1785, 48th AIAA/ASME/ASCE/AHS/ASC Structures, Structural Dynamics, and Materials Conference, Honolulu, Hawaii, Apr. 23-26, 2007.

[8] Bilgen, O., Kochersberger, K. B., and Inman, D. J. 2009. "Macro-Fiber Composite Actuators for a Swept Wing Unmanned Aircraft," *Aeronautical Journal*, Special issue on Flight Structures Fundamental Research in the USA, publication of Royal Aeronautical Society, **113**(1144).

[9] Bilgen, O., Kochersberger, K. B., Inman, D. J. 2010a. "Macro-Fiber Composite Actuated Simply-Supported Thin Morphing Airfoils," *Journal of Smart Materials and Structures*, **19**, 055010.

[10] Bilgen, O., Kochersberger, K. B., Inman, D. J. 2010b. "Novel, Bi-Directional, Variable Camber Airfoil via Macro-Fiber Composite Actuators," *AIAA Journal of Aircraft*, **47**(1), pp. 303-314.

[11] Paradies, R., Ciresa, P. 2009. "Active wing design with integrated flight control using piezoelectric macro fiber composites," *Smart Materials and Structures*, **18**, doi:10.1088/0964-1726/18/3/035010.

[12] Wickramasinghe, V. K., Chen, Y., Martinez, M., Kernaghan, R., Wong, F. 2009. "Design and Verification of a Smart Wing for an Extremely-Agile Micro-Air-Vehicle," AIAA 2009-2132, 50th AIAA/ASME/ASCE/AHS/ASC Structures, Structural Dynamics, and Materials Conference, Palm Springs, California, 4 - 7 May 2009.

[13] Butt, L., Day, S., Sossi, C., Weaver, J., Wolek, A., Bilgen, O., Inman, D.J., Mason, W.H. 2010a. "Wing Morphing Design Team Final Report 2010," Virginia Tech Departments of Mechanical Engineering and Aerospace and Ocean Engineering Senior Design Project, Blacksburg, VA.

[14] Butt, L., Bilgen, O., Day, S., Sossi, C., Weaver, J., Wolek, A., Inman, D.J., Mason, W.H. 2010b. "Wing Morphing Design Utilizing Macro Fiber Composite," Society of Allied Weight Engineers (SAWE) 69th Annual Conference, Virginia Beach, VA, Paper Number 3515-S.

[15] Bilgen, O., Butt, L.M., Day, S.R., Sossi, C.A., Weaver, J.P., Wolek, A., Mason, W.H., Inman, D.J. 2011. "A Novel Unmanned Aircraft with Solid-State Control Surfaces: Analysis and Flight Demonstration," 52nd AIAA/ASME/ASCE/AHS/ASC Structures, Structural Dynamics, and Materials, Denver, CO.

[16] Wilkie, W. K., Bryant, G. R., High, J. W., "Low-Cost Piezocomposite Actuator for Structural Control Applications," *SPIE 7th Annual International Symposium on Smart Structures and Materials*, Newport Beach, CA, 2000.

[17] High, J. W. and Wilkie, W. K., "Method of Fabricating NASA-Standard Macro-Fiber Composite Piezoelectric Actuators," NASA/TM-2003-212427, ARL-TR-2833.

[18] Hagood, N. W., Kindel, R., Ghandi, K., and Gaudenzi, P., "Improving Transverse Actuation using Interdigitated Surface Electrodes," SPIE Paper No. 1917-25, pp. 341-352, *North American Conference on Smart Structures and Materials*, Albuquerque, NM, 1993.

[19] Bilgen, O., Kochersberger, K. B., Inman, D. J., 2010, "Novel, Bi-Directional, Variable Camber Airfoil via Macro-Fiber Composite Actuators," *AIAA Journal of Aircraft*, **47**(1), pp. 303-314.

[20] MATLAB, Computer Software, version R2010b, [http://www.mathworks.com/products/matlab/]

[21] Drela, M., "XFOIL 6.9 User Primer, XFOIL: Subsonic Airfoil Development System," Massachusetts Institute of Technology. [http://web.mit.edu/drela/Public/web/xfoil/xfoil_doc.txt]

[22] Drela, M. 1989. 'XFOIL: An Analysis and Design System for Low Reynolds Number Airfoils,' *Conference on Low Reynolds Number Airfoil Aerodynamics*, University of Notre Dame, June 1989.

[23] ANSYS, Computer Software, version 13.0, [http://www.ansys.com/products/ansys13-new-features.asp]

[24] Goldberg D., 1989, "Genetic Algorithms in search, optimization and machine learning", Addison-Wesley.

ADAPTIVE AERONAUTICAL STRUCTURES DEMONSTRATION ON A MODULAR DESIGNED MICRO AERIAL VEHICLE

C-M Kuo[1] and C Boller[1,2]

[1] Chair of Testing and Quality Assurance, Saarland University,

[2] Fraunhofer Institute Nondestructive Testing IZFP, Campus E3.1, 66123 Saarbrücken/Germany

ABSTRACT

Demonstration of the performance of adaptive structures on air vehicles in general has been a rather difficult subject. Different reasons such as cost, risk, actuator capability, time and possibly others have prevented performance of adaptive aeronautical structures to be demonstrated exhaustively. Although operating at lower Reynolds numbers a means to alleviate some of the reasons preventing smart technologies to be applied is to demonstrate those adaptive structures' capabilities on a micro aerial vehicle (MAV) which is what is presented along this article. Based on a modular MAV design it is shown how within minutes if not even seconds wings, tails or the propulsion systems can be easily changed resulting in differences of the MAV's performance. Principally based on the same fuselage this allows different features of adaptive structures to be performance and analyzed such as a change in a wing's thickness, aspect ratio, stiffness or angle of attack, or a vector thrust propulsion system, before an adaptive structures' solution is practically realized. The performance of all these features has been demonstrated in flight tests and the results obtained have been validated through analytical and numerical analysis, mainly from the point of flight performance stability and manoeuvrability which will be described and explained throughout the article. The effects of passive versus active adaptive wing will be briefly explained. Special emphasis is also made with regard to a vector thrust propulsion principle which besides enhancing manoeuvrability also allows a MAV's payload and/or endurance to be enhanced significantly.

INTRODUCTION

A micro aerial vehicle (MAV) is a non-conventional small and hence unmanned aircraft that faces a challenge because its size aerodynamically (low Reynolds' numbers) as well as structurally. Since an MAV is small and light weight, its structure and resulting aerodynamics are often designed for one flight condition only. However this does limit an MAV's performance, specifically for a fixed wing one, which is designed for a comparatively long distance flight at high speed but may have to maneuver significantly when being used for observation with a sensor system attached such as a camera or any other type for sensing device providing a continuous and hence time dependent signal. Flight stability has also a significant impact on sensor signal quality, where adaptive structures can significantly contribute. Furthermore efficiency in flight performance does also lead to a longer endurance which helps a sensing mission to be optimized.

During the early times of smart structural design around twenty years ago a lot of emphasis has been placed on aspects such as attenuation of dynamic loads by means of an active wing-fuselage interface (based on piezoceramics), flutter suppression and vibration reduction by means of adaptive stiffness tuning and adaptive control of the wing camber (in these cases the application of shape memory alloys were seen to be efficient), active internal noise cancellation, adaptive stiffness control, or adaptive wing-engine pylons [1]. Different of those aspects have been initially explored but failed final realization mainly as a result of an actual system's complexity but also as a matter of cost. Overviews on developments with respect to adaptive structures in aeronautics can be found in [2-7].

Shape control and thus actively influencing flow of aerodynamic profiles is an ultimate desire in aeronautics where expectations are high with respect to adaptive structures. As a consequence, different programmes were launched in the past, where the Smart Wing Programme [8] run in the USA in the early 90ies can be considered as the pilot study. It was quickly learned that neither actuators possibly machined from bulk shape memory material nor piezoelectric wafers attached to an aerodynamic profile's surface would meet any requirements mainly on a real aeronautical structure for reasons of the energy required or the additional weight imposed. It could therefore be very quickly concluded that any solution for adaptive wings would only hold if they would still stay with the principles of conventional solid state actuators and that these actuators could be made from an actuation material such as a piezoelectric. The next step therefore resulted in a much more conventional mechanical solution actuated by piezoelectric travelling wave ultrasonic motors [9]. This solution was then built into a 30% downscaled model of an uninhabited combat air vehicle of which the control surfaces consisted of a conventional flap solution on the left side of the aircraft and a segmented continuously deforming smart solution on the right side. Along a wind tunnel test at 0.8 Mach wind speed and 300 psf dynamic pressure the smart solution showed a 17% improvement in rolling moment coefficients at 15 degrees of control surface deflection when compared to the conventional flap solution [10].

The Smart Wing Programme together with various other programmes related to adaptive aerodynamic profiles was placed under the NASA Morphing Wing Programme [11] which emphasized a strategic direction and the need to place different disciplines under one umbrella. Another major DARPA programme run was the Compact Hybrid Actuator Programme (CHAP) from which SAMPSON [12] emerged as a key project. SAMPSON dealt with an adaptive air inlet duct of the engine of an F-15 that allowed the cowl to rotate, the lip to deflect, the air intake wall to deflect and the lip to blunt. This was achieved by mainly using SMA actuators being either configured as a rod of 60 SMA wires, or wires placed in a flex skin panel. Wind tunnel tests were performed to determine the gains in noise reduction. Other solutions for engine noise reduction include chevrons around the engine exhaust which are actuated by SMA actuators in accordance to an aircraft's flight level position.

Studying adaptive aeronautical structures at smaller scales inhibits other challenges. The advantage of operating at those scales is the lower cost, lower risk and time in realizing different prototypes and exploring different technologies. This article therefore describes different ideas of adaptive aeronautical structures for multi-role mission demand including wing thickness and stiffness variation, a variable V-tail and a vector thrust mechanism which have been developed over the past and have been published in more explicit detail in [13,14].

WING THICKNESS VARIATION

Looking at effects in nature a bird can morph its wing to perform different flight conditions. One of those features is that a bird's wing tends to morph to a thicker profile when it is flying in a gust and to a thinner profile during steady flight. Such a principle can even be applied to a MAV when the wing consists of an upper and lower panel and forces are applied in a way this is schematically shown in Fig. 1.

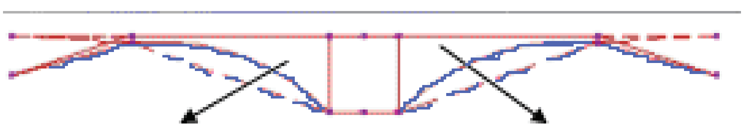

Figure 1: Front view of the MAV showing when the wing is fully extracted (dashed line) and fully contracted (solid line).

The dynamic change of the wing shape can even further result in dynamic forces that may have an influence on the stability of the MAV. However, simulation of the fully dynamic behaviour within Fluid-Structure-Interaction (FSI) to understand the dynamic behaviour does require very large computational power. To simplify verification of the wing thickness effect three discrete model wings have been generated (see Fig.2.) which allowed this effect to be understood.

Figure 2: Morphing-wing MAV CAD models

The wing shape schematically described in Fig. 1 has been modeled by 3D FE assuming Depron the material. A vector of force in the y and x direction was applied onto the bottom plane of the wing, which can be seen in the Fig.3 left (front view of the MAV wing) and the resulting deformation as a dashed line on the right hand side of Fig. 3. For a 300 mm span MAV a max. wing thickness change of 7 mm was determined.

Following the FE model, a simple ground test model was built for validation. Fig.4 shows the two MAV wing conditions (note the lines indicated are a highlight of the wing shape), extracted (left) and contracted (right) when a pulling force is applied.

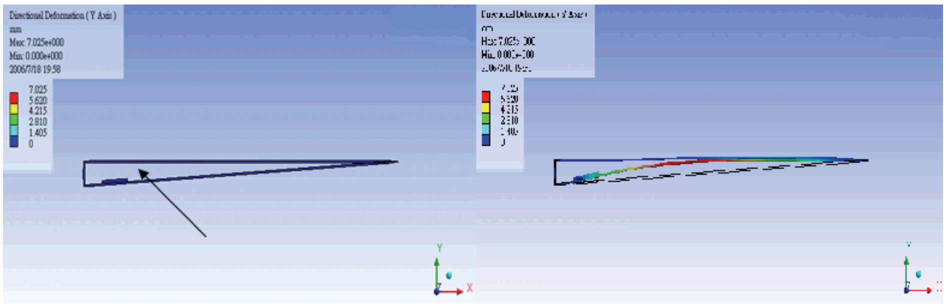

Figure 3: 3D FE model of the morphing wing fully extracted (left) and fully contracted (right).

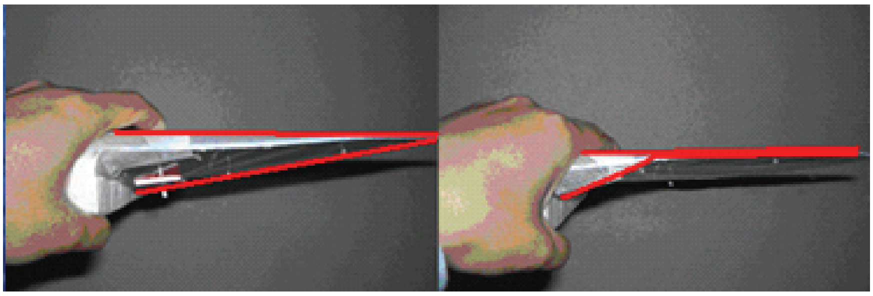

Figure 4: Ground prototype showing fully extracted wing (left), and the fully contracted wing (right).

Since the FE model deformation shape agrees with the hardware model, CFD and stability modeling could be carried out for the 3 different wing shapes shown in Fig.2. By using all the force and momentum results from the CFD analysis a longitudinal stability model was generated. The MAV was subjected to very small sudden changes in velocity *u*, with the response of settling time (5% rule) to be 22 seconds for the fully extracted wing, and 33 seconds for the fully contracted wing respectively as shown in Fig. 5, where the x axis is time in seconds, and y-axis is the change in velocity.

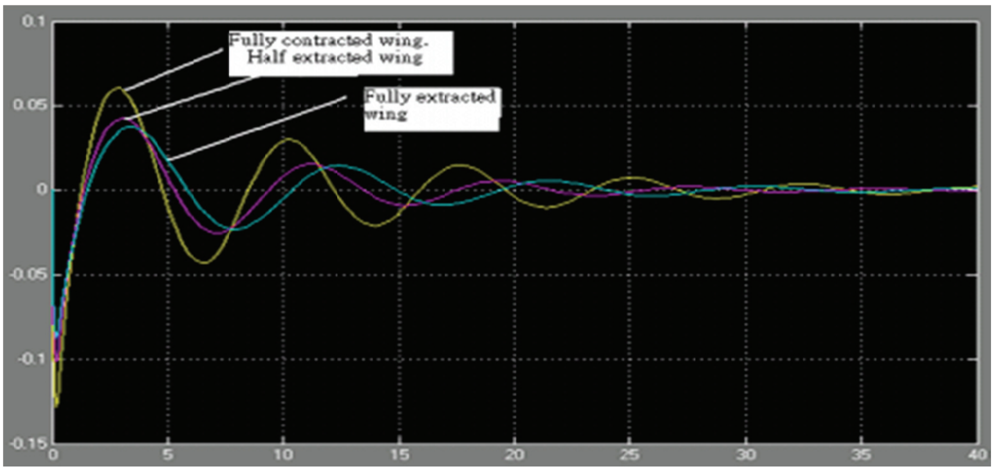

Figure 5: Longitudinal results in changing vertical velocity

The settling time is related to the value of the damping ratio, and the experiment shows that the higher the thickness of a wing is the higher the damping ratio of the wing becomes, which in other words means, a thicker wing has a better natural stability, which results in better performance when flying in gusty winds.

To realize the wing thickness change in hardware and during flight normal R/C servos were installed as actuators inside the wing such as shown in Fig. 6 below. This solution allowed the wing thickness to be changed during flight of the MAV from the ground.

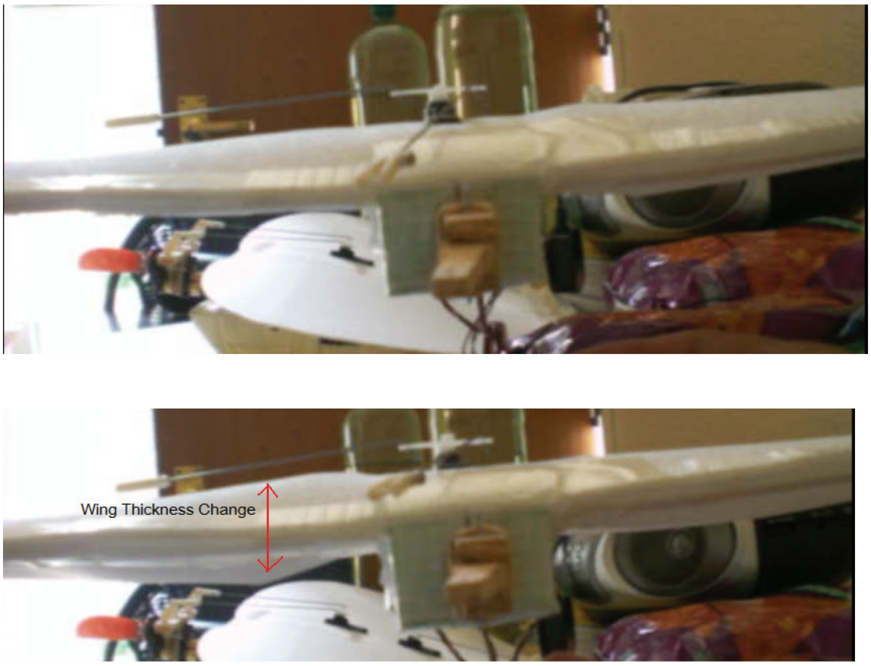

Figure 6: Dynamic morphing-wing prototype: fully contracted (top) and fully extracted (bottom).

Following the simulation the thicker wing MAV shows better natural stability. Flight tests performed for validation were focused on the pilot's review considering not only flight stability but also overall flight efficiency in terms of flight time. For comparative reasons all three different wing thicknesses were tested separately but on the same day to cope for similarity in weather conditions. The recorded flight times and a pilot's review on the stability are listed in Tables 1 and 2 below.

MAV wing model	Flight time (min)
1. Fully contracted	>20
2. Half-extracted	18~20
3. Fully extracted	< 18

Table 1: Comparison of flight times recorded

MAV wing model	Natural stability	Manoeuvrability
Fully contracted	Less	Good
Half extracted	Better but more thrust required	Slightly less than before.
Fully extracted	Best but power consuming	Clearly reduced.

Table 2: Flight stability recorded by pilot

The flight results show that the simulated results follow the trend with the thicker wing providing the better stability and the thinner wing the higher endurance. Hence a wing being able to adapt the variable conditions such as in gusts could be a great advantage for a MAV's stability and endurance.

ADAPTIVE WING STIFFNESS

Background

Since MAV configurations allow a variety of different aerodynamic profile configurations to be tested this may allow fairly unconventional and hence even adaptive aerodynamic profile designs to be determined. It is known that birds and insects can change the flexibility of their wings remarkably and that they can use this capability to enhance their flight performance. The MAV group at the University of Florida [15] was possibly the first group to explore the effect of enhanced MAV wing flexibility. It was found that their flexible wing had a higher lift coefficient at higher angles of attack, which also resulted in a major increase in the stall angle when compared to conventional rigid wings. However what was also found was that flexible wings result in an increasing effect of fluid-structure interaction and that this needs to be analyzed in terms of aeroelastic behavior [14].

Multiple one-way Fluid-Solid Interaction

The theory behind multiple one-way fluid structure interaction (FSI) is that once the CFD model has been calculated, the results are passed to the FE model to determine the deformation and stress. This deformation, which includes twisting and bending of the aerodynamic profile considered, is passed back to the parameters in the CAD model, so that a new CAD model of the deformed wing can be generated. The new CAD model is later used to generate the CFD mesh, and converted to a CFD model again for simulation; thus, the step is repeated until the de-formation converges when compared to the previous CAD model. This method is more computation efficient since there is a separation of the structure and the CFD model. Therefore the memory consumption is much lower and there is no 'negative value' of the cell deformation of the wing because the mesh is rebuilt in each iteration step. The resulting process of this procedure is shown in Fig. 7.

In order to find out what parameters are required for the CAD model modification, a sample FSI result model is used, which can be seen in Fig.8. The resulting deformation image is superimposed to the normal CAD model (with 1:1 ratio) to work out the exact parameters which are required to be added into the CAD model.

The main parameters for the wing deformation are the displacement along the y axis (global coordinate system form Fig.8) and wing twist. Inserting these two parameters into the CAD drawing allows the model to deform and twist whatever the value is required, which leads to a flexible CAD model. Fig.9a. shows twisting of the wing and Fig.9b bending of the wing in y-axis respectively.

Stability Modelling and Comparison with Rigid Wing MAV

Simulation of the longitudinal and lateral stability was performed for a flexible and a rigid wing. Fig.10 shows the result for the longitudinal stability, which demonstrates an enhancement in natural stability when making the wing more flexible in excess of the gains already achieved in lift. Determination of the lateral stability becomes more complex since the wing will become asymmetric in the XY plane during a lateral disturbance. A 5 degree yaw will lead the left wing to behave asymmetrically to the right. This requires the natural stability model to be rewritten, while still allowing the parallel FSI approach mentioned before to be applied. Fig.11 shows the resulting wing deflections in which the asymmetries between the left- and right-hand wing deflections can be observed.

A comparison in lateral stability between the rigid- and the flexible-wing models is shown in terms of change in side-slip rate, roll rate, yaw rate and roll angle in Figs.12 to 15. It can be seen that an increase in flexibility reduces the roll rate significantly and thus the roll angle, with no significant penalties in the side-slip rate. The yaw rate may increase slightly and yawing will behave slightly different, which may have an effect on the size of the fin rudder and possible control algorithms to be applied. The results obtained can be taken to explain why a flexible wing may result in better flight performance, at least up to a certain degree. Further details can be found in [16].

Prototyping and Test Flight

The various approaches described above were prototyped in hardware and test flown. Due to realizing a prototype in a very short time followed by a test flight, results of the test flight have been judged by the pilot only, with detailed wind tunnel tests, autonomous flights and integrated sensors still to follow. The prototypes considered for the test flight were the rigid-wing model as a reference, added by a flexible-wing model, where a single front spar was left only when compared to the rigid wing, where three spars have been used for stiffening. To get the stiffening realised the spars were stuck into a fixing hole in the fuselage. All other components of the MAV, including the fin, were the same when compared to the reference MAV (rigid wing MAV).

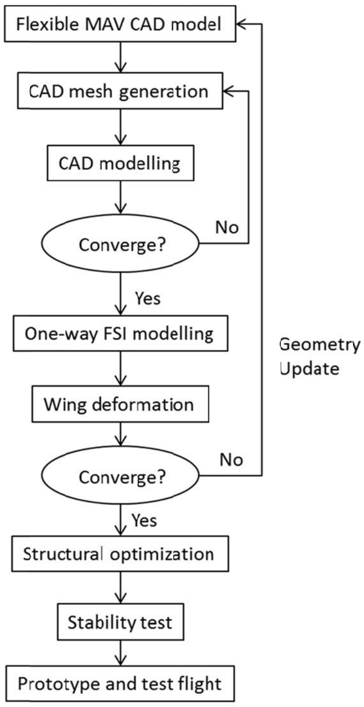

Figure 7: Flow chart of multiple one-way FSI for a flexible-wing MAV

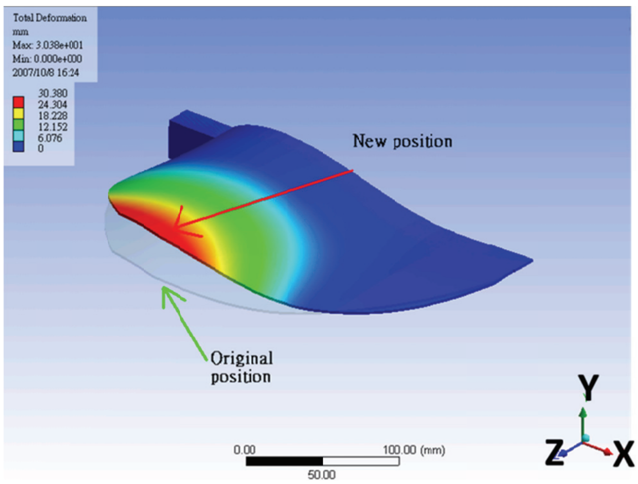

Figure 8: FSI results, showing the original model and deformation (shape) of the wing

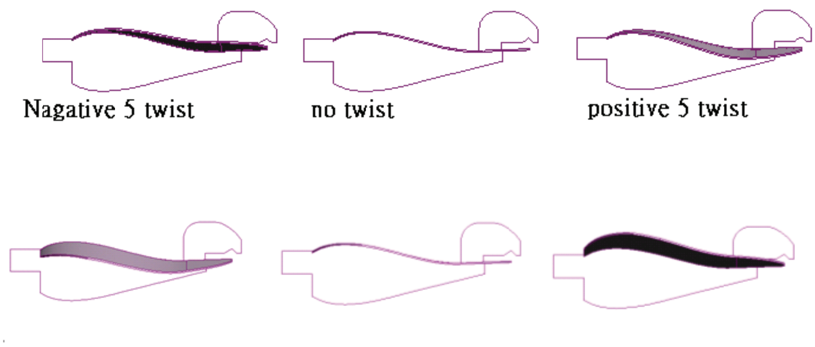

Figure 9: Wing twist (top) and wing bending 20 mm down (bottom left) and 20 mm up (bottom right) configurations

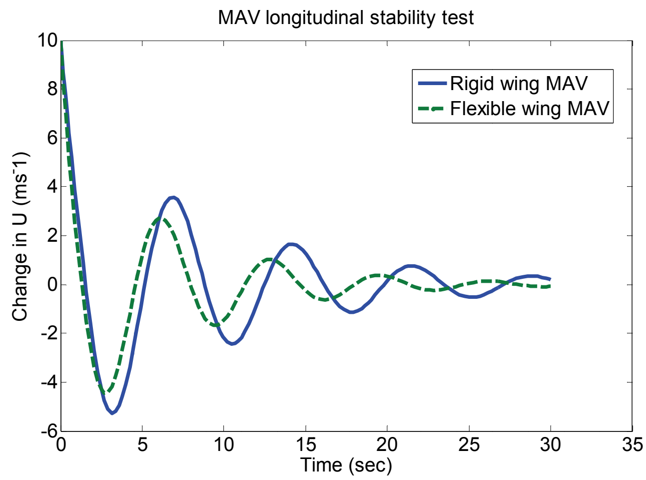

Figure 10: Longitudinal stability modelling result

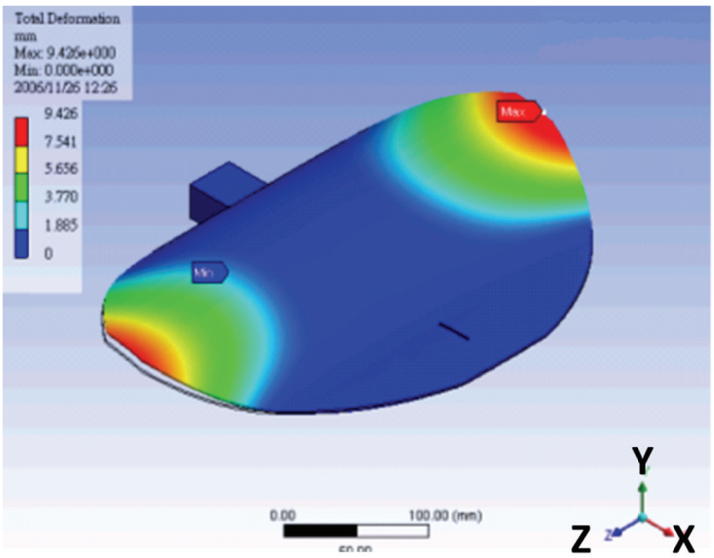

Figure 11: FSI results of the MAV in side-slip

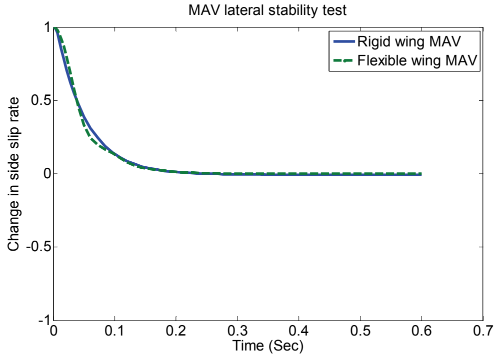

Figure 12: Lateral stability modelling in terms of change in side-slip rate

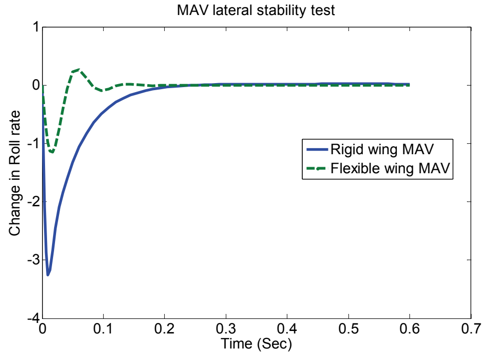

Figure 13: Lateral stability modelling in terms of change in roll rate.

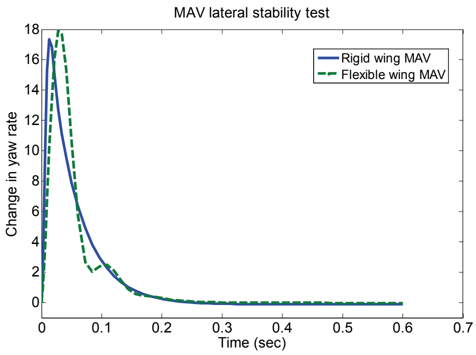

Figure 14: Lateral stability modelling in terms of yaw rate.

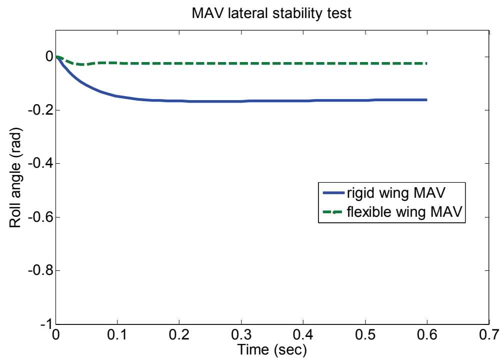

Figure 15: Lateral stability modelling in terms of roll angle

Flight tests were done in windy conditions. The flexible-wing MAV turned out to be more stable when compared to the rigid-wing MAV, which was felt by the pilot through easier handling and longer endurance, resulting from less power being required to stabilize the MAV. However, the flexible-wing MAV shows a disadvantage in hand launch capability and maneuverability being less due to the higher natural stability. Table 3 provides a summary of the observations made during flight. Another practical advantage of the flexible-wing MAV model is its ease in back-packaging. Fig.16 shows how it can be easily rolled and stored in a tube of the size of a large 2 liter PET bottle being also a means for safe transportation of the MAV.

Rigid wing	Flexible wing
• Less stable • Good maneuverability • Less controllable during gusty wind conditions	• More stable in gusts (but more thrust required) • Gliding distance slightly less • Difficult to control during take off • Easier packing • Less damage after crash
>20 min endurance	>22 min endurance

Table 3: Flight observations with rigid- and flexible-wing MAVs

VARIABLE V-TAIL MAV (CONTROL SURFACES)

Background

MAVs are on the scale of birds in terms of size and speed. Therefore biomimetic inspiration is allowed with respect to aerodynamics and stability control. Bio-inspiration here been related to active morphing and a passive flexible wing in a way this is shown in Fig. 17. For MAVs directional control is either by a rudder or vector thrust while directional stability is largely provided by the vertical tail. However, birds and insects do not have any vertical tail, but still can maintain their lateral stability. The main reason why birds do not need a vertical tail is because propulsion is provided by the wings. However, since weight of the MAV is small, torque generated by the propeller needs to be countered not just by the thrust angle, but also by the vertical tail.

Figure 16: Assembled MAV and container (left) packed MAV (right)

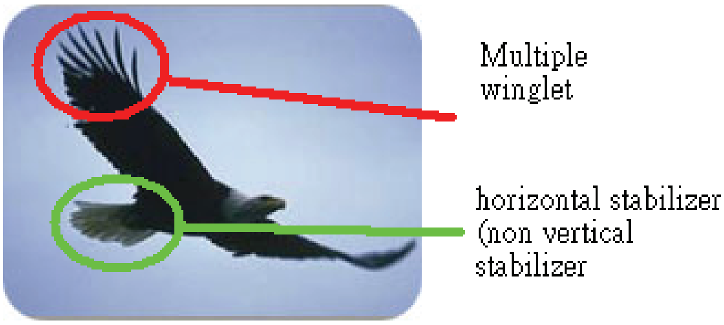

Figure 17: A bird's wing during flight.

Considering the overall dimension of the MAV, the vertical tail is the only part that occupies a significant dimension in the Z axis as can be seen from Fig. 18.

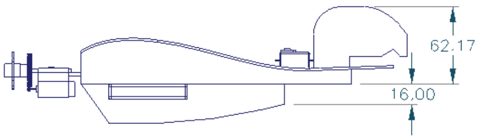

Figure 18: MAV vertical tail with dimensions (unit mm).

Stability Analysis

Longitudinal: The resulting effect of the V-tail on the short and long period motion can be seen from the data plotted in Fig. 19. It is observed that the period motion is rather short (less than 0.5 sec), which means that the displacement of the MAV in Z-direction is not significant. The V-tail configuration shows better longitudinal stability compared to the original rigid wing with the highest damping ratio to occur at 20 degrees (see Table 4)..

Lateral: The point of using the variable V-tail is to enhance stability and this in lateral direction. Therefore, analysis of the lateral stability of the variable V-tail on an MAV becomes very important.

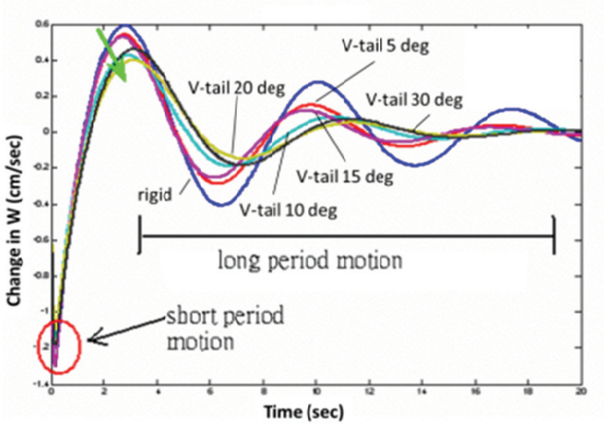

Figure 19: Longitudinal motion in W (vertical). Short period motion (circle) and damping ratio increases for the long period motion (arrow).

Lateral stability can be divided into three different modes of motion: spiral, roll and Dutch roll. Table 4 summarizes the results of each of the modes considered. It can be seen that the spiral mode only has a very short time (less than 0.02 seconds), which means the roll mode is dominant. The Dutch roll has a very long period, which indicates the MAV's high stability. This is because the motion will only be visible if the MAV flies in a perfect condition for 12 min. Fig. 20 shows the results for different positive-angle V-tail MAVs in a sudden 5° side-slip motion compared to the original MAV. The original MAV has a clearly better stability in side-slip, due to the size of the vertical tail which can hardly be beaten. The V-tail angle has been controlled by one remote controlled servo only (Fig.21).

	Spiral		Roll		Dutch roll		
Angle of the V-tail	ω_n [Hz]	Period [sec]	ω_n [Hz]	Period [sec]	Damping ratio	Period [sec]	ω_n [Hz]
5	2247.9	0.002795	1.5	4.18879	0.003507	1791.6	25.94
10	632.67	0.009931	0.24	26.17994	0.001393	4510.6	73.15
15	523.28	0.001201	0.48	13.08997	0.003563	1763.3	47.54
20	560.88	0.011202	142.61	0.44059	0.008282	758.6	2.837
30	353.55	0.017772	0.57	11.02313	0.00403	1559	45.16

Table 4: Results of the lateral motion of the V-tail MAV

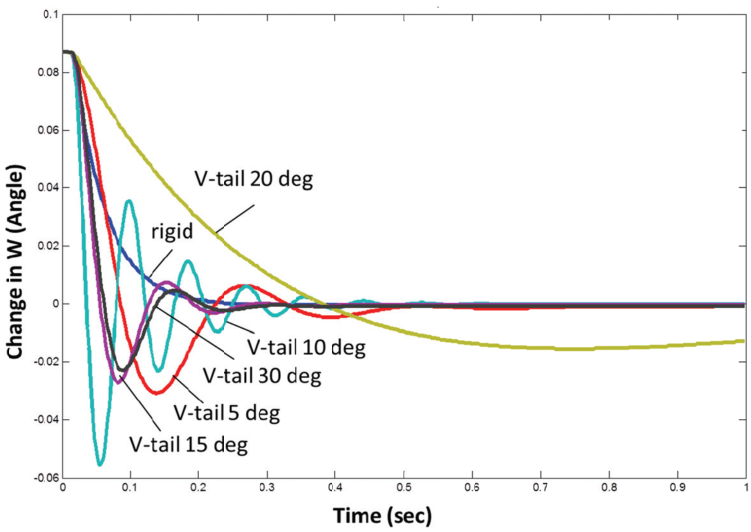

Figure 20: Side-slip motion of the positive angle V-tail MAV compared to original rigid wing

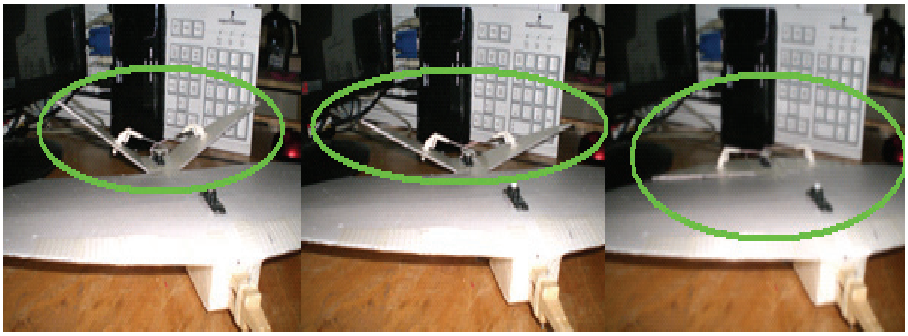

Figure 21: V-tail at different angles (controlled by servo).

Flight Test Analysis

A summary of the flight tests performed and qualitative observations made is provided in Table 5. Tests were only possible to be performed with a V-tail angle of > 5 deg due to poor flight stability otherwise. A condition where the MAV performs similar to the rigid wing is at a V-tail angle of 20 deg, which can also be observed from the numerical results shown in Fig. 20 and is a proof of the numeric model's validity.

Angle of V-tail (degree)	Can it take off?	Stability (compared with reference MAV)	Flight speed (compared with reference MAV)	Response to direction control
30	Yes	Less	Slightly faster	Faster
25	Yes	Less	Slightly faster	Faster
20	Yes	Very close, slightly less	Slightly faster	Similar
15	Yes	Less	Faster	Faster
10	No	A lot less	Similar	Similar
5	No	No flight test	No flight test	No flight test
0	No	No flight test	No flight test	No flight test

Table 5: Flight results of the V-tail MAV

VECTOR THRUST MAV

Background

MAVs are intended to operate in urban areas. This requires high manoeuvreability, being not in the nature of a fixed wing MAV. Control surfaces have good efficiency when the dynamic pressure is high [17], however, this is not the case in low Reynolds' number aerodynamics. In order to increase the efficiency of yaw and bank moment at low speed, a constant force therefore needs to be present. For this reason a1 degree of freedom (DOF) thrust vectoring can be deployed.

Vector Thrust Control Modelling

The combination of a vector thrust system and conventional control surfaces is complex, not just in terms of the mechanical system, but also with regard to the mathematical model. To simplify the problem, the rudder (control surface) is therefore fixed. Forward thrust provided by the motor is 120 g (1.2 N), and for comparison, the deflection is also set to 5 degrees, such that only a small amount of side force will be created, which can be seen in

Fig.22. Also, since now the propeller wash is in an angle it increases the angle of attack (AoA) on the vertical tail a momentum is generated that makes the MAV to turn to the right (Fig. 23). Since this side force is activated by pilot input, the only matrix which needs to change is the lateral control derivative, and the main values needed to change are (see [18]):

$$dY = 120 \cdot 9.81 \cdot \cos 85 = 0.102 N,$$

$$dCy = \frac{dY}{QS} = 0.01426, \text{ and}$$

$$Cy\zeta r = \frac{dCy}{dr} = 0.1634,$$

where r is the motor deflection angle and the other parameters are summarized in a table in the appendix at the end of this article. This leads to

$$Y\varsigma r = \frac{QSCy\zeta r}{m} = 11.09.$$

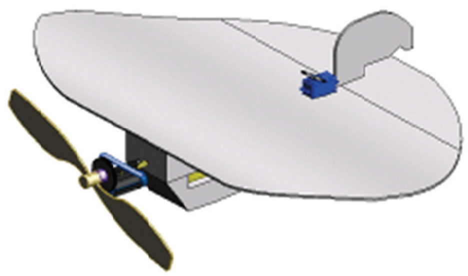

Figure 22: CAD model of fully assembled MAV

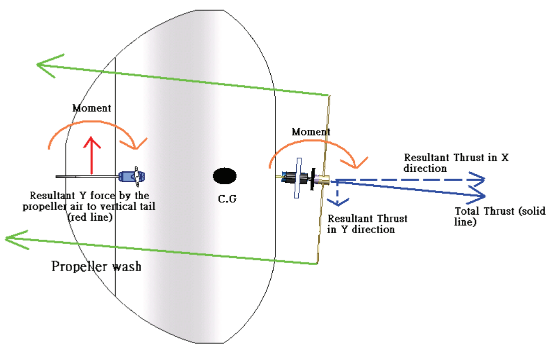

Figure 23: Schematic of how ‘side’ thrust is created by deflection of the thrust line.

This is the same for $N\varsigma r$ for,

$$dN = dY \cdot length = 0.102 \cdot 0.121 = 0.012342 Nm,$$

where the length is the distance between the propeller and the centre of gravity (CG).

$$dCn = \frac{dN}{QSb} = 4.289 \cdot 10^{-3},$$

$$Cn\zeta r = \frac{dCn}{dr} = 0.04915,$$

This leads to

$$N\zeta r = \frac{QSCn\zeta r}{Iz} = -176.02\,.$$

These two values are then put back into the control model and compared with the 'original' model. It can be seen from the simulation results shown in Fig.24 that the vector thrust system can create more roll and yaw angle with the same amount of servo input provided. Due to the size of the motor for the vector thrust version the position of the battery had to be shifted which led to a slight shift of the CG and moment of inertia as well and further contributed to an enhancement of the overall natural stability when compared to the original MAV model [13]. Flight results obtained are shown in Table.6. The simple vector thrust unit proved to be more effective than the normal control surface in both simulation and test flight, leading to an increase in the MAVs endurance by more than 20%, based on the flight testing results obtained. Moreover maneuverability has increase significantly without altering natural stability.

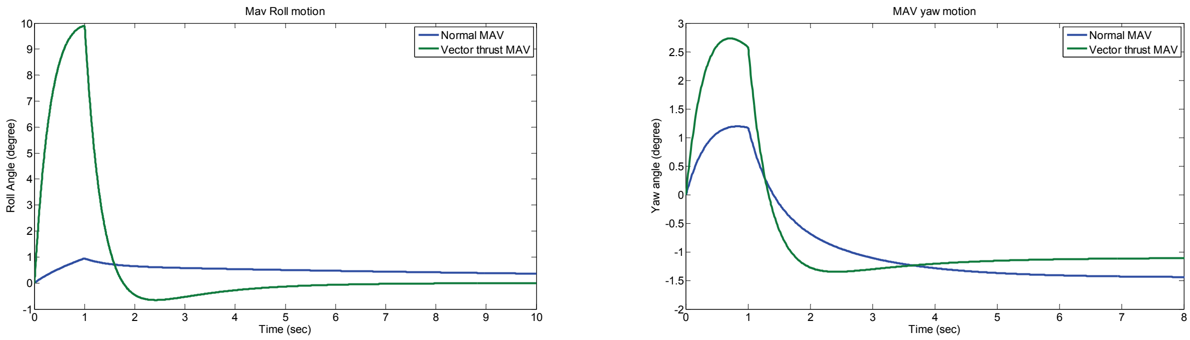

Figure 24: Simulated results with control input and initial disturbance

Wind tunnel testing

In order to confirm the results of the mathematical simulation of the vector thrust MAV, a wind tunnel test was carried out. Normally a full wind tunnel test does involve a 6 degrees of freedom (DOF) force balance to measure all aerodynamic forces and moments applied on the MAV. Since a 6 DOF force balance is a huge investment specifically within the scales of an MAV an easier means of measurement was determined by using a force balanced limited to 2 axes only. Such a force balance being used to measure lift and drag of a MAV only and is shown on Fig. 25 (right) simply needed to be turned around the vertical axis to measure the side forces as shown in Fig. 25 (left). Each of the forces along the 3 axes were recorded and later processed in MATLAB where the results are matching the simulated results really well, which can be seen from the results shown on Figs. 26 - 28.

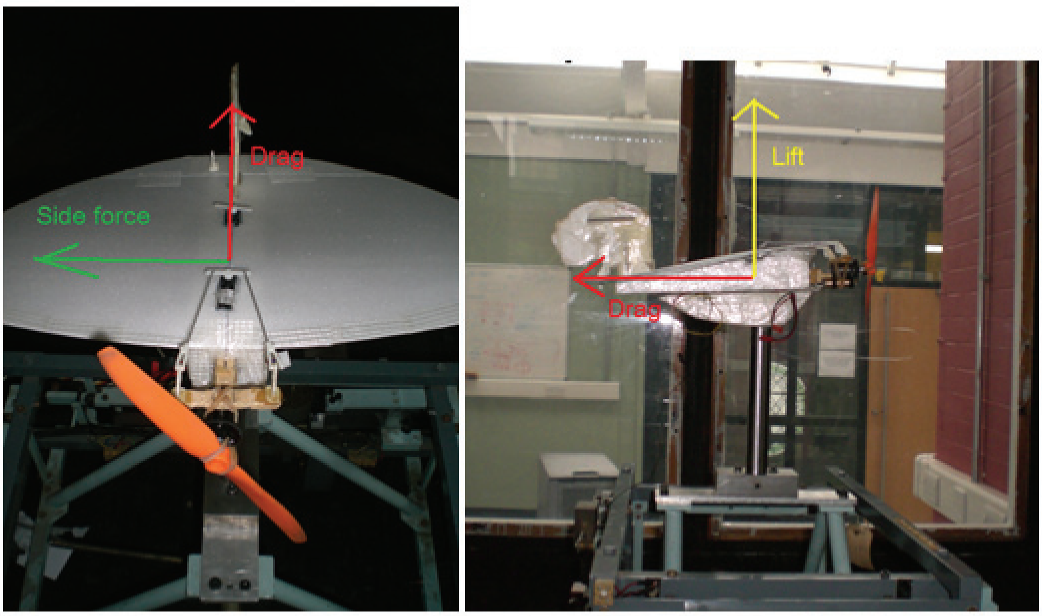

Figure.25. MAV set up for the Wind tunnel test

Apart from flight stability and control modeling test in wind tunnel, of the static force measurement experiment were also carried out. This experimental is simple but also proved the evident of usefulness of vector thrust on the MAV. The set up was that the MAV is originally sit in 0m/s wind speed, and side force is then recorded when the vector thrust is activated, then, this force value is latter used to compare with the side force value when the flow speed is set to be in the cruise speed (8m/s).

Flow speed (m/s)	0	8
Total side force (N)	0.24	0.28

Table. 6. The results of static side force test for the vector thrust MAV.

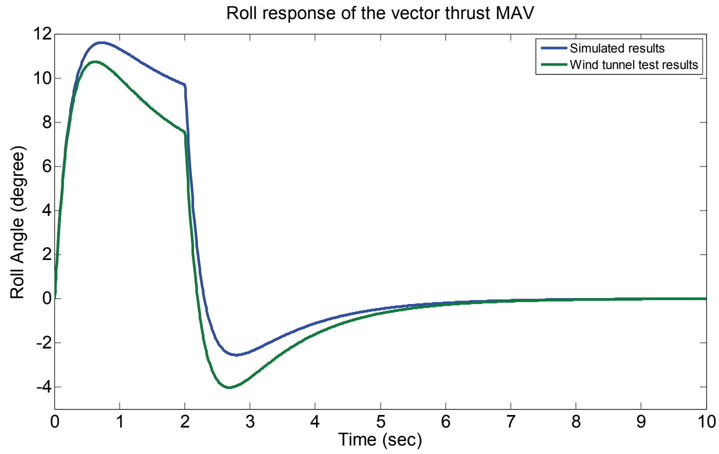

Figure.26. Roll response

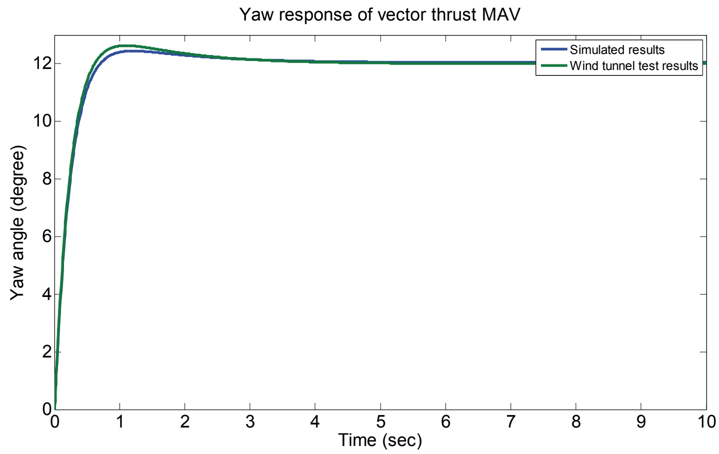

Figure.27. Yaw response

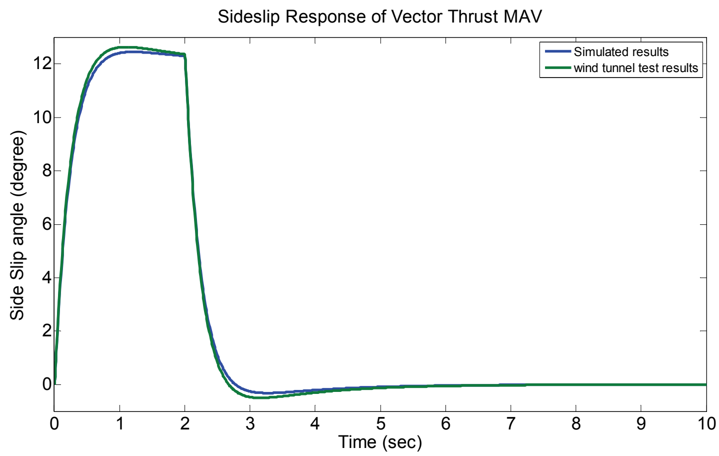

Figure.28. Sideslip Response

Result from Table.6 shows that more side force was generated when the MAV is in the cruise, this is because apart from the side force from the thrust, also some aerodynamic forces are formed from the wing, which cause the MAV turns more.

MAV type	Maneuvera-bility	Flight time	Stability
Normal (with 1500 kv motor)	All right	25+ min	Good
Smaller motor	All right	40+ min	Good
Vector thrust	Very good	50+ min	Good

Table 7: Flight endurance, maneuverability and stability results of the MAVs

CONCLUSIONS

The modular design of an MAV allows a variety of technology options to be explored in relatively short term. This even applies to adaptive and hence morphing aircraft features. Designing an aircraft such as an MAV on a modular basis has the advantage that different components can be easily replaced by others without having to replace the rest of the aircraft. Although operating at different Reynolds numbers MAVs can serve as a valuable first attempt to demonstrate the effectiveness of adaptive structures aircraft technology at rather low cost when compared to large scaled manned aircraft.

When considering adaptive structures different of a structure's condition can be easily validated as a static display before any of the actuation principles have to be developed. Wing thickness is an issue with regard to an aircraft's maneuverability and this even for small as well as for large aircraft. A thicker wing however generates more drag and hence consumes more energy and it is thus that actuation mechanism must exist, that allows the wing to become thicker only when there is a need. In the case described here this has been simply done by a RC-controlled servo that mainly 'bumped' the wing skin. However more sophisticated solutions may be considerable in the sense of a smart/adaptive morphing structure.

Another adaptive effect of significance is the variation in wing stiffness. A softer wing provides more stability and even enhanced endurance together with ease in packaging when compared to the rigid where maneuverability is superior. A means on having spars with adaptive stiffness in that regard looks to be a solution of specific interest. Flight stability is also controlled by control surfaces where V-tails are an interesting option to be pursued with MAVs and may be also with manned aircraft too. Again actuation can be provided with a simple servo actuator providing remarkable flight performance improvements indeed.

Vector thrust propulsion has indicated that it cannot only enhance an MAV's maneuverability but also endurance and payload. This concept is worth to be explored in much more detail in the future and has possibly the largest effect of all adaptive structures concepts explored here so far.

Principally the introduction of adaptive structures concepts with aeronautical vehicles is an approach very much worth to be pursued. However the partially large deformations induced by the actuators used can cause structural problems such as fatigue and fracture of the structure in the longer term. Hence the bigger the aeronautical structure becomes the bigger this problem may become and it therefore that the exploration of adaptive aeronautical structures may be first done at the small scale, not just from a cost issue point of view only.

REFERENCES

[1] Breitbach E.J., 1991: *Research Status on Adaptive Structures in Europe;* Proc. of 2nd Joint Japan/US Conf. on Adaptive Structures; Technomic Sc. Publ.

[2] Chopra I (Ed.), 1996: Special Issue on *Application of Smart Structures Technology to Rotorcraft Systems*; Smart Mater. & Struct., **5**, Nr. 1

[3] Gandhi F (Ed.), 2001: Special Issue on *Rotorcraft Applications*; Smart Mater. & Struct., **10**, Nr. 1

[4] McGowan A.-M. R., A.E. Washburn, L.G. Horta, R.G. Bryant, D.E. Cox, E.J. Siochi, S.L. Padula and N.M. Holloway, 2002: *Recent Results from NASA's Morphing Project;* Proc. of SPIE Vol. 4698; pp. 97 – 111

[5] Garcia, E., 2002: *Smart Structures and Actuators: Past, Present, and Future*; SPIE Vol. 4698, pp. 1 - 12

[6] Loewy R.G., 1997; *Recent Developments in Smart Structures with Aeronautical Applications*; Smart Materials and Structures, Vol. 6, No. 5, pp. R11 – R42

[7] Giurgiutiu, V., 2000: *Review of Smart-Materials Actuation Solutions for Aeroelastic and Vibration Control;* J. Int. Mat. Syst. & Struct., **11**, pp. 525 - 544

[8] Kudva J.N. et al., 1999: *Overview of the DARPA/AFRL/NASA Smart Wing Program;* SPIE Vol. 3674, pp. 230 – 236

[9] Kudva J.N., B. Sanders, J. Pinkerton-Florance and E. Garcia, 2001: *Overview of the DARPA/AFRL/NASA Smart Wing Phase 2 Program;* SPIE Vol. 4332, pp. 383 – 389

[10] Scherer L.B., C.A. Martin, B. Sanders, M. West, J. Florance, C. Wieseman, A. Burner and G. Fleming, 2002: *DARPA/AFRL Smart Wing Phase 2 Wind Tunnel Test Results;* SPIE Vol. 4698, pp. 64 – 75

[11] McGowan A.-M. R., A.E. Washburn, L.G. Horta, R.G. Bryant, D.E. Cox, E.J. Siochi, S.L. Padula and N.M. Holloway, 2002: *Recent Results from NASA's Morphing Project;* Proc. of SPIE Vol. 4698; pp. 97 – 111

[12] Pitt D.M., J.P. Dunne, E.V. White, 2002: *SAMPSON smart inlet design overview and wind tunnel test; Part 1 – Design overview; Part II – Wind tunnel test;* Proc. of SPIE Vol. 4698; pp. 13 – 36

[13] Kuo C-M, 2008: *Adaptive MAV Design*, PhD Thesis, The University of Sheffield/UK

[14] Kuo C-M, C Boller and N Qin, 2006: "*Adaptive MAV interns of aerodynamic, mission capability and energy efficiency";* Proc. of 2nd European Workshop on Micro Aerial Vehicles, Braunschweig/Germany

[15] Mujahid A. et al : *Design of the university of Florida surveillance and endurance Micro air vehicles*; University of Florida 2003

[16] Kuo C-M, C Boller and N Qin, 2007: "*Enhancing MAV Stability in Gusty Wind by Wing Flexibility-Analyses and Flight Tests*"; 22nd International UAV Conference, Bristol,

[17] Snell S. A, Enns D. F. "Nonlinear Inversion Flight control of A Super maneuverable Aircraft". Journal of Guidance, Control & Dynamics. Vol. 15, No 4, 1992

[18] Barnes W. McCormick. "Aerodynamics Aeronautics and Flight Mechanics". John Wiley & Sons, Inc, 2nd edition

APPENDIX

Aircraft modeling

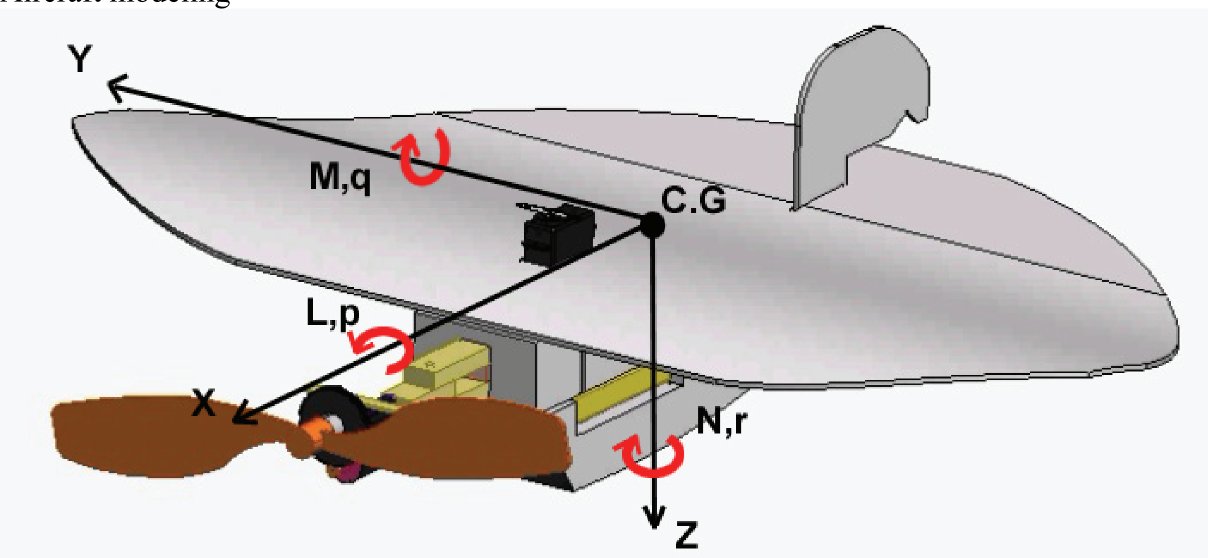

	Roll axis x	Pitch axis y	Yaw axis z
Angular rate	p	q	r
Velocity components	u	v	w
Aerodynamic force components	X	Y	Z
Aerodynamic moment component	L	M	N
Moment of inertia about each axis	Ix	Iy	Iz
Products of inertia	Iyz	Ixz	Ixy

Cy: Side force coefficient

Cy ξ r: Side force coefficient with rudder angle (in this case, vector thrust angle)

Cn: Yaw moment coefficient

Cn ξ r: Yaw moment coefficient with rudder angle (in this case, vector thrust angle)

Y ξ r: Side force with rudder angle (in this case, vector thrust angle)

N ξ r: yaw moment with rudder angle (in this case, vector thrust angle)

Smart technologies, materials and structures encompass sensing, actuation and control capabilities to be combined from a systems approach happening on a macro, meso or even micro scale. Smart technologies have triggered a variety of new research areas including condition and damage monitoring, passive and active damping or morphing. This book is an insight into latest development of those technologies from a fundamentals, modeling and applications point of view.

ISBN 978-3-8396-0577-6

9 783839 605776